Offshore Wind Turbine Foundation Design

Passon, Patrik ; Branner, Kim; Larsen, Søren Ejling; Hvenekær Rasmussen, Jørgen

Publication date:
2015

Document Version
Publisher's PDF, also known as Version of record

Offshore Wind Turbine Foundation Design

Department of Wind Energy PhD Report 2015

Patrik Passson

DTU Wind Energy PhD-0044 (EN)
ISBN: 978-87-93278-23-3

March 2015

DTU Vindenergi
Institut for Vindenergi

Authors: Patrik Passon

Title: Offshore Wind Turbine Foundation Design

Department: DTU Wind Energy

DTU Wind Energy PhD-0044 (EN)
ISBN: 978-87-93278-23-3
March 2015

Project Period:
2011.11.01 – 2015.03.31

Education:
Doctor of Philosophy

Field:
Wind Energy

Supervisors:
Kim Branner
Søren Ejling Larsen
Jørgen Hvenekær Rasmussen

Sponsorship:
Industrial PhD Programme

ISBN:
978-87-93278-23-3

Technical University of Denmark
Department of Wind Energy
Frederiksborgvej 399
Bygning 118
4000 Roskilde
Telephone 46775470

kibr@dtu.dk

www.vindenergi.dtu.dk

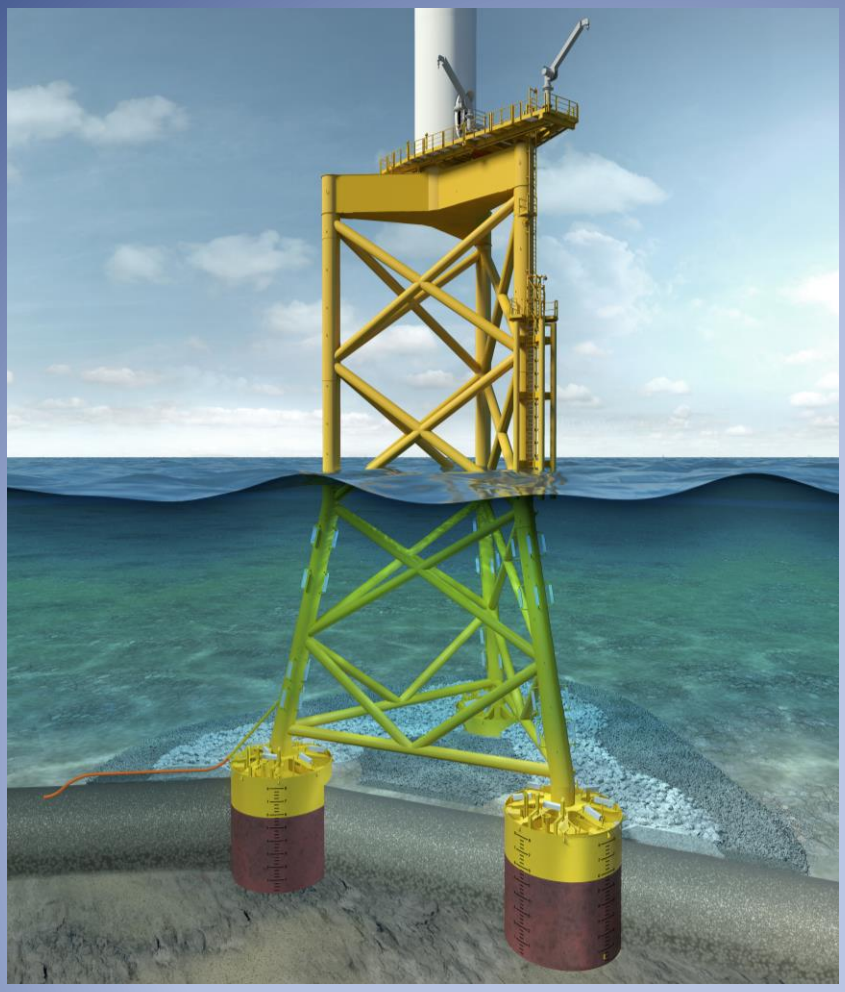

Offshore Wind Turbine Foundation Design

Selected Topics from the Perspective of a Foundation Designer

Patrik Passon

Technical University of Denmark
Department of Wind Energy

and

RAMBØLL Wind and Towers

Offshore Wind Turbine Foundation Design

Selected Topics from the Perspective of a Foundation Designer

by

Patrik Passon

Submitted for the degree of
Doctor of Philosophy

DTU Wind Energy PhD-0044 (EN)

March 2015

Preface

This dissertation “Offshore Wind Turbine Foundation Design” is submitted in partial fulfillment of the requirements for obtaining the degree Doctor of Philosophy. The work was carried out from 1st October 2011 to 31st March 2015 at RAMBØLL Wind & Towers as well as at the Department of Wind Energy on DTU RISØ Campus, Technical University of Denmark. I was granted a fellowship for my PhD studies under the Industrial PhD Fellowship Programme of the Ministry of Science, Technology and Innovation, Denmark in 2011. The financial support for my PhD studies was provided by RAMBØLL Wind & Towers and the Ministry of Science, Technology and Innovation. Their financial support is greatly appreciated.

I thank my supervisors, Kim Branner & Søren Ejling Larsen from DTU Wind Energy and Jørgen Hvenekær Rasmussen from RAMBØLL Wind & Towers (now DONG Energy), for their support throughout all phases of the project. I also thank Klaus Andersen from RAMBØLL Wind & Towers for his support on management level and for helping me to find undisturbed time in the finalization of the PhD project. My special thanks go to Arturo Rodríguez Tsouroukdissian from ALSTOM Wind as well as Anders Sørrig Mouritzen from DONG Energy for their unconditional and relentless support despite the busy schedules in their daily work. I know how hard it can be to squeeze in the extra work next to your project responsibilities and therefore appreciate very much the swift and good support you provided in the article review processes in every single case! Furthermore, I thank my colleagues from the RAMBØLL for all their support in general and Jesper Skourup, Natalia Quero Prat, Jacob Fisker Jensen, Ronnie Refstrup Pedersen, Tim Fischer, Thomas von Borstel, Marcos Álvarez Gómez and Henrik Bisgaard Clausen in particular for their support in the review process of this thesis.

I thank Bas Kuilman and gratefully acknowledge his support by providing full access to the met-ocean database of the Gemini Offshore Wind Farm project on behalf of Typhoon Offshore. Furthermore, I thank Jørgen Nørlev and gratefully acknowledge his support by providing full access to the detailed met-ocean database of the Veja Mate Offshore Wind Farm project on behalf of Veja Mate Offshore Holding GmbH and K2 Management GmbH. Furthermore, I thank DONG Energy A/S for letting me use various data and material from the Borkum Riffgrund 1 & 2 projects. This allowed for application of realistic wind-wave climate conditions in the investigations of this thesis.

I also thank Wolf-Jürgen Gerasch, my dynamics lecturer during my civil engineering studies, whose introduction to the field of dynamics and support in my chosen diploma thesis topic on earthquakes helped a lot to keep the studies fun and challenging. It was also an excellent preparation for the exciting field of offshore wind energy.

In addition I wish to thank my other colleagues, friends and especially family for fruitful discussions, helpfulness and moral support during the project. In particular, Dahlan Mahyudin Jr. and Kim Mittendorf contributed significantly in the review process of this thesis.

Last but not least, I want to express my very special thanks in honorable memory to Sten Frandsen. Sten provided very valuable support and honest encouragement to take a restart on my PhD project. Thank you, Sten!

Summary

Offshore wind energy has greatly matured during the last decade with an annually installed energy capacity exceeding 1 GW. A key factor for further large-scale development of offshore wind energy is a cost of energy reduction. Given for example the drop in oil price since summer 2014, which has continued into 2015 it is even more important to drive down the costs of energy for renewable energy sources such as offshore wind energy in order to arrive at a sustainable future on a global level.

Cost of energy reductions for offshore wind turbines (OWTs) can be achieved by optimizations on different disciplines such as the structural design, fabrication and installation. In all cases it is very important to carefully assess the mutual influences of the different disciplines and the overall costs of energy. Different subsystems of the OWT such as the foundation or control system require on one hand the involvement of specialists with different technical backgrounds and on the other hand considerations of the whole OWT system and the mutual influences of the subsystems.

For example, accurate design loads are essential for cost-efficient and safe foundation designs. However, such accurate loads can only be established under proper consideration of the dynamics of the whole system requiring adequate models of the individual subsystems and environment. This is due to the fact that OWTs introduce complex interactions between individual subsystems and the environment. Hence, a thorough understanding of the overall OWT system is essential for the establishment of accurate design loads and the subsequent optimization of individual subsystems as part of an overall optimization.

In the present thesis, the design of OWT foundations is approached from the perspective of a foundation designer starting with a general introduction of the design process. The complexity of this particular field is emphasized by consideration of a variety of topics covering different foundations types and aspects throughout the design process. Focus is on structural modelling, environmental modelling and load calculations as already established in literature and design practice. Methods and approaches of the selected topics are assessed with respect to their influences on the dynamics of the system and design loads in order to evaluate their applicability in the design process. The investigations comprise new as well as existing methods and approaches.

In design practice, the modelling of the structure as well as of the environment is often based on simplifications. For the environmental conditions, this is e.g. due to the fact that the combined, directional wind and wave climate consists of an impractically large amount of combinations of met-ocean parameters for load calculations purposes, which is consequently handled by application of condensed wind-wave correlations. A new damage equivalent wind-wave correlation method is introduced in the present thesis and assessed against alternative methods. It is shown that only the new method allows for a damage equivalent preservation of long-term, full wave climates throughout the entire support structure, while the alternative methods may introduce severe errors due to an insufficient consideration of the dynamics throughout the whole system.

In the detailed design process, condensed wind-wave correlations are typically subjected to sequential load calculation approaches in an iterative and collaborative process between foundation designer and wind turbine manufacturer. Involvement of these different design parties may be motivated by various aspects such as

introduction of state-of-the-art design expertise and tools from individual fields of technology. However, the collaboration requires special load calculation methods and simplifications of individual subsystem models in the design process due to different tools, expertise and design responsibilities of both parties. It is shown in the present thesis, how various aspects, such as the load calculation approach or the foundation model in the aero-elastic analysis, influence the dynamics and may thereby potentially introduce design load errors on the conservative or non-conservative side if not considered adequately.

Different types of OWT foundations have individual characteristics and show differences in the interactions with other subsystems leading to varying requirements regarding structural modelling, environmental modelling and load calculations in the design process. Hence, it is important to carefully assess particular aspects in the specific context of OWTs and individual foundation type characteristics. For example, modelling and load calculation approaches for jacket type foundations of OWTs are often inherited from existing experiences of monopile type foundations or from their counterparts in the offshore oil & gas industry. However, severe errors may be introduced due to different dynamic characteristics and loading conditions in case the inherited approaches are not adjusted adequately for the individual requirements of jacket type foundations for OWTs. For example, quasi-static foundation load calculation approaches as often applied for jacket foundations of substations or jackets from the offshore oil & gas industry may introduce severe errors when applied to jacket foundations for OWTs e.g. due to differences in the loading conditions. However, in case of monopiles for OWTs quasi-static foundation load calculation approaches are applicable despite the fact that loading conditions are similar to their jacket counterparts. This is due to differences in the structural dynamic characteristics, e.g. the pronounced coupling of local foundation modes with higher global modes for jacket foundations of OWTs do not occur for monopiles. In the present thesis, the investigations cover monopile and jacket type foundations as representatives of individual characteristics and individual requirements of different bottom-mounted foundation types for OWTs.

The present thesis is complemented by various aspects from the industrial work of the author emphasizing the industrial character of the PhD project.

Summary in Danish

Offshore vindenergi er i høj grad modnet i det seneste årti med en årligt installeret kapacitet på mere end 1 GW. En vigtig faktor for den videre udvikling af offshore vindenergi i stor målestok, er en reduktion af de samlede udgifter til produceret energi. I betragtning af for eksempel faldet i olieprisen siden sommeren 2014 og dens fortsatte fald ind i 2015, er det endnu vigtigere at sænke omkostningerne til etablering af vedvarende energikilder såsom offshore vindenergi, for at nå frem til en bæredygtig fremtid på et globalt plan.

Reduktion af udgifter til energi produceret af havvindmøller kan opnås ved optimering indenfor forskellige discipliner, såsom strukturelt design, produktion og installation. Indenfor et hvert område det vigtigt nøje at vurdere de gensidige påvirkninger og dermed de samlede omkostninger til energien. Forskellige delsystemer, som fundamentet eller vindmøllens styresystem kræver både involvering af specialister med forskellige tekniske kompetencer og håndtering af det samlede system og den indbyrdes indflydelse mellem undersystemerne.

Omkostningseffektive og pålidelige strukturer kræver præcise designbelastninger. Præcise belastninger kan kun etableres under hensyntagen til dynamikken i hele systemet, hvilket der kræver nøjagtige modeller af de enkelte delsystemer og miljøet. Dette skyldes at havvindmøller involverer komplekse samspil mellem de enkelte delsystemer og miljøet. Derfor er det afgørende at have en indgående forståelse for det samlede system inklusive vindmølle og fundament for at bestemme præcise designbelastninger, som herefter kan benyttes til optimering af delsystemerne med øje for en overordnet strukturel optimering.

I nærværende afhandling er dette emne behandlet ud fra en fundamentsdesigners synspunkt, startende med en generel introduktion af designprocessen. Kompleksiteten af det pågældende område understreges ved en gennemgang af forskellige fundamenttyper og designaspekter in designprocessen. Fokus er på strukturel modellering og modellering af miljøet samt tilgange til lastberegning. Metoder og tilgange for de valgte emner er vurderet med hensyn til deres indflydelse på dynamikken i systemet og design belastninger for at vurdere deres anvendelighed i designprocessen. Undersøgelserne omfatter såvel nye som eksisterende metoder og tilgange.

I praksis foretages modelleringen af strukturen og de klimatiske forhold ofte på basis af forenklinger i de anvendte designmetoder. Med hensyn til de klimatiske forhold skyldes dette, at det fulde kombinerede og retningsbestemte vind- og bølgeklima ellers ville resultere i en uhåndterlig mængde kombinationer af parametre i selve lastberegningen. Derfor anvendes her kondenserede korrelationer mellem vind og bølger. En ny metode med en skades-ækvivalent korrelation mellem bølger og vind introduceres i denne afhandling, og metoden opvejes mod alternative metoder. Det kan vises at kun 'bølgekondenseringsmetoden' er i stand til at beskrive det relevante skadesækvivalente bølgeklima for hele strukturen, hvorimod de alternative metoder risikerer at introducere alvorlige fejl på grund af manglende hensyntagen til systemets samlede dynamik.

De kondenserede vind- og bølgekorrelationer anvendes typisk sekventielt i den detaljerede designfase med iterative lastberegninger, som foregår i et samarbejde mellem fundamentdesigner og vindmølleproducenten. Involvering af flere parter i denne designprocess er motiveret af forskellige årsager, herunder et ønske om at bruge de mest specialiserede ekspertiser og designværktøjer fra forskellige teknologier. Denne proces kræver specielle beregningsmetoder og forenklede modeller af delsystemerne i designprocessen grundet de forskellige

værktøjer og ekspertiser, der anvendes i begge parters designs og ansvarsområder. Det er påvist, hvordan forskellige aspekter i begge parters designs påvirker systemets dynamik, der potentielt kan introducere fejl i de beregnede designlaster, som kan være både konservative og ukonservative.

Forskellige typer fundamenter til offshore vindmøller har individuelle egenskaber og udviser forskelle i samspil med andre delsystemer, der medfører forskellige krav til strukturel modellering, modellering af miljø og lastberegninger i designprocessen. Derfor er det vigtigt nøje at vurdere særlige aspekter i den konkrete sammenhæng og individuelle fundamenttypers karakteristika. Eksempelvis er designmetoder til offshore vindmøllejackets ofte taget direkte fra eksisterende erfaringer med design af monopælefundamenter eller design af offshore jackets til olie- og gasindustrien. Dette kan introducere fejl på grund af forskellige dynamiske egenskaber og belastningsforhold i de forskellige systemer, med mindre beregningsmetoderne tilpasses kravene til nøjagtig beregning af jacketfundamenter til offshore vindmøller. For eksempel er den kvasistatiske metode, som ofte benyttes til olie&gas jacketstrukturer, ikke tilstrækkelig for vindmøllefundamenter på grund af blandt andet den anderledes belastning. For monopæle til havvindmøller kan den kvasistatiske metode dog oftest godt benyttes på trods af at belastningerne er sammenlignelige med lasterne på jackets. Dette skyldes forskelle i dynamiske egenskaber, hvor kobling mellem globale egensvingningsformer og lokale vibrationer i krydsafstivningen forekommer i jackets, men som naturligvis ikke ses ved monopæle. Denne afhandling omhandler monopæle og jacketstrukturer som repræsentative typer af pælefunderede fundamenter for havvindmøller.

Denne afhandling er endvidere suppleret med forskellige henvisninger til design af virkelige offshore vindmøllefundamenter udført af forfatteren, som understreger den industrielle karakter af afhandlingen.

List of Publications

The present thesis is written as a collection of scientific publications. It includes a joint introduction which describes the background for the publications together with a presentation of the main conclusions and results. The publications included in the thesis are the following:

Paper 1

Passon P, Branner K (2014). Load calculation methods for offshore wind turbine foundations. *Ships and Offshore Structures*, Vol.9, No.4, pages 433-449.

Paper 2

Passon P, Branner K (2015). Condensation of long-term wave climates for the fatigue design of hydrodynamically sensitive offshore wind turbine support structures. *Ships and Offshore Structures, (in press, currently available online)*

Paper 3

Passon P (2015). Damage Equivalent Wind-Wave Correlations on Basis of Damage Contour Lines for the Fatigue Design of Offshore Wind Turbines. *Renewable Energy, (in press, currently available online)*

The publications listed above can be found in the second part of this thesis. In addition, other relevant publications have been established by the author. These publications are not included since they have been published prior to the start of the industrial PhD project in 2011. The publications not included in the thesis are:

Passon P (2002). Modelling of soil-structure interactions for monopiles and non-linear wave theories. *M.Sc Thesis, Hannover University. Hannover, Germany.*

Passon P, Kühn M (2005). State-of-the-art and Development Needs of Simulation Codes for Offshore Wind Turbines. *Copenhagen Offshore Wind Energy Conference. Copenhagen, Denmark.*

Passon P, Kühn M (2005). Research Program of the Utgrunden Demonstration Offshore Wind Farm - Final Report: Part I - Load and Eigenfrequency Measurement. *Wintus GmbH. Aichtal, Germany*.

Passon P (2006). Memorandum: Derivation and Description of the Soil-Pile-Interaction Models. *IEA-Annex XXIII Subtask 2. Stuttgart, Germany.*

Passon P, Kühn M (2006). Offshore-Windenergieanlagen mit verzweigten Tragstrukturen unter kombinierter Wind- und Wellenanregung. *VDI-Tagung Baudynamik, ISSN: 0083-5560, Vol. 1941, Pages 401ff. Kassel, Germany.*

Passon P, Kühn M (2007). OC3-Benchmark aeroelastischer Simulationsprogramme für Offshore Windenergieanlagen. *Gigawind 5. Symposium, April 18, Tagungsbeiträge (Proceedings), pages 80-85. Hannover, Germany.*

Passon P, Kühn M, Butterfield S, Jonkman J, Camp T, Larsen TJ (2007). OC3–Benchmark Exercise of Aero-elastic Offshore Wind Turbine Codes. *TORQUE2010, Science of Making Torque from Wind Conference. Copenhagen, Denmark.*

Passon P (2008). Aero-Elastic Design Tool for Bottom-Mounted Offshore Wind Turbines. *Deliverable D4.3.2 (WP4: Offshore Foundations and Support Structures). Stuttgart, Germany.*

Passon P (2010). Design of Offshore Wind Turbine Foundations in Deeper Water. *TORQUE2010, Science of Making Torque from Wind. Crete, Greece.*

Table of Contents

Abbreviations, Nomenclature and Definitions

Abbreviations

OWT	Offshore wind turbine	FLS	Fatigue limit state
FEED	Front-end engineering design	ULS	Ultimate limit state
RNA	Rotor-nacelle-assembly	SLS	Servicability limit state
FD	Foundation designer	ALS	Accidental limit state
WTM	Wind turbine manufacturer	SCD	Wave scatter matrix or wave scatter diagram
DOF	Degree of freedom	DEL	Damage equivalent load
DLC	Design load case	DCL	Damage contour line
LCT	Load case table		

SE06	Guyan type superelement based on a condensation of the foundation DOF to 6 generalized DOF at interface between tower and foundation
SE36	Craig-Bampton type superelement based on the SE06 superelement complemented with 30 internal modes

Nomenclature

1P	[Hz]	Rotor frequency.
3P	[Hz]	Three times rotor frequency; corresponds to blade passing frequency at tower for three-bladed turbine.
6P	[Hz]	Six times rotor frequency.
9P	[Hz]	Nine times rotor frequency.
a	[-]	Axial induction factor.
b	[m]	Blade element chord length.
c	[m/s]	Resulting inflow velocity at a blade element.
c_D	[-]	Drag coefficient (function of angle of attack).
c_L	[-]	Lift coefficient (function of angle of attack).
d	[-]	Fatigue damage.
d_a	[-]	Isolated aerodynamic damage.
d_h	[-]	Isolated hydrodynamic damage.
d_{ah}	[-]	Combined aerodynamic and hydrodynamic damage equivalent stress range.
$d_{i,j}^*$	[-]	Unit damage for sea-state with wave height $H_{s,i}$ and wave period $T_{p,j}$.
$d_{i,j}$	[-]	Actual damage for sea-state with wave height $H_{s,i}$ and wave period $T_{p,j}$ (based on probability $p_{i,j}$).
$d_{i,j,s}^*$	[-]	Theoretical fatigue damage of the sea-state $H_{s,i}$ - $T_{p,j}$ in case the full probability of occurrence p_k is applied.
d_k	[-]	Actual damage for wind speed class k (based on probability p_k).
$\boldsymbol{D}^*$	[-]	Unit damage matrix, containing elements $d_{i,j}^*$.
$\boldsymbol{D}$	[-]	Damage matrix, containing elements $d_{i,j}$.
$\boldsymbol{D_s}^*$	[-]	Scaled damage matrix, containing elements $d_{i,j,s}^*$.
EI_f	[Nm^2]	Bending stiffness of an equivalent cantilever beam.

dF_D	[N]	Aerodynamic drag force at a blade element.
dF_I	[N]	Aerodynamic in-plane force at blade element in oscillation-free case.
dF_L	[N]	Aerodynamic lift force at blade element.
dF_T	[N]	Aerodynamic thrust force at blade element in oscillation-free case.
F_T	[N]	Aerodynamic rotor thrust.
F_u	[N]	Jacket member axial load.
F_v	[N]	Jacket member in-plane shear load.
F_w	[N]	Jacket member out-of-plane shear load.
$F_{u,eq}$	[N]	Damage equivalent axial load, aligned with local brace *u*-axis.
$F_{v,eq}$	[N]	Damage equivalent in-plane shear load, aligned with local brace *v*-axis.
$F_{w,eq}$	[N]	Damage equivalent out-of-plane shear load, aligned with local brace *w*-axis.
F_x	[N]	Force in global x-direction.
F_y	[N]	Force in global y-direction.
F_z	[N]	Force in global z-direction.
$F_{x,eq}$	[N]	Damage equivalent shear load, aligned with *x*-axis.
$F_{y,eq}$	[N]	Damage equivalent shear load, aligned with *y*-axis.
$F_{z,eq}$	[N]	Damage equivalent axial load, aligned with *z*-axis.
H_s	[m]	Significant wave height.
$H_{s,i}$	[m]	Significant wave height for wave height class *i*.
$H_{s,k}$	[m]	Associated significant wave height for wind speed class *k*.
L_f	[m]	Fixity length of an equivalent cantilever beam.
m	[-]	*S-N* curve slope.
M_u	[Nm]	Jacket torsion moment around local brace *u*-axis.
M_v	[Nm]	Jacket in-plane moment around local brace *v*-axis.
M_w	[Nm]	Jacket out-of-plane moment around local brace *w*-axis.
$M_{u,eq}$	[Nm]	Damage equivalent torsion moment around local brace *u*-axis.
$M_{v,eq}$	[Nm]	Damage equivalent in-plane bending moment around local brace *v*-axis.
$M_{w,eq}$	[Nm]	Damage equivalent out-of-plane bending moment around local brace *w*-axis.
M_x	[Nm]	Moment in global *x*-direction.
M_y	[Nm]	Moment in global *y*-direction.
M_z	[Nm]	Moment in global *z*-direction.
$M_{x,eq}$	[Nm]	Damage equivalent bending moment around *x*-axis.
$M_{y,eq}$	[Nm]	Damage equivalent bending moment around *y*-axis.
$M_{z,eq}$	[Nm]	Damage equivalent torsion moment around *z*-axis.
N_{eq}	[-]	Equivalent number of cycles.
$N_{eq,i}$	[-]	Equivalent number of cycles for direction *i*.
n_{ref}	[-]	Reference number of cycles.
$p_{i,j}$	[-]	Probability of occurrence for sea-state with wave height $H_{s,i}$ and wave period $T_{p,j}$.
p_k	[-]	Probability of occurrence for wind speed class *k*.
r	[m]	Radial distance of blade element from rotor axis.

t	[m]	Blade element thickness.
T_p	[s]	Peak period.
$T_{p,j}$	[s]	Peak period for wind period class *j*.
$T_{p,k}$	[s]	Peak period for wind speed bin *k*.
T_z	[s]	Mean period or zero up-crossing period.
$\dot{u}_{RNA}$	[m/s]	RNA oscillation velocity (fore-aft).
v	[m/s]	Undisturbed wind speed.
v_k	[m/s]	Mean wind speed at hub height for wind speed class *k*.
v_{out}	[m/s]	Cut-out wind speed.
α	[deg]	Angle of attack.
$\Delta_{SE06}(t)$	[kN,kNm]	Interface load vector with errors in the interface response at time t due to application of the SE06.
ΔdF_I	[N]	Difference of aerodynamic in-plane force at blade element compared to oscillation-free case.
ΔdF_L	[N]	Difference in aerodynamic lift force at blade element compared to oscillation-free case.
ΔdF_T	[N]	Difference of aerodynamic thrust force at blade element compared to oscillation-free case.
ΔF_I	[N]	Difference of aerodynamic in-plane force at one rotor blade compared to oscillation-free case.
ΔF_T	[N]	Difference of aerodynamic rotor thrust force compared to oscillation-free case.
ΔM_I	[Nm]	Difference of aerodynamic in-plane rotor moment compared to oscillation-free case.
$\Delta\sigma$	[N/mm^2]	Stress range.
$\Delta\sigma_a$	[N/mm^2]	Isolated aerodynamic damage equivalent stress range.
$\Delta\sigma_h$	[N/mm^2]	Isolated hydrodynamic damage equivalent stress range.
$\Delta\sigma_{ah}$	[N/mm^2]	Combined aerodynamic and hydrodynamic damage equivalent stress range.
κ_{ip}	[-]	Exponent to sine profile for $\xi_{aero,ip}$ contribution to $\xi_{\mathrm{aero},\varphi}$ in misaligned cases.
κ_{op}	[-]	Exponent to cosine profile for $\xi_{aero,op}$ contribution to $\xi_{\mathrm{aero},\varphi}$ in misaligned cases.
$\xi_{aero,ip}$	[-]	Equivalent damping ratio for in-plane aerodynamic damping.
$\xi_{aero,op}$	[-]	Equivalent damping ratio for out-of-plane aerodynamic damping.
$\xi_{aero,\varphi}$	[-]	Equivalent damping ratio for effective, directional aerodynamic damping.
ξ_{add}	[-]	Estimation on in-plane aerodynamic damping at cut-out wind speed v_{out}.
ξ_s	[-]	Total structural damping ratio, including all damping contributions except aerodynamic damping.
ρ	[kg/m^3]	Air density.
φ_{WaWi}	[deg]	Effective wind-wave misalignment angle for aerodynamic damping on hydrodynamic responses.
Ω	[1/s]	Angular velocity of the rotor.

Definitions

Figure 1 shows the definitions and denotations of the offshore wind turbine subsystems as used in this thesis.

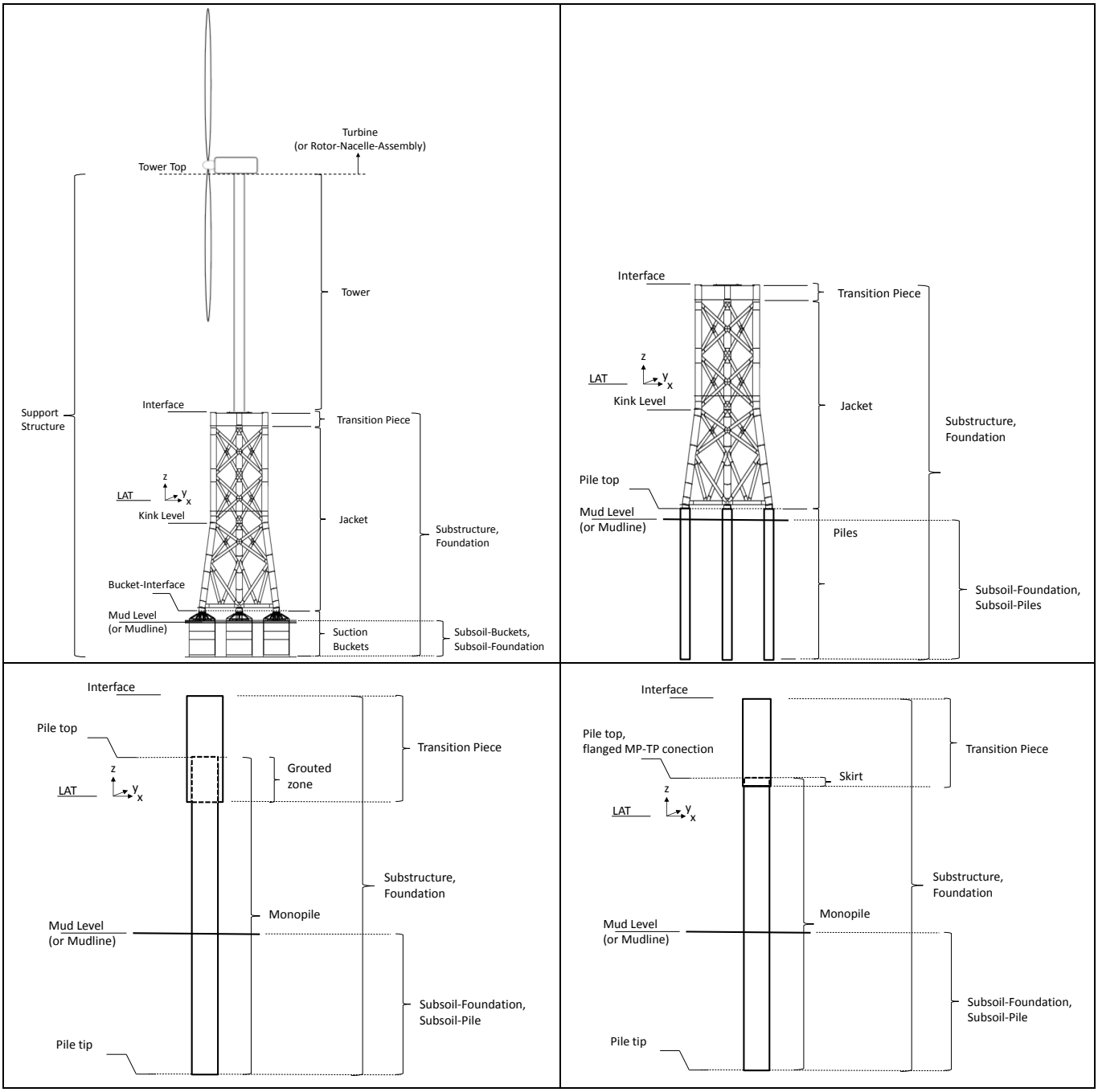

Figure 1: Definitions and denotations for subsystems of offshore wind turbines.

1 Introduction

Offshore wind farm installations have been considerably grown in size and number over the last decade and an even further world-wide increase is expected on a medium-term scale for the future. For example, the Danish Energy Strategy [100] calls for a substantial increase in renewable energy in order to achieve complete independence of fossil fuels by 2050. A major contributor in the renewable energy mix is wind energy which reached a share of 39% for the electricity consumption in 2014 which is an increase of 6% compared to 2013 according to Energinet.dk [92], [93].

Similar plans for an increased share of renewable energy in the energy mix are formulated in many other countries around the world. That strategy often includes the construction of new offshore wind farms as can be observed in the United Kingdom, Germany, The Netherlands, Belgium and France. According to a wind energy scenario for 2020 from EWEA [94] offshore wind energy could cover 2.4% of the EU electricity consumption in a pessimistic scenario and 3.5% in an optimistic scenario and the numbers for onshore wind installations are even roughly four times higher. This may not seem like a lot, but it needs to be kept in mind that larger scale offshore wind energy installations started only rather recently and that this scenario covers only a short term horizon. In light of these facts, it is clear that the path leads in direction of significantly larger contributions of offshore wind energy to the EU electricity consumptions. However, the optimistic EWEA scenario and further development of offshore wind energy can only be achieved by substantial cost reductions. Figure 2 shows the annual and cumulative capacities of European offshore wind farm installations till 2014.

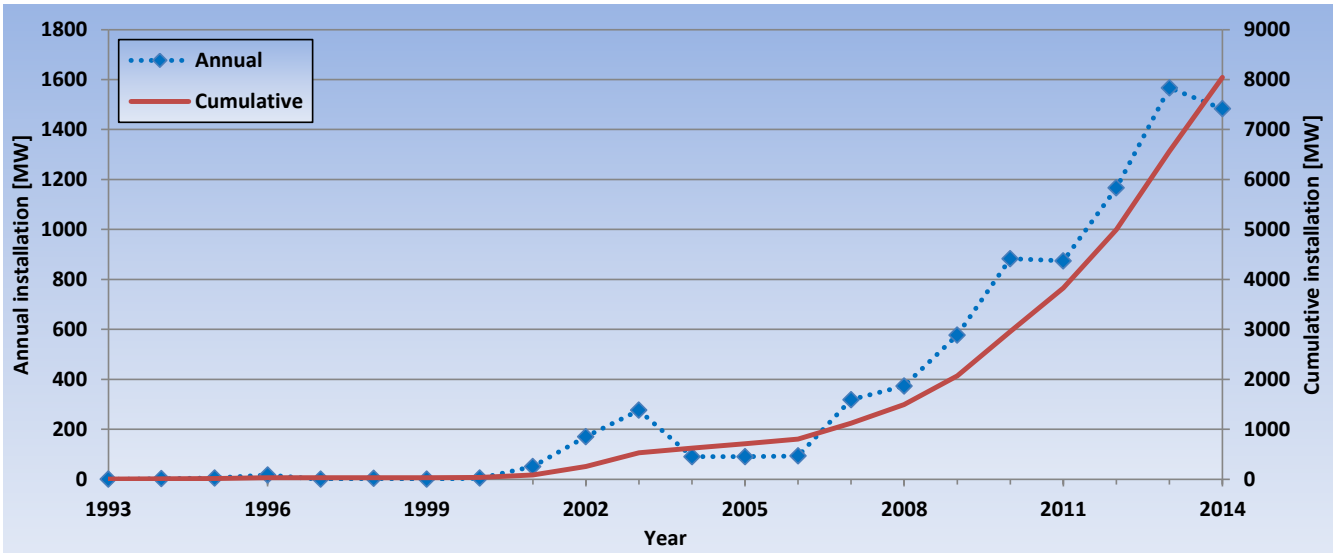

Year	1993	1994	1995	1996	1997	1998	1999	2000	2001	2002	2003	2004	2005	2006	2007	2008	2009	2010	2011	2012	2013	2014
Annual	0	2	5	17	0	3	0	4	51	170	276	90	90	93	318	373	577	883	874	1166	1567	1483
Cumulative	5	7	12	29	29	32	32	36	86	256	532	622	712	804	1122	1495	2072	2955	3829	4995	6562	8045

Figure 2: Annual & cumulative capacities [MW] of European offshore wind farm installations according to EWEA [96].

The main challenge for future offshore wind farm installations is to drive down the cost of energy. Figure 3 from BVG associates [90] shows an example of a cost break down for a typical 500MW offshore wind farm with

monopile foundations. It can be seen that the fabrication and installation of foundations are major cost items introducing approximately 20% of the overall project costs. The importance of cost optimized offshore wind turbine foundations is therefore strongly related to the economic viability and further development of offshore wind energy. Furthermore, it is of course very important as well to ensure safety and reliability in the designs of offshore wind farms.

The trend towards larger water depths and turbine sizes in combinations with large variations of site-specific soil conditions impose further challenges to the design, fabrication and installation of foundations. These challenges are addressed by different types of foundation concepts in order to maintain economic feasibility of the offshore wind turbines. The most suitable foundation type is assessed in a site- and project-specific manner accounting also for recent developments in installation and fabrication techniques.

Cost-efficient and reliable designs of offshore wind turbines require an integrated design approach, as described by Kühn et al. [39], as well as calculation of accurate design loads. Such accurate design loads can only be obtained under consideration of the dynamics of the whole offshore wind turbine which requires for example aero-elastic simulations with simultaneous aerodynamic and hydrodynamic loading as shown by numerous publications; see e.g. Passon [60].

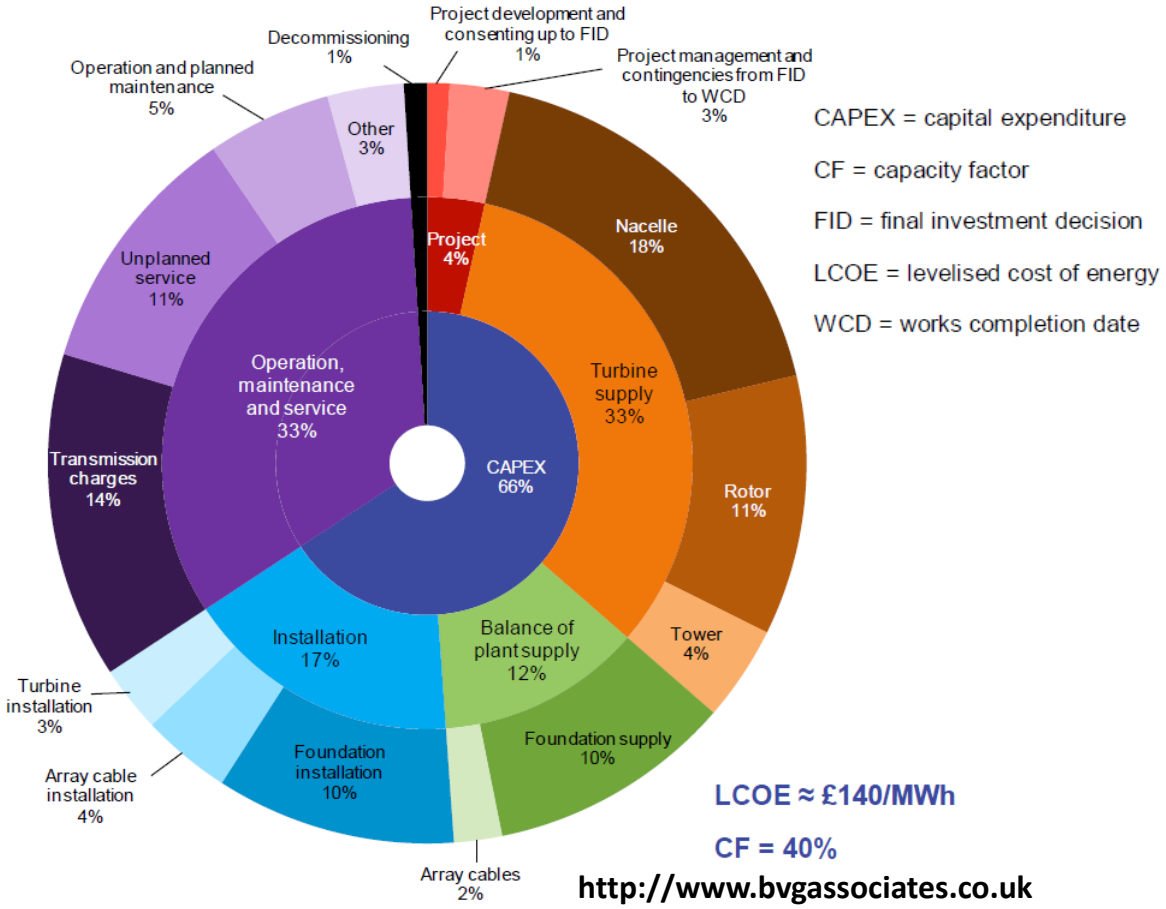

Figure 3: Offshore wind farm cost breakdown, from BVG associates [90].

The present thesis focuses on the importance of dynamics in the context of accurate design load calculations for bottom-mounted offshore wind turbine foundations. Various aspects throughout the different stages of the detailed design process are investigated and discussed due to their relevance for a proper consideration of the overall dynamics. Despite the focus on foundations, the investigated aspects, models and methods are relevant for design load calculations of other subsystems as well, such as the tower. Furthermore, it is emphasized that the denotation *accurate design loads* must always be critically questioned since the actual accuracy of loads do also depend on assumptions introduced by the governing design standards or guidelines and the quality of the available met-ocean database. In the context of the present thesis, the denotation accurate design loads is to be understood in relation to the aforementioned constraints. For example, the question is how well the design loads represent the environmental parameters of the underlying met-ocean database and not how accurate the underlying met-ocean database represents the real site specific environmental parameters.

In the context of the desired cost reductions for offshore wind energy the question is how the costs are related to more accurate design loads in the design process? In order to answer to this question it is necessary to distinguish between two scenarios:

- In the first scenario, the improved accuracy is achieved by a reduction of conservatism, leading to reduced design loads. It is obvious that this may lead to more cost-efficient designs.

- In the second scenario, the improved accuracy has been achieved by a reduction of non-conservatism, leading to more reliable designs. This is important for the prevention of failures and the costly consequences.

The investigations and results of the present thesis cover both scenarios. In the context of the first scenario it is for example shown that the application of simplified foundation superelement representations in the aero-elastic simulation model may lead to highly conservative design loads in case of jacket foundations. More accurate and less conservative design loads are obtained by application of more adequate superelement formulations. An example for the second scenario is provided by the introduction of a new damage equivalent wind-wave correlation method in this thesis. The new method is assessed against existing methods and it is shown that this new method allows for a damage equivalent preservation of long-term, full wave climates throughout the entire support structure while the alternative methods lead to severe underestimations of hydrodynamic fatigue damages.

The selection of investigated aspects for the design of offshore wind turbine foundations in the present thesis covers only a part of all relevant aspects in the design process of offshore wind turbines. Nevertheless, the author expects that a proper consideration of the findings from this PhD thesis can form a considerable contribution towards more cost-efficient and safe designs of future offshore wind turbines.

1.1 Objective of the thesis

This thesis presents results and recommendations on different aspects of an integrated design approach for the foundation where of the dynamic behaviour of the whole offshore wind turbine is taken into account. The basic scientific-technical hypothesis is:

Significant improvements in terms of economics and safety of bottom-mounted wind turbine foundations can be achieved through an integrated design approach under proper consideration of the dynamics of the whole offshore wind turbine.

The proof of the scientific-technical hypothesis and the necessary improvements of related models and methods form the core output of the present thesis. In this context, the improvements of economics and safety are mainly implied through improvements in the accuracy of calculated design loads. The objective is to add knowledge to the following questions for the scientific and industrial community in the context of foundation designs for offshore wind turbines:

- How to establish proper wind and wave parameters for fatigue load calculations?
- How to introduce proper integrated models in the design process of the offshore wind turbine?
- How to obtain foundation loads for the design of the foundation?

Both, the objective and investigations for this industrial PhD project are strongly influenced by the industrial and scientific work performed by the author. On one hand the scientific experiences are introduced from various research projects such as the UpWind project [21] and the OC3 project [57], [58], [34], [35], [77] since 2002. On the other hand, the work as a designer and technical consultant in many foundation design projects introduced complementary industrial experiences. This practical component of the work comprises a total of 13 detailed designs and more than 20 front-end engineering designs as well as conceptual and feasibility design studies for offshore wind turbine foundations and other offshore structures since 2006. In this context, focus has been given on primary steel design, load and structural modelling, soil-structure interactions, load iterations and general optimization of design load case setups.

Complementary research and development in the scientific and industrial community is very important and requires a mutual understanding of the needs and constraints in each domain. The present thesis, as a result of an industrial PhD project, is intended to address this aspect and is furthermore intended to form a contribution to the ongoing task of closing the gap between the industrial and scientific communities.

1.2 Outline of the thesis

The core of the present thesis is a collection of papers comprising of three submitted journal papers. This is complemented by contents and findings of various additional conference papers, research reports, memos as well as from practical work by the author prior to and during the industrial PhD project. The main issues and results are further discussed and tied together in Chapter 1 - 6 of the joint introduction. In particular, it is shown how the dynamic behaviour of the complete offshore wind turbine system can be captured accurately for the following aspects:

- Modelling of wind-wave parameters for integrated load calculations.
- Modelling of structural subsystems and excitations.
- Load calculation approaches in the design process.

In Chapter 2, the design process of offshore wind turbine foundations is described together with a brief discussion of the different characteristics of monopile and jacket type foundations. Individual aspects investigated in the following chapters and journal papers are highlighted and put into the global context of the design process, mainly from the perspective of a foundation designer.

In Chapter 3, superimposed and integrated load calculation approaches as well as load calculation methods for the foundation are discussed. Individual aspects on the superimposed load calculation approach are exemplarily introduced and discussed from the perspective of the foundation designer. Complementary to the dynamic load expansion methods introduced in the corresponding paper 1 [61], the applicability of quasi-static load expansion methods for jacket foundations is addressed as well.

In Chapter 4, the relevance of damping is briefly addressed for hydrodynamically sensitive offshore wind turbines. Hydrodynamic drag damping and aerodynamic damping under consideration of misaligned wind-wave conditions are addressed in more detail.

In Chapter 5, aspects related to the damage equivalent wind-wave correlation method as developed in paper 3 [63] are addressed. The main focus is on the influence of damping, comparison with alternative wave lumping approaches and the introduction of an modified approach in case of limited data in the met-ocean database.

In Chapter 6, simplified structural modelling approaches for individual subsystems are discussed for different stages in a sequentially integrated load calculation process. Focus is on the applicability of low-fidelity models used by the wind turbine manufacturer and foundation designer with respect to calculations of design loads and modal properties.

Chapter 7 summarizes the conclusions and recommendations for current design practices and future work.

The three journal papers are appended after the joint introduction. Furthermore, the papers are also included in the reference section.

Paper 1 [61] addresses dynamic load calculation methods in the foundation load expansion as part of a sequentially integrated load calculation approach. A new inverse dynamics based method is introduced and compared against existing methods. While accurate results are obtained by all investigated methods the new inverse dynamics based method has the distinct advantage of a higher degree of flexibility for available design

tools but requires an additional step in the calculation procedure. The paper is complemented by Chapter 3 and 6.

Paper 2 [62] introduces a condensation approach for long-term wave climates leading to a substantially reduced number of different sea-states for load simulation purposes while preserving the dynamic response in a damage equivalent manner.

Paper 3 [63] is an extension of the long-term wave climate condensation from paper 2 [62] towards the required correlation of wind and wave parameters for aero-elastic load simulations with simultaneous aerodynamic and hydrodynamic loads. The paper is complemented by Chapter 5.

2 Design of Offshore Wind Turbines

This chapter introduces relevant aspects from the design process of offshore wind turbines (OWTs). The discussions and descriptions are mainly provided from the perspective of a foundation designer and based on the most common approaches in the design process observed by the author during the last decade. However, it should be noted that many variations exist in design practice. Generally, these variations depend on project constraints and involved design parties. A detailed summary of all these variations is outside the scope of this introduction and is therefore disregarded. Instead the present chapter discusses selected aspects from the design process in detail.

OWTs are complex systems showing significant interactions of the individual subsystems, the loads and the environment. Figure 4 provides an overview of the most important interactions. It should be noted that further influences exist such as from wake effects of neighboring wind turbines or the grid connection.

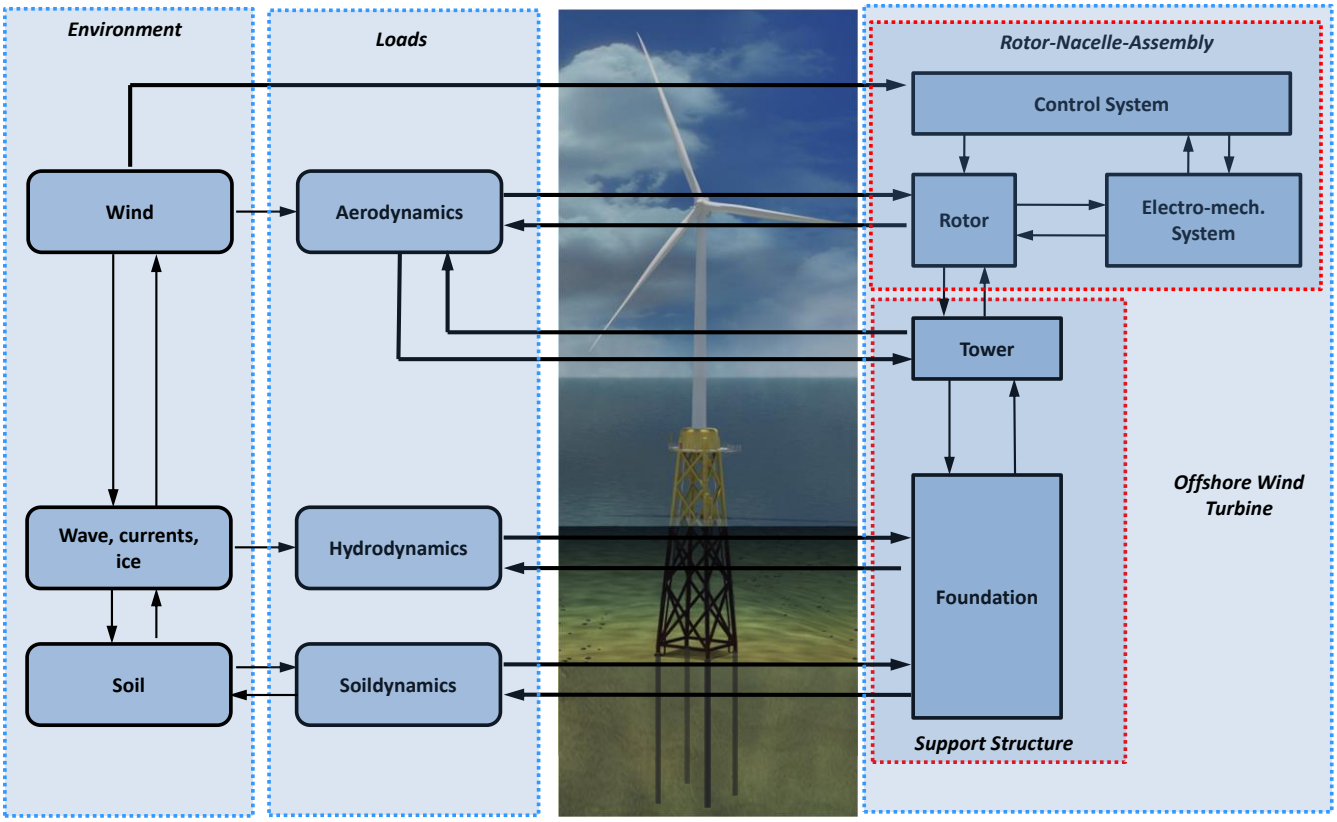

Figure 4: Interactions between OWT subsystems, loads and environment.

Highly specialized design tools and approaches based on thorough expertise in the respective fields of technology are required for a safe and economic design of the individual subsystems. Therefore, the design of OWTs is an iterative process comprising numerous tasks and involving several expert parties such as the wind turbine manufacturer (WTM), foundation designer (FD), met-ocean experts, geotechnical expert, fabricator, installation contractor and certifier. This is indicated in Figure 5 for the example of selected parties that have been involved in DONG Energy's pilot project of a three-legged jacket on suction buckets at the Borkum

Riffgrund 1 location. Depending on the design phase, task and strategy the individual expert parties are involved in an isolated or collaborative manner. However, the design of the main subsystems i.e. foundation, tower and rotor-nacelle-assembly (RNA) is traditionally performed by different parties. Therefore, at some point in the design process, the individual design parties have to include adequate subsystem models, environmental parameters and constraints, such as lifting capacities, from the other parties involved. For example, the FD needs to include an adequate description of the tower and RNA obtained from the WTM while the WTM needs to include in their models an adequate description of the foundation and hydrodynamic loads from the FD. More innovative design approaches aim at a stronger integration of individual aspects and subsystems in the design process. For example, nowadays the FD acts sometimes also as the geotechnical expert, met-ocean expert and performs the overall support structure design based on aero-elastic load simulations. The aforementioned aspects are further discussed in this as well as in the following chapters.

Figure 5: Involved parties for DONG Energy's Borkum Riffgrund 1 jacket project, from Schiedek [65].

This chapter starts with a brief overview of different design criterions as well as monopile and jacket type foundations. Monopiles and jackets are considered by the author as the most popular and promising bottom-mounted foundation types today and are therefore in focus of the present thesis. The following sections address the different phases of the design process as well as load calculation tools used for the investigations in the present thesis. This chapter concludes with some considerations on innovative design approaches.

2.1 Limit state and natural frequency design requirements

The design of OWT foundations is based on a large variety of design tasks and analyses of design criterions in order to ensure that the relevant limit states are not exceeded and the allowable turbine specific natural frequency ranges are maintained. Descriptions of the involved analyses for all limit states have been published by many authors; see e.g. Devaney [18]. Therefore, only a brief summary is provided here. A limit state is defined as a state beyond which the structure does not satisfy the design criterions anymore; see e.g. DNV-C101 [83] or IADC [99]. Limit state categories are:

- **Fatigue limit state (FLS)**
  FLS analyses are performed to verify sufficient resistance to the cumulative fatigue damages due to repeated loads during life time including transportation, installation, service and decommissioning.
- **Ultimate limit state (ULS)**
  ULS analyses are performed to verify the maximum load-carrying resistance of all structural components of the OWT, i.e. sufficient strength and stability under design loads, as well as for the soil.
- **Serviceability limit state (SLS)**
  SLS analyses are performed to verify that the structural behavior under characteristic loads does not exceed given SLS design criteria such as for example permanent rotation limits for the RNA.
- **Accidental limit state (ALS)**
  ALS analyses are performed to verify that the structural integrity or behavior after an operational failure or accidental event.

For the foundation, the limit state analyses may comprise drivability analyses, scour calculation and ship collision analyses. Details on individual design criteria and limit state analyses can be found in the relevant design guidelines and standards such as DNV-J101 [84], GL [86] or BSH [82]. However, it should be kept in mind that scope and accuracy of the corresponding analyses differs in the preliminary and detailed design phase.

A special topic for onshore and offshore wind turbines is the natural frequency design because these structures have a design requirement on the allowable range for the first natural frequency. This is introduced in order to avoid resonance effect from *1P* (rotor speed) and *3P* (blade passing frequency of a three-bladed turbine) dependent on the particular turbine type, see Damgaard [15] or van der Tempel & Molenaar [70]. Thus support structures have to be designed in order to meet the natural frequency requirement or alternatively the wind turbine controller has to be adjusted in order to allow for additional natural frequency ranges. Such wind turbine controller based extensions of allowable frequency ranges can for example be achieved by definition of a rotor speed exclusion window, which has been demonstrated for the Utgrunden offshore wind farm, see Kühn et al. [42].

In design practice, the methods in paper 1 [61] are applied for foundation load calculations in FLS, ULS and SLS. Further details on load calculation approaches are discussed in Chapter 3 and 6. The publications dealing with the long-term wave climate condensation (paper 2 [62]) and the wind-wave correlation (paper 3 [63]) are intended for a damage equivalent description of wind-wave parameters for load calculations in FLS. This is complemented by further discussions in Chapter 5. Selected modelling aspects for all analyses and the natural frequency design are discussed in Chapter 6.

2.2 Monopile and jacket foundations

Different types of foundations exist for OWT and an even larger number of solutions have been discussed in the maturing phase of the offshore wind energy technology. With focus on bottom-mounted solution, the concepts established today comprise of mainly jackets, monopiles, tripods and gravity based foundations for the submerged part and pile(s) as well as suction buckets for the sub-soil part. Figure 6 provides an overview of the share of different foundation types[1] installed at European offshore wind farms at the end of 2013 and 2014[2] according to EWEA [95], [96].

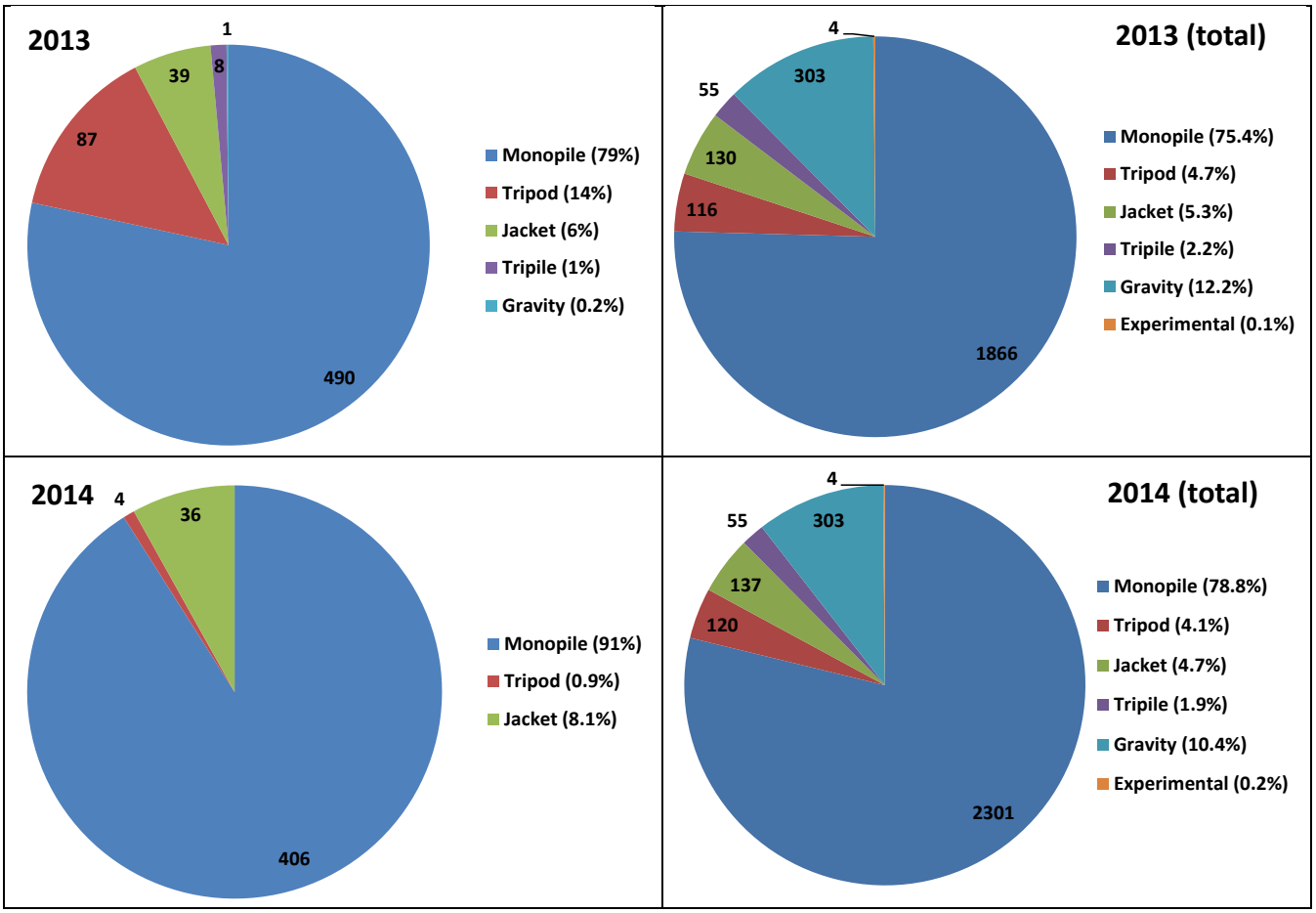

Figure 6: Installed foundation types in European offshore wind farms in 2013 (top, left) & 2014[2] (bottom, left) and in total at the end of 2013 (top, right) & 2014[2] (bottom, left).

In the present thesis, focus is on monopiles as the most popular bottom-mounted foundation concept and on jacket type foundations which represent a promising alternative for future installations with larger turbines at deeper water. Brief summaries of these concepts are provided here with more focus on the jacket due to the higher structural complexity and more innovative character for offshore wind applications.

[1] Experimental foundations in the figure include also floating type foundations.
[2] The numbers for jackets in 2014 provided by EWEA [96] contain an error; updated numbers have not been made available prior to publication of the present thesis.

The decision between monopile and jacket foundation for an offshore wind farm is mainly based on economic considerations and typically taken already in the preliminary design phase as described in section 2.3.1. It is therefore very important to be able to make reasonable cost estimates for designs of each type of foundation on basis of limited data. Fischer [98] provided a simplified cost estimate of 2€/kg for monopiles and 4-6€/kg for jackets. In reality, more complex cost functions are required for an economic comparison between monopiles and jackets. For example, the lower mass of the jacket is beneficial for the lifting capacities required for installation while the larger dimensions (footprint) introduce larger requirements for storage. Furthermore, it should be kept in mind that the fabrication costs for jackets might be considerably reduced once subjected to large scale installation, e.g. due to the development of improved assembly strategies.

It should be noted that certain variations exist for certain constructive details of monopile and jacket type foundations. For example, the jacket can be designed with different transition pieces, as three- or four-legged jackets with piles or suction buckets. However, the general characteristics of monopiles and jackets are not affected by these variations of structural and constructive details. The reader is referred to De Vries [17], Arshad & O'Kelly [1] and Damgaard [15] for a more detailed overview of alternative foundation concepts.

Monopile

A monopile structure is formed by a single tubular pipe-like structure which is driven, drilled or vibrated into the seabed. Aerodynamic and hydrodynamic loads are mainly transferred as shear forces and bending moments through the structure. However, axial loads (especially due to gravity) and torsion exist as well and are of particular interest for the geotechnical design. Shear forces and overturning moments are transferred as lateral loads into the seabed. The transfer of overturning moments is achieved by a rotation of the pile which utilizes lateral resistances in opposite directions on each side of the pile relative to the point of rotation. Torsion moments are transferred to the soil mainly by shaft friction of the pile while axial forces are transferred by shaft friction and compression at the pile tip. The connection between the tower and monopile is typically established by a transition piece. This transition piece carries the secondary steel structures like boat landings and access ladders and is attached to the monopile most commonly by a grouted or flanged connection.

To date, monopiles are the most popular foundation concept for OWT. In the past, the monopile was assumed to be feasible only for shallow to medium water depths up to 30m while other foundation concepts such as tripods or jackets were expected for larger water depths as reflected by numerous publications; see e.g. Ashuri & Zaaijer [2] or Esteban et al. [20]. However, in the offshore wind industry there is an economic interest to increase the range of applicability for monopiles towards larger turbines and water depths due to the simplicity and relatively low fabrication costs compared to e.g. jacket type foundations. Hence, longer monopiles with larger diameters, such as so-called XXL-monopiles, have attained the focus of the industry; compare e.g. Willecke & Fischer [79]. This is also reflected by current design activities comprising monopile foundations up to approximately 35-40m water depth for turbine sizes of 6MW and beyond. Diameters are exceeding 8m so far, but even larger monopiles are expected in the future.

Characteristics

- Well proven and relatively simple concept.
- Low manufacturing costs and proven installation methods[3].
- Applicability in soft and stiff soil, but sensitive to the soil conditions.
- Prone and sensitive to scour.
- Relatively high mass to stiffness ratio.
- Single, large diameter tubular member attracts large wave forces.
- Large modal deflections in the submerged zone (compared to jackets).

The relatively high mass to stiffness ratios leads to a tendency of lower natural frequencies for the first global bending mode in fore-aft and side-side direction compared to jackets, i.e. being located close to upper limit of *1P* (rotor speed frequency) and therefore closer to the excitation frequencies for fatigue relevant sea states. As a consequence, monopiles are sensitive to hydrodynamic excitations with significant dynamic amplifications in the vicinity of the first global bending mode. Furthermore, the large diameter and the relatively large modal deflections of the first global bending mode in the submerged zone introduce large hydrodynamic excitations compared to jackets. Both, the dynamic amplifications as well as large forces affect the hydrodynamic responses of the first global bending mode for monopiles in a cumulative, unfavourable manner. Therefore monopiles are hydrodynamically sensitive structures.

Increasing top masses, as for example introduced by increasing RNA sizes, lead to a natural frequency reduction of the first global bending modes. This is an unfavourable effect since it further increases the hydrodynamic responses to fatigue relevant sea states. Higher global stiffness for the first global bending mode leads to increased natural frequencies, which can efficiently be achieved by increased diameters. However, very large diameters might introduce buckling and installation problems, if not limited by current fabrication facilities. Furthermore, increased diameters in the submerged zone result in increased hydrodynamic fatigue loads[4].

On the other hand, the closed cross-sectional shape introduces a relatively high torsional stiffness and therefore a tendency towards higher global torsion frequencies compared to jackets.

Jacket foundation

The jacket foundation concept is characterized by a number of main legs which are stiffened by transverse braces. The legs are typically connected to the soil by piles or in more recent designs also by suction buckets. Aerodynamic, hydrodynamic and gravity loads are mainly transferred as axial loads through the members of the structure, but the members also experience certain shear forces, bending moments and even torsion. The transfer of global loads into the soil differs significantly from monopiles. Shear forces and torsion moments are transferred as lateral loads into the seabed. Axial loads and overturning moments are mainly transferred as axial compressive and tensile forces. In case of the overturning moments this is achieved by load couples in opposite directions at the individual legs, utilizing the distance of the legs in the footprint as lever arms. The

[3] Also innovative installation methods are available e.g. based on vibrations.
[4] Hydrodynamic fatigue loads are approximately proportional to the square of the diameter since dominated by inertia loads.

connection between the tower and jacket is established by a transition piece. In contrast to monopiles, the jacket does also carry secondary steel structures like boat landings and access ladders.

Compared to monopiles, jackets are expected to become economic feasible for larger water depths as reflected by numerous publications e.g. Fischer [98]. Jacket foundations are currently most common in combination with piles. However, alternative configurations with suction buckets are currently investigated especially by DONG Energy as illustrated for the prototype installation in Figure 7. Successful installation of this prototype and initial lessons learned indicate promising prospects for the suction bucket as a feasible alternative to piles; compare e.g. Schiedek [65]. However, suction buckets are sensitive to tensile loading. Therefore, one of the main advantages for jackets compared monopiles, i.e. the relatively low mass, might lead to problems for the geotechnical design in case of suction buckets.

Figure 7: Suction bucket jacket foundation at the Borkum Riffgrund 1 offshore wind farm (Photo from DONG Energy).

Characteristics

- Rather new concept for offshore wind energy applications, allowing for easy installation with lighter equipment (compared to monopiles).
- High manufacturing cost due to complex structural layout.
- Applicability in soft and stiff soil, less sensitive to the soil conditions (compared to monopiles).

- Prone to scour, but not as sensitive to scour as monopiles.
- Relatively high stiffness to mass ratio.
- Composed of small-diameter members in space-frame configuration, therefore hydrodynamically transparent structure which does not attract large wave forces.
- Low modal deflections in the submerged zone due to high stiffness to mass ratio compared to tower.
- Prone to local dynamic effects.

The space-frame layout of jackets leads to higher global stiffness which allows for designs with lower steel consumption for the primary structure in comparison to monopiles. However, despite the lower mass, the jacket is often disqualified due to higher fabrication cost per kg.

Compared to monopiles, the relatively high stiffness to mass ratio of jackets leads to a tendency of higher natural frequencies for the first global bending mode in fore-aft and side-side direction i.e. being located close to lower limit of *3P* (blade passing frequency). This is typically also further away from the excitation frequencies of fatigue relevant sea states. Actually, the high stiffness of jacket type foundations for OWT leads often to natural frequencies in the *3P* range which requires either controller adjustments to increase the allowable frequency range such as rotor speed exclusion windows or design changes. A reduction of the first natural frequency by design changes in the support structure is most efficiently controlled by tower adjustments, for example by increasing the hub height and tower length, rather than changes in the jacket.

In consequence of the typically high natural frequency, the first global bending mode is less sensitive to hydrodynamic excitations. Furthermore, the small diameters of legs and braces together with the relative smaller modal deflections of the first global bending mode in the submerged zone introduce rather small hydrodynamic excitations compared to monopiles. Both, the small dynamic amplifications, as well as small exciting forces, affect jackets in a cumulative, favourable manner regarding hydrodynamic responses of the first global bending mode. Therefore, jackets are hydrodynamically insensitive structures.

Increasing top masses, as for example introduced by increasing RNA sizes, lead to a natural frequency reduction of the first global bending mode. This is in many cases a favourable effect since it decreases the natural frequency of the first global bending mode without a significant increase of the hydrodynamic responses.

An increase of global stiffness for the first global bending mode can efficiently be achieved by increasing the footprint which also reduces the axial member loads from global overturning moments. However, increased footprint dimensions also increases the unbraced lengths of brace members which might introduce buckling problems, vortex induced vibrations or enhanced local dynamic effects.

Jacket type foundations with long, slender brace member might experience local dynamic effects as investigated by Kjetså & Saaghus [38]. These local dynamic effects are typically introduced from couplings of higher global bending modes with local brace modes and may introduce a substantial influence on the fatigue lives of the neighbouring tubular joint connections. Vortex induced vibrations introduce another relevant source for local dynamics of brace members.

Figure 8 shows the first three global bending mode shapes of an OWT with a jacket type foundation. The RNA is modelled as a lumped mass with corresponding mass moments of inertia (not shown in the figure). For the first mode, it can be seen that the modal displacements are large in the tower and that the jacket braces stay in the brace planes. However, the higher modes show pronounced in-plane and out-of-plane brace deformations which are superimposed to the global modes and thereby forming coupled local-global modes.

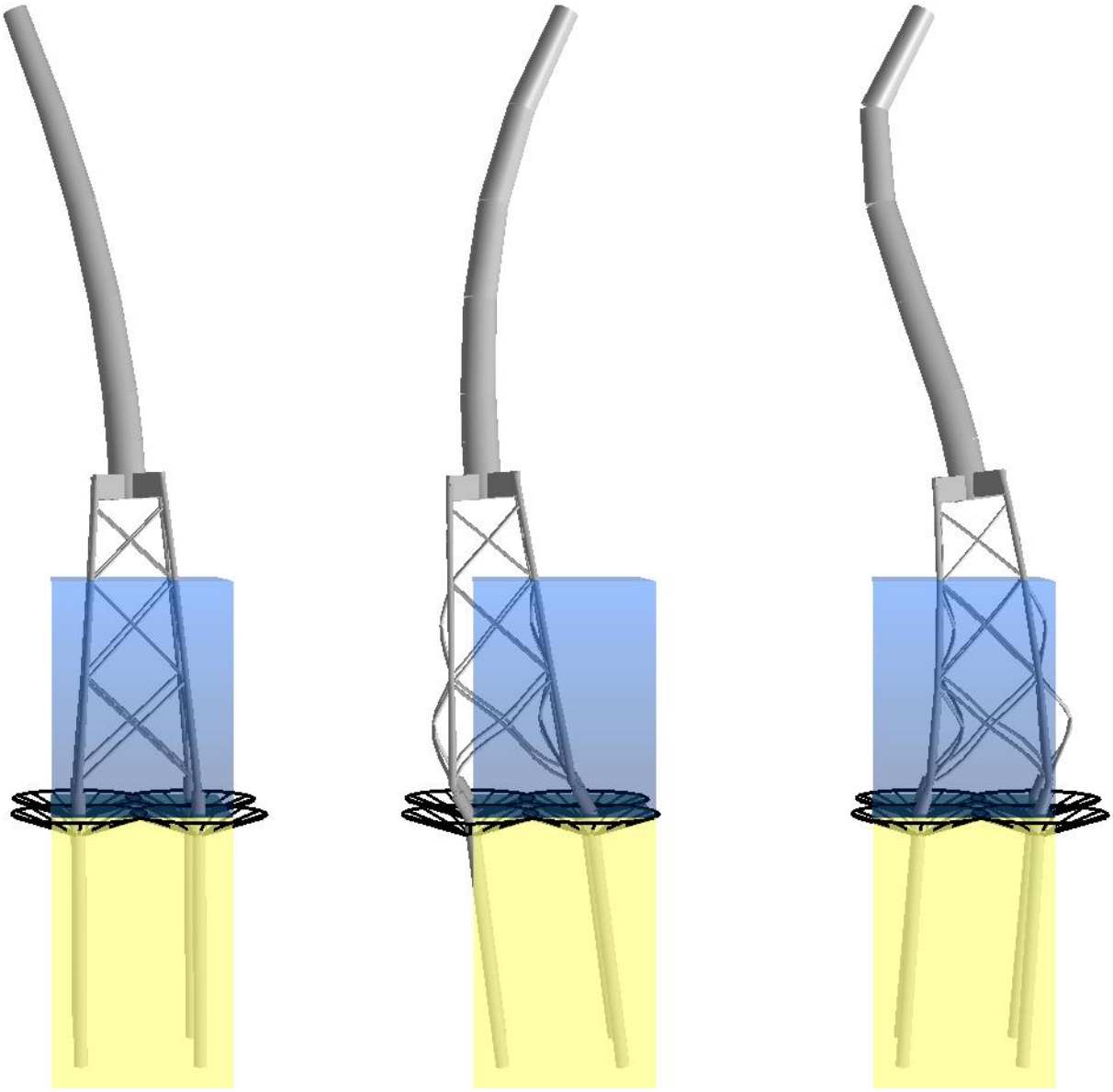

Figure 8: Global bending modes in fore-aft direction. 1st mode (left), 2nd mode (centre) and 3rd mode (right).

2.3 Design phases in the life cycle of offshore wind turbines

The life cycle of an offshore wind farm can be divided into a number of phases. The individual phases are briefly summarized here. More detailed descriptions of the design phases for the OWT foundation are provided in sections 2.3.1 and 2.3.2.

1. Pre-feasibility phase
This phase is intended for site scouting and initial desktop studies on wind resource and other site conditions.

2. Preliminary design phase
This phase comprises initial site surveys, concept, feasibility and front-end engineering design (FEED) studies based on actual, but still limited site information (geotechnical, geophysical, met-ocean) as well as the evaluation of permitting/environmental issues and the technical/financial feasibility, see section also 2.3.1.

3. Planning phase
This phase involves planning and permitting activities, environmental impact assessment, detailed site investigations (wind, geophysical, geotechnical, met-ocean, bathymetry, various environmental surveys) in order to prepare for the detailed design, various engineering studies to determine, wind farm layout, cable routes/corridors, procurement and contracting. This planning phase is executed in parallel to the preliminary design phase with certain interactions, e.g. detailed site investigations could be used as input for FEED studies while conceptual design results are used for the environmental impact assessment.

4. Detailed design phase
This phase concerns the detailed design the offshore wind farm including foundation and tower design, potential controller tuning, cabling/grid connection system, offshore substation as well as procurement and contracting, see section 2.3.2 for more details.

5. Construction phase
This phase concerns the manufacturing and installation of turbines, towers, foundations, cables and offshore high voltage substation for the offshore wind farm.

6. Operation phase
During this phase, the wind farm is in operation, producing power while being monitored, maintained and serviced by the operator.

7. Decommissioning phase
During this phase, all components are removed from the site and subsequently processed for scrapping, recycling or other means of disposal. The decommissioning phase might be complemented or (partially) substituted by a repowering phase. Such initiatives are currently discussed and supported by increased condition monitoring activities.

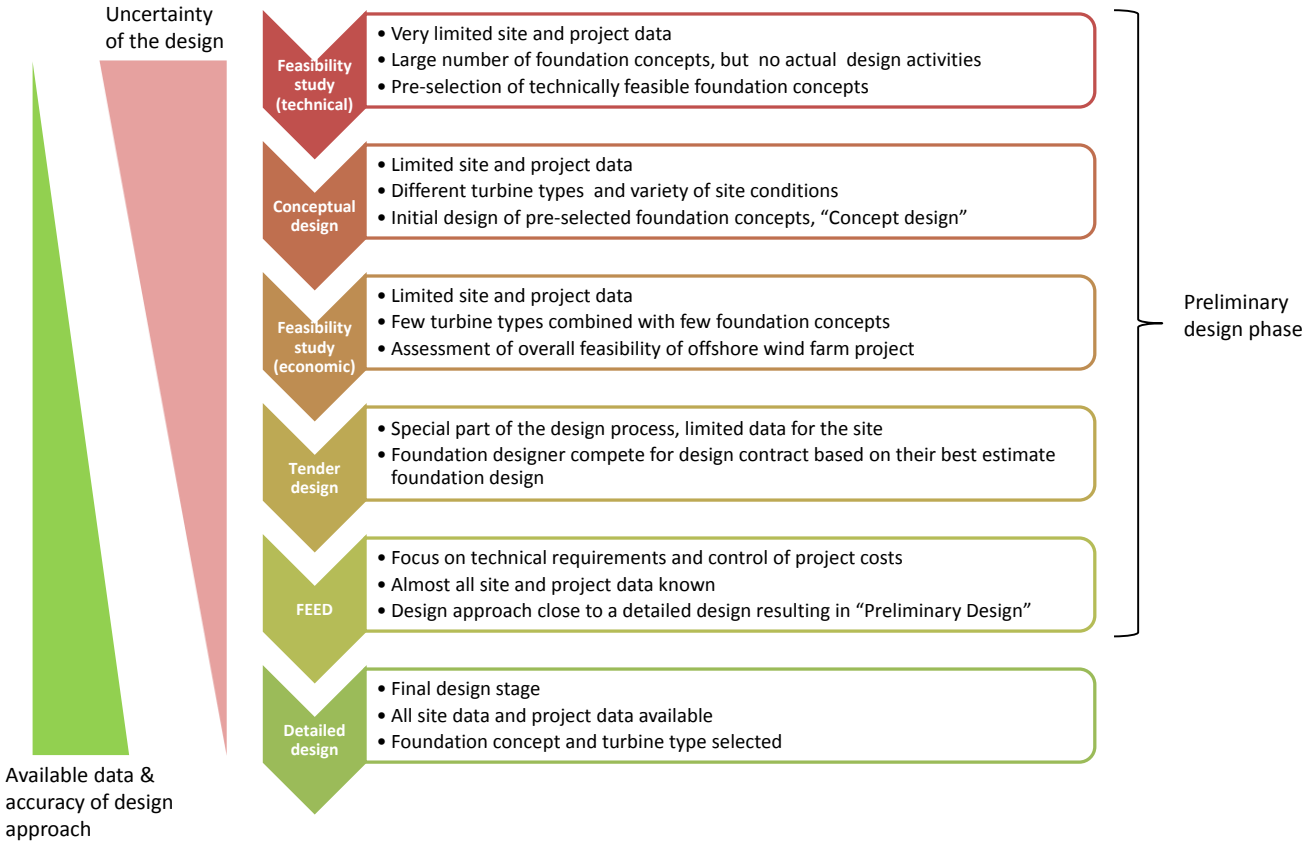

Figure 9: Design stages in the design process.

As shown in this life cycle summary of a typical offshore wind farm project, the actual design process has two subsequent phases, the preliminary design phase and the detailed design phase. Investigations of the foundation as an integral part of the OWT are performed in several, subsequent design stages before maturing into the detailed design phase as indicated in Figure 9. The design tasks and studies of the individual stages in the preliminary design phase are based on an increasing amount of site- and project-data as well as more sophisticated and accurate load calculation approaches. At the same time, the uncertainty of the design, e.g. in terms of number of investigated foundation concepts and turbine types, as well as dimensions of the foundation are reduced by each design stage.

However, in actual design practice the individual design stages are not always present in the preliminary design phase. For example, FEED studies are mainly performed in case of innovative design solutions and often the conceptual design is used for the project feasibility study (economic) too. The tender design is a somewhat special part of the design process, performed simultaneously by different FDs in a competitive manner.

In reality, there is an additional design phase for the turbine type, i.e. the RNA. However, the RNA is designed mainly in a project-independent manner and is therefore only briefly discussed in the following on basis of a subsystem based categorization of the design process. For this subsystem based categorization, the design is divided into support structure and RNA with the support structure being further divided into foundation and tower.

Support structures for OWTs are designed specifically for a given RNA type and project site. Typically only one or a few tower configurations are designed for an offshore wind farm while especially the foundations are designed specifically even for the individual locations within the wind farm. This individual foundation design is very important for the economic feasibility as shown by Carstens, Nielsen & Hansen [7] for the Kentish Flats offshore wind farm.

Contrary to the tower and foundations the RNA is designed in a project- and site-independent manner prior actual offshore wind farm design project. This is achieved by a validation of suitability for uniform RNA designs (type class) for a variety of sites covering a predefined range of environmental conditions. These environmental conditions can e.g. be taken from the IEC 61400 series guidelines [87], [88] in order to demonstrate conformity with respect to the corresponding guideline, which results in a type certification. Actual, site- and project-specific design loads in the design process of OWTs are used to verify that the loading conditions from the type certification are not exceeded. The only RNA item subjected to more site- and project-specific design activities is typically the control system. Here, the objective is typically related to performance optimization, load mitigation or the establishment of rotor speed exclusion windows in order to allow for extended natural frequency ranges in the support structure design. The latter aspect has for example been demonstrated for the Utgrunden offshore wind farm as summarized by Passon & Kühn [54].

2.3.1 Preliminary design phase

The main objective of the preliminary design phase is to generate all relevant key parameters for financial planning in the economic decision process, but also for preparation of the detailed design phase. Typically, different support structure concepts and turbine types are studied prior to selection of the most feasible combination for a particular site and project and prior to entering the detailed design phase. The preliminary design phase starts often several years before the detailed design phase with very limited data about the site and project. Interactions between the WTM and FD are rather limited at most preliminary design stages. The design stages from Figure 9 are further described in the following, but it is emphasized again that large variations exist in design practice, dependent on the developer, country and location of the project as well as on the selected design solution. In the present thesis, focus is on certain aspects of the detailed design phase. The individual design stages of the preliminary design phase are therefore only briefly described. However, the importance of a good preliminary design in the context of an optimized detailed design solution is further addressed in section 2.3.2.

Feasibility studies (technical)

For the foundations, the preliminary design phase is initialized by studies of the technical feasibility of different foundation concepts. This is based on an assessment of the very limited site data and potential turbine types with respect to the characteristics of different foundation concepts rather than on actual foundation design activities. The purpose is to identify technically feasible and unfeasible foundation concepts in order to optimize the available resources in the next design stages.

Conceptual design studies

In the conceptual design phase, the identified technically feasible foundation concepts are designed for a selection of turbine types. Focus of conceptual design studies is typically on the primary structure with rough approximations of the secondary structures, e.g. from experience. Available site and project data are still rather limited and require the FD to complement missing information with assumptions or parameter variations. For example, this is often valid for the soil conditions. The geotechnical survey is an expensive task and requires knowledge of the actual position of the individual OWTs. Consequently, the conceptual foundation designs are established e.g. individually for soft and stiff soil conditions. Design loads are obtained from a superimposed load calculation approach according to section 3.2.

The goal of this design stage is the establishment of initial design ideas for foundation types and geometries as well as corresponding cost estimates as function of e.g. turbine type, soil conditions and/or water depth. The purpose of these conceptual foundation designs studies is to support on an initial economic feasibility assessment on project level as well as to further narrow down the range of foundation concepts for the following design stages. As a guideline, the level of accuracy, measuring for instance the cost of the foundations, is in the area of +/- 15 to 25% compared to the final detailed design.

Feasibility studies (economic)

The starting point for feasibility studies at this design stage are the technically and economically most attractive conceptual designs from the previous design stage. The number of different turbine types and foundation concept combination is therefore further limited while often more detailed site and project data are available. In some cases even improved aerodynamic loads are provided by the WTM on basis of aero-elastic simulations with the foundation from the conceptual design and the actual (available) site conditions due to the importance of this design stage. This allows for maturing the individual foundation designs with more detailed consideration of the secondary structures therefore converging further towards the final design.

The purpose of the economic feasibility studies is the selection of the most favorable combinations of foundation concept and turbine type for the potential project. This is based on more accurate foundation design solutions than in the previous phases. The resulting foundation designs are used to support in the assessment of economic feasibility of the overall offshore wind farm project and subsequent preparation of the allocation of corresponding financial resources.

Despite the fact that important decisions are based on the outcome of this stage, the design is often based on superimposed load calculation approaches according to section 3.2 with very limited site and project data. It should be noted, that the uncertainty from the limited data and simplified load calculation approach might differ significantly for different foundation concepts. Therefore, it is important that the uncertainties from the required simplifications and assumption are minimized and thoroughly assessed for the individual design solutions. This design stage is concluded with a scheme design as a starting point into the detailed design phase. As a guideline, the level of accuracy, measuring the cost of the foundations, is in the area of +/- 10 to 15% compared to the final detailed design.

Tender design

The purpose of the tender design is to assist a) the developer in the preparation of the documentation for the foundation tender package or b) to assist potential contractors in the preparation of a foundation design for their bid. The foundation design is performed for the selected, most favourable combination of foundation concept and turbine type from the previous design stages. The level of detail and requirements is typically provided by the developer through employer's requirements documents. Often the developer awards the foundation design contract to a contractor in a competition phase. In such competition phases, the focus of the individual FDs is typically on the design optimization within the allowed boundaries given by the available background information. The accuracy of the foundation design in this design stage is extremely important for the contractor since foundation contracts are often based on a fixed price. A too optimistic tender design of the foundation might therefore lead directly to a loss in profit. That risk is further increased by the fact that the available site data and turbine loading information is still rather limited at this design stage and that the design is based on a superimposed load calculation approach according to section 3.2. The corresponding foundation design serves as the preliminary design for the detailed design phase unless a more accurate design is obtained, for example from a FEED study. As a guideline, the level of accuracy, measuring for instance the cost of the foundations, is in the area of +/- 10 to 15% compared to the final detailed design.

Front-End Engineering Design (FEED)

The purpose of the FEED is to support in the identification of technical requirements and risks as well as of the main costs for the project, e.g. for cost control purposes in the execution phase. Focus is given on a particular foundation concept in combination with a particular turbine type or sometimes also on certain innovative subsystems or components. Site and project data are (at least) almost completely available and furthermore, the WTM is typically involved in the FEED phase as well. Load calculation approaches correspond to detailed designs, i.e. using integrated models according to section 3.1. The corresponding foundation design serves as the preliminary design for the detailed design phase. As a guideline, the level of accuracy, measuring for instance the cost of the foundations, is in the area of +/- 5 to 10% compared to the final detailed design.

2.3.2 Detailed design phase

The second and final design stage is the detailed design. Focus is given on the combination of one particular foundation concept with one particular turbine type. However, some sites require also a mix of foundation concepts due to a large variability in site conditions, in particular water depths and soil conditions. Starting point for the foundation design is the final preliminary design from the preliminary design phase. It should be noted that the work scope in a detailed design can vary quite significantly e.g. due to different requirements in different countries. For example, offshore wind farm installations in the exclusive economic zone, i.e. outside the 12 mile zone, in Germany require approvals by the Federal Office of Navigation and Hydrography (BSH). Next to a certification in accordance to the chosen design guidelines this requires compliance with the BSH-Standard [82] and procedures.

The deliverables of the detailed design foundation package include design drawings and a number of design reports suitable for certification of the design by an independent verification body. Design drawings need to be provided in sufficient level of detail in order to allow for production and subsequent installation of the

structures. Once the detailed design foundation package has been approved by the developer and a 3rd party certification body, it will typically form the basis of a fabrication and installation package

The detailed design of OWT foundations requires cooperation and close communication of the FD with numerous parties during the design process as indicated in Figure 5. This includes for example the foundation fabricator and installation contractor in order to ensure compatible foundation dimensions with their equipment. However, focus is on the calculation of design loads in the context of the present thesis and therefore mainly the interfaces towards the WTM are addressed.

Site and project data are completely available in the detailed design phase, which includes the individual locations in the wind farm and location-specific soil conditions. Furthermore, the WTM is directly involved and responsible for the design of the superstructure, i.e. tower and RNA. WTM and FD collaborate in order to establish a load calculation approach corresponding to section 3.1. Such a sequentially integrated load calculation approach requires the combination of sophisticated subsystem models and loads from different parties and different highly specialized tools. The aerodynamic loads from the WTM are applied simultaneously with the hydrodynamic loads from the FD in the aero-elastic simulation. The number of load combinations[5] as realizations of the design load cases (DLCs) from the selected design standard/guideline is in the order to 2000-10000 for each, the ULS and FLS load cases. Furthermore, the FD provides a dynamically equivalent foundation description which needs to be incorporated into the integrated OWT model for the aero-elastic analysis by the WTM. The corresponding model and load exchanges are critical items in the design process, i.e. prone to be the source of design errors. A smooth and efficient design process requires therefore:

- Clear and well-defined interfaces with respect to deliverables regarding the structural configuration, loads, coordinate systems, data formats, file identification and calculated DLCs.
- Clear understanding of the DLCs and load iteration process.
- Adequate modelling capabilities of the involved parties.
- Adequate model and load verification.

Figure 10 provides an overview of the steps in the design load calculation process of a detailed design. Starting point for the design load iteration process is the establishment of a load case table (LCT) summarizing and describing the individual realizations of all DLCs in step 0. This is followed by design iteration loops that comprise load iteration loops in steps 1-3 for establishment of the design loads. Details on the individual steps are provided in this section, while a brief summary of the load iteration is also provided in section 3.1. A new load iteration loop is required in case of significant design changes after step 3. With respect to the design loads, a large change of the relevant modal properties, compare section 2.1, can for example be used as a classification of significant design changes. Such a change in the relevant modal properties is accompanied by a change of the global dynamic responses and therefore introducing a deviation from the design loads of the last load iteration loop. In design practice it is decided on a case-by-case base (often supported by additional assessments) if a new load iteration loop is required.

[5] In the present thesis, a load combination is defined as a load realization for a combination conditions such as environmental (e.g. wind speed, waves) and operational (e.g. normal power production).

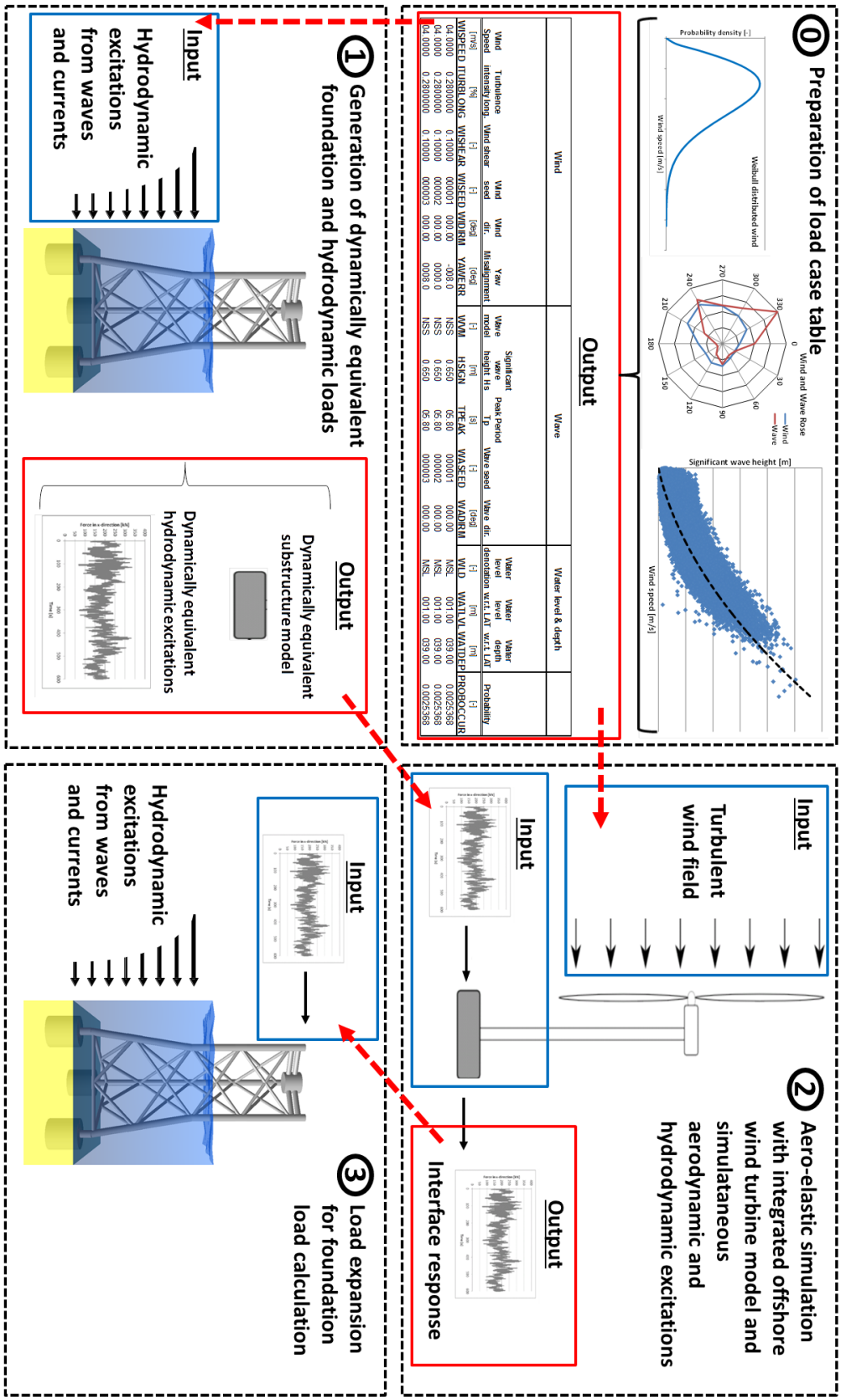

Figure 10: Design load calculation steps in detailed design process (top) and example load case table for 3 load combinations (bottom).

Design load case & load file						Wind				Wave				Current		Water level & depth		Time series parameter	Probability
File name / identification	DLC IEC 61400-3	Load case description	Analysis type	Seed group index	Load factor	Wind model	Wind Speed	Turbulence intensity long.	Wind shear	Wind seed	Wind dir.	Yaw error	Wave model	Significant wave height Hs	Peak Period Tp	Wave seed	Wave dir.	Wave spreading factor	Current Model	Current dir.	Ref. Current Speed	Water level w.r.t. LAT	Water depth w.r.t. LAT	Length of initialisation	Length of time series (after initialisation)	Probability
Num																									
[-]	[-]	[-]	[-]	[-]	[-]	[-]	[m/s]	[%]	[-]	[-]	[deg]	[deg]	[-]	[m]	[s]	[-]	[deg]	[-]	[-]	[deg]	[m/s]	[-]	[m]	[s]	[s]	[-]
0001	DLC12_0001	Normal power production	FLS	0001	1.000	NTM	4	0.27	0.14	1	000.00	352.0	NSS	0.55	06.16	1	000.00	01.0000	NCM	000.00	00.028	MSL	1.25	32.5	100	600	0.0003586
0002	DLC12_0002	Normal power production	FLS	0001	1.000	NTM	4	0.27	0.14	2	000.00	000.0	NSS	0.55	06.16	2	000.00	01.0000	NCM	000.00	00.028	MSL	1.25	32.5	100	600	0.0003586
0003	DLC12_0003	Normal power production	FLS	0001	1.000	NTM	4	0.27	0.14	3	000.00	008.0	NSS	0.55	06.16	3	000.00	01.0000	NCM	000.00	00.028	MSL	1.25	32.5	100	600	0.0003586

However, a very common practical constraint for the maximum number of load iterations between FD and WTM in the detailed design process is actually introduced by project time schedules. Time schedules of most detailed design projects do not allow for more than two load iterations and therefore the number of design loops for the global design, as indicated in Figure 11, is limited as well. Refinements of the design during each design loop correspond to design optimization. Due to the limited number of design loops, a good preliminary design is required as a starting point in order to achieve a sufficiently optimized design solution.

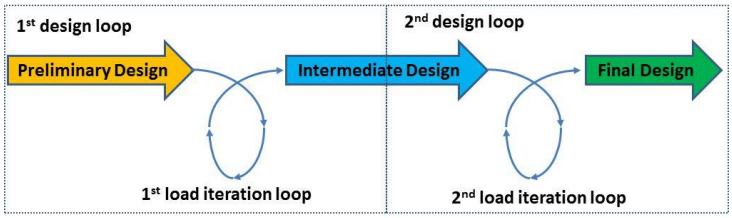

Figure 11: Detailed design based on 2 design loops.

Step 0 - LCT preparation

An example for a LCT is shown in Figure 10 for three load combinations of the normal power production DLC 1.2 according to IEC61400-3 [88]. Here, the LCT is split into four blocks in the figure in order to fit the page size. The LCT is established in a joint effort between the FD and WTM in order to ensure capturing of all relevant load combinations for each subsystem. It should be noted, that the design loads for almost each load combination in the LCT can only be established in a joint effort between the WTM and FD since each party needs to generate parts of the simultaneous excitations.

A LCT describes the complete set of simulation parameters for every single load combination of each DLC. Establishment of a complete set of simulation parameters per load combination requires e.g. a correlation of met-ocean parameters in order to capture their simultaneous effect in the load calculation. All relevant met-ocean parameters are therefore organized by primary parameters and associated parameters. Primary parameters form the general structure of the LCT and are defined a priori due to their project-specific but not site-specific character. Primary parameters are marked green in Figure 10.

Example: *For a wind turbine the normal power production DLC 1.2 is simulated for all wind speeds in the power production range (e.g. 3-25m/s) in 2m/s intervals and each combination of wind and wave direction (e.g. assuming in each case 12 directions for 30 degree sectors). Each combination of "wind speed - wind direction - wave direction" is simulated for 3 yaw error scenarios (e.g. -8, 0 and 8 degree) and for 2 turbulence and wave seeds per case. Without any further knowledge of the actual site, the overall form of DLC 1.2 can already be established in the LCT, resulting in 11·12·12·3·2 = 9504 load combinations with pre-defined values for the parameter wind speed, wind direction, wave direction, yaw error and turbulence seed. It should be noted that this large number of load combinations is reduced in design practice based on zero probability of occurrence cases and experiences of the FD and WTM.*

On the other hand the associated parameters are site-, project- and structure-specific. For example, it is required to derive the associated wave parameter and probabilities for the given primary parameters of each load combination. Associated parameters are marked yellow in Figure 10. Note, that in reality a range of wave parameter can occur per combination primary parameter.

For example, the met-ocean database may include wave scatter diagrams (SCD) or better wave scatter matrices, as outlined in Figure 12, as full wave climate representations conditioned on combinations of "wind speed - wind direction - wave direction", i.e. per primary parameter combination. There can potentially be occurrences of many different H_s-T_p combinations dependent on the resolution of the SCDs and the individual primary parameter combination. Given the already rather large amount of combinations of primary parameter it is clear that a lumping of the associated parameters is required in order to be applicable for load simulation and design purposes. Often the whole SCD per primary parameter combination is condensed to only one representative H_s-T_p combination.

	Class *j*	1	2	····	17
	Tp [s]	0.0-1.0	1.0-2.0	····	16.0-17.0
Class *i*	*Hs* [m]				
1	9.00-9.25	$p_{1,1}$	$p_{2,1}$	····	$p_{17,1}$
2	8.75-9.00	$p_{1,2}$	$p_{2,2}$	····	$p_{17,2}$
3	8.50-8.75	$p_{1,3}$	$p_{2,3}$	····	$p_{17,3}$
····	····	····	····	····	····
35	0.50-0.75	$p_{1,35}$	$p_{2,35}$	····	$p_{17,35}$
36	0.25-0.50	$p_{1,36}$	$p_{2,36}$	····	$p_{17,36}$
37	0.00-0.25	$p_{1,37}$	$p_{2,37}$	····	$p_{17,37}$

Figure 12: Exemplary SCD format with H_s bins of 0.25m, T_p bins of 1.0s and probabilities of occurrence $p_{i,j}$.

Representative associated parameters depend on the limit state design situation, often damage equivalent parameters are used in FLS and maximum parameters in ULS. A damage equivalent wind-wave correlation approach that allows for preservation hydrodynamic fatigue damage from the full wave climate has been developed in paper 3 [63] based on an extension of the wave lumping approach introduced in paper 2 [62]. Further topics related to the modelling of environmental parameters in the detailed design process are addressed in Chapter 5.

Step 1 – Generation of dynamically equivalent foundation and loads

The first step of the load iteration loop is intended to establish a detailed model of the foundation structure and the corresponding hydrodynamic loads. In the beginning of the detailed design process this is based on the results of the preliminary design phase, e.g. from the FEED study. Later in the detailed design process the foundation design is based on design loads established in previous load iteration loops.

An adequate representation of structural foundation characteristics requires rather detailed descriptions of the relevant foundation aspects. Dependent on the actual foundation configuration, this can for example comprise the following items:

- Local joint flexibilities.
- (Directional) influence of appurtenances on hydrodynamic loads and mass distribution
- Marine growth influence.
- Scouring or scour protection.
- Superelement[6] representations of the tubular joints and transition piece.
- Corrosion allowance.

[6] A superelement is an individual finite element obtained from a group or set of finite elements for example by substructuring techniques; see Felippa [97] for further details.

Furthermore, this step contains the modelling of (non-linear) soil-structure interactions (together with a corresponding linearization for the aero-elastic simulations) as well as the generation of wave kinematics for the hydrodynamic loads. Both items have been addressed extensively in available literature; see e.g. Passon [52], [55] for monopiles and extreme waves. The generation of directional hydrodynamic loads under consideration of currents is typically based on Morison formula where the time varying hydrodynamic coefficients are based on the actual flow conditions and structural configuration. The foundation structure is assumed to be rigid for the generation of the hydrodynamic loads, i.e. no relative wave kinematics terms are considered in the Morison formula.

The established detailed foundation subsystem models including soil-structure interactions and hydrodynamic loads are then available in the FD modelling tool. For example, this can be based on a finite element description with system matrices for the foundation and load vectors for the time series of hydrodynamic loads of every single load combination in the LCT. It is then required to describe the FE system of foundation model and hydrodynamic loads in an adequate way for the aero-elastic simulation e.g. on basis of an adequate superelement formulation. Subsystem modelling aspects are further discussed in Chapter 6.

Step 2 – Aero-elastic simulations with the integrated OWT model

Integration of the foundation model including soil-structure interactions and hydrodynamic loads into the OWT model of the WTM yields an integrated model of the overall OWT under simultaneous aerodynamic and hydrodynamic loads and the controller characteristics according to Figure 4 and Figure 14.

It should be noted that no hydrodynamic damping from the relative kinematics term in the Morison formula can be utilized in case of pre-defined hydrodynamic loads (i.e. water particle kinematics are not available in the aero-elastic simulation). However, hydrodynamic damping from the relative kinematics term in the Morison formula is in most cases also not applicable for monopile or jacket type foundations as shown in section 4.2.

The responses as results of the aero-elastic simulations for each load combination are provided to the FD in terms of loads and/or kinematics at pre-defined locations for a load expansion throughout all parts of the foundation. Integrated load calculation approaches are further discussed in Chapter 3.

Step 3 – Load expansion for the foundation

The dynamic responses from aero-elastic simulations in step 2 have to be expanded to the final design loads throughout all parts of the detailed foundation model in the design tool of the FD. Locations for the extraction of dynamic responses for the FD are for example the interface between tower and foundation as well as the mudline level. The dynamic responses are typically extracted as load, deformation and acceleration components in all six directions at the location under consideration. Often not all of these load and kinematic components are subjected to the load expansion directly, but used for load and model verification, i.e. comparison of the direct responses from the aero-elastic simulations with those established in the foundation load expansion. Different load expansion methods exist, but their applicability depends on the characteristics of the foundation type under consideration. A selection of dynamic foundation load expansion methods have been assessed in paper 1 [61] for a jacket type foundation structure. This is complemented by further investigations and discussions in Chapter 3.

2.4 Load simulation tools for offshore wind turbines

Load simulation tools with sophisticated modelling approaches for the structure and environmental loads exist for offshore structures and wind turbines. Due to the fast development of offshore wind energy and the ever increasing need for more complex models and more accurate load calculations, both types of tools have experienced significant improvements over the last decade. OWTs require modelling and load calculation capabilities from both types of tools, which is often established by a coupling of these tools or alternatively by extension of an existing onshore wind turbine tool. The resulting solution constitutes an integrated load simulation tool for OWTs. However, in the context of OWT foundation design and the corresponding design load calculations the actual modelling capabilities of loads and structures can be very different for individual solutions. An overview of modelling capabilities for a selection of aero-elastic load simulation tools for OWTs has been provided by Passon [53], [59] in 2005 and 2008 which has been updated by Vorpahl et al. [77] in 2013.

Nowadays, trends in design practice are not exclusively going towards fully integrated load calculation and design tools with detailed modelling and design capabilities for all subsystems. Instead, the most popular solution in design practice is based on a sequentially integrated approach for the load simulations as illustrated in section 3.1. This approach uses loads and models from a tool for offshore structures and from an aero-elastic tool for wind turbine in order to establish an integrated model of the OWT for load calculation purposes. An advantage of this approach is the possible utilization of the strengths and experiences of state-of-the-art tools and subsystem models from both, the wind turbine community and offshore structure community. However, it does also require the involvement of interface specialists, ensuring that the individual subsystem models and loads are coupled consistently and adequately in order to obtain the overall integrated OWT system model for calculation of design loads.

For load calculation purposes in this thesis, the tools used at Ramboll Wind & Towers are applied, i.e. ROSAP [64] and LACflex. A brief description of both tools is provided in the following; for further information the reader is referred to Ramboll [103].

LACflex is an aero-elastic simulation platform allowing for load calculations and performance analyses of onshore and offshore wind turbines. The program is based on FLEX5 [50] which is one of the most verified and frequently used aero-elastic load simulation tools in the industry, see e.g. Vorpahl et al. [77].

LACflex simulates 20-30 times faster than real-time on a single processor core due to the efficient condensation of the foundation, tower and RNA degrees of freedom (DOFs), i.e. the total OWT is described by only 28 generalized DOFs in the basic version as summarized in Table 1.

The program supports customized models of mechanical, electrical and control systems. Substantial modifications of the original FLEX5 code have been introduced to the program. As a result, subsystem models and the controller can easily be incorporated from other programs since LACflex has a direct interface for external loads, foundation models and controllers, e.g. as dynamic link libraries. Furthermore, the foundation can be simulated with a user-defined number of DOF following the extension approach from Passon [59], instead of the limitation to only 6 DOFs in the basic FLEX5 version.

Table 1 Degrees of freedom and reference coordinate systems for the subsystems in FLEX5, from Passon [59]

	Subsystem	DOF resp. subsystem mode	DOF number	Reference coordinate system
Support Structure	Foundation	x-translation	1	$\mathbf{F_{Sys}}$
		z- translation	2	$\mathbf{F_{Sys}}$
		y-rotation	3	$\mathbf{F_{Sys}}$
		y- translation	4	$\mathbf{F_{Sys}}$
		z-rotation	5	$\mathbf{F_{Sys}}$
		x-rotation	6	$\mathbf{F_{Sys}}$
	Tower	1st fore-aft	7	$\mathbf{T_{Sys}}$
		2nd fore-aft	8	$\mathbf{T_{Sys}}$
		1st lateral	9	$\mathbf{T_{Sys}}$
		2nd lateral	10	$\mathbf{T_{Sys}}$
Rotor-Nacelle-Assembly	Nacelle	x-rotation	11	$\mathbf{K_{Sys}}$
		y-rotation	12	$\mathbf{K_{Sys}}$
	Drive Train	z-rotation (shaft rotation[1])	13	$\mathbf{R_{Sys}}$
		x-rotation (bending)	14	$\mathbf{R_{Sys}}$
		y-rotation (bending)	15	$\mathbf{R_{Sys}}$
		z-rotation (torsion[2])	28	$\mathbf{R_{Sys}}$
	1st Blade	1st flap	16	$\mathbf{V_{1,Sys}}$
		2nd flap	17	$\mathbf{V_{1,Sys}}$
		1st edge	18	$\mathbf{V_{1,Sys}}$
		2nd edge	19	$\mathbf{V_{1,Sys}}$
	2nd Blade	1st flap	20	$\mathbf{V_{2,Sys}}$
		2nd flap	21	$\mathbf{V_{2,Sys}}$
		1st edge	22	$\mathbf{V_{2,Sys}}$
		2nd edge	23	$\mathbf{V_{2,Sys}}$
	3rd Blade	1st flap	24	$\mathbf{V_{3,Sys}}$
		2nd flap	25	$\mathbf{V_{3,Sys}}$
		1st edge	26	$\mathbf{V_{3,Sys}}$
		2nd edge	27	$\mathbf{V_{3,Sys}}$

[1]- rotation of the drive train resp. the low speed shaft described as rigid body motion
[2]- torsional stiffness of the drive train resp. the low speed shaft

ROSAP is the acronym for Ramboll Offshore Structural Analysis program Package. The program package has been continuously developed by Ramboll for more 30 years and is a state-of-the-art simulation and design platform for marine structures. ROSAP has been used for the design of the majority of offshore oil & gas structures in the Danish part of the North Sea as well as for the design of the majority of OWT foundations worldwide.

The program package consists of various program modules of which ROSA is the main program. ROSA is a finite element program for offshore structures and can perform static or dynamic (incl. spectral & transport) analyses of spatial frames and truss structures as well as piping systems subjected to various kinds of loads (gravity, acceleration, transport, temperature, pressure, buoyancy, wave, current & wind). The structures may be modelled with non-linear soil-structure interactions, which are established internally in ROSA or defined

externally by the user. Furthermore, soil curves can be subjected to automatic or user-defined linearization approaches; see e.g. Passon [52], [55] for further details on a load specific linearization approach.
Many other relevant aspects for offshore structures are supported, such as the automatic generation of local joint flexibilities in tubular joints based on geometric properties and/or loads. Another important feature is the interface for superelement representations of selected components of the structure such as joints or the transition piece as well as the possibility for generation of superelements.

In difference to a pure load simulation tool, ROSAP consists of numerous pre- and post-processing program modules. This includes modules for generation of wave kinematics, model & result visualization, stress and stability checks as well as fatigue checks according to various design standards, etc. Furthermore, ROSAP allows for fast and extensive model parameter variations and provides utilities for a quick result assessment. Therefore, ROSAP is considered as an integrated design and load simulation platform.

SHEILA is the acronym for SHell Execution of Integrated Large Analyses. The program is used to organize the execution of multiple repetitive analyses such as time domain fatigue analysis for wind turbine foundations or parameter variations for structural optimization studies in the design process including distribution of calculation packages to a dedicated computer calculation cluster. SHEILA controls the pre-processing, e.g. for establishment of wave kinematics, simulations as well as the post-processing of results, e.g. for calculation of fatigue damages. Furthermore, SHEILA is used to control coupled ROSAP-LACflex (sequentially integrated) simulations by handling the model and load transfer files on basis of shared simulation parameters as taken from the LCT described in section 2.3.2.

Coupled ROSAP- LACflex solution

Large efforts have been put into the task of coupling aero-elastic wind turbine tools with sophisticated offshore tools in the past. Hald & Høgedahl [29] presented an idea for an efficient and practical approach for the FLEX5 code [50] based on the reduction method by Craig-Bampton [9]. This approach introduces an extension of the existing Guyan [26] type reduction approach for the foundation in FLEX5 by additional consideration of so-called internal modes. An actual application and investigation of the coupling of FLEX5 with a finite element based offshore structure tool by using the Craig-Bampton reduction method for the foundation has been presented by Passon [59] within the UpWind project [102]. This has been successfully reproduced and continued by Kaufer et al. [36] with the same FLEX5 version. Van der Valk & Voormeeren [72] showed that a foundation representation based on a Guyan reduction with only six interface DOFs might significantly overestimate the potential energy of the dynamic response in case of jacket-type space frame structures. However, in case of a Craig-Bampton reduction with a small amount of internal modes of the same foundation the potential energy could be preserved very well.

Although Passon's [59] integration approach could also be applied for LACflex and ROSA, the author has decided for a simpler coupling alternative as the more efficient solution. This coupling solution follows generally the sequentially integrated load calculation approach explained in section 3.1. For that purpose, enhanced interfaces have been implemented in ROSAP and LACflex ensuring fully compatible transfer files. On one hand, this allows for a direct application of ROSAP-generated foundation model and load files in LACflex as indicated in Figure 13. On the other hand, LACflex-generated load and kinematic output files from the aero-

elastic analyses can be directly applied in ROSAP. Furthermore, the ROSAP-LACflex calculations are controlled by SHEILA and the (same) parameters from the LCT such as wind speeds, wave heights, wind and wave directions, probabilities and the simulation time.

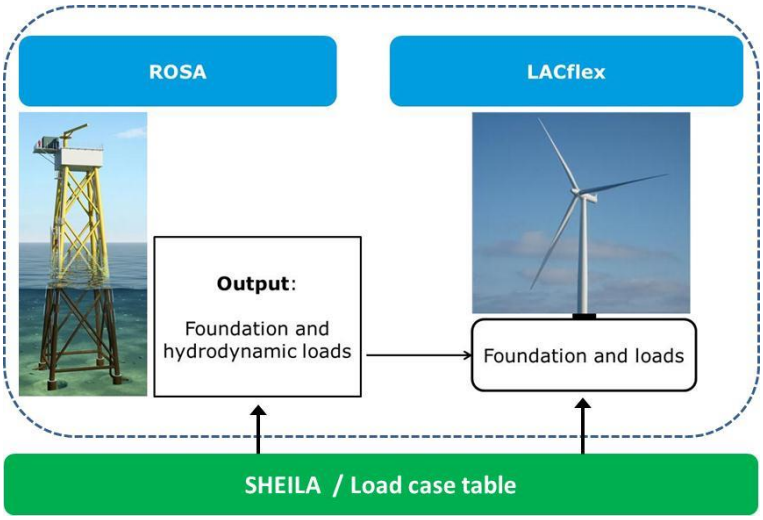

Figure 13: Coupling of ROSA and LACflex on foundation system matrix and load vector level controlled by SHEILA and the LCT.

In this simple coupling approach, the integrated OWT system model is established by introduction of the ROSAP finite element based foundation system matrices and load vectors in LACflex according to Figure 14. This approach ensures that identical foundations and hydrodynamic loads are used in both tools since the system matrices and load vectors represent a complete description of the structural foundation and hydrodynamic loads with all relevant modelling features from ROSAP. However, for practical applications the Craig-Bampton [9] reduction technique is often applied to the foundation.

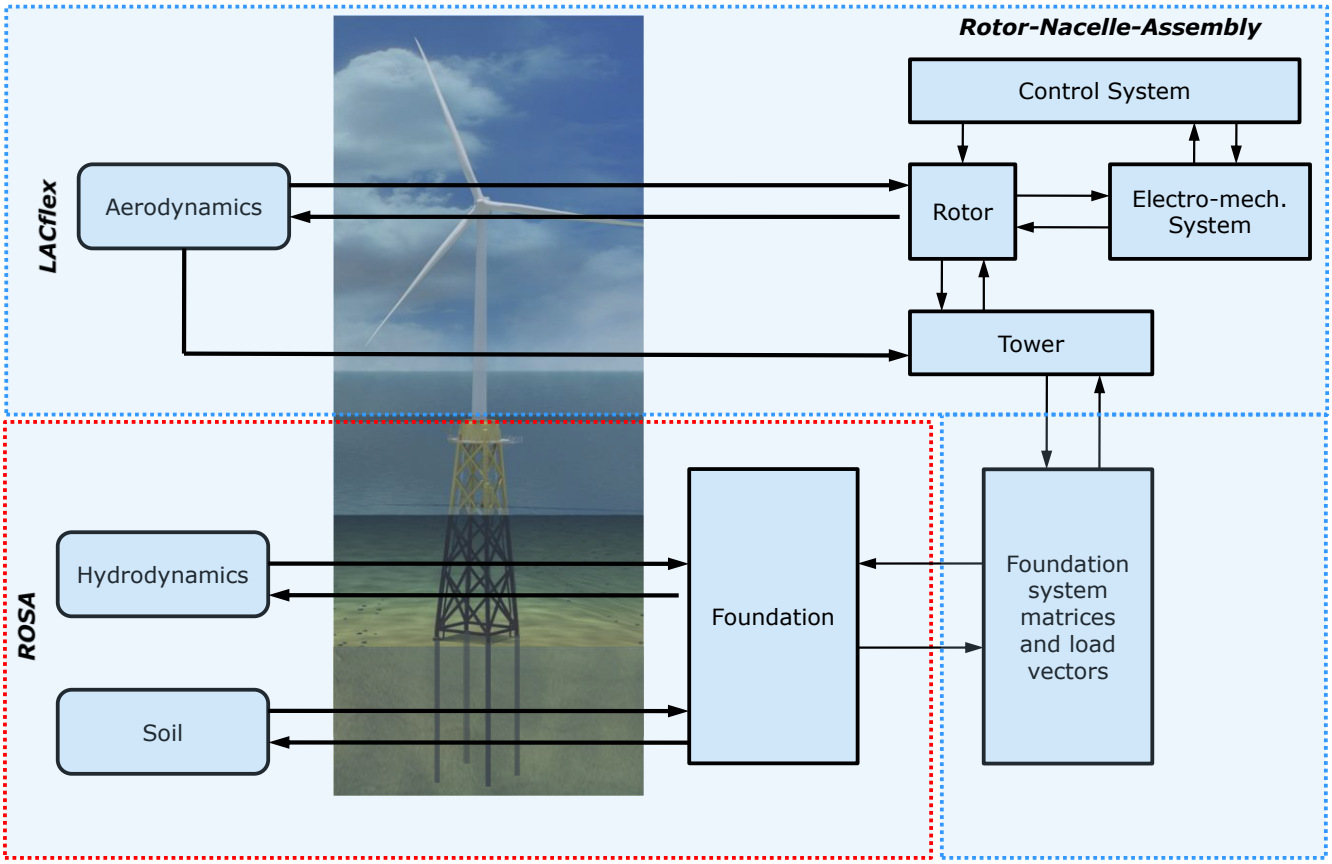

Figure 14: Integrated OWT model in LACflex with foundation and loads from ROSA.

Compared to a full integration of the LACflex and ROSAP codes this rather simple coupling has the following advantages:

- Independent maintenance, updates and modification performed by individual experts with specialized backgrounds on either the aero-elastic LACflex code or the offshore structure simulation platform ROSAP.
- Independent quality assurance approaches for new versions of each tool.
- Clear and well-defined interfaces. These interfaces are also used in load iterations with external parties, such as the WTMs. In fact, the established LACflex-ROSAP interfaces have been reproduced by various WTMs and applied in several detailed design projects.

On the other hand, the main disadvantage is the need for three steps in the design load calculations rather than only one in case of a full integration. However, this is nowadays hardly a problem since simulations are typically performed simultaneously on many computers with rather large processor and memory capacities in clusters. Furthermore, one might be concerned with a loss of accuracy in the aero-elastic simulations. This could be due to the fact that the foundation model is linearized, thereby missing the non-linear soil-structure interactions of the foundation in the aero-elastic simulations. However, the applicability of typical non-linear soil curves such as p-y curves according to API-LRFD [81] for dynamic analyses is questionable since these curves are defined with the same loading and unloading path, i.e. completely disregarding the hysteretic character of real soil responses under dynamic loading. It is therefore common design practice to linearize the foundation and soil-structure interactions for the aero-elastic analyses in the sequentially integrated load calculation approach while the non-linear soil behavior is e.g. considered for the load expansion in ULS. In this context, it has been shown by Damgaard et al. [14] that the non-linear soil-structure interactions of monopiles can be captured reasonably well with simplified, linearized soil-structure interaction models in FLS. Another concern might be introduced from the fact that the hydrodynamic forces are calculated by Morison's formula[7] for rigid structures, i.e. without the use of relative water particle velocities for direct consideration of hydrodynamic drag damping. This item is further discussed in section 4.2, showing that Morison's formula with relative water particle velocities due to the flexibility of the structure is for most configurations of monopile and jacket foundations not applicable. The established coupled ROSAP-LACflex solution has therefore many advantages while potential disadvantages are limited.

[7] The Morison formula is provided in section 4.2 for flexible structures consideration of relative fluid particle kinematics in Eq. 10 and for rigid structures in Eq. 9.

2.5 Innovative design approaches

Traditional detailed design approaches for the support structure are based on sequentially integrated load calculations according to section 3.1 with a split of design responsibilities between the WTM and FD according to section 2.3.2. Both aspects have been applied and optimized throughout many offshore wind farm designs during the last decade. As a result, efficient and well-defined load iterations interfaces do often exist between the various WTMs and FDs for the detailed design process. Nevertheless, the turn-around time of load and model transfer files in this load iteration process is still a determining factor for the maximum possible number of design and load iteration loops that can fit into the project schedule. Only two or three load iterations are performed in most detailed design projects, despite the fact that this limits the possibility to converge at the most optimal support structure design. The reason for this long turn-around time in the load iteration process is related to the associated design tasks at the individual steps in the design loop rather than to the actual load simulations.

For example, the FD establishes a foundation design in internal design loops on basis of available information on loads as well as on the superstructure and provides the WTM subsequently with a corresponding model and set of hydrodynamic loads. The WTM establishes an integrated OWT model and performs aero-elastic load simulations in order to design the tower (and potentially modifies the controller) in internal load calculation and design loops, while keeping the foundation and hydrodynamic loads unchanged. After converging at a sufficient tower design solution, updated design loads for the new superstructure configuration and the unchanged foundation are forwarded to the FD for an assessment and potential re-design of the foundation. In consequence, the two subsystems, tower and foundation, of the support structure are designed and optimized individually.

The individual design of the tower and foundation subsystems might lead to a suboptimal solution for the overall support structure due to the limited number of design (optimization) loops in the time schedule as well as due to the fact that the optimization of one subsystem can lead to a suboptimal design of the other subsystem. For example, a mass optimization of the tower might result in a softer superstructure which needs to be balanced by a stiffer foundation in order to fulfil the natural frequency design criterions according to section 2.1. In case of monopile foundations this increased foundation stiffness might be achieved by increased diameters which lead to increased hydrodynamic loads and in consequence to the need of larger wall-thicknesses throughout the support structure. In total, this can very well lead to increased overall support structure cost despite of the optimization of the tower. Furthermore, the tower bottom diameter has a large influence on the minimum monopile and transition piece diameter in the submerged zone. Therefore, it might be beneficial to introduce the tower bottom diameter as a design parameter for an overall support structure optimization, which is often not utilized due to challenging project schedules in nowadays design practice.

Given the limitations from the limited number of design (optimization) loops and from the individual foundation and tower subsystem design, it might very well be possible to utilize further optimization potentials for the support structure design by certain modifications of the traditional design approach. In particular, the integrated support structure design approach as indicated in Figure 15 seems promising.

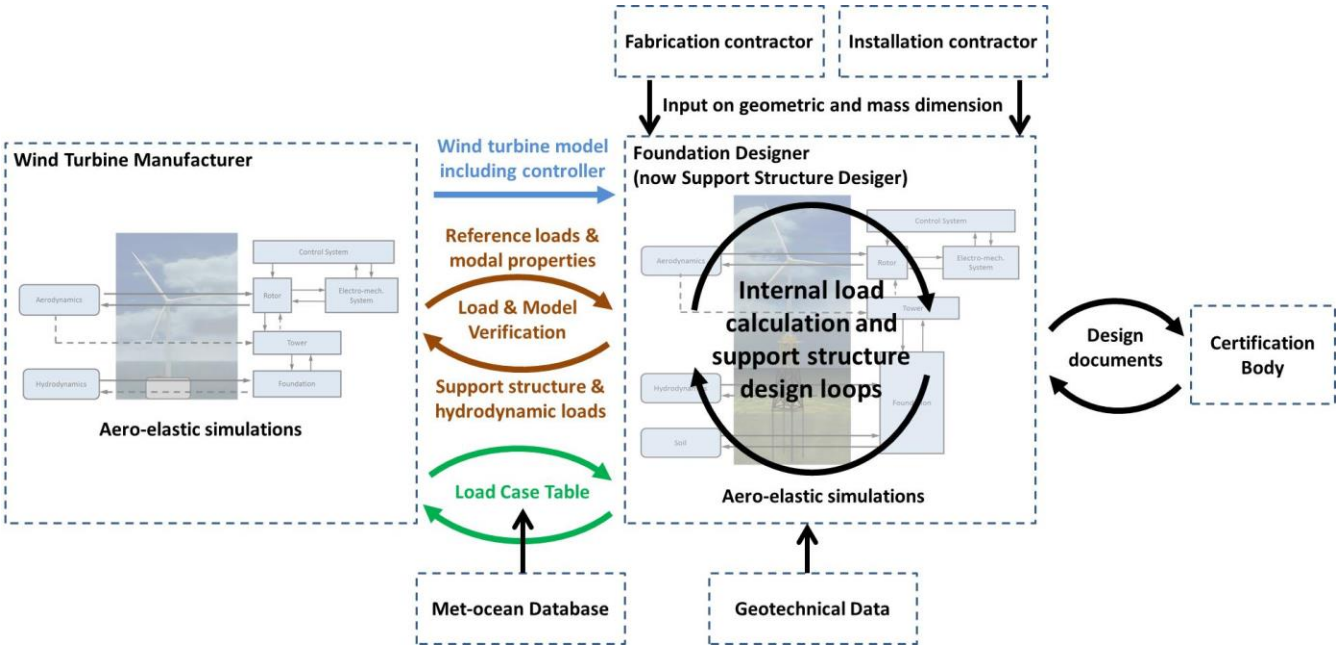

Figure 15: Innovative design approach with interactions from the perspective of the FD.

Here, the support structure is designed as one unit as e.g. discussed by Kühn et al. [39] instead of the individual design of foundation and tower. Haghi et al. [27] demonstrated the potential for considerable weight savings on support structure level in an example scenario by re-designing an actual OWT support structure. Furthermore, the foundation (or now support structure) designer performs internal aero-elastic load simulations with the integrated OWT model in internal design loops. This allows for quicker and consequently more design loops and therefore potentially higher degrees of cost optimization for the complete support structure. The value of such cost optimizations for the support structure might be substantial when assuming a 24% share of the support structure cost on the overall costs according to Figure 3.

This innovative approach to the support structure design requires the availability of an adequate coupled aero-elastic wind turbine tool and offshore tool for the calculations of the FD, similar to the coupled ROSAP-LACflex solution from section 2.4. Furthermore, the WTM would now provide the FD with a sufficiently detailed description of the RNA including controller for establishment of an integrated OWT model in the aero-elastic tool. In principle, these RNA and controller descriptions correspond to those provided to the certifying body for their independent load calculations, thereby not resulting in additional workload during the design process.

Furthermore, the existing load and model exchange interfaces from the traditional design approach would be maintained between the WTM and FD. However, for the support structure design, these interfaces would now only be used for model and load verification purposes rather than for design load calculations. For the RNA design loads, on the other hand, the WTM would still use the input on the foundation and hydrodynamic loads from the traditional approach for their integrated OWT model which would then be also complemented with an adequate tower description.

Other items and interfaces from the traditional design approach remain unchanged. For example, in the initialization phase the WTM and FD establish the LCT in a joint effort on basis of e.g. the met-ocean database.

Information on either soil profiles or directly on soil-structure interactions are provided by the geotechnical expert. Furthermore, a cost efficient support structure design requires still a close collaboration of the FD with e.g. the fabrication and installation contractor already at an early stage of the design process. This is due to the fact that optimizations of the total support structure costs can only be achieved by the simultaneous consideration of all cost items in the design process, such as for material, fabrication, installation and potentially also for scour protection

Analogously, the FD could also improve the quality and accuracy of the support structure design in the preliminary design phase by aero-elastic simulations with the integrated OWT model. This might not only lead to different conclusions on the most feasible foundation concept, but also help to improve the accuracy in the economic planning process.

2.6 Summary

The approaches taken within the individual design phases of an offshore wind turbine have an essential influence on the costs and safety. A typical traditional design process for offshore wind turbines can be split into a preliminary and detailed design phase, each with a different amount, quality and utilization of available information. Furthermore, the traditional approach for the design of individual offshore wind turbine subsystems involves different design parties, such as the foundation designer and wind turbine manufacturer. Dependent on the design phase, task and strategy these individual design parties are acting in an isolated or collaborative manner.

Innovative design approaches aim at a stronger integration of the overall structural design and requirements from the individual design parties with the goal of cost optimization. For example, this can be achieved in case the support structure is designed as one unit by the foundation designer instead of the traditional separation into tower design by the wind turbine manufacturer and foundation design by the foundation designer. In the same context, it would be very beneficial if the individual design parties perform independent integrated design load calculations with aero-elastic tools instead of the currently popular, but more time consuming sequentially integrated load calculation approach. On one hand, this would allow to increase the number of design iteration & optimization loops which are connected to the number of load iteration loops and even allow to assess unconventional design solutions in parallel or to introduce major design changes in case of unforeseen, short-term changes in the project database without compromising the project schedule. On the other hand it would also reduce the rather significant limitations and uncertainties from the required simplifying modelling and load assumption in early phases of the preliminary design process. The implications from these simplifying modelling and load assumption in the early stage of the offshore wind turbine lifecycle are potentially very different for different foundation concepts. Corresponding improvements would consequently more appropriately account for the importance of preliminary design solutions since they serve as crucial input for global project decision processes, e.g. on the foundation concept selection or the overall project feasibility assessment.

Such innovative design approaches allowing for independent, integrated load calculations with aero-elastic offshore wind turbine models by the individual design parties are therefore beneficial in the preliminary and detailed design phase. However, despite the potential advantages current design practice is typically still based on superimposed load calculation approaches in the preliminary design phase and sequentially, integrated load calculation approaches in the detailed design phase.

3 Load Calculation Approaches

Designing OWTs is an iterative process comprising numerous tasks due to the complexity introduced from the various interactions and subsystems as illustrated in Figure 4. This requires different fields of expertise and technology which is typically addressed by involvement of different design parties with design responsibilities for individual subsystems. These design parties are mainly the WTM responsible for the design of the superstructure and the FD, responsible for the foundation design.

The expertise and design responsibility for individual subsystems is reflected by the particular load simulation and design tools of the WTM and FD, i.e. the models and tools employed by the WTM and FD differ substantially from each other. On one hand, the WTM uses an aero-elastic design tool dedicated to all relevant details of the tower and RNA, such as the controller behaviour and a detailed aerodynamic description of the blades, while the foundation structure is represented by a simplified, but dynamically equivalent model. On the other hand, the FD applies a tools dedicated to a detailed description of all relevant foundation structure aspects, such as soil-structure interactions, local joint flexibilities or appurtenances, while especially the RNA is modelled in a simplified manner, thereby not allowing for aero-elastic simulations.

A central task in the design process is the calculation of global loads which are subsequently used for the subsystem and component design. Global loads are commonly calculated by either superimposed or integrated load calculation approaches with different types of system and subsystem models. Applicability of the superimposed or integrated load calculation approach depends on the design phase as well availability of data and tools as discussed by Passon & Kühn [56], [101]. Both load calculation approaches and underlying system and subsystem models have been addressed by various authors and are therefore only briefly addressed in this section. The reader is referred to Kühn [41], van der Tempel [71] and Passon [60] for further details.

3.1 Integrated load calculation approach

Fully integrated load calculation approaches aim at the simultaneous consideration of all interactions between subsystems and loads according to Figure 4. Design load calculations are commonly based on a sequentially integrated load calculation approach as described in paper 1 [61] and briefly summarized below. The underlying subsystem models and loading conditions are assembled to an integrated model in a joint effort by the WTM and FD before subjected to aero-elastic simulations. This requires an exchange of loads and models in adequate formats for the respective design tools. It is very important to ensure a proper representation of the individual subsystems and loading components in order to capture the correct dynamic behaviour and response in the aero-elastic analysis.

For the foundation such a proper representation in the aero-elastic load simulation tool is based on two criterions:

- Compatible with modelling approaches supported by the aero-elastic load simulation tool.
- Accurate representation of the dynamic behaviour.

The FD and WTM should therefore have a thorough understanding regarding characteristics and dynamic behaviour of their particular subsystems and loads within the integrated OWT model as well as of the available modelling approaches in the aero-elastic load simulation tool. For the example case of a superelement representation of a jacket type foundation in the aero-elastic analysis, it is important to choose a proper formulation and sufficient number of DOFs. Furthermore, the load expansion approach must be sufficient to capture dynamic effects in the foundation adequately. Significant errors on the conservative and non-conservative side can occur due to an inappropriate selection of the foundation formulation and load expansion as shown in section 3.3 and 6.1 or by van der Valk & Voormeeren [72].

Loads for the OWT design are established in three subsequent steps of an iterative load simulation process performed by the FD and the WTM as described in Cahpter 2 and paper 1 [61]. The individual steps and data exchange items of the sequential load calculation approach are indicated in Figure 16 and explained below.

In the first step, the FD creates a detailed model of the foundation and hydrodynamic loads with a tool specialized on the modelling of offshore structures and hydrodynamic loads. Both, the foundation structure and hydrodynamic loads are subsequently extracted and described in an adequate format for the WTM. Next to the description of the foundation structure and hydrodynamic loads, the FD provides the WTM typically with additional information relevant for the establishment of the integrated model and for verification purposes. This can include descriptions of the foundation geometry, modal properties, hydrodynamic load summaries, soil data and structural damping of the support structure.

In the second step, the WTM establishes an integrated OWT model for the used aero-elastic simulation tool by incorporation of the FDs foundation model description, hydrodynamic loads and structural damping. The integrated OWT model is subsequently used for comprehensive aero-elastic load simulations including e.g. simultaneous aerodynamic and hydrodynamic loads as well as the controller behaviour. Time series of interface responses are extracted for each simulated load case and send back to the FD.

In the third step, the FD uses an adequate load expansion procedure in order to calculate the design loads throughout the foundation structure. For that purpose, the interface response time series from the aero-elastic simulations of the second step needs to be combined with the direct loading on the foundation structure as established in the first step. Synchronization of the loads from the first and second step is important in order to ensure consistency of the hydrodynamic response contribution of the interface loads with the direct hydrodynamic loading. Depending on the type of foundation structure and the overall model and loading information the load expansion approach can be based on:

- Quasi-static approach according to Passon [60].
- Dynamic according to paper 1 [61].
- Direct expansion as shown for Guyan [26] and Craig-Bampton [9] based superelements by Passon [59].

The reader is referred to Van der Valk et al. [73] for a detailed assessment of the aforementioned approaches as well as to section 3.3 for additional information.

This sequentially integrated load calculation approach in the design process has advantages and disadvantages. However, the main reasons for application of this approach rather than complete design load calculation by each individual design party are:

- Protection of confidential data, in particular related to the RNA.
- Individual design responsibilities.
- Particular fields of expertise.
- Sophisticated load simulation and design tools for individual design tasks and subsystems.

It is important to note the following limitations of the described sequentially integrated load calculation approach. The aero-elastic analysis is limited to linear foundation descriptions and application of the Morison formula for rigid structures according to Eq. 9, thereby disregarding the hydrodynamic drag damping. Both items have been addressed for the coupled ROSAP-LACflex solution in section 2.4. Furthermore, due to the involvement of different parties the sequentially integrated load calculation approach is more time consuming than internal load iterations as described in section 2.5. This is an important disadvantage. However, efficient and well-described interfaces between the WTM and FD as well as the use of a common LCT according to section 2.3.2 allows for considerable improvements on the turn-around times. It is the author's experience that such improvements can maximize the number of design iteration loops which is typically beneficial for the overall project economy due to optimized support structures.

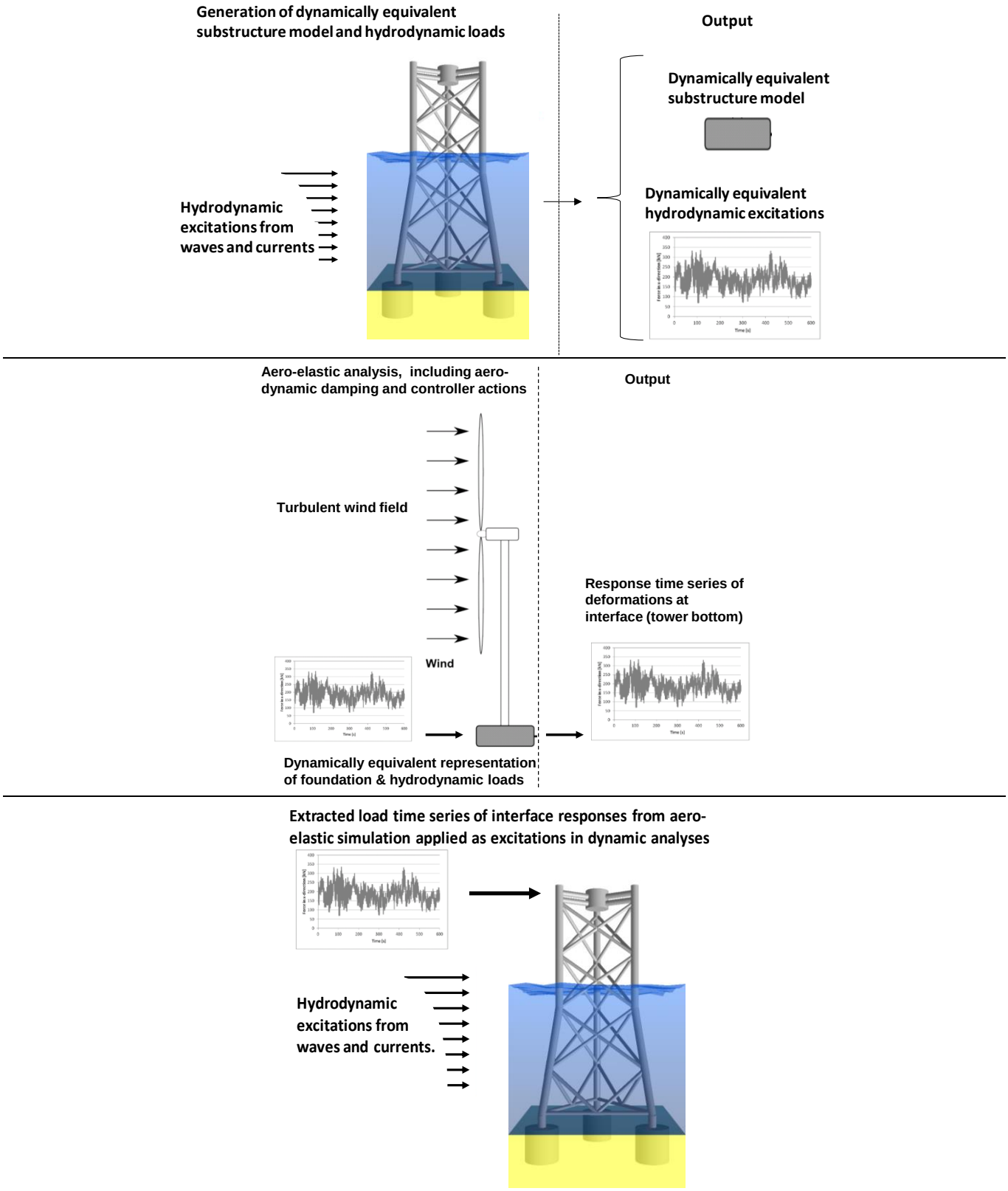

Figure 16: Subsequent steps in the sequentially integrated load calculation approach.

3.2 Superimposed load calculation approach

Superimposed load calculation approaches are typically reserved to preliminary design phases in today's design practice. The idea of the superimposed load calculation approach is based on the superposition of results obtained from a load calculation with isolated aerodynamic load and another load calculation with isolated hydrodynamic loads. The isolated load calculation models are basically simplified versions of the fully integrated model as indicated in Figure 17.

Aerodynamic responses are obtained from aero-elastic load calculations under consideration of the support structure including soil-structure interactions, tower, RNA including control system and aerodynamic excitations. For that purpose, hydrodynamic loading is disregarded by consideration of only calm sea conditions, i.e. without waves or currents. However, the influence from water added mass and contained mass on the natural frequencies is considered in the aerodynamic response due to the presence of the water.

Hydrodynamic responses are obtained from dynamic load calculations under consideration of the support structure including soil-structure interactions, tower, RNA without control system and hydrodynamic excitations. In case of hydrodynamically sensitive foundations, it might be necessary to increase structural damping in order to account for aerodynamic damping in the hydrodynamic response, see e.g. Passon [56].

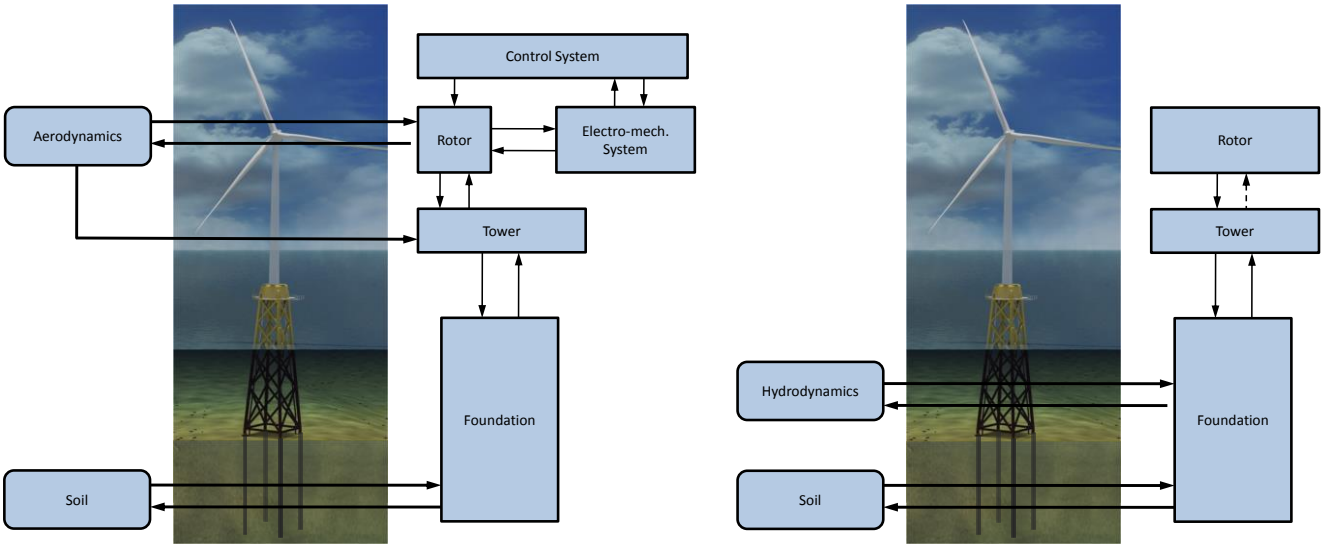

Figure 17: Modelling approach for calculation of the isolated aerodynamic response (left) and isolated hydrodynamic response (right).

The aerodynamic response and hydrodynamic response are subsequently combined to obtain the total response. So far, the results from the aerodynamic and hydrodynamic analysis have been addressed in a rather general way as responses instead of specific quantities such as loads. The reason for this generalization is the large variety of possible approaches to these combination phases encountered by the author in design practice. For example, the combination may be based on time series level for loads, deformations or directly for stresses. Furthermore, it is e.g. also very common to combine extreme peak loads in ULS and DELs or damages in FLS. However, details of the combination approach are only briefly addressed in the present thesis since focus is on the detailed design process and integrated load calculations.

As indicated, superimposed load calculation approaches are typically limited to the preliminary design phase. The scenario of identical models shown in Figure 17 and discussed before is somewhat idealized and almost never present in the preliminary design phase, except for FEED studies. Instead, the superimposed load calculation approach is based on different design parties, tools, models and limited site conditions. A less accurate, but more realistic scenario for foundation design studies in the preliminary design phase is therefore described exemplarily in the following. However, deviations from this scenario do often occur in design practice.

3.2.1 Isolated aerodynamic responses

Aerodynamic responses are calculated for ULS and FLS conditions on basis of aero-elastic simulations by the WTM as indicated in Figure 18. However, the direct involvement of the WTM is actually very limited in large parts of the preliminary design phase and so is the availability of site conditions and interactions between the FD and WTM. The aerodynamic loads are therefore often calculated in a site- and project-independent manner using a superstructure configuration with a particular turbine and a tower based on approximated dimensions, e.g. from a previous detailed design. The generic foundation is often based on a pre-selected concept with estimated dimensions based on experiences or simplified design loads. A key parameter for these generic structures is the natural frequency which is in most cases based on a soft-stiff design within *1P* and *3P*. The aerodynamic loads are generated for estimated wind conditions, commonly assuming unidirectional wind. In FLS the wind is based on a generic Weibull distribution and generic turbulences while extreme wind conditions, are used in ULS. It is important to apply calm sea conditions in case of hydrodynamic sensitive structures such as monopiles, in order to avoid a conservative double consideration of wave dynamics in the subsequent combination of aerodynamic and hydrodynamic responses. In consequence, only generic and project-independent aerodynamic responses are available. A positive recent trend in the offshore wind energy industry is a more active involvement of the WTM in the preliminary design phase. This often results in improved aerodynamic responses based on the site-specific wind climate and a site- and project-specific conceptual foundation design, thereby reducing the uncertainty from the generic wind climate and foundation.

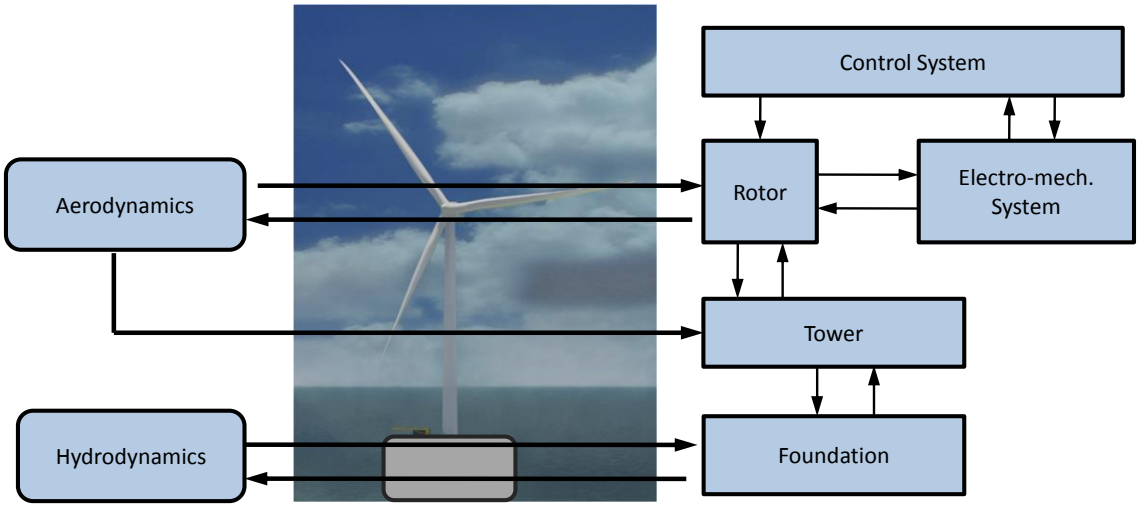

Figure 18: Aero-elastic simulation for isolated aerodynamic response.

3.2.2 Isolated hydrodynamic responses

Hydrodynamic responses are calculated with specialized offshore design tools under consideration of site-specific wave climate information such as directional SCDs by the FD. This allows for detailed modelling of the foundation under consideration of site- and structure specific hydrodynamic loads in dynamic, but not aero-elastic, simulations as indicated in Figure 19.

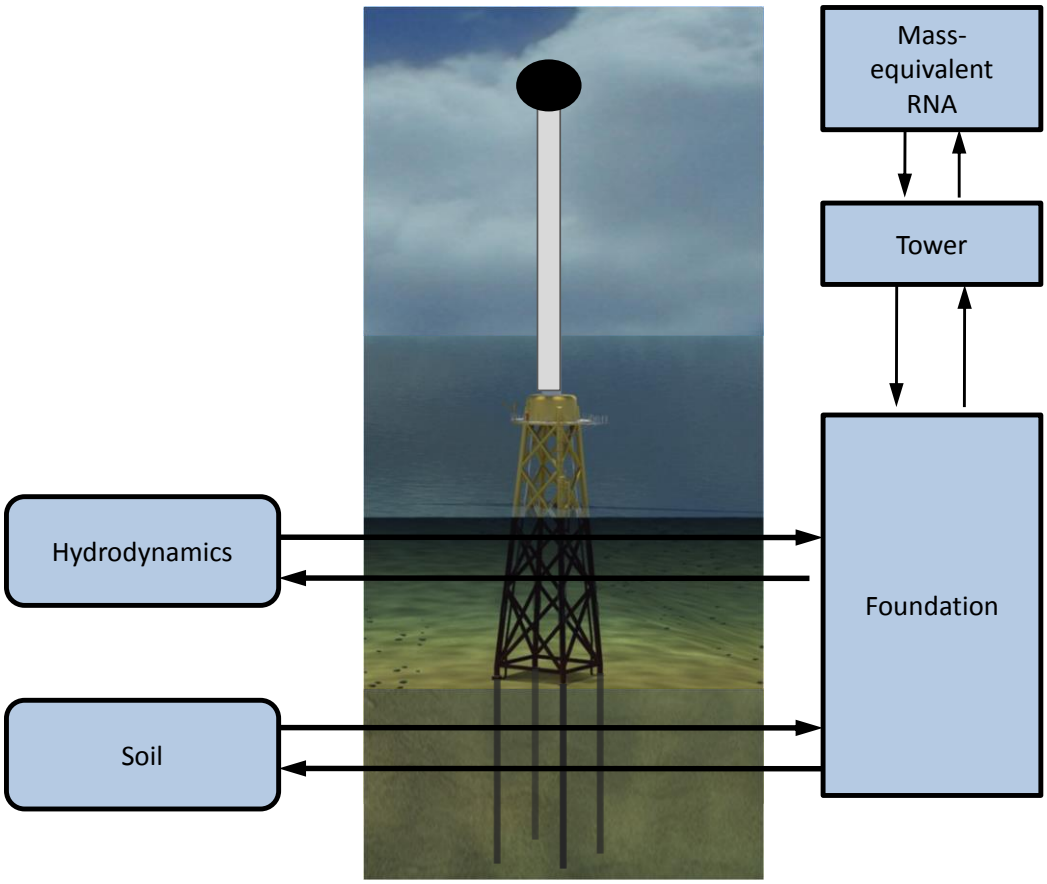

Figure 19: Dynamic simulation for isolated hydrodynamic response.

The superstructure is modelled as a generic tower and mass-equivalent RNA representation based on descriptions of the WTM. Information on the wave climate is often available while information on the soil is often limited. Therefore, only generic soil condition based on estimations are applied. Furthermore, it is important to account adequately for aerodynamic damping in the dynamic simulations. In case of available data from the WTM the aerodynamic damping is taken into account by increased structural damping dependent on e.g. wind speeds, wind-wave misalignments and assumptions on the technical availability. However, aerodynamic damping information is in many cases not available requiring estimates from the FD. A value of 4% critical damping has been suggested by Van der Tempel [71] and is often applied in design practice. Observations of the author indicate that this is a rather conservative value and that a more realistic average value for modern OWTs is in the order of 6-7% critical damping for aligned wind-wave conditions during power production.

3.2.3 Simplified combination approaches for aerodynamic and hydrodynamic responses

It is important for the involved design parties to provide a detailed description of the conditions and assumptions used for establishment of the isolated loads and the load combinations in order to avoid misunderstandings and potential design errors due to wrong assumptions in the superposition. Such errors can for example occur in case the supposedly isolated aerodynamic loads contain portions of hydrodynamic responses or in case of misunderstandings regarding the directional assumptions for the aerodynamic loads, e.g. unidirectional wind vs. generic wind rose. In particular, the following assumptions influence the accuracy of the (generic) aerodynamic loads for the site and structure under consideration:

- Interface and hub height of the generic structure.
- Wind distribution.
- Turbulence intensities.
- Modal properties.

Similarly, the hydrodynamic loads need to be carefully assessed in a site- and project-specific context. However, this is not addressed here.

The combination of aerodynamic and hydrodynamic loads is performed by the FD for the foundation design studies in the preliminary design phase. Ideally, aerodynamic loads are provided as time series at interface between tower and foundation. However, current design practice is more commonly based on only damage equivalent loads (DELs) in FLS and extreme (minimum and maximum) loads in ULS instead of time series. In FLS, an advantage of time series is the possibility to utilize cancellation effects as shown by Passon & Kühn [56] or to properly account for the load dependent stress concentration factors in tubular joints of jackets. In ULS, the main advantage is that design loads result from the actual constellation of aerodynamic and hydrodynamic responses and thereby removing the need for assumptions to find design driving extreme combination.

Dependent on the availability of data the FD is typically required to pre-process the generic aerodynamic responses prior to combination with the hydrodynamic loads or responses. For example, generic aerodynamic fatigue loads are often provided as DELs based on unidirectional wind conditions. Application of such unidirectional aerodynamic DEL might yield conservative load assumptions for one direction, but non-conservative e.g. for the perpendicular direction. The corresponding aerodynamic fatigue loads are therefore modified in accordance to actual site-specific wind rose prior to superposition with the site- and structure-specific hydrodynamic loads. DELs are based on a reference *S-N* curve slope m and an equivalent number of cycles N_{eq}. Directional DELs are established for all directions i from the unidirectional DELs by a rotation of the DEL direction and scaling of the unidirectional N_{eq} on basis of the directional probabilities p_i of the actual wind rose according to Eq. 1.

$$N_{eq,i} = p_i \cdot N_{eq} \qquad \text{Eq. 1}$$

Eq. 1 makes use of the linear damage accumulation hypothesis according to Palmgren [51] and Miner [44]. It should be noted that this is only one example of the required pre-processing activities for the isolated (generic) aerodynamic responses. Further pre-processing aspects are related to the assumptions on the tower length,

wind distribution, turbulence intensities, etc. However, the treatment of such details is part of the individual FD expertise and is as such not published here.

FLS combination of aerodynamic and hydrodynamic fatigue damages in the preliminary design phase

Based on the findings from Kühn [40] in the OptiOWECS project the combined aerodynamic and hydrodynamic damage equivalent stress range $\Delta\sigma_{ah}$ can be approximated by Eq. 2 on basis of the isolated aerodynamic and hydrodynamic damage equivalent stress ranges $\Delta\sigma_a$ and $\Delta\sigma_h$.

$$\Delta\sigma_{ah} \approx (\Delta\sigma_a^2 + \Delta\sigma_h^2)^{1/2} \quad \text{Eq. 2}$$

However, for certain design tools it might be required to perform the combination on damage level rather than on stress range level. For that purpose, the relations between damage and stress range in Eq. 3 and Eq. 4 needs to be taken into account.

$$d \approx \Delta\sigma^m \quad \text{Eq. 3}$$

$$d^{1/m} \approx \Delta\sigma \quad \text{Eq. 4}$$

Introduction of Eq. 4 in Eq. 2 leads to the combination on damage level in Eq. 5.

$$d_{ah} \approx \left(d_a^{2/m} + d_h^{2/m}\right)^{m/2} \quad \text{Eq. 5}$$

Example: *Figure 20 shows an assumed S-N curve with an inverse slope of m=5 as well as the stresses and damages for different ratios of the equivalent aerodynamic and hydrodynamic stress range for a reference number of cycles of $n_{ref} = 10^3$.*
Here, an assumed aerodynamic stress range of $\Delta\sigma_a$ = 40 N/mm² is combined with hydrodynamic stress ranges $\Delta\sigma_h$ as a fraction of the aerodynamic stress range. The stress ratio $\Delta\sigma_h/\Delta\sigma_a$ varies from 2.5% to 100%, thereby covering scenarios from one dominant stress component to equal stress components in the combination. The combined aerodynamic and hydrodynamic stress range $\Delta\sigma_{ah}$ according to Eq. 2 is shown together with the corresponding damage $d_{ah}(\Delta\sigma_{ah})$. The isolated aerodynamic fatigue damage d_a is calculated directly from $\Delta\sigma_a$, n_{ref} and the S-N curve. Analogously, the hydrodynamic fatigue damage d_h is derived on basis of $\Delta\sigma_h$, n_{ref} and the S-N curve. The combined aerodynamic and hydrodynamic fatigue damage $d_{ah,cal}$ is obtained from d_a and d_h with Eq. 5. It is obvious that the damage distributions $d_{ah,cal}$ and $d_{ah}(\Delta\sigma_{ah})$ for the combination approaches based on Eq. 2 and Eq. 5 are identical.

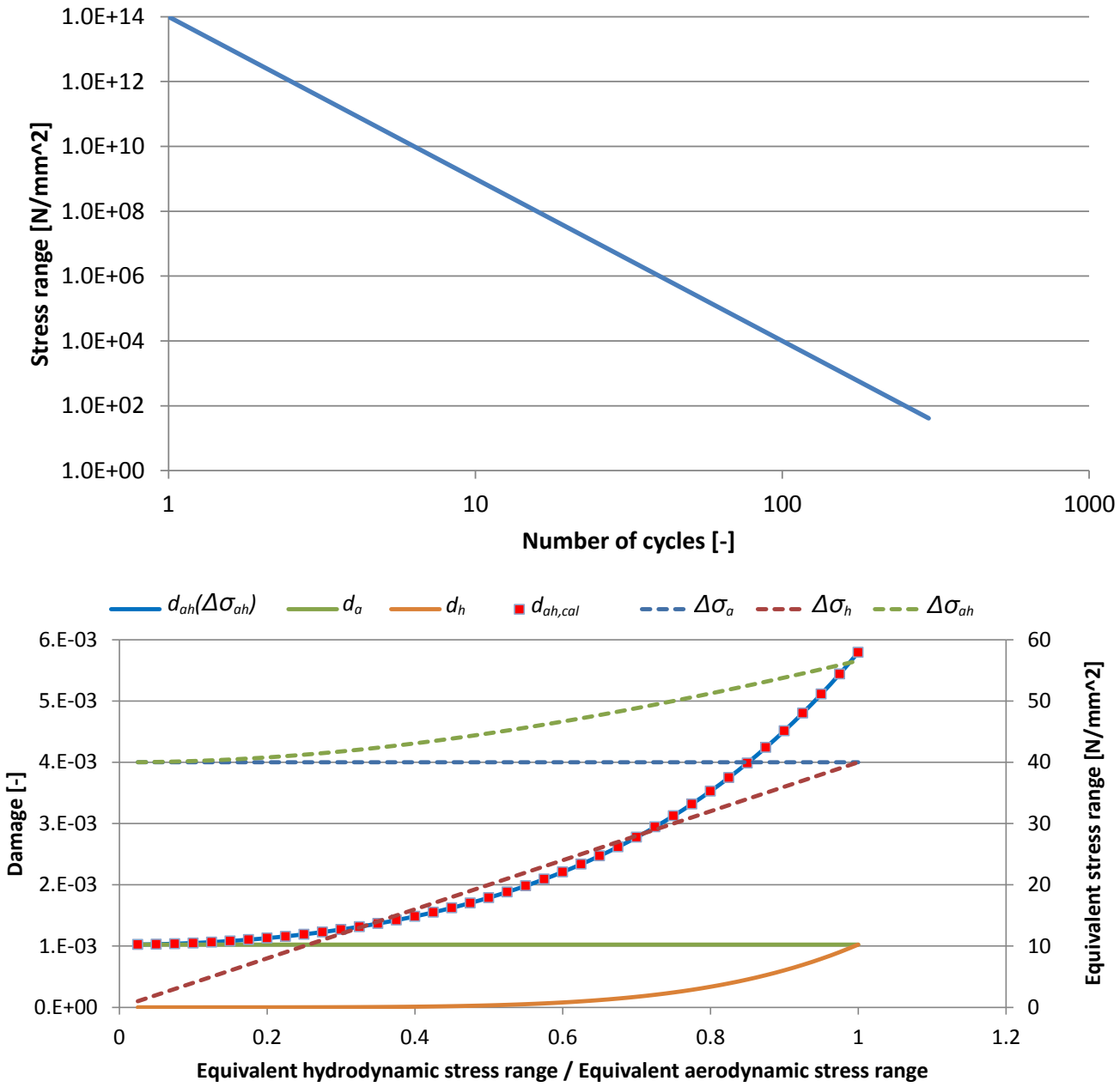

Figure 20: Generic *S-N* curve (upper) and combination of aerodynamic and hydrodynamic fatigue damage (lower).

Concluding remarks:

The DEL based design approach allows for a quick and approximate fatigue assessment. However, the designer needs to be aware of the uncertainty introduced from the underlying assumptions and structure under consideration. For example, it should be noted that the accuracy of DELs for fatigue design purposes, in particular for jacket type structures, is very questionable. This is mainly due to the fact that DELs are not sufficient for capturing of the local dynamic behaviour within the jacket (see section 3.3) and due to the strong dependency of actual load patterns for determination of stress concentration factors in the tubular joints.

ULS combination of aerodynamic and hydrodynamic loads in the preliminary design phase

As mentioned before, the ULS design is often not based on a combination of aerodynamic and hydrodynamic loads on time series level. Instead, the FD is typically provided with extreme aerodynamic loads L_{aero} in terms of maximum loads $L_{max,aero}$ extracted from the governing load cases by the WTM for combination with the hydrodynamic loads L_{hydro}. Alternatively, the extreme loads are provided in terms of extreme load statistics of the corresponding time series including e.g. mean values. Several combination approaches have been observed and applied by the author in design practice for estimating the extreme values of linear combinations of aerodynamic and hydrodynamic loads. Here, only selected aspects are addressed.

Foundation designs in ULS are often based on 50-year wind and wave extreme events reflecting DLC 6.1 and 6.2 from IEC61400-3 [88] during the preliminary design phase. In that case the extreme wave is correlated with the extreme wind since extreme waves are wind generated[8]. However, the individual realizations of the extreme wind and the extreme wave form two independent stochastic processes with respect to the occurrence of their respective peak loads. The corresponding extreme values of the wind load time series and wave load time series are therefore uncorrelated in this short-term consideration and it is very unlikely that the aerodynamic load and hydrodynamic load attain their maxima (or minima) at the same time. A combination of the worst aerodynamic loads with the worst hydrodynamic loads according to Eq. 6 is therefore too conservative and might very well lead to a premature disqualification of a foundation design in the preliminary design phase.

$$L_{max} = L_{max,aero} + L_{max,hydro} \qquad \text{Eq. 6}$$

Instead, alternative combination approaches are preferred in order to avoid too conservative design loads. An example is the following combination approach which is to some extend inspired by Turkstra [68]. Turkstra's combination rule states that the maximum load can be approximated as the sum of the maximum load from of the principal load effect and the arbitrary-point-in-time value of the remaining (secondary) load effects. In application for ULS design of OWT foundation Turkstra's rule is modified in accordance to Eq. 7, i.e. the maximum combined load L_{max} for all individual locations in the foundation is found as the worse of the maximum aerodynamic load $L_{max,aero}$ (considered as principal load effect) combined with the mean of the hydrodynamic load $L_{mean,hydro}$ (considered as secondary load effect) and vice versa.

$$L_{max} = \max \begin{cases} L_{max,aero} + L_{mean,hydro} \\ L_{mean,aero} + L_{max,hydro} \end{cases} \qquad \text{Eq. 7}$$

Alternatively, the combination of loads is often based on scaled extreme loads according to Eq. 8. The scale factors α_{aero} and α_{hydro} can be based on experiences from detailed designs of similar projects. Based on experiences from design practice, the author recommends values between 0.4 and 0.8 for design purposes.

$$L_{max} = \max \begin{cases} L_{max,aero} + \alpha_{hydro} \cdot L_{max,hydro} \\ \alpha_{aero} \cdot L_{max,aero} + L_{max,hydro} \end{cases} \qquad \text{Eq. 8}$$

[8] Exceptions are e.g. tsunamis.

3.2.4 Combination of aerodynamic and hydrodynamic responses for jackets

The combination of aerodynamic and hydrodynamic time-domain responses is rather robust for jacket type foundation structures. This is due to the fact that jacket type structures are typically not hydrodynamically sensitive.

This is illustrated in an exemplary FLS load scenario for two OWT configuration with the NREL 5MW [33] turbine. The OWT configurations are based on a soft and stiff piled jacket type foundation as described in Table 2 and Figure 21. The load scenario consists of aligned wind-wave load combinations corresponding to DLC 1.2 of IEC61400-3 [88].

Table 2 Summary of the investigated piled jacket configurations

Configuration	**H33H**	**S33N**
Site conditions		
Water depth	32m	35m
Soil type	Dense Sand	Lose Sand
Local scour depth	0.0m	3.66m
Rotor-Nacelle-Assembly		
Turbine size	5MW	
Tower height	90m	
Foundation		
Top width	13.0m	
Base width	21.0m	
x-brace levels	3	
Number of legs	3	
Horizontal mudbrace	Yes	No
Pile stickup	0.5m	3.5m

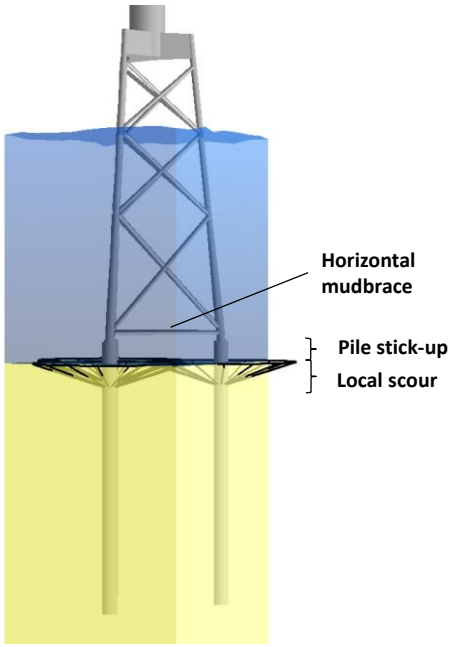

Figure 21: Generic jacket with piles.

A reference set of loads and joint fatigue lives is calculated by the sequentially integrated load calculation approach with simultaneous aerodynamic and hydrodynamic loads as introduced in the next section 3.1. For the superimposed approach, aerodynamic interface responses are obtained from the aero-elastic analysis according to step 2 of the sequentially integrated load calculation approach, however, without application of hydrodynamic loads. The hydrodynamic loads are only applied in the force-controlled, dynamic load expansion according to paper 1 [61] corresponding to step 3 of the sequentially integrated load calculation approach. This means that the superstructure inertia loads from the global dynamic responses to the hydrodynamic excitations are missing in the foundation load expansion which would introduce a potentially very non-conservative situation for monopile type foundations.

Figure 22 shows the ratios of joint fatigue lives obtained from the superimposed load calculation approach relative to those obtained from the integrated load calculation approach exemplarily for one side of both jacket configurations. Nodes are denoted by 6 alphanumeric characters while the connected element names are given by 5 alphanumeric characters in the figure. The corresponding minimum joint fatigue life ratios on the

brace and chord side are provided in the red boxes attached to the brace side, together with the corresponding element names. Fatigue life calculations in all tubular joints are based on *S-N* curves taken from DNV-OS-J101 [84]. It can be seen that an excellent agreement is achieved for all tubular joints of both jacket configurations despite the fact that inertia loads from the superstructure are missing in the hydrodynamic response of the superimposed approach.

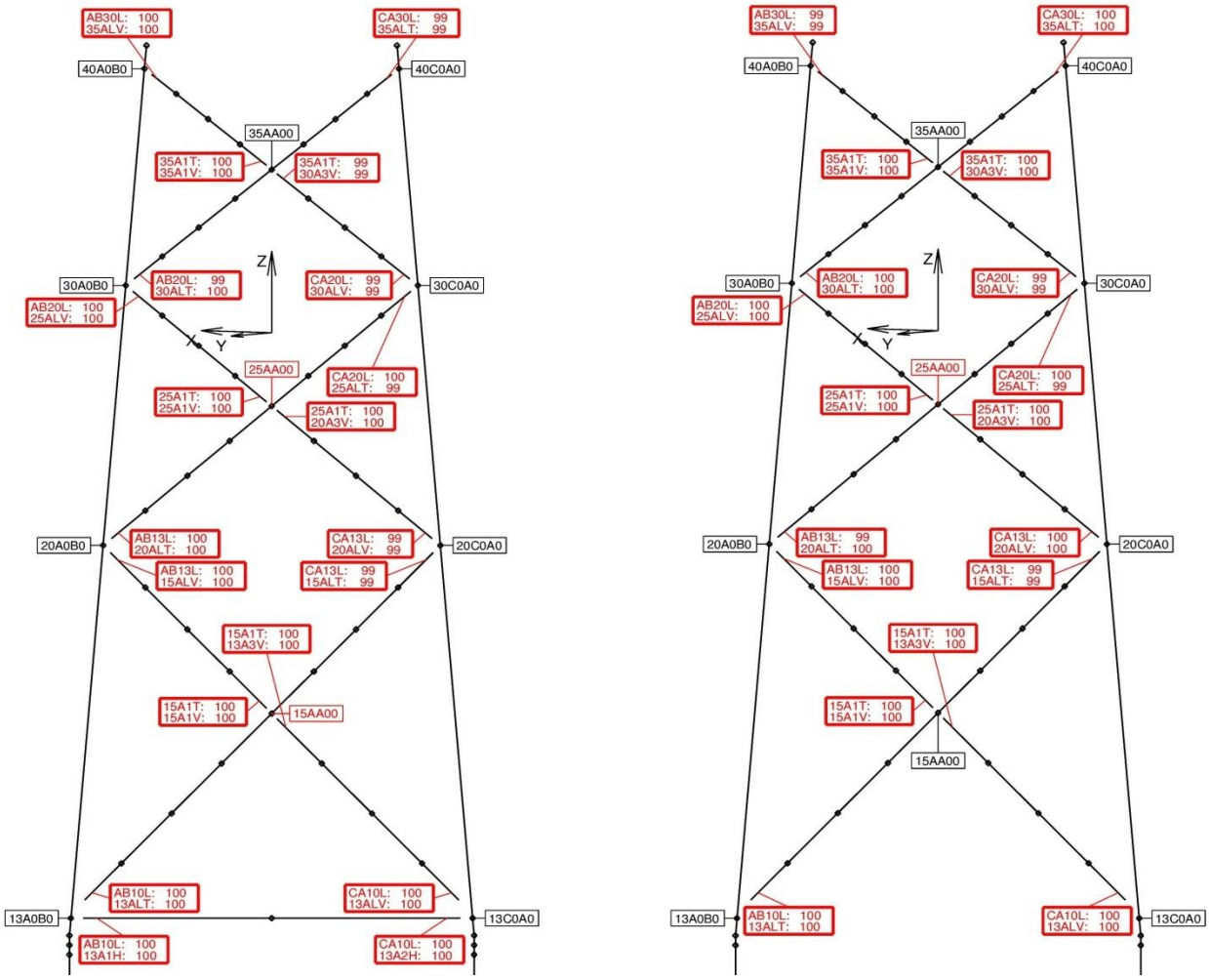

Figure 22: Ratio of joint fatigue lives from the superimposed and integrated load calculation approach in [%] for the configurations H33H (left) and S33N (right).

It has been verified before that the contributions of the superstructure to the hydrodynamic responses, in terms of inertia loads, are rather limited for the investigated OWT configurations. This introduces a certain robustness to the superimposed load combination approaches. However, the quasi-static loading contributions of the hydrodynamic loads are still relevant locally. This is shown in Figure 23 by the ratios of joint fatigue lives obtained from only the isolated aerodynamic loads relative to those obtained from simultaneous aerodynamic & hydrodynamic loads exemplarily for one side of both jacket configurations. It can be seen that some joint fatigue lives, in particular in the vicinity of the still water level, are significantly overestimated when disregarding the hydrodynamic loads.

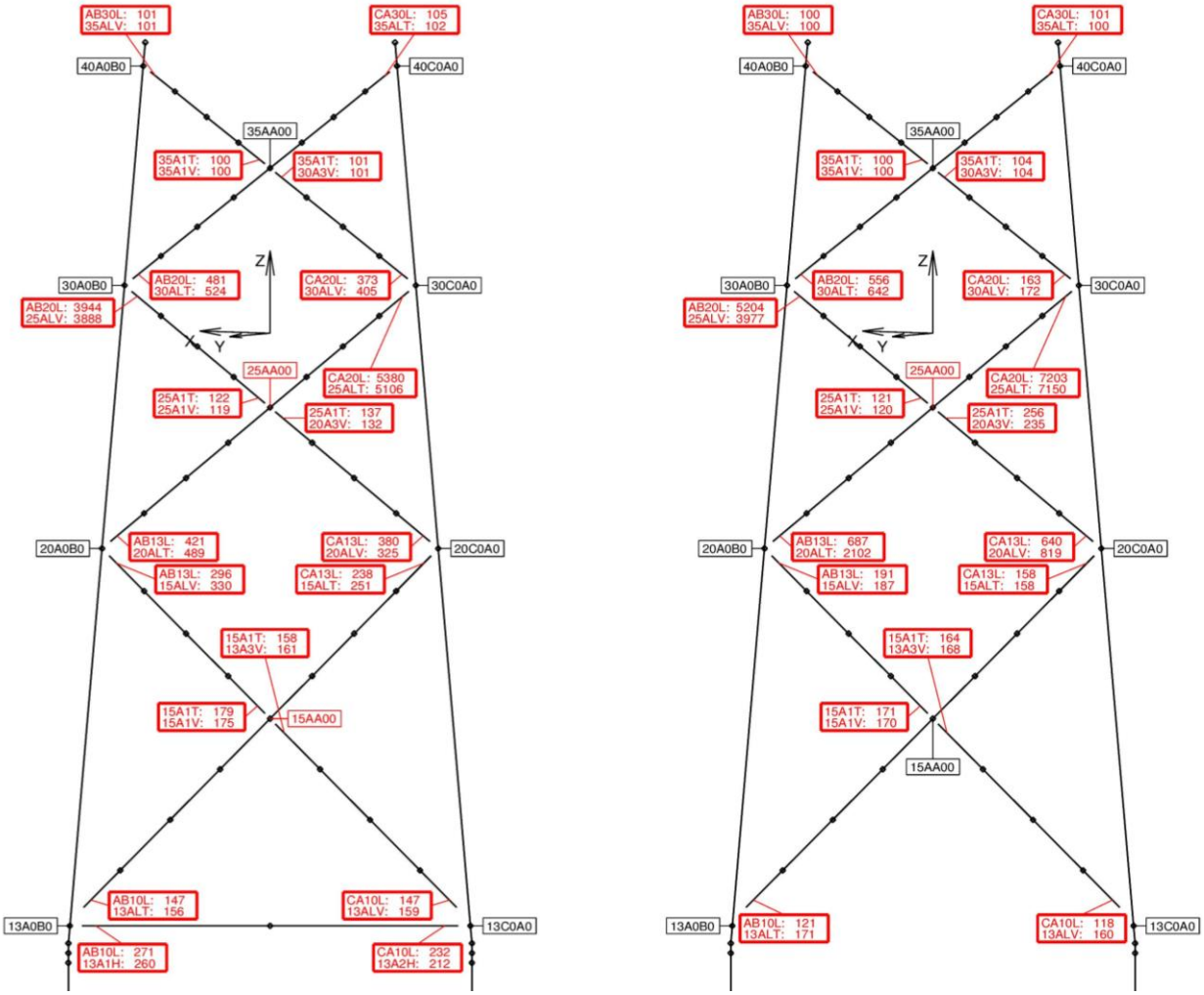

Figure 23: Ratio of joint fatigue lives from isolated aerodynamic loads and simultaneous aerodynamic & hydrodynamic loads in [%] for the configurations H33H (left) and S33N (right).

3.3 Foundation load expansion

A central part of the load iteration approach for the FD is the foundation load expansion as explained in section 3.1 and indicated at the bottom of Figure 16.

Paper 1 [61] introduces different dynamic load expansion methods and demonstrates their applicability for an exemplary jacket type foundation. Quasi-static load expansion methods exist as well; see e.g. Passon [60]. However, quasi-static methods are often reserved for monopiles in design practice. The quasi-static load expansion is summarized in Figure 24 and would for example replace the force-controlled, dynamic load expansion at the bottom of Figure 16 in the sequentially integrated load calculation approach. For a jacket configuration, Passon [60] demonstrated that it is very important to consider the inertia loads of the foundation. This section addresses the applicability of quasi-static approaches for jacket foundations.

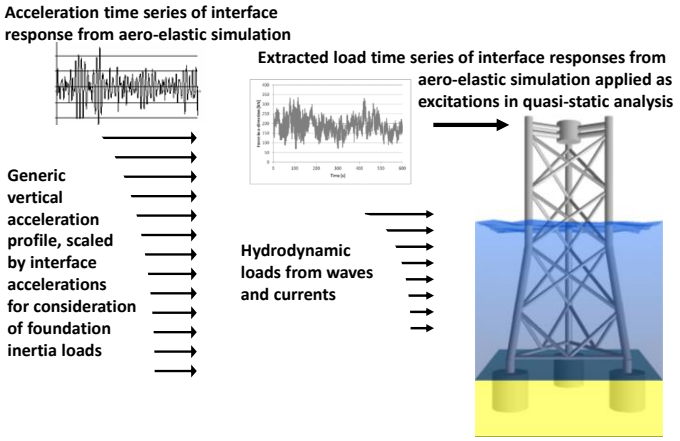

Figure 24: Quasi-static load expansion.

It is important to understand the accuracy and applicability and limitations of the quasi-static load expansion method in case of jacket type foundations. For that purpose, the force-controlled quasi-static load expansion method as described by Passon [60] and the force-controlled, dynamic load expansion method from paper 1 [61] are compared in an exemplary FLS load scenario for the two OWT configurations H33H and S33N from the previous section 3.2.4. The quasi-static load expansion is performed twice, i.e. with and without a generic acceleration profile according to Figure 24. The generic acceleration profile is applied as a simple linear, vertical profile with a value of 1 at the top (interface) and a value of 0.1 at the bottom (mudline). The FLS load scenario is based on aligned wind-wave combinations of DLC 1.2 from IEC61400-3 [88] for the Borkum Riffgrund 2 offshore wind farm project from DONG Energy A/S. Interface loads and accelerations are obtained from aero-elastic simulations in LACflex and are subsequently subjected to a load expansion in ROSAP.

Figure 25 and Figure 26 shows the calculated ratios of joint fatigue lives from the quasi-static load expansion, with and without application of a generic acceleration profile, relative to those obtained from the dynamic load expansion. For simplicity, only one side of both jacket configurations is depicted. Nodes are denoted by 6 alphanumeric characters while the connected element names given by 5 alphanumeric characters. The corresponding minimum joint fatigue life ratios on the brace and chord side are provided in the red boxes attached to the brace side, together with the corresponding element names. Fatigue life calculations in all tubular joints are based on *S-N* curves taken from DNV-OS-J101 [84].

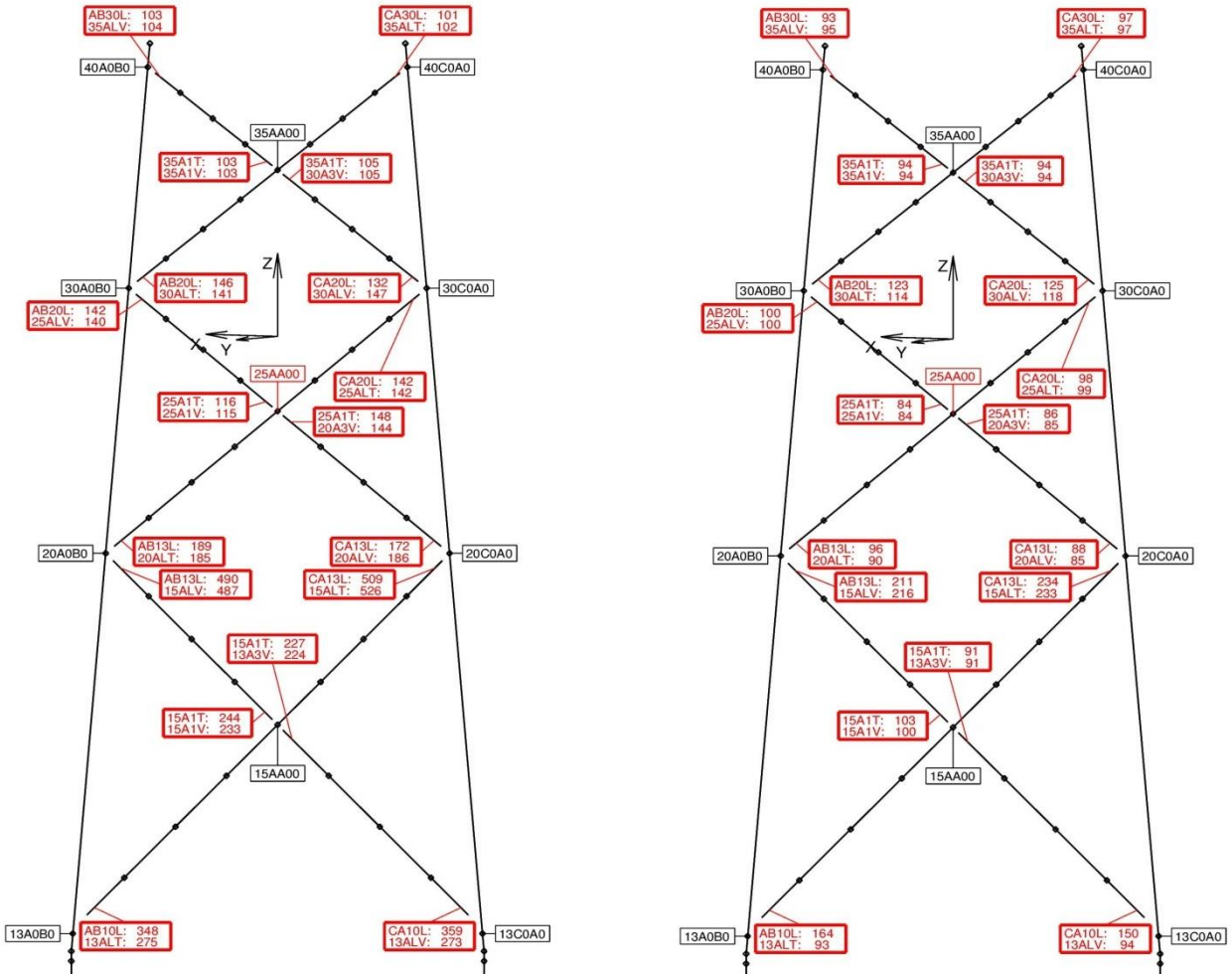

Figure 25: Ratio of joint fatigue lives from the quasi-static and dynamic load expansion in [%] for the configurations S33N. Quasi-static load expansion without (left) and with (right) foundation inertia loads from accelerations.

Reasonable approximation of the joint fatigue lives are obtained in upper bay of both configurations with the quasi-static method. Application of the generic acceleration profile has only a minor influence. In the centre bay, the joint fatigue lives are overestimated by the quasi-static method without the generic acceleration profile. Application of the generic acceleration profile leads to less severe overestimations of the joint fatigue lives for the stiff configuration H33H and even to slightly underestimated joint fatigue lives for the soft configuration S33N. For the lowest bay, the joint fatigue lives are significantly overestimated by the quasi-static method without the generic acceleration profile. Even though, that application of the generic acceleration profile in the quasi-static load expansion leads to considerable reductions, the remaining overestimation are still very high.

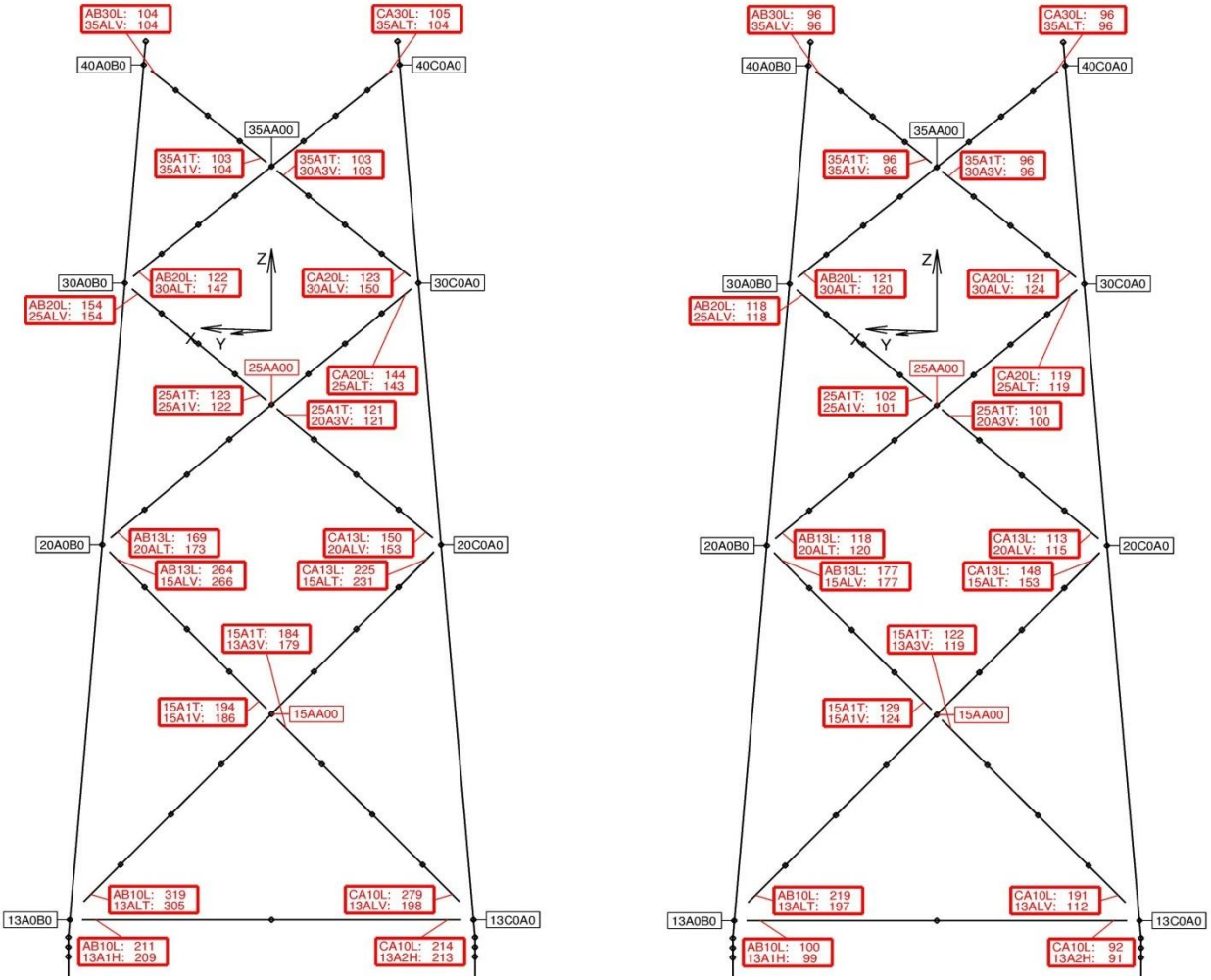

Figure 26: Ratio of joint fatigue lives from the quasi-static and dynamic load expansion in [%] for the configurations H33H. Quasi-static load expansion without (left) and with (right) foundation inertia loads from accelerations.

The joint fatigues lives of configuration S33N and H33H are overestimated by the quasi-static load expansion without the generic acceleration profile. Furthermore, both configurations show a strong tendency towards increasing overestimations at the lower bays as well as large variations in the overestimations for the individual joints. These observations are also valid in case the generic acceleration profile is considered for the quasi-static load expansion, although the overestimations are significantly reduced. It is concluded, that OWT jacket dynamics are not considered adequately by the quasi-static load expansion approaches, presumably due to the presence of the local modes according to Figure 8, which introduces a high risk for unsafe design solutions.

The author expects that a better approximation could be obtained by an adjustment of the vertical acceleration profile for consideration of the inertia loads. Nevertheless, such an adjustment would be iterative and require knowledge of the actual fatigue lives as e.g. obtained from a dynamic load expansion. The dynamic load expansion method is therefore superior for jackets and should be preferred in a detailed design situation while quasi-static approaches with application of a generic acceleration profile might be used for initial assessments of fatigue lives in the preliminary design phase.

4 Aerodynamic Damping and Hydrodynamic Drag Damping for OWT

This chapter starts with a general discussion of the influence of damping on the design loads for hydrodynamic sensitive OWTs and subsequently addresses hydrodynamic drag damping and aerodynamic damping for the design of OWT. Focus is on aerodynamic damping which is discussed for various aspects such as:

- Misaligned wind-wave scenarios.
- Methods for determination.
- Simplified engineering models.

Hydrodynamic drag damping, on the other hand, is discussed only briefly with focus on the applicability of the relative velocity form of the Morison formula. Other sources of damping are material damping, soil damping, hydrodynamic radiation damping and installed damper devices such as tuned mass dampers. However, these damping sources are discussed in detail within the present thesis.

Generally, the estimation of actual damping values is rather difficult for the support structure design of OWTs. It is the experience of the author that some numerical approaches, e.g. according to Cook & Vandiver [11], may lead to rather conservative damping estimations for monopile structures. Instead, generic values are often applied for the effective structural damping, i.e. comprising all damping contributions except aerodynamic damping and damping from additional damping devices, in the design process.

Effective structural damping values for OWT with monopile foundations according to current research, measurements and design guidelines are summarized below:

- GL recommends about 1.1-1.5% according to Gujer [25].
- ISO 19902 [89] recommends 1.0-2.0% in Annex A 12.3.12.
- Damgaard et al. [12] found a lower limit of >0.95% with 0.58% from soil damping from measurements
- Tarp-Johansen et al. [67] found 1.91% critical damping from measurements at the Horns Rev 1 wind farm and 0.99-1.23% critical damping from calculations with 0.58-0.8% from soil damping
- Devriendt et al. [16] found 1.05% critical damping from measurements at the Bligh Bank wind farm.
- Versteijlen et al. [75] found 1.5-3.0% critical damping from measurements at the Burbo wind farm.

As common practise in industrial projects, the effective structural damping for the design of monopile foundations is applied as 1% (critical), which corresponds to the lower limit found in the aforementioned literature.

Furthermore, an even lower value of approximately 0.5% critical damping is often applied for the support structure design of OWTs with jacket foundations. This is acceptable since jackets are not dynamically sensitive to hydrodynamics. Here, the relevant dynamic loads are introduced from (rotor) aerodynamics in fore-aft direction during operation, which are directly subjected to aerodynamic damping as the dominant damping source, i.e. the additional structural damping contributions are rather small in comparison.

4.1 Damping considerations for hydrodynamic sensitive OWT in FLS

Hydrodynamic sensitive OWTs are characterized by substantial global dynamic responses due to hydrodynamic excitations from typical fatigue sea states. For example, monopile based OWT configurations with large RNAs which are located at deeper water sites are hydrodynamically sensitive. The following discussions are therefore based on such types of monopile configurations. Due to the substantial global dynamic responses, the total effective damping is obviously very important for hydrodynamically sensitive OWTs and has therefore a significant influence on the loads for the FLS design. The total effective damping depends on various aspects such as actual operational conditions of the turbine, wind and wave conditions including wind-wave misalignment, soil.

In most situations the aerodynamic damping due to the aero-elastic behaviour is the main damping source. Substantial aerodynamic damping contributions are experienced during power production of the turbine. The aerodynamic response is effectively damped in such situations. However, the effective aerodynamic damping for the hydrodynamic excitations depends strongly on the actual wind-wave misalignment as further discussed in section 4.3. In case of aligned or only slightly misaligned wind-wave conditions, aerodynamic damping is typically the governing damping contribution during power production of the turbine. However, the FLS design also comprises many situations without or with very limited effective aerodynamic damping, e.g. when the turbine is idling due to a fault or for large wind-wave misalignments. In such cases the remaining damping, often summarized as structural damping, for the hydrodynamic responses is rather limited. For load simulation purposes the structural damping is often defined explicitly as viscous damping. Effective structural damping values in design practice range often in the order of 0.9 ± 0.3 % of critical damping according to the author's experience; see also e.g. Gujer [25].

The governing DLCs for the support structure design in FLS based on IEC61400-3 [88] are often the normal power production DLC1.2 and idling DLC7.2. Table 3 summarizes indicatively the probabilities of occurrence for typical North Sea conditions and effective damping conditions for the hydrodynamic excitations in case of different misalignment scenarios for both DLCs.

Table 3 Indicative overview of effective damping conditions and probabilities for DLC1.2 and DLC7.2 according to IEC61400-3 [88].

DLC	Misalignment	Effective damping	Probability
1.2	0 degree (aligned)	High	High
	30 degree	Medium high	High
	60 degree	Medium low	Medium
	90 degree	Low	Low
7.2	All cases	Low	Low

In particular for DLC7.2 and the 90 degree misalignment case for DLC1.2 the structure experiences almost no aerodynamic damping in the wave direction. Consequently, the contribution to the overall fatigue damage from these situations can be very significant for hydrodynamic sensitive structures despite a) the rather low probability of occurrence and b) the very limited contribution from aerodynamic loads. The effective structural damping is therefore extremely important for these cases.

The influence of the effective damping is now investigated for some exemplary scenarios under hydrodynamic loading. The investigations are based on the NREL 5MW turbine configuration with a monopile foundation at 30m water depth and with a 1st natural frequency of 0.29Hz as illustrated in Figure 27.

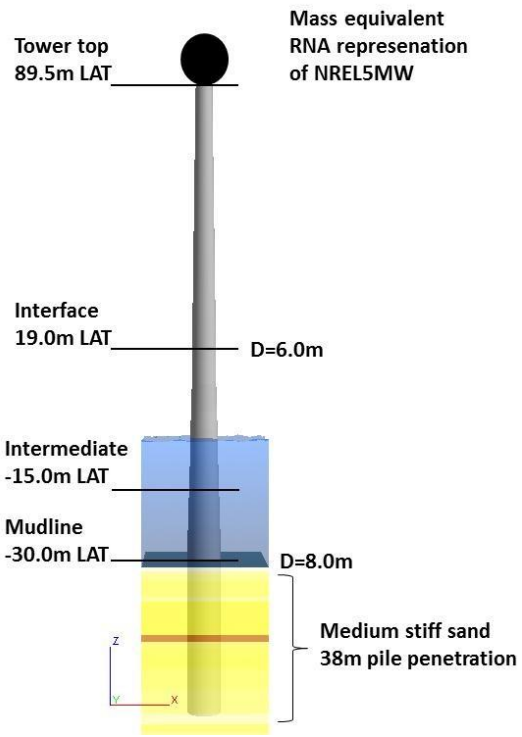

Tp [s]	0.50	1.50	2.50	3.50	4.50	5.50	6.50	7.50	8.50	9.50	10.50
Hs [m]											
7.6											
7.3											
7.0											
6.7											
6.4											
6.1											
5.8											
5.5											
5.2											
4.9											
4.6											
4.3											
4.0											
3.7											
3.4											
3.1											
2.8											
2.5											
2.2											
1.9											
1.6											
1.3											
1.0											
0.7											
0.4											
0.1											

Figure 27: OWT configuration and wave scatter matrix with markings for investigated sea states.

Isolated hydrodynamic loads are generated for the exemplary selection of marked sea states in the H_s-T_p scatter matrix on the right-hand side of Figure 27. The exemplary OWT configuration is subjected to these isolated hydrodynamic loads in a dynamic analysis under consideration of different values of total equivalent structural damping, comprising the combined effect of structural and aerodynamic damping. The high damping cases represent low misalignment situations during normal power production while low damping cases represent high misalignment conditions and/or cases in which the turbine is not operating. For all sea states and damping scenarios normalized fatigue damages are calculated at the mudline, interface, tower top and an intermediate position between mudline and interface as indicated in Figure 27. The normalized damages are calculated for equal (unit) probabilities on basis of the same *S*-*N* curve with a slope of *m*=5 in all cases.

The resulting normalized damage over damping distributions are summarized in Figure 28. The figure contains a large amount of information e.g. on the characteristics of the structure, influence of damping and dynamics of the selected sea states. However, in the context of this section focus is on the influence of damping. Therefore, only a brief example on the available information from the figure is provided at the end of this section.

The most important observation from the figures is that the damping has a very strong influence on the calculated fatigue damages especially in the low damping regions up to approximately 2-3% of critical damping

for all levels and sea states. Here, over-proportional high hydrodynamic fatigue damages can be observed at low damping scenarios.

When comparing the damage distributions in the practically relevant ranges of structural damping, i.e. approximately 0.9 ± 0.3 % of critical damping, it is clear that a good damping estimation is crucial for accurate calculations of design loads in FLS. For the same reason, designers and developers aim for an utilization of all possible damping sources motivated by the apparent cost optimization potentials. Any improvement in the damping estimation for increased effective structural damping is certainly a valid and valuable source for future cost optimizations of OWT. However, the designer must carefully assess the validity of the individual damping contributions in order to avoid unsafe OWT designs based on underestimated design loads as addressed in the following section 4.2.

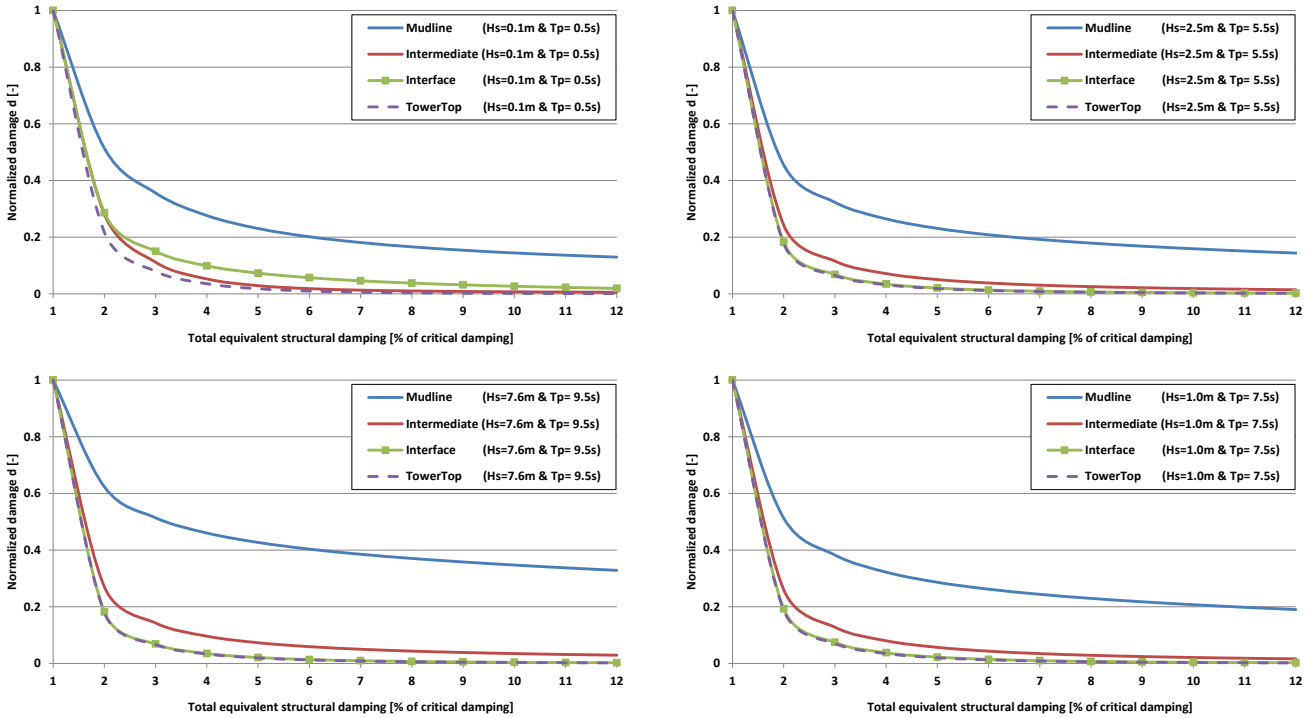

Figure 28: Normalized damage over damping distribution at different levels for different sea-states.

Exemplary assessment of available information in Figure 28: *The damping effect is quite significant for all levels, but has the least influence on the damages at Mudline. The reason is related to the individual loading contributions to the total response. The hydrodynamic responses at Mudline contain contributions from the global dynamics as well as from the direct quasi-static loading on the submerged part of the structure while both Interface and Tower top loads are pure dynamic responses without any quasi-static contributions from direct hydrodynamic loads. The Intermediate level is in the submerged zone and experiences hydrodynamic loads with both dynamic contributions as well as direct hydrodynamic loading similar, but not as pronounced as at Mudline. The damping affects only the dynamic part of the response while the quasi-static contribution from direct hydrodynamic loading is not affected. Consequently, the damping effect on the damages at Mudline is less pronounced than for the other levels. Furthermore, it can be seen from the normalized damage distribution at Mudline that the smallest dynamic amplification occurs for T_p=9.5s in comparison to the remaining cases and thus leads to the lowest influence of damping on the damage.*

4.2 Hydrodynamic drag damping

The sequentially integrated load calculation approach according to section 3.1 does not account for relative water particle kinematics in the Morison formula. It is the experience of the author that this has often been understood as a major disadvantage of the sequentially integrated load calculation approach due to the apparent loss of hydrodynamic drag damping. In this context, stakeholders of commercial offshore wind farm projects have often have high expectations on cost optimization potentials by consideration of hydrodynamic drag damping via the relative velocity form of the Morison formula as e.g. briefly discussed for jackets by King et al. [37]. However, the present section shows that the relative velocity form of the Morison formula is only applicable in special cases for monopile and jacket type foundations of OWTs.

Hydrodynamic drag damping from fluid-structure interaction effects can be considered by application of the Morsion formula with relative kinematics in load simulations for OWTs. Alternatively, it is also possible to increase the structural damping by an equivalent portion of hydrodynamic drag damping. However, both approaches for consideration of hydrodynamic damping are rather complicated in design practice of bottom-mounted OWT with monopile or jacket type foundations. On one hand, the estimation of equivalent hydrodynamic damping is not straightforward due to the lack of proper methods for the design of OWTs. On the other hand, the applicability of the relative kinematics formulation in the Morison formula is limited for practical purposes as briefly addressed in this section.

The Morison formula for calculation of sectional forces under consideration of only fluid kinematics is summarized in Eq. 9, i.e. the structure is assumed rigid for calculation of the hydrodynamic forces.

$$f_N(t) = \rho(1 + c_A)A\dot{v} + \frac{1}{2}\rho c_D D v|v| \qquad \text{Eq. 9}$$

In case relative kinematics are considered due to the flexibility of the structure, the rigid case Morison formula can be rewritten according to Eq. 10, i.e. the structural kinematics are now considered directly together with the fluid kinematics. This allows for consideration of the hydro-elastic behaviour of the OWT and may lead to a favourable hydrodynamic drag damping effect.

$$f_N(t) = \rho A\dot{v} + \rho c_A A(\dot{v} - \ddot{x}_s) + \frac{1}{2}\rho c_D D(v - \dot{x}_s)|(v - \dot{x}_s)| \qquad \text{Eq. 10}$$

with

$f_N(t)$	Sectional force per length unit at time t, normal to member axis [N/m]
ρ	Mass density of the fluid [kg/m^3]
c_A	Added mass coefficient (with cross-sectional area as reference area) [-]
c_D	Drag coefficient [-]
D	Diameter or typical cross-sectional dimension [m]
A	Cross sectional area [m^2]
v	Fluid particle (wave and/or current) velocity [m/s]
$\dot{v}$	Fluid particle acceleration [m/s^2]
$\dot{x}_s$	Velocity of member normal to axis [m/s]
$\ddot{x}_s$	Acceleration of member normal to axis [m/ s^2]

Numerous load calculation tools support the use of relative velocities in the Morison formula; see e.g. Passon [58]. Application of the relative velocity form according to Eq. 10 is generally an adequate modelling approach for floating type OWT. However, in case of bottom-mounted OWT with monopile or jacket type foundations the designer is often limited to the rigid form according to Eq. 9. This is, on one hand, introduced from the sequentially integrated modelling approach as described in section 3.1. On the other hand, the actual fluid-structure interactions are not adequately described by Eq. 10 for fixed (non-compliant) offshore structures, which cover also typical configurations of bottom-mounted OWT foundations. This has been investigated by various authors such as Moe & Verley [47], [48] or Laya et al. [43], but can also be found in design standards and guidelines.

According to ISO19902 [89], section 9.8.3.4 of Annex A, the relative velocity formulation of the Morison formula should not be used at all. The following is taken directly from ISO19902 [89]:

"*For fixed structures, the relative velocity formulation of Morison's equation should not be used for regular or random waves. When the displacement of the structure is less than the diameter of a representative member and the motion of the structure is at a high frequency compared to the frequency(ies) of the wave(s), the motion of an individual member interacts with its own wake and does not develop the hydrodynamic actions predicted by the relative velocity formulation of Morison's equation (see A.9.5.2.3 and, for example, Reference [A.9.8-4]). Using relative velocity would have the same effect on the dynamic analysis as using too large a value of the damping. In this situation, as the damping force and the environmental action do not interact, the use of a formulation with absolute water particle velocities is more realistic. The associated viscous damping coefficient should be estimated in the absence of waves.*"

According to DNV-RP-C205 [85], the applicability of Eq. 10 depends on the value of a parameter V_R, with unconditional applicability in case of $V_R \geq 20$.

$$V_R = \frac{\left(v_c + \pi \frac{H_s}{T_z}\right) T_n}{D} \qquad \text{Eq. 11}$$

with

$\left(v_c + \pi \frac{H_s}{T_z}\right)$	Particle velocity approximation close to wave surface [m/s]
v_c	Current velocity [m/s]
H_s	Significant wave height [m]
T_z	Zero up-crossing period [s]
T_n	Period of structural oscillations [s]
D	Member diameter [m]

Eq. 11 is now evaluated for a wide range of H_s-T_z combinations and different assumptions on the structural oscillations in case of exemplary monopile and jacket configurations.

Example 1: Optimistic Monopile Scenario

In this scenario a monopile configuration is considered. The period of structural oscillation, i.e. T_n=4s, is taken on basis of an assumed 1st natural frequency of 0.25Hz. Furthermore, rather optimistic conditions are assumed in order to achieve a large parameter V_R, i.e.:

- Small monopile diameter of D=4.5m.
- Large current velocity[9] of v_c=1m/s (represents an extreme current rather than a fatigue current).

Table 4 summarizes the resulting parameters V_R for a H_s-T_z SCD. It can be seen that a threshold value of $V_R \geq 20$ is achieved only for a region of very low practical relevance (green) while the majority of the H_s-T_z combinations has a value of $V_R < 20$ and even <10. The relative Morison equation for consideration of hydrodynamic drag damping in analogy to aerodynamic damping should therefore be avoided for the design of monopile type foundation structures.

Table 4 Scatter matrix of parameter V_R for D=4.5m, v_c=1m/s and T_n=4s.

T_z[s]	0.5	1.5	2.5	3.5	4.5	5.5	6.5	7.5	8.5	9.5	10.5
H_s[m]											
10.0	56.7	19.5	12.1	8.9	7.1	6.0	5.2	4.6	4.2	3.8	3.5
9.5	53.9	18.6	11.5	8.5	6.8	5.7	5.0	4.4	4.0	3.7	3.4
9.0	51.2	17.6	10.9	8.1	6.5	5.5	4.8	4.2	3.8	3.5	3.3
8.5	48.4	16.7	10.4	7.7	6.2	5.2	4.5	4.1	3.7	3.4	3.1
8.0	45.6	15.8	9.8	7.3	5.9	5.0	4.3	3.9	3.5	3.2	3.0
7.5	42.8	14.9	9.3	6.9	5.5	4.7	4.1	3.7	3.4	3.1	2.9
7.0	40.0	13.9	8.7	6.5	5.2	4.4	3.9	3.5	3.2	2.9	2.8
6.5	37.2	13.0	8.1	6.1	4.9	4.2	3.7	3.3	3.0	2.8	2.6
6.0	34.4	12.1	7.6	5.7	4.6	3.9	3.5	3.1	2.9	2.7	2.5
5.5	31.6	11.1	7.0	5.3	4.3	3.7	3.3	2.9	2.7	2.5	2.4
5.0	28.8	10.2	6.5	4.9	4.0	3.4	3.0	2.8	2.5	2.4	2.2
4.5	26.0	9.3	5.9	4.5	3.7	3.2	2.8	2.6	2.4	2.2	2.1
4.0	23.2	8.3	5.4	4.1	3.4	2.9	2.6	2.4	2.2	2.1	2.0
3.5	20.4	7.4	4.8	3.7	3.1	2.7	2.4	2.2	2.0	1.9	1.8
3.0	17.6	6.5	4.2	3.3	2.8	2.4	2.2	2.0	1.9	1.8	1.7
2.5	14.9	5.5	3.7	2.9	2.4	2.2	2.0	1.8	1.7	1.6	1.6
2.0	12.1	4.6	3.1	2.5	2.1	1.9	1.7	1.6	1.5	1.5	1.4
1.5	9.3	3.7	2.6	2.1	1.8	1.7	1.5	1.4	1.4	1.3	1.3
1.0	6.5	2.8	2.0	1.7	1.5	1.4	1.3	1.3	1.2	1.2	1.2
0.5	3.7	1.8	1.4	1.3	1.2	1.1	1.1	1.1	1.1	1.0	1.0

[9] It should be noted that currents can even be disregarded in FLS according to IEC61400-3 [88].

Example 2: Optimistic Jacket Scenario

In this scenario for a jacket configuration some rather optimistic conditions are assumed in order to achieve a large parameter V_R, i.e.:

- Small member diameter of D=0.5m (e.g. braces).
- Large current velocity of v_c=1m/s (represents an extreme current rather than a fatigue current).
- Period of structural oscillation taken as T_n=4s, corresponding to a relatively low 1st natural frequency of 0.25Hz for jackets.

A larger number H_s-T_z combinations in the SCD correspond to values of $V_R \geq 20$ as shown in Table 5 with favourable conditions for the diameter, current velocity and period of structural oscillations. However, even in this very optimistic scenario a certain range of practically relevant H_s-T_z combinations show values of $V_R < 20$.

Table 5 Scatter matrix of parameter V_R for D=0.5m; v_c=1m/s and T_n=4s.

T_z[s]	0.5	1.5	2.5	3.5	4.5	5.5	6.5	7.5	8.5	9.5	10.5
H_s[m]											
10.0	510.7	175.6	108.5	79.8	63.9	53.7	46.7	41.5	37.6	34.5	31.9
9.5	485.5	167.2	103.5	76.2	61.1	51.4	44.7	39.8	36.1	33.1	30.7
9.0	460.4	158.8	98.5	72.6	58.3	49.1	42.8	38.2	34.6	31.8	29.5
8.5	435.3	150.4	93.5	69.0	55.5	46.8	40.9	36.5	33.1	30.5	28.3
8.0	410.1	142.0	88.4	65.4	52.7	44.6	38.9	34.8	31.7	29.2	27.1
7.5	385.0	133.7	83.4	61.9	49.9	42.3	37.0	33.1	30.2	27.8	26.0
7.0	359.9	125.3	78.4	58.3	47.1	40.0	35.1	31.5	28.7	26.5	24.8
6.5	334.7	116.9	73.3	54.7	44.3	37.7	33.1	29.8	27.2	25.2	23.6
6.0	309.6	108.5	68.3	51.1	41.5	35.4	31.2	28.1	25.7	23.9	22.4
5.5	284.5	100.2	63.3	47.5	38.7	33.1	29.3	26.4	24.3	22.6	21.2
5.0	259.3	91.8	58.3	43.9	35.9	30.8	27.3	24.8	22.8	21.2	20.0
4.5	234.2	83.4	53.2	40.3	33.1	28.6	25.4	23.1	21.3	19.9	18.8
4.0	209.1	75.0	48.2	36.7	30.3	26.3	23.5	21.4	19.8	18.6	17.6
3.5	183.9	66.6	43.2	33.1	27.5	24.0	21.5	19.7	18.3	17.3	16.4
3.0	158.8	58.3	38.2	29.5	24.8	21.7	19.6	18.1	16.9	15.9	15.2
2.5	133.7	49.9	33.1	26.0	22.0	19.4	17.7	16.4	15.4	14.6	14.0
2.0	108.5	41.5	28.1	22.4	19.2	17.1	15.7	14.7	13.9	13.3	12.8
1.5	83.4	33.1	23.1	18.8	16.4	14.9	13.8	13.0	12.4	12.0	11.6
1.0	58.3	24.8	18.1	15.2	13.6	12.6	11.9	11.4	11.0	10.6	10.4
0.5	33.1	16.4	13.0	11.6	10.8	10.3	9.9	9.7	9.5	9.3	9.2

Example 3: Optimistic Jacket Scenario for higher modes

Dynamic responses of OWT with jacket type foundations may contain substantial contributions of higher modes as exemplarily shown in section 6.1.5. The previous scenario from example 2 is therefore re-assessed for oscillations in higher modes:

- Small member diameter of D=0.5m (e.g. braces).
- Large current velocity of v_c=1m/s (represents rather an extreme current than a fatigue current).
- Period of structural oscillation taken as T_n=1s, corresponding to a relatively low 2nd global bending frequency of 1.00Hz for OWTs with jacket foundations.

Table 6 summarizes the resulting parameters V_R for a range of H_s-T_z combinations. It can be seen that a threshold value of $V_R \geq 20$ is achieved only for a region of very low practical relevance (green) while the majority of the H_s-T_z combinations in the SCD correspond to values of $V_R < 20$ and even <10. Due to the potentially substantial contribution of higher modes in the dynamic response of OWT with jacket foundations, the relative Morison equation for consideration of hydrodynamic drag damping should be avoided.

Table 6 Scatter matrix of parameter V_R for D=0.5m; v_c=1m/s and T_n=1s.

T_z[s]	0.5	1.5	2.5	3.5	4.5	5.5	6.5	7.5	8.5	9.5	10.5
H_s[m]											
10.0	127.7	43.9	27.1	20.0	16.0	13.4	11.7	10.4	9.4	8.6	8.0
9.5	121.4	41.8	25.9	19.1	15.3	12.9	11.2	10.0	9.0	8.3	7.7
9.0	115.1	39.7	24.6	18.2	14.6	12.3	10.7	9.5	8.7	8.0	7.4
8.5	108.8	37.6	23.4	17.3	13.9	11.7	10.2	9.1	8.3	7.6	7.1
8.0	102.5	35.5	22.1	16.4	13.2	11.1	9.7	8.7	7.9	7.3	6.8
7.5	96.2	33.4	20.8	15.5	12.5	10.6	9.2	8.3	7.5	7.0	6.5
7.0	90.0	31.3	19.6	14.6	11.8	10.0	8.8	7.9	7.2	6.6	6.2
6.5	83.7	29.2	18.3	13.7	11.1	9.4	8.3	7.4	6.8	6.3	5.9
6.0	77.4	27.1	17.1	12.8	10.4	8.9	7.8	7.0	6.4	6.0	5.6
5.5	71.1	25.0	15.8	11.9	9.7	8.3	7.3	6.6	6.1	5.6	5.3
5.0	64.8	22.9	14.6	11.0	9.0	7.7	6.8	6.2	5.7	5.3	5.0
4.5	58.5	20.8	13.3	10.1	8.3	7.1	6.3	5.8	5.3	5.0	4.7
4.0	52.3	18.8	12.1	9.2	7.6	6.6	5.9	5.4	5.0	4.6	4.4
3.5	46.0	16.7	10.8	8.3	6.9	6.0	5.4	4.9	4.6	4.3	4.1
3.0	39.7	14.6	9.5	7.4	6.2	5.4	4.9	4.5	4.2	4.0	3.8
2.5	33.4	12.5	8.3	6.5	5.5	4.9	4.4	4.1	3.8	3.7	3.5
2.0	27.1	10.4	7.0	5.6	4.8	4.3	3.9	3.7	3.5	3.3	3.2
1.5	20.8	8.3	5.8	4.7	4.1	3.7	3.4	3.3	3.1	3.0	2.9
1.0	14.6	6.2	4.5	3.8	3.4	3.1	3.0	2.8	2.7	2.7	2.6
0.5	8.3	4.1	3.3	2.9	2.7	2.6	2.5	2.4	2.4	2.3	2.3

Example 4: Realistic Jacket Scenario

In this scenario for a jacket configuration, some more realistic conditions are assumed in comparison to the scenario from example 2:

- Medium member diameter of D=0.7m (for braces; leg members have typically larger diameters).
- Small current velocity of v_c=0.1m/s.
- Period of structural oscillation taken as T_n=3.33s, corresponding to a 1st natural frequency of 0.30Hz which is a representative value for jackets according to author's experiences.

The values for V_R are summarized for the H_s-T_z combinations in Table 7. It can be seen that the threshold value of $V_R \geq 20$ is exceeded only for a region of rather low practical relevance, since such sea states hardly occur. The majority of typically FLS relevant H_s-T_z combinations in the SCD correspond to values of $V_R < 20$. Therefore, the relative velocity form of the Morison formula according to Eq. 10 should be avoided for most members of jacket type foundations.

Table 7 Scatter matrix of parameter V_R for D=0.7m; v_c=0.1m/s and T_n=3.33s.

T_z[s]	0.5	1.5	2.5	3.5	4.5	5.5	6.5	7.5	8.5	9.5	10.5
H_s[m]											
10.0	299.4	100.1	60.3	43.2	33.7	27.6	23.5	20.4	18.1	16.2	14.7
9.5	284.4	95.1	57.3	41.0	32.0	26.3	22.3	19.4	17.2	15.4	14.0
9.0	269.5	90.1	54.3	38.9	30.4	24.9	21.2	18.4	16.3	14.6	13.3
8.5	254.5	85.2	51.3	36.8	28.7	23.6	20.0	17.4	15.4	13.8	12.6
8.0	239.6	80.2	48.3	34.6	27.0	22.2	18.9	16.4	14.5	13.1	11.9
7.5	224.7	75.2	45.3	32.5	25.4	20.9	17.7	15.4	13.7	12.3	11.2
7.0	209.7	70.2	42.3	30.4	23.7	19.5	16.6	14.4	12.8	11.5	10.4
6.5	194.8	65.2	39.3	28.2	22.1	18.1	15.4	13.4	11.9	10.7	9.7
6.0	179.8	60.3	36.3	26.1	20.4	16.8	14.3	12.4	11.0	9.9	9.0
5.5	164.9	55.3	33.4	24.0	18.7	15.4	13.1	11.4	10.1	9.1	8.3
5.0	149.9	50.3	30.4	21.8	17.1	14.1	12.0	10.4	9.3	8.3	7.6
4.5	135.0	45.3	27.4	19.7	15.4	12.7	10.8	9.4	8.4	7.6	6.9
4.0	120.0	40.3	24.4	17.6	13.8	11.3	9.7	8.4	7.5	6.8	6.2
3.5	105.1	35.3	21.4	15.4	12.1	10.0	8.5	7.5	6.6	6.0	5.5
3.0	90.1	30.4	18.4	13.3	10.4	8.6	7.4	6.5	5.8	5.2	4.7
2.5	75.2	25.4	15.4	11.2	8.8	7.3	6.2	5.5	4.9	4.4	4.0
2.0	60.3	20.4	12.4	9.0	7.1	5.9	5.1	4.5	4.0	3.6	3.3
1.5	45.3	15.4	9.4	6.9	5.5	4.6	3.9	3.5	3.1	2.8	2.6
1.0	30.4	10.4	6.5	4.7	3.8	3.2	2.8	2.5	2.2	2.0	1.9
0.5	15.4	5.5	3.5	2.6	2.1	1.8	1.6	1.5	1.4	1.3	1.2

Concluding summary

The applicability of the relative velocity form of the Morison formula according to Eq. 10 has been assessed on basis of Eq. 11 from DNV-RP-C205 [85] for a large number of sea-states applied on different structural configurations and oscillation conditions. It has been shown that Eq. 10, for implicit consideration of hydrodynamic drag damping, is in most cases not applicable for monopiles or typical jacket configurations. Even though the relative velocity form of the Morison formula according to Eq. 10 could be applied for some sea-state conditions in case of small diameter jacket members and lower frequency oscillations, the practical benefit of hydrodynamic damping is limited. This is due to the fact that jackets are typically not hydrodynamic sensitive as shown in section 3.2.4. However, in case of monopiles, the author recommends to subject the hydrodynamic drag damping effect to further studies in order to assess if any damping contributions can be utilized for design purposes since even a small damping portion can help to reduce fatigue damages as illustrated in section 4.1.

4.3 Aerodynamic damping

Global dynamics of modern variable speed, pitch-controlled wind turbines are significantly influenced by their aero-elastic behavior and controller characteristics. For typical aerodynamic designs of wind turbine rotors a substantial damping contribution results from the aero-elastic behavior of the wind turbine in operation, i.e. the aerodynamic damping. Aerodynamic damping is mainly introduced from rotor aerodynamics of the oscillating wind turbine although additional contributions are also introduced from the aerodynamic drag loading on the tower and RNA. However, in this section focus is on the main contribution from the rotor aerodynamics. For detailed descriptions on rotor aerodynamics and aerodynamic design of wind turbine rotors the reader is referred to Hansen [30] and Gasch & Twele [23], [24].

The aerodynamic damping effect is typically many times larger than the combined damping effect from all other contributions such as material damping, soil damping and hydrodynamic damping. Consideration of the aerodynamic damping effect is therefore essential for a realistic description of the global dynamics, in particular for simultaneous aerodynamic and hydrodynamic excitations. In this context, the aerodynamic damping contribution is of crucial importance for economic designs of hydrodynamic sensitive OWT support structures. However, it should be noted that aerodynamic damping is a directional effect with the largest magnitude in fore-aft direction while only small contributions are available for the side-side direction. This is an important fact which can lead to substantially increased hydrodynamic responses in case of misalignment between wind direction and wave direction. Several authors have addressed the aerodynamic damping effect such as Kühn [41] and Valamanesh & Myers [69]. Therefore, only a brief summary is provided here with focus on aerodynamic damping contributions from rotor aerodynamics in out-of-plane direction. This summary is complemented with further discussions and results for the effective directional aerodynamic damping in case of misaligned wind and wave directions and the provision of a simple engineering model for estimation of the aerodynamic damping in such cases.

4.3.1 Out-of-plane aerodynamic damping

This section illustrates in a simplified manner the aerodynamic conditions at the rotor during global oscillations of the OWT leading to aerodynamic damping effects. Focus is on out-of-plane aerodynamic damping. However, it should be noted that a certain portion of in-plane aerodynamic damping exists as well and is addressed in the following sections. The descriptions and assumptions for the out-of-plane aerodynamic damping are largely based on Kühn [41]. Additional consideration on in-plane and out-of-plane aerodynamic damping are provided by Hansen [31] and Brøndsted & Nijssen [5], however, with focus on individual rotor blades and aerodynamic stability. Furthermore, this section is based on descriptions using blade element momentum theory approach; see e.g. Hansen [30].

The following simplifying assumptions are used:

- Aerodynamic damping only introduced from rotor aerodynamics.
- Limitation to fore-aft oscillations for out-of-plane damping and to side-side oscillations for in-plane damping.
- Only translational deformations considered for the RNA.

- No yaw error.
- Only attached flow for the wind turbine in operation with steady state conditions, e.g. constant rotor speed Ω, blade pitch angle, axial induction factor a and uniform wind.

These assumptions are not valid in reality due to e.g. turbulence in the wind, the variable rotor speed and varying pitch angles of modern OWT. However, this simplified scenario provides valuable insight and a basic understanding of the aerodynamic damping effect which is useful for the extension to cases with misaligned wind and wave directions.

Oscillations of the support structure and RNA influence the aerodynamic conditions at the rotor blades by introduction of an additional velocity component in upwind and downwind direction. In consequence, the individual rotor blade elements experience slight changes in the effective wind speed v and therefore in the resulting inflow velocity c and angle of attack α. The changed angle of attack leads to a change in the lift coefficient $c_L(\alpha)$. With the air density ρ, chord length b, and thickness t the resulting lift force at the blade element dF_L is calculated by Eq. 12.

$$dF_L = 0.5 \cdot \rho \cdot c_L(\alpha) \cdot c^2 \cdot (t \cdot b) \qquad \text{Eq. 12}$$

The out-of-plane aerodynamic damping effect is exemplarily illustrated in Figure 29 for one oscillation cycle of the OWT in fore-aft direction. In the upper row, the individual states of the oscillation are shown.

The second row in Figure 29 shows the effective inflow velocity components at the cross section of a rotor blade element in distance r from the rotor axis. Individual inflow velocities components are $v(1 - a)$ from the wind, $\dot{u}_{RNA}$ from RNA fore-aft oscillations and the in-plane velocity Ωr as introduced from the rotor speed Ω.

The resulting total inflow velocity c has an angle of attack α relative to the blade chord which determines the lift coefficient $c_L(\alpha)$ as shown in the third row of Figure 29.

The fourth row in Figure 29 shows the corresponding aerodynamic forces at the blade element including changes in the lift force dF_L from varying inflow velocities c and lift coefficients $c_L(\alpha)$ compared to the oscillation-free case. Due to the minor influence of (rotor) drag loads in the aerodynamic damping the changes for the drag coefficient $c_D(\alpha)$ and drag force at the blade element dF_D are disregarded for simplicity.

The rotor thrust force at the bladed element dF_T is obtained from projections of dF_L and dF_D perpendicular to the rotor plane.

The oscillation cycle in Figure 29 is divided in four stages (sorted into the four columns):

- In stage 1, the oscillation has reached its maximum amplitude in upwind direction and the oscillation velocity is therefore equal to zero. The effective wind speed $v(1 - a)$ experienced by the rotor is equal to the oscillation-free case.
- In stage 2, the RNA experiences the maximum oscillation velocity in downwind direction with zero amplitude of the oscillation. Since the RNA moves in direction of the wind, the effective wind speed at the blade element is reduced by the oscillation velocity of the RNA to $v(1 - a) - \dot{u}_{RNA}$. This leads to a decreased inflow velocity compared to the oscillation-free case. The angle of attack and therefore the lift coefficient are decreased leading to a lower lift force dF_L and (projected) thrust force dF_T at the

blade element. The thrust force at the blade element dF_T is changed by ΔdF_T in comparison to the oscillation-free case. The sum of ΔdF_T from all blade elements leads to a decrease ΔF_T in rotor thrust. Compared to the oscillation-free case the difference ΔF_T in rotor thrust is an additional force, which is superimposed to the undisturbed rotor thrust F_T against the current oscillation direction and thus effectively acting as a damping force.

- In stage 3, the oscillation has reached its maximum amplitude in downwind direction and the oscillation velocity is therefore equal to zero. The effective wind speed experienced by the rotor is equal to the oscillation-free case.
- In stage 4, the RNA experiences the maximum oscillation velocity in upwind direction with zero amplitude of the oscillation. Since the RNA moves against wind direction, the effective wind speed at the blade element is increased by the oscillation velocity of the RNA to $v(1 - a) + \dot{u}_{RNA}$. This leads to an increased inflow velocity compared to the oscillation-free case. The angle of attack and therefore the lift coefficient are increased which leads to a higher lift force dF_L and (projected) thrust force dF_T at the blade element. The thrust force at the blade element dF_T is changed by ΔdF_T in comparison to the oscillation-free case. The sum of ΔdF_T from all blade elements leads to an increase ΔF_T in rotor thrust. Compared to the oscillation free case the difference ΔF_T in rotor thrust can be interpreted as a force which is superimposed to the undisturbed rotor thrust F_T against the current oscillation direction and therefore acting as a damping force.

The difference in rotor thrust ΔF_T due to the fore-aft oscillations is the aerodynamic damping force. The damping coefficient c_{aero} is obtained by Eq. 13 according to Cerda Salzmann & van der Tempel [8]. Here, T' is the change in rotor thrust F_T corresponding to ΔF_T and dV_d is the change in effective wind speed $v(1 - a)$ perpendicular to the rotor plane corresponding to $\dot{u}_{RNA}$.

$$c_{aero} = \frac{T'}{dV_d} = \frac{\Delta F_T}{\dot{u}_{RNA}} \qquad \text{Eq. 13}$$

The resulting out-of-plane aerodynamic damping ratio, i.e. for fore-aft direction, is denoted as $\xi_{aero,op}$. The corresponding in-plane component, i.e. for side-side direction, is denoted as $\xi_{aero,ip}$.

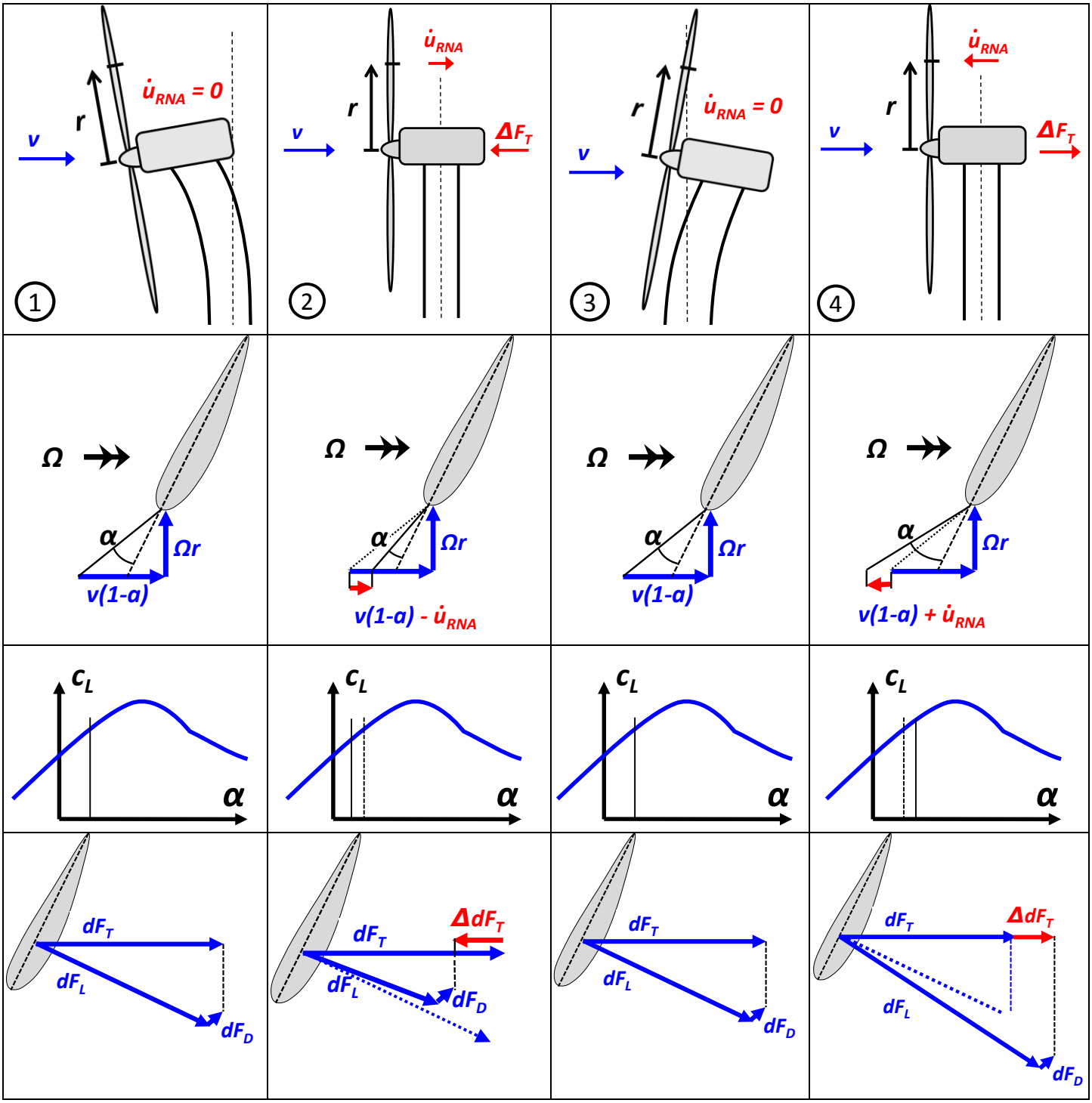

Figure 29: Illustration of the aerodynamic damping effect during four stages of an oscillation cycle.

4.3.2 Directionality of aerodynamic damping

So far, the aerodynamic damping has only been considered for the main directions, i.e. fore-aft direction resulting in out-of-plane damping $\xi_{aero,op}$ and side-side direction resulting in in-plane damping $\xi_{aero,ip}$. However, situations with misaligned wind and wave directions are also very common at typical offshore sites. Such misaligned conditions are quite significant, in particular for the design of hydrodynamic sensitive structures like monopile based OWTs. It is therefore very important to understand how much aerodynamic damping can be expected in such situations. This section discusses the effective aerodynamic damping for hydrodynamic excitations in misaligned wind-wave cases in a simplified manner in order to establish a general model from a geometric point of view. For that purpose, it is assumed that the oscillation responses introduced from the (misaligned) hydrodynamic excitations are simply superimposed to the oscillation responses introduced from the aerodynamic excitations. The simplified model described in this section is complemented by results from simulations in the following sections.

Figure 30 shows the conditions for an exemplary scenario of 60 degree misalignment between wind and wave direction. Due to the misalignment of the wave neither the out-of-plane damping $\xi_{aero,op}$ nor the in-plane damping $\xi_{aero,ip}$ can fully contribute to the effective aerodynamic damping in wave direction $\xi_{aero,\varphi}$. Instead it is expected that the effective aerodynamic damping for the wave direction contains contributions from the in-plane and out-of-plane damping dependent on the misalignment angle φ.

Some theoretical considerations on the dependency of the out-of-plane damping contribution to the effective aerodynamic damping in wave direction $\xi_{aero,\varphi}$ are provided below. Here, the same simplifying assumptions as in section 4.3.1 are used.

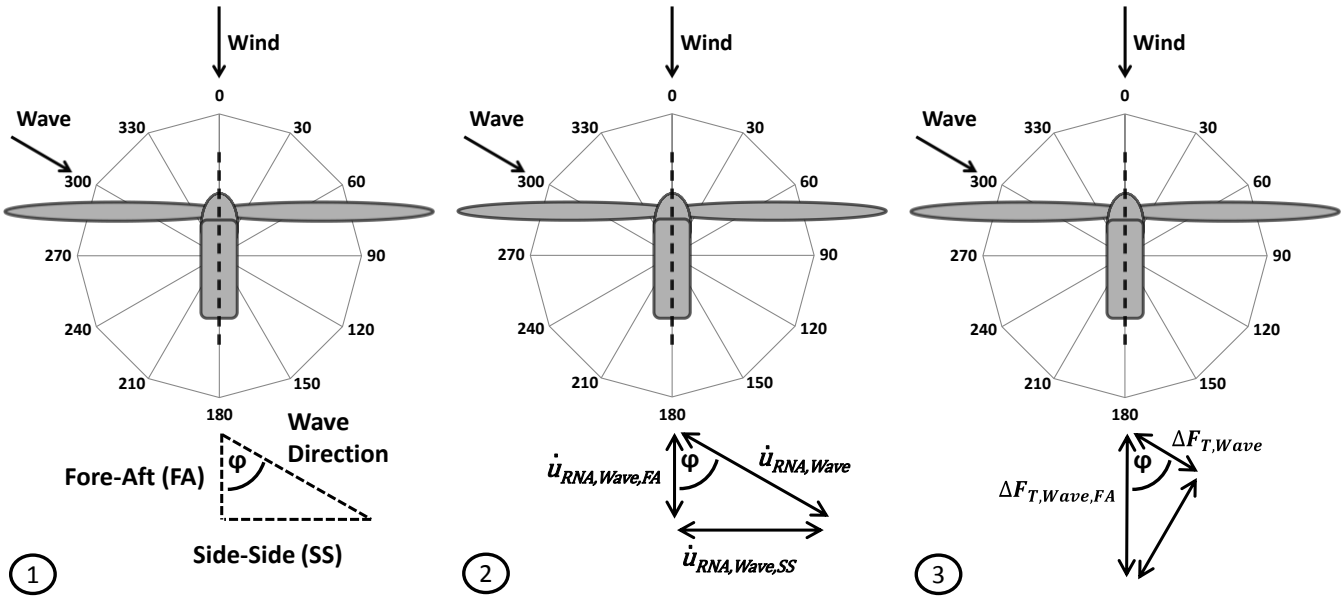

Figure 30: Effective aerodynamic damping in case of misaligned wind and wave direction.

In the left part of Figure 30 it can be seen that the wind direction is aligned with the fore-aft (FA) direction while the wave direction is misaligned by φ = 60 degree. The middle part of Figure 30 shows that wave excitations lead to oscillations in and against wave direction with the oscillation velocity $\dot{u}_{RNA,Wave}$ on RNA level. The projection of wave induced RNA oscillation velocities in fore-aft direction $\dot{u}_{RNA,Wave,FA}$ is calculated by Eq. 14.

$$\dot{u}_{RNA,Wave,FA} = \dot{u}_{RNA,Wave} \cdot cos(\varphi) \quad \text{Eq. 14}$$

Wave induced oscillations of the RNA in fore-aft direction $\dot{u}_{RNA,Wave,FA}$ introduce differences in lift force $\Delta dF_{L,Wave,FA}$ and thrust force $\Delta dF_{T,Wave,FA}$ at the blade element as shown in section 4.3.1. For simplicity, the differences $\Delta dF_{L,Wave,FA}$ and $\Delta dF_{T,Wave,FA}$ are assumed to be approximately proportional to the square of the RNA oscillation velocity projected in fore-aft direction $\dot{u}_{RNA,Wave,FA}$. Integration of $\Delta dF_{T,Wave,FA}$ over the whole rotor leads to the overall thrust force difference from the wave in fore-aft direction $\Delta F_{T,Wave,FA}$ which is therefore also proportional to the square of $\dot{u}_{RNA,Wave,FA}$ according to Eq. 15.

$$\Delta F_{T,Wave,FA} \sim (\dot{u}_{RNA,Wave,FA})^2 \quad \text{Eq. 15}$$

Furthermore, it should be noted that the relation in Eq. 15 is only a linearized approximation obtained when disregarding the non-linear influence from changes in the angle of attack α. Inserting Eq. 14 in Eq. 15 leads to the proportionality relation in Eq. 16 between the overall difference in thrust force $\Delta F_{T,Wave,FA}$ in fore-aft direction and wind-wave misalignment angle φ.

$$\Delta F_{T,Wave,FA} \sim cos^2(\varphi) \quad \text{Eq. 16}$$

The thrust force $\Delta F_{T,Wave,FA}$ is the aerodynamic damping force for wave induced oscillations in fore-aft direction. However, only the projection of $\Delta F_{T,Wave,FA}$ in wave direction $\Delta F_{T,Wave}$ according to Eq. 17 is effectively damping the oscillations from the wave excitations.

$$\Delta F_{T,Wave} = \Delta F_{T,Wave,FA} \cdot cos(\varphi) \quad \text{Eq. 17}$$

Under consideration of Eq. 16 and Eq. 17 the proportionality relation between misalignment angle φ and the effective aerodynamic damping force $\Delta F_{T,Wave}$ according to Eq. 18 can be established.

$$\Delta F_{T,Wave} \sim cos^3(\varphi) \quad \text{Eq. 18}$$

Using Eq. 18 in Eq. 13 leads to the proportionality relation of the effective aerodynamic damping coefficient $c_{aero,\varphi}$ for wave excitations and the misaligned wave direction φ in Eq. 19.

$$c_{aero,\varphi} \sim cos^3(\varphi) \quad \text{Eq. 19}$$

The critical damping ratio ξ is the ratio of the damping coefficient and the critical damping coefficient $c_{crit} = 2\sqrt{km}$ with the modal stiffness k and the modal mass m.

$$\xi = \frac{c}{c_{crit}} \quad \text{Eq. 20}$$

It is important to note that c_{crit} is not constant for different directions due to differences in the modal mass as introduced from especially the RNA. However, for simplicity this is disregarded here and the proportionality relation in Eq. 19 is extended to the directional aerodynamic damping according to Eq. 21.

$$\xi_{aero,op,\varphi} \sim \xi_{aero,op} \cdot cos^3(\varphi) \quad \text{Eq. 21}$$

Analogously, the directional aerodynamic damping contribution from in-plane damping is obtained by Eq. 22.

$$\xi_{aero,ip,\varphi} \sim \xi_{aero,ip} \cdot sin^3(\varphi) \quad \text{Eq. 22}$$

The cubic proportionality relations in Eq. 21 and Eq. 22 result from the simplifying assumptions on the proportionality relation in Eq. 15, i.e. assuming that the overall thrust force difference from the wave in fore-aft direction $\Delta F_{T,Wave,FA}$ is proportional to the square of $\dot{u}_{RNA,Wave,FA}$. For the establishment of the engineering estimate in section 4.3.4, the cubic exponents in Eq. 21 and Eq. 22 are therefore replaced by the generalized exponents κ_{op} and κ_{ip} in Eq. 23 and Eq. 24.

$$\xi_{aero,op,\varphi} \sim \xi_{aero,op} \cdot cos^{\kappa_{op}}(\varphi) \quad \text{Eq. 23}$$

$$\xi_{aero,ip,\varphi} \sim \xi_{aero,ip} \cdot sin^{\kappa_{ip}}(\varphi) \quad \text{Eq. 24}$$

The total effective, directional aerodynamic damping is the sum of the in-plane and out-of-plane contribution according to Eq. 25.

$$\xi_{aero,\varphi} = \xi_{aero,op,\varphi} + \xi_{aero,ip,\varphi} \quad \text{Eq. 25}$$

4.3.3 Determination of aerodynamic damping

Aerodynamic damping is considered implicitly in aero-elastic simulations with fully integrated tools such as FLEX5 [50]. However, under certain conditions it might be required to perform calculations without a direct consideration of the aero-elastic behaviour and controller. This could be relevant for:

- Simplified superimposed load calculation approaches in the preliminary design phase.
- Determination of damage equivalent wind-wave correlations as addressed in paper 3 [63].
- Specialized simulations without aero-elastic tools such as dynamic ice load calculations.

In such cases the effective aerodynamic damping must be modelled in a simplified manner, e.g. by increasing the structural damping to an equivalent total structural damping. It is therefore important to understand and derive the aerodynamic damping characteristics of the OWT in operation. In this context, Kühn [41] provided an overview of two methods for determination of the aerodynamic damping of a given wind turbine in power production. The methods are based on non-linear time domain simulations and numerical linearization. Further, a summary of various closed-form solutions is provided by Cerda Salzmann & van der Tempel [8]. It should be noted that all presented closed form solutions are limited to the out-of-plane damping $\xi_{aero,op}$ from the rotor aerodynamics, while other contributions are disregarded.

Here, the aerodynamic damping is estimated from non-linear time domain simulations, as demonstrated by Passon & Kühn [56], since this approach allows for capturing all contributions for the aerodynamic damping effect. However, in extension to the aforementioned publications also the effective aerodynamic damping is assessed for directions which are misaligned from the wind in order to address misaligned wind-wave direction

scenarios. For that purpose an aero-elastic simulation is performed for each combination of wind speed and misalignment angle under consideration of all relevant conditions including turbulence, waves and controller behavior. The RNA translation responses in direction of the wave, i.e. misaligned to the wind by the angle φ, from these simulations constitute the reference values. A second set of simulations is performed afterwards using the same conditions as for the first set. However, also an additional, short-duration, impact load is introduced on the nacelle in direction of the wave at a predefined point in time. Relative to the simulations without the impact load, this results in a superimposed free decaying vibration response. The decay of the vibration depends on the total damping, i.e. not only the aerodynamic damping.

The above is exemplarily shown in Figure 31 for the vibrations of the RNA applying an impulse load at 10s. The upper part of the figure shows the RNA translation response for both cases. The free decaying vibration can now easily be extracted by subtraction of the reference case response from the response including the impact load as shown in the lower part of the figure. Here, it is assumed that the impact load is introduced for a very short duration and then completely removed such that the peaks are equal to the amplitudes of the free decaying vibration around zero.

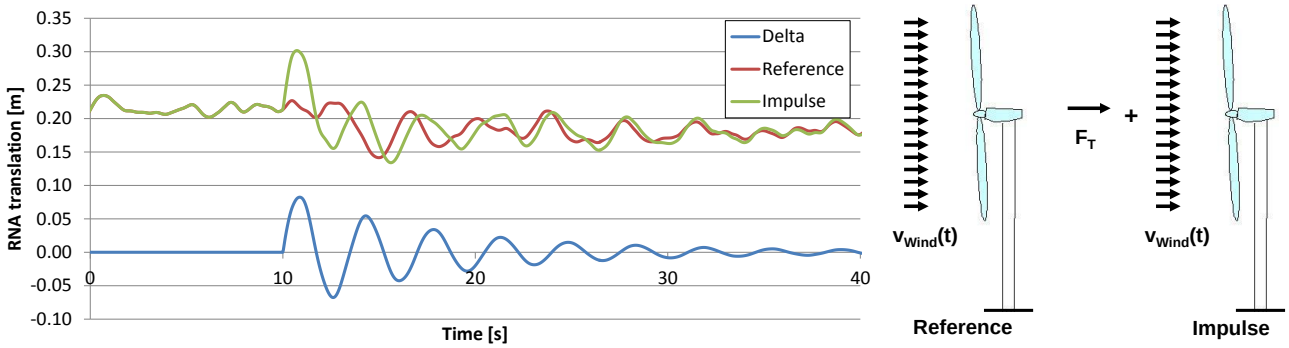

Figure 31: Establishment of a free decaying vibration from the overall vibrations of the two time domain simulations.

The logarithmic damping decrement Λ is the natural logarithm of the ratio of the amplitudes of any two successive peaks x in the free decaying vibration according to Eq. 26.

$$\Lambda = \frac{1}{n} ln\left(\frac{x_i}{x_{i+n}}\right) \qquad \text{Eq. 26}$$

Here, the index i represents an arbitrary peak with the amplitude x_i while x_{i+n} is the amplitude at n peaks later. The damping ratio ξ is then found from the logarithmic decrement according to Eq. 27.

$$\xi = \frac{\Lambda}{2\pi} \qquad \text{Eq. 27}$$

Cautious attention must in particular be given for conditions close to rated wind as the transition from variable speed to constant speed and from constant to variable blade pitch angles may distort the results of the damping assessment based on non-linear time domain simulations.

It should be noted that derived explicit aerodynamic damping by the aforementioned methods are of an approximate character. For example, yawing of the turbine due to the influence of the three-dimensional turbulent wind field as well as the presence of yaw errors have an influence on the instantaneous effective

misalignment angle and the aerodynamic damping. Furthermore, Damgaard et al. [13] found by experimental testing that the cross-wind modal damping increased proportionally up to rated wind speed while stagnation or decreasing modal damping occurred for higher wind speeds. They concluded that a considerable portion of aerodynamic damping might be available in cross-wind direction due to coupling effects between the lowest fore-aft and side-side wind turbine modes. However, this behaviour could not be reproduced by fully coupled wind turbine simulations where proportional damping is present for the entire operational mean wind speed range.

4.3.4 Engineering estimate for misaligned aerodynamic damping

Generally, the aerodynamic damping can be derived for all misalignment conditions as shown in section 4.3.3. However, it is also possible to scale the out-of-plane damping $\xi_{aero,op}$ and the in-plane damping $\xi_{aero,ip}$ on basis of the effective misalignment angle φ_{WaWi} in order to approximate the effective damping value $\xi_{aero,\varphi}$ for misaligned conditions. This requires prior knowledge of only $\xi_{aero,op}$ and $\xi_{aero,ip}$ and can be based on Eq. 28. Under consideration of Eq. 21 and Eq. 22, the exponents κ_{op} and κ_{ip} would both take the value 3. However, the considerations leading to these equations are based on simplified assumptions. The validity of Eq. 28 is therefore extended by keeping the exponents κ_{op} and κ_{ip} as general values.

$$\xi_{aero,\varphi}(v,\varphi_{WiWa}) \approx \xi_{aero,op}(v,\varphi_{WiWa}) \cdot cos^{\kappa_{op}}(\varphi_{WiWa}) + \xi_{aero,ip}(v,\varphi_{WiWa}) \cdot sin^{\kappa_{ip}}(\varphi_{WiWa}) \qquad \text{Eq. 28}$$

Based on experience from a limited range of real and fictive wind turbines, the author recommends values between 2.5 and 3 for the exponents κ_{op} and κ_{ip} for practical applications in case no more detailed information is available. The effective misalignment angle varies in the range $0 \leq \varphi_{WaWi} \leq 90$ and can be determined from Table 8 for given combinations of wind direction φ_{Wind} and wave direction φ_{Wave}.

Table 8 Effective misalignment φ_{WaWi} [degree] for directional wind-wave combinations.

Wind direction φ_{Wind} [degree]	0	30	60	90	120	150	180	210	240	270	300	330
Wave direction φ_{Wave} [degree]												
0	0	30	60	90	60	30	0	30	60	90	60	30
30	30	0	30	60	90	60	30	0	30	60	90	60
60	60	30	0	30	60	90	60	30	0	30	60	90
90	90	60	30	0	30	60	90	60	30	0	30	60
120	60	90	60	30	0	30	60	90	60	30	0	30
150	30	60	90	60	30	0	30	60	90	60	30	0
180	0	30	60	90	60	30	0	30	60	90	60	30
210	30	0	30	60	90	60	30	0	30	60	90	60
240	60	30	0	30	60	90	60	30	0	30	60	90
270	90	60	30	0	30	60	90	60	30	0	30	60
300	60	90	60	30	0	30	60	90	60	30	0	30
330	30	60	90	60	30	0	30	60	90	60	30	0

The parameters in Eq. 28 are further discussed and assessed in the next section on basis of non-linear time domain simulation results according to the methodology described in the previous section. The resulting scale factor for all possible misalignment angles in the range of 0 - 360 degrees are shown exemplarily for $\kappa_{op} = \kappa_{ip} = 3$ in Figure 32.

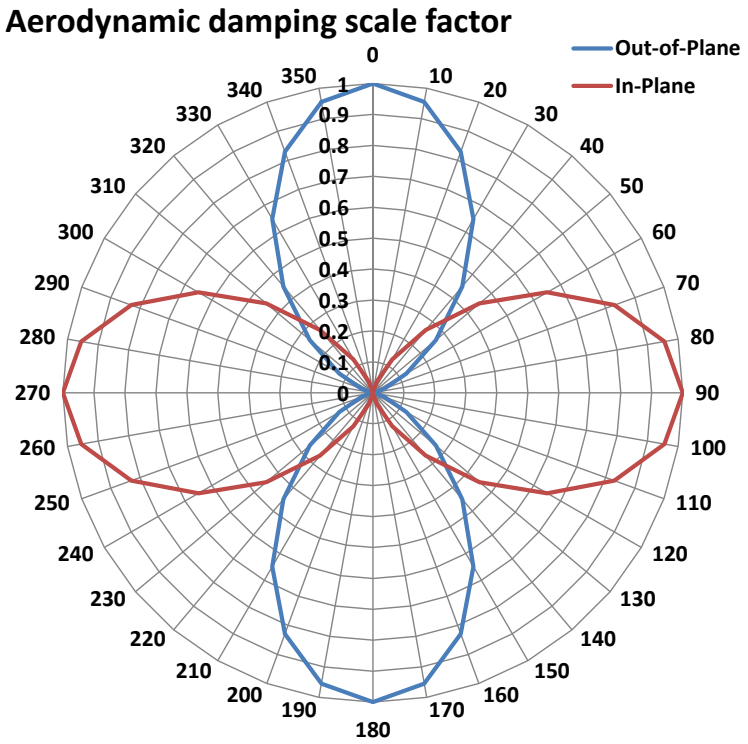

Figure 32: Scale factor on aerodynamic damping for different wind-wave misalignment angles.

4.3.5 Example scenario

In this section, the aerodynamic damping is determined on basis of non-linear time domain simulations according to section 4.3.3 and compared to approximated values obtained from Eq. 28. For that purpose an exemplary OWT configuration with monopile foundation at 30m water depth and the NREL 5MW turbine [33] is established. The wind field is modelled as three dimensional turbulent wind with the longitudinal turbulence intensities according to Figure 33. The lateral and vertical turbulence intensities

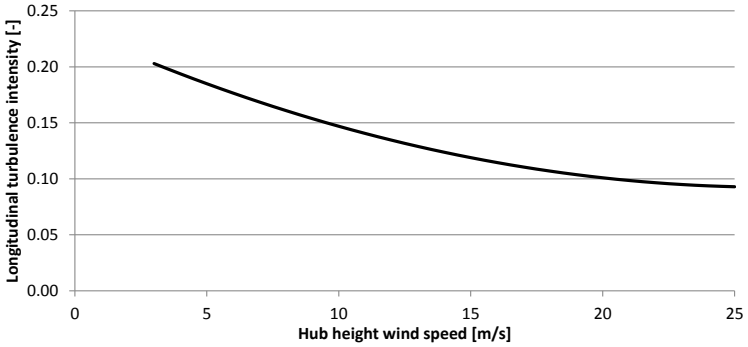

Figure 33: Longitudinal turbulence intensity over wind speed.

are applied as 0.8 and 0.5 times the longitudinal component. No yaw error is included, however, the yaw system is enabled in the model. Waves are modelled on basis of one representative sea state with H_s = 1m and T_p = 4s for all wind speeds and misalignments. The structural damping is included as ξ_s = 1% of critical damping on the first global bending mode of the OWT.

The assessment comprises the full power production wind speed range v = 3 – 25m/s and the wind-wave misalignment angles φ = 0, 30, 60 and 90 degrees. The aerodynamic damping is determined for the wave direction, i.e. misaligned to the aligned (mean) wind and rotor direction. Figure 34 shows the resulting calculated total damping values $\xi_{total,\varphi}(v, \varphi)$. It can be seen from Figure 34 that significant variations exist around 11-13m/s, i.e. around rated wind speed. This is a result of highly non-linear effects due to transitions from the variable rotor speed region to the rated rotor speed region and from constant blade pitch angles to varying blade pitch angles as introduced by the controller.

The aerodynamic damping $\xi_{aero,\varphi}(v, \varphi)$ is obtained by subtraction of the (constant) structural damping ξ_s from the total damping $\xi_{total,\varphi}(v, \varphi)$ according to Eq. 29.

$$\xi_{aero,\varphi}(v,\varphi) = \xi_{total,\varphi}(v,\varphi) - \xi_s \qquad \text{Eq. 29}$$

Figure 34 also shows that the total damping for 90 degrees misalignment increases with the wind speed. As the structural damping ξ_s is constant over wind speed this damping contribution is expected being in-plane aerodynamic damping $\xi_{aero,ip}$. This increase of $\xi_{aero,ip}$ is approximately proportional to the square of the wind speed.

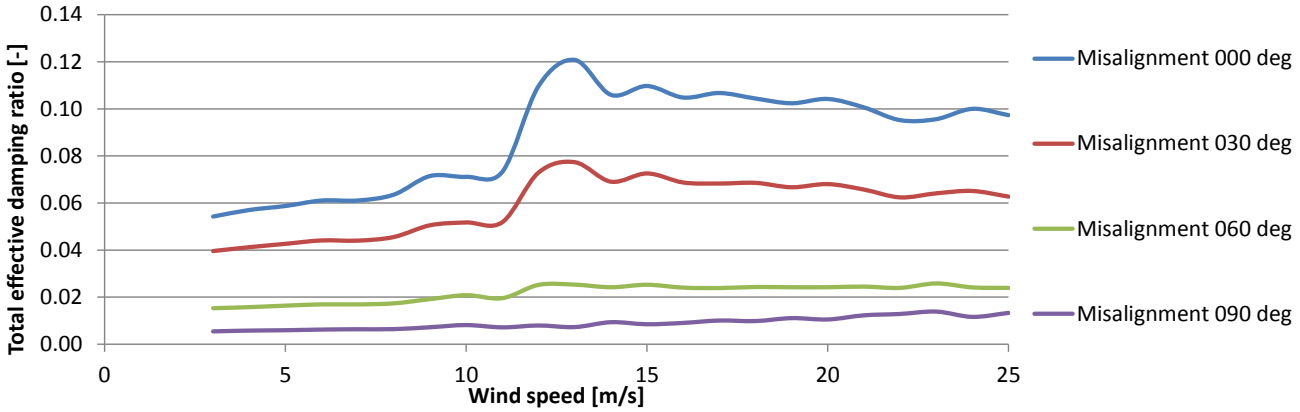

Figure 34: Calculated total damping $\xi_{total,\varphi}(v, \varphi)$.

It should be noted that aerodynamic damping information in terms of equivalent structural damping ratios is often not available for design purposes. However, in cases with available information on aerodynamic damping the information is typically limited to out-of-plane damping $\xi_{aero,op}$, while in-plane damping $\xi_{aero,ip}$ is very rarely available and effective aerodynamic damping values for misaligned cases is practically never available. In cases without detailed information on in-plane aerodynamic damping, Eq. 30 can be used as estimation.

$$\xi_{aero,ip} \approx \frac{v^2}{v_{out}^2}\xi_{add} \qquad \text{Eq. 30}$$

Here, v is the (mean) wind speed at hub height, v_{out} is the cut-out wind speed and ξ_{add} is the additional damping ratio at v_{out}. Unless more accurate values are known, the author recommends using values of ξ_{add} between 0.5 and 1.2 based on experience from a limited range of real and fictive wind turbines. In particular, ξ_{add} = 0.8 seems to give reasonable fits. Inserting Eq. 30 into Eq. 28 would also allow for estimation of the effective directional aerodynamic damping $\xi_{aero,\varphi}$ in accordance to Eq. 31.

$$\xi_{aero,\varphi} \approx \xi_{aero,op} \cdot cos^{\kappa_{op}}(\varphi_{WiWa}) + \frac{v^2}{v_{out}^2} \xi_{add} \cdot sin^{\kappa_{ip}}(\varphi_{WiWa}) \qquad \text{Eq. 31}$$

Figure 35 shows the calculated aerodynamic damping together with the approximated values for all wind speeds and misalignment cases 30, 60 and 90 degree based on the parameters ξ_{add} = 0.8, κ_{op} = κ_{ip} = 3. It can be seen that the aerodynamic damping approximation is rather good for the 30 and 90 degree misalignment cases, while the approximation for the 60 degree case is on the conservative side.

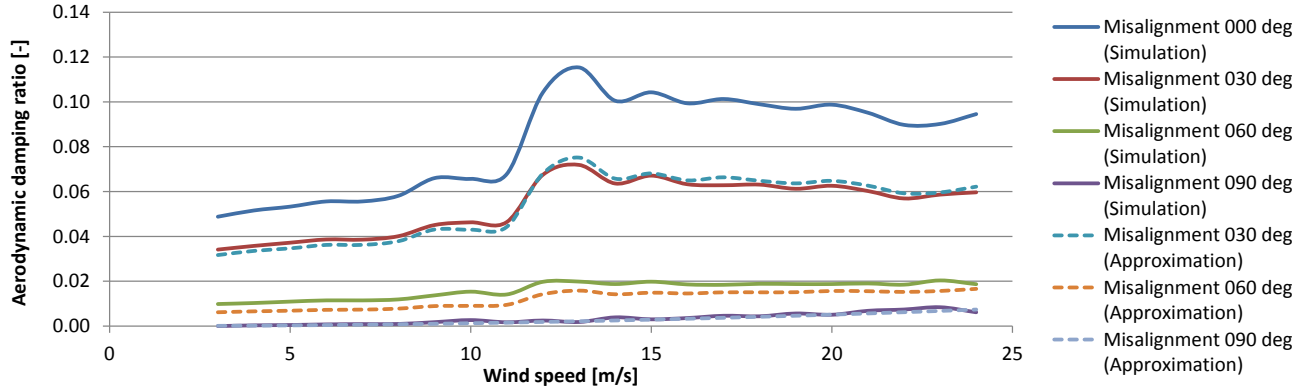

Figure 35: Aerodynamic damping $\xi_{aero,\varphi}(v, \varphi)$ from simulations and approximations with ξ_{add} = 0.8 and κ_{op} = κ_{ip} = 3.

Much better results for the 60 degree misalignment case are obtained for ξ_{add} = 0.9, κ_{op} = 2.7 and κ_{ip} = 3 as shown in Figure 36. However, the approximated aerodynamic damping values are now non-conservative for wind speeds above rated in the 30 degree misalignment case.

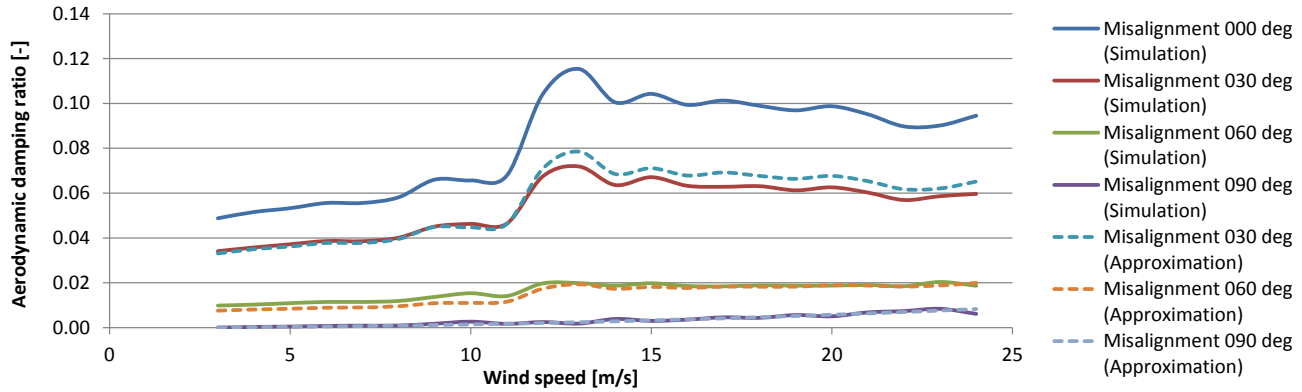

Figure 36: Aerodynamic damping $\xi_{aero,\varphi}(v, \varphi)$ from simulations and approximations with ξ_{add} = 0.9, κ_{op} = 2.7 and κ_{ip} = 3

Both examples show that the assumption of a cubic relation between wind-wave misalignment angle and the effective aerodynamic damping according to Eq. 21 and Eq. 22 in section 4.3.2 leads to reasonable, but approximate results.

4.3.6 Summary

A proper consideration of damping properties for offshore wind turbines is rather important in the dynamic calculation of design loads. Aerodynamic damping introduces potentially the largest contribution to the effective overall damping and is implicitly considered at each time step by aero-elastic simulation models in integrated or sequentially integrated load calculation approaches. It is also possible to define aerodynamic damping explicitly as equivalent structural damping. However, such explicit aerodynamic damping quantities have to be considered as approximations. Nevertheless, an explicit definition of effective aerodynamic damping and application as equivalent structural damping is required for the isolated hydrodynamic response calculation of superimposed approaches in case of hydrodynamic sensitive structures such as monopile based OWTs. Disregarding this damping source could potentially lead to very conservative estimations of the hydrodynamic contribution in the total loads for hydrodynamic sensitive structures.

Furthermore, an explicit definition of effective aerodynamic damping is also beneficial for the calculation of lumped waves in damage equivalent wind-wave correlations. However, sufficient information on explicitly defined, effective aerodynamic damping, in particular for misaligned wind-wave cases, is often not available for the foundation designer. Instead, the foundation designer can often only apply simplified rule-of-thumb values, e.g. in the order of 4% of critical damping, without any differentiation for misalignment cases despite the potentially significant relevance for the fatigue design loads. The author recommends therefore a consequent definition of explicit aerodynamic damping properties in the design process. For that purpose, a new approximation method of effective aerodynamic damping for hydrodynamic loading in case of misaligned wind-wave conditions has been introduced in this thesis. Application of this method requires the availability of aerodynamic damping reference values, at least for aligned wind-wave conditions, and has been assessed for a generic OWT. Reasonable approximations of the effective aerodynamic damping have been achieved for misaligned wind-wave cases. The investigations show also that the assumption of a cubic relation between wind-wave misalignment angle and the effective aerodynamic damping can be used as an initial estimate. However, further validation is required for individual, real offshore wind turbine configurations and site conditions.

5 Damage Equivalent Modelling of Wind-Wave Correlations

A range of H_s-T_p combinations can occur per set of mean wind speed, wind direction and wave direction for a specific site constituting the long-term wave climate. This wave climate is typically described by directional SCDs containing individual probabilities $p_{i,j}$ for $i=1..n$ wave height classes $H_{s,i}$ and $j=1..m$ wave period classes $T_{p,j}$. Detailed met-ocean databases comprise of SCDs for the wind and wave direction for each $k=1..n_{wind}$ wind speeds v_k. This results potentially in a plethora of varying wind and wave parameters for the complete wind-wave climate and would therefore be impractical to address by load calculations for the design of OWTs in FLS even with state of the art computing.

Consequently, it is important to reduce the number of wind-wave parameter combinations for FLS design purposes, which is achieved by condensation or lumping of the long-term wave climate. Paper 2 [62] introduces a damage equivalent wave lumping method which allows for preservation of the hydrodynamic fatigue damage distribution from the underlying full wave climate as expressed by a SCD. Furthermore, paper 3 [63] introduces an extension towards the required wind-wave correlations for design load calculation purposes of OWTs in FLS. The new approach from paper 3 [63] allows for condensation of a full wave climate per wind speed, wind direction and wave direction, expressed as a SCD, to only one damage equivalent sea state represented by a significant wave height and peak period while preserving the hydrodynamic fatigue damages throughout the OWT structure.

This chapter is intended to complement the investigations in paper 3 [63] on the new damage equivalent wind-wave correlation method. For that purpose the following aspects are addressed:

- Different effective damping conditions.
- Assessment of alternative wave lumping approaches.
- Modified approach in case of limited data availability in met-ocean databases.

Further, the wave lumping method from paper 2 [62] and the damage equivalent wind-wave correlation method from paper 3 [63] make use of a unit damage matrix $\boldsymbol{D}^*$ containing fatigue damages d for individual H_s-T_p combinations of a SCD. This unit damage matrix is addressed for a time domain based derivation in section 5.1.

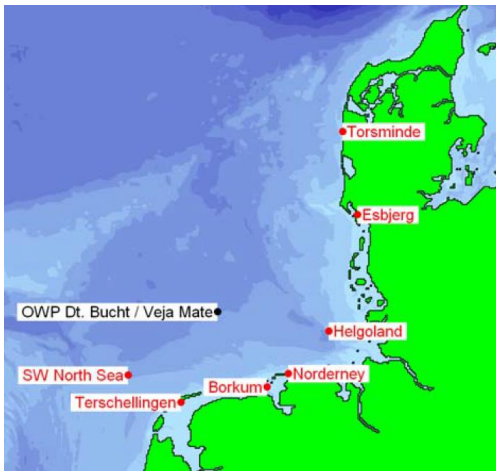

Figure 37: Location of the planned Veja Mate offshore wind farm

For the present chapter, met-ocean data are taken from the Veja Mate project which is planned as a 400MW offshore wind farm located at 40m water depth within the German exclusive economic zone in the North Sea as shown in Figure 37. The project is developed by Veja Mate Offshore Holding GmbH and their representative K2 Management GmbH with Siemens Wind Power's SWT-6.0-154 wind turbines and monopile type foundations designed by Rambøll Wind. The Veja Mate database is property of Veja Mate Offshore Holding GmbH and can as such not be fully enclosed. Therefore, the corresponding quantities and relations of the met-ocean data, such as SCDs and wind distributions, are only shown in a qualitative manner in the present thesis.

5.1 Unit damage matrices

The unit damage matrix $\boldsymbol{D}^*$ contains fatigue damages d for each individual H_s-T_p combination of a SCD. The individual damages d are obtained from dynamic calculations in the time or frequency domain assuming unit probabilities for each H_s-T_p combination. Here, only the time domain based approach in Figure 38 is briefly summarized since this approach is also taken in paper 2 [62] & paper 3 [63]. Details for a frequency domain based approach can e.g. be found in Barltrop & Adams [3], Hapel [32] and Seidel [66].

For each H_s-T_p combination in the SCD a number of irregular wave time series is established. The number and length of these time series must be sufficiently large to account for the stochastic character of the irregular waves as shown e.g. by Haid et al. [28] for floating type OWTs, which is also further addressed at the end of this section. The OWT structure is then subjected to the irregular waves in dynamic analyses. Responses from the dynamic analyses are extracted and processed via the Rainflow Counting method in order to obtain stress spectra. The stress spectra are subsequently subjected to a *S-N* curve for calculation of the fatigue damage d.

Similarly to the derivation of DELs, the establishment of the unit damages elements $d_{i,j}^*$ in $\boldsymbol{D}^*$ is based on representative configuration parameters, e.g. with respect to the OWT structure, damping, location of damage extraction and *S-N* curve slope m. Further details on the influence of configuration parameters are provided in section 4.2 of paper 2 [62].

Following the linear damage accumulation hypothesis according to Palmgren [51] and Miner [44], actual fatigue damages $d_{i,j}$ can be obtained by simple scaling of the unit damages $d_{i,j}^*$ in $\boldsymbol{D}^*$ with actual probabilities $p_{i,j}$ from the SCD. This is illustrated in Figure 39, according to Eq. 32, for calculation of actual damages $d_{i,j}$ in the damage matrix $\boldsymbol{D}$ for each $H_{s,i}$-$T_{p,j}$ sea-state in the SCD.

$$d_{i,j} = p_{i,j} \cdot d_{i,j}^* \qquad \text{Eq. 32}$$

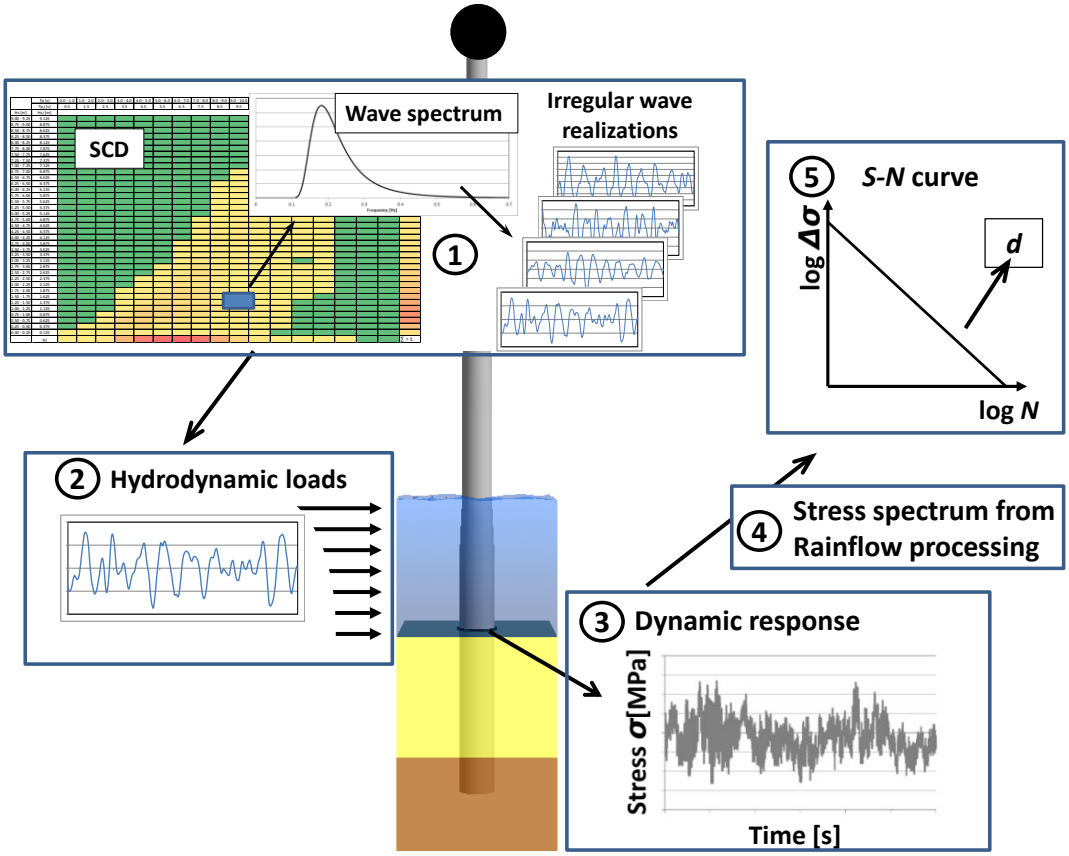

Figure 38: Time domain based calculation of damage per H_s-T_p combination

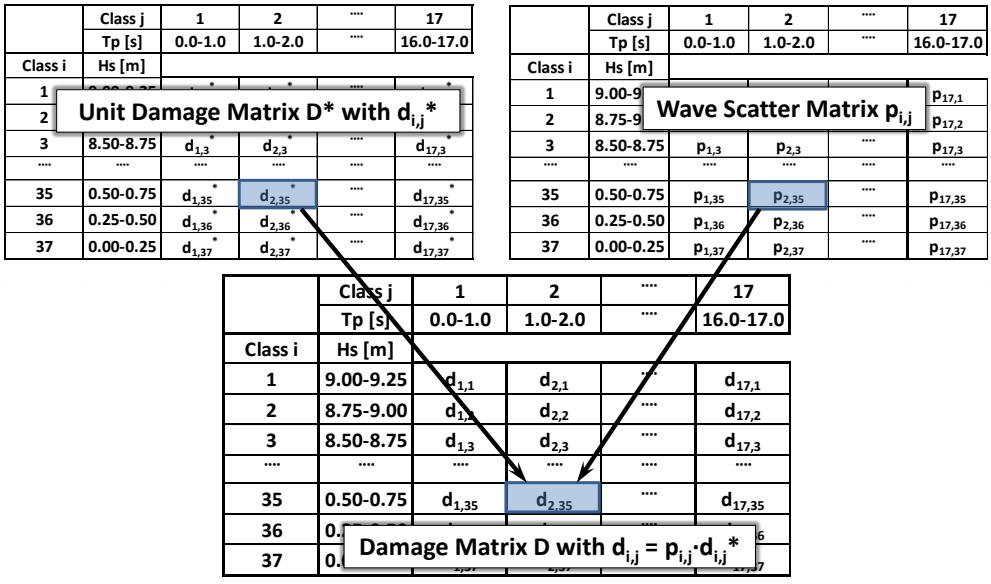

Figure 39: Illustration of damage calculation with the ***D****.

In time domain based calculations of the unit damage matrix $\boldsymbol{D}^*$, the stochastic uncertainties from the irregular wave realizations must be carefully assessed. In the following, this is exemplarily illustrated for the influence of the total wave realizations length on the calculated hydrodynamic fatigue damages. For that purpose, the structure and Veja Mate based met-ocean conditions for aligned wind and waves coming from west according to paper 3 [63] are taken into account.

Each element in the unit damage matrix is established on the basis of 600s simulations and for up to 200 seeds. For example, the 200 seed case correspond to a total simulation length of 200·600s = 120000s (=33.3hrs) per sea-state. The derived significant wave height and peak period of the lumped waves and the resulting damages over wind speed at interface and mudline levels are shown in Figure 40 and Figure 41 for different (total) wave length realizations (number of seeds). It can be seen that variations in damage equivalent sea state parameters and the corresponding fatigue damages occur mainly for the case of 10 seeds (i.e. corresponding to ten 600s wave realizations). Hence, a larger number of seeds should be used. The 200 seeds case is sufficient to address the stochastic character of the individual wave realizations.

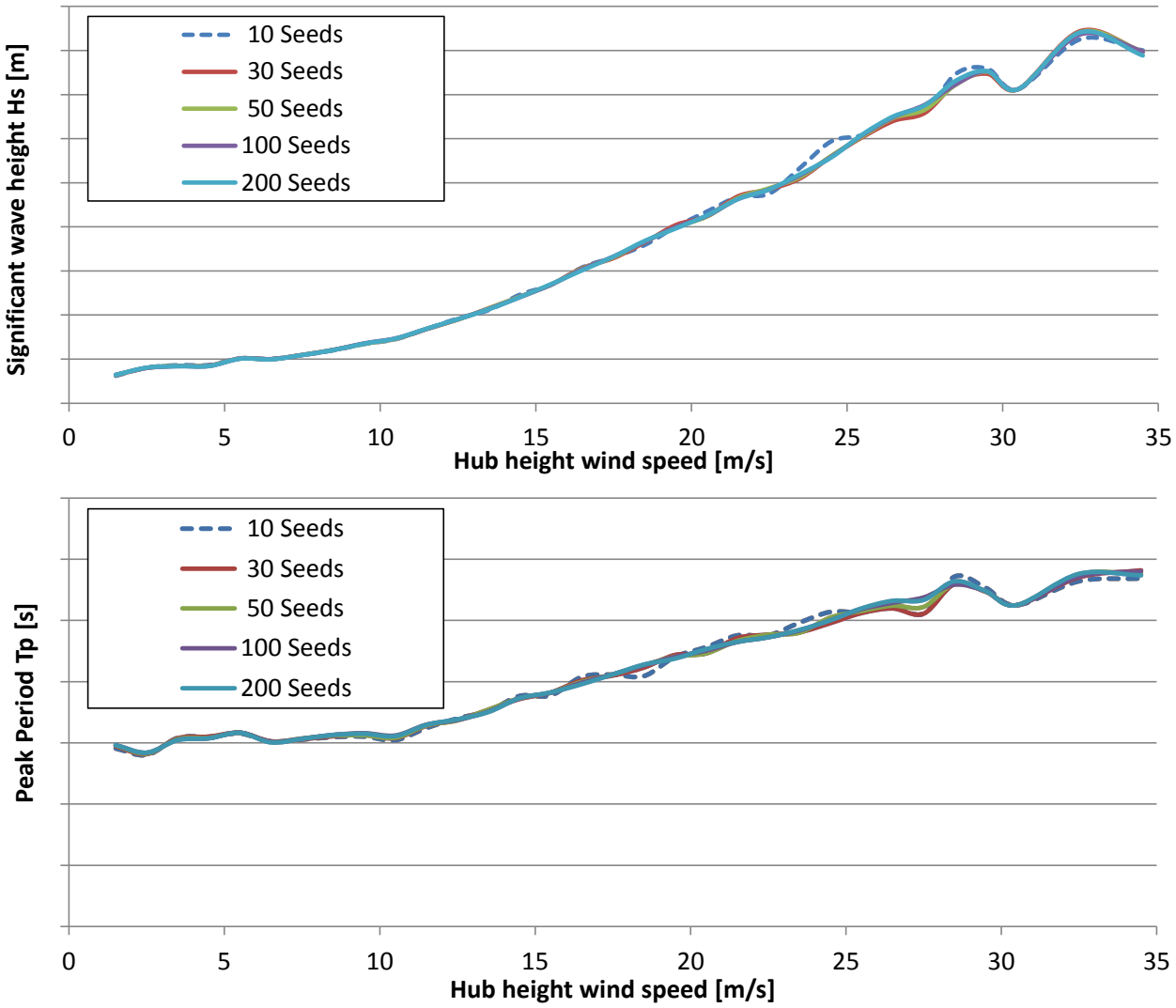

Figure 40: Derived significant wave height (upper) and peak period (lower) of the lumped waves over wind speed for different numbers of seeds.

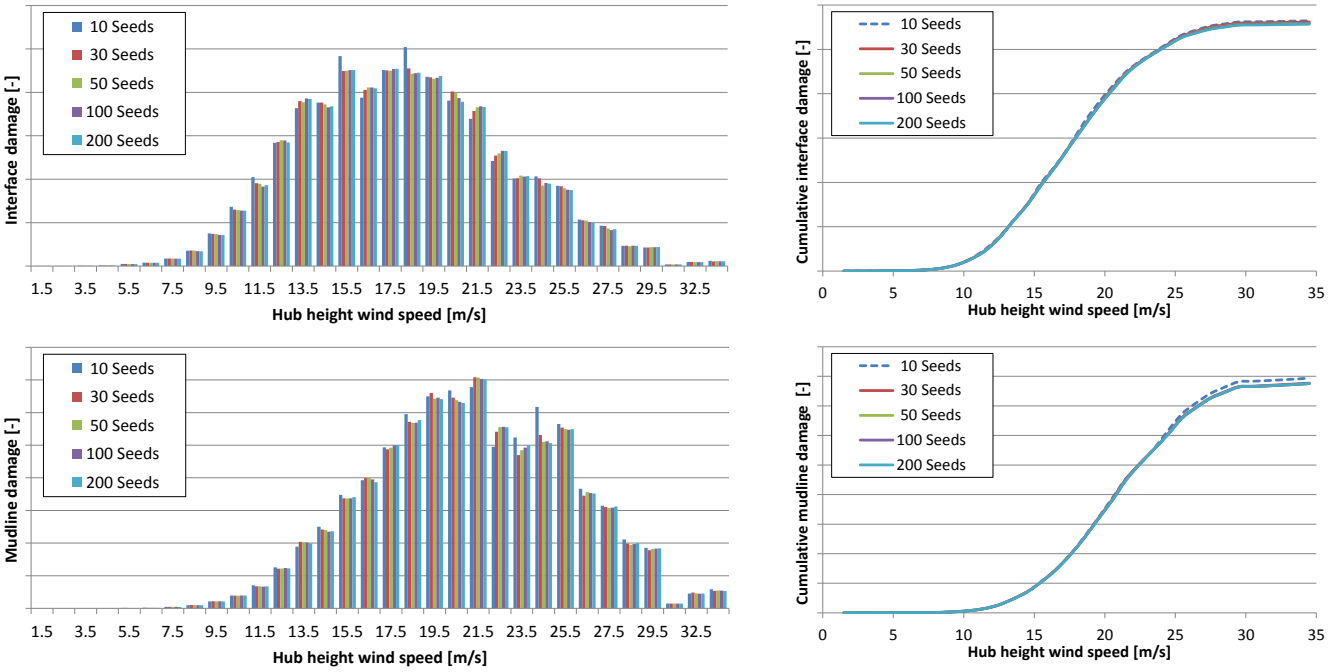

Figure 41: Resulting individual (left) and cumulative (right) hydrodynamic fatigue damage distribution at interface level (upper) and mudline level (lower) over wind speed for different numbers of seeds.

5.2 Influence of damping

Damping has a significant influence on the hydrodynamic responses and consequently on the fatigue damages for hydrodynamic sensitive OWTs as seen in section 4.1. Paper 2 [62] demonstrates that the applied damping conditions are important for the derivation of damage equivalent, lumped wave parameters. Aerodynamic damping might be the dominant damping source for the turbine in operation. However, the effective aerodynamic damping and therefore the effective total damping varies a lot during lifetime due to different operational states and wind-wave misalignment as shown in section 4.3.

This section addresses the sensitivity of fatigue damages from lumped waves derived for different damping conditions using the new damage equivalent wind-wave correlation method from paper 3 [63]. For this purpose the met-ocean database from the Veja Mate Offshore Wind Farm project is used together with the NREL 5MW based OWT with a monopile foundation in 30m water depth from section 4.3.5. Sea-state parameters for the lumped waves are derived for different damping conditions. These damping conditions are based on the effective total damping for the hydrodynamic response at different wind speeds, wind-wave misalignments and operational states corresponding to DLCs 1.2 and 6.4 from the IEC61400-3 [88]. Furthermore, a minimum (only structural) and a maximum effective damping scenario are taken into account for the exemplary OWT configuration.

Table 9 summarizes the distribution of wind speeds and damping conditions for the individual scenarios. The wave lumping, in accordance to the damage equivalent wind-wave correlation method from paper 3 [63], is performed for all combinations of wind and wave direction under consideration of the damping conditions listed in Table 9 for the individual wind speed bins. The total effective damping ratios vary between 1% and 12% critical damping.

Table 9 Distribution of wind speed ranges and total damping conditions in different scenarios.

Wind-wave correlation scenario	**Wind speed range [m/s]**	**Total effective damping**
DLC6.4 (parked outside power production range)	1-2 & 26-34	1% critical
DLC1.2 (normal power production)	3-25	according to section 4.3.5
Structural Damping (minimum)	1-34	1% critical
Maximum Damping (maximum)	1-34	12% critical

The Mudline level and Tower top level are used as the two locations to derive the damage equivalent sea-state parameters from the intersections of the corresponding damage contour lines (DCLs). The derived damage equivalent sea-state parameters of the lumped waves are subsequently used for calculations of hydrodynamic fatigue damages. Furthermore, hydrodynamic fatigue damages are calculated for the full wave climate in terms of SCDs and under consideration of the damping conditions in DLC1.2 and 6.4 for each combination of wind speed, wind direction and wave direction. The resulting hydrodynamic fatigue damages from the full wave climate are then compared with the hydrodynamic fatigue damages obtained from damage equivalent sea-state parameters based on the different damping scenarios. Figure 42 shows the four locations within the OWT used for the hydrodynamic fatigue damage comparison.

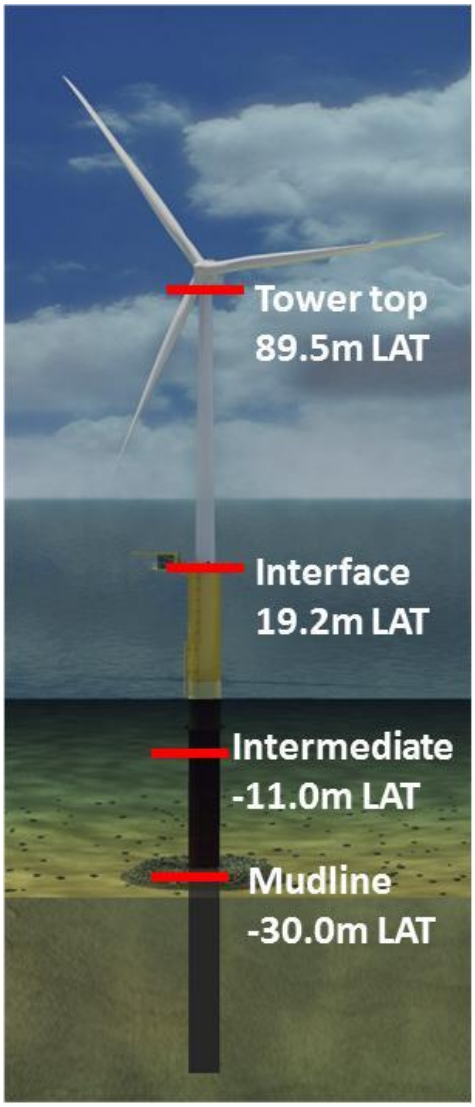

Figure 42: Locations for assessment of hydrodynamic fatigue damage.

Figure 43 to Figure 46 show the normalized individual and cumulative hydrodynamic fatigue damages from the full and lumped wave climates over wind speeds exemplarily for waves from 270 degrees, as this is the wave direction with the highest probability of occurrence, in combination with different misalignment conditions. Hydrodynamic fatigue damages for the full wave climate and the different lumped waves are calculated with damping conditions corresponding to DLC1.2 and 6.4 according to Table 9. However, the sea-state parameters of the lumped waves have been derived for different damping conditions in order to assess the corresponding sensitivity, i.e.:

- Actual damping conditions, i.e. corresponding to DLC1.2 and 6.4 according to Table 9.
- Structural damping conditions, i.e. 1% critical damping, also corresponding to DLC7.2 according to Table 9.
- Maximum damping conditions, i.e. 12% critical damping.

The results in Figure 43 to Figure 46 contain a lot of information, such as the trend of decreasing probabilities for high wind speeds with increasing misalignment angle or the relative importance of hydrodynamics at different operational conditions and locations in the OWT. Furthermore, the figures also show the total effective damping and normalized probability of occurrence. However, focus is on the representation of the full wave climate by the lumped waves using the damage equivalent wind-wave correlation method from paper 3 [63].

The hydrodynamic fatigue damages from the full wave climates are captured rather accurately with the lumped waves based on the actual damping conditions, i.e. corresponding to DLC1.2 and 6.4 according to Table 9. Here, the largest difference in the total cumulative hydrodynamic fatigue damage is approximately 4% and occurs for the intermediate location of the 60 degree wind-wave misalignment case in Figure 45.

Generally, the hydrodynamic fatigue damages are also captured accurately with the lumped waves based on only the structural damping conditions. Here, the largest difference in the total cumulative hydrodynamic fatigue damage is approximately 6% and occurs at Mudline level of the 60 degree wind-wave misalignment case in Figure 45. Application of structural damping conditions for the derivation of lumped wave sea-state parameters according to the damage equivalent wind-wave correlation method from paper 3 [63] seems therefore to be an acceptable alternative in cases without detailed information on the aerodynamic damping and hence on the total effective damping.

The lumped waves based on the maximum structural damping conditions introduce the largest deviations from the actual hydrodynamic fatigue damages of the full wave climate. Large difference for individual wind speeds occur for situations of low total effective damping such as the parked cases of DLC6.4 at high wind speeds in Figure 43. The largest difference in the total cumulative hydrodynamic fatigue damage is approximately 11% and occurs at Tower top level and Interface level of the 90 degree wind-wave misalignment case in Figure 46.

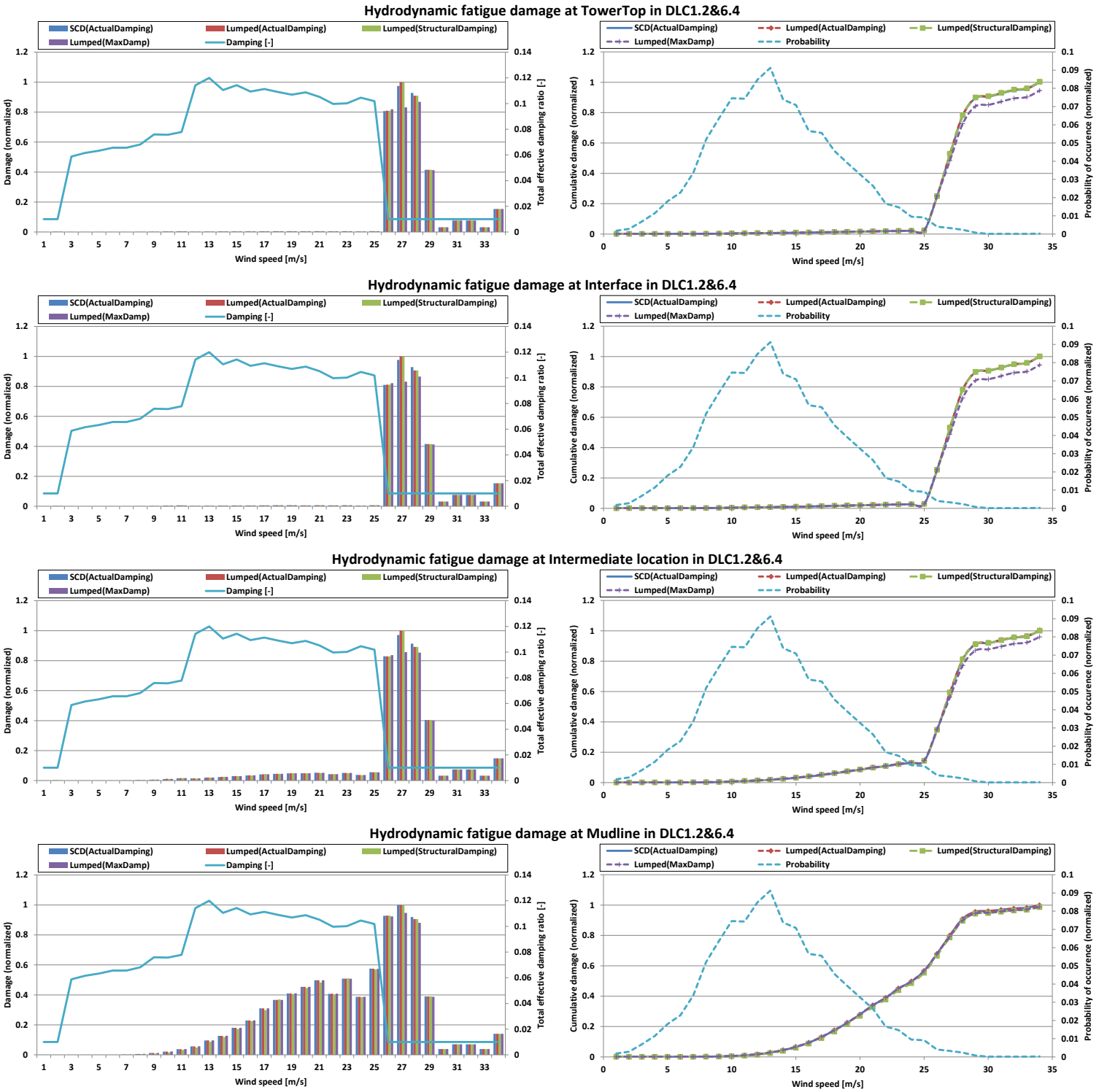

Figure 43: Distribution of hydrodynamic fatigue damage from full wave climate and lumped waves together with damping and probability of occurrence over wind speed at different locations for waves from 270 degree and wind from 270 degree.

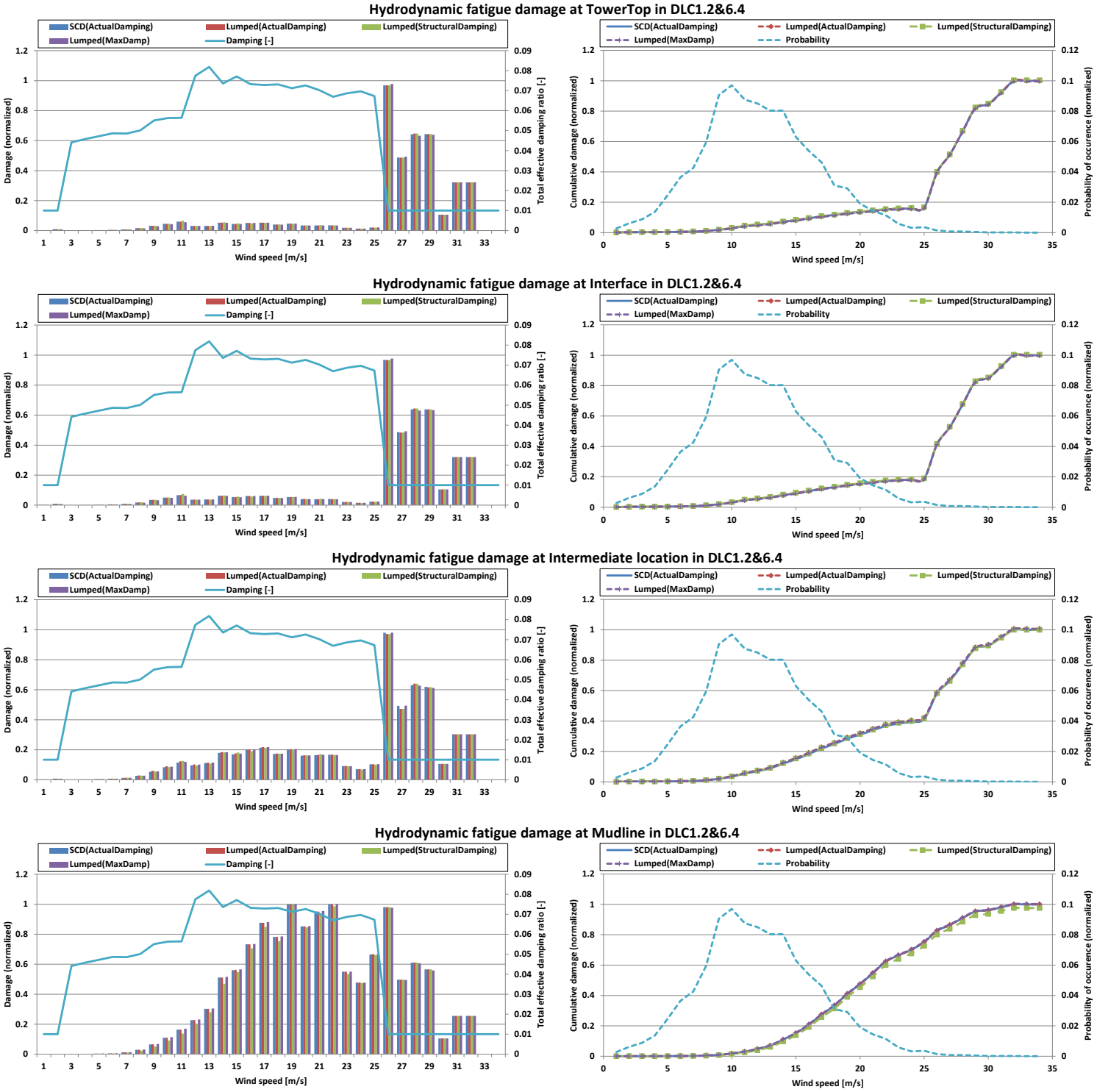

Figure 44: Distribution of hydrodynamic fatigue damage from full wave climate and lumped waves together with damping and probability of occurrence over wind speed at different locations for waves from 270 degree and wind from 240 degree.

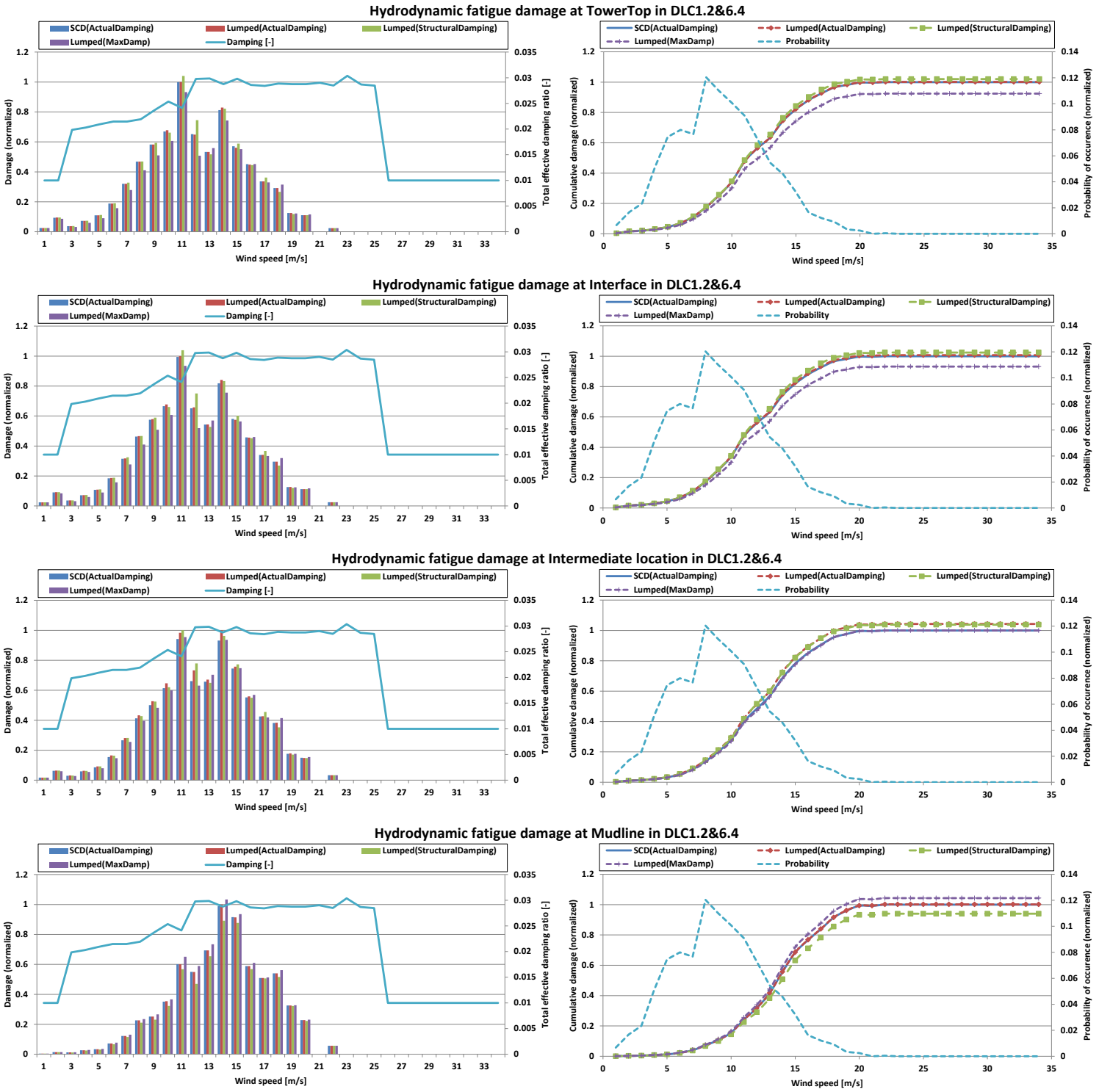

Figure 45: Distribution of hydrodynamic fatigue damage from full wave climate and lumped waves together with damping and probability of occurrence over wind speed at different locations for waves from 270 degree and wind from 210 degree.

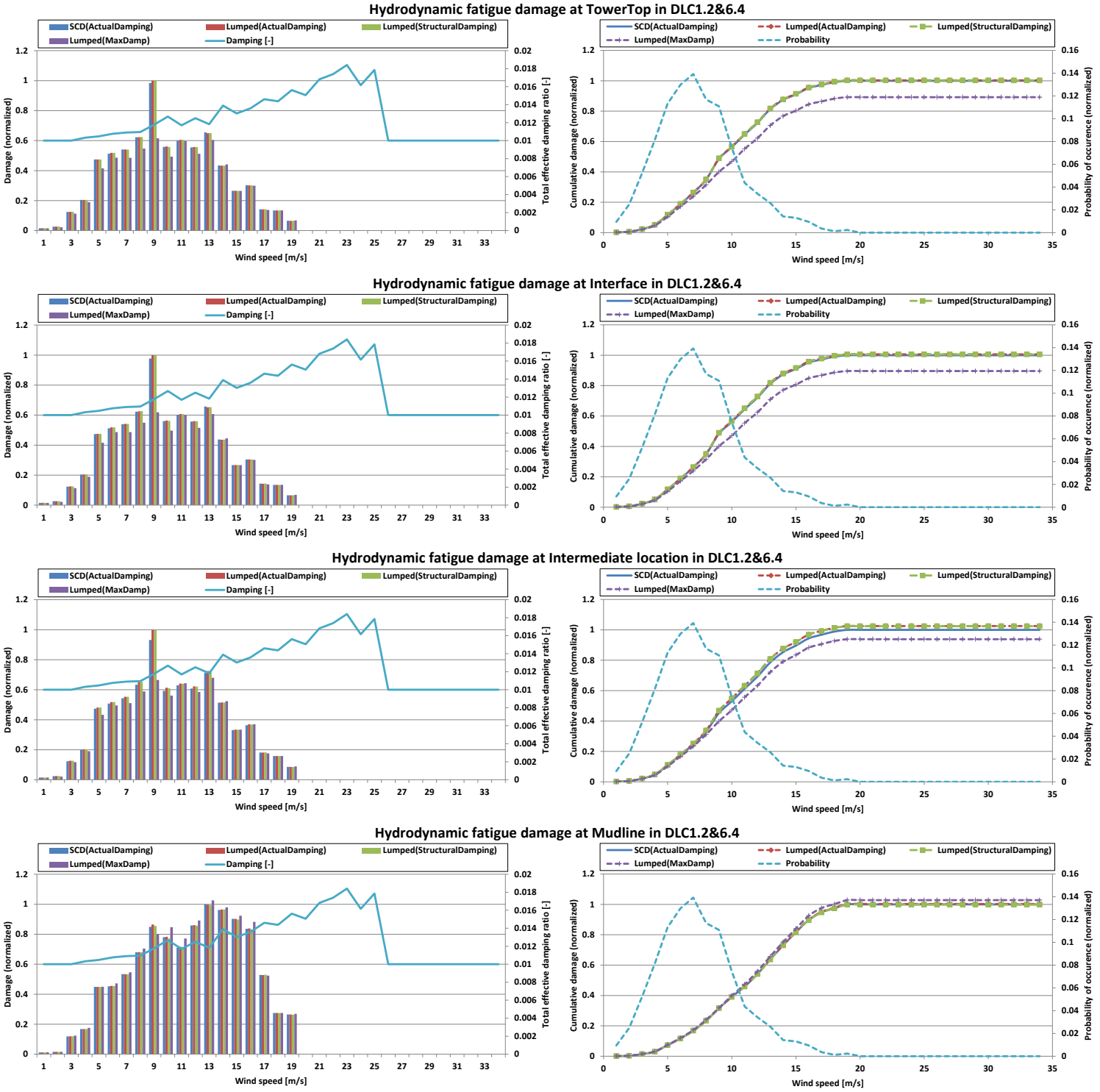

Figure 46: Distribution of hydrodynamic fatigue damage from full wave climate and lumped waves together with damping and probability of occurrence over wind speed at different locations for waves from 270 degree and wind from 180 degree.

5.3 Alternative wave lumping approaches for wind-wave correlations

This section assesses the lumped waves of selected wind-wave correlation approaches by comparing hydrodynamic fatigue damages with the full wave climate for hydrodynamic sensitive structures in extension to the investigations performed in paper 3 [63]. The following approaches are subjected to the investigations in this section:

- Damage equivalent approach according to paper 3 [63], hereinafter denoted as Passon's approach.
- Probability based averaging of sea-state parameters according to paper 3 [63].
- Iterative, damage equivalent approach according to Kühn [41].
- Damage equivalent approach according to Seidel [66].

All approaches are briefly described in paper 3 [63]. The wave lumping of a SCD for a given wind speed bin v_k, wind direction and wave direction is established by the condensation of all combinations for the $i=1..n$ wave height classes $H_{s,i}$ and $j=1..m$ wave period classes $T_{p,j}$ to only one representative set of $H_{s,k}$ and $T_{p,k}$. It should be noted that Mittendorf [45] studied further wind-wave correlation approaches. However, these are mainly suited for hydrodynamic insensitive structures such as jackets and therefore not subjected in the following investigations.

Comparison of hydrodynamic fatigue damage from the different wave lumping approaches

Hydrodynamic fatigue damages are now calculated for the different wave lumping approaches and compared to results obtained for the full wave climate represented by SCDs. The same OWT configuration with waves from 270 degrees, as introduced in the previous section 5.2, is applied again. The main difference to the investigations in paper 3 [63] is the use of damping conditions according to Table 9 corresponding to DLC1.2 and 6.4 with misalignment cases between 0 and 90 degrees. Figure 47 to Figure 50 show the normalized individual and cumulative hydrodynamic fatigue damages at the four locations marked in Figure 42. Furthermore, the figures show the total effective damping and normalized probability of occurrence over wind speeds.

The probability based averaging approach results in acceptable approximations of the hydrodynamic fatigue damages from the full wave climate for the 30 degree misalignment cases in Figure 48. Furthermore, only slightly non-conservative hydrodynamic fatigue damage approximations are obtained for the aligned cases in Figure 47. However, significant non-conservative hydrodynamic fatigue damages are calculated in comparison to the full wave climate for the high misalignment (and low effective damping) scenarios of 60 and 90 degree in Figure 49 and Figure 50.

Kühn's [41] and Seidel's [66] approach yields in all misalignment cases very good hydrodynamic fatigue damages at Mudline level. This is introduced from the fact that the sea-state parameters of their lumped waves have been derived on basis of target damage levels from the full wave climate at this specific reference location. Furthermore, good approximations of hydrodynamic fatigue damages from the full wave climate are obtained for all locations in the aligned and 30 degree misalignment cases in Figure 47 and Figure 48 with differences up to 4.8%. However, larger differences on the non-conservative side are present at all locations

other than at Mudline level for the high misalignment (and low effective damping) scenarios of 60 and 90 degree in Figure 49 and Figure 50.

The best overall agreement of hydrodynamic fatigue damage for all misalignment cases and locations is obtained with Passon's wind-wave correlation approach from paper 3 [63]. The largest differences occur at the intermediate location with 4.3% for the 60 degree misalignment case in Figure 49 and with 2.5% for the 90 degree misalignment case in Figure 50. In both cases, the differences are small and on the conservative side.

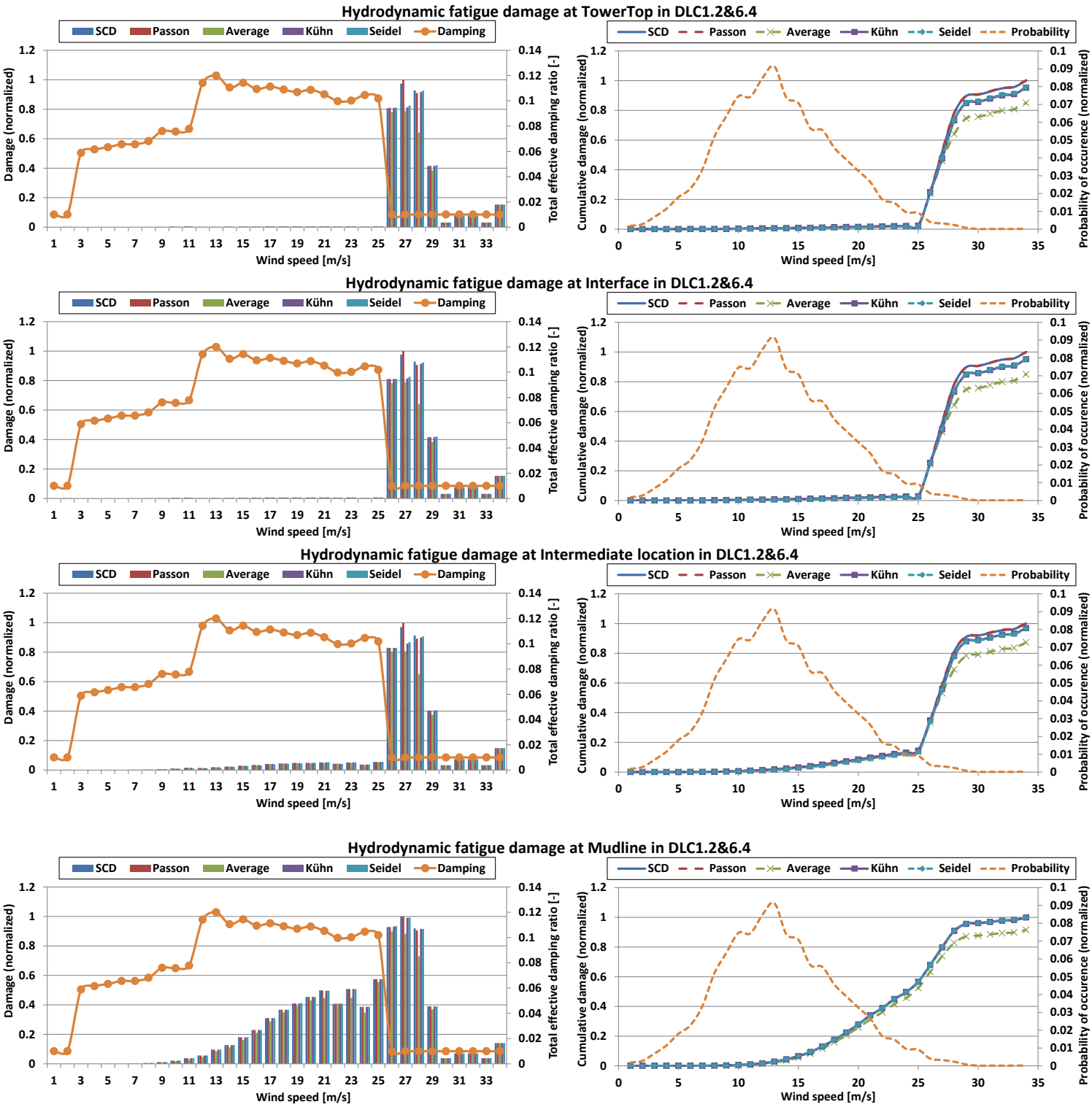

Figure 47: Distribution of hydrodynamic fatigue damage from full wave climate and lumped waves together with damping and probability of occurrence over wind speed at different locations for waves from 270 degree and wind from 270 degree.

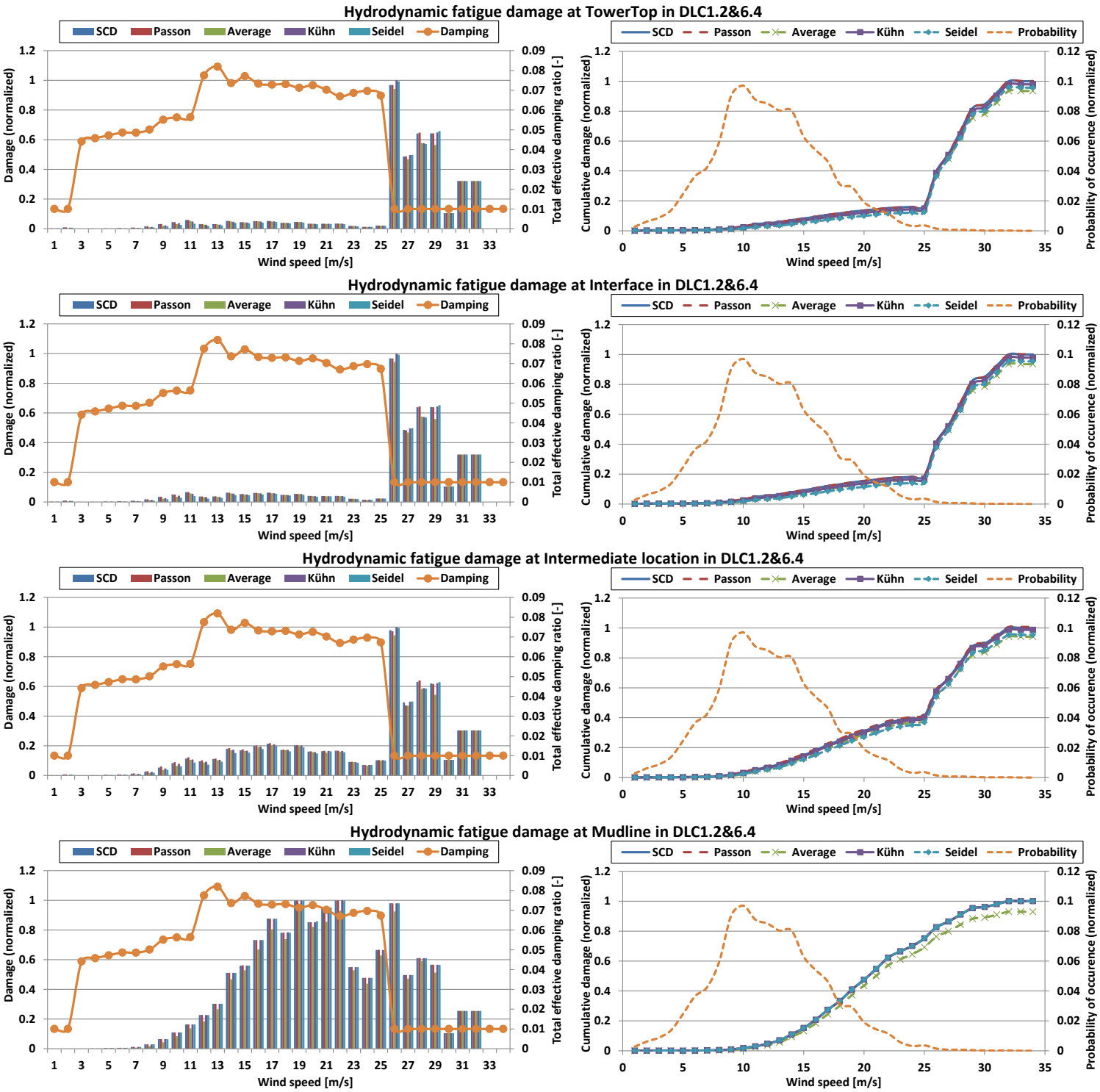

Figure 48: Distribution of hydrodynamic fatigue damage from full wave climate and lumped waves together with damping and probability of occurrence over wind speed at different locations for waves from 270 degree and wind from 240 degree.

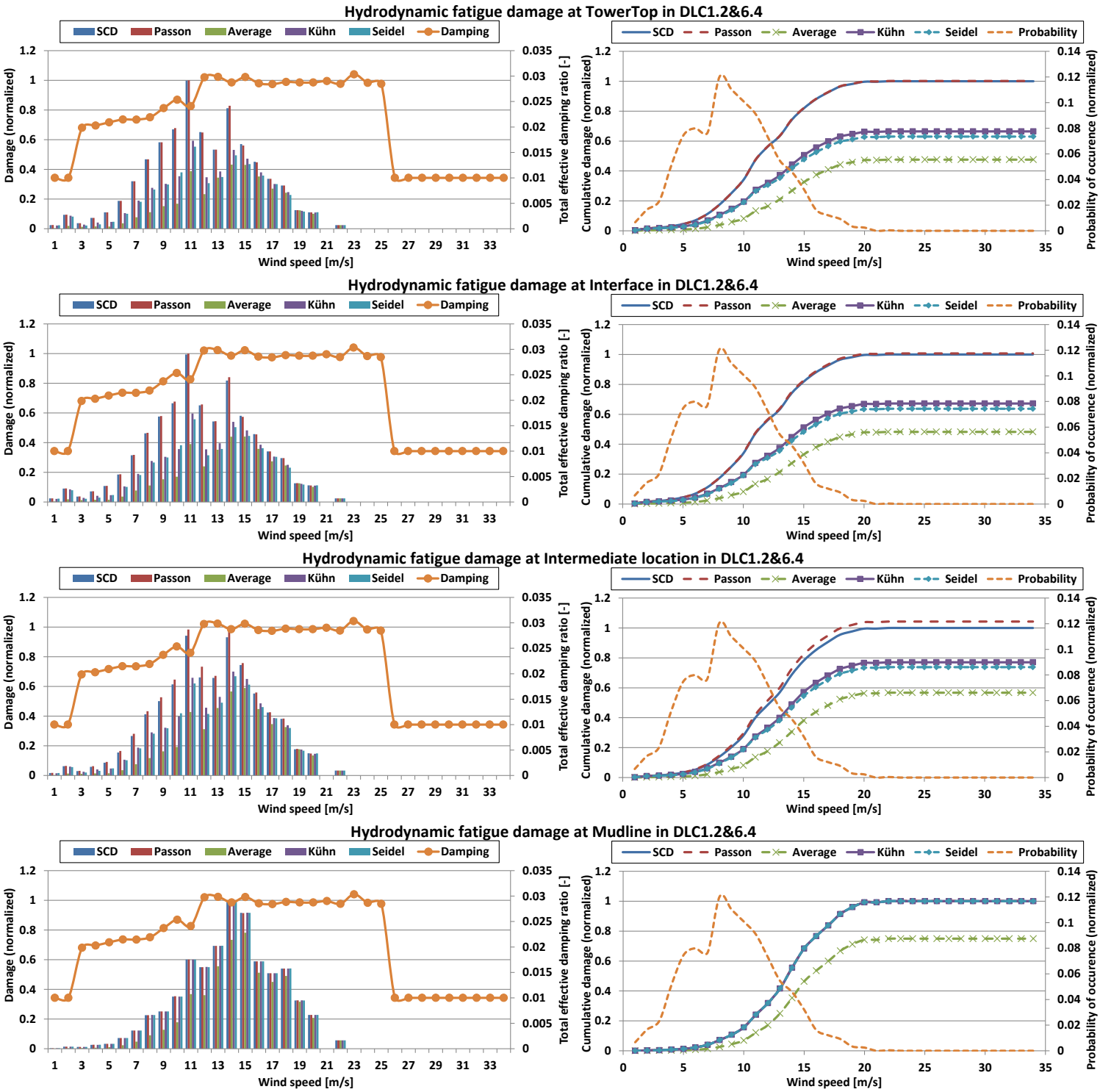

Figure 49: Distribution of hydrodynamic fatigue damage from full wave climate and lumped waves together with damping and probability of occurrence over wind speed at different locations for waves from 270 degree and wind from 210 degree.

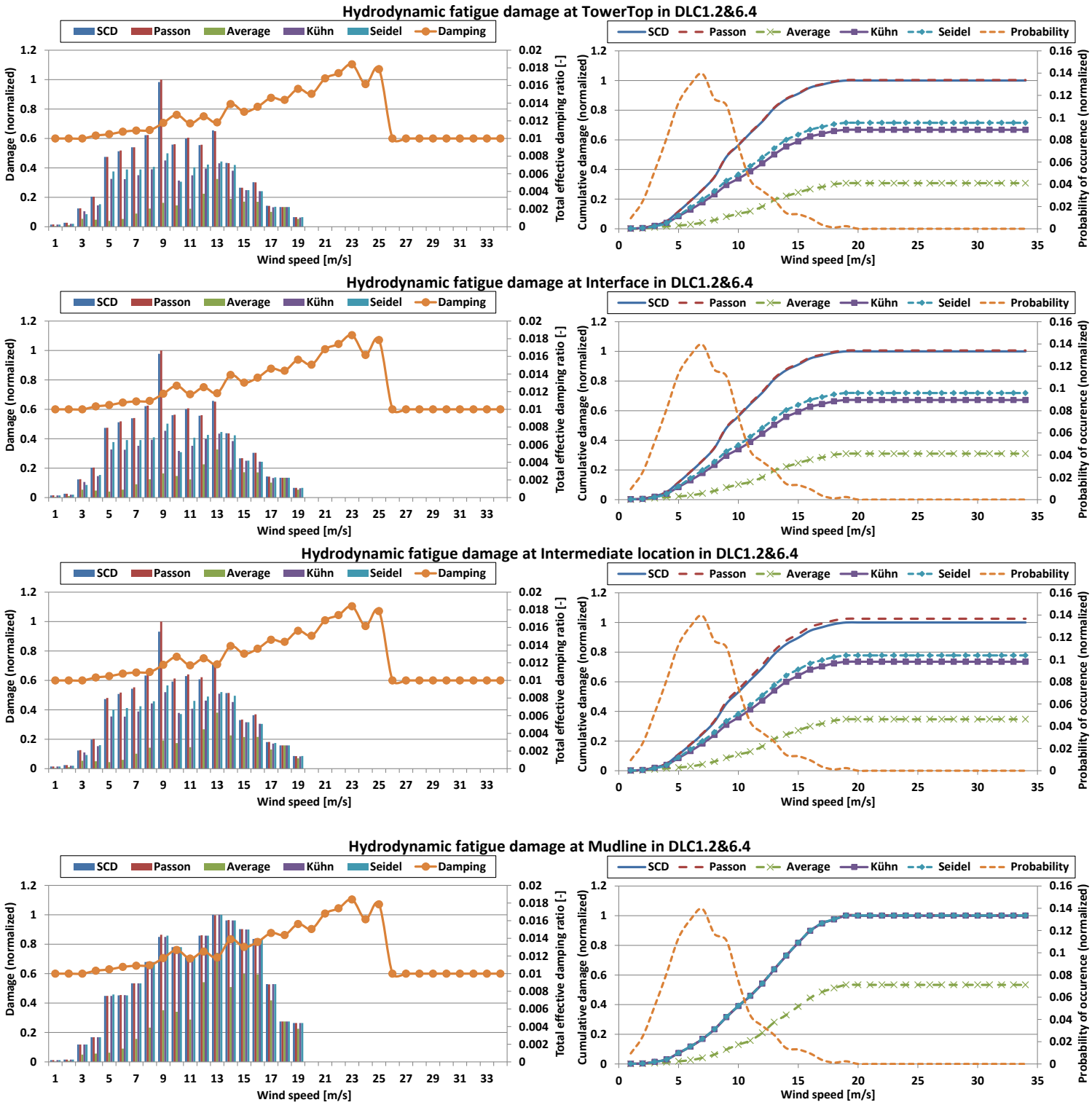

Figure 50: Distribution of hydrodynamic fatigue damage from full wave climate and lumped waves together with damping and probability of occurrence over wind speed at different locations for waves from 270 degree and wind from 180 degree.

The individual wind-wave misalignment cases for v_k=11m/s are investigated in more detail for the different wave lumping approaches. Figure 51 shows exemplarily the scaled damage surfaces and target damage levels at different locations in the structure for waves from 270 degree and wind from 180 degree as perspective view and top view.

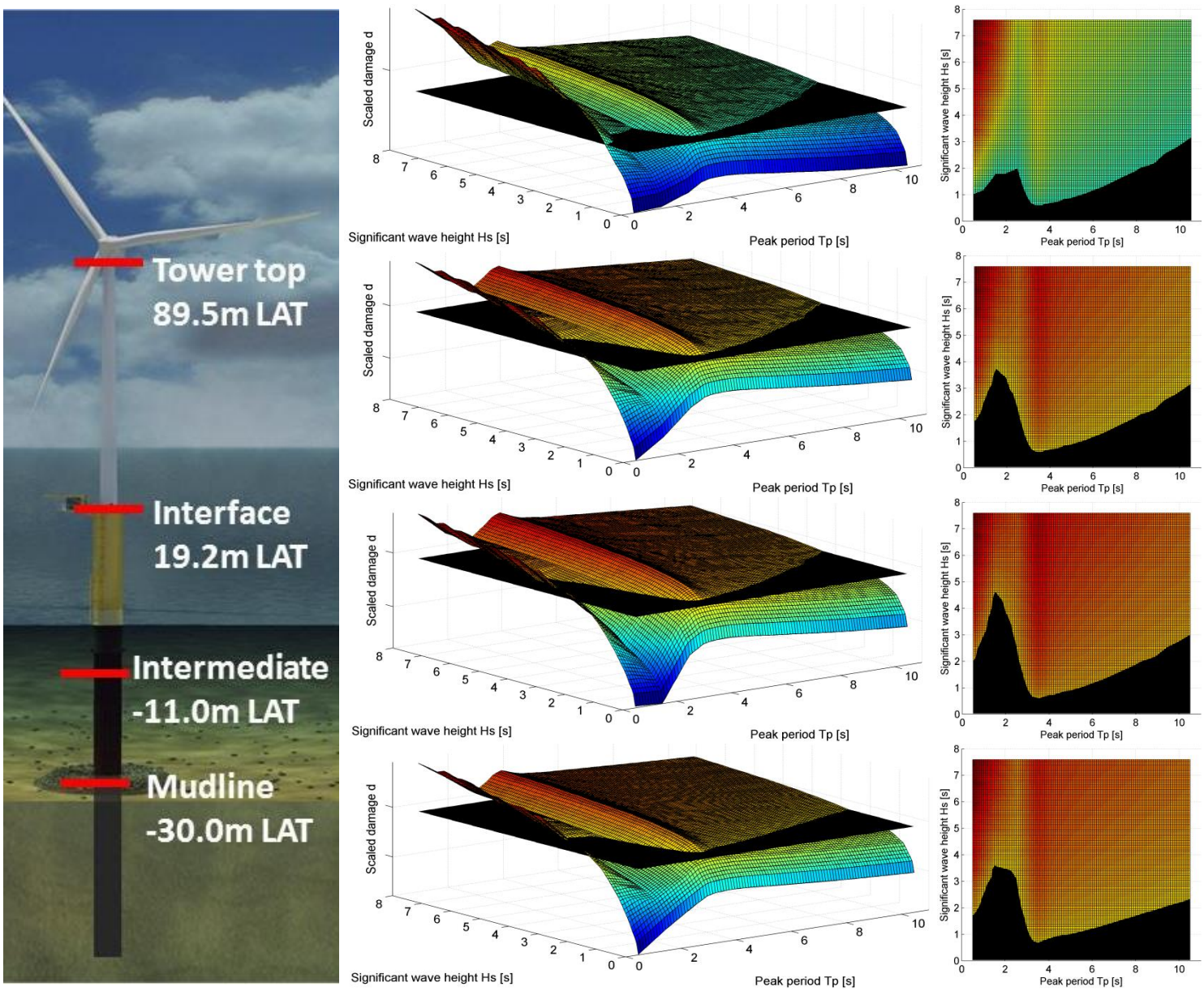

Figure 51: Scaled damage surface and target level in perspective view (centre) and top view (right) at Tower top, Interface, Intermediate and Mudline levels for v_k=11m/s, waves from 270 degree and wind from 180 degree.

The resulting DCLs at Tower top, Interface, Intermediate and Mudline levels are shown for the investigated misalignment cases in Figure 52 to Figure 55, together with the calculated sea-state parameters from all different wave lumping approaches.

As indicated in Figure 50, the approaches from Kühn [41] and Seidel [66] yield sea-state parameters on the Mudline level DCLs of all misalignment cases, but not on the DCL of any of the three other levels for any of the misalignment cases. However, in particular, for the low misalignment cases with waves from 270 degree and wind from either 270 or 240 degree, the resulting sea-state parameters of the lumped waves are rather close to the DCLs at Tower top, Interface and the Intermediate levels. This closeness results in good approximations of hydrodynamic fatigue damages as observed in Figure 47 and Figure 48.

The averaging approach yields sea-state parameters that are generally not located on any DCL, therefore introducing fatigue damage differences at all locations. However, the sea-state parameters are significantly closer to DCLs and the DLC intersections for the low misalignment cases. This leads to smaller errors in the hydrodynamic fatigue damages compared to the high misalignment cases.

Only Passon's damage equivalent wind-wave correlation method from paper 3 [63] yields sea-state parameters at the intersection of all DCLs, hence maintaining damage equivalency at all locations.

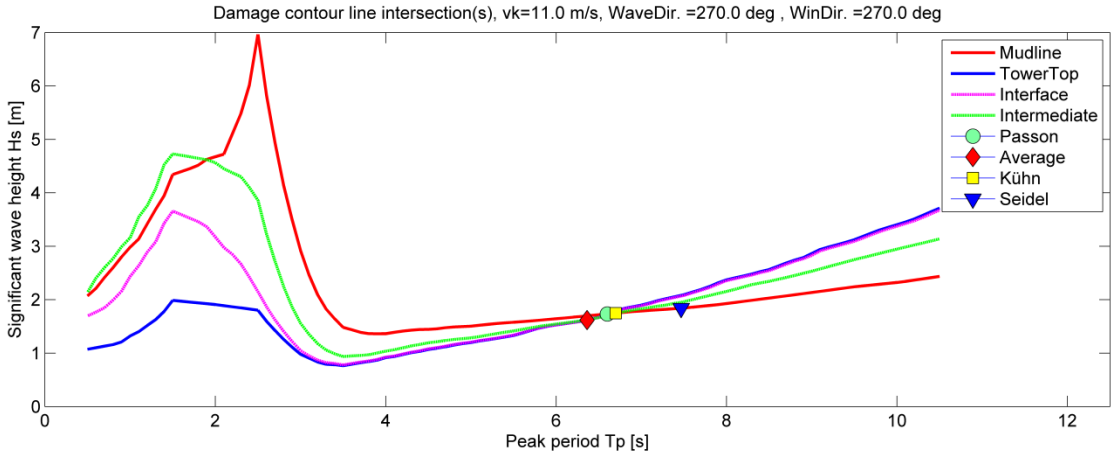

Figure 52: DCLs at Tower top, Interface, Intermediate and Mudline levels and calculated sea-state parameters of the corresponding lumped wave from different approaches at v_k=11m/s for 0 degree wind-wave misalignment.

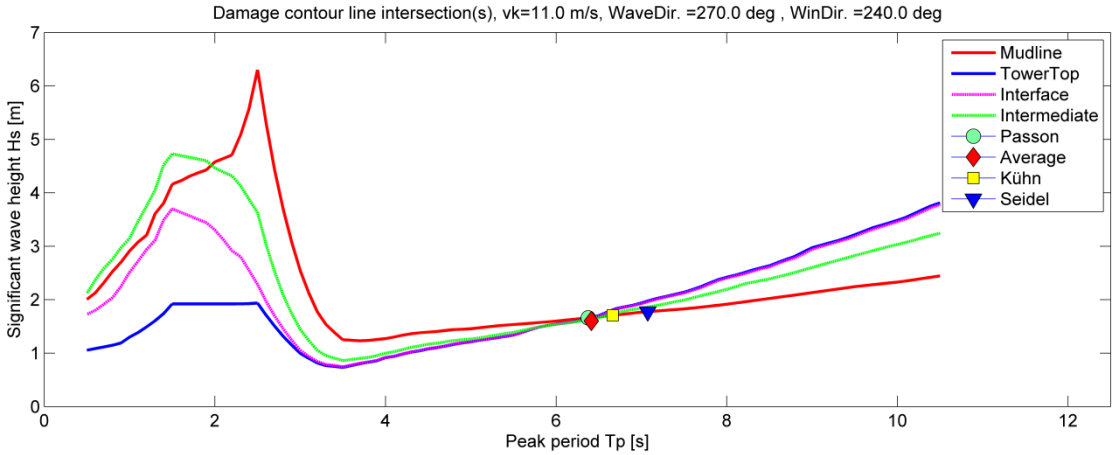

Figure 53: DCLs at Tower top, Interface, Intermediate and Mudline levels and calculated sea-state parameters of the corresponding lumped wave from different approaches at v_k=11m/s for 30 degree wind-wave misalignment.

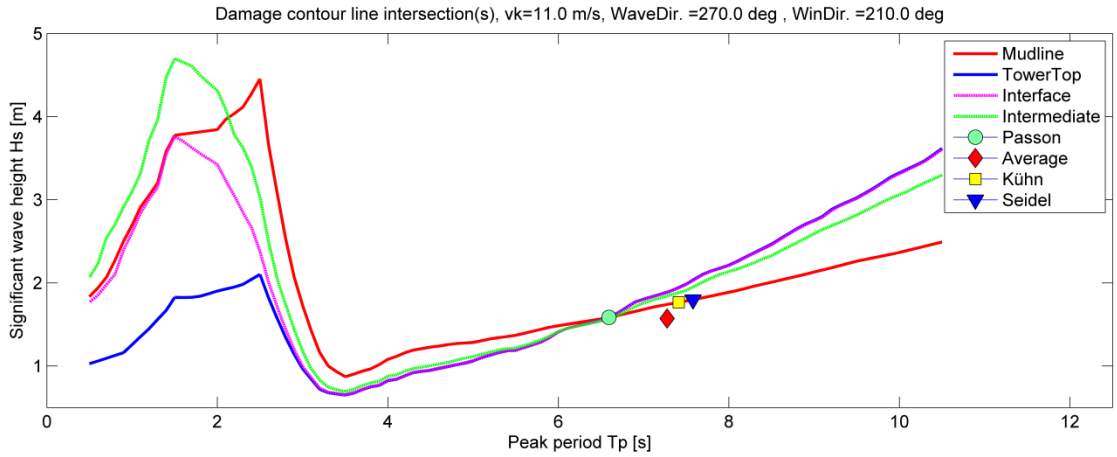

Figure 54: DCLs at Tower top, Interface, Intermediate and Mudline levels and calculated sea-state parameters of the corresponding lumped wave from different approaches at v_k=11m/s for 60 degree wind-wave misalignment.

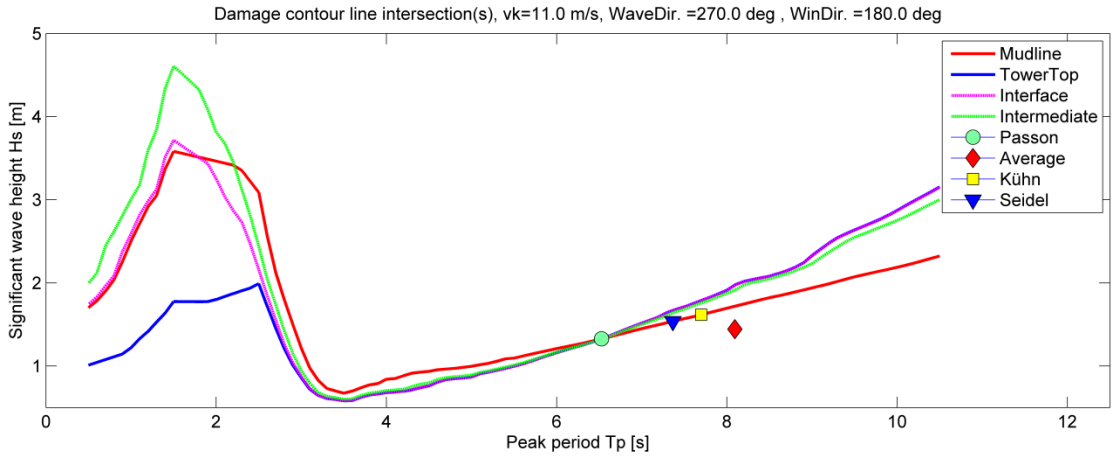

Figure 55: DCLs at Tower top, Interface, Intermediate and Mudline levels and calculated sea-state parameters of the corresponding lumped wave from different approaches at v_k=11m/s for 90 degree wind-wave misalignment.

5.4 Limited availability of met-ocean databases

The author has frequently observed that only marginal wind and wave distributions are available for detailed designs of offshore wind farms, requiring that missing information on wind-wave joint occurrences have to be supplemented on basis of reasonable assumptions. Ideally, these assumptions allow for obtaining an adequate hydrodynamic (target) damage distribution over wind speeds. Due to the high practical relevance, such a scenario is addressed in this section. In this context an alternative, simplified calculation approach which combines elements from Mittendorf's [46] correlation method on basis of equal cumulative probabilities and the new damage equivalent method from paper 3 [63]. Furthermore, the implications on the hydrodynamic fatigue damage over wind speed from this simplified approach are briefly assessed. For practical applications, however, it is strongly emphasized to aim for a detailed met-ocean database and an adequate approach for derivation of the hydrodynamic fatigue damage over wind speeds such as introduced in paper 3 [63].

The starting point for the simplified calculation approach of hydrodynamic fatigue damage over wind speed is the establishment of a wind speed – wave height correlation based on only marginal wind and wave distributions. It should be noted that this wind speed – wave height relation is required for establishment of an approximation of the hydrodynamic damage over wind speed distribution. For a particular wind-wave direction, these marginal distributions are typically described by a Weibull distribution for the wind and one SCD for the waves. In this case, the wave climate is thus not described by an SCD for each individual wind speed bin, but only one SCD covering all wind speeds i.e. corresponding to the sum of the SCD for the individual wind speeds. The correlation of significant wave heights to wind speeds can be based on the condition of equal non-exceedance or cumulative probabilities as described by Mittendorf [46]. The individual steps of the wind speed – wave height correlation process are shown in Figure 56 and described below.

Based on the directional Weibull distribution for the wind, the non-exceedance probability $F(v)$ is determined for the upper bound v_u and lower bound v_l of each wind speed class v_k under consideration. For the SCD, the sum of probabilities over wave periods $T_{p,j}$ results in the total probability p_i for the individual wave height classes $H_{s,i}$. This allows for establishment of the cumulative probability distribution over wave heights $F(H_s)$. Similarly to the wind speed distribution $F(v)$ the non-exceedance probability $F(H_s)$ is calculated for the upper class value $H_{s,u}$ and lower class value $H_{s,l}$ for each wave height class i in the SCD. It should be noted that the wave height classes i in the SCD do not correspond to the wind speed classes k. However, as mentioned before, it is assumed that a relation between wind speed and wave height can be established on basis of equal cumulative probabilities.

The upper and lower limits $H_{s,u,k}$ and $H_{s,l,k}$ for each wave height class $H_{s,k}$ associated to each individual wind speed class v_k can therefore be interpolated from $F(H_s)$ assuming the same non-exceedance probabilities as the corresponding upper and lower limit wind speed for wind speed class v_k. The result is a unique wind speed – wave height relation for each wind-wave direction as indicated in Figure 56.

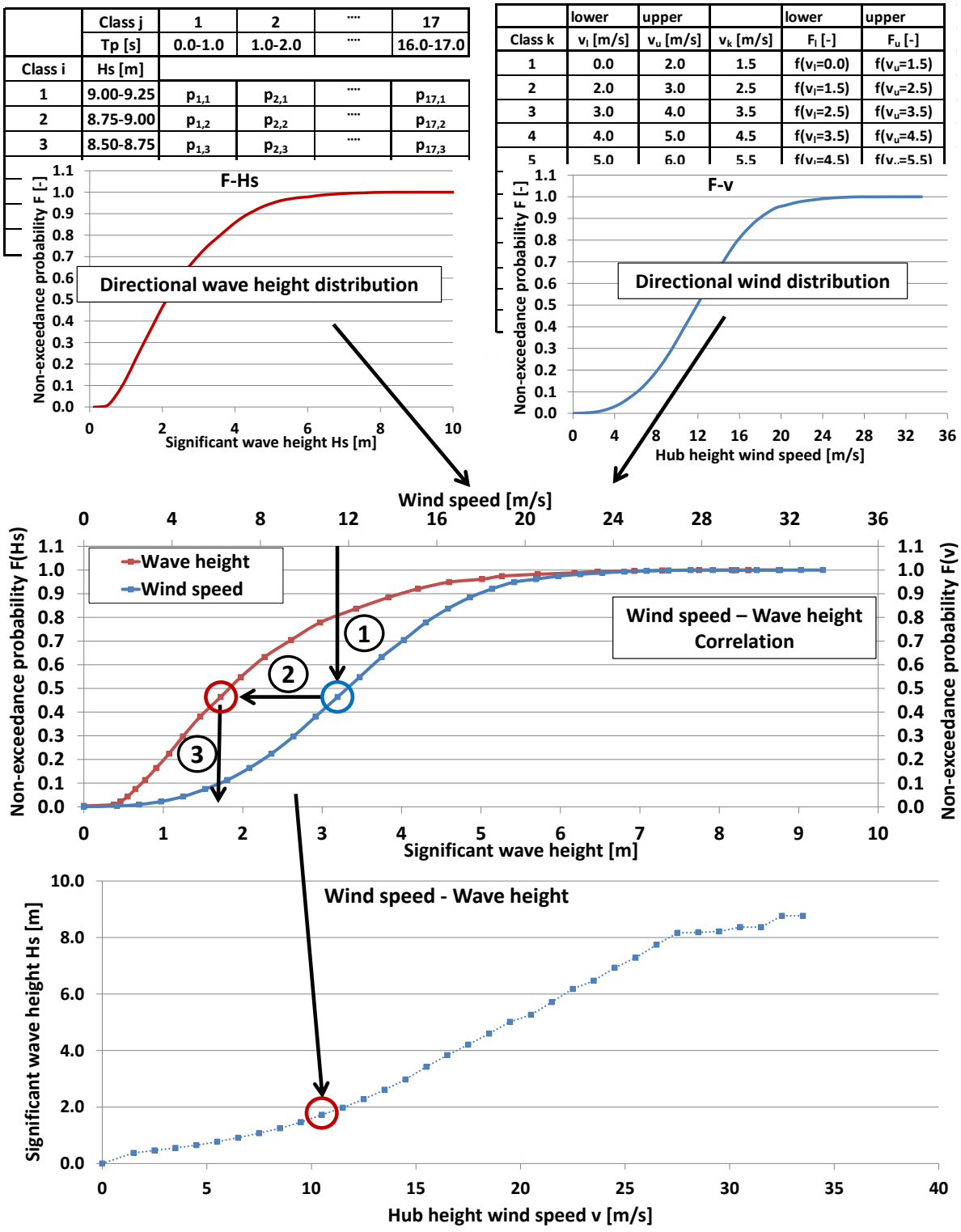

Figure 56: Correlation of wind speeds and wave heights, exemplarily shown for v_k=11.5m/s and $H_{s,k}$=1.85m.

Based on the established combinations of wind speed, probability and wave height, the hydrodynamic fatigue damages over wind speeds are subsequently calculated in accordance to the process illustrated in Figure 57 using the damage matrix $\boldsymbol{D}$. First the damage matrix $\boldsymbol{D}$ is calculated on basis of the unit damage matrix $\boldsymbol{D}^*$ and the SCD according to Eq. 32 from section 5.1. The sum of the fatigue damages over wave periods $T_{p,j}$ results in the total damage d_i for the individual wave height classes $H_{s,i}$. This allows for establishment of the cumulative fatigue damage distribution over wave heights $d_{cum}(H_s)$. Secondly, the upper and lower values of the cumulative fatigue damage distribution $d_{cum,u,k}$ and $d_{cum,l,k}$ are calculated for the upper and lower wave heights $H_{s,u,k}$ and $H_{s,l,k}$ by interpolation from $d_{cum}(H_s)$. This allows for calculation of target damage levels according to Eq. 33 for each wind speed class v_k and subsequent application of the wind-wave correlation approach from paper 3 [63].

$$d_k = d_{cum,u,k} - d_{cum,l,k} \qquad \text{Eq. 33}$$

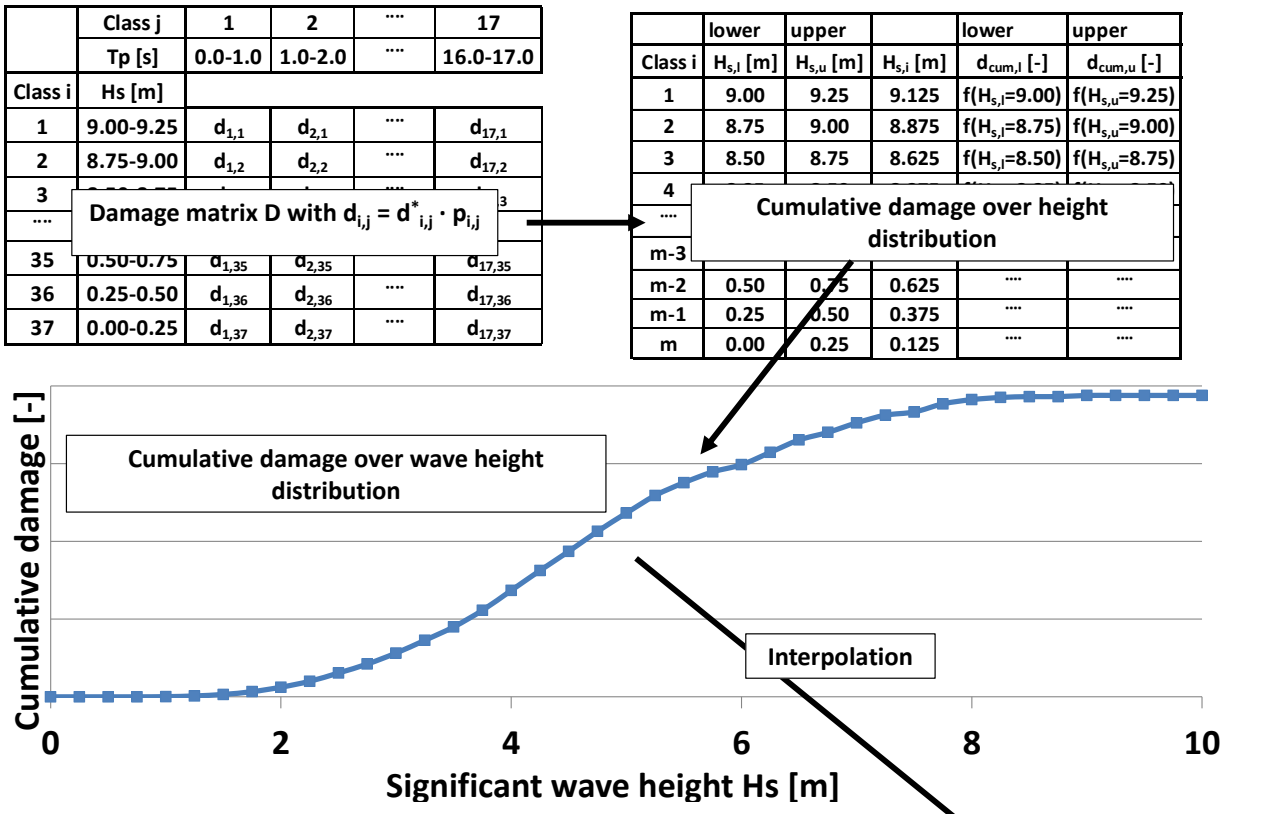

	Class j	1	2	....	17
	Tp [s]	0.0-1.0	1.0-2.0	....	16.0-17.0
Class i	Hs [m]				
1	9.00-9.25	$d_{1,1}$	$d_{2,1}$	....	$d_{17,1}$
2	8.75-9.00	$d_{1,2}$	$d_{2,2}$	....	$d_{17,2}$
3					
....					
35	0.50-0.75	$d_{1,35}$	$d_{2,35}$		$d_{17,35}$
36	0.25-0.50	$d_{1,36}$	$d_{2,36}$	....	$d_{17,36}$
37	0.00-0.25	$d_{1,37}$	$d_{2,37}$	....	$d_{17,37}$

	lower	upper		lower	upper
Class i	$H_{s,l}$ [m]	$H_{s,u}$ [m]	$H_{s,i}$ [m]	$d_{cum,l}$ [-]	$d_{cum,u}$ [-]
1	9.00	9.25	9.125	$f(H_{s,l}=9.00)$	$f(H_{s,u}=9.25)$
2	8.75	9.00	8.875	$f(H_{s,l}=8.75)$	$f(H_{s,u}=9.00)$
3	8.50	8.75	8.625	$f(H_{s,l}=8.50)$	$f(H_{s,u}=8.75)$
4					
....					
m-3					
m-2	0.50	0.75	0.625	....	....
m-1	0.25	0.50	0.375	....	....
m	0.00	0.25	0.125	....	....

	lower	upper				lower	upper				lower	upper	
Class k	v_l [m/s]	v_u [m/s]	v_k [m/s]	$F_{k,l}$ [-]	$F_{k,u}$ [-]	$H_{s,k,l}$ [m]	$H_{s,k,u}$ [m]	$H_{s,k}$ [m]	p_k [-]	$d_{cum,k,l}$ [-]	$d_{cum,k,u}$ [-]	d_k [-]
1	0.0	2.0	1.5	$f(v_l=0.0)$	$f(v_u=1.5)$	$f(F\|v_l=35.5$ m/s)	$f(F\|v_u=36.5$ m/s)	$f(H_{s,l}, H_{s,u})$	F_u-F_l	$f(H_{s,k,l})$	$f(H_{s,k,u})$	$d_{cum,u} - d_{cum,l}$
2	2.0	3.0	2.5	$f(v_l=1.5)$	$f(v_u=2.5)$	$f(F\|v_l=34.5$ m/s)	$f(F\|v_u=35.5$ m/s)	....	....	....	....	....
....	....	....	....	....	....	....	....	....	....	....	....	....
n-1	36.0	37.0	36.5	....	....	....	....	....	....	....	....	....
n-1	37.0	38.0	37.5	....	....	....	....	....	....	....	....	....

Figure 57: Calculation process of hydrodynamic fatigue damages over wind speed.

This simplified approach is based on joint distribution assumptions for the marginal wind and wave distributions in order to establish the required (hydrodynamic) target fatigue damage over wind speed relation. It should be noted that the term 'simplified' refers to the necessary assumption on the wind-wave joint distribution and the approximate character of the established damages over wind speeds. However, the actual calculation procedure for the simplified approach is more complex and cumbersome in comparison to the approach based on detailed SCD information over wind speeds, wind directions and wave directions introduced in paper 3 [63]. The initial wave height over wind speed relations are only used for determination of the (hydrodynamic) target fatigue damage over wind speed. Alternatively, this could also have been based on a wave period over wind speed relation. In both cases only the established hydrodynamic fatigue damage over wind speed relations are used in the final wind-wave correlation step.

An interesting question is, how well the simplified approach can approximate the actual distribution of hydrodynamic fatigue damages over wind speed? Normally, this cannot be assessed since the reason for application of the simplified approach is the lack of adequate joint property information on the wind-wave climate. However, all information is available for the Veja Mate site and therefore this assessment is performed for the exemplary OWT configuration from section 5.2 under consideration of a scenario with only structural damping.

The 'reference' case is established on basis of the detailed met-ocean database using the SCDs for the individual wind speeds in a direct damage over wind speed calculation. The 'simplified' case, on the other hand, follows the simplified approach on basis of only marginal wind and wave distributions introduced in this section. Figure 58 shows the actual distribution of individual and cumulative (normalized) fatigue damages over wind speeds for the reference case in comparison to the results obtained for the simplified case. From the cumulative damage distribution, it can be seen that the total fatigue damage is the same in both cases as could be expected since the total wave climate is the same for both cases. However, significant differences are present for fatigue damage at individual wind speeds with a pronounced shift of damages towards higher wind speeds for the reference case.

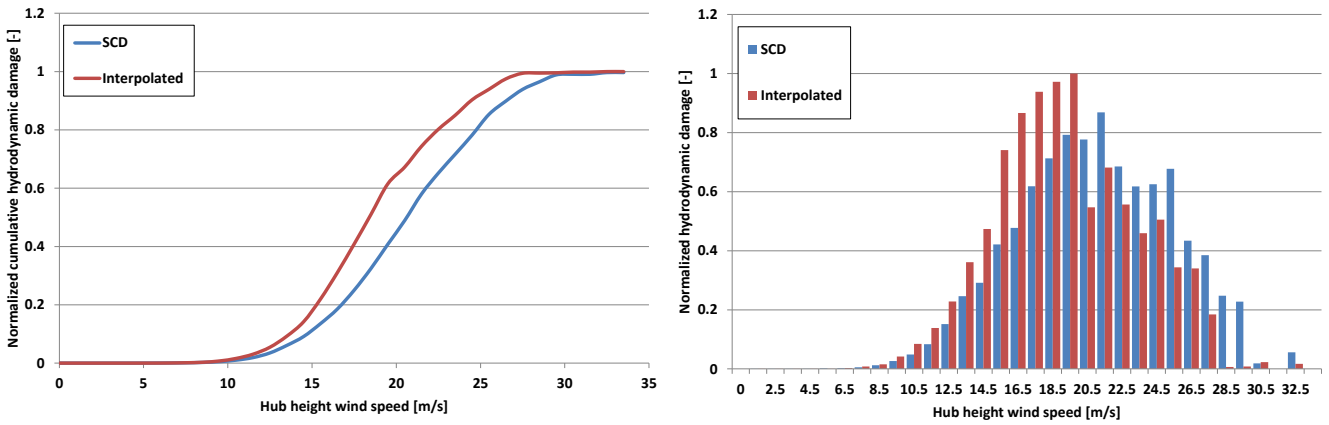

Figure 58: Normalized distribution of cumulative (left) and individual (right) hydrodynamic fatigue damage over wind speeds.

Although equal total hydrodynamic fatigue damages have been obtained, a negative impact on the accuracy of the combined wind-wave fatigue is expected for the simplified case. This is due to the non-linear influence of the individual damage contributions from wind and waves to the combined fatigue damage. Therefore, the author recommends further assessments of the simplified approach. Such assessments should focus on the influence generated from the shifted damage distribution on the final wind-wave correlations and the resulting combined wind-wave fatigue damages. This requires aero-elastic simulations of simultaneous wind-wave loading combinations with the aim to clarify whether conservative or non-conservative total wind-wave fatigue loads are obtained by the simplified approach.

5.5 Summary

An adequate representation of the site-specific wind-wave joint distribution is essential for the calculation of accurate fatigue design loads and therefore for cost-efficient and safe designs of offshore wind turbines. For the example of typical North Sea sites, a rather wide range for the combination of sea-states and wind speeds can potentially occur for individual combinations of wind direction and wave direction. This would result in an impractically large amount of design load simulations in case all these combinations are addressed individually in the design process. In current design practice, the wave climate is therefore most commonly subjected to lumping approaches while the full wind climate[10] is maintained, resulting in equivalent wind-wave correlations for design purposes. Such wind-wave correlations contain a substantially reduced amount of wind and wave parameter combinations compared to the actual wind-wave climate. Preservation of the hydrodynamic fatigue distribution from the full wave climate is an important aspect in this wind-wave correlation. In the particular case of hydrodynamic sensitive structures such as offshore wind turbines with monopile foundations an adequate consideration of the dynamics is therefore required in the establishment of wind-wave correlations for design purposes. However, only a few wind-wave correlation methods exist for the fatigue design of offshore wind turbines and none of them take the dynamics of the full structure adequately into account.

A new wind-wave correlation method has therefore been developed in paper 3 [63] which is based on the work carried out in paper 2 [62]. The new method addresses the current lack of wind-wave correlation methods with an adequate consideration of dynamics for the fatigue design of hydrodynamic sensitive offshore wind turbines and has been assessed and compared to alternative methods. The investigations show that only the lumped wave climate of the new method allows for the preservation of the hydrodynamic fatigue damages from the full wave climate throughout the offshore wind turbine structure.

The calculations for the assessment of the new method have been based on a limited set of conditions. However, real offshore wind turbines are subjected to a large variety of fatigue relevant conditions during their lifetime. Therefore, the author recommends further investigations of the influence from such conditions in future studies similar to the investigations of different conditions in paper 2 [62]. In this context, the influence from different damping conditions in the establishment of the damage equivalent wind-wave correlations and the resulting hydrodynamic fatigue damage distributions has been investigated. In comparison to reference results with the total effective damping, i.e. including aerodynamic damping contributions, it has been shown that hydrodynamic fatigue damages are also captured rather well in case the lumped waves are derived on basis of only the structural damping conditions without aerodynamic damping. Application of structural damping conditions for the derivation of lumped wave sea-state parameters according to the new damage equivalent wind-wave correlation method from paper 3 [63] seems therefore to be an acceptable alternative where no detailed information on the aerodynamic damping is available.

In addition, the author recommends detailed investigations on the validity range of damage equivalent wind-wave correlations from the new method with respect to changes in the structural configuration. Such changes

[10] This refers only to the mean wind speed distributions which are typically expressed by directional Weibull distributions. However, the effective turbulence levels per wind speed are obtained from lumping approaches as well; see e.g. Frandsen [22].

occur during the optimization process within the detailed design phase of the support structures for offshore wind turbines. In the same context, the author recommends to perform large scale verification on basis of aero-elastic simulations of simultaneous wind and wave loading from the wind-wave correlations with the lumped wave climate in comparisons to the full scatter of wind-wave parameter from the full wind and wave climate.

The new method requires a detailed met-ocean database with respect to information on the wind and wave climate as well as wind-wave joint occurrence parameters. However, this is in practice not always available. Therefore an alternative, but simplified approach which is based on a combination of Mittendorf's [46] correlation method on basis of equal cumulative probabilities and the new damage equivalent method from paper 3 [63] has been introduced for design situations with limited met-ocean data. The simplified approach has been assessed in a calculation example by comparison to fatigue results obtained from the full wave climate. It has been demonstrated that the same total hydrodynamic fatigue damage is obtained from the simplified approach. However, significant differences are present for hydrodynamic fatigue damage at individual wind speeds with a pronounced shift of damages towards higher wind speeds for the full wave climate. Although equal total hydrodynamic fatigue damages have been obtained, a negative impact on the accuracy of the combined wind-wave fatigue is expected for the simplified approach. Therefore, the author recommends subjecting this simplified approach to further investigations with simultaneous wind-wave loading in aero-elastic simulations.

6 Simplified Modelling Approaches in the Design Process

Models for the analysis of OWTs may be categorized by different aspects such as the fidelity, i.e. the level of detail in the numerical model including the consideration of interactions between the different parts of the OWT. Different model fidelities have to be considered for individual model types in the design process, i.e. component, subsystem and integrated system models.

Component models deal with single parts such as grouted connections, blades, tubular joints or suction buckets. Modelling and calculations of these individual parts are required for dimensioning, optimisation and certification as well as for derivation of equivalent, but simplified representations in subsystem or system models. Dependent on the actual objectives, such component models ranges from very crude to very detailed. For example, very detailed component models are required for the design of secondary steel items or for individual suction buckets and the surrounding soil as shown in Figure 59.

Subsystem models on the other hand consist of a group of components, e.g. the foundation or the RNA. Those subsystems are modelled relatively detailed with respect to the global subsystem behaviour, relevant interactions and environmental loads, while individual components are often modelled in a simplified manner. For example, FDs apply detailed subsystem models of the foundation for load calculation purposes as explained in paper 1 [61]. However, for other design purposes, such as the natural frequency design or for model verification activities, the RNA needs to be modelled by the FD as well. In such cases, the RNA is often modelled as a lumped mass with corresponding mass moments of inertia by the FD as indicated in Figure 59. This simplification can be motivated by various reasons such as by limited modelling capabilities for RNA specific aspects in the FD's tool.

Integrated system models as indicated in Figure 4 deal with the OWT as a whole unit by considering all interactions between the subsystems and environment as completely as practically possible. Integrated system models of OWTs require a high degree of complexity on a global level in order to deal simultaneously with e.g. aerodynamics, dynamics of the electrical and control system, structural dynamics of the rotor, drive train and support structure, soil-structure interactions and environmental loads. For practical applications such as for load calculations of several thousand design load combinations this high global complexity of integrated system models is achieved at the expense of a lower degree of detail for the individual subsystem and component models. The reasons for the simplifications are often a mix of limited modelling capabilities on component and subsystem level in the integrated OWT load simulation tools and too demanding computational requirements from the detailed subsystem or component models in the aero-elastic simulations.

Many publications exist on state-of-the-art high-fidelity modelling approaches for integrated system models, subsystem models and the numerous component models. Of course, their development and improvement is very important for more accurate modelling and load calculation capabilities. However, the present chapter is intended to focus on simplified (low-fidelity) modelling approaches on subsystem level instead, as this is frequently required in actual design practice, in particular for sequentially integrated load calculation approaches. Reasons for such requirements have been exemplarily addressed in the previous paragraph.

Muskulus & Schafhirt [49] promote the idea of automatic transformations from one level of detail to another in the context of early and advanced design stages, corresponding to the preliminary and the detailed design

phases. In the author's experience, such an automatic transformation is equally beneficial in the sequentially integrated load calculation approach. In design practice, this is often based on model reduction techniques. However, it is very important to ensure a sufficient fidelity of the simplified models in the context of the corresponding analysis in order to avoid errors in the dynamic behaviour and calculated design loads.

The objective of this chapter is to illustrate how to model selected, individual subsystems and components in a simplified manner while preserving accuracy for the intended calculation purpose. The selected modelling aspects are based on some of the constraints most frequently encountered by the author during the last decade.

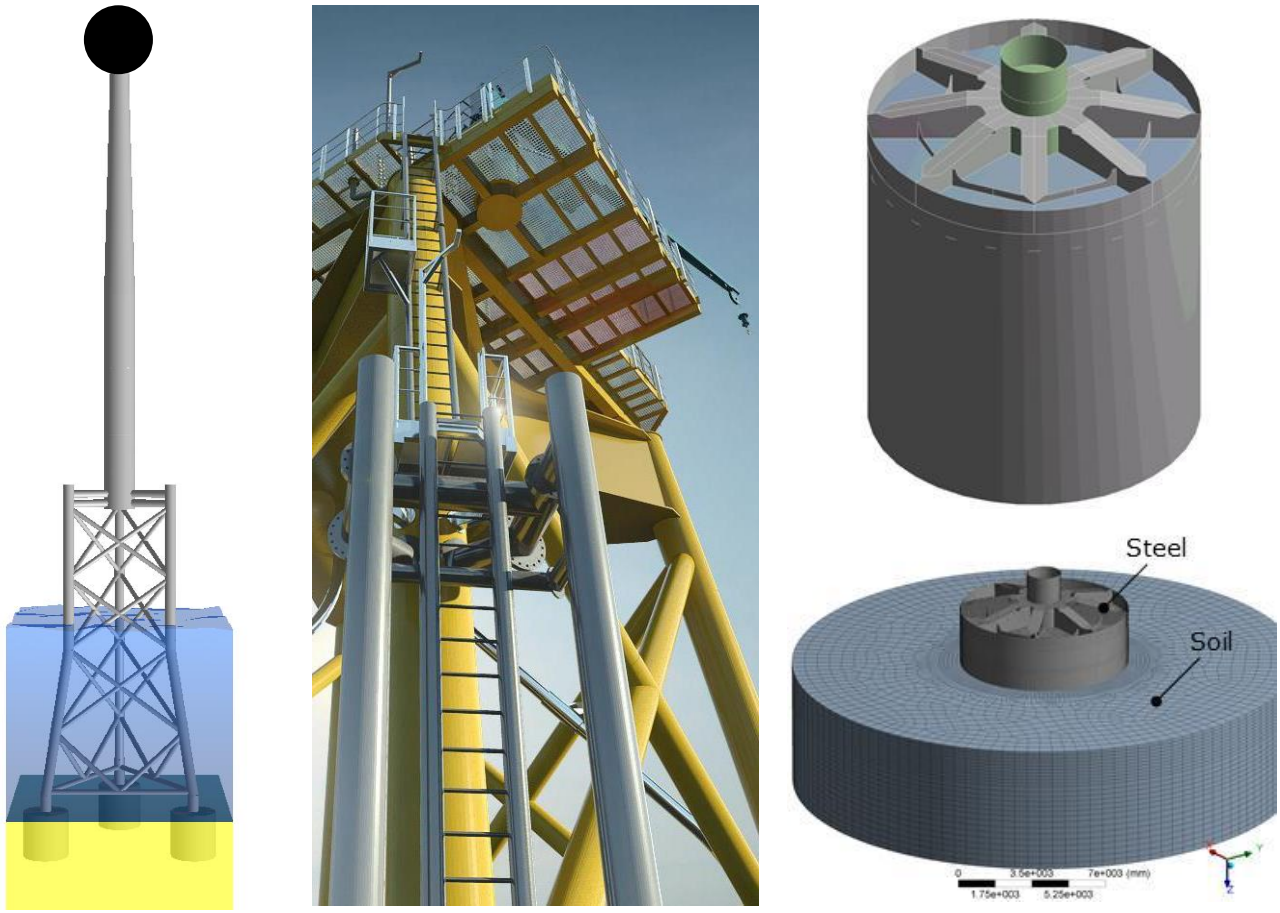

Figure 59: OWT with detailed subsystem model of support structure (left) and component models for secondary steel (middle) and a suction bucket together with the soil (upper and lower right).

6.1 Foundation model reduction by substructuring

Several methods exist in order to reduce the size of OWT models by condensation of a number of DOFs from subsystem- or component models. By this, the dimensions of system matrices as well as load vectors are reduced, allowing for fast analyses as well as efficient load and data exchange processes. In some case, a model reduction is simply required to cope with limitations in the modelling capabilities of the applied tool. A good example is the establishment of 3D finite element based transition piece models for the connection of a jacket with a tubular tower. Most tools for OWTs do not support the required degree of detail in their modelling capabilities to establish a good representation of these structures. Therefore, the detailed transition piece model has been established by an equivalent beam framework in some cases. However, this is a rather time consuming and iterative process. A more efficient solution is the replacement of the complex 3D finite element model by a superelement representation in the foundation subsystem model as well as in the integrated system model. The superelement might be obtained by an appropriate substructuring or model reduction technique.

Similar approaches exist for other components and have often been adopted from the offshore industry such as superelement representations of tubular joints which has already been introduced by Bouwkamp et al. [4] in 1981 and is nowadays frequently applied for OWT jackets. The reader is referred to Voormeeren [76] for further details on the use of model reductions for various components and subsystem models in the integrated OWT model.

This section focuses on model reduction approaches for the whole foundation subsystem as often applied for aero-elastic load simulations in design practice. In the experience of the author, the most common reduction approaches for the foundation are based on substructuring techniques according to Guyan [26] and Craig-Bampton [9]. Here, the foundation is first isolated from the OWT and described by a group of finite elements. The foundation subsystem is then condensed into a superelement by the FD and subsequently integrated into the overall OWT model by the WTM. Integrated OWT models with foundation superelements can then be subjected to the various dynamic analyses. These substructuring approaches are well known from other fields of technology such as spacecraft design; see e.g. chapter 17 in Wijker [78].

The investigations in this section address different aspects regarding applicability and performance of Guyan [26] type SE06 superelements and Craig-Bampton [9] type SE36 superelements for jacket foundations in FLS load calculations. Both are further introduced in section 6.1.1. Fatigue loads and damages obtained from application of the SE36 superelements are used as reference results for the assessment of the SE06 superelements. This assumption is confirmed by the investigations in section 6.1.2 and section 6.1.6.

Both, the Guyan and Craig-Bampton, reduction approaches aim for a condensation of the DOFs of the detailed foundation subsystem model and loads from the FD while maintaining the relevant dynamic properties. Nowadays, the primary motivation for the foundation model reduction is not introduced by limitations of processor and memory capacities of current computers although the resulting improvements of the simulation times are still considered quite beneficial. Instead, the main reasons are modelling constraints in the aero-elastic simulation tools. This is briefly illustrated for two examples related to the basic FLEX5 [50] code together with possible solutions.

Example 1: *FLEX5 reserves only a maximum of 6 generalized DOFs for the foundation. The overall OWT system matrices are established under consideration of a foundation reduction approach corresponding to Guyan [26] as described by Passon [59], i.e. the foundation model and loads are condensed to only the 6 DOFs at interface between tower bottom and foundation. An efficient extension of the 6 foundation DOFs in FLEX5 can be achieved by introduction of a Craig-Bampton [9] type substructuring approach as described by Hald & Høgedahl [29] and demonstrated by Passon [59].*

Example 2: *Introduction of an additional (and potentially flexible) number of DOFs into the fixed system of FLEX5 foundation DOFs according to Table 1 forms the most essential modification of the basic FLEX5 code when extended towards a Craig-Bampton [9] type substructuring approach. From that point of view the step towards a foundation representation by full system matrices and load vectors may seem trivial. However, the basic FLEX5 code uses the explicit Runge-Kutta-Nystrøm time integration method, see Øye [50], which is only conditionally stable and therefore requires a minimum time step size with respect to the maximum natural frequency of the system. Introduction of full foundation system matrices may result in very high values for the largest natural frequencies and would therefore require impractically small time step sizes to achieve numerical stability. Here, an implicit time integration method such as the generalized-α method according to Chung & Hulbert [10] could be used instead. This is for example implemented for LACflex and ROSAP, thereby allowing selections of time step sizes based on accuracy considerations rather than on numerical stability.*

6.1.1 Influence of different jacket foundation superelement formulations in the FLS design

Van der Valk & Voormeeren [72] assessed the applicability of different superelement formulations and load expansion approaches for the UpWind jacket from Vemula [74]. They found that an error is introduced in the aero-elastic analysis in case the foundation is represented on basis of a Guyan type condensation with only 6 interface DOFs (SE06). Furthermore, they showed that application of a Craig-Bampton type foundation description on basis of the same 6 interface DOFs, however, complemented with a few internal modes helped to reduce the error to insignificant levels.

While the findings from Van der Valk & Voormeeren [72] are generally valid, it is important to establish a better understanding of the errors introduced from the SE06 superelement in terms of sources and magnitudes in order to assess the applicability for individual jacket type foundation configurations. This is now further investigated for the fatigue lives of joints in different jacket foundation configurations using the NREL 5MW [33] turbine on a generic 90m tower. Fatigue loads are calculated for aligned wind-wave combinations in DLC 1.2 according to IEC61400-3 [88] from the Borkum Riffgrund 2 offshore wind farm project which has been provided by DONG Energy A/S. Reference results are obtained from a second set of calculations using a Craig-Bampton type foundation description on basis of the same 6 interface DOFs as used for SE06 together with 30 internal modes, denoted as SE36.

The assessment is performed for different jacket type foundation configurations with piles and suction buckets as indicated in Figure 60. All piled configurations are described individually and in more detail in Table 10. The purpose of the different configurations is to assess the influence of global stiffness variations as well as of different structural configurations on the error introduced from the SE06 superelement.

The three-legged jacket on suction buckets corresponds to the softest, preliminary configuration for the Borkum Riffgrund 2 offshore wind farm project and has been provided by DONG Energy A/S.

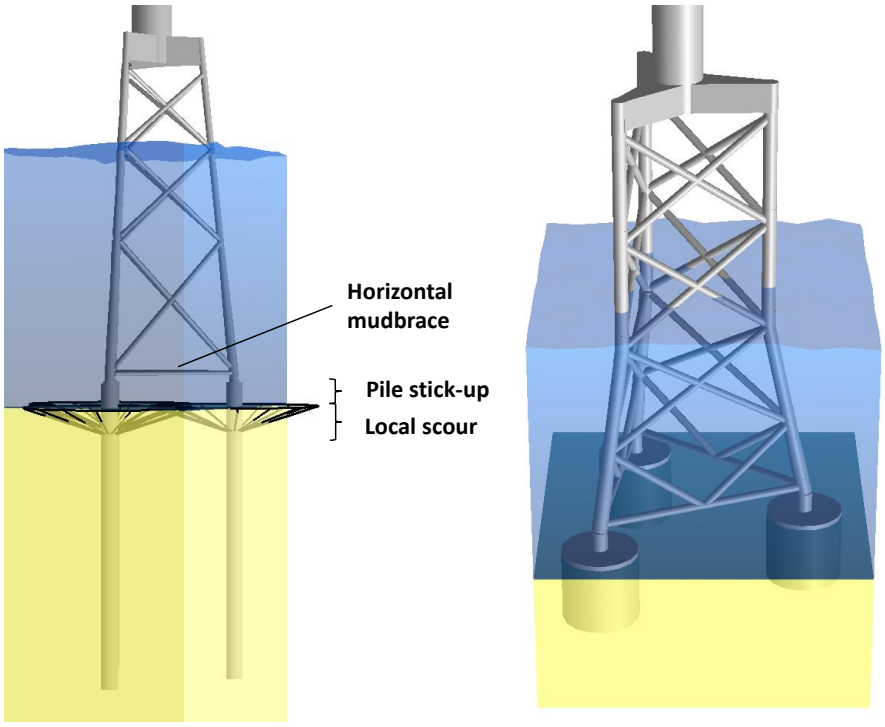

Figure 60: Jackets with piles and suction buckets.

Table 10 Summary of the investigated piled jacket configurations.

Configuration	H33H	H33N	S33H	S33N	H34H
Water depth	32m	32m	35m	35m	32m
x-brace levels	3	3	3	3	3
Number of legs	3	3	3	3	4
Pile stickup	0.5m	0.5m	3.5m	3.5m	0.5m
Local scour depth	0m	0m	3.66m	3.66m	0m
Soil type	Dense Sand	Dense Sand	Lose Sand	Lose Sand	Dense Sand
Horizontal mudbrace	Yes	No	Yes	No	Yes

Table 11 summarizes the eigenfrequencies of selected global modes of the integrated OWT model with the different foundation configurations and the different superelement representations of the foundation together with the 1st eigenfrequency of the isolated foundation configurations as applied for the load expansion, i.e. the foundation without the tower and RNA as illustrated at the bottom of Figure 16. It is noticeable that the eigenfrequencies of the first global bending modes in both directions are identical for the SE06 and SE36 foundation representation in the integrated model. Furthermore, the eigenfrequencies of the 2nd global bending modes (fore-aft) for the OWT models with the soft foundation configurations S33H & S33N and the SE06 superelement are very close to the 1st eigenfrequency of the isolated foundation.

Table 11 Natural frequencies [Hz] of the different OWT and foundation configurations for SE36 and SE06.

Foundation configuration and representation in OWT model		Eigenfrequencies of integrated OWT				Isolated, full foundation
		1st global bending mode		2nd global bending mode		
Configuration	Superelement	fore-aft	side-side	fore-aft	side-side	1st mode
H33H	**SE36**	0.230	0.232	1.630	1.573	2.202
	SE06	0.230	0.232	1.656	1.592	
H33N	**SE36**	0.230	0.231	1.607	1.554	2.139
	SE06	0.230	0.231	1.637	1.576	
S33H	**SE36**	0.228	0.229	1.137	1.112	1.247
	SE06	0.228	0.229	1.229	1.206	
S33N	**SE36**	0.228	0.227	1.131	1.098	1.230
	SE06	0.228	0.227	1.200	1.157	
H34H	**SE36**	0.237	0.239	1.612	1.566	2.073
	SE06	0.237	0.239	1.639	1.586	

Loads are obtained in a sequentially integrated load calculation approach according to section 3.1 with aero-elastic load simulations in LACflex. For the aero-elastic calculations the individual foundation configurations are first represented by the SE36 superelement and subsequently by the SE06 superelement formulation, thereby generating two sets of interface loads. Both sets of interface loads are subjected to force-controlled, dynamic load expansions which are performed in ROSAP on the full foundation model including a subsequent calculation of fatigue lives in all tubular joints of the structure. Fatigue loads and damages obtained from application of the SE36 superelements contain only insignificant error levels. This has been confirmed by additional investigations of the author, but is only shown exemplarily for the convergence behavior of the soft configuration S33N in section 6.1.2. This reflects also the practical experiences of the author from various detailed design projects and FEED studies. Convergence has in all cases already been achieved with 12-15 internal modes of the Craig-Bampton superelement. Nevertheless, Craig-Bampton type superelements with 30

internal modes are often used in design practice in order to be on the safe side. For the present investigations, results obtained from the SE36 superelements are used as reference for the assessment of the SE06 superelements.

Figure 61 to Figure 63 show the ratios of (minimum) joint fatigue lives obtained from interface loads of the SE06 superelement relative to the SE36 superelement for one side of each jacket configuration. Nodes are denoted by 6 alphanumeric characters while the connected element names are given by 5 alphanumeric characters in the figures. The joint fatigue life ratios on the brace and chord side are provided in the red boxes attached to the brace side, together with the corresponding element names. Fatigue life calculations in all tubular joints are based on *S-N* curves taken from DNV-OS-J101 [84].

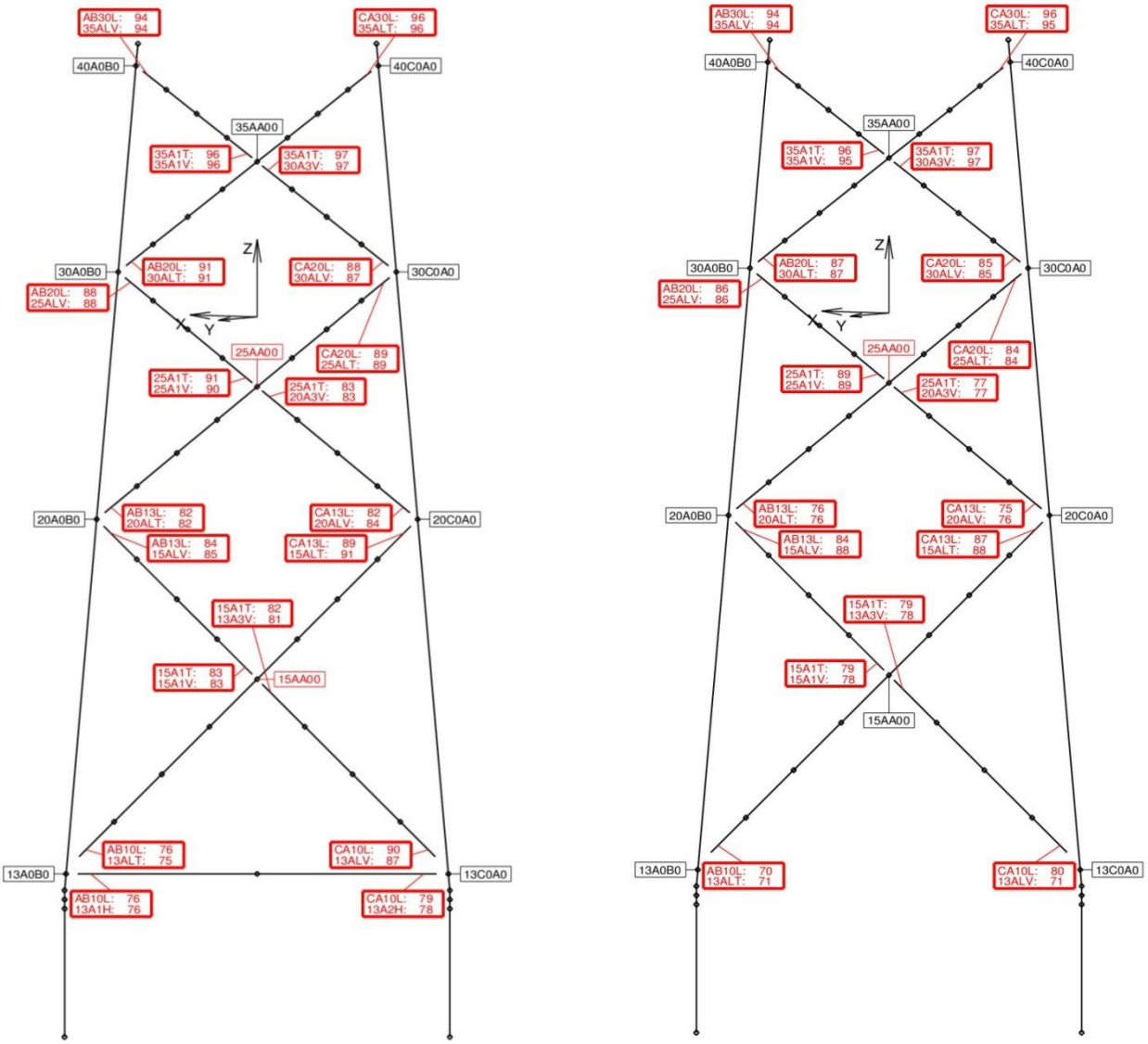

Figure 61: Joint fatigue lives from the SE06 superelement relative to the SE36 superelement in [%] for the stiff configuration H33H (left) and H33N (right).

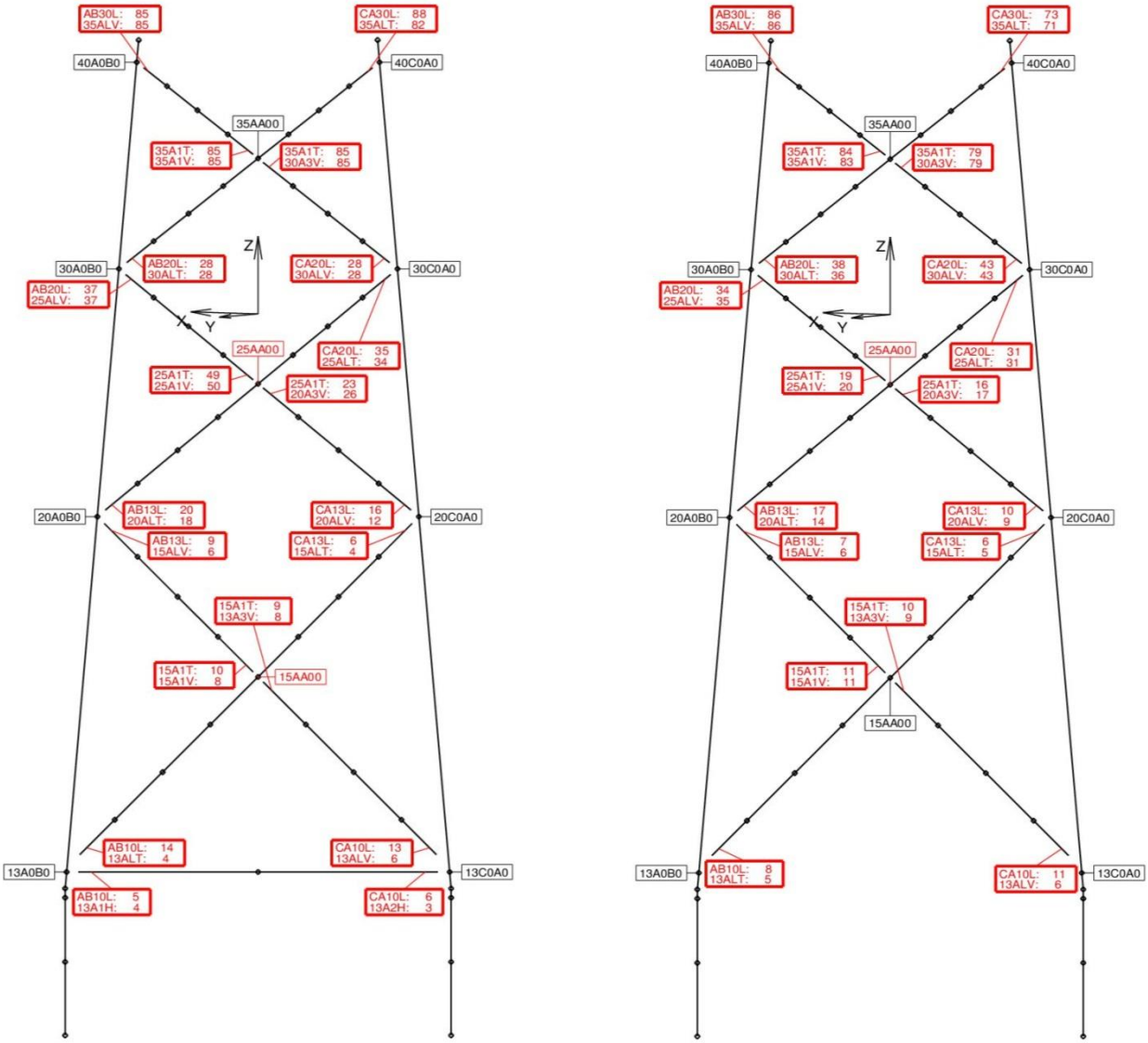

Figure 62: Joint fatigue lives from the SE06 superelement relative to the SE36 superelement in [%] for the soft configurations S33H (left) and S33N (right).

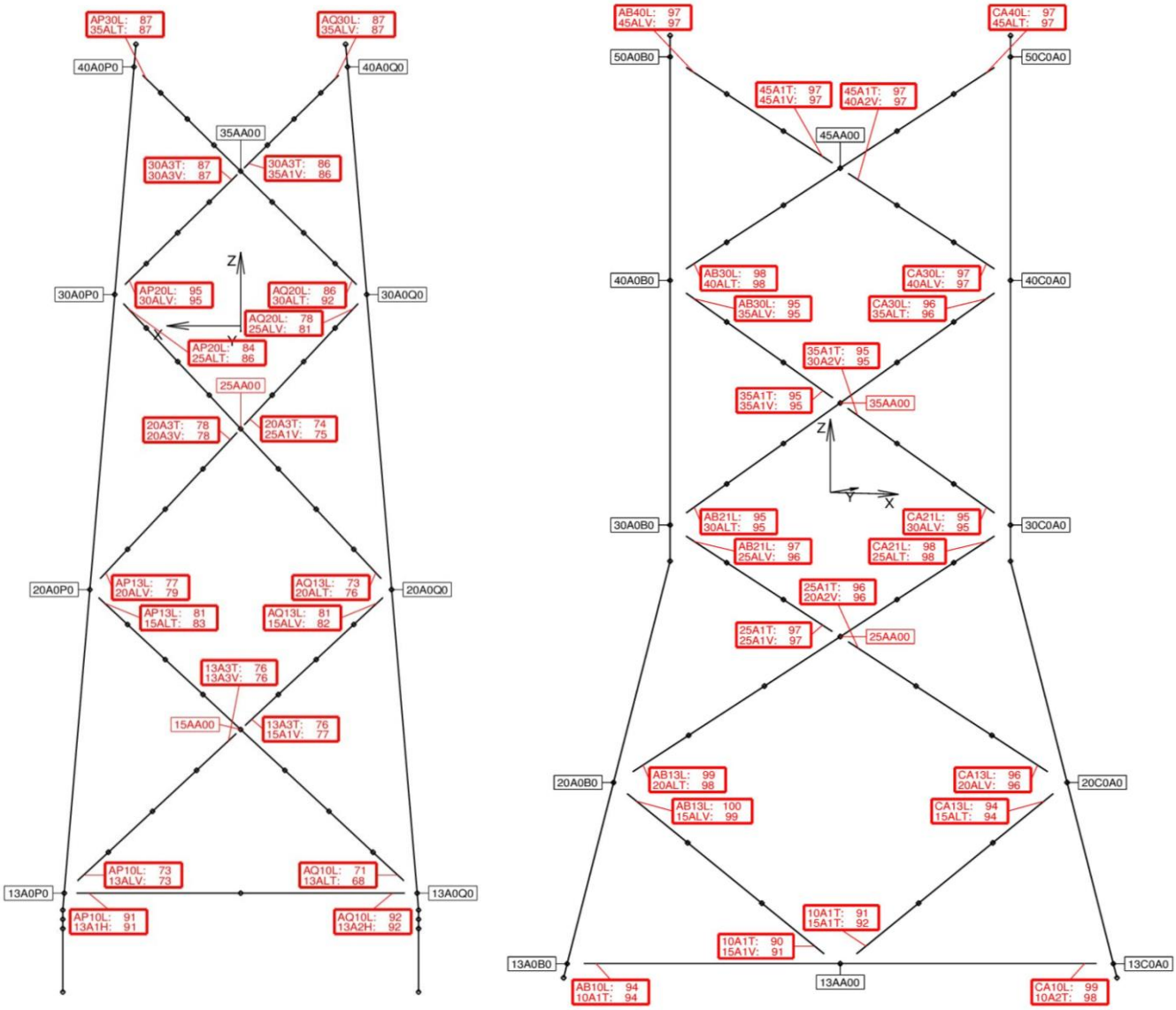

Figure 63: Joint fatigue lives from the SE06 superelement relative to the SE36 superelement in [%] for the stiff configuration H34H (left) and the preliminary Borkum Riffgrund 2 jacket configuration (right).

Different magnitudes of errors can be observed for the calculated joint fatigue lives from the SE06 and SE36 superelements loads dependent on the individual jacket configuration. Van der Valk et al. [73] concluded that the differences are introduced from a missing spectral and/or spatial convergence and that application of the SE06 superelement is conservative for the joint fatigue lives. The results for all investigated configurations in Figure 61 to Figure 63 confirm the latter conclusion.

The best agreement between tubular joint fatigue lives from the SE06 and SE36 superelements is achieved for the preliminary Borkum Riffgrund 2 jacket with suction buckets. This configuration is globally very stiff and has also the stiffest soil-structure interactions due to the suction buckets. However, no quantitative description can be provided here since the corresponding foundation configuration is property of DONG Energy A/S. The stiff piled configurations H33H, H33N and H34H also show reasonable agreements, but with much less accuracy than achieved for the suction bucket configuration, especially in the lower part of the structures. However, very large errors occur for the SE06 superelements of the soft configurations S33H and S33N, especially in the lower part. Here, the worst case fatigue lives for the SE06 superelement are as low as 3% compared to those obtained from the SE36 superelement.

A trend seems therefore to be that the error for the joint fatigue lives from application of the SE06 superelement is smaller for stiffer configurations. However, it has also been shown in Table 11 that the 2nd global bending eigenfrequency (fore-aft) of the OWT with the soft foundation configurations and the SE06 superelement are also very close to the 1st eigenfrequency of the isolated foundation. This result in significant artificial dynamic excitations of the isolated foundation structure in the dynamic load expansion with the SE06 interface loads which is confirmed by the investigations in the sections 6.1.5 and 6.1.6.

Based on the large range of errors observed in Figure 61 to Figure 63, the following preliminary conclusions are drawn:

Application of the SE06 superelement for jacket foundations of OWTs can result in a large range of errors for the fatigue design, e.g. dependent on the structural configuration. Therefore, the author recommends in general using more detailed superelement representations for jacket type foundations.

Despite this general conclusion from the investigated examples it is not always possible to apply detailed superelement representations such as the SE36 superelement in design practice. This might be a result of limitations in the modelling capabilities of the applied tools such as for the basic version of FLEX5 [50]. Design load calculations would therefore still be based on the SE06 superelement type and the question on how to minimize the error in the design becomes extremely important. Furthermore, Figure 61 to Figure 63 show clearly that the accuracies in joint fatigue lives for the SE06 superelement cover a large range between the individual configurations. A designer would therefore be interested in the following questions:

- Is it possible to make a simple assessment whether the SE06 superelement allows for reasonable results or how many internal modes should be used as a minimum for Craig-Bampton type superelements?
- Can load calculations on basis of the SE06 superelement be improved?

Both questions are briefly addressed in the following sections.

6.1.2 Influence of internal modes for Craig-Bampton type jacket foundation superelements

The large differences in some joint fatigue lives for the soft configurations experienced in section 6.1.1 signifies the questions whether the SE36 superelement description is sufficient or how many superelement DOFs are required as a minimum to obtain converged fatigue lives. For that purpose, the joint fatigue lives for the jacket configuration S33N from section 6.1.1 are re-calculated under consideration of the following foundation superelement representations:

- 6 DOFs i.e. Guyan type with foundation condensed to 6 interface DOF (SE06).
- 8-36 DOFs i.e. Craig-Bampton type on basis of SE06 complemented with 2-30 internal modes.

Figure 64 shows the calculated normalized joint fatigue lives over the number of superelement DOFs for the following exemplary joints at the upper, middle and lower jacket bay according to denotations in Figure 62:

- 40A0B0-35ALV, i.e. upper bay joint at brace element 35ALV & node 40A0B0.
- 25AA00-25A1V, i.e. middle bay joint at brace element 25A1V & node 25AA00.
- 13A0B0-13ALT, i.e. lower bay joint at brace element 13ALT & node 13A0B0.

Furthermore, Figure 64 shows the modal mass from all DOFs of the internal superelement modes relative to the total modal mass $m_{2nd\text{-}FA}$ in the 2nd fore-aft bending mode of the OWT. Based on the eigenvector $\boldsymbol{\Phi}_{2nd\text{-}FA}$ for the 2nd fore-aft mode and the system mass matrix $\boldsymbol{M}$ of the OWT, the total modal mass $m_{2nd\text{-}FA}$ is calculated in accordance to Eq. 34.

$$m_{2nd\text{-}FA} = \boldsymbol{\Phi}_{2nd\text{-}FA}{}^{T} \cdot \boldsymbol{M} \cdot \boldsymbol{\Phi}_{2nd\text{-}FA} \qquad \text{Eq. 34}$$

The modal mass of the internal foundation modes for the 2nd fore-aft mode is obtained in the same way. However, only mass matrix elements from the DOFs of the internal modes are considered in the mass matrix while all other contributions are set to zero.

The relative modal mass contribution of the internal modes converges at 12% of the total modal mass of the 2nd fore-aft mode. This is considered to be a significant contribution for the dynamic behavior of this mode which may lead to noticeable errors when missing in the dynamic analysis due to an insufficient selection of internal modes.

Analogously to Figure 62, it can be seen that all joint fatigue lives are underestimated for the SE06 superelement and that the underestimation increases towards the lower parts of the structure. The relative modal mass of the internal foundation modes is of course at zero, since no internal modes are included in this superelement. Increasing the number of superelement DOFs, i.e. increasing the number of the internal modes, quickly results in convergence of fatigue lives in all joints as well as in convergence of relative modal mass of the internal modes. However, the joint fatigue life convergence in the lower part of the structure requires slightly more internal superelement modes compared to the upper part. For the superelement with 2 internal modes a normalized joint fatigue life of 0.996 is achieved for joint 40A0B0-35ALV while only a value of 0.72 is achieved for joint 13A0B0-13ALT. Furthermore, the modal mass of the internal modes is 9% of the total modal mass which corresponds to 75% of the convergence value, i.e. 12%. This is similar to the normalized joint fatigue life for joint 13A0B0-13ALT. In this context, a strong relation between the normalized fatigue life of the

lowest joint 13A0B0-13ALT and the relative modal mass of the internal foundation modes can be observed over the number of superelement DOFs.

An important observation is that the fatigue lives for all considered tubular joints converged in case the relative modal mass of the internal modes is converged. Based on this observation and practical experience, the author recommends ensuring the convergence of the modal mass[11] of the internal modes for the 2nd fore-aft mode when selecting the number of internal modes for the Craig-Bampton type foundation superelement. Furthermore, section 6.1.5 and 6.1.6 indicate that significant errors in the dynamic response can occur for the 1st and 2nd torsion mode as well. Hence, the author recommends extending the convergence criterion to these torsion modes[12].

Consequently, the following criterion for selection of the minimum number of internal modes for Craig-Bampton type superelements of jacket foundations can be formulated:

The number of internal superelement modes must be sufficient to ensure convergence of the corresponding modal mass of the internal modes in the 1st torsion and 2nd fore-aft mode of the OWT.

[11] This is equivalent to the convergence of the relative modal mass from the internal modes.
[12] In design practice, the 2nd torsion mode is typically not relevant for the fatigue design of the foundation. Therefore, the 2nd torsion is not included in the following criterion.

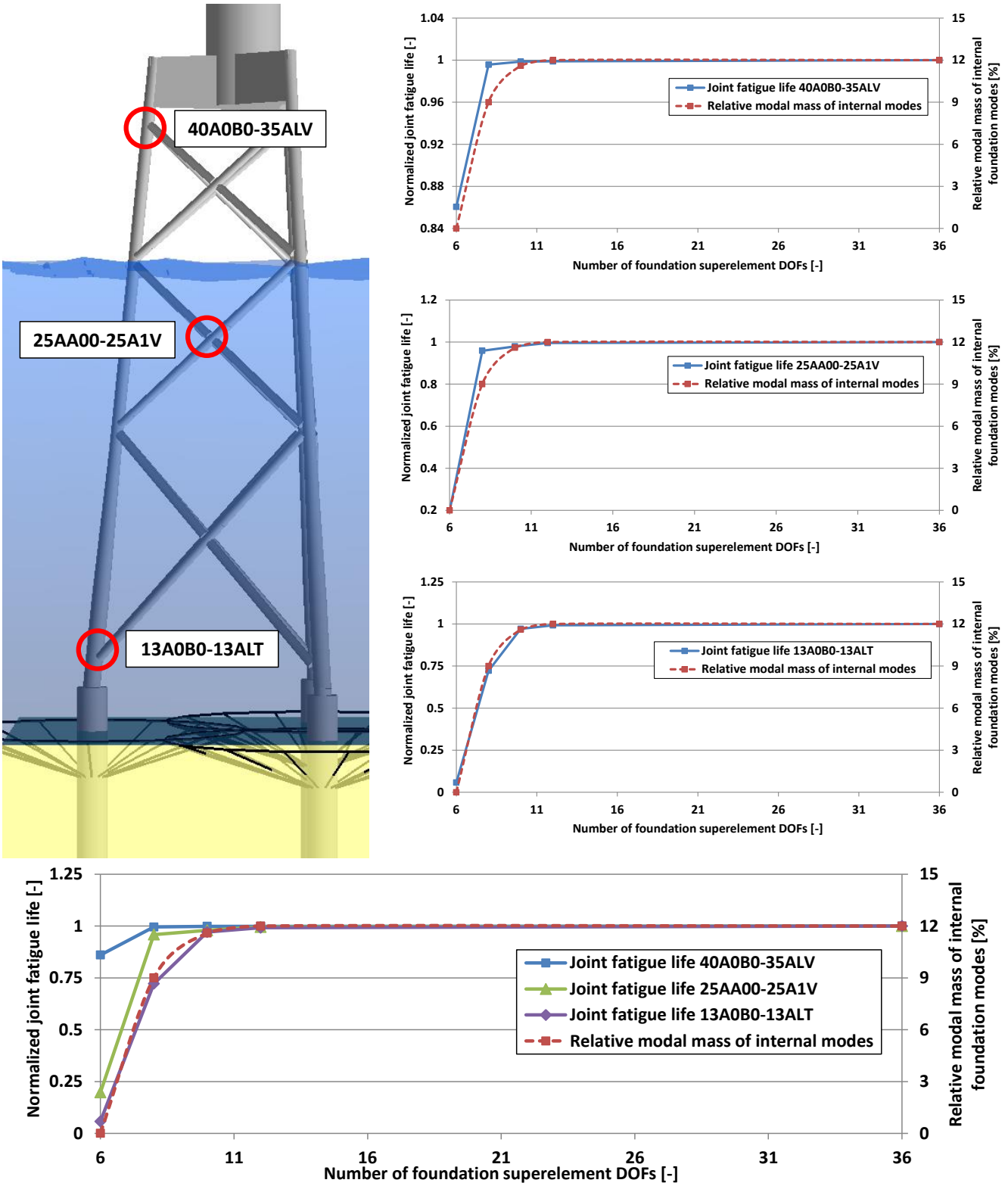

Figure 64: Joint fatigue lives & relative modal mass of internal modes over the number of foundation superelement DOFs for the soft configuration S33N; plotted individually (right) and together (bottom) for the different locations (left).

So far, it has been investigated, how many internal modes are required for an adequate Craig-Bampton based superelement representation for the dynamic calculations in FLS in order to obtain convergence in the joint fatigue lives. This question has been discussed for the example of the soft foundation configuration S33N leading to further insight on and a criterion for the bad performance of the SE06 foundation superelement. However, another interesting question concerns the reason for the bad performance of the SE06 foundation superelement in the sequentially integrated load calculations. This question is further addressed in sections 6.1.3, 6.1.5 and 6.1.6 where it is shown that:

- Firstly, application of SE06 foundation superelements in the aero-elastic analysis leads to errors in the dynamic interface responses.
- Secondly, these interface response errors lead to artificial dynamic excitations of the foundation structure in force-controlled, dynamic load expansions, i.e. the member loads contain amplified interface response errors. The magnitude and frequency interval of these amplified member load errors depend on the modal properties of the full OWT model in relation to the foundation model.

This means that only the first error type, i.e. interface response errors in the aero-elastic simulation, is directly introduced from the SE06 foundation superelement. In the following, the source for this error is briefly discussed in a simplifying but illustrative manner.

The SE06 superelement is based on a Guyan type reduction, also denoted as static condensation, and can be obtained by numerical or analytical approaches. On one hand, the very efficient and straightforward numerical approach, based on transformations of the foundation mass and stiffness system matrices as well as of the load vector, is implemented in most finite element based tools such as ROSA. The analytical approach, on the other hand, is e.g. implemented for monopile foundation models in the basic FLEX5 code, but could be applied for jackets as well. Both approaches are described in detail by many publications; see e.g. Passon [59]. Therefore, only some basic aspects are provided here in order to establish the basis for the further discussion about the suitability of SE06 type superelement for the S33N jacket foundation.

The *6-by-6* mass and stiffness matrices, $\boldsymbol{M}_{SE06}$ and $\boldsymbol{K}_{SE06}$, for the SE06 foundation superelement are obtained from (static) deformation modes $\boldsymbol{\Phi}_i$ corresponding to the i=1,..,6 interface DOFs. For that purpose, unit deformations are introduced individually for each of the six interface DOFs as boundary conditions while the remaining interface DOFs are fixed. No other loads or forced deformations are introduced. The resulting foundation deformation shape due to the forced unit deformation of the i^{th} interface DOF is the (static) deformation mode $\boldsymbol{\Phi}_i$. The required (interface) loads to introduce these six unit deformation states $\boldsymbol{\Phi}_i$ are subsequently used to form the flexibility matrix $\boldsymbol{H}$ and, by inversion, the stiffness matrix $\boldsymbol{K} = \boldsymbol{H}^{-1}$. Furthermore, the (static) deformations modes $\boldsymbol{\Phi}_i$ are used as shape functions for calculation of the mass matrix elements. The mass matrix element m_{ij} of the superelement matrix $\boldsymbol{M}_{SE06}$ is obtained with the foundation mass matrix $\boldsymbol{M}$ and the (static) deformations modes $\boldsymbol{\Phi}_i$ and $\boldsymbol{\Phi}_j$ for the i^{th} and j^{th} interface DOF by Eq. 35.

$$m_{ij} = \boldsymbol{\Phi}_i^T \cdot \boldsymbol{M} \cdot \boldsymbol{\Phi}_j \qquad \text{Eq. 35}$$

For the soft foundation configuration S33N, the six (static) deformations modes[13] or shape functions for the mass and stiffness matrix of the SE06 superelement, are shown in Figure 65.

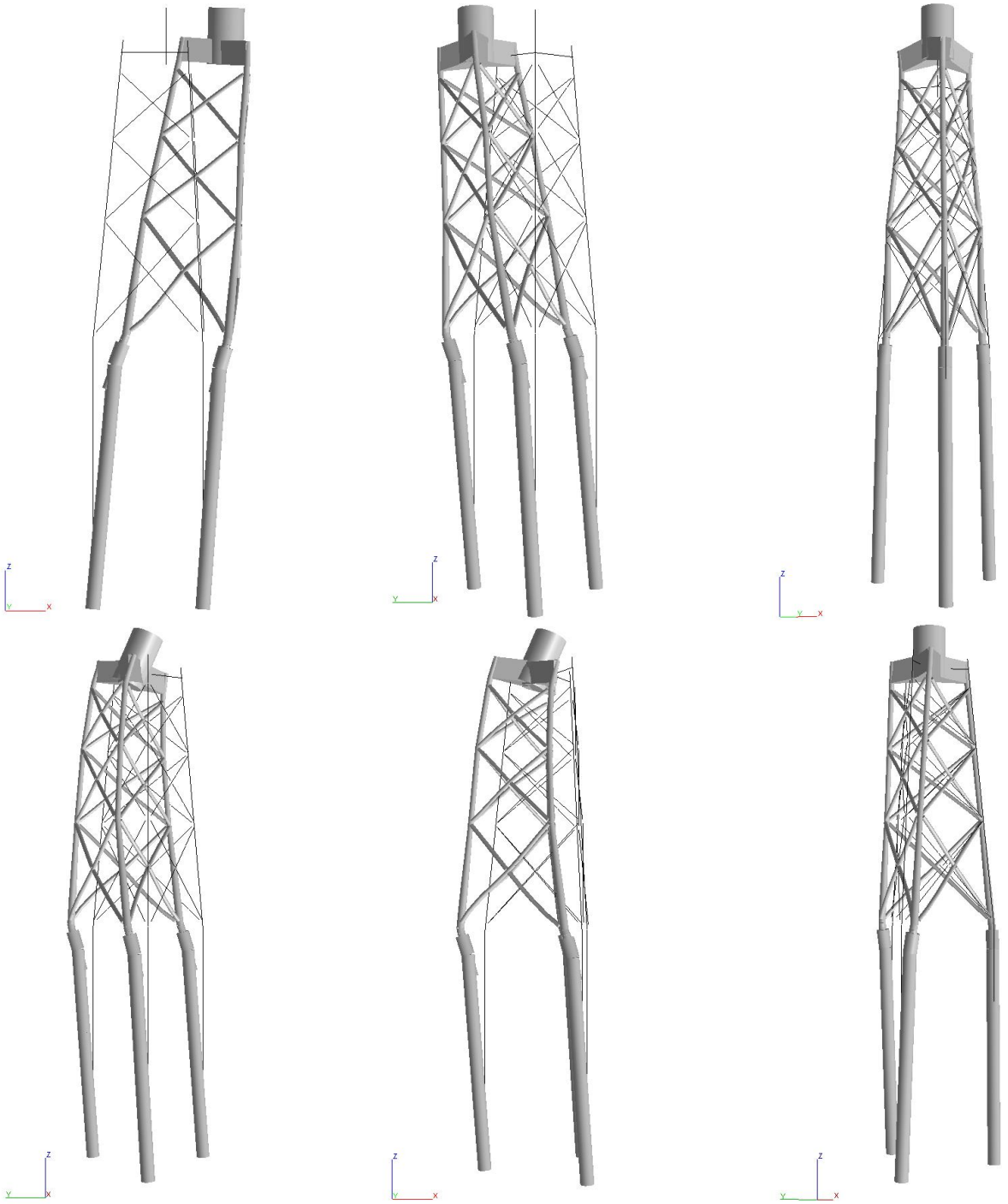

Figure 65: Static deformation modes of the soft configuration S33N (for the mass matrix calculation of the SE06 superelement) for translational (top) and rotational (bottom) unit deformation of the interface DOF.

[13] Sea and soil conditions are not shown in the plots as focus is on the deformation shapes. Furthermore, the plots do not show the curvature of the subsoil part of the piles.

Figure 66 shows the (dynamic) OWT mode shapes for the 1st and 2nd fore-aft mode as well as for the 1st torsion mode. For the foundation, it can be seen that very pronounced local out-of-plane brace modes are part of the 2nd fore-aft bending mode, in particular for the lowest bay. None of the six (static) deformations modes, i.e. the shape functions of the SE06 superelement, in Figure 65 show similar local out-of-plane brace deformations. Hence, the 2nd fore-aft mode cannot be well approximated by any linear combination of the six shape functions in Figure 65. Due to these limitations of the shape functions, the author expects that the SE06 superelement might not represent dynamic behaviour of the 2nd fore-aft bending mode adequately.

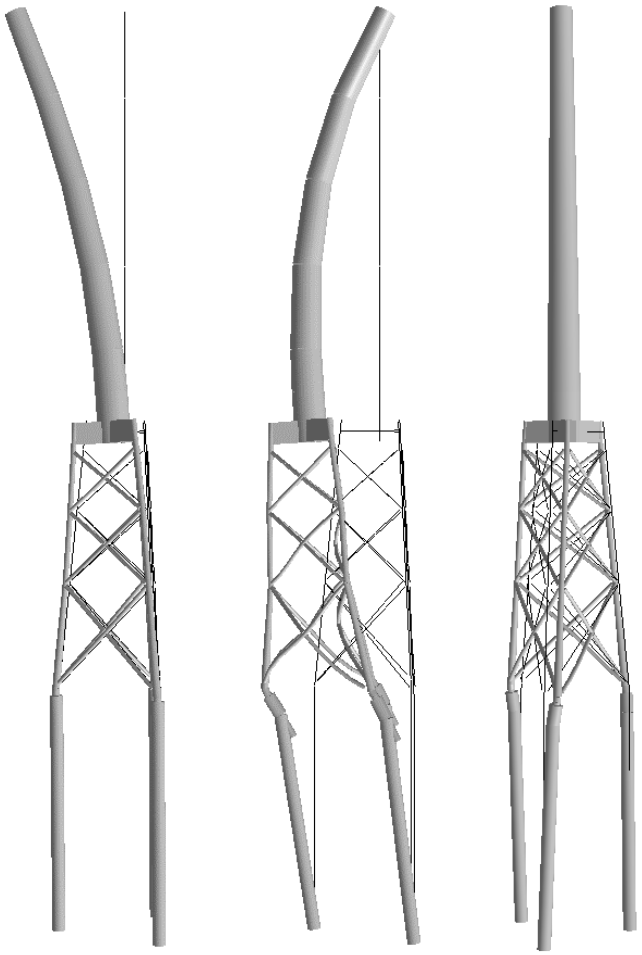

Figure 66: 1st mode (left) and 2nd mode (centre) global bending modes in fore-aft direction and 1st torsion mode (right).

Although section 6.1.5 and 6.1.6 confirm the poor performance of the SE06 superelement for the dynamic behaviour of the 2nd fore-aft bending mode, a conclusive confirmation of the assumed influence from the local out-of-plane brace modes is not provided. However, it has been shown that an amendment of the SE06 superelement with a few internal modes lead to significant improvements regarding the dynamic behaviour of the 2nd fore-aft bending mode.

For example, Figure 64 shows that the calculated fatigue life for the lowest joint 13A0B0-13ALT is only at 3% of the value compared to the converged solution. Consideration of the first two internal modes for the foundation superelement of the soft configuration S33N increases in to calculated fatigue life to 72% of the converged solution while consideration of the first four internal modes increases in to calculated fatigue life to 97%. Similar approximations, i.e. 74% and 97% of the convergence value, are obtained for modal mass of the internal modes for the 2nd fore-aft bending mode. The question is why do the first internal modes improve the accuracy of the calculated fatigue lives as well as of the 2nd fore-aft bending mode?

Figure 67 shows the first four internal modes of the soft foundation configuration S33N. The first two modes on the left side are bending modes with pronounced local out-of-plane brace modes at the two lowest bays. The third mode is a torsion mode and the fourth mode is again a bending mode with pronounced local out-of-plane brace bending modes at the lowest bay. It can be seen that, in particular, the first two internal modes complement the shape functions from the (static) unit deformation modes in Figure 65 well with respect to representations of the foundation part of 2nd fore-aft bending mode in Figure 66.

The author expects that the complementation of the superelement shape functions from the static unit deformation modes by the internal modes allow for a more accurate approximation of the 2nd fore-aft bending mode. This leads to the more accurate representation of dynamic behaviour from the 2nd fore-aft bending mode in the aero-elastic analysis with the corresponding Craig-Bampton type superelement.

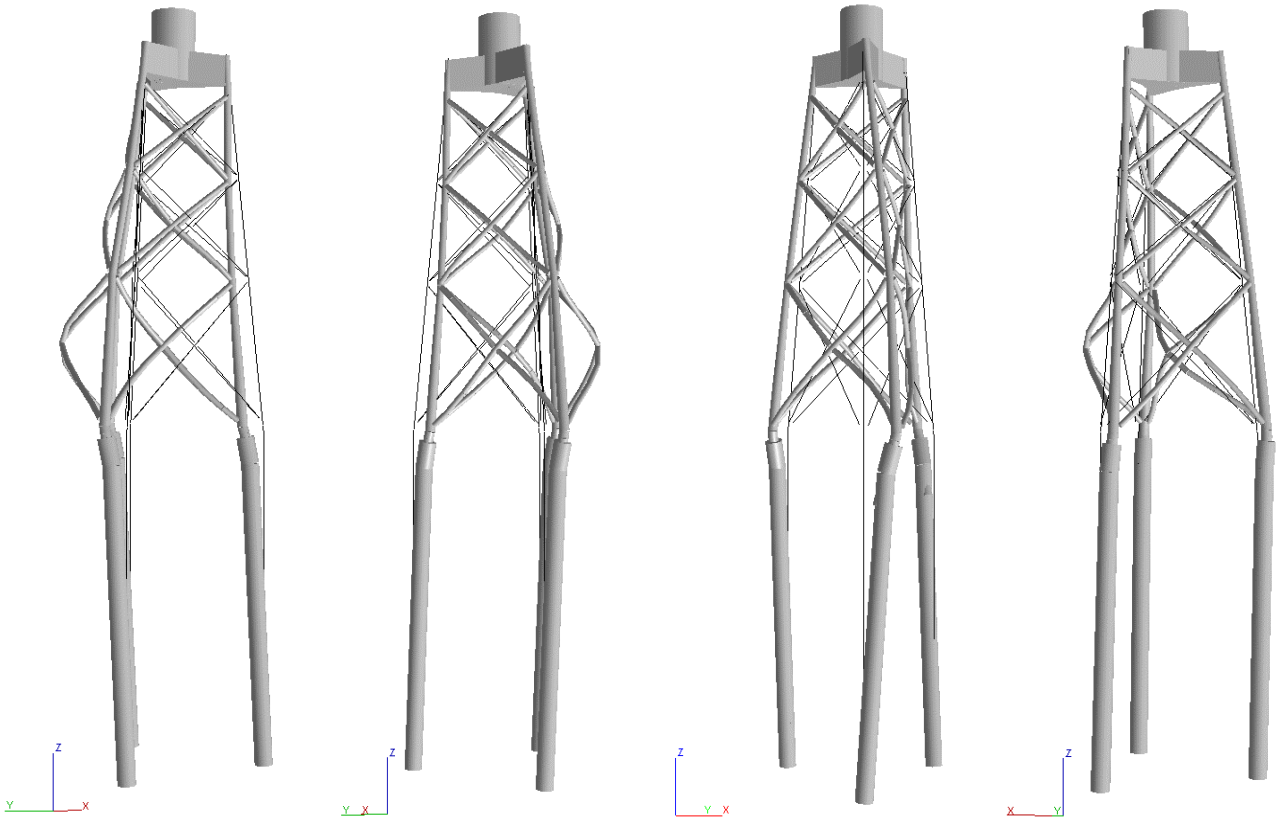

Figure 67: First four internal modes, i.e. for fixed interface.

6.1.3 Force-controlled, dynamic load expansions for different foundation superelements

Load calculations in section 6.1.1 followed a sequentially integrated approach according to section 3.1. Interface loads have been obtained by aero-elastic calculations with LACflex while fatigue loads in the foundation structure are obtained by a subsequent force-controlled, dynamic load expansion according to paper 1 [61] in ROSAP. Details on the force-controlled load expansion approach are provided e.g. by Van der Valk et al. [73]. Here, only a brief description in the context of the performed investigations is provided.

The equations of motion of the total OWT structure consist of a part describing the superstructure (tower and RNA) and a part describing the foundation (e.g. represented by the SE06 or SE36 superelement) together with the corresponding loads. The equations of motion according to Eq. 36 in terms of the system mass matrix $\boldsymbol{M}$, damping matrix $\boldsymbol{C}$, stiffness matrix $\boldsymbol{K}$, acceleration vector $\ddot{\boldsymbol{u}}$, velocity vector $\dot{\boldsymbol{u}}$, deformation vector $\boldsymbol{u}$ and load vector $\boldsymbol{f}$ are solved for at each time step t in the aero-elastic analysis.

$$\boldsymbol{M}\ddot{\boldsymbol{u}}(t) + \boldsymbol{C}\dot{\boldsymbol{u}}(t) + \boldsymbol{K}\boldsymbol{u}(t) = \boldsymbol{f}(t) \qquad \text{Eq. 36}$$

The equation of motion can also be written in dual form according to Eq. 37 separating the system matrices into a part describing the superstructure (index S) and a part describing the foundation (index F). The compatibility condition $\boldsymbol{B}\boldsymbol{u}(t) = \boldsymbol{0}$ is introduced in order to ensure that interface displacements and rotations are the same for the superstructure and the foundation.

$$\begin{cases} \boldsymbol{M}^S\ddot{\boldsymbol{u}}(t) + \boldsymbol{C}^S\dot{\boldsymbol{u}}(t) + \boldsymbol{K}^S\boldsymbol{u}(t) - \boldsymbol{f}^S(t) = -\boldsymbol{B}^{S^T}\boldsymbol{\lambda}(t) \\ \boldsymbol{M}^F\ddot{\boldsymbol{u}}(t) + \boldsymbol{C}^F\dot{\boldsymbol{u}}(t) + \boldsymbol{K}^F\boldsymbol{u}(t) - \boldsymbol{f}^F(t) = -\boldsymbol{B}^{F^T}\boldsymbol{\lambda}(t) \\ \boldsymbol{B}\boldsymbol{u}(t) = \boldsymbol{0} \text{ (compatibility cond.)} \end{cases} \qquad \text{Eq. 37}$$

$\boldsymbol{\lambda}(t)$ are Lagrangian multipliers and $\boldsymbol{B}^*$ are Boolean matrices (0 and 1 entities) related to the interface DOFs. The Lagrangian multipliers are in fact the internal interface forces and moments as calculated in the aero-elastic analysis of the integrated OWT in step 2 of the sequentially integrated load calculation approach according to Figure 16.

The exact foundation response can now be determined by solving the equations of motion in Eq. 38 for the foundation corresponding to step 3 of the sequentially integrated load calculation approach according to Figure 16.

$$\boldsymbol{M}^F\ddot{\boldsymbol{u}}(t) + \boldsymbol{C}^F\dot{\boldsymbol{u}}(t) + \boldsymbol{K}^F\boldsymbol{u}(t) - \boldsymbol{f}^F(t) = -\boldsymbol{B}^{F^T}\boldsymbol{\lambda}(t) \qquad \text{Eq. 38}$$

The foundation load vector $\boldsymbol{f}^F(t)$ contains the direct loads on the foundation, i.e. in particular the hydrodynamic loads, from step 1 of the sequentially integrated load calculation approach, and $-\boldsymbol{B}^{F^T}\boldsymbol{\lambda}(t)$ contains the interface forces and moments.

However, an error is introduced for the force-controlled, dynamic load expansion according to Eq. 38 in case the interface loads have been obtained from aero-elastic calculations with an in-sufficient foundation model such as the simplified SE06 superelement for jacket type foundations. This error can be understood as an additional loading $\Delta_{SE06}(t)$, such that Eq. 38 is re-written as Eq. 39.

$$\boldsymbol{M}^F\ddot{\boldsymbol{u}}(t) + \boldsymbol{C}^F\dot{\boldsymbol{u}}(t) + \boldsymbol{K}^F\boldsymbol{u}(t) - \boldsymbol{f}^F(t) = -\boldsymbol{B}^{F^T}\boldsymbol{\lambda}(t) + \Delta_{SE06}(t) \qquad \text{Eq. 39}$$

Van der Valk et al. [73] concluded that the error introduced from the SE06 superelement only has a small effect on the results for the wind turbine, while the influence on the foundation is more significant. The latter conclusion has been assessed in section 6.1.1 of this thesis for a variety of soft and stiff jacket type configurations, showing that the SE06 superelement can be applied in certain cases while a large error on the conservative side is introduced especially for the soft configurations.

The additional loading due to the error term $\Delta_{SE06}(t)$ in Eq. 39 can introduce pronounced, artificial dynamic excitations of the foundation structure in the load expansion calculation as shown in section 6.1.5 and 6.1.6. This may lead to scenarios with rather conservative foundation design loads and a substantial underestimation of joint fatigue lives.

6.1.4 Force-controlled, dynamic load expansions with increased damping

Joint fatigue lives are now re-calculated for the S33N configuration with interface loads from the SE06 and SE36 foundation superelement according to section 6.1.1, however with varying damping conditions in the force-controlled, dynamic load expansion with the interface loads from the SE06 superelement.

The structural damping ratio is applied as a realistic value of 1% critical damping on the first mode in the aero-elastic load simulation for the OWT with the SE06 and SE36 foundation models in LACflex. The load expansion with the loads from the SE36 superelement is also performed with 1% critical damping while load expansion calculations with loads from the SE06 superelement are performed with 1% critical damping as well as with increased structural damping conditions, i.e. 2.5%, 3% and 3.5% critical damping.

The resulting joint fatigue lives from load expansion calculations with loads from the SE06 superelement and different damping conditions are shown as ratios to those obtained with the SE36 superelement loads and 1% critical damping in Figure 68. It can be seen that the joint fatigue lives are substantially underestimated in case the actual damping ratio of 1% is applied for the SE06 superelement loads. The increased critical damping of 2.5% and 3.0% leads to better, yet not accurate approximations of the joint fatigue lives. In the 3% critical damping case, it can even be seen that the fatigue lives are slightly overestimated in some joints. More pronounced overestimations in the joint fatigue lives occur for the 3.5% critical damping case which may therefore lead to a non-conservative FLS design, in particular in the lower part of the foundation.

Dynamic load expansion approaches with increased damping might be considered in case the aero-elastic simulations can only be performed with SE06 foundation superelements, e.g. due to limitations in the applied tools. However, the FD must be very careful and, if possible, assess the applied damping conditions thoroughly in order to avoid non-conservative FLS designs. Increased damping conditions in dynamic load expansions for interface loads from the SE06 foundation superelement are further assessed in section 6.1.5.

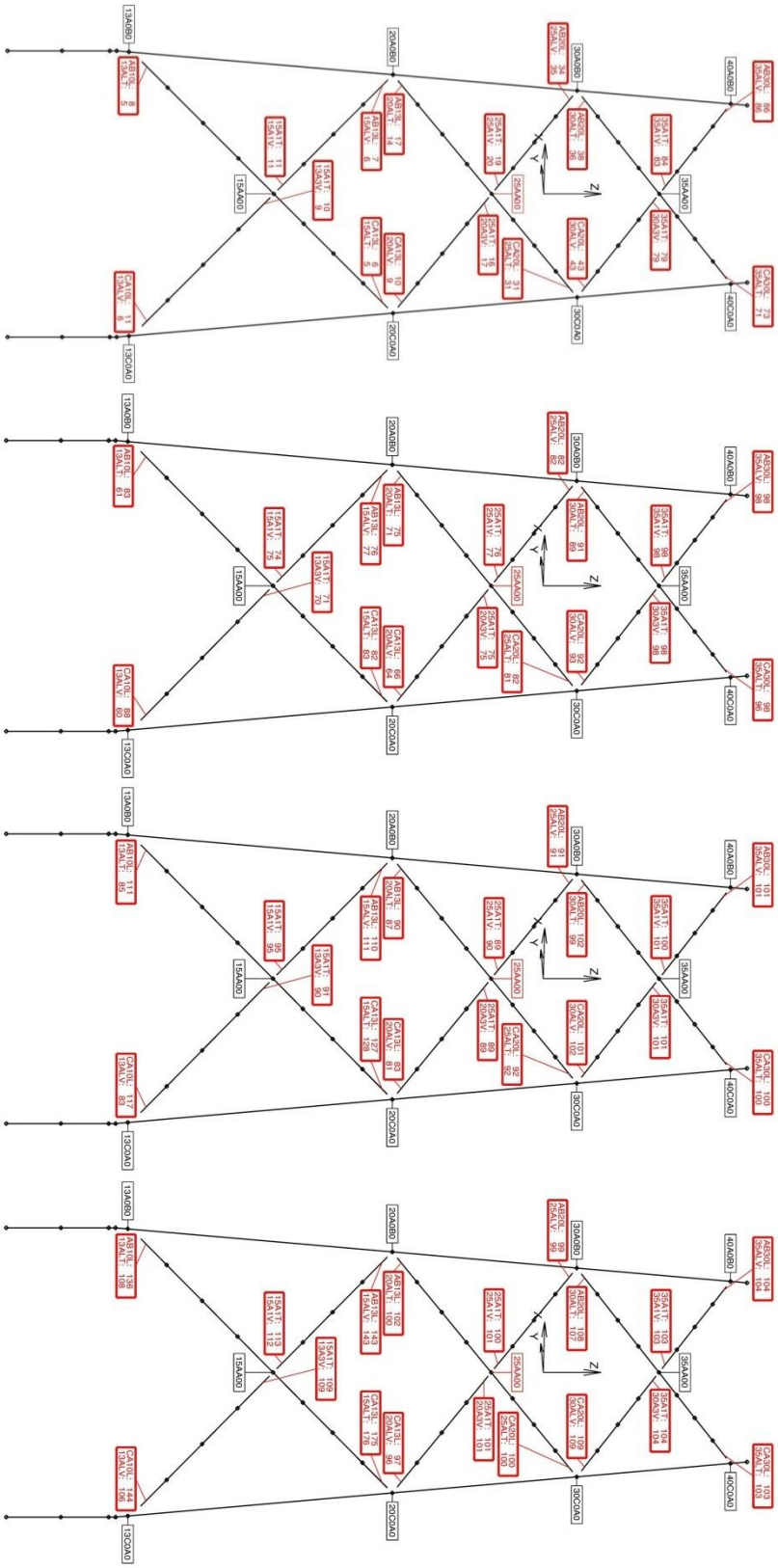

Figure 68: Ratio of joint fatigue lives from the SE06 and SE36 superelement in [%] for the soft configuration S33N for the actual damping of 1% (left), 2.5% (centre left), 3% (centre right) and 3.5% (right).

6.1.5 Detailed assessment of individual load combinations

In this section, the OWT configuration with the soft foundation configuration S33N from section 6.1.1 is assessed in more detail for one exemplary load combination. For the selection of this particular load combination, the fatigue damages are extracted individually for all load combinations in an arbitrary hotspot of the joint 13A0B0-13ALT according to Figure 64. Figure 69 shows the resulting damage distribution as a function of hub height wind speed for the SE36 superelement and the relative differences for the SE06 superelement. As indicated by the differences, the damages are always conservative[14] for the SE06 superelement.

It can be seen that the load combinations for the hub height wind speed v=15m/s, i.e. above rated wind speed of the NREL 5MW [33] turbine, introduce large fatigue damage contributions and also large differences between SE36 and SE06 for the considered tubular joint. Therefore, an exemplary load combination for v=15m/s is investigated in more detail.

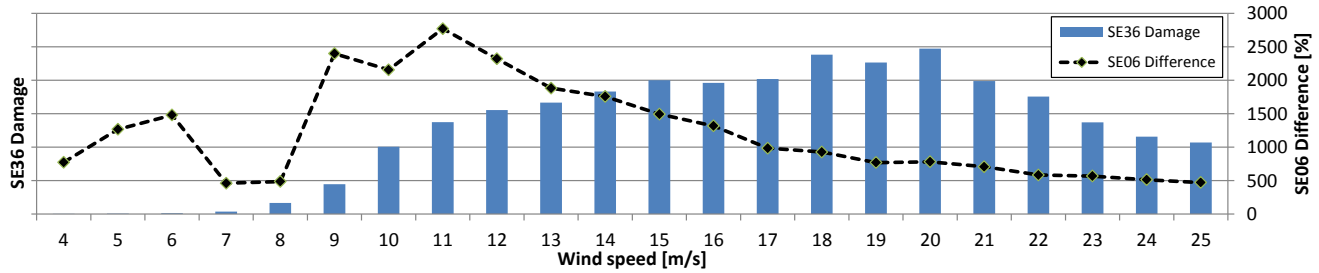

Figure 69: Fatigue damage distribution over wind speed at an arbitrary hotspot in the joint 13A0B0-13ALT (brace side).

The investigations in this section are primarily based on comparisons of results obtained with the SE36 and SE06 superelements. This includes fatigue damage ratios from using SE06 relative to SE36 on the chord and brace side over the circumference of the tubular joint 13A0B0-13ALT as well as assessments of dynamic load responses at interface and in the brace 13ALT.

The damage distribution in Figure 69 shows that high damage contributions are introduced from high wind speed cases. For monopiles and tubular joints in the upper bays of jackets, one can expect a different distribution, i.e. with more pronounced damage contributions around the rated wind speed. For convenience, the damage over wind speed in an arbitrary hotspot of joint 40A0B0-35ALV (according to Figure 64) is shown in Figure 70, but not further discussed.

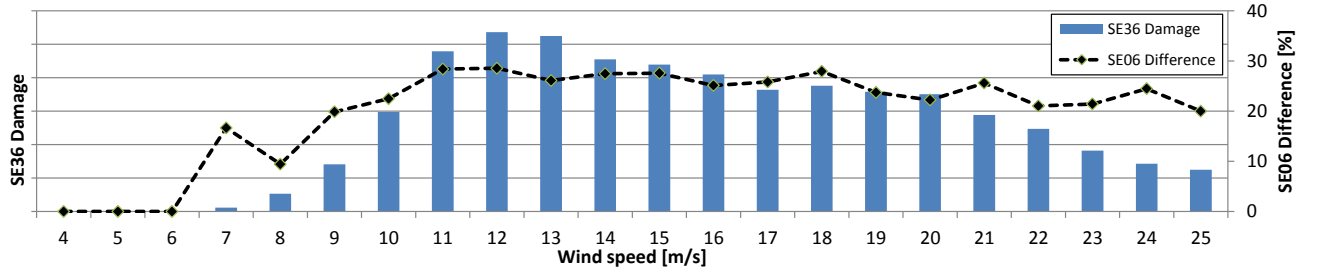

Figure 70: Fatigue damage distribution over wind speed at an arbitrary hotspot in the joint 40A0B0-35ALV (brace side).

[14] This observation is also valid for all other investigated cases (real and theoretical) by the author. However, it should also be mentioned that small fatigue damage underestimations have occasionally been introduced by the SE06 superelement for certain load combinations in individual hotspots, even though the total damage has always been conservative.

Load combination at *v*=15m/s for the soft configuration S33N

An exemplary load combination for the wind speed *v*=15m/s is now assessed in more detail. Figure 71 shows the fatigue damage ratios, i.e. the fatigue damages from SE06 relative to those from SE36, around the circumference on the chord and brace side of joint 13A0B0-13ALT. For convenience, the figure also shows a 100% threshold line, i.e. corresponding to the theoretical case in which the same fatigue damage is obtained from SE06 and SE36. It can be seen, that the fatigue damages are overestimated up to 1500% by application of SE06. The different ratios on opposite sides of the circumference are introduced by differences in the corresponding stress concentration factors which are determined according to Efthymiou [19].

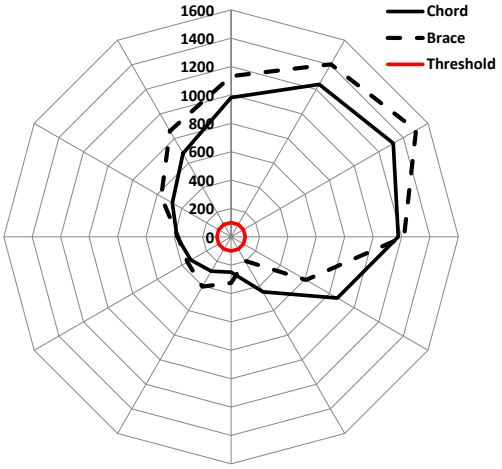

Figure 71: Joint fatigue damage ratios [%] from SE06 relative to SE36 around the circumference in joint 13A0B0-13ALT.

Table 12 summarizes the damage equivalent interface loads from SE36 and SE06 assuming unit probabilities of the time series for *v*=15m/s and a lifetime of 25 years. Furthermore, the table shows the errors in terms of relative differences between the DELS from SE36 and SE06.

It can be seen that the errors are rather small with the largest overestimation being 4.6% for the damage equivalent horizontal shear force in fore-aft direction $F_{eq,x}$. Furthermore, the damage equivalent horizontal shear force in side-side direction $F_{eq,y}$ and axial load $F_{eq,z}$ are even underestimated by application of the SE06 foundation superelement.

Table 12: Damage equivalent interface loads from SE36 and SE06 for N_{ref}=10^8 and *m*=5.

	$F_{eq,x}$ [kN]	$F_{eq,y}$ [kN]	$F_{eq,z}$ [kN]	$M_{eq,x}$ [kNm]	$M_{eq,y}$ [kNm]	$M_{eq,z}$ [kNm]
SE36	361	177	119	14152	29068	5560
SE06	378	172	116	14146	29184	5628
Error [%]	*4.7*	*-2.8*	*-2.5*	*0.0*	*0.4*	*1.2*

The interface responses are directly obtained from the aero-elastic simulations under the same conditions for the SE06 and SE36 superelement. Hence, no influences from the force-controlled, dynamic load expansion are included and errors are directly introduced from the foundation superelement SE06.

Figure 72 shows 50s time series samples of selected interface responses from the SE06 and SE36 super-elements as well as the differences between both. The differences from all load components constitute the error term $\Delta_{SE06}(t)$ for the force-controlled, dynamic load expansion in Eq. 39. For the present example, the errors are small at interface, as also indicated by the DELs in Table 12.

However, under consideration of the large damage differences at joint 13A0B0-13ALT in Figure 71, the following preliminary conclusion on the applicability of the SE06 superelement is drawn:

Small errors in the DELs and the time series of the interface responses cannot be used as an indication for acceptable accuracy of calculated joint fatigue lives by the SE06 superelement.

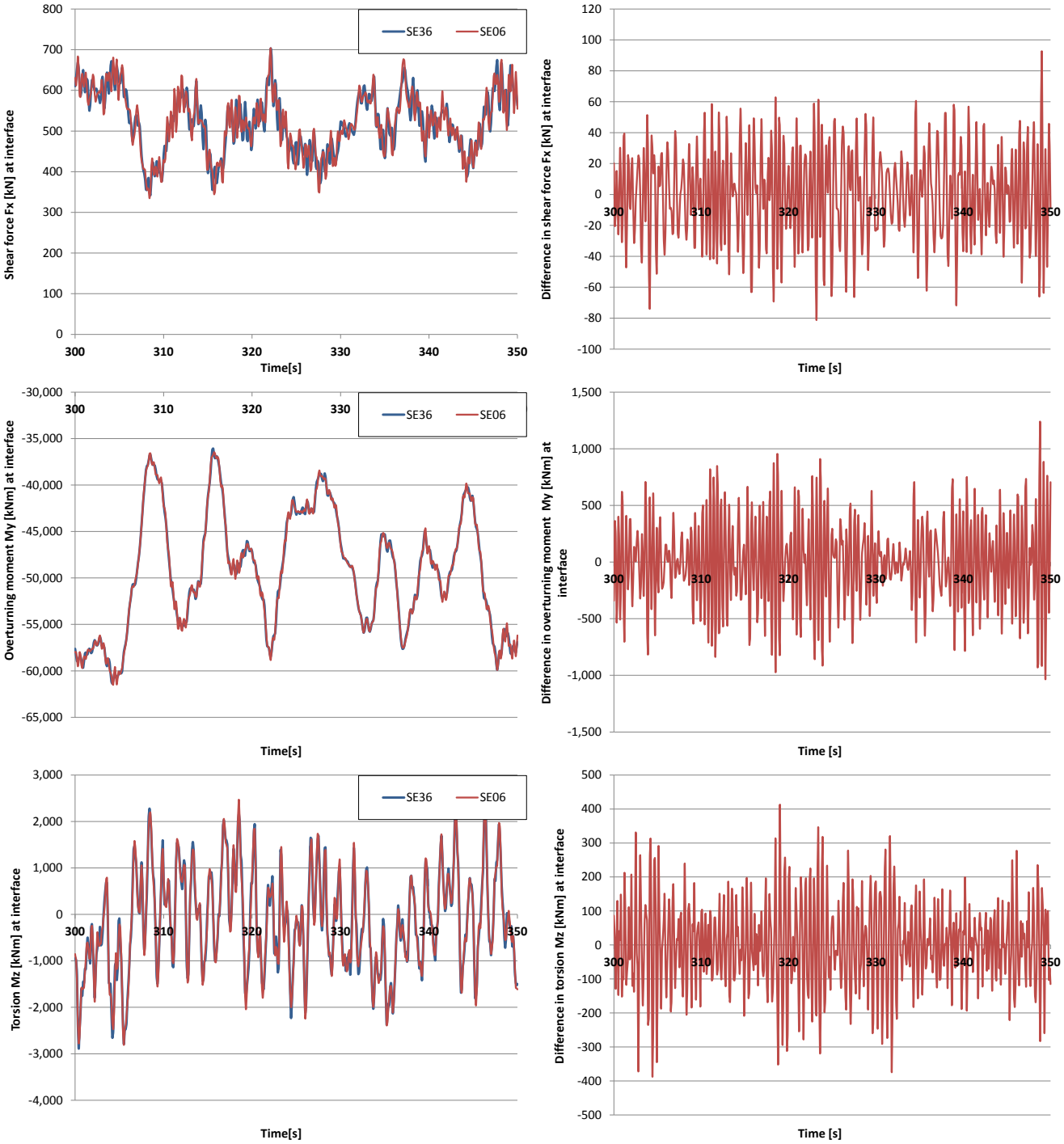

Figure 72: Sample response time series (left) and absolute errors (right) at interface from SE36 and SE06. Horizontal shear load F_x (top), overturning moment M_y (centre) and torsion M_z (bottom).

The following investigations of responses in the frequency domain cover frequencies beyond the 1st and 2nd bending modes from Table 11. Therefore, Table 13 provides additional information regarding the eigenfrequencies of various modes for the OWT with the SE36 and SE06 foundation superelement.

Table 13 Eigenfrequencies [Hz] of the different modes for SE36 and SE06.

Mode	global bending						torsion	1st mode of full foundation without superstructure
	fore-aft			side-side				
	1st	2nd	3rd	1st	2nd	3rd	1st	
SE36	0.228	1.131	2.002	0.227	1.098	1.839	0.954	1.23
SE06	0.228	1.200	2.259	0.227	1.157	2.406	0.955	
Difference [%]	*0.0*	*6.1*	*12.8*	*0.0*	*5.4*	*30.8*	*0.1*	

Figure 73 and Figure 74 show the power spectral densities of all interface responses as obtained by SE06 and SE36 as well as the corresponding total errors, i.e. the power spectral density differences between SE36 and SE06. Furthermore, the figures show the *1P* - *9P* excitations and the 1st eigenfrequency of the foundation S33N without superstructure. Good agreement between SE06 and SE36 is achieved for all responses at lower frequencies, i.e. covering the 1st bending eigenfrequency as well *1P* and *3P* excitations up to 1Hz.

Pronounced horizontal shear responses F_x (fore-aft) at interface can be observed in the power spectral densities for the excitations *1P* to *6P*. The largest differences in terms of overestimations are located in the vicinity of the 2nd global bending modes (fore-aft and side-side) of the OWT with the SE06 foundation superelement, i.e. around 1.10Hz to 1.25Hz. An error peak is found directly at the frequency of *6P* and the 2nd fore-aft bending mode (SE06). This is reasonable as the structural responses are typically more pronounced around the eigenfrequencies. In the same way, the small underestimation just before 1.10Hz can be explained by the fact that the response from the OWT with the SE36 superelement contains more energy due to the close vicinity to the 2nd global bending modes (fore-aft and side-side). Furthermore, distinct underestimations and overestimations are present in the range of 1.75Hz to 2.0Hz and 2.25Hz to 2.40Hz. On one hand, the frequency interval for the underestimations corresponds roughly to the eigenfrequency range of the 3rd global bending modes (fore-aft and side-side) of the OWT with the SE36 foundation superelement. On the other hand, the frequency interval for the overestimations corresponds roughly to the eigenfrequency range of the 3rd global bending modes (fore-aft and side-side) of the OWT with the SE06 foundation superelement.

Similar observations can be made for the horizontal shear force F_y (side-side). However, in comparison to the results for the horizontal shear force F_x (fore-aft), the power spectral densities of the responses as well as of the differences are lower by at least an order of magnitude for the higher frequencies. Furthermore, the error peak in the range 1.10Hz to 1.25Hz is now found at the frequency of the 2nd side-side bending mode (SE06) instead of the frequency of the 2nd fore-aft bending mode (SE06). The total error in the power spectral densities seems to be more pronounced for the underestimations than for the overestimations which is in alignment with the results for the damage equivalent load $F_{y,eq}$ in Table 12.

It is interesting to note, that both modes, fore-aft and side-side, can be recognized in the responses and errors of the horizontal shear force component F_x, although F_x supposedly corresponds to the fore-aft direction. The horizontal interface shear force F_x is based on an global earth-fixed coordinate system. With respect to the mean wind direction and by disregarding any yaw errors the global x-direction corresponds to the fore-aft

direction in this exemplary load combination. However, the global *x*-direction is not always completely aligned with the fore-aft direction during the load simulation, e.g. due to the consideration of three-dimensional turbulent wind and the corresponding yawing of the turbine. In consequence, the responses of the side-side modes can be observed in the responses and errors of the horizontal shear force F_x as well. For the same reason, the responses of the fore-aft modes can be observed in the responses and errors of the horizontal shear force F_y. In design practice, this effect might even be more pronounced due to couplings of the fore-aft and side-side mode.

It is shown at the end of this section, that mainly the errors in F_x and F_y lead to errors in the foundation member loads and joint fatigue lives for the present example. Therefore, the results for the remaining interface load components are only discussed briefly.

The overturning moments M_x and M_y show errors in roughly the same frequency regions as the horizontal shear forces in F_x and F_y. The main difference is that the responses for M_x and M_y are underestimated by the OWT with the SE06 superelement in the region of 1.10Hz to 1.25Hz while overestimated for the horizontal shear forces F_x and F_y. Furthermore, the most pronounced differences are found in terms of overestimations at the eigenfrequency range of the 3rd global bending modes (fore-aft and side-side) of the OWT with the SE06 foundation superelement, i.e. around 2.25Hz to 2.40Hz.

The axial interface responses F_z seems to agree generally very well between SE06 and SE36. However, very narrow error peaks in terms of underestimations and overestimations are located around 1.25Hz.

Differences in the torsion responses M_z mainly occur around 1.75Hz which corresponds to the 2nd torsion mode of the OWT. Here, the responses are overestimated by the OWT with the SE06 superelement. However, the differences are relatively small in comparison to the energy contents at lower frequencies such as *3P*. Furthermore, small differences in terms of underestimations occur also around *6P*.

The eigenfrequency of the 2nd fore-aft bending mode according to Table 11 is close to the *6P* excitations in the current example. The resulting excitations and pronounced responses of the 2nd fore-aft bending mode are beneficial for the present investigations since this particular mode has an important influence for the fatigue design of jacket foundations and the applicability of SE06 superelements. However, jacket designs with the 2nd fore-aft bending mode in close vicinity to *6P* excitations (at rated rotor speed) should be avoided in design practice.

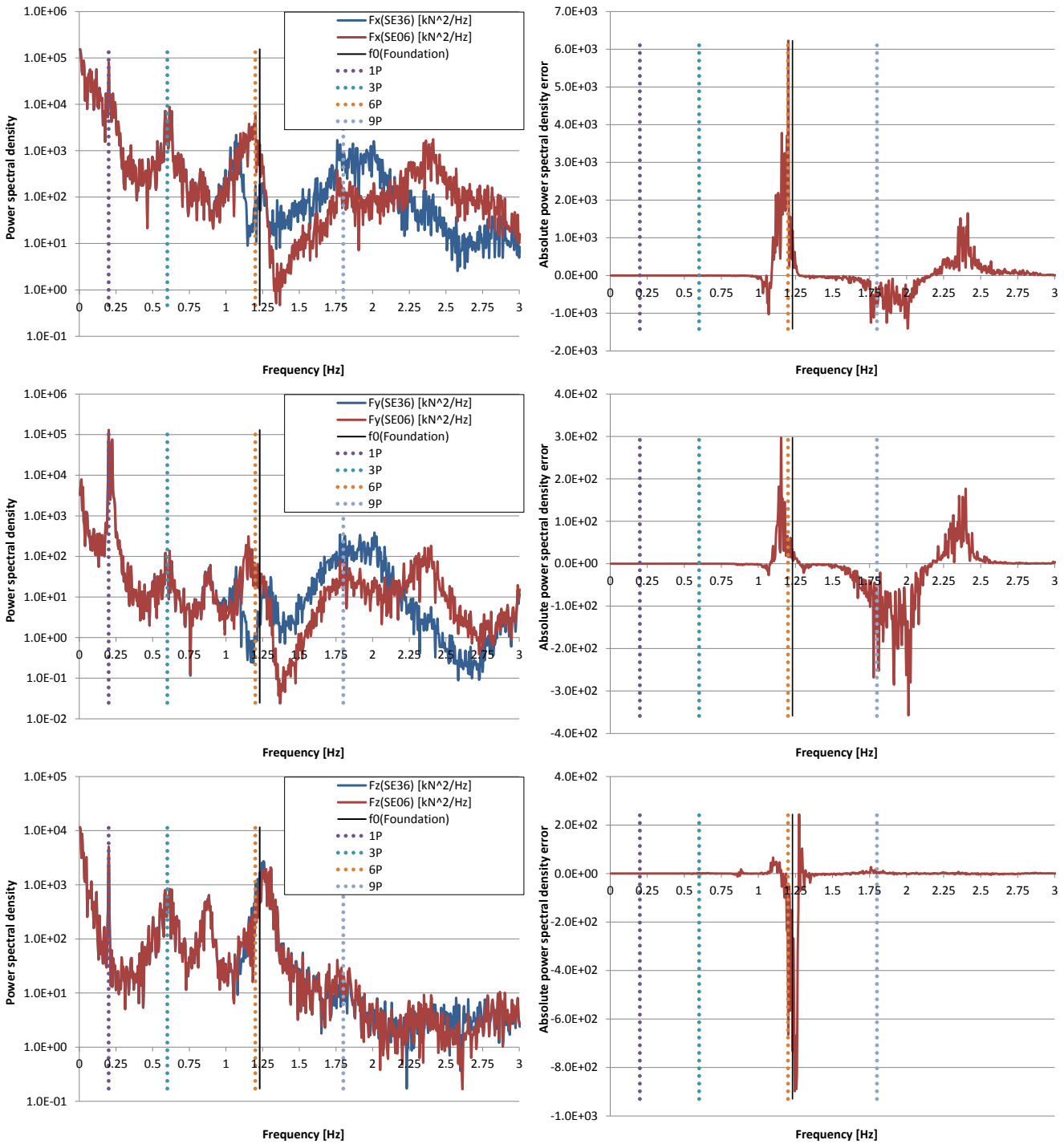

Figure 73: Distribution of power spectral densities (left) and total errors (right) over frequency for interface responses from SE36 and SE06. Horizontal shear load F_x (top) & F_y (centre) and axial load F_z (bottom).

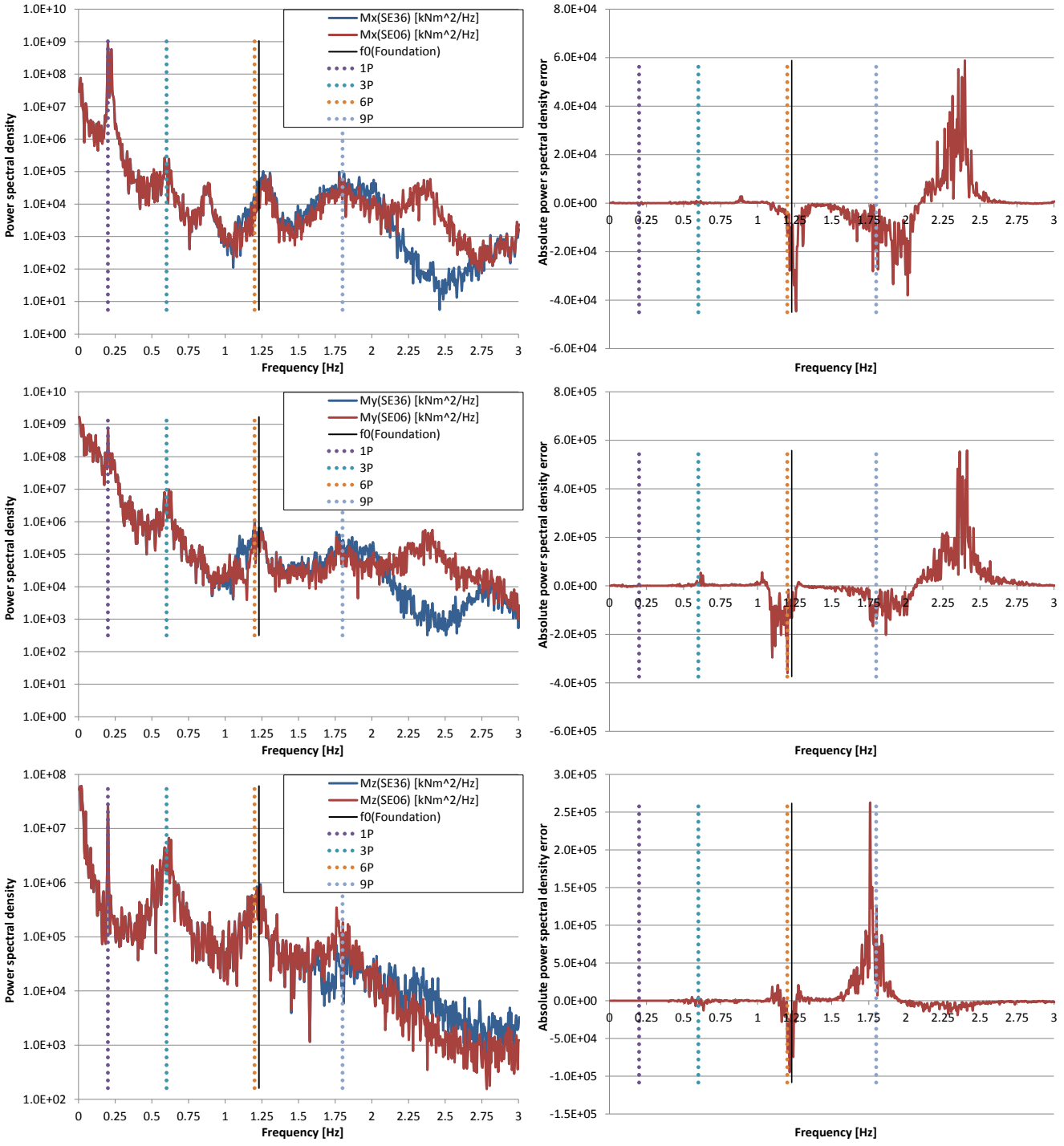

Figure 74: Distribution of power spectral densities (left) and total errors (right) over frequency for interface responses from SE36 and SE06. Overturning moments M_x (top) & M_y (centre) and torsion M_z (bottom).

Foundation loads are calculated on basis of the interface responses from the SE06 and SE36 superelements in a force-controlled, dynamic load expansion as described in paper 1 [61]. Figure 75 shows the soft foundation configuration S33N, as applied for the load expansion, together with the first eigenmode[15]. According to section 6.1.3, the possibility of artificial dynamic excitations from the error term $\Delta_{SE06}(t)$ in Eq. 39 might be expected. These excitations lead to artificial dynamic foundation responses and, in consequence, to artificially increased foundation loads. The increased foundation loads are most pronounced for members in the bottom of the structure. On one hand, this is due to the fact that increased foundation inertia loads from the upper part of the structure are transferred down into the soil. On the other hand, the eigenmode in Figure 75 shows pronounced local in-plane and out-of-plane brace deformations for the lower bays which introduce additional loads in the neighbouring tubular joints when excited. The trend for increasing artificial foundation loads towards the bottom of the structure is verified by the decreasing relative joint fatigue lives for the soft foundation configuration S33N in Figure 62.

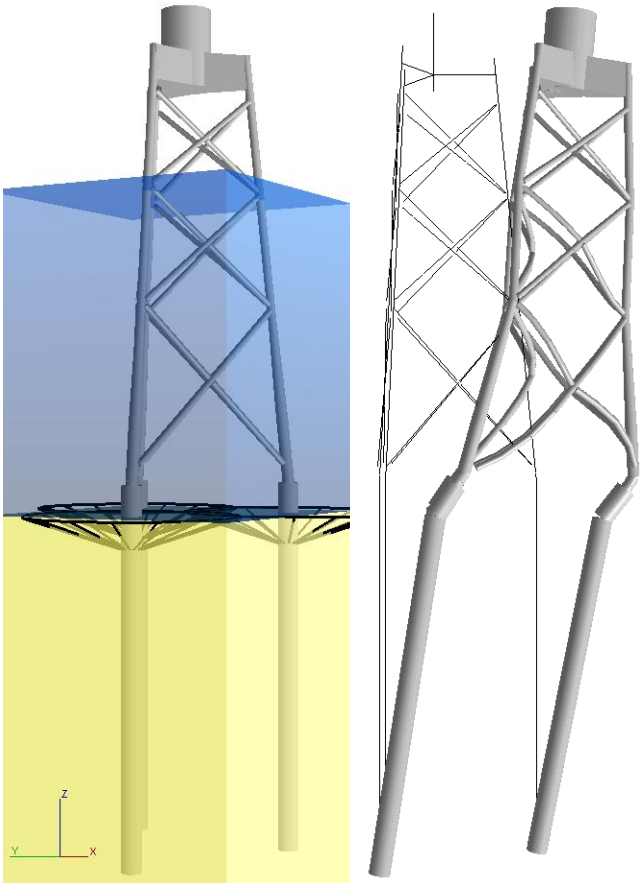

Figure 75: Soft configuration S33N and first eigenmode.

Table 14 and Table 15 summarize the damage equivalent member loads in the braces at joints 13A0B0-13ALT and 40A0B0-35ALV (see Figure 64) as obtained from SE36 and SE06. The DELs are calculated under the assumption of unit probabilities of the time series for v=15m/s and a lifetime of 25 years. In difference to interface, the brace member DELs loads are provided on basis of local coordinate systems with the u-axis being parallel to the member axis, the v-axis being in-plane and the w-axis being out-of-plane of the (undeformed) x-brace plane.

For the upper bay member loads of brace 35ALV in Table 14, it can be seen that the axial load $F_{eq,u}$ constitutes the largest load component. The error is similar to the errors for the interface loads in Table 12 and therefore not very large.

Table 14: Damage equivalent loads in brace 35ALV at node 40A0B0 from SE36 and SE06 for N_{ref}=10^8 and m=5.

	$F_{eq,u}$ [kN]	$F_{eq,v}$ [kN]	$F_{eq,w}$ [kN]	$M_{eq,u}$ [kNm]	$M_{eq,v}$ [kNm]	$M_{eq,w}$ [kNm]
SE36	248.9	4.1	1.8	7.4	15.2	26.2
SE06	258.5	4.4	2.1	8.2	15.8	26.5
Error [%]	*3.9*	*7.3*	*16.7*	*10.8*	*3.9*	*1.1*

[15] The mode shape plot does not show the curvature of the subsoil part of the piles.

The axial load $F_{eq,u}$ constitutes also the largest load component for the lower bay member loads of brace 13ALT in Table 15. Although still lower than the axial loads, the in-plane and out-of-plane bending moments $M_{eq,v}$ and $M_{eq,w}$ introduce more significant contributions. Both, axial load as well as bending moments from the SE06 superelement show large errors despite the small errors in the interface DELs according to Table 12.

Table 15: Damage equivalent loads in brace 13ALT at node 13A0B0 from SE36 and SE06 for $N_{ref}=10^8$ and $m=5$.

	$F_{eq,u}$ [kN]	$F_{eq,v}$ [kN]	$F_{eq,w}$ [kN]	$M_{eq,u}$ [kNm]	$M_{eq,v}$ [kNm]	$M_{eq,w}$ [kNm]
SE36	409.9	5.9	13.4	6.8	78.4	78.5
SE06	601.6	9.1	23.0	10.8	117.0	142.3
Difference [%]	*46.8*	*54.2*	*71.6*	*58.8*	*49.2*	*81.3*

The increasing error magnitude from the upper bay member 35ALV to the lower bay member 13ALT can also be observed in the corresponding relative joint fatigue lives in Figure 62.

Figure 76 shows 50s time series samples of the axial load F_u, the in-plane bending moment M_v and the out-of-plane bending moment M_w in brace 13ALT at node 13A0B0 as well as the differences between the SE06 and SE36 results. The errors are relatively large for all three load components. Although the total errors are larger for the interface responses in Figure 72, the brace member loads show larger relative errors, i.e. relative to the underlying load component. This is also indicated by the small errors of the interface DELs in Table 12 and the large errors of the member DELs in Table 15.

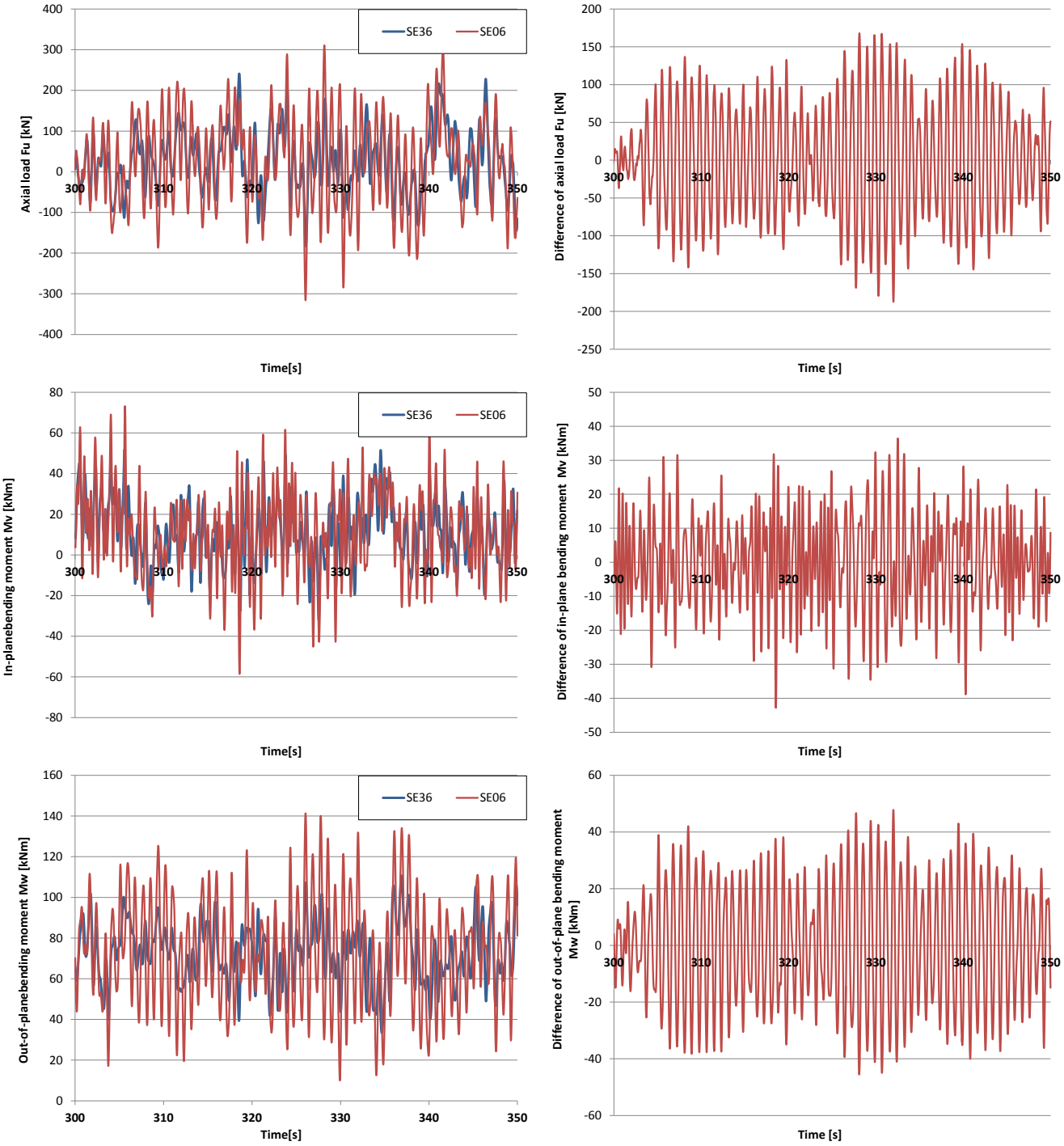

Figure 76: Sample response time series (left) and total errors (right) at element 13ALT from SE36 and SE06. Axial load F_u (top), in-plane moment M_v (centre), out-of-plane moment M_w (bottom).

Figure 77 and Figure 78 show the power spectral densities of all local member loads in brace 13ALT at node 13A0B0 as obtained from the SE06 and SE36 interface loads in the force-controlled, dynamic load expansion. In addition, the load expansion results for the SE06 interface loads are also provided for an increased damping case of 3.5% structural damping (critical), denoted is as DampSE06. In accordance to section 6.1.4, the increased damping is only applied to the foundation structure in the load expansion. Furthermore, Figure 77 and Figure 78 show the total power spectral density errors from SE06 and DampSE06, i.e. the differences to the reference results from SE36.

As for the interface responses, good agreement is achieved between SE36 and SE06 for all responses at lower frequencies, i.e. covering the 1st global OWT bending eigenfrequency as well *1P* and *3P* excitations up to 1Hz. This is also valid for the increased damping case DampSE06.

In the following discussion of results, focus is on the most severe member loads as indicated by DELs in Table 15, i.e. the axial load F_u as well as the in-plane and out-of-plane bending moments M_v and M_w.

The largest differences between SE06 and SE36 occur as overestimations around 1.20Hz for all load components, i.e. at the eigenfrequency of the 2nd fore-aft bending mode of the OWT with SE06 superelement. As shown in Figure 73 and Figure 74, this coincides with the overestimation errors in the horizontal shear loads F_x and F_y at interface while all other interface load components introduce errors in terms of underestimations. Therefore, the member load errors around 1.20Hz are assumed to be mainly introduced from the errors in horizontal shear loads F_x and F_y at interface. This assumption is verified at the end of this section.

Further errors between SE06 and SE36 can particularly be observed for the in-plane bending moment component M_v at the frequency 1.75Hz which coincides with the error in the interface torsion M_z at the 2nd torsion mode of the OWT. Both, the axial load F_u and the out-of-plane bending moment component M_w show an error at this frequency as well. However, their error magnitudes are much less pronounced in comparison to the error at the 2nd fore-aft bending mode of the OWT with SE06 superelement. Furthermore, pronounced errors in terms of overestimations are found for the in-plane bending moment M_v in freqcuency range of the 3rd global bending modes (fore-aft and side-side) of the OWT with the SE06 foundation superelement, i.e. around 2.25Hz to 2.40Hz. In comparison to the results for the axial load F_u and out-of-plane bending moment M_w, the errors in the frequency regions 1.75Hz and 2.25Hz to 2.40Hz for the in-plane bending moment M_v can be recognized as higher frequency oscillations in Figure 76.

An interesting observation for all member load components is related to the fact that the power spectral densities are practically always overestimated for the SE06 case despite the pronounced underestimations of some interface responses at some frequencies.

Significant reductions of the errors in all member load components at joint 13A0B0-13ALT can be observed for the increased damping case DampSE06. This behavior supports the assumption from section 6.1.3, i.e. that the additional loading due to the error term $\Delta_{SE06}(t)$ in Eq. 39 introduces artificial dynamic excitations of the foundation structure in the dynamic load expansion calculation. However, Figure 77 and Figure 78 show also underestimations in the power spectral densities in case of DampSE06 which is aligned with overestimation of fatigue live in the corresponding tubular joint in Figure 68 of section 6.1.4.

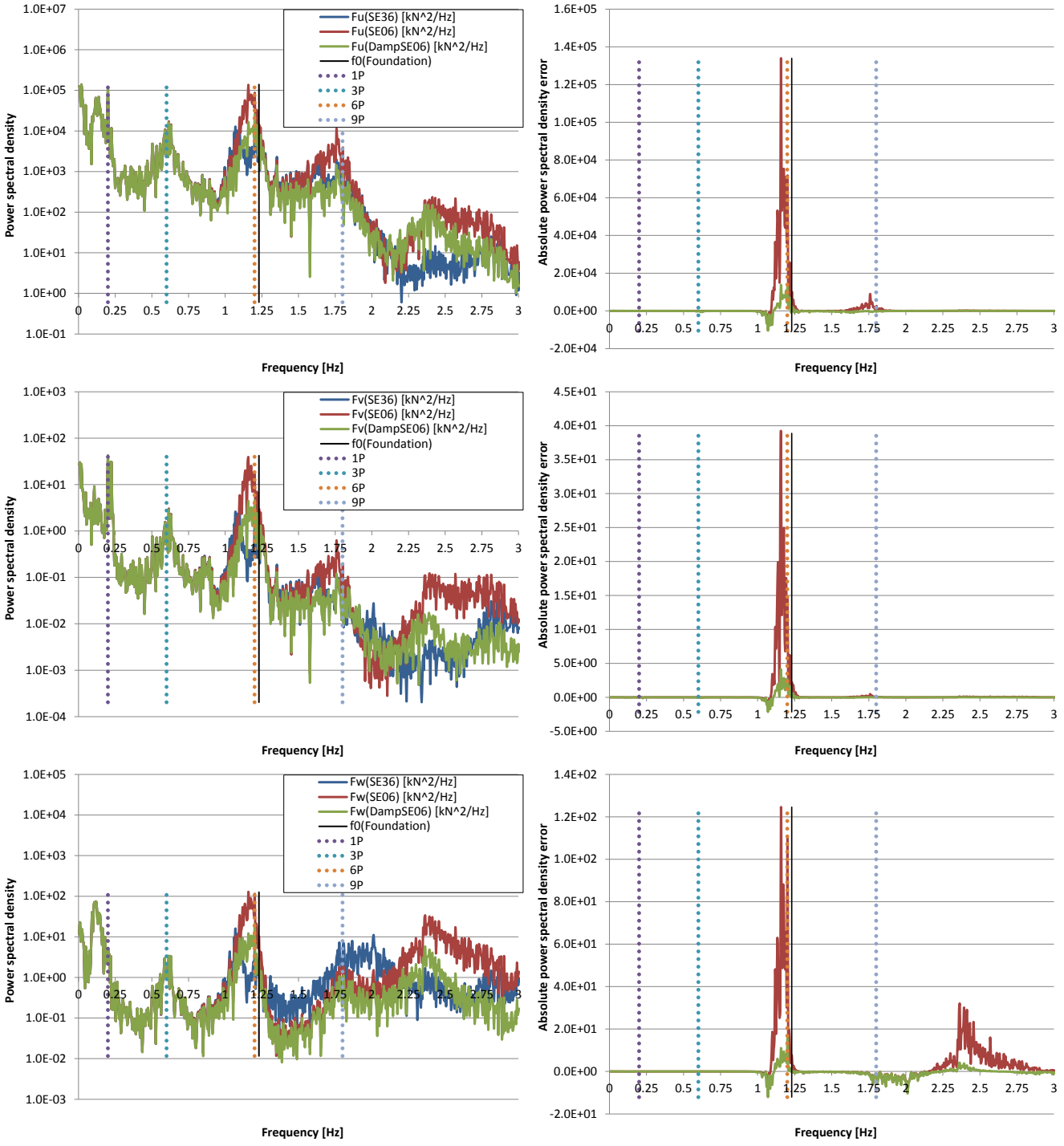

Figure 77: Distribution of power spectral densities (left) and total errors (right) over frequency for element 13ALT at tubular joint node 13A0B0. Axial load F_u (top), in-plane shear F_v (centre), out-of-plane shear F_w (bottom).

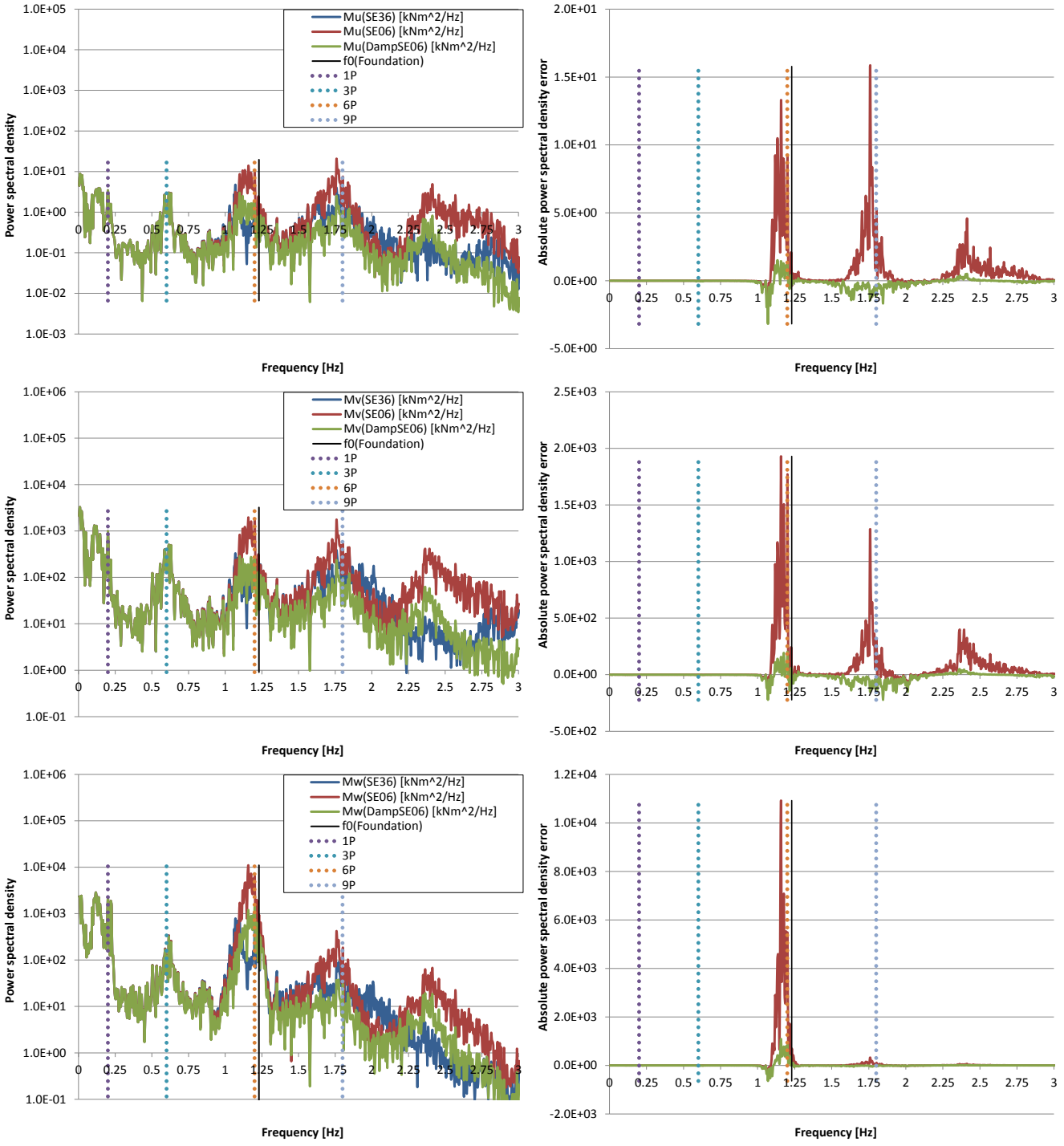

Figure 78: Distribution of power spectral densities (left) and total errors (right) over frequency for element 13ALT at tubular joint node 13A0B0. Torsion M_u (top), in-plane moment M_v (centre), out-of-plane moment M_w (bottom).

Influence from the error of individual interface load components in the load expansion

As shown above, fatigue damages in the tubular joint 13A0B0-13ALT are significantly overestimated by application of the interface loads from SE06 and the error over frequency in the power spectral density differs for the individual load components. However, a quantifiable correlation between the individual interface load errors and the joint fatigue damages is not available due to the dynamic character of the relation between interface and foundation responses. For the exemplary load combination at v=15m/s, it is briefly investigated how the errors of individual interface load components from SE06, i.e. corresponding to the error term $\Delta_{SE06}(t)$ in Eq. 39, contribute to the fatigue damage overestimation in the tubular joint 13A0B0-13ALT.

For that purpose, two additional force-controlled, dynamic load expansions and subsequent fatigue damage calculations are established. The individual interface loads components F_x, F_y, F_z, M_x, M_y and M_z for these load expansions are taken either from the SE06 or the SE36 interface response time series.

- For the first case, the horizontal shear loads F_x and F_y from SE36 are taken together with the moments M_x, M_y, M_z and the axial load F_z from SE06.
- For the second case, the moments M_x, M_y, M_z and the axial load F_z from SE36 are taken together with the horizontal shear loads F_x and F_y from SE06.

The mix of interface load components for the dynamic load expansion introduces a certain loss in the correlation between individual load components such as between F_x and M_y. However, this loss of correlation is limited to higher frequency contents while it is reasonably well preserved for the lower frequency contents which govern the overall responses. This can be seen in the time series samples of Figure 79 and in the power spectral density distributions from Figure 73 and Figure 74. Therefore, the mix of load components from the SE36 and SE06 interface responses is an acceptable simplification for the purpose of this investigation.

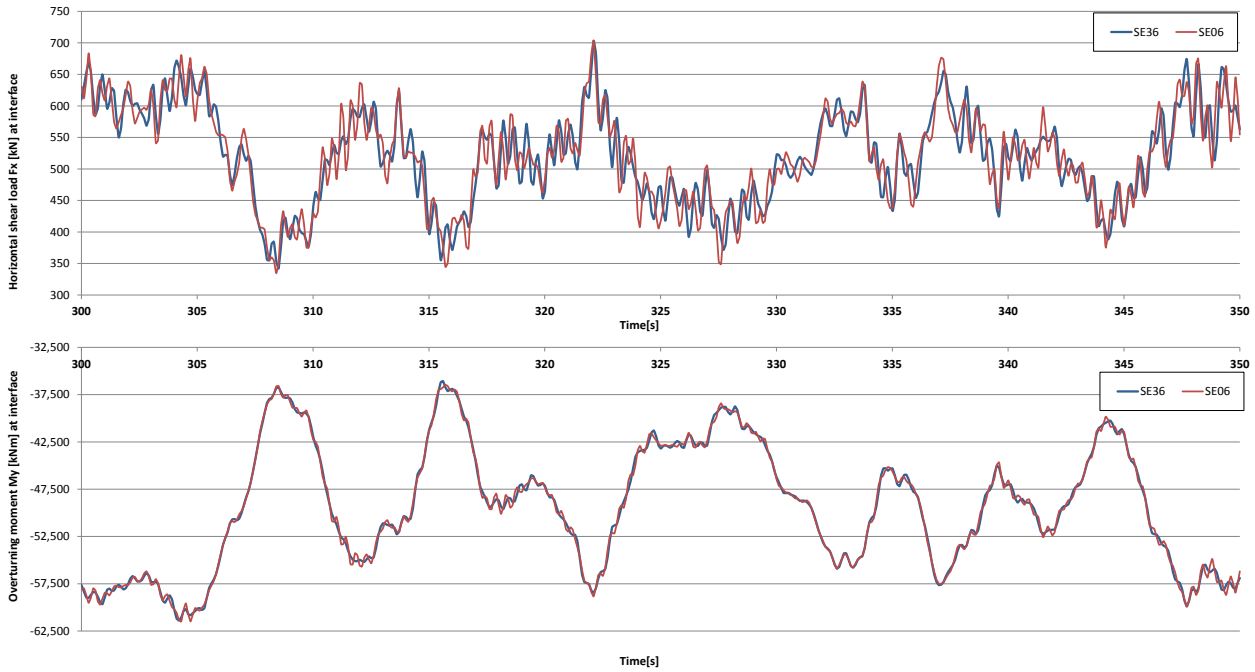

Figure 79: Sample time series of horizontal shear load F_x (top) and overturning moments M_y (bottom) from SE36 and SE06.

The resulting fatigue damage ratios, i.e. the fatigue damages for the constructed cases relative to those from SE36, are shown in Figure 80 for the tubular joint 13A0B0-13ALT. For convenience, the figure also shows a 100% threshold line. Deviations from the 100% threshold line constitute fatigue damage errors in the constructed cases since the results from SE36 are considered correct, which has been verified by the investigations in section 6.1.2.

In comparison to the results from Figure 71, i.e. without mixing of load components, it can be seen that:

- The fatigue damage errors are substantially reduced for the first case (left plot). In particular, the large errors on the right side of the joint are almost completely removed. On the left side of the joint the errors are still reduced substantially.
- For the second case (right plot), the large errors on the right side of the joint are hardly affected. However, significant error reductions are achieved again on the left side of the joint.

Hence, the conclusion is that the errors in the horizontal shear loads F_x and F_y from SE06 have a dominant influence on the fatigue damage overestimation in the tubular joint while the influence of the errors in the moments M_x, M_y, M_z and the axial load F_z from SE06 is more limited.

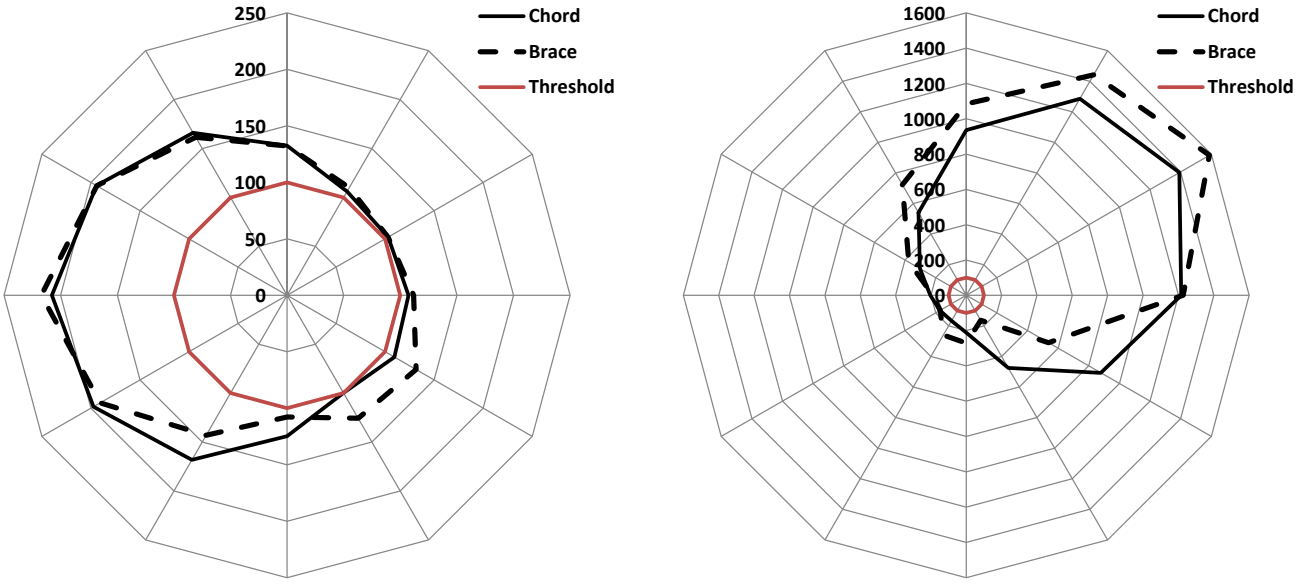

Figure 80: Joint fatigue damage ratios [%] from mixed SE06-SE36 load components relative to SE36 around the circumference in joint 13A0B0-13ALT.
Left: Load component F_x and F_y from SE36 mixed with F_z, M_x, M_y and M_z from SE06.
Right: Load components F_z, M_x, M_y and M_z from SE36 mixed with F_x and F_y from SE06.

6.1.6 Influence of modal properties for different superelement formulations

This section focuses on how fatigue damage errors from SE06 are influenced by the modal properties of the foundation structure in relation to the total OWT. For that purpose two scenarios with different loading conditions and different eigenfrequencies are investigated in more detail.

Load combination at *v*=15m/s for the soft configuration S33N with a modified superstructure

Similar to section 6.1.5 the soft foundation configuration S33N from section 6.1.1 is now assessed for a load combination at the wind speed *v*=15m/s. However, in difference to the previous investigations, the superstructure is modified for the calculation of the interface responses. The change of the superstructure is introduced in order to assess further the influence from the 2nd global (fore-aft) bending mode of the OWT in relation to the 1st mode of the foundation structure while the foundation configuration remains unchanged. For that purpose, the tower stiffness is increased in order to increase the 2nd global (fore-aft) bending mode eigenfrequency slightly while at the same time the RNA mass is increased in order limit the corresponding increase of the 1st fore-aft bending mode eigenfrequency. Table 16 compares the first two global bending eigenfrequencies for the modified OWT as obtained with the SE06 and SE36 foundation superelements. The 1st eigenfrequency of the foundation, which is used for the dynamic load expansion, is at 1.23Hz. Furthermore, the 2nd global bending frequencies are again overestimated by the SE06 superelement.

Table 16 Natural frequencies of the OWT with the S33N foundation configuration for SE36 and SE06.

Mode	1st bending		2nd bending	
	fore-aft	side-side	fore-aft	side-side
SE36	0.276	0.277	1.168	1.150
SE06	0.276	0.277	1.301	1.260
Difference [%]	0.0	0.0	11.4	11.2

It can be seen that the eigenfrequency for the OWT model with the SE06 foundation superelement is larger while the eigenfrequency for the OWT model with the SE36 foundation superelement is lower compared to the eigenfrequency of the isolated foundation. However, in absolute numbers, the 2nd fore-aft bending eigenfrequencies for the OWT with the SE06 and SE36 foundation superelements and the 1st foundation eigenfrequency are similar, differing only by 5-6%.

Figure 81 shows the fatigue damage ratios, i.e. the fatigue damages from superelement SE06 relative to those from superelement SE36 in percent, around the circumference on the chord and brace side of joint 13A0B0-13ALT. The figure shows also the 100% threshold line, i.e. corresponding to the theoretical case in which the same fatigue damage is obtained from SE06 and SE36. It can be seen, that the fatigue damages are overestimated up to

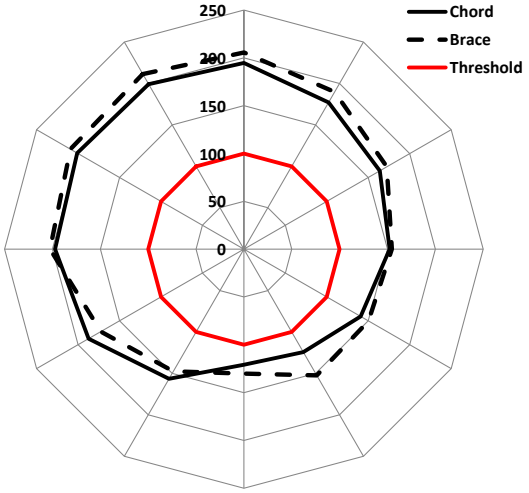

Figure 81: Joint fatigue damage ratios from SE06 relative to SE36 in [%] around the circumference in node 13A0B0 (element 13ALT).

approximately 200% due to application of SE06. This is significantly less than for the exemplary *v*=15m/s case of the original OWT configuration in Figure 71.

Figure 82 shows the power spectral densities of the interface shear force responses as obtained by SE06 and SE36 as well as the corresponding total errors, i.e. the power spectral density differences between SE36 and SE06, together with *1P*, *3P*, *6P* and *9P* excitations, the 1st eigenfrequency of the isolated foundation and the 2nd fore-aft eigenfrequencies of the OWT model with the SE06 and SE36 superelement.

Focusing on the frequency range of the largest error, i.e. in the vicinity of the 2nd global bending modes, *6P* and the 1st foundation mode, the following observations can be made in comparison to the results for exemplary case of the original OWT configuration in Figure 73 of the previous section 6.1.5:

- The largest error for F_x is approximately three times lower in magnitude but occurs at the same frequency, i.e. at *6P*.
- The largest error for F_y is similar in magnitude but occurs at a higher frequencies, i.e. at the 2nd global (side-side) bending mode of the OWT with the SE06 superelement.

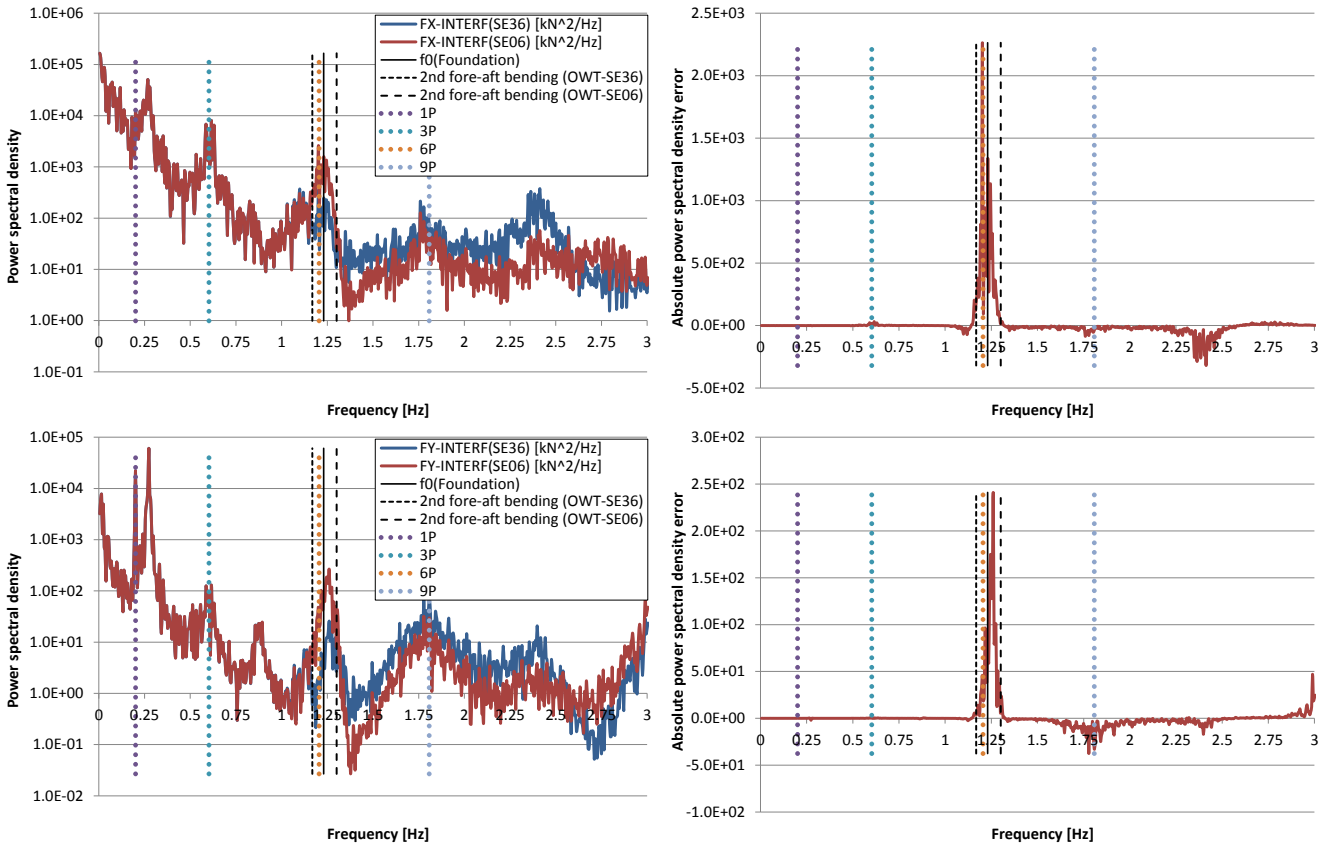

Figure 82: Distribution of power spectral densities (left) and total errors (right) over frequency for interface responses from SE36 and SE06. Horizontal shear load F_x (top) and F_y (bottom).

Table 17 to Table 19 summarize the damage equivalent loads from the SE36 and SE06 superelements at interface and in the braces 35ALV (node 40A0B0) and 13ALT (node 13A0B0) according to Figure 64. The DELs are calculated by assuming unit probabilities of the time series for *v*=15m/s and a lifetime of 25 years.

The interface responses are not influenced by the force-controlled, dynamic load expansion since they are directly obtained from the aero-elastic simulations. Therefore, errors are directly introduced from the foundation superelement SE06. Similar to the exemplary case at *v*=15m/s in the previous section 6.1.5, the errors are rather small. Furthermore, the DELs at interface are overestimated again by the SE06 superelement.

Table 17: Damage equivalent interface loads from SE36 and SE06 for $N_{ref}=10^8$ and $m=5$.

	$F_{eq,x}$ [kN]	$F_{eq,y}$ [kN]	$F_{eq,z}$ [kN]	$M_{eq,x}$ [kNm]	$M_{eq,y}$ [kNm]	$M_{eq,z}$ [kNm]
SE36	323	125	220	7925	21243	5546
SE06	328	126	228	8012	21362	5615
Error [%]	*1.5*	*0.8*	*3.6*	*1.1*	*0.6*	*1.2*

The damage equivalent loads in brace 35ALV and 13ALT according to Table 18 and Table 19 are obtained in a force-controlled, dynamic load expansion with interface loads from the SE36 and SE06 superelements. The loads are provided on basis of a local member coordinate system with the *u*-axis being parallel to the member axis, the *v*-axis being in-plane and the *w*-axis being out-of-plane of the (undeformed) x-brace plane.

Table 18: Damage equivalent loads in brace 35ALV at node 40A0B0 from SE36 and SE06 for $N_{ref}=10^8$ and $m=5$.

	$F_{eq,u}$ [kN]	$F_{eq,v}$ [kN]	$F_{eq,w}$ [kN]	$M_{eq,u}$ [kNm]	$M_{eq,v}$ [kNm]	$M_{eq,w}$ [kNm]
SE36	250.6	3.1	1.4	6.1	11.2	19.9
SE06	256.0	3.1	1.5	6.3	11.5	20.0
Difference [%]	*2.2*	*0.0*	*7.1*	*3.3*	*2.7*	*0.5*

The DELs in 35ALV and 13ALT from SE36 are similar to those obtained from the exemplary case at *v*=15m/s in Table 14 and Table 15 of the previous section 6.1.5, with the axial load $F_{eq,u}$ being the largest component. However, the error magnitudes from SE06 are substantially reduced.

Table 19: Damage equivalent loads in brace 13ALT at node 13A0B0 from SE36 and SE06 for $N_{ref}=10^8$ and $m=5$.

	$F_{eq,u}$ [kN]	$F_{eq,v}$ [kN]	$F_{eq,w}$ [kN]	$M_{eq,u}$ [kNm]	$M_{eq,v}$ [kNm]	$M_{eq,w}$ [kNm]
SE36	395.3	5.3	10.7	6.6	75.3	74.7
SE06	439.0	6.0	11.4	8.3	87.4	88.9
Difference [%]	*11.1*	*13.2*	*6.5*	*25.8*	*16.1*	*19.0*

Figure 83 and Figure 84 show the time series and power spectral densities of the local brace member loads at joint 13A0B0-13ALT as obtained from the SE06 and SE36 interface loads in the force-controlled, dynamic load expansion together with the total errors from SE06 with respect to SE36. It can be seen that the errors are significantly reduced in comparison to Figure 76, Figure 77 and Figure 78 from the previous example in section 6.1.5 which is in line with the reductions of DELs in Table 19.

Focusing on the frequency range of the largest error, i.e. in the vicinity of the 2nd global bending modes, *6P* and the 1st foundation mode it can be seen that the errors are significantly reduced in comparison to the results for the exemplary *v*=15m/s case of the original OWT configuration in Figure 77 and Figure 78. For the load components F_u and M_w the error is reduced approximately by a factor of six and for the in-plane moment M_v the reduction is even larger.

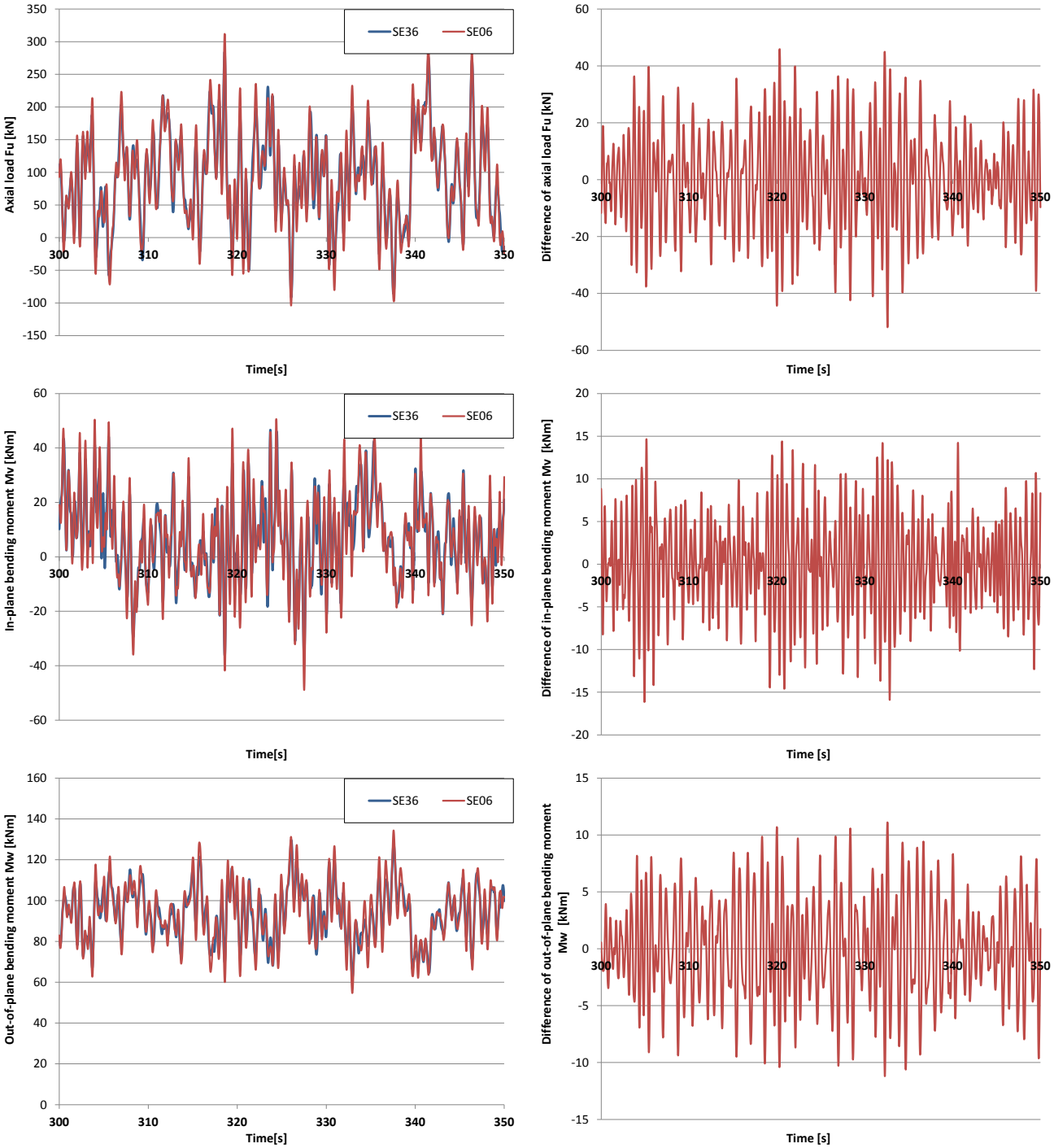

Figure 83: Sample response time series (left) and total errors (right) at element 13ALT from SE36 and SE06. Axial load F_u (top), in-plane moment M_v (centre), out-of-plane moment M_w (bottom).

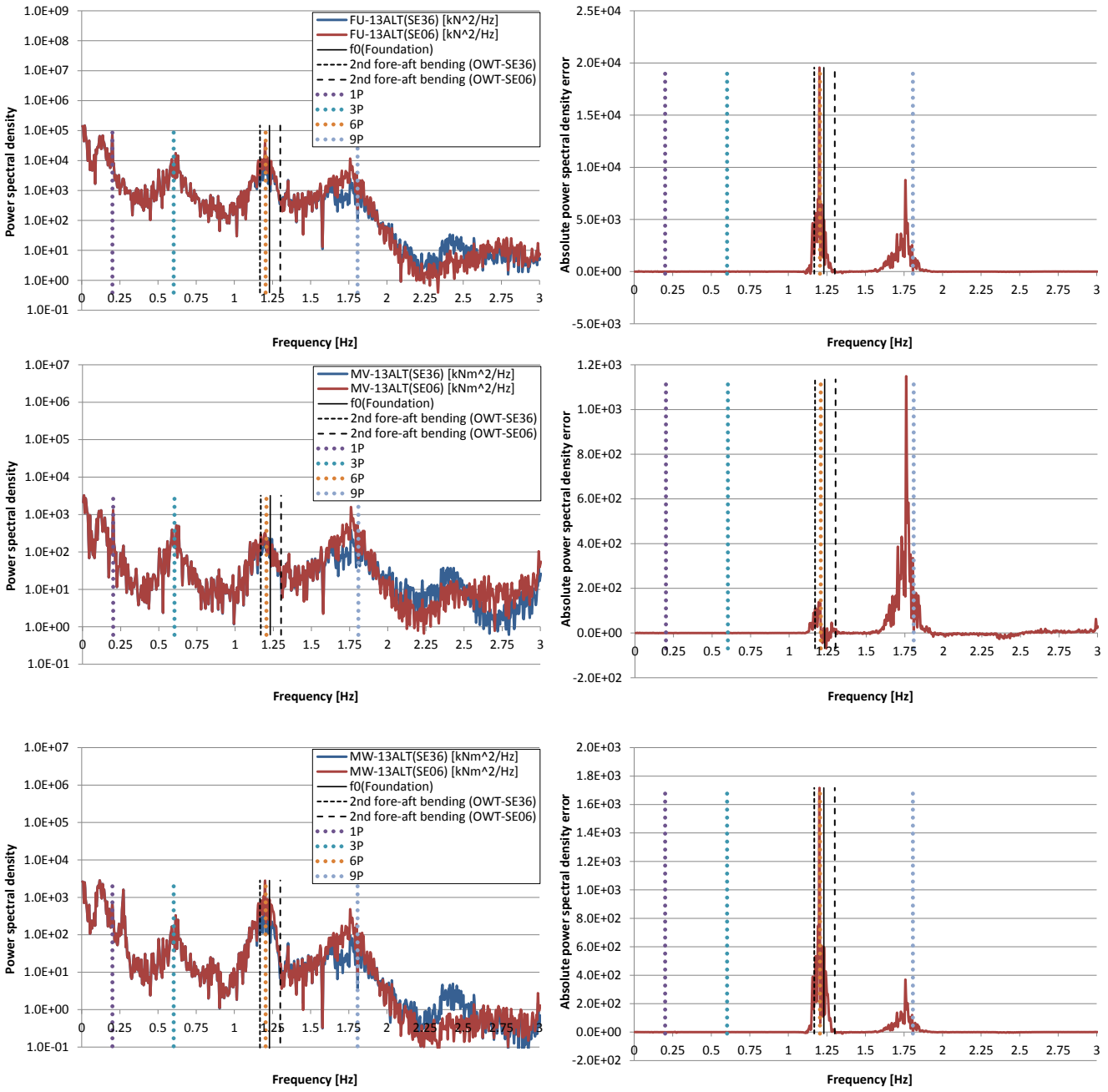

Figure 84: Distribution of power spectral densities (left) and total errors (right) over frequency for element 13ALT at tubular joint node 13A0B0. Axial load F_u (top), in-plane moment M_v (centre), out-of-plane moment M_w (bottom).

In terms of fatigue load accuracy, the SE06 foundation superelement performs considerably better for the OWT configuration in this example compared to the OWT configuration in the previous section 6.1.5, although the only difference is introduced to the superstructure. This difference changed the eigenfrequency constellations of the 1st foundation mode and the 2nd fore-aft bending modes of the OWT with the SE36 and the SE06 superelement.

Detailed assessment of responses in the vicinity of the 2nd global OWT bending mode & 1st foundation mode

In this example, a generic OWT model at a water depth of 38m is subjected to generic tower top excitations in a specific frequency region in dynamic analyses by ROSAP. No detailed RNA representation is required for the dynamic analyses in this example. Therefore, the RNA is represented in a simplified manner by a discrete top mass with associated mass moments of inertia. The superstructure is attached to a 3-legged, piled jacket foundation as illustrated in Figure 85. Superstructure and foundation have been established such that the eigenfrequency of the 2nd global OWT bending mode is very close to the eigenfrequency of the 1st mode of the isolated foundation.

Dynamic analyses are performed for the OWT model with the detailed foundation, hereinafter denoted as the full structure, as well as for the OWT model with a SE06 and SE36 superelement representation of the foundation. The resulting dynamic responses in terms of interface loads from the full structure are compared to the loads obtained with SE36 and SE06 foundation superelement. Furthermore, the brace member loads at the marked tubular joint in Figure 85 as calculated directly with the full structure are compared to results obtained by a force-controlled, dynamic load expansion with the SE36 and SE06 superelement.

Selected eigenfrequencies for the OWT with all three foundation representations as well as for the isolated foundation are summarized in Table 20. It can be seen that the eigenfrequencies for the 1st global bending modes of the OWT are identical for all foundation representations. Furthermore, the same eigenfrequencies for the 2nd global bending modes of the OWT are obtained for the full foundation and the SE36 superelement representation of the foundation, while eigenfrequencies are overestimated by almost 10% for the OWT with the SE06 superelement representation of the foundation. The eigenfrequency for the 1st mode of the isolated foundation is very close to the eigenfrequencies for the 2nd global bending modes of the OWT with full foundation and the SE36 superelement representation of the foundation. Furthermore, the 1st global torsion eigenfrequency for the OWT is 0.910Hz for the full foundation model as well as for the SE36 superelement and 0.915Hz for the OWT with the SE06 superelement.

Table 20 Natural frequencies [Hz] OWT with different foundation representations and for the isolated foundation.

Foundation representation in OWT model	Integrated OWT model				Isolated, full foundation
	1st bending mode		2nd bending mode		
	fore-aft	side-side	fore-aft	side-side	1st mode
Full	0.303	0.302	1.018	1.014	1.031
SE36	0.303	0.302	1.018	1.014	
SE06	0.303	0.302	1.108	1.100	

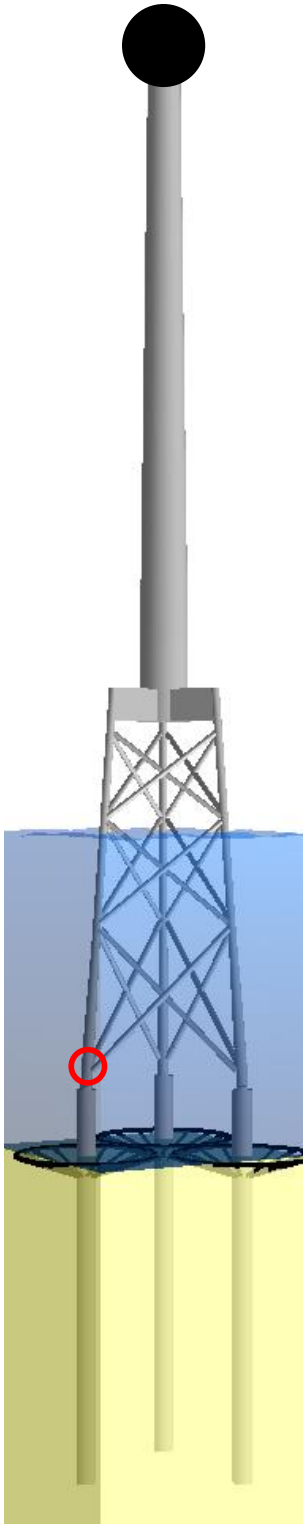

Figure 85: Generic OWT model.

Generic time series of excitations in terms of horizontal fore-aft shear force $F_{x,top}$ and torsion $M_{z,top}$ have been established for a specific frequency interval at tower top which is briefly introduced in the following.

The generation of the shear force time series $F_{x,top}(t)$ is based on the generic power spectrum in Figure 86. Only the frequency interval from 0.75Hz to 1.261Hz contains energy in order to ensure excitations of the OWT's 1st torsion mode and 2nd global (fore-aft) bending mode. Furthermore, the excitations in this frequency interval allows also for investigations of the 1st foundation mode behavior in the dynamic load expansion.

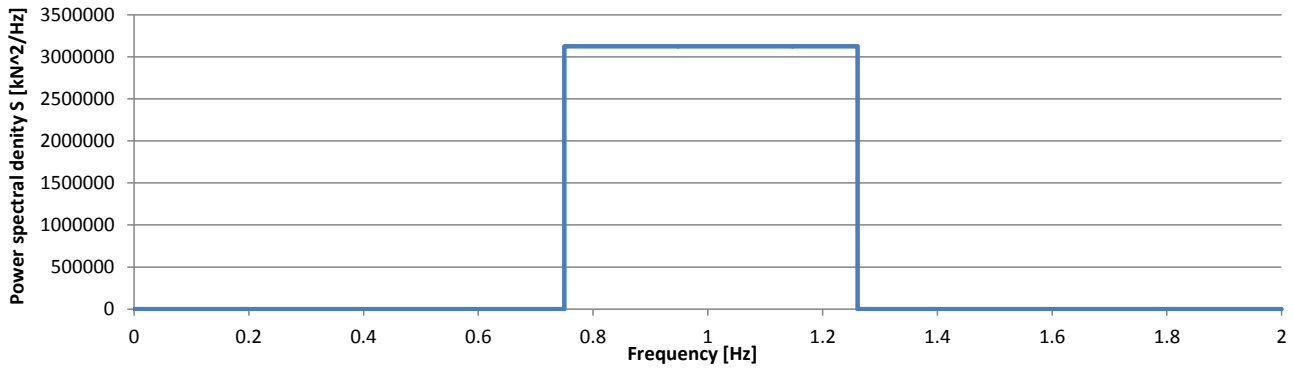

Figure 86: Generic power spectral density distribution $S(f)$ for the horizontal shear force $F_{x,top}$.

The time series generation is based on a Fourier transformation. This requires a discretization of the spectrum into n intervals, each with the constant frequency width Δf. Each interval i is represented by the power spectral density $S(f_i)$ at the frequency f_i which is used for establishment of the amplitude a_i of the i^{th} harmonic component. The time series realization for the shear force $F_{x,top}$ is based on the generation and superposition of n(=512) harmonic components and an arbitrarily chosen mean value of 200kN according to the in Eq. 40.

$$F_{x,top}(t) = 200 + \sum_{i=1}^{n} a_i \cdot cos(\omega_i t + \theta_i) \qquad \text{Eq. 40}$$

with

$a_i = 2 \cdot \sqrt{S(f_i) \cdot \Delta f}$	Amplitude of the i^{th} harmonic component
Δf = 0.001Hz	(Constant) frequency width for each harmonic component
$\omega_i = 2\pi f_i$	Angular frequency of the i^{th} harmonic component
θ_i	Random phase for the i^{th} harmonic component

Only the generic 600s time series for the shear force $F_{x,top}$ has been established directly. The time series for the torsion $M_{z,top}$ is obtained by mirroring the time series $F_{x,top}$ and scaling with the factor 5. Figure 87 shows exemplarily the first 100s of both time series.

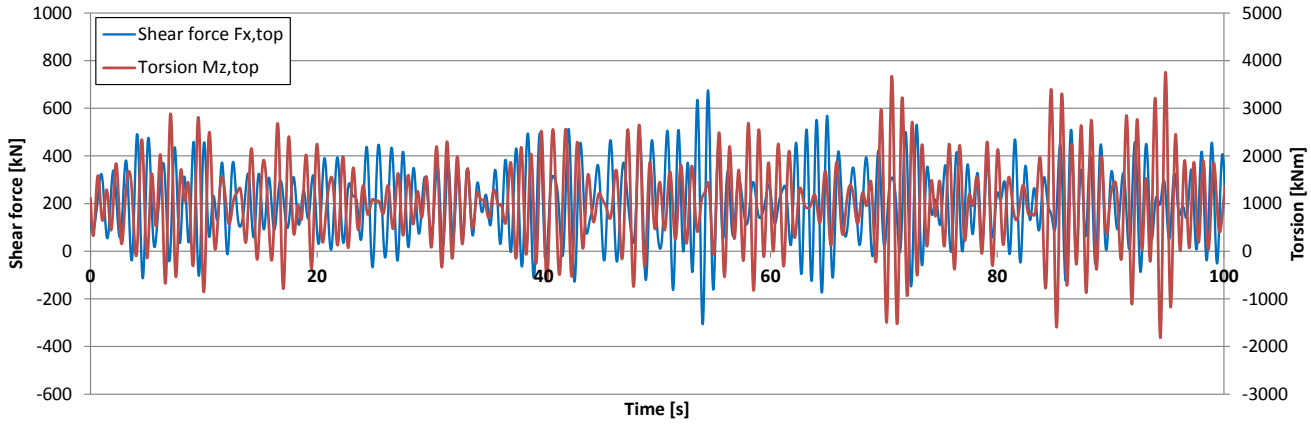

Figure 87: Sample for the established tower top shear force and torsion time series $F_{x,top}$ and $M_{z,top}$.

Figure 88 shows the power spectral densities of selected interface responses from the OWT model with different foundation representations and the corresponding absolute errors of the SE36 and SE06 foundation superelements when compared to the full foundation. The results for the dynamic analysis with the SE36 superelement agree well with the reference results of the full foundation model. However, the results for the SE06 superelement contain significant errors. The errors in shear force F_x and overturning moment M_y are located in the vicinity of the 2nd global (bending) modes. Note, that the energy content of the overturning moment M_y obtained from the OWT with the SE06 foundation superelement is:

- underestimated in the vicinity of the 2nd global (bending) mode of the OWT with the full foundation.
- overestimated in the vicinity of the 2nd global (bending) mode of the OWT with the SE06 foundation.

In the vicinity of the 1st global torsion eigenfrequency, the error in the torsion response M_z from the SE06 foundation superelement shows a similar behavior as the overturning moment M_y in the vicinity of the 2nd global (bending) modes.

Figure 89 shows the power spectral densities of selected local brace member loads at the marked joint in Figure 85. Furthermore, Figure 89 shows the corresponding total errors from the SE06 and SE36 foundation superelement in comparison to the results from the full foundation model. The member loads for the SE06 and SE36 superelements are obtained in a force-controlled, dynamic load expansion while the member loads for the full foundation model are obtained directly, i.e. without the load expansion. Only the responses for the OWT with the SE06 foundation superelement contain substantial errors near the same frequencies as the errors in the interface loads shown in Figure 88. However, the axial member load F_u and the out-of-plane member bending moment M_w at the foundation's 1st mode eigenfrequency are significantly more pronounced in comparison to the interface loads. This supports the assumption from section 6.1.3 i.e. that the error term $\Delta_{SE06}(t)$ in Eq. 39, which represents the errors in the power spectral densities of interface responses in Figure 88, leads to artificial dynamic excitation of the 1st mode of the isolated foundation in the force-controlled, dynamic load expansion.

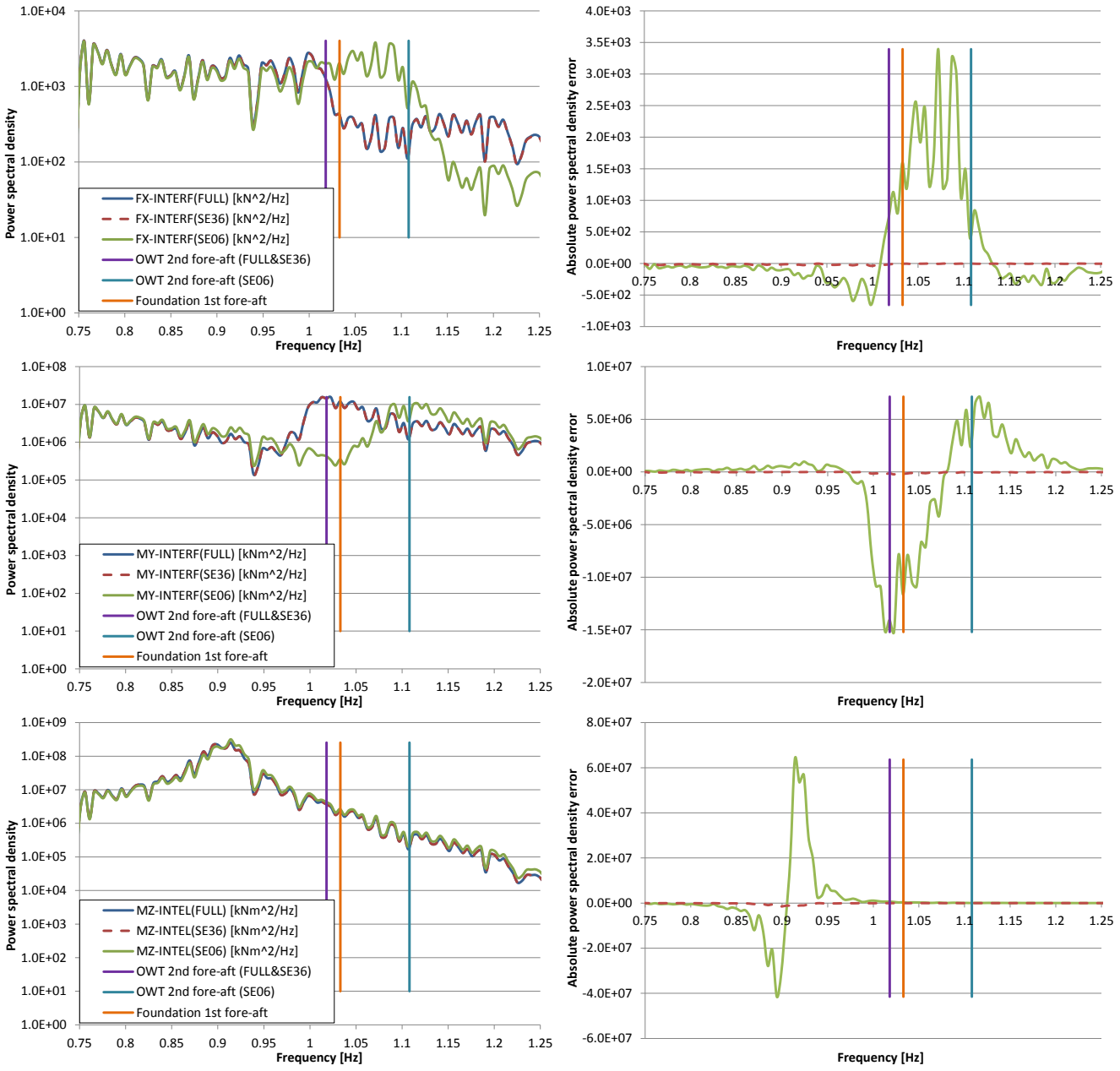

Figure 88: Distribution of power spectral densities (left) and absolute errors (right) over frequency for interface responses from SE36 and SE06. Horizontal shear load F_x (top), overturning moment M_y (centre) and torsion M_z (bottom).

Similar to the example in the previous section 6.1.5, the interface responses from SE06 are substantially overestimated and underestimated at various frequencies. However, in difference to the previous examples it can be seen that also the member responses from SE06 are substantially underestimated at certain frequencies. The largest underestimations from SE06 occur at the 1st global torsion eigenfrequency of the OWT with the full foundation model as well as with the SE36 foundation superelement. Such underestimations indicate the theoretical possibility for corresponding fatigue damage underestimations by the SE06 superelement as briefly introduced in the previous section 6.1.5.

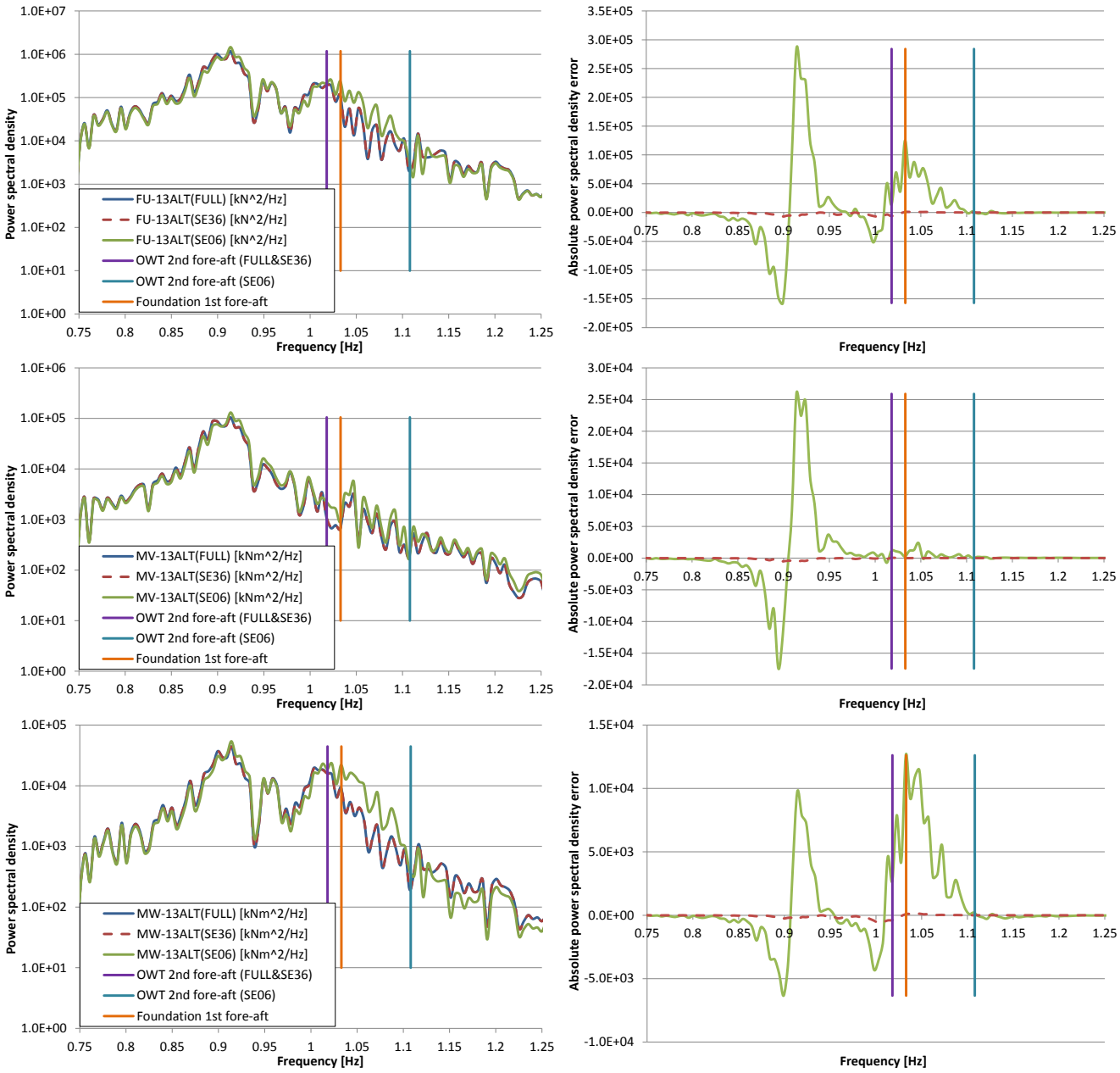

Figure 89: Distribution of power spectral densities (left) and absolute errors (right) over frequency for element 13ALT at tubular joint node 13A0B0. Axial load F_u (top), in-plane moment M_v (centre), out-of-plane moment M_w (bottom).

Based on the findings of this section, the following conclusion is drawn for SE06 superelements:

The performance of SE06 jacket foundation superelements, e.g. measured by the accuracy of calculated fatigue loads and lives, does not only depend on the foundation configuration, but also on the configuration of the superstructure, and therefore the integrated OWT configuration, as well as on the characteristics of loading.

6.1.7 Summary

The focus in section 6.1 is on the applicability and performance of different superelement formulations for jacket foundations in FLS load calculations. In particular, Guyan [26] type SE06 superelements of different foundation and OWT configurations are assessed against reference results, in terms of fatigue loads and damages, from corresponding Craig-Bampton [9] type SE36 superelements.

Section 6.1.1 demonstrates the general possibility of errors in calculated fatigue damages from application of SE06 foundation superelements for a selection of OWT configurations. Conservative results, in terms of tubular joint fatigue lives, are obtained in all cases by the SE06 superelements leading to the general conclusion that application of SE06 superelements is conservative for the FLS design. This behavior is confirmed by further investigations of individual load combinations in section 6.1.5 and 6.1.6. However, it is also shown that the energy contents of individual interface and foundation member load components from the SE06 superelement may be underestimated at individual frequencies. This can be taken as an indication for the theoretical possibility of non-conservative fatigue damage calculations with the SE06 superelement. However, based on the author's experiences with actual and theoretical structures, a scenario of non-conservative FLS designs due to application of the SE06 superelement is considered very unlikely in design practice.

Furthermore, section 6.1.1 shows that the SE06 performance differs greatly for individual foundation and OWT configurations as well as for the individual tubular joints. For example, the SE06 superelement leads to very extreme underestimations of tubular joints fatigue lives for the investigated soft foundation configurations S33N and S33H while a very reasonable approximation of the actual tubular joint fatigue lives is achieved for the preliminary Borkum Riffgrund 2 structure. Application of the SE06 foundation superelement may potentially result in uneconomic design solutions and a large uncertainty on the level of conservatism. Therefore, the author recommends in general the use of Craig-Bampton type superelements, similar to SE36, with a sufficient number of internal modes instead of Guyan based SE06 superelements for jacket foundations of OWT.

The influence from the number of internal modes for Craig-Bampton type foundation superelements, similar to SE36, is assessed in more detail for the soft foundation configuration S33N in section 6.1.2. It is shown that the modal mass convergence of the internal modes for the 2nd fore-aft bending mode leads also to a convergence of the calculated fatigue lives in the investigated tubular joints. On basis of these results and practical experiences, the author recommends that the number of internal superelement modes should at least be large enough to ensure modal mass convergence of the internal modes in the 1st torsion as well as the 2nd fore-aft bending mode of the OWT.

The aforementioned soft foundation configurations S33N and S33H show a close proximity between the eigenfrequency of the 2nd global (fore-aft) bending mode of the OWT with the SE06 superelement and the 1st mode of the isolated foundation as summarized in Table 11. It appears that this has an influence on the calculated error in the joint fatigue damages. More specifically, it is assumed in section 6.1.3 that errors in the interface responses as introduced from SE06 foundation superelements in the aero-elastic OWT analyses lead to artificial excitations of the 1st foundation mode in the force-controlled, dynamic load expansion. This assumption is supported by the investigations of individual load combinations in section 6.1.5 as well as by the

investigation of different OWT configurations and loading conditions in section 6.1.6. In section 6.1.5, it is shown that even small errors in the interface responses can lead to large errors in foundation loads and fatigue lives. A conclusion is therefore, that small errors in the DELs and time series of interface responses cannot be used as an indication for acceptable accuracy of calculated joint fatigue lives by the SE06 superelement.

Section 6.1.5 shows for an exemplary tubular joint of the soft foundation configuration S33N that a significant portion of the overall fatigue damage error due to application of the SE06 superelement is introduced from errors in the shear force components of the interface loads. Furthermore, these shear force errors are particularly pronounced in the vicinity of the 1st mode of the isolated foundation. As a result of the force-controlled, dynamic load expansion with these erroneous interface responses from SE06, very pronounced errors are present in the same frequency region for the member responses of an exemplary brace.

The soft foundation configuration S33N is further investigated in section 6.1.6. However, compared to section 6.1.1, a tuned superstructure configuration is used. This leads to a larger eigenfrequency distance between the 2nd fore-aft bending mode of the OWT with the SE06 foundation and the 1st mode of the foundation without superstructure, i.e. as used for the dynamic load expansion. The error in the interface and member loads as well as in the tubular joint fatigue lives due to application of the SE06 superelement is substantially reduced in comparison to the example from section 6.1.5.

Furthermore, another tuned OWT configuration is established in section 6.1.6. For this OWT configuration, the eigenfrequency of the 2nd fore-aft bending mode of the OWT the SE36 superelement is very close to the 1st foundation mode. The eigenfrequency of the 2nd fore-aft bending mode of the OWT with the SE06 foundation is located at a larger distance to the 1st foundation mode. Furthermore, the OWT with the full foundation model is used as a reference for the investigations in this example. The eigenfrequencies of the 2nd fore-aft bending modes from the OWT model with the full foundation and the OWT model with the SE36 foundation superelement are equal. The investigations are performed for generic tower top excitations covering the range of the 1st torsion modes and the 2nd fore-aft bending modes of all OWT models. Reference results are established in a dynamic analysis of the complete model including a direct calculation of foundation loads instead of the force-controlled, dynamic load expansion.

On one hand, it is shown that the SE36 superelement allows for a very accurate calculation of interface responses over the whole frequency range of excitations and also for very accurate calculations of foundation member loads in the load expansion.

On the other hand, it is shown that the SE06 superelement leads (again) to errors in the interface responses in the vicinity of the 1st torsion mode and the 2nd fore-aft bending mode. These errors are transferred into the member loads of the foundation by the force-controlled, dynamic load expansion. Furthermore, a pronounced error peak is present in the vicinity of the 1st foundation mode for some member load components. However, this error peak is not present in the underlying interface loads, which supports the assumption from section 6.1.3, i.e. that errors in the interface responses from OWT with the SE06 foundation superelement introduce artificial excitations of the 1st foundation mode in force-controlled, dynamic load expansions.

In design practice, FDs might encounter situations in which the application of SE06 foundation superelements for jacket type foundations of OWT cannot be avoided, e.g. due to modelling limitations of the applied aero-

elastic tool. In such cases, the FD could consider to increase the damping artificially in the force-controlled, dynamic load expansion. It is shown in section 6.1.4 and 6.1.5 that this can help to reduce the conservatism in the calculated FLS design loads. However, the definition of proper damping conditions is very difficult for such cases in design practice since no reference results are available. Furthermore, it should be considered, that too high damping values can lead to overestimations of fatigue lives and therefore to unsafe design solutions.

6.2 Superstructure modelling

A detailed model of the superstructure, i.e. tower and RNA, is mainly required for the aero-elastic analysis and component design of tower and RNA. These activities are traditionally performed by the WTM according to the constellation in a sequentially integrated load calculation approach as described in section 3.1. The use of the superstructure model by the FD is therefore limited to the following activities:

- Natural frequency design of the foundation.
- Model verification activities with the WTM.
- Ship collision analysis.
- Potentially for inverse dynamics load expansion method as introduced in paper 1 [61].
- Derivation of damage equivalent wind-wave correlations according to paper 3 [63]

For those design activities, the FD typically applies a simplified superstructure model with a mass equivalent representation of the RNA in terms of a discrete mass and a set of associated mass moments of inertia as indicated on the left side in Figure 59. These mass properties and location of the discrete RNA mass are provided together with a description of the tower including mass properties of the internals by the WTM. Although the description of such a simplified superstructure model seems to be rather simple and straightforward it is often the source of misunderstandings and errors if not addressed carefully by the involved parties and if the limitations of the simplified superstructure are not properly taken into account.

For example, limitations are introduced from disregarding the flexibility of the RNA components due to the reduction of the detailed RNA model to the aforementioned mass equivalent representation. Furthermore, errors and misunderstandings might be introduced from disregarding the flexibility of the connection between tower and RNA or application of different types of beam formulations for the tower model such as Euler-Bernoulli beams vs. Timoshenko beams.

The simplified superstructure representation is typically sufficient for the natural frequency design of the foundation since it allows for a good match on the relevant natural frequencies, i.e. the first global bending frequencies (fore-aft and side-side). This is due to the fact that first global bending frequencies are rather robust against the aforementioned sources of limitations and errors. However, a more accurate yet still simple representation might be beneficial for e.g. model verification activities, the ship collision analysis or identification of mode couplings in jacket type foundations.

This section introduces and investigates an alternative superstructure modelling approach for the design tasks of the FD. The idea is based on a model exchange similar to typical foundation descriptions for the WTM, i.e. based on system matrices in a finite element based model rather than on re-modelling of a simplified superstructure representation. This allows the FD to incorporate a superstructure model for the corresponding design tasks which is more similar to that used by the WTM. Of course, such a superstructure representation is still linear and can therefore not reflect variations introduced from different rotor speeds, pitch angles or operational conditions. However, it does still introduce a significant improvement compared to simple mass equivalent representation of the RNA.

The alternative superstructure modelling approach is demonstrated for FLEX5 and ROSAP, i.e. the FLEX5 system matrices of the superstructure as described by the DOFs according to Table 1 are incorporated into ROSAP. For that purpose an exemplary OWT configuration with a monopile foundation at 30m water depth and the NREL 5MW turbine [33] is established and subjected to modal analyses for different modelling approaches.

For the investigations, a full foundation model is established in ROSAP and subsequently reduced to the six DOF at the top of the foundation by static condensation according to Guyan [26], i.e. corresponding to SE06 as described in section 6.1. The reduced foundation is subsequently applied in FLEX5 and subjected to a modal analysis with a flexible RNA model. Table 21 summarizes the FLEX5 results in terms of natural frequencies and modal mass distribution over the individual DOFs for the first seven modes.

Table 21 Natural frequencies in ROSAP and FLEX5 for the first seven eigenmodes.

		Natural frequencies [Hz]						
ROSAP (Full Foundation)		0.288	0.289	0.647	0.669	0.689	0.913	1.003
ROSAP (Red. Foundation)		0.288	0.289	0.647	0.669	0.689	0.923	1.028
FLEX5 (Red. Foundation)		0.288	0.289	0.647	0.669	0.689	0.923	1.027
DOF Nr.	**DOF Type**	**Modal mass distribution [%] of eigenvectors in FLEX5**						
1	Foundation u_x	0	0	0	0	0	0	0
2	Foundation u_z	6	17	0	1	1	13	60
3	Foundation φ_y	8	24	0	0	0	-3	-15
4	Foundation u_y	17	6	0	0	0	40	20
5	Foundation φ_z	24	8	0	0	0	-10	-5
6	Foundation φ_x	0	0	1	0	0	0	0
7	Tower : Long1	11	33	0	1	0	6	23
8	Tower : Long2	0	0	0	1	0	1	0
9	Tower : Lat1	34	11	0	0	0	17	8
10	Tower : Lat2	0	0	0	0	0	4	0
11	Nacelle Yaw	0	0	8	0	0	0	0
16	Blade1: flap1	0	1	0	46	49	0	3
17	Blade1: flap2	0	0	0	0	0	0	0
18	Blade1: edge1	0	0	0	0	0	15	0
19	Blade1: edge2	0	0	0	0	0	0	0
20	Blade2: flap1	0	0	45	25	25	0	0
21	Blade2: flap2	0	0	0	0	0	0	0
22	Blade2: edge1	0	0	0	0	0	9	2
23	Blade2: edge2	0	0	0	0	0	0	0
24	Blade3: flap1	0	0	45	25	25	0	0
25	Blade3: flap2	0	0	0	0	0	0	0
26	Blade3: edge1	0	0	0	0	0	9	2
27	Blade3: edge2	0	0	0	0	0	0	0

In addition, the table summarizes also the corresponding natural frequencies obtained from ROSAP with the FLEX5 superstructure model for both, the full foundation model and the reduced foundation model as applied in FLEX5. A very good agreement is achieved between FLEX5 and ROSAP for all seven modes in case the same reduced foundation model is applied to both. It is therefore concluded that the FLEX5 superstructure model is incorporated adequately into ROSAP. However, mode 6 and 7 for ROSAP with the full foundation model shows

up to 2.5% lower natural frequencies compared to the models with the reduced foundation. These modes correspond to the 2nd fore-aft and side-side bending mode and the differences are introduced from the model reduction of the foundation. In this case, the most accurate results are obtained from the ROSAP model with the full foundation and the FLEX5 superstructure representation.

Now the modal analyses are repeated with a rigid RNA model in order to compare the alternative, detailed RNA representation with the mass equivalent RNA representation of the traditional superstructure modelling approach by the FD. Table 23 summarizes the results for the first four modes comprising the 1st and 2nd global bending mode in fore-aft and side-side direction. Again, a very good agreement is achieved between FLEX5 and ROSAP in case the same reduced foundation model is applied to both while differences occur for the 2nd global bending modes towards the ROSAP model with the full foundation.

Table 22 Natural frequencies in ROSAP and FLEX5 for the first two global bending eigenmodes in fore-aft and side-side direction.

		Natural frequencies [Hz]			
ROSAP (Full Foundation)		0.289	0.290	0.971	0.984
ROSAP (Red. Foundation)		0.289	0.290	0.993	1.007
FLEX5 (Red. Foundation)		0.289	0.290	0.993	1.007
DOF Nr.	**DOF Type**	**Modal mass distribution [%] of eigenvector in FLEX5**			
1	Foundation u_x	0	0	0	0
2	Foundation u_z	6	18	21	65
3	Foundation φ_y	8	24	-5	-17
4	Foundation u_y	17	6	64	22
5	Foundation φ_z	24	8	-16	-5
6	Foundation φ_x	0	0	0	0
7	Tower : Long1	11	33	8	25
8	Tower : Long2	0	0	1	1
9	Tower : Lat1	34	11	26	8
10	Tower : Lat2	0	0	2	0

In comparison to Table 21, it can be seen in Table 22 that the 1st global bending modes in fore-aft and side-side direction are almost unchanged and well represented by all modelling approaches, while larger differences can be observed for the corresponding 2nd global bending modes. The largest differences occur for the configurations corresponding to the traditional modelling approaches of a full foundation with a rigid RNA in the offshore tool and the reduced foundation with a flexible RNA in the aero-elastic tool according to Table 23.

Table 23 Natural frequencies in ROSAP and FLEX5 for the first two global bending eigenmodes in fore-aft and side-side direction.

	Natural frequencies [Hz]			
ROSAP (Full Foundation, rigid RNA)	0.289	0.290	0.971	0.984
FLEX5 (Red. Foundation, flexible RNA)	0.288	0.289	0.923	1.027
Difference [%]	0.3	0.3	5.2	-4.2

6.3 Soil-structure interaction models for monopile structures in aero-elastic analyses

Modelling approaches of the soil and soil-structure interactions for integrated OWT models have been discussed in many publications, e.g. by Zaaijer [80] or Passon [52] for monopiles. For example, the three soil-structure interaction models for monopiles according to Figure 90 as provided by Passon [55] have been investigated within the OC3 project [35]. The first model, on the left, is an equivalent cantilever beam which introduces a modified form of the well-known apparent fixity length model. For the second model, in the centre, a set of coupled translational and rotational single springs is established which constitutes effectively a stiffness matrix. The third model captures more accurately the sub-soil part of the monopile. Here, linear and uncoupled, lateral springs are distributed over the length of the pile. All three models are linear i.e. based on a linearization of the non-linear soil-pile interactions.

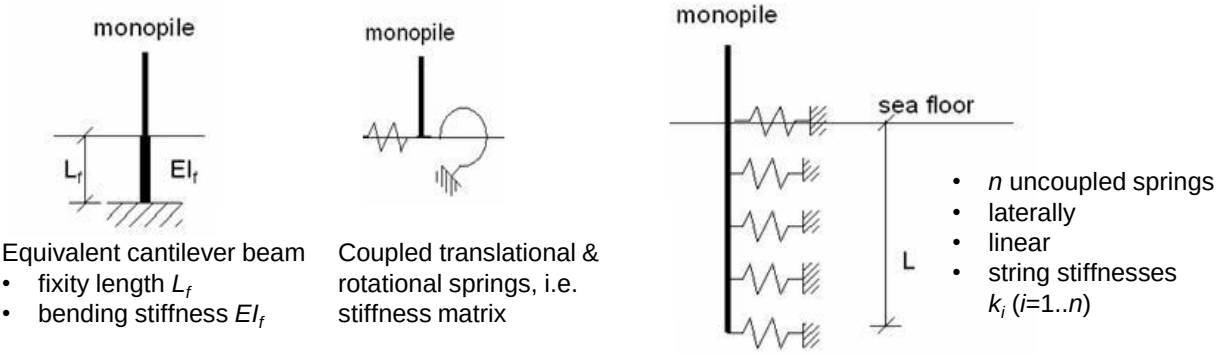

Figure 90: Typical soil-structure interaction models for monopiles in aero-elastic analyses.

This section focuses exemplarily only on the equivalent cantilever beam[16] for monopile type foundations as developed by the author in 2005 and first published in 2006 for the OC3 project. Although, the equivalent cantilever beam model does not allow for detailed calculations of loads below mudline it has been proven rather beneficial since it can be applied in almost all aero-elastic codes including the basic version of the FLEX5 code [50] and allows for a dynamically equivalent representation of the linearized soil-structure interactions in the global model. However, only the derivation of the equivalent cantilever beam model is summarized here since the model has already been subjected by various investigations and publications, e.g. Jonkman et al. [34] or Bush & Manuel [6].

The basic idea for this modelling approach is the replacement of the sub-soil part of the monopile by a fictive cantilever beam that is a statically equivalent representation of the actual (linearized) soil-structure interactions. The linearization of the soil-structure interactions and the derivation of the geometry and material properties of the cantilever beam are performed in two subsequent steps. For the linearization a representative set of shear force F and overturning moment M are applied at mudline of a detailed, non-linear soil-structure interaction model, which results in a deflection w and rotation φ at mudline. In order to obtain the same deformations w and φ for a cantilever Euler-Bernoulli beam with a discrete shear force F and moment M on the free end as shown in Figure 4 it is required to fulfil equations Eq. 41 and Eq. 42. However, the cantilever beam length l and bending stiffness EI are not yet known.

[16] Also denoted as modified apparent fixity length approach

$$\frac{l^3}{3\cdot EI}\cdot F+\frac{l^2}{2\cdot EI}\cdot M=w \qquad \text{Eq. 41}$$

$$\frac{l^2}{2\cdot EI}\cdot F+\frac{l}{EI}\cdot M=\varphi \qquad \text{Eq. 42}$$

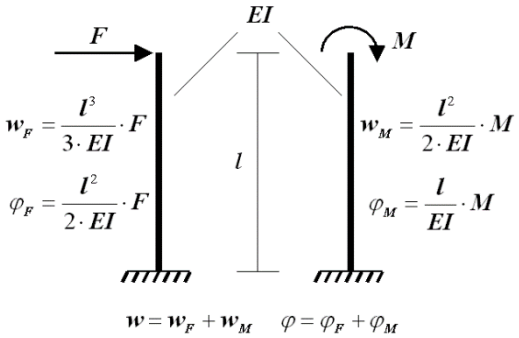

Figure 91: Cantilever Euler-Bernoulli beam analogy.

When dividing Eq. 41 by Eq. 42 and bringing the right side expression to the left side the following expression is obtained. The bending stiffness is removed from Eq. 43 leaving the length l as the only unknown.

$$\frac{l}{3}\cdot\frac{2\cdot l\cdot F+3\cdot M}{l\cdot F+2\cdot M}-\frac{w}{\varphi}=0 \qquad \text{Eq. 43}$$

Eq. 43 is a 2nd order polynomial of the fixity length l. Solution of the polynomial leads to the two expressions given in Eq. 44.

$$l_{1,2}=\begin{bmatrix}\frac{1}{4\cdot\varphi\cdot F}\cdot\left(-3\cdot\varphi\cdot M+3\cdot w\cdot F+\left[9\cdot\varphi^2\cdot M^2+30\cdot\varphi\cdot w\cdot F\cdot M+9\cdot w^2\cdot F^2\right]^{0.5}\right)\\ \frac{1}{4\cdot\varphi\cdot F}\cdot\left(-3\cdot\varphi\cdot M+3\cdot w\cdot F-\left[9\cdot\varphi^2\cdot M^2+30\cdot\varphi\cdot w\cdot F\cdot M+9\cdot w^2\cdot F^2\right]^{0.5}\right)\end{bmatrix} \qquad \text{Eq. 44}$$

In general, either l_1 or l_2 is positive while the other value is negative. However, at least one positive value should be found for l. The fictive bending stiffness can then be calculated by equations Eq. 45 or Eq. 46 which are derived from Eq. 41 and Eq. 42.

$$EI=\frac{F\cdot l^3}{3\cdot w}+\frac{M\cdot l^2}{2\cdot w} \qquad \text{Eq. 45}$$

$$EI=\frac{F\cdot l^2}{2\cdot\varphi}+\frac{M\cdot l}{\varphi} \qquad \text{Eq. 46}$$

The calculated length l and bending stiffness EI are used as the fixity length L_f and the bending stiffness EI_f of the equivalent cantilever beam. Finally, the mass distribution of the cantilever beam can be chosen such that approximately the same mass as for the real sub-soil pile is achieved. This rough mass approximation is typically acceptable for practical purposes since the actual mass properties of this part of the support structure have a minor influence on the relevant modal properties for the overall dynamic response.

The author recommends assessing the applicability of this equivalent cantilever beam carefully in case Timoshenko beam formulations are used by the applied tools.

7 Summary, Conclusions and Recommendations for Future Work

Various aspects on the design of offshore wind turbine foundations have been studied and discussed in the present thesis. These aspects are mainly related to the structural modelling, load calculations and consideration of met-ocean conditions in the design process of offshore wind turbine monopile and jacket foundations. Main emphasis has been on the proper representation of the selected aspects for load calculation purposes in order to avoid errors in the global and local dynamics and to enhance the accuracy of the design loads for offshore wind turbines. The aim is to further improve the understanding of these complex and dynamic structures in the scientific and industrial community as well as to provide improved modelling approaches for the individual design phases in order to enable for more cost efficient and safe designs of offshore wind turbines. This chapter provides a summary and conclusions of the explored topics together with recommendations for future work.

The studies in the present thesis are performed for monopile and jacket foundations in order to account for the different characteristics of individual foundation types. For example, jackets are hydrodynamically less sensitive but structurally more complex than monopiles. This leads to more demanding requirements on the jacket foundation representation for the integrated offshore wind turbine model, but less demanding requirements on the simultaneous aerodynamic and hydrodynamic loading in aero-elastic simulations.

The present thesis deals with a variety of facets and has strong focus on practical applications. This is chosen in order to acknowledge and emphasise the complex dynamic behaviour of offshore wind turbines as well as the industrial character of the PhD project and the manifold aspects in the design process of offshore wind turbines from the perspective of a foundation designer.

The main conclusions are:

- Innovative design approaches with a strong integration of the individual subsystems in the design process in combination with independent, integrated load calculations by the individual design parties are expected to have significant cost optimization potentials.
- Guyan [26] superelements that are based on a static condensation of the foundation to only the six interface DOFs, i.e. SE06 superelements, might introduce small errors in the aero-elastic analysis of OWT with jacket foundations. However, these errors might be amplified severely in the subsequent dynamic load expansion for the calculation of foundation loads.
- The errors of the SE06 superelement for jacket foundations can be avoided in case the superelement is complemented by a sufficient number of internal modes corresponding to a Craig-Bampton [9] superelement. A lower limit for a sufficient number of internal modes is introduced from the convergence of the total modal mass of internal modes in the 2nd fore-aft bending mode of the OWT.
- Dynamic load expansion approaches are required for OWTs with jacket foundations. Quasi-static load expansion approaches introduce errors due to an insufficient representation of the foundation inertia loads. These errors can vary to a large extent.

- The new inverse dynamics based load expansion approach from paper 1 [61] is more time consuming than the force- and deformation-controlled approaches, but offers more flexibility for application in different tools.
- The effective aerodynamic damping for the hydrodynamic response is reduced in case of misaligned wind and waves. With respect to the rotor orientation and wind direction, this reduction corresponds approximately to the absolute cosine-cubed value of the wind-wave misalignment angle φ, i.e. $|\cos^3(\varphi)|$, for the out-of-plane damping and to the absolute sine-cubed value of the wind-wave misalignment angle φ, i.e. $|\sin^3(\varphi)|$, for the in-plane damping.
- The establishment of wind-wave correlations for the calculation of design loads in FLS is typically based on a condensation of the long-term wave climate. It is important to preserve the hydrodynamic fatigue damages throughout the structure in the wave climate condensation. In case of hydrodynamically sensitive structures such as monopiles, this requires a proper consideration of the dynamics.

In the following, the investigations, discussions and recommendations of the individual topics from the present theses are briefly summarized.

Design approach

An essential influence on the costs and safety of offshore wind turbines is introduced by the approaches taken within the individual design phases. The design process can be split into a preliminary and detailed design phase, each characterized by application of models with different fidelities as well as the availability of data and its quality. Furthermore, a typical traditional design process involves different design parties, such as the foundation designer, geotechnical designer and wind turbine manufacturer. The different design parties are responsible for the design of individual subsystems. Depending on the design phase, task and strategy, these design parties are acting in an isolated or collaborative manner. Such traditional design approaches have been applied for the majority of today's offshore wind farm projects and have, in many cases, lead to efficient standardized collaborations between individual design parties. Nevertheless, the author recommends the implementation of innovative design approaches with the goal of cost optimization. This can be achieved by a stronger integration of the design of different subsystems. An example would be the design of the complete support structure as one unit thereby replacing the traditional split into tower design by the wind turbine manufacturer and foundation design by the foundation designer.

In the same context, the author recommends replacing, or just complementing, the time consuming sequentially integrated load calculation approach with independent integrated design load calculations by the individual design parties. This would allow for an increased number of design iteration & optimization loops in the design process while simultaneously reducing the design duration. Furthermore, the author expects that independent integrated design load calculations might also prove beneficial in the preliminary design process. Besides that, it could potentially reduce the significant limitations and uncertainties from required simplifying modelling and load assumption. Such improvements would account for the importance of preliminary design solutions because they serve as crucial input to the global project decision processes, e.g. on the foundation concept selection or the overall project feasibility assessment. However, current design practice is typically still

based on superimposed load calculations in the preliminary design phase and sequentially integrated load calculations in the detailed design phase. Here, potential advantages might be utilized by a substitution or supplementation in terms of independent integrated load calculations by the individual design parties.

Low-fidelity models in the design process

The sequentially integrated load calculation approach is typically characterized by application of different subsystem models for the individual tools of the involved design parties. For example, high-fidelity models of the foundation are applied by the foundation designer while low-fidelity models of the foundation are often applied in the integrated offshore wind turbine model by the wind turbine manufacturer. It is important to understand what kind of low-fidelity or simplified subsystem models can be applied with sufficient accuracy for the corresponding analyses of the individual design tasks. Such simplified modelling approaches have been exemplarily introduced in terms of monopile soil-structure interaction models for the aero-elastic analysis by the wind turbine manufacturer and in terms of a superstructure model for the natural frequency analysis by the foundation designer.

However, the main focus has been on investigations of substructuring methods according to Guyan [26] and Craig-Bampton [9] in relation to jacket type foundations in the aero-elastic load simulations. These studies comprise different structural configurations and assessments of modal properties, tubular joint fatigue life as well as energy distributions of interface responses and local foundation member responses as obtained by aero-elastic analyses and subsequent force-controlled, dynamic load expansions. An error is introduced in the interface responses from the aero-elastic analyses in case the foundation is represented by a Guyan [26] type superelement which is based on a condensation of the foundation to only the six interface degrees of freedom (SE06). Such errors can be avoided in case the SE06 superelement is complemented by a number of internal modes corresponding to a Craig-Bampton [9] type foundation superelement. In the present thesis the number of internal modes is typically set to 30 resulting in a SE36 superelement.

In sequentially integrated load calculations, the aero-elastic interface responses from the integrated offshore wind turbine model are subjected to load expansions in order to obtain design loads throughout the foundation. The interface response errors from the SE06 superelement can lead to artificial, dynamic foundation excitations in force-controlled, dynamic load expansions. Therefore, the error in the interface responses is not only transferred but also amplified in the foundation load calculation process. The artificial dynamic excitations and resulting error in the foundation design loads may become large if the energy of the error from the underlying interface responses is located in close vicinity to the 1st bending mode of the isolated foundation model used in the load expansion. This scenario has been observed in case the eigenfrequency of the 2nd fore-aft bending mode of the offshore wind turbine using the SE06 superelement is close to the 1st mode of the isolated foundation. In this case, very large errors have been introduced in the foundation loads and fatigue lives in case the 2nd fore-aft bending mode is subjected to severe dynamic excitations in the aero-elastic load simulations. In addition, it has been shown that the artificial, dynamic excitations are considerably reduced in case of the eigenfrequency for this 2nd fore-aft bending mode is located further away from the 1st foundation mode. However, conservative results for the fatigue design in terms of tubular joint fatigue lives have been obtained for all investigated configurations for the SE06 superelement, even though the level of

conservatism shows rather extreme ranges over the individual configurations. Hence, the application of Guyan type SE06 superelement is not recommended for offshore wind turbine jacket foundations. Instead, the SE06 superelement should for example be extended such as shown for the Craig-Bampton type superelements with a sufficient number of internal modes.

It is possible that application of the Guyan type SE06 superelement for jacket foundations cannot be avoided in the design process, e.g. due to limitations of the applied tools. In such cases the foundation designer needs to consider carefully how to avoid or minimize artificial dynamic foundation excitations from interface response errors in the load expansion step. In case of monopile type foundations, quasi-static approaches are most commonly chosen as it allows capturing the design loads accurately. A corresponding application of quasi-static load expansion approaches for jackets would of course completely eliminate the occurrence of such artificial dynamic excitation. However, quasi-static methods allow in general only for rough approximations of the design loads in case of jacket type foundations and are therefore not sufficient for the design of cost efficient and safe structures. The foundation designer might therefore consider increasing the damping artificially in the force-controlled, dynamic load expansion in order to damp the artificial dynamic excitations. Although it has been demonstrated that this can help reducing the errors in the calculated fatigue design loads, it should be kept in mind that it is very difficult to define proper artificially increased damping conditions in design practice. In particular too high damping values can lead to overestimations of fatigue lives and thereby to an unsafe design.

Foundation load expansion approaches

The force-controlled approach for dynamic load expansions has been applied for the majority of investigations in the present thesis. However, a new dynamic load expansion method based on inverse dynamics has been developed and assessed in paper 1 [61] for long-term and short-term fatigue scenarios using an offshore wind turbine with jacket foundation. The assessments include the validation of the new method by comparison with other dynamic load expansion methods, i.e. force-controlled and deformation-controlled. It has been demonstrated that identical long-term and short-term fatigue results can be obtained by all three dynamic load expansion methods. However, the new inverse dynamics based approach requires additional calculation steps and might therefore be considered the least efficient approach for normal design practice. On the other hand, the new approach grants a higher degree of flexibility since it can be applied in situations with given deformation responses using tools that allow only for application of force-controlled load expansions and vice versa. Despite the additional calculation step, this flexibility and applicability for different design tools and types of dynamic responses offers a considerable advantage for the inverse dynamics based approach over the force- and deformation-controlled approaches. In addition, the author expects that the inverse dynamics method could potentially also be used for design tasks of offshore wind turbine subsystems beyond the application of calculating foundation loads. Therefore, the author recommends assessing the potential of the inverse dynamics method in a broader context for offshore wind turbine design purposes, such as e.g. controller optimisation for load mitigation purposes.

Explicit aerodynamic damping approximations in the design process

The damping properties for offshore wind turbines are very important in the dynamic calculations of design loads. From the various damping sources, aerodynamic damping introduces the potentially largest contribution to the effective overall damping and is implicitly considered at each time step by aero-elastic simulation models in integrated or sequentially integrated load calculation approaches. In addition, explicit aerodynamic damping approximations might be required in some design situations for hydrodynamic sensitive structures such as monopile based OWTs, e.g. for the isolated hydrodynamic response calculation of superimposed load calculation approaches. However, explicit values of effective aerodynamic damping are often not available in design practice, particularly for the important wind-wave misalignment cases, leaving foundation designers with simplified rule-of-thumb approximations. Therefore, a new approximation method on the effective aerodynamic damping for hydrodynamic loading in case of misaligned wind-wave conditions has been introduced in the present thesis. Application of this method requires the availability of aerodynamic damping reference values at least for aligned wind-wave conditions and has been exemplarily demonstrated and assessed for a generic offshore wind turbine. Reasonable approximations of the effective aerodynamic damping have been achieved for the misaligned wind-wave cases. However, the author recommends further investigations on the new approximation method for individual, real offshore wind turbine configurations and site conditions.

The effective aerodynamic damping for the hydrodynamic loads is small to almost non-existent when the turbine is not operational and/or there is a high effective misalignment of wind and wave direction. Such low damping scenarios are particularly important for fatigue loading in hydrodynamic sensitive structures. A proper consideration of the remaining damping sources is therefore of crucial importance for cost efficient and safe designs in the preliminary and detailed design phase. For example, several aero-elastic load simulation tools allow for utilization of hydrodynamic drag damping by considering water particle velocities relative to the oscillating structure. However, it has been shown that this is generally not applicable for monopiles and only for a limited amount of cases applicable to jackets. It has also been demonstrated by superimposed load calculation examples that the aerodynamic damping is not very relevant for the hydrodynamic response of jackets. This indicates also that benefits from hydrodynamic drag damping would be limited as well. In case of hydrodynamic sensitive structures the author recommends further studies on the utilizable contributions from all damping sources in general. This could include specific studies on any applicable hydrodynamic drag damping since even small contributions might be beneficial in fatigue relevant low damping situations.

Damage equivalent wind-wave correlations for the fatigue design

An adequate representation of the site-specific wind-wave joint distribution is essential for the calculation of accurate fatigue design loads in order to obtain cost-efficient and safe designs of offshore wind turbines. However, consideration of all individual combinations of wind and wave parameters for each combination of wind direction and wave direction would generally result in an impractically large amount of design load simulations. In current design practice, the wave climate is therefore most commonly subjected to lumping approaches while the full wind climate, with respect to the mean wind speed distribution, is maintained. However, the effective turbulence per wind speed is typically obtained from damage equivalent lumping

approaches as well. This results in equivalent wind-wave correlations for design purposes. Such wind-wave correlations can potentially lead to a substantial reduction of wind-wave parameter combinations for design load calculation purposes, but also introduce challenges on the preservation of the hydrodynamic fatigue distribution in comparison to the underlying full wave climate. An adequate consideration of the dynamics is therefore required in the equivalent wind-wave correlations for design purposes, in particular for hydrodynamic sensitive structures. This has been addressed by the development of a new wind-wave correlation method in paper 3 [63] which is based on the preliminary work carried out in paper 2 [62]. The new method focuses on an adequate consideration of dynamics for the fatigue design of hydrodynamic sensitive offshore wind turbines and allows for preservation of hydrodynamic fatigue damages from the full wave climate throughout the structure. For a selection of alternative methods, it has also been shown that the same high accuracy in damage equivalency throughout the structure might not always be achieved. Instead, some of these methods allow for hydrodynamic fatigue damage preservation at individual locations within the offshore wind turbine structure, while only approximating the hydrodynamic fatigue damage in the remaining parts.

Furthermore, the influence from different damping assumptions on the new wind-wave correlation method from paper 3 [63] has been assessed. It has been shown that hydrodynamic fatigue damages are approximated well if the lumped waves are derived on basis of only the structural damping conditions without aerodynamic damping. The derivation of lumped waves under consideration of only structural damping conditions therefore seems to be an acceptable approximation in cases without corresponding information on the total effective damping.

However, the calculations for the assessment of the new method and the alternative methods have been based on a limited set of parameter combinations compared to the large variety of fatigue relevant conditions for offshore wind turbines during their lifetime. Therefore, the author recommends investigating the influence from such conditions. These investigations can be similar to the studies in paper 2 [62]. In the same context, the author recommends investigating the validity range of damage equivalent wind-wave correlations from the new method as a function of changes in the structural configuration. Such changes can e.g. occur during the optimization process of the support structures within the detailed design phase for offshore wind turbines. Finally, the author recommends performing large scale verifications of the new method based on aero-elastic simulations with simultaneous wind and wave loading.

References

[1] Arshad M, O'Kelly BC (2013). Offshore wind-turbine structures: a review. Proceedings of the ICE - Energy, Volume 166, Issue 4, 01 November 2013 , pages 139 –152. DOI: 10.1680/ener.12.00019

[2] Ashuri T, Zaaijer MB (2007). Review of design concept, methods and considerations of offshore wind turbines. European Offshore Wind Conference 2007, 10 pp., Germany.

[3] Barltrop N, Adams A (1991). Dynamics of fixed Offshore Structures, 3. Edition. Butterworth Heinemann 1991.

[4] Bouwkamp JG, Hollings JP Maison BF, Row DG (1981). Effects of joint flexibility on the response of offshore towers. In Proceedings - Annual Offshore Technology Conference — Volume 4, Pages 455

[5] Brøndsted P, Nijssen R (2013). Advances in wind turbine blade design and materials. Woodhead Publishing. (Woodhead Publishing Series in Energy; No. 47).

[6] Bush E, Manuel L (2009). The influence of foundation modelling assumption on long-term load prediction for offshore wind turbines. Proceedings of the ASME 28th International Conference on Ocean, Offshore and Arctic Engineering. OMAE2009. May 31 – June 5, 2009, Honolulu, Hawaii. Available from: http://www.ce.utexas.edu/prof/Manuel/Papers/BushManuel_OMAE2009-80050.pdf (Accessed at: 15th December 2014)

[7] Carstens H, Nielsen HB, Hansen HM (2004). Lowering costs by individual design of foundation structures. EWEC2004, London, UK. Available from: http://wind.nrel.gov/public/SeaCon/Proceedings/Copenhagen.Offshore.Wind.2005/documents/papers/Low_cost_foundations/H.Carstens.pdf (Accessed at: 15th December 2014)

[8] Cerda Salzmann DJ, Van der Tempel J (2005). Aerodynamic damping in the design of support structures for offshore wind turbines. Copenhagen Offshore Wind Energy Conference. Copenhagen, Denmark.

[9] Craig RR, Bampton MDD (1968). Coupling of Substructures for Dynamic Analysis. AIAA Journal, Vol. 6, No. 7, pp. 1313-1319.

[10] Chung J, Hulbert GM (1993). A Time Integration Algorithm for Structural Dynamics With Improved Numerical Dissipation: The Generalized-a Method J. Appl. Mech. 60(2), pp. 371-375 ; doi:10.1115/1.2900803

[11] Cook MF, Vandiver JK (1982). Measured and predicted dynamic response of a single pile platform to random wave excitation. Proceedings from Offshore Technology Conference, pages 637-645, Houston.

[12] Damgaard M, Andersen JKF, Ibsen LB, Andersen LV (2012). Natural Frequency and Damping Estimation of an Offshore Wind Turbine Structure. Proceedings of the Twenty-second International Offshore and Polar Engineering Conference. International Society of Offshore & Polar Engineers, 2012. p. 300-307 (International Offshore and Polar Engineering Conference. Proceedings; No. 22).

[13] Damgaard M, Andersen LV, Ibsen LB (2014). Assessment of dynamic substructuring of a wind turbine foundation applicable for aeroelastic simulations. John Wiley & Sons, Ltd. Wind Energy. DOI: 10.1002/we.1763.

[14] Damgaard M, Zaniab V, Andersen LV, Ibsen LB (2014). Effects of soil–structure interaction on real time dynamic response of offshore wind turbines on monopiles. Engineering Structures Volume 75, 15 September 2014, Pages 388–401

[15] Damgaard M (2014). Dynamic Properties of Offshore Wind Turbine Foundations. PhD Thesis. ISSN 1901-7294. DCE Thesis No. 65. Department of civil engineering, Aalborg University, Denmark.

[16] Devriendt C, Jordaens PJ, de Sitter G, Guillaume P (2013) Damping estimation of an Offshore Wind Turbine on a Monopile Foundation. IET Renewable Power Generation,7(4): pages 401–412.

[17] de Vries WE(2007). Assessment of bottom-mounted support structure types with conventional design stiffness and installation techniques for typical deep water sites. Deliverable D4.2.1 (WP4: Offshore Foundations and Support Structures).

[18] Devaney, LC (2012). Breaking Wave Loads and Stress Analysis of Jacket Structures Supporting Offshore Wind Turbines [Thesis]. Manchester, UK: The University of Manchester; 2012.

[19] Efthymiou M (1988). Development of SCF formulae and generalised influence functions for use in fatigue analysis Offshore Tubular Joints. Published in: Conference Proceedings of the Offshore Tubular Joints Conference (OTJ '88); 1988; London, UK.

[20] Esteban M, Lopes-Gutierrez J, Diez J and Negro V (2011) Foundations for offshore wind farms. Proceedings of the 12th International Conference on Environmental Science and Technology, pp. 516–523. Rhodes, Greece.

[21] Fichaux N, Beurskens J, Jensen PH, Wilkes P (2011). Design Limits and Solutions for Very Large Wind Turbines—A 20 MW Turbine Is Feasible. UpWind Report; European Wind Energy Association. Brussels, Belgium.

[22] Frandsen S (2005). Turbulence and turbulence-generated structural loading in wind turbine clusters, Risø national laboratory, Denmark, Report R1188.

[23] Gasch R, Twele J (2007). Windkraftanlagen: Grundlagen, Entwurf, Planung und Betrieb. 5te Auflage, Vieweg+Teubner Verlag. ISBN-13: 978-3835101364

[24] Gasch R, Twele J (2012). Wind Power Plants - Fundamentals, Design, Construction and Operation. 2nd edition. Springer Berlin Heidelberg. ISBN: 978-3-642-22937-4.

[25] Gujer P. (2005). Overall Damping for Piled Offshore Support Structures,Guideline for the Certification of Offshore Wind Turbines. Germanischer Lloyd, WindEnergie, Edition.
Available from: http://www.gl-group.com/pdf/1.d._Overall_Damping_for_Piled_Offshore_Support_Structures.pdf
(Accessed at: 31st December 2014)

[26] Guyan RJ (1965). Reduction of Stiffness and Mass Matrices. AIAA Journal, Vol. 3, No. 2, pp. 380-380.

[27] Haghi R, Ashuri T, van der Valk PLC, Molenaar DP (2012). Integrated multidisciplinary constrained optimization of offshore support structures. In: The science of making torque from wind, Oldenburg, Germany; 2012.

[28] Haid L, Stewart G, Jonkman J, Robertson A, Lackner M, Matha D (2013). Simulation-length requirements in the loads analysis of offshore floating wind turbines. In: Proceedings of the 32nd international conference on ocean, offshore and arctic engineering, Nantes, France; 2013. Available from (preprint): http://www.nrel.gov/docs/fy13osti/58153.pdf (Accessed 19th January 2015)

[29] Hald T, Høgedal M (2005). Implementation of a finite element foundation module in Flex5 using Craig-Bampton substructuring, European Offshore Wind 2005, Copenhagen

[30] Hansen M OL (2007). Aerodynamics of Wind Turbines. 2nd edition ISBN-13: 978-1844074389

[31] Hansen MH (2007). Aeroelastic instability problems for wind turbines Wind Energy. Vol. 10, No. 6, pp. 551–577. DOI: 10.1002/we.242

[32] Hapel, KH (1990). Festigkeitsanalyse dynamisch beanspruchter Offshore-Konstruktionen. Braunschweig: Vieweg. ISBN: 978-3-528-06368-9

[33] Jonkman J, Butterfield S, Musial W, Scott G (2007). "Definition of a 5MW reference wind turbine for offshore systems development," National Renewable Energy Laboratory, Golden, Colorado.

[34] Jonkman J, Butterfield S, Passon P, Larsen TJ, Camp T, Nichols J, Azcona J, Martinez A (2007). Offshore Code Comparison Collaboration within IEA Wind Annex XXIII: Phase II Results Regarding Monopile Foundation Modeling. Proceedings of the IEA European Offshore Wind Conference. Berlin, Germany.
Available from: http://www.nrel.gov/docs/fy08osti/42471.pdf (Accessed at: 15th December 2014)

[35] Jonkman J, Musial W (2010). Offshore Code Comparison Collaboration (OC3) for IEA Task 23 Offshore Wind Technology and Deployment. IEA Wind Task 23 Subtask 2 Final Report, March 31, 2010. Available from:
http://www.nrel.gov/docs/fy11osti/48191.pdf (Accessed at: 15th December 2014)

[36] Kaufer D, Cosack N, Böker C, Seidel M, Kühn M (2009). Integrated Analysis of the Dynamics of Offshore Wind Turbines with Arbitrary Support Structures. Proceedings of European Wind Energy Conference (EWEC 2009).

[37] King J, Cordle A, McCann G (2013). Cost Reductions in Offshore Wind Turbine Jacket Design using Integrated Analysis Methods and Advanced Control. Proceedings of the Twenty-third (2013) International Offshore and Polar Engineering, Vol.1, pp233-241

[38] Kjetså A, Saaghus LJ (2010). Local Dynamics of Offshore Wind Turbine Jacket Sub-structures [Master's Thesis]; June 2010; Trondheim, Norway: Norwegian University of Science and Technology.

[39] Kühn M, Harland LA, Bierbooms WAAM, Cockerill TT, Ferguson MC, Göransson B, van Bussel GJW, Vugts JH (1998). Final Report Opti-OWECS: Volume 1 - Integrated Design Methodology for Offshore Wind Energy Conversion Systems. ISBN 90-76468-02-8. Institute for Wind Energy, Delft University of Technology. Delft, The Netherlands.

[40] Kühn M (1999). Design optimisation of an offshore wind energy converter by means of tailored dynamics. European Wind Energy Conference and Exhibition (EWEC 99).Nice, France

[41] Kühn M (2001). Dynamics and Design Optimisation of Offshore Wind Energy Conversion Systems. Dissertation, Technische Universiteit Delft, ISBN 90-76468-07-9. Delft, The Netherlands.

[42] Kühn M, Cheng PW, Dahlberg J-A, Duffy J, Jacquemin J, Torbjörn T, Passon P, Pettersson J (2005). Utgrunden Offshore Wind Farm: Results of 5 years of Operation and Research. Copenhagen Offshore Wind Energy Conference. Copenhagen, Denmark.

[43] Laya EJ, Connor JJ, Sunder SS (1984). Hydrodynamic Forces on Flexible Offshore Structures. Journal of Engineering Mechanics (ASCE), Vol. 110, No. 3, pp. 433-448.

[44] Miner MA (1945). Cumulative damage in fatigue. J Appl Mech;12: A159–A64.

[45] Mittendorf KE (2006). Hydromechanical Design Parameters and Design Loads for Offshore Wind Energy Converters. Dissertation, Institut fuer Stroemungsmechanik, Universität Hannover, Bericht Nr. 71/2006.

[46] Mittendorf KE (2009). Joint Description Methods of Wind and Waves for the Design of Offshore Wind Turbines. Marine Technology Society Journal. 43(3):23-33. DOI:10.4031/MTSJ.43.3.2.

[47] Moe G, Verley RLP (1978). An Investigation into the Hydrodynamic Damping of Cylinders Oscillated in Steady Rurrents of Various Velocities. Report of River and Harbour Laboratory, Norwegian Institute of Technology.

[48] Moe G, Verley RLP (1980).Hydrodynamic Damping of Offshore Structures in Waves and Currents. Proceedings of the Offshore Technology Conference, Paper No. 3798.

[49] Muskulus M, Schafhirt S (2014). Design Optimization of Wind Turbine Support Structures—A Review. Journal of Ocean and Wind Energy. Vol. 1, No. 1, February 2014, pp. 12–22. ISSN 2310-3604.

[50] Øye S (1999). FLEX5 manual. Technical report, Technical University of Denmark (Department of Fluid Mechanics), Copenhagen, Denmark.

[51] Palmgren A (1924). Die Lebensdauer von Kugellagern. Zeitschrift des Vereins Deutscher Ingenieure;68:339–41.

[52] Passon P (2002). Modelling of soil-structure interactions for monopiles and non-linear wave theories. M.Sc Thesis, Hannover University. Hannover, Germany.

[53] Passon P, Kühn M (2005). State-of-the-art and Development Needs of Simulation Codes for Offshore Wind Turbines. Copenhagen Offshore Wind Energy Conference. Copenhagen, Denmark.

[54] Passon P, Kühn M (2005). Research Program of the Utgrunden Demonstration Offshore Wind Farm - Final Report: Part I - Load and Eigenfrequency Measurement. Wintus GmbH. Aichtal, Germany.

[55] Passon P (2006). Memorandum: Derivation and Description of the Soil-Pile-Interaction Models. IEA-Annex XXIIII Subtask 2. Stuttgart, Germany.

[56] Passon P, Kühn M (2006). Offshore-Windenergieanlagen mit verzweigten Tragstrukturen unter kombinierter Wind- und Wellenanregung. VDI-Tagung Baudynamik, ISSN: 0083-5560, Vol. 1941, Pages 401ff. Kassel, Germany.

[57] Passon P, Kühn M (2007). OC3-Benchmark aeroelastischer Simulationsprogramme für Offshore Windenergieanlagen. Gigawind 5. Symposium, April 18, Tagungsbeiträge (Proceedings), pages 80-85. Hannover, Germany.

[58] Passon P, Kühn M, Butterfield S, Jonkman J, Camp T, Larsen TJ (2007). OC3–Benchmark Exercise of Aero-elastic Offshore Wind Turbine Codes. TORQUE2010, Science of Making Torque from Wind Conference. Copenhagen, Denmark.

[59] Passon P (2008). Aero-Elastic Design Tool for Bottom-Mounted Offshore Wind Turbines. Deliverable D4.3.2 (WP4: Offshore Foundations and Support Structures). Stuttgart, Germany.

[60] Passon P (2010). Design of Offshore Wind Turbine Foundations in Deeper Water. TORQUE2010, Science of Making Torque from Wind. Crete, Greece.

[61] Passon P, Branner K (2014). Load calculation methods for offshore wind turbine foundations. Ships and Offshore Structures, Vol.9, No.4, pages 433-449. doi: 10.1080/17445302.2013.820108. Available from: http://www.tandfonline.com/doi/citedby/10.1080/17445302.2013.820108#.VN-Z-C5tzff (Accessed at: 23rd February 2015)

[62] Passon P, Branner K (2015). Condensation of long-term wave climates for the fatigue design of hydrodynamically sensitive offshore wind turbine support structures. Ships and Offshore Structures (in press). doi: 10.1080/17445302.2014.967994. Available from: http://www.tandfonline.com/doi/abs/10.1080/17445302.2014.967994#.VN-ZpS5tzfe (Accessed at: 23rd February 2015)

[63] Passon P (2015). Damage Equivalent Wind-Wave Correlations on Basis of Damage Contour Lines for the Fatigue Design of Offshore Wind Turbines. Renewable Energy, Volume 81, September 2015, Pages 723–736.

[64] ROSAP. 2014. Ramboll Offshore Structural Analysis Program Package, Version 4.80. (Confidential). Copenhagen, Denmark.

[65] Schiedek D (2014). Praxiserfahrung beim Bau des Offshore Windparks Borkum Riffgrund 1 und Pilotanlage mit Suction Bucket Jacket. Presentation from 2. Schallschutz-Tagung Berlin

[66] Seidel, M (2014). Wave induced fatigue loads on monopiles - New approaches for lumping of scatter tables and site specific interpolation of fatigue loads. Conference Proceedings IWEC, Hannover.

[67] Tarp-Johansen NJ, Andersen L, Christensen ED, Mørch C, Frandsen S (2009). Comparing Sources of Damping of Cross-Wind Motion. European Offshore Wind 2009: Conference & Exhibition. The European Wind Energy Association. Available from: http://proceedings.ewea.org/offshore2009/allfiles2/406_EOW2009presentation.pdf. (Accessed at: 15th November 2014)

[68] Turkstra CJ (1970). Theory of Structural Design Decisions. SM Studies Series No. 2, Solid Mechanics Division, University of Waterloo, Ontario, Canada.

[69] Valamanesh V, Myers A (2014). Aerodynamic Damping and Seismic Response of Horizontal Axis Wind Turbine Towers. J. Struct. Eng., 140(11), 04014090.

[70] van der Tempel J, Molenaar DP (2002). Wind turbine structural dynamics – A review of the principles for modern power generation, onshore and offshore, Wind Engineering 26, No. 4, pages 211–220.

[71] van der Tempel J. (2006) Design of Support Structures for Offshore Wind Turbines. Dissertation, Technische Universiteit Delft, Delft, The Netherlands.

[72] van der Valk PLC, Voormeeren S (2012). An overview of modelling approaches for complex offshore wind turbine support structures. Published in: Conference Proceedings of ISMA2012 International Conference on Noise and Vibration Engineering. Leuven, Belgium.

[73] van der Valk PLC, Voormeeren SN, de Valk PC, Rixen D (2014). Dynamic Models for Load Calculation Procedures of Offshore Wind Turbine Support Structures: Overview, Assessment and Outlook. ASME doi:10.1115/1.4028136. (In press)

[74] Vemula, NK (2010). Design Solution for the UpWind Reference Offshore Support Structure. Deliverable D4.2.5 (WP4: Offshore Foundations and Support Structures). Ramboll Wind Energy, Esbjerg

[75] Versteijlen WG, Metrikine AV, Hoving JS, Smid E, de Vries W. (2011) Estimation of the Vibration Decrement of an Offshore Wind Turbine Support Structure Caused by its Interaction with soil. Proc of the EWECA Offshroe 2011 Conference, Amsterdam.

[76] Voormeeren SN (2012). Dynamic Substructuring Methodologies for Integrated Dynamic Analysis of Wind Turbines. Dissertation. ISBN: 9789491104107. Technische Universiteit Delft, Delft, The Netherlands.

[77] Vorpahl F, Strobel M, Jonkman J, Larsen TJ, Passon P, Nichols J (2013). Verification of aero-elastic offshore wind turbine design codes under IEA Wind Task XXIII. Wind Energy, April 2014, Volume 17, Issue 4, pages 519–547.

[78] Wijker J (2008). Spacecraft Structures. ISBN: 978-3-540-75552-4. Springer.

[79] Willecke A, Fischer T (2013). Large monopiles for offshore wind farms in the German North Sea. Conference on Maritime Energy. May 2013. Hamburg, Germany.

[80] Zaaijer, MB (2002). Foundation models for the dynamic response of offshore wind turbines. Marine Renewable Energy Conference (MAREC), Newcastle, UK, September 2002. Available at: http://lr.home.tudelft.nl/fileadmin/Faculteit/LR/Organisatie/Afdelingen_en_Leerstoelen/Afdeling_AEWE/Wind_Energy/Research/Publications/Publications_2002/doc/Zaaijer_MAREC_Foundation.pdf (Accessed: 15th December 2014)

Design guidelines and standards

[81] API-LRFD (1993). Recommended Practice for Planning, Designing and Constructing Fixed Offshore Platforms – Load and Resistance Factor Design. American Petroleum Institute, Recommended practice 2A-LRFD, 1st edition.

[82] BSH-Standard (2007). BSH-No: 7005: Design of Offshore Wind Turbines.
Available at: http://www.bsh.de/en/Products/Books/Standard/7005eng.pdf (Accessed at 12th November 2014)

[83] DNV-OS-C101 (2011). Design of Offshore Steel Structures, General (LRFD Method). Offshore Standard. Det Norske Veritas AS.

[84] DNV-OS-J101 (2014). Design of Offshore Wind Turbine Structures. Offshore Standard. Det Norske Veritas AS.

[85] DNV-RP-C205 (2014). Environmental Conditions and Envirionmental Loads. Offshore Standard. Det Norske Veritas AS.

[86] GL-COWT (2012). Guideline for the Certification of Offshore Wind Turbines. Rules and Guidelines, IV – Industrial Services, Part 2. Germanischer Lloyd.

[87] IEC 61400-1 (2005). IEC 61400-1: Wind Turbines – Part 1: Design Requirements. 3rd Edition. International Electrotechnical Commission (IEC).

[88] IEC 61400-3 (2009). IEC 61400-3: Wind Turbines – Part 3: Design Requirements for Offshore Wind Turbines. 1st Edition. International Electrotechnical Commission (IEC).

[89] ISO 19902 (2007). Petroleum and natural gas industries — Fixed steel offshore structures. First Edition.

Online reference

[90] BVG Associates (2013). Offshore wind: Industry's journey to £100/MWh – Cost breakdown and technology transition from 2013 to 2020. Available at:
http://www.bvgassociates.co.uk/Portals/0/publications/BVG%20Offshore%20wind%20industry%27s%20journey%20to%20%C2%A3100%20per%20MWh%201305.pdf
(Accessed: 10th November 2014)

[91] Design Basis-Upwind deep water site, Rev0_v09, 13.10.2009
Available at: http://repository.tudelft.nl/assets/uuid:a176334d-6391-4821-8c5f-9c91b6b32a27/276271.pdf
(Accessed: 12th November 2014)

[92] Energinet (2013). Available at:
http://www.energinet.dk/EN/El/Nyheder/Sider/2013-var-et-rekordaar-for-dansk-vindkraft.aspx
(Accessed: 10th November 2014)

[93] Energinet (2014). Available at:
http://energinet.dk/EN/El/Nyheder/Sider/Vindmoeller-slog-rekord-i-2014.aspx
(Accessed: 25th February 2015)

[94] EWEA (2014). Wind Energy Scenarios for 2020. A report by the European Wind Energy Association - July 2014. Available at:
http://www.ewea.org/fileadmin/files/library/publications/reports/EWEA-Wind-energy-scenarios-2020.pdf
(Accessed: 10th November 2014)

[95] EWEA (2014). The European offshore wind industry - key trends and statistics 2013. January 2014
Available at: http://www.ewea.org/fileadmin/files/library/publications/statistics/European_offshore_statistics_2013.pdf
(Accessed: 1st December 2014)

[96] EWEA (2015). The European offshore wind industry - key trends and statistics 2014. January 2015
Available at: http://www.ewea.org/fileadmin/files/library/publications/statistics/EWEA-European-Offshore-Statistics-2014.pdf
(Accessed: 30th January 2015)

[97] Felippa CA (2004). Introduction to Finite Element Methods. Chapter10 Superelements and Global-Local Analysis. Department of Aerospace Engineering Sciences and Center for Aerospace Structures. University of Colorado. Available at:
http://www.colorado.edu/engineering/cas/courses.d/IFEM.d/IFEM.Ch10.d/IFEM.Ch10.pdf
(Accessed: 16th January 2015)

[98] Fischer T (2011). Project UpWind Executive Summary – WP4: Offshore Foundations and Support Structures. Available at: http://www.upwind.eu/Publications/~/media/UpWind/Documents/Publications/4%20-%20Offshore%20Foundations/WP4_Executive_Summary_Final.ashx (Accessed: 12th November 2014)

[99] IADC Lexicon. Available at: http://www.iadclexicon.org (Accessed: 12th November 2014)

[100] Klimakommissionen (2010). Green Energy. The road to a Danish energy system without fossil fuels, Klimakommissionen - Danish commission on climate change policy. http://www.ens.dk/sites/ens.dk/files/dokumenter/publikationer/downloads/green_energy.pdf (Accessed: 10th November 2014)

[101] Passon P, Kühn M (2005). IEA Expert Meeting: Offshore Modeling Needs Workshop. Available at: http://www.ieawind.org/task_23/Subtask_2S_docs/Meeting%2002_Risoe/Passon.pdf (Accessed: 10th November 2014)

[102] UpWind Project. Available at: www.upwind.eu (Accessed: 12th November 2014)

[103] Ramboll Wind. Available at: http://www.ramboll.com/services/energy/wind-energy/offshore-wind-consulting (Accessed: 16th November 2014)

Paper 1: Load Calculation Methods for Offshore Wind Turbine Foundations

Authors:	Patrik Passon, Kim Branner
Submitted to:	Journal '*Ships and Offshore Structures'*
Status:	Published.
Remarks:	This is an Author's Accepted Manuscript of an article published at 06th August 2013 in the Journal '*Ships and Offshore Structures'*, Vol.9, No.4, pages 433-449 (DOI: 10.1080/17445302.2013.820108), © 2013 Taylor & Francis.
	Available online from: http://www.tandfonline.com/doi/citedby/10.1080/17445302.2013.820108#.VN-Z-C5tzff
	Free access until 31st December 2015 from following link: http://explore.tandfonline.com/page/est/engineering-computer-science-technology-most-read-2014/civil-engineering-top-10-2014

Load calculation methods for offshore wind turbine foundations

Patrik Passon[1], Kim Branner[2]

[1]*RAMBOLL Wind, Esbjerg, Denmark*

[2] *Department of Wind Energy, Technical University of Denmark, Roskilde, Denmark*

Patrik Passon. Email: pkp@ramboll.com. Ramboll, Adgangsvejen 3, 6700 Esbjerg, Denmark,

Load calculation methods for offshore wind turbine foundations

Calculation of design loads for offshore wind turbine foundations are typically performed in a joint effort between wind turbine manufactures and foundation designers. Ideally, both parties would apply the same fully integrated design tool and model for that purpose. However, such solutions are rather limited as it would require exchanging confidential data and the need of sophisticated modelling capabilities for all subsystems of the offshore wind turbine. In practise this leads to an iterative and sequential load calculation process involving different design tools. In this process the wind turbine manufacturer provides the foundation designer with dynamic responses obtained from aero-elastic simulations at a pre-defined interface. These responses are subsequently expanded to the corresponding dynamic responses in all structural parts of the foundation. In this article a novel load calculation method, for the expansion to dynamic foundation responses based on an inverse dynamics algorithm, is introduced and described in detail. Furthermore, a summary of load calculations methods currently applied for the design of bottom-mounted offshore wind turbines foundations is provided and compared with the proposed method. While emphasis is given to jacket type foundations the methods are considered applicable for other bottom-mounted foundation types as well. All load calculation methods are applied and evaluated for an exemplarily fatigue design scenario from the perspective of a foundation designer in order to establish more confidence in these methods. The article concludes with an assessment and recommendation for all presented load calculation methods.

Keywords: offshore wind; foundation design; load calculation methods; inverse dynamics

Nomenclature

u_i	Deflection in direction i = x,y,z	φ_i	Rotation w.r.t axis/direction i = x,y,z
F_i	Force in direction i = x,y,z	M_i	Moment w.r.t axis/direction i = x,y,z
$f(t)$	magnitude of excitation at time t	$f(t_i)$	Discrete form of $f(t)$, i.e. vector description
$u(t)$	Magnitude of dynamic response to excitation f at time t	$u(t_i)$	Discrete form of $u(t)$ at time t_i
$h(t)$	Impulse response function (IRF) to a unit impulse at time t	$h(t_i)$	Discrete impulse response function (DIRF) of at time t_i
τ	Time interval between impulse and corresponding response	$\boldsymbol{H}(t_i)$	Matrix form of $h(t_i)$ for multiple, simultaneous excitation and response signals
t	Time	t_i	Time, i^{th} time step
OWT	Offshore wind turbine	RNA	Rotor-nacelle-assembly
WTM	Wind turbine manufacturer	FD	Foundation designer
SDOF	Single degree of freedom	MDOF	Multi degree of freedom
IRF	Impulse response function	DIRF	Discrete impulse response function

1. Introduction

The design of offshore wind turbine (OWT) subsystems such as the foundation, tower and controller requires expertise from different fields of technology. In practise, this is realised by involvement of specialised parties, typically a wind turbine manufacturer (WTM) and a foundation designer (FD), each with their own tools and models which are specifically developed for their respective design tasks. However, the individual subsystems of OWT show a high degree of interactions e.g. resulting from the pronounced dynamic behaviour of wind turbines. Design load calculations for all OWT subsystems are therefore performed in a joint effort between the WTM and FD resulting in an integrated, multidisciplinary design approach. The fully integrated OWT model is shown in Figure 1 including environmental and loading conditions as well as all potential interactions. The figure also shows an actual modelling approach as often applied in practise for the design of individual subsystems. ***[Figure 1 below here]***

Design loads for OWT subsystems are typically established in a sequential, multi-step design process due to the involvement of different parties and models. Such an approach introduces the necessity to exchange information regarding structural properties of all relevant subsystems as well as loads at one or more pre-defined interfaces, often the connection between the tower and foundation subsystem. In consequence, this often leads to a situation in which the FD applies a simplified representation of the tower and the rotor-nacelle-assembly (RNA) while the WTM applies a simplified representation of the foundation. Each of these models being sufficient for their corresponding design and load calculation tasks, but neither of them sufficient to perform the overall OWT design and load calculation individually. Therefore, the WTM performs aero-elastic simulations with an integrated offshore wind turbine model which is established with a foundation representation and hydrodynamic loads provided by the FD. From these aero-elastic simulations, the WTM then provides the FD with the dynamic responses at the interface location.

These responses are then subsequently expanded to corresponding dynamic responses in all parts of the foundation in the FD model.

This article addresses applicable load calculation methods for the expansion of interface responses in case of bottom-mounted, space-frame foundations such as jackets from the perspective of the FD. For that purpose a brief summary of the design load calculation process is provided in section 2 followed by an overview existing load calculation methods in section 3. A novel method which is based on inverse dynamics is introduced in section 4. In section 5 all load calculation methods are applied and evaluated for an exemplarily fatigue design situation from the FD's perspective using an OWT with a jacket type foundation at a generic offshore site. Finally, summary and conclusions are provided in section 6.

2. Design load calculation process for OWT

Design loads for OWT foundations are jointly established by the WTM, responsible for the RNA and tower design, and the FD responsible for the foundation design as outlined in the Introduction and indicated in Figure 1. In the context of the present article the foundation is defined as the structure below tower bottom. Furthermore, the connection between the tower and the foundation is in the following denoted as the interface while the RNA and tower are denoted as the superstructure. All relevant loads such as simultaneous aerodynamic and hydrodynamic loads need to be considered for the design of the individual components and subsystems of the OWT. These loads are typically established in three subsequent steps after an initial step of preparation for each design iteration loop as outlined in Figure 2:

1. The WTM receives hydrodynamic loads as well as a foundation model in a form applicable for the particular aero-elastic tool from the FD. Here, a preliminary foundation design is used in the initial design loop. This preliminary foundation design is typically established on basis of limited loading information.
2. The WTM performs detailed aero-elastic analyses with an integrated OWT model under consideration of all loads such as simultaneous aerodynamic and hydrodynamic loading. The calculated dynamic responses are used to design the superstructure. At the end of this step time series of load and/or deformation responses at interface are provided to the FD.
3. The FD applies the provided interface responses together with all other loads acting directly on the foundation in order to calculate the corresponding dynamic responses in all parts of the structure.

[Figure 2 near here]

A repetition of the design loop described above is required in case of significant foundation

design changes. The models and tools employed by the WTM and FD can differ significantly from each other as they need to address and focus on very different aspects and subsystems. For example, the WTM uses aero-elastic design tools dedicated to all relevant details of the superstructure, such as the controller behaviour and a detailed structural and aerodynamic description of the blades, while the foundation structure often is represented by a dynamically equivalent, but simplified model. The FD, on the other hand, applies often non-aero-elastic tools dedicated to a detailed description of all relevant foundation structure aspects, such as non-linear soil-structure interactions, while especially the RNA is modelled in a simplified manner.

3. Existing load calculation methods

Expansion of foundation loads from dynamic interface responses requires methodologies of high accuracy such that the resulting design loads in all parts of the foundation are captured adequately. In case of bottom-mounted, space frame structures such as jackets this requires a high precision method in order to capture the dynamics correctly in the design loads. For example, the braces of jacket foundations for OWT can be prone to local dynamics as shown by e.g. Böker (2010) and Kjetså & Saaghus (2010). This local dynamic behaviour of the braces influences the resulting stresses significantly, in particular in the neighbouring connection to the jacket legs.

This section provides a brief summary of typical load calculation methods for the load expansion step in the design of bottom-mounted, space-frame OWT foundations, namely the deformation controlled approach and the force controlled approach. It should be noted that both approaches are also applicable for monopile type foundations.

The same first step is required for the force and deformation controlled approach within the overall load calculation process between the FD and WTM. This first step is the generation of a dynamically equivalent foundation model and corresponding hydrodynamic loads by the FD. Foundation model and loads are subsequently applied within the integrated OWT model of the WTM in accordance to Figure 2 and Figure 3. The reader is referred to Van der Valk & Voormeeren (2012) for a more detailed description and evaluation of selected modelling approaches in this first step. ***[Figure 3 below paragraph]***

It should be noted that certain development activities towards fully integrated design tools, shared by the WTM and FD, with detailed subsystems models on all levels of the load calculation process exist, see Passon (2008). However, large scale application of such tools and models for the design of OWT is not expected in the short-term future.

3.1. Deformation controlled approach

The deformation controlled approach, subsequently denoted as ‘Def-Ctrl’, as described by Seidel et al. (2005) is indicated in Figure 4. Dynamic responses in terms of interface deformation time series for all six DOF, i.e. u_x to φ_z, are generated by aero-elastic simulations of the integrated OWT model corresponding to step 2 in Figure 2. These response time series are then applied as deformation boundary conditions at the interface together with the hydrodynamic loads acting directly on the foundation in a dynamic analysis of the foundation structure without the superstructure.

[Figure 4 below paragraph]

3.2. Force controlled approach

The force controlled approach, subsequently denoted as ‘For-Ctrl’, as described by Van der Valk & Voormeeren (2012) is indicated in Figure 5. Dynamic responses in terms of interface load time series for all six load components, i.e. F_x to M_z, are generated by aero-elastic simulations of the integrated OWT model corresponding to step 2 in Figure 2. These response time series are then applied as external loads at the interface together with the hydrodynamic loads acting directly on the foundation in a dynamic analysis of the foundation structure without the superstructure.

[Figure 5 below paragraph]

4. Foundation load calculation based on inverse dynamics

This section presents an alternative calculation method based on inverse dynamics for the expansion of foundation loads according to Figure 2. Starting from the convolution integral method the inverse dynamics approach is developed as a set of coupled, inverse discrete impulse response functions (DIRF). For further details the reader is referred to Bayo et al. (1988) and Bayo & Moulin (1989).

4.1. Convolution Integral Method

Responses of linear, time-invariant systems to general dynamic excitations can be derived on basis of the convolution integral method, also known as the Duhamel integral method. Theory and practical application of this method is well covered in many articles and textbooks e.g. Meirovitch (1980).

The basic idea is to establish an impulse response function (IRF) to capture the system characteristics by relating a unit impulse excitation to the dynamic system response. A general dynamic excitation can be regarded as a sequence of impulses. The individual responses to these impulses are described by IRF scaled by the actual magnitude of the impulse. The total response to the dynamic excitation at any given time t is then obtained by superposition of the individual scaled IRF at time τ prior to time t.

The general form of this approach is described by the integral in Eq. 1:

$$u(t) = \int_0^t f(\tau)h(t-\tau)d\tau \qquad \text{Eq. 1}$$

with

$u(t)$	magnitude of dynamic response to excitation f at time t
$f(t)$	magnitude of excitation at time t
$h(t)$	impulse response function (IRF) to a unit impulse at time t

A discretized form of the integral expression from Eq. 1 is typically applied for computer aided dynamic calculations of complex structural systems:

$$u(t_i) = \sum_{\tau=0}^{t_i} f(\tau)h(t_i - \tau) \qquad \text{Eq. 2}$$

4.2. Convolution Integral based algorithm for dynamic response calculations

This section introduces an algorithm for the discretized convolution integral in Eq. 2 in a slightly different form for single degree of freedom (SDOF) systems as shown in Figure 6.

The DIRF based approach to solve the dynamics of SDOF systems is based on the following three steps. ***[Figure 6 near here]***

1) *Generation and sampling of the IRF*

   The continuous IRF *h(t)* is calculated in a linear dynamic analysis for the considered SDOF system. Here, *h(t)* represents the load at the fixation point of the model shown in Figure 6. The underlying unit impulse is established by a ramped load that increases from zero to unity within one time step of the size *dt* and subsequently decreases down to zero within the next time step. Subsequently, the calculated IRF is discretized and sampled in an array $h(t_i)$ for all $t_i = 0..N$ time steps with $N = (T/dt)$ and *T* being the total length of the considered time series. The first element *h(0)* corresponds to the initial time step at *t=0s* which is neglected for further use of $h(t_i)$. The example unit impulse, IRF and DIRF are shown in Figure 7. ***[Figure 7 near here]***

2) *Discretization and sampling of the excitations*

The excitations are discretized and sampled similar to the DIRF. As indicated in Figure 8 the excitation function in terms of forces $f(t)$ is sampled in the array $f(t_i)$ using time step sizes of dt. Furthermore, an array with change in excitation force is established as $\Delta f(t_i) = f(t_i)-f(t_{i-1})$, with $\Delta f(0)=0$. For time T of the excitation function the arrays $f(t_i)$ and $\Delta f(t_i)$ consist of $i = 0..N$ elements with $N = (T/dt)$. For convenience, T and the time step dt are assumed to be equal for the discretization the excitation function $f(t)$ and IRF $h(t)$.

[Figure 8 near here]

3) *Calculation of responses $u(t_i)$ for the excitations $f(t_i)$*

The elements of the response time series $u(t_i)$ to the excitations $f(t_i)$ are calculated successively on basis of the established DIRF $h(t_i)$ and excitation differences $\Delta f(t_i)$ following the algorithm in Eq. 3.

$$
\begin{aligned}
u(0) &= f(0) \\
u(1) &= u(0) + \Delta f(1) \cdot h(1) \\
u(2) &= u(1) + \Delta f(1) \cdot h(2) + \Delta f(2) \cdot h(1) \\
&\vdots \\
u(t_i) &= u(t_i - 1) + \sum_{j=1}^{i} (\Delta f(t_j) \cdot h(t_{i+1} - t_j))
\end{aligned}
\qquad \text{Eq. 3}
$$

Generally, the response can be calculated for various properties, such as deflections or loads, dependent on the DIRF. Here, $u(t_i)$ can for example represent the load response at the fixation of the system shown in Figure 6. Initial conditions at $t=0s$ are based on a static equilibrium with $u_0 = u(0) = f(0)$, i.e. velocity and acceleration are zero.

4.3. Development of an inverse dynamics algorithm

So far, the discrete form of the convolution integral method has been introduced as a possibility to calculate responses to general dynamic excitations for linear, time-invariant SDOF systems. This section presents an algorithm for application of the method the other way around, i.e. to generate an excitation signal for a specific dynamic response of a given linear, time-invariant system. For this purpose the discrete form of the convolution integral as established in section 4.2 is reformulated into an algorithm that allows solving for excitations based on responses while keeping the DIRF. The established algorithm is subsequently extended to MDOF systems.

4.3.1. Inverse dynamics for SDOF systems

A DIRF based algorithm to solve dynamic problems for a given linear SDOF system and an arbitrary excitation time series has been provided in Eq. 3. These equations can be transformed such that it is possible to calculate the corresponding excitation time series $f(t_i)$ via the excitation differences $\Delta f(t_i)$ for a specific dynamic response time series $u(t_i)$ and a given SDOF system characterized by its DIRF $h(t_i)$. Again, the initial conditions at $t=0s$ are based on a static equilibrium with $f_0 = f(0) = u(0)$. Eq. 4 introduces the inverse dynamics algorithm to solve successively for the excitation differences $\Delta f(t_i)$ for all time steps $t_i = 1..N$, which are subsequently used to establish the corresponding excitation time series $f(t_i)$.

$$
\begin{aligned}
&f(0) = u(0) \\
&\Delta f(1) = \frac{[u(1) - u(0)]}{h(1)} && \rightarrow f(1) = f(0) + \Delta f(1) \\
&\Delta f(2) = \frac{[u(2) - u(1)] - \Delta f(1) \cdot h(2)}{h(1)} && \rightarrow f(2) = f(1) + \Delta f(2) \\
&\quad \vdots \\
&\Delta f(t_i) = \frac{[u(t_i) - u(t_i - 1)] - \sum_{j=1}^{i-1} (\Delta f(t_j) \cdot h(t_{i+1} - t_j))}{h(1)} && \rightarrow f(t_i) = f(t_{i-1}) + \Delta f(t_i)
\end{aligned}
\qquad \text{Eq. 4}
$$

4.3.2. Inverse dynamics for MDOF systems

The inverse dynamics approach in Eq. 4 is now extended to MDOF systems. However, in order to limit the complexity of the problem, just six degrees of freedom (DOFs) are considered. These six DOFs represent 3 perpendicular translations and 3 perpendicular rotations in a Cartesian x-, y-, z-coordinate system with the corresponding forces and moments F_x, F_y, F_z, M_x, M_y, M_z. Excitations are now represented by time series of six load components $\boldsymbol{f}(t_i) = [f_x(t_i)\ f_y(t_i)\ f_z(t_i)\ m_x(t_i)\ m_y(t_i)\ m_z(t_i)]^T$ and analogously the load responses are represented by $\boldsymbol{F}(t_i) = [F_x(t_i)\ F_y(t_i)\ F_z(t_i)\ M_x(t_i)\ M_y(t_i)\ M_z(t_i)]^T$. Each component in $\boldsymbol{f}$ and $\boldsymbol{F}$ is a time series of $t_i = 0..N$ elements with $N = T/dt$ according to the length of the time series T and the selected time step size dt.

The DIRF is now established by subsequent application of individual unit impulse loads $f_{x(unit)}$, $f_{y(unit)}$, $f_{z(unit)}$, $m_{x(unit)}$, $m_{y(unit)}$ and $m_{z(unit)}$ and calculation of the corresponding system responses in terms of all six load components per unit impulse load. The individual time series of load component responses to the individual unit impulse loads are stored in a compact *6x6* DIRF matrix per time step i and the corresponding time t_i as:

$$\boldsymbol{H}(t_i) = \begin{bmatrix} h_{f_{x(unit)},F_x} & \cdots & h_{f_{x(unit)},M_z} \\ \vdots & \ddots & \vdots \\ h_{m_{z(unit)},F_x} & \cdots & h_{m_{z(unit)},M_z} \end{bmatrix} = \begin{bmatrix} h_{1,1} & \cdots & h_{1,6} \\ \vdots & \ddots & \vdots \\ h_{6,1} & \cdots & h_{6,6} \end{bmatrix} = h_{k,n} \quad \text{for} \quad \begin{cases} k = 1..6 \\ n = 1..6 \end{cases}$$

For example, $h_{fy(unit),Mz}$ in $\boldsymbol{H}(t_i)$ represent load component M_z of the system response to the unit impulse load $f_{y(unit)}$. For convenience, an index notation is used for the entries in the DIRF matrix, expressing them as $h_{k,n}$ with:

$k = 1..6$ for the unit impulse loads $f_{x(unit)}$, $f_{y(unit)}$, $f_{z(unit)}$, $m_{x(unit)}$, $m_{y(unit)}$ and $m_{z(unit)}$

$n = 1..6$ for response components F_x, F_y, F_z, M_x, M_y and M_z to the unit impulse load

Substitution of the scalar terms in Eq. 4 by the vectors of responses $\boldsymbol{F}(t_i)$ and difference in excitation loads $\boldsymbol{\Delta f}(t_i) = [\Delta f_x(t_i)\ \Delta f_y(t_i)\ \Delta f_z(t_i)\ \Delta m_x(t_i)\ \Delta m_y(t_i)\ \Delta m_z(t_i)]^T$ as well as by the matrix of the DIRF $\boldsymbol{H}(t_i)$ leads to the inverse dynamics algorithm for MDOF systems summarized in Eq. 5. Again, this allows to solve successively for the differences $\boldsymbol{\Delta f}(t_i)$ in the excitation vector for all time steps $i = 1..N$ which in turn allows to subsequently calculate the corresponding excitation vector $\boldsymbol{f}(t_i)$ for time step i. The initial conditions at $t=0s$ are based on a static equilibrium with $\boldsymbol{f_0} = \boldsymbol{f}(0) = \boldsymbol{F}(0)$.

Note, that $\boldsymbol{H}(1)^{-1}$ represents the inverse of the matrix formed by the elements $h_{k,n}$ at time step $t_i=1$ corresponding to peak of the individual unit impulse loads and that this inverse matrix needs to be derived only once.

$$
\begin{aligned}
&\boldsymbol{f}(0) = \boldsymbol{F}(0) \\
&\Delta\boldsymbol{f}(1) = [\boldsymbol{F}(1) - \boldsymbol{F}(0)] \cdot \boldsymbol{H}(1)^{-1} && \rightarrow \boldsymbol{f}(1) = \boldsymbol{f}(0) + \Delta\boldsymbol{f}(1) \\
&\Delta\boldsymbol{f}(2) = \big([\boldsymbol{F}(2) - \boldsymbol{F}(1)] - \Delta\boldsymbol{f}(1) \cdot \boldsymbol{H}(2)\big) \cdot \boldsymbol{H}(1)^{-1} && \rightarrow \boldsymbol{f}(2) = \boldsymbol{f}(1) + \Delta\boldsymbol{f}(2) \\
&\vdots \\
&\Delta\boldsymbol{f}(t_i) = \left([\boldsymbol{F}(t_i) - \boldsymbol{F}(t_i - 1)] - \sum_{j=1}^{i-1}[\Delta\boldsymbol{f}(t_j) \cdot \boldsymbol{h}(t_i + 1 - t_j)]\right) \cdot \boldsymbol{H}(1)^{-1} && \rightarrow \boldsymbol{f}(t_i) = \boldsymbol{f}(t_i - 1) + \Delta\boldsymbol{f}(t_i)
\end{aligned}
\qquad \text{Eq. 5}
$$

The inverse dynamics algorithm in Eq. 5 can easily be implemented for computer aided applications allowing for efficient calculations of excitation time series for given responses and MDOF systems characterized by the DIRF $\boldsymbol{H}(t_i)$.

4.4 Inverse dynamics approach for load calculations of OWT foundations

The steps of the inverse dynamics approach, subsequently denoted as ‘Inv-Dyn’, for foundation load expansion are indicated in Figure 9. A dynamically equivalent foundation together with hydrodynamic loads is extracted from the detailed FD model in step 1 required for the aero-elastic

simulations by the WTM. This step fully corresponds to first step in the ‘Def-Ctrl’ and ‘For-Ctrl’ approach introduced in section 3. Furthermore, this step is used to generate isolated hydrodynamic interface responses in a dynamic analysis of the FD model as required in step 3. The equivalent foundation model and hydrodynamic loads are included in the aero-elastic OWT model by the WTM in step 2 resulting in an integrated OWT model and simultaneous aerodynamic and hydrodynamic excitations. This aero-elastic model is then subjected to a dynamic analysis from which response time series for all six load components, i.e. F_x to M_z, are extracted at interface. These response time series contain both the aerodynamic response as well as the dynamic part of the hydrodynamic response and are subjected to the inverse dynamics algorithm in step 3. For that purpose the inverse dynamics algorithm from Eq. 5 is applied using the DIRF for all six load components at interface of the FD model. However, the hydrodynamic interface responses as generated in step 1 have to be subtracted from the interface responses generated in step 2 prior to application of the inverse dynamics algorithm. This is required in order to avoid a double application of the dynamic part of the hydrodynamic response from the superstructure in step 4 as the generated, artificial interface excitations are applied simultaneously with the hydrodynamic excitations on the foundation structure in a dynamic analysis. The FD model in step 4 is the same as in step 1 and 3, consisting of a detailed foundation model and a simplified superstructure configuration. Generation of the artificial interface excitation time series from interface responses obtained in step 1 and 2 introduces an additional, intermediate step compared to the ‘Def-Ctrl’ and ‘For-Ctrl’ approach. ***[Figure 9 near here]***

It should be noted that the superstructure could be removed in the intermediate step of the inverse dynamics as well as in the subsequent dynamic load calculation. This would make the inverse dynamics approach for generation of the interface excitations unnecessary as the resulting interface excitations are identical to the interface responses from step 2 since the interface forms a

free end. In this special case the inverse dynamics approach is reduced to the ‘For-Ctrl’ approach. Analogously, the inverse dynamics approach would be reduced to the ‘Def-Ctrl’ approach in case of deformation based DIRFs when omitting the superstructure.

5. Load calculation method comparison

This section presents an assessment of all three introduced load calculation methods. For that purpose, a representative fatigue scenario from the perspective of a FD is introduced in section 5.1 by generic met-ocean conditions and a generic OWT model. Ideally, the load calculation methods should be evaluated against results obtained by a fully integrated design tool modeling the OWT in accordance with Figure 1. However, since such a tool is not available the results from the individual load calculation methods are compared with each other establishing a sufficient level of confidence in case of good agreement.

Dynamic interface response time series are generated by aero-elastic simulations with RamFlex[1] for a selection of representative fatigue load cases with simultaneous aerodynamic and hydrodynamic loading conditions. The OWT model in RamFlex consists of a detailed superstructure model and a dynamically equivalent representation of the foundation. The interface response time series together with the direct hydrodynamic loads on the foundation structure are subsequently applied for calculation of all responses in the foundation structure on basis of the different load calculation methods as introduced in the previous sections, i.e. the 'Def-Ctrl', 'For-Ctrl' and 'Inv-Dyn' approach. For that purpose, a detailed model of the foundation and hydrodynamic excitations are established in the simulation platform ROSAP[2] (2012). In case of the 'Inv-Dyn' approach, the detailed foundation model is complemented by a simplified representation of the superstructure consisting of a detailed tower model and a mass equivalent representation of the RNA.

---

[1] RAMBOLLs version of the FLEX5 code from Øye (1999a, 1999b)

[2] RAMBOLL Offshore Structure Analysis Package, a finite element based in-house software package of RAMBOLL for offshore structures

Selected long-term and short-term fatigue results in the foundation structure are compared in section 5.2 for the individual load calculation methods. These results are then discussed together with additional aspects for the evaluation of all load calculation methods in section 5.3.

5.1. Offshore wind turbine model and generic site conditions

The well-known generic NREL 5MW wind turbine (Jonkman et al., 2007) in combination with a piled jacket foundation and tubular steel tower are used for the present investigations. The piled jacket foundation consists of four legs and four bays of x-bracings as indicated in Figure 10. Table 1 summarizes the main structural parameters. ***[Figure 10 & Table 1 below here]***

The generic site is established with medium stiff soil and a water depth of 31m. Met-ocean conditions for the long term fatigue scenario consist of aligned wind and wave conditions for 12 directions in accordance to the wind-wave rose in Figure 11. Wind conditions on hub height level are described by an omni-directional Weibull distribution with a scale parameter of A = 11.19m/s and a form factor of k = 2.35. Turbulences are generated in accordance to the UpWind site conditions as described by Fischer et al. (2010). ***[Figure 11 below here]***

Table 2 summarizes the combined omni-directional wind, wave and current parameters for all simulated load cases. The long-term fatigue setup includes only normal power production conditions (wind speed bins 5 – 23m/s in Table 2) and idling conditions outside the power production range of the turbine (wind speed bin 3.5m/s and 30m/s in Table 2). For simplicity each load combination has been simulated with only one random seed for generation of turbulences and irregular waves resulting in a total of 144 load combinations (short-term fatigue cases). Probabilities for the individual short-term fatigue cases have been assigned in accordance to the aforementioned omni-directional Weibull distribution and aligned wind-wave rose. ***[Table 2 below here]***

5.2. Comparison of fatigue results from all load calculation methods

In this section fatigue results obtained by the ‘For-Ctrl’, ‘Def-Ctrl’ and ‘Inv-Dyn’ load calculation method are compared. Long-term fatigue results are compared on basis of damages in selected tubular joints and short-term fatigue results are compared on basis of load and deformation time series at selected locations within the jacket structure.

5.2.1. Long-term fatigue results

The long-term fatigue assessment of the individual load calculation methods is performed by comparison of minimum fatigue lives at different locations on the chord and brace side of all tubular joints exemplarily for one side of the jacket. All 144 directional fatigue load cases weighted with their respective probabilities of occurrence are taken into account for the calculation of fatigue lives. Stress concentration factors for the tubular joints are determined according to Efthymiou (1988). S-N curves for calculation of fatigue damages in all tubular joints are taken from DNV-OS-J101 (2011). The naming of tubular joints and location of the extracted minimum fatigue lives is chosen in accordance to the following convention: *Node – Chord element 1 – Chord element 2 – Brace*.

Node and element names for one flat side of the jacket are shown together with an example for the denotation of joint ‘*20A0Q0-AQ13L-AQ20L-20AAT*’ in Figure 12. Here, the minimum fatigue lives are extracted at the connection of brace element *20AAT* to the chord elements *AQ13L* and *AQ20L* in node *20A0Q0*. It should be noted, that each element in Figure 12 is furthermore composed from 4 sub-elements. However, this additional discretization is not shown for a more convenient visualization. ***[Figure 12 below here]***

Figure 13 shows fatigue lives for the chord and brace side of all tubular joints for one side of the jacket as calculated by the individual load calculation methods. For convenience the individual joint fatigue lives have been normalized to unity with respect to the ‘For-Ctrl results. The

agreement is considered very well as differences are less than 0.5% for all tubular joint. ***[Figure 13 below here]***

5.2.2. Short-term fatigue results

One exemplarily load combination from the long-term fatigue load setup has been selected as a representative short-term fatigue load case for further assessment. The selected load case represents normal power production at 13m/s wind speed with wind and waves coming from East-South-East. A total of 60 distributed load and deformation response sensors throughout the jacket structure have been assessed in terms of time series, power spectral densities and statistics for the individual load calculation methods. The sensor locations (each comprising of 6 deformations and 6 load components) together with the wind-wave direction in relation to the foundation orientation are indicated in Figure 14. ***[Figure 14 below here]***

The observed agreement between the individual load calculation methods is very good for all 60 sensors. However, the results presented here are limited to the following two sensors:

1. Axial load for the submerged brace element *20AAT* at node *20A0Q0*
2. Out-of-plane deflection in submerged node *25A0Q0*

Figure 15 and Figure 16 show the time series, power spectral densities and statistics for the two sensors as obtained by the individual load calculation methods. It should be noted that the presented power spectral densities and statistics reflect the whole 600s duration of the corresponding time series while only 40s are extracted for the shown time series in order to allow for a more convenient illustration. Furthermore, the relevant natural frequencies and exciting rotational frequencies are shown in the power spectral density plots. A distinct peak around 0.9Hz can be observed in both power spectral density distributions. This peak is assumed to result from interactions between the 1st blade edge mode and the rotational frequency 1P resulting in

backward rotor whirl. The reader is referred to Petersen et al. (1998) for a more detailed description of this phenomenon. ***[Figure 15 and Figure 16 below here]***

5.3. Evaluation of the load calculation methods

This section evaluates the three load calculation methods under consideration of different aspects, which are practical constraints, accuracy and efficiency.

5.3.1. Practical constraints and flexibility

No particular practical constraints were present for the fatigue design example in this article. However, this may not be the case in commercial applications for OWT foundation designs, as typically only a narrow selection of appropriate, dedicated design tools exist. The 'Def-Ctrl' approach for example requires application of time varying deformation boundary conditions as excitations. While this is typically a supported feature in general purpose tools such as *ANSYS*® it might not be a supported approach in all specialized design tools dedicated to the design of OWT foundations. However, both the 'For-Ctrl' and 'Inv-Dyn' approach can be applied in all design tools known to the authors. Furthermore, limited information in terms of interface responses might be available in particular situations i.e. either loads or deformations; while the 'For-Ctrl' approach depends on available responses in terms of loads the 'Def-Ctrl' approach is limited to scenarios with available deformation responses. Here, the 'Inv-Dyn' approach is considered superior in terms of flexibility as it can be applied for both types of responses. Furthermore, the 'Inv-Dyn' approach does allow for a transformation between load and deformation responses, which e.g. is useful in a situation with available deformation responses but a limitation on the application of load excitations in the chosen design tool. For that purpose the DIRF $\boldsymbol{H}(t_i)$ in section 4.3.2 has simply to be established for a load impulse and deformation response in order to generate load excitation time series from given deformation response time series.

5.3.2. Accuracy

Confidence in the accuracy of all three load calculation methods could be established on basis the exemplary design scenario as almost identical results have been achieved. It is therefore concluded that all three load calculation methods are equally applicable with respect to accuracy. However, additional validation studies for all load calculation methods against results obtained from a fully integrated model with detailed subsystem models are recommended in order to conclude on the overall accuracy.

5.3.3. Efficiency

Both, the ‘For-Ctrl’ and ‘Def-Ctrl’ approach are more favourable than the ‘Inv-Dyn’ approach in terms of efficiency. This is due to the additional steps required for the ‘Inv-Dyn’ approach, i.e. generation of the hydrodynamic interface responses and generation of the equivalent interface excitations. No particular advantages or disadvantages on the efficiency are present for the ‘For-Ctrl’ and ‘Def-Ctrl’ approach when compared to each other.

5.3.4. Recommendations for selection of the optimal load calculation method

The individual load calculation methods introduce advantages and disadvantages on different aspects. As these aspects might have higher or lower relevance dependent on the particular situation and requirements it is not possible to provide a general recommendation towards application of one method in preference to another method. Instead it is recommended to assess the advantages and disadvantages of the individual methods in context of the particular task in order to select the optimal method.

6. Conclusions

A summary and assessment of load calculation methods for the design of bottom-mounted, space frame type offshore wind turbine foundations has been presented in this article. In this context a novel approach based on inverse dynamics has been developed and compared to two alternative approaches i.e. force controlled and deformation controlled. This is done for an exemplarily fatigue design scenario from the perspective of a foundation designer. Ideally, results obtained by the three load calculation methods should be verified on basis of a fully integrated model. However, such a model has not been available for the investigations presented in this article. Confidence in the three methods is instead generated by the fact that identical long-term and short-term fatigue results are obtained by all methods. Despite the identical results for all methods the novel, inverse dynamics based approach requires additional calculation steps and might be considered the least efficient approach. On the other hand the novel approach grants a higher degree of flexibility compared to both other approaches as it can even be applied in situations with given deformation responses in a tool that allows only for application of loads in dynamic analyses as well as the other way around. This flexibility and resulting applicability for all design tools and types of dynamic response data is a considerable advantage of the inverse dynamics based approach over the force and deformation controlled approach despite the additional calculation step. Nevertheless, a conclusive recommendation on one particular method should not be provided. Instead, it is recommended to assess their applicability and individual benefits in the context of the particular application purpose and under consideration of the aspects highlighted in section 5.3.

In addition, it is expected that inverse dynamics for the design of offshore wind turbine subsystems has potentials even beyond the application of calculating foundation loads. It is therefore highly recommended to assess the potentials of the inverse dynamics method in a

broader context for offshore wind turbine design purposes, such as e.g. controller optimisation for load mitigation purposes.

References

Bayo E, Movaghar R, Medus M. 1988. Inverse Dynamics of a Single-Link Flexible Robot. Analytical and Experimental Results, International Journal of Robotics and Automation. 3:150–157.

Bayo E, Moulin H. 1989. An Efficient Computation of the Inverse Dynamics of Flexible Manipulators in the Time Domain. Published in: Conference Proceedings of the IEEE Conference on Robotics and Automation; May 1989; Scottsdale, Arizona.

Böker C. 2010. Load simulation and local dynamics of support structures for offshore wind turbines [dissertation]; February 2010; Hannover, Germany : University of Hannover.

DNV-OS-J101. 2011. Design of Offshore Wind Turbine Structures; September 2011; Offshore Standard Det Norske Veritas AS.

Efthymiou M. 1988. Development of SCF formulae and generalised influence functions for use in fatigue analysis Offshore Tubular Joints. Published in: Conference Proceedings of the Offshore Tubular Joints Conference (OTJ '88); 1988; London, UK.

Fischer T., de Vries W., Schmidt B. 2010. Upwind Design basis; September 2010; Stuttgart, Germany.

Jonkman J, Butterfield S, Musial W, Scott G. 2007. Definition of a 5MW reference wind turbine for offshore systems development; February 2007; Golden, Colorado: National Renewable Energy Laboratory.

Kjetså A., Saaghus L.J. 2010. Local Dynamics of Offshore Wind Turbine Jacket Sub-structures [Master's Thesis]; June 2010; Trondheim, Norway: Norwegian University of Science and Technology.

Meirovitch L. 1980. Computational Methods in Structural Dynamics. The Netherlands: Sijthoff-Nordhoff.

Øye S. 1999a. FLEX5, Short description for FLEX4 users; 1999; Copenhagen, Denmark: Technical University of Denmark.

Øye S. 1999b. FLEX5 manual; 1999; Copenhagen, Denmark: Technical University of Denmark.

Passon P. 2008. Design tool for multi-member bottom-mounted support structures, UpWind deliverable D4.3.2; 2008; Stuttgart, Germany.

Petersen JT, Thomsen K, Madsen HA. 1988. Local Blade Whirl and Global Rotor Whirl Interaction. August 1998. Roskilde, Denmark: Risø National Laboratory.

ROSAP. 2012. Ramboll Offshore Structural Analysis Program Package, Version 4.46. Copenhagen, Denmark.

Seidel M, von Mutius M, Rix P, Steudel D. 2005. Integrated analysis of wind and wave loading for complex support structures of Offshore Wind Turbines. Published in: Conference Proceedings of Copenhagen Offshore Wind 2005; October 2005; Copenhagen, Denmark.

Van der Valk PLC, Voormeeren S. 2012. An overview of modelling approaches for complex offshore wind turbine support structures. Published in: Conference Proceedings of ISMA2012 International Conference on Noise and Vibration Engineering; September 2012; Leuven, Belgium.

FIGURES

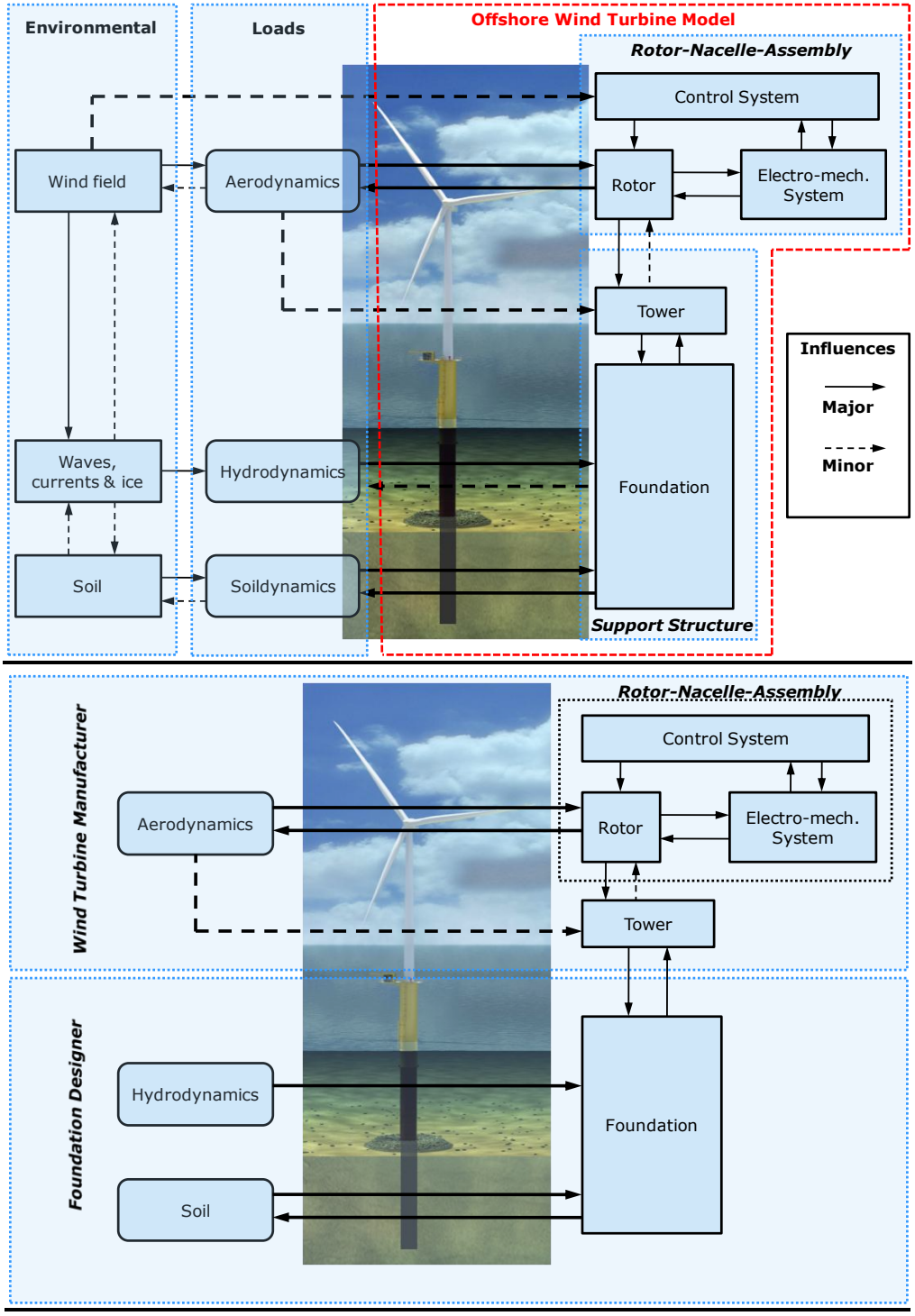

Figure 1: Fully integrated model for OWT (upper) and practical modelling approach for subsystem designs (lower)

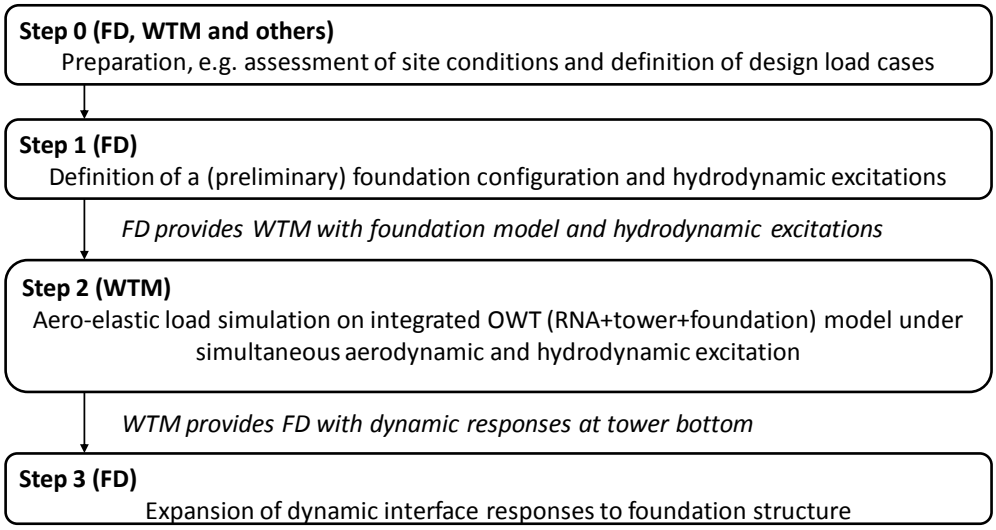

Figure 2: Stepwise approach for calculation of OWT foundation loads

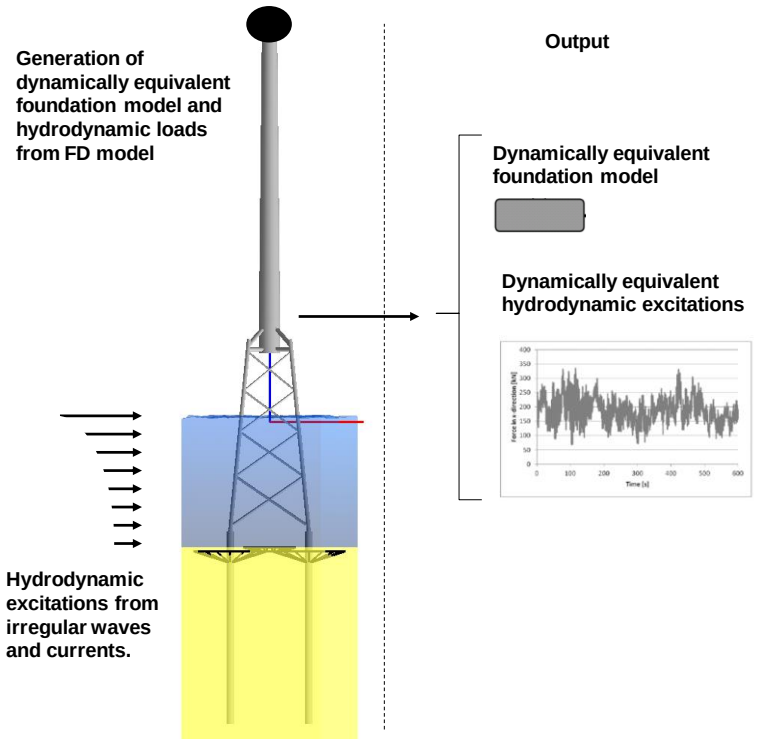

Figure 3: Equivalent foundation and hydrodynamic excitation generation from the FD model

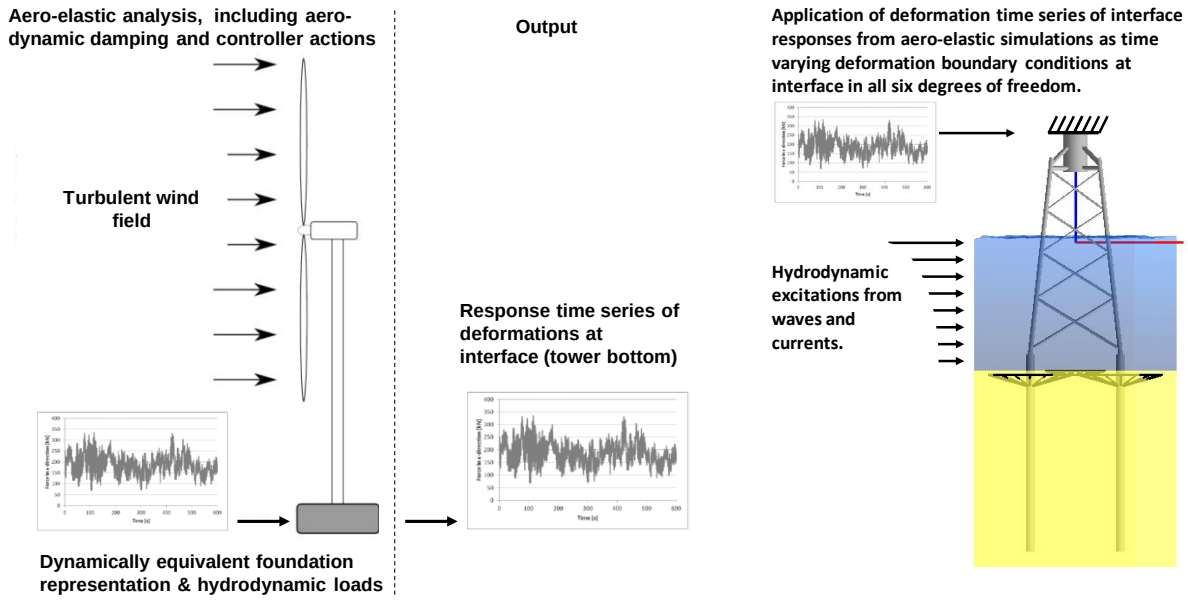

Figure 4: Models and loading configurations for the deformation controlled approach

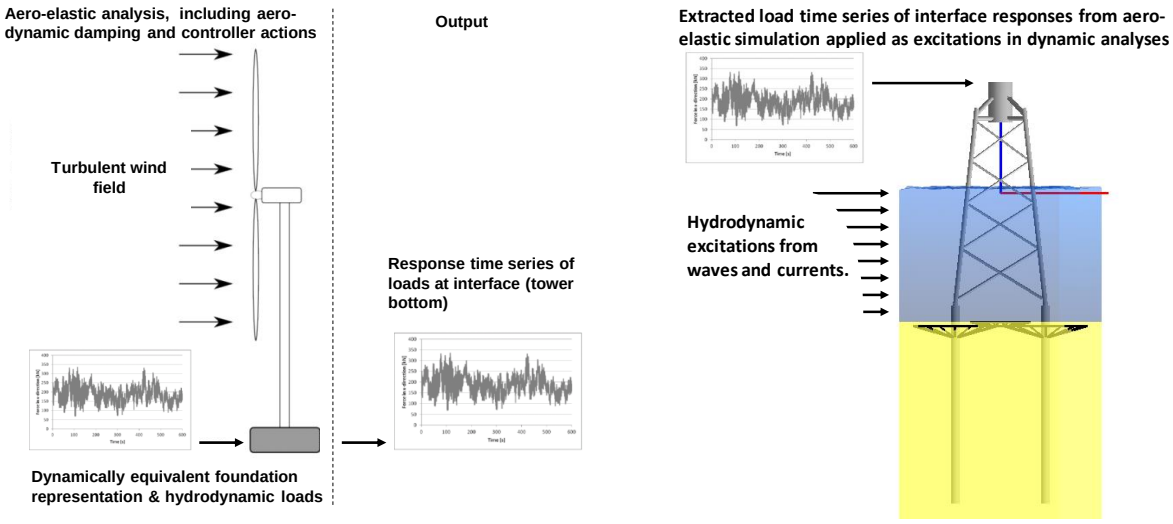

Figure 5: Models and loading configurations for the force controlled approach

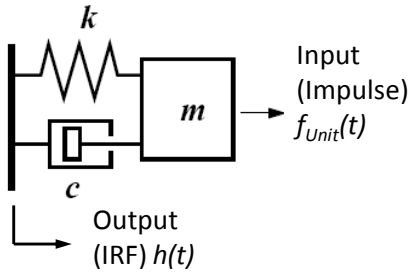

Figure 6: Example SDOF system

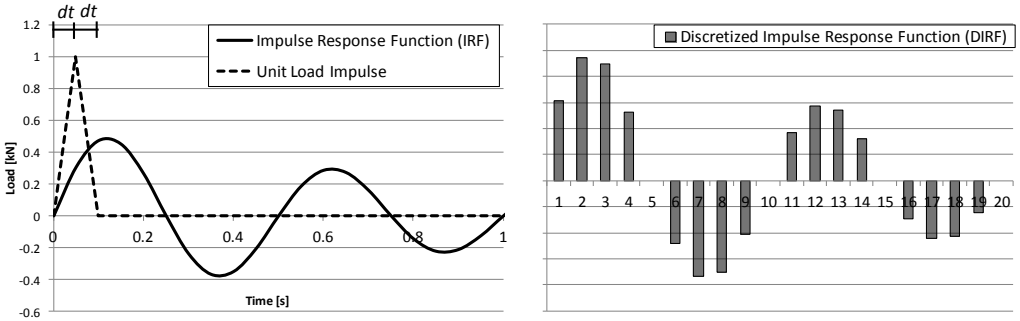

Figure 7: Unit load impulse together with IRF (left) and DIRF (right)

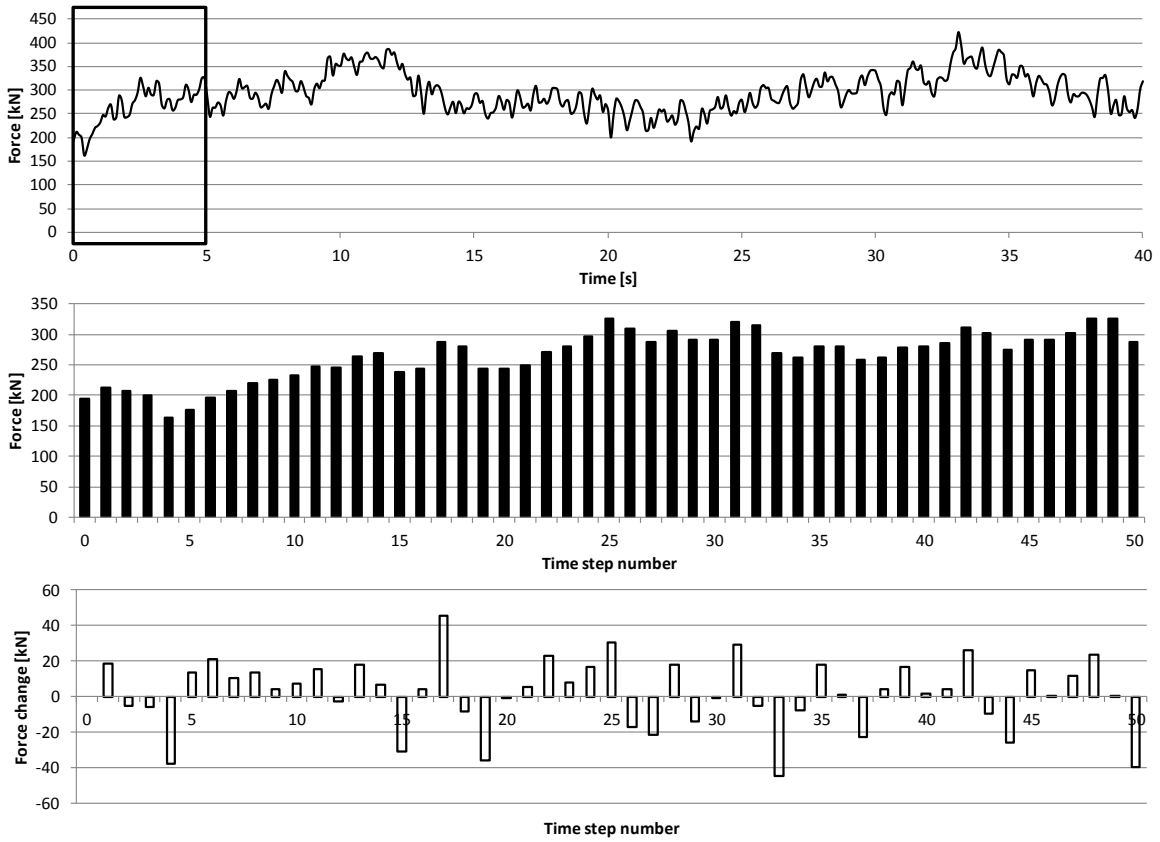

Figure 8: A load function *f(t)* (upper) is discretized and sampled for time step sizes *dt* in the vector $\boldsymbol{f}(t_i)$ (centre) and further sampled for load differences per time step in the vector $\Delta\boldsymbol{f}(t_i)$

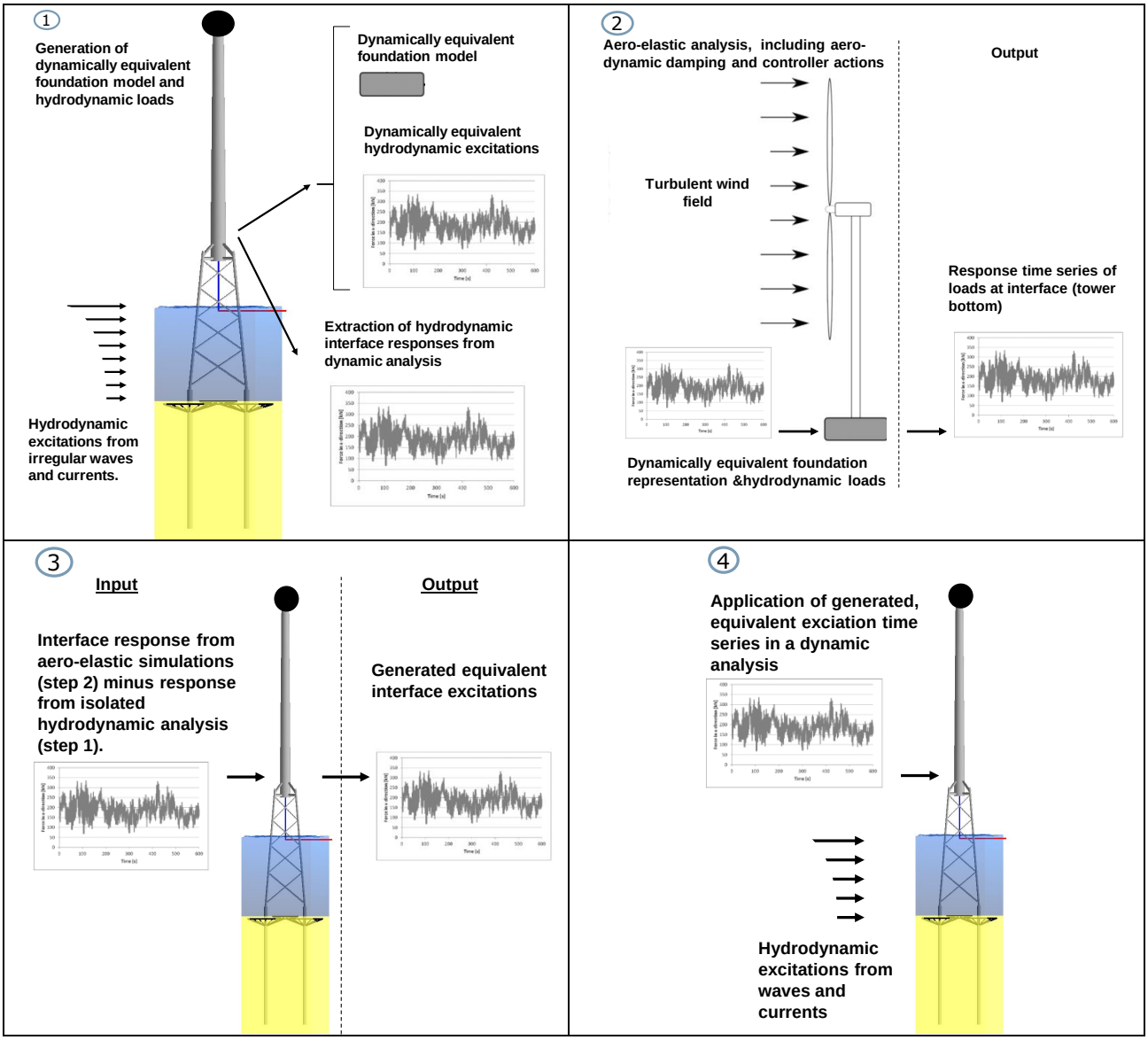

Figure 9: Four subsequent steps for load calculations based on inverse dynamics

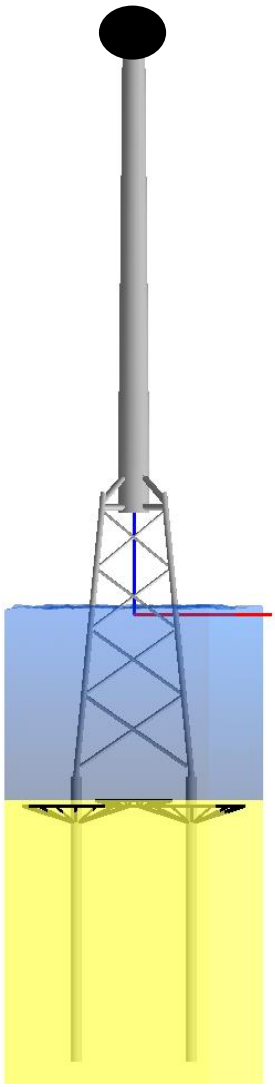

Figure 10: OWT model in ROSAP

Table 1: Offshore wind turbine model parameter

WTG Parameters	
Mass of RNA [ton]	350
Hub height elevation wrt LAT [m]	100.0
Conical tower parameters	
Tower top diameter [mm]	4000
Tower bottom diameter [mm]	5500
(Constant) wall thickness [mm]	38
Tower length [m]	72
Jacket and pile parameters	
Top base width [m]	11.0
Bottom base width [m]	20.0
Leg diameter [mm]	1000
Leg wall thickness [mm]	30-50
Brace diameter [mm]	450-630
Brace wall thickness [mm]	18-35
Pile diameter [mm]	1829
Pile wall thickness [mm]	25-50
Pile penetration [m]	45.0

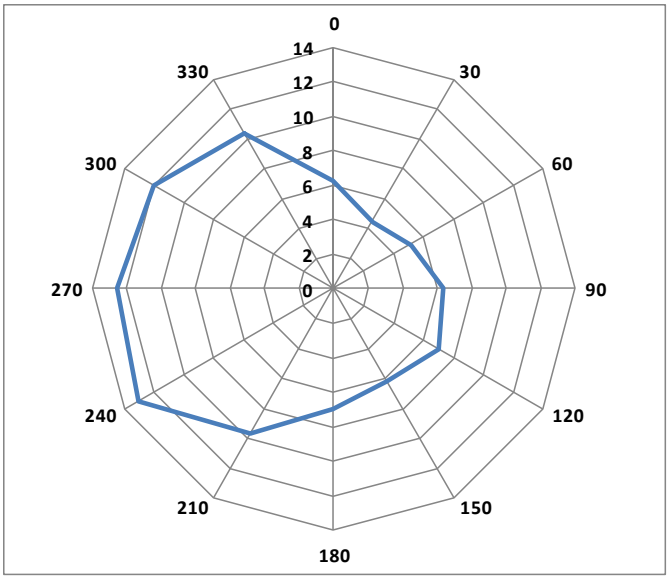

Figure 11: Wind-wave rose for the generic site

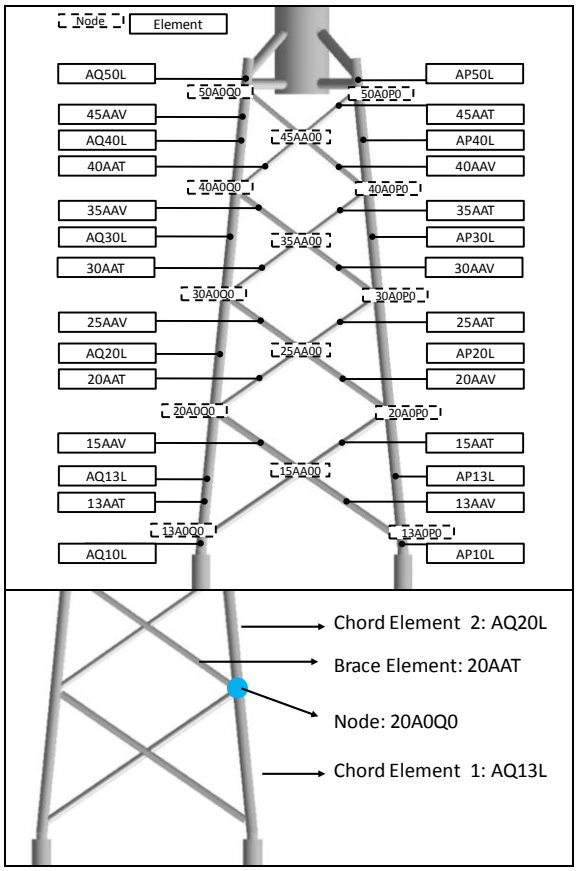

Figure 12: Nodes and elements on one flat face of the jacket (upper) and example denotation of one tubular joint (lower)

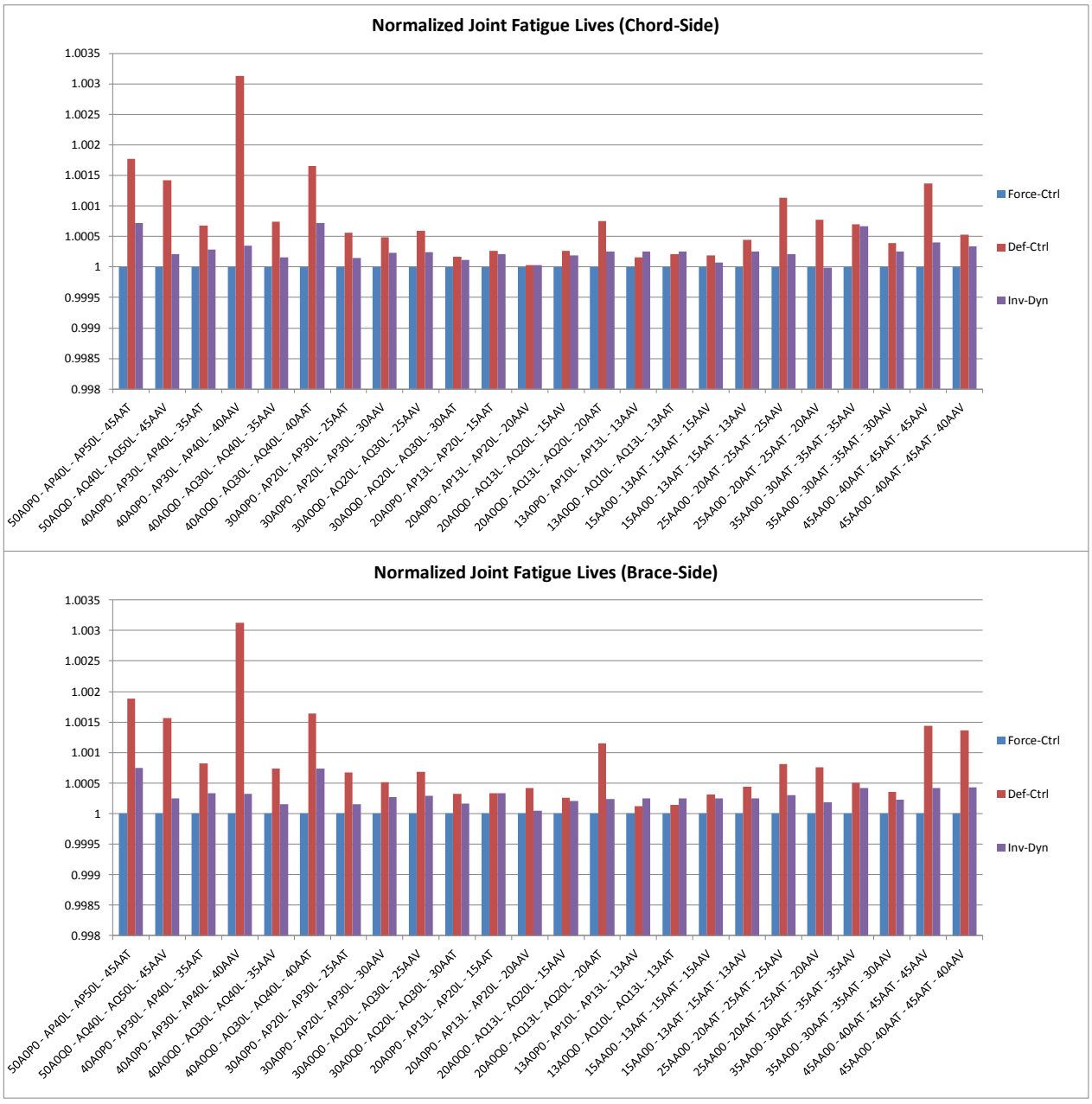

Figure 13: Normalized fatigue lives for all tubular joints on one flat face side of the jacket

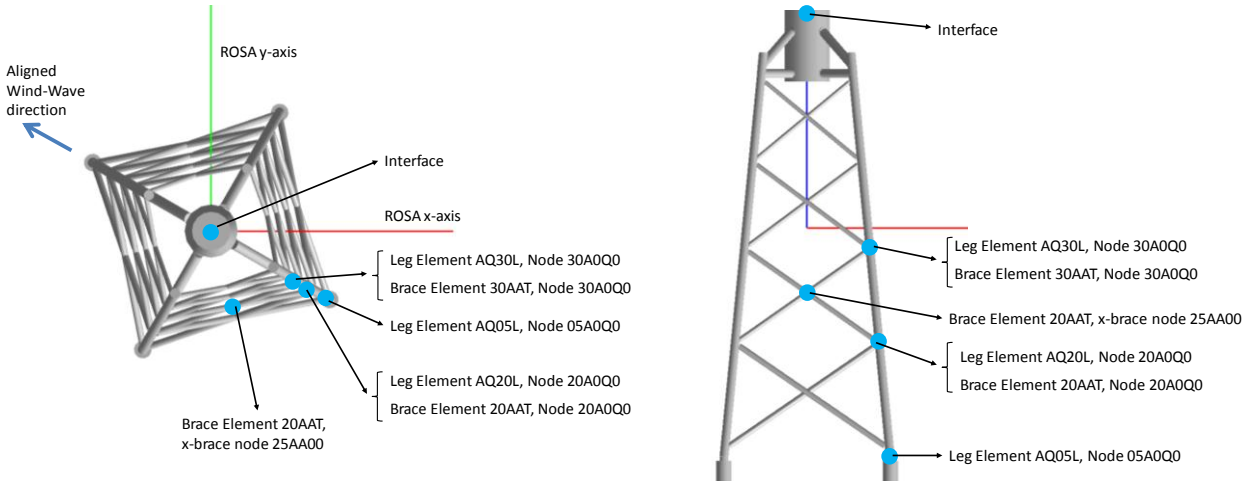

Figure 14: Location of the assessed load and deformation sensors

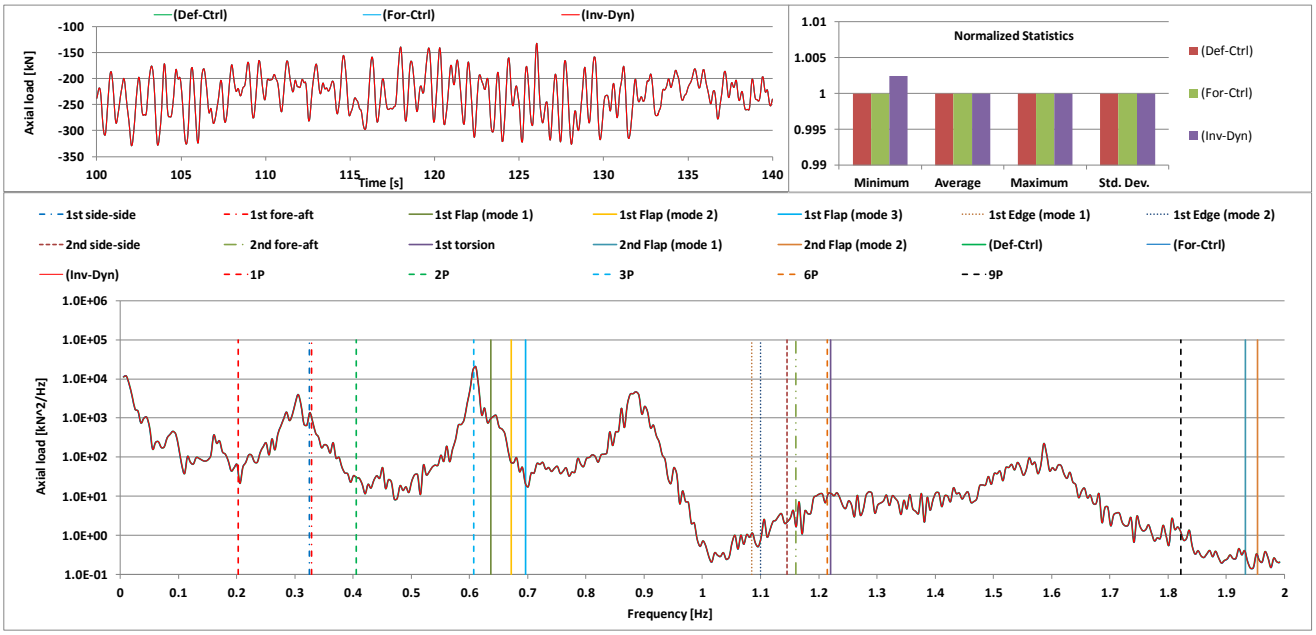

Figure 15: Comparison of axial load response in element 20AAT at node 20A0Q0 for the individual load calculation methods. Time series (upper left), statistics (upper right) and power spectral densities (lower)

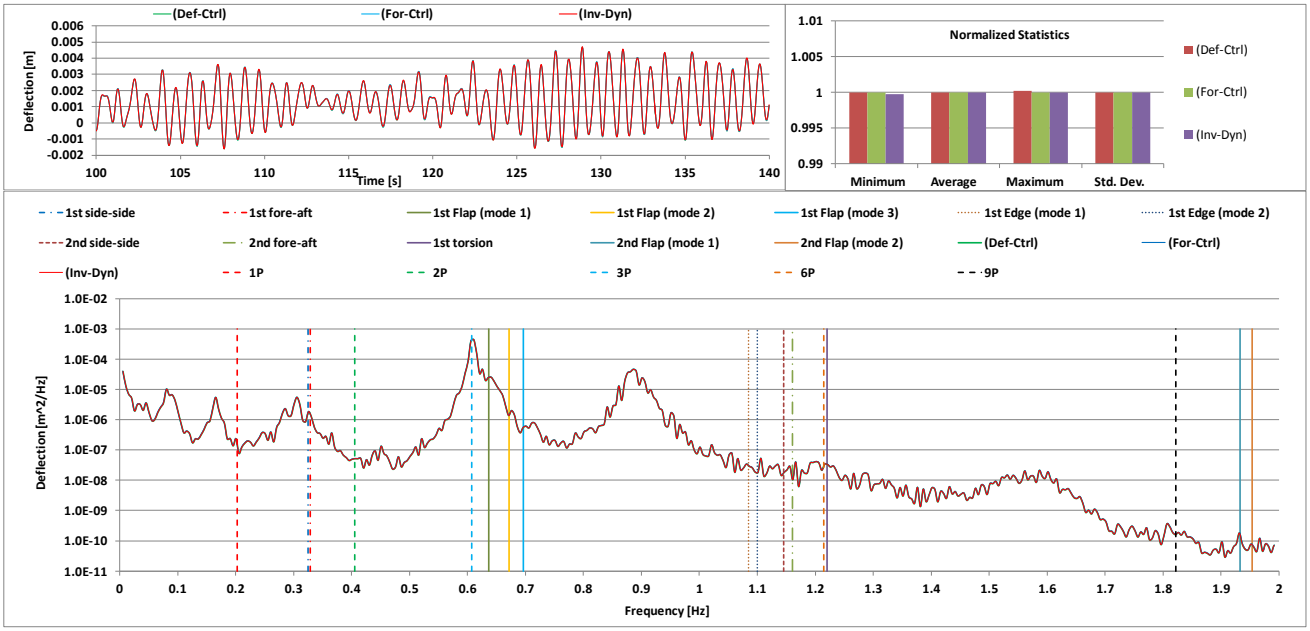

Figure 16: Comparison of out-of-plane deflection response in node 25AA00 for the individual load calculation methods. Time series (upper left), statistics (upper right) and power spectral densities (lower)

Tables

Table 2: Correlation of wind, wave and current parameters

Mean wind speed on hub height	Turbulence intensity	Significant wave height	Peak period	Reference current speed (wind induced)	Omni-directional probability
v_{hub}	I	H_s	T_p	$v_{c,wind,ref}$	p
[m/s]	[%]	[m]	[s]	[m/s]	[%]
3.5	21.7	0.60	4.20	0.04	8.530
5	18.7	0.91	4.88	0.06	12.112
7	16.7	1.25	5.43	0.08	15.886
9	15.6	1.46	5.61	0.10	17.076
11	14.8	1.81	5.83	0.12	15.628
13	14.4	2.18	6.19	0.14	12.377
15	14.0	2.61	6.55	0.16	8.539
17	13.7	3.06	7.17	0.19	5.147
19	13.5	3.61	7.66	0.21	2.710
21	13.3	4.18	7.98	0.23	1.247
23	13.2	4.78	8.44	0.25	0.501
30	12.8	5.63	9.07	0.33	0.246

Paper 2: Condensation of Long-Term Wave Climates for the Fatigue Design of Hydrodynamically Sensitive Offshore Wind Turbine Support Structures

Authors:	Patrik Passon, Kim Branner
Submitted to:	Journal '*Ships and Offshore Structures'*
Status:	Published online, currently in press.
Remarks:	This is an Author's Accepted Manuscript of an article published at 13th October 2014 in the Journal '*Ships and Offshore Structures'*, currently in press (DOI: 10.1080/17445302.2014.967994), © 2014 Taylor & Francis.
	Available online from: http://www.tandfonline.com/doi/abs/10.1080/17445302.2014.967994#.VN-ZpS5tzfe

Condensation of long-term wave climates for the fatigue design of hydrodynamically sensitive offshore wind turbine support structures

Patrik Passon[1], Kim Branner[2]

[1]*RAMBOLL Wind, Esbjerg, Denmark*

[2] *Department of Wind Energy, Technical University of Denmark, Roskilde, Denmark*

Patrik Passon. Email: pkp@ramboll.com. Ramboll, Adgangsvejen 3, 6700 Esbjerg, Denmark,

Condensation of long-term wave climates for the fatigue design of hydrodynamically sensitive offshore wind turbine support structures

Cost-efficient and reliable fatigue designs of offshore wind turbine support structures require an adequate representation of the site-specific wind-wave joint distribution. Establishment of this wind-wave joint distribution for design load calculation purposes requires typically a correlation of the marginal wind and wave distribution. This is achieved by condensation of the site-specific wave climate in terms of wave period or wave height lumping, subsequently used as input for a correlation with the corresponding wind climate. The quality of this resulting wind-wave correlation is especially important for hydrodynamically sensitive structures since the applied met-ocean parameters have a non-linear influence on calculated fatigue design loads. The present article introduces a new wave lumping method for condensation of the wave climate. The novelty is predominantly based on refined equivalence criterions for fatigue loads aiming at preservation of the fatigue damage distribution over either the wave height or wave period distribution. This new method is assessed in comparison with different other traditional wave lumping methods on basis of the site-specific wave climate for the offshore wind farm project Gemini which has kindly been made available by the developer Typhoon Offshore. It is shown that the new method allows for a significantly better preservation of the hydrodynamic fatigue in comparison to the traditional methods.

Keywords: offshore wind; support structure; fatigue design; wave lumping

Nomenclature

H_s	Significant wave height [m]	$H_{s,i}$	i^{th} significant wave height class [m]
T_p	Peak period [s]	$T_{p,j}$	j^{th} peak period class [s]
T_z	Mean or zero-crossing (either up or down) period [s]	$T_{z,j}$	j^{th} mean period class [s]
$p_{i,j}$	Probability of i^{th} significant wave height class $H_{s,i}$ and j^{th} peak period class $T_{p,j}$ in wave scatter diagram	$d_{i,j}$	Fatigue damage of i^{th} significant wave height class $H_{s,i}$ and j^{th} peak period class $T_{p,j}$ in wave scatter diagram
p_i	Probability of i^{th} significant wave height class $H_{s,i}$ over all peak period classes $T_{p,j}$	d_i	Fatigue damage of i^{th} significant wave height class $H_{s,i}$ over all peak period classes $T_{p,j}$
p_j	Probability of j^{th} peak period class $T_{p,j}$ over all significant wave height classes $H_{s,i}$	d_j	Fatigue damage of j^{th} peak period class $T_{p,j}$ over all significant wave height classes $H_{s,i}$
γ	Peak shape parameter	m	*S-N* curve slope
N_{Hs}	Number of significant wave height classes in wave scatter diagram	N_{Tp}	Number of peak period classes in wave scatter diagram
D	Damage scatter matrix	D^*	Unit damage scatter matrix
OWT	Offshore wind turbine	SCD	Wave scatter diagram
DEWH	Damage equivalent wave height	DEM	Damage equivalent moment
DEWP	Damage equivalent wave period	MEWH	Damage equivalent wave height based on *S-N* curve slope m

1. Introduction

Offshore wind turbines (OWTs) are subjected to dynamic wind and wave loading governing the fatigue design of the support structures. Calculations of these loads for OWT are typically performed in a joint effort between wind turbine manufactures and foundation designers. In this constellation the support structure is divided into two subsystems, i.e. the upper tower subsystem and the lower foundation subsystem which is subjected to direct hydrodynamic loading. An overview of the load calculation process and methods for OWT foundations can be found in Passon & Branner (2014). Establishment of corresponding fatigue design load cases for OWTs depend on the availability and quality of site-specific met-ocean databases which often differ for individual offshore wind farm projects. In consequence there is no unique method for the derivation of wind-wave joint distributions as well as the subsequent extraction of site-specific met-ocean parameters for the individual fatigue design load combinations. A common scenario for available met-ocean data comprise long-term wave climates represented by directional, two-dimensional wave scatter diagrams (SCDs) as well as directional Weibull distributions for the wind. An example SCD is shown in Figure 1 summarizing probabilities of occurrence $p_{i,j}$ of $i=1,..,N_{Hs}$ classes of significant wave heights $H_{s,i}$ and $j=1,..,N_{Tp}$ classes of peak periods $T_{p,j}$[1].

[Figure 1 below here]

In practise, the establishment of the wind-wave joint distribution is based on a condensation of the long-term wave climate for example by definition of only one representative peak period $T_{p,i}$ per significant wave height class $H_{s,i}$ replacing the actual range of wave period classes $T_{p,j}$. The wave climate condensation is required in order to obtain a reasonable number of wind-wave load

[1] Sometimes SCDs are also available for mean periods $T_{z,j}$ instead, or even in addition.

combinations for the fatigue load simulations as well as to allow for application of wind-wave correlation methods e.g. according to Mittendorf (2009). This condensation is achieved by wave height or period lumping of the full fatigue wave climate, hereinafter denoted as wave lumping.

Nowadays trends towards larger wind turbines installed at deeper water often lead to rather pronounced dynamic wave fatigue loads for example in case of monopile foundations. OWT support structures with pronounced or even dominant wave fatigue loads are denoted as hydrodynamically sensitive structures in this article. Due to this hydrodynamic sensitivity the monopile is often replaced by jacket structures in case of larger wind turbines installed at deeper water. However, its rather simple geometry and relatively low fabrication cost makes the monopile still a competitive foundation concept compared to jackets hence it is attractive to increase the feasibility range of monopiles. This introduces high accuracy requirements on the fatigue equivalency of lumped wave climate representations in order to avoid negative impacts on the cost efficiency or safety of the structure.

This article addresses lumping methods of long-term wave statistics for the fatigue design of hydrodynamically sensitive OWT support structures. Application of various wave lumping methods have been observed frequently by the authors in past offshore wind farm designs as well as in research projects such as in the UpWind project by Fischer et al. (2010). These traditional methods typically aim on either a preservation of the wave height distribution while establishing an associated, lumped distribution of wave periods or the other way around. However, fatigue equivalency is generally not fulfilled by the traditional wave lumping methods especially in cases of hydrodynamically sensitive OWT support structures since dynamics are disregarded in the lumping assumption. A new method is therefore developed and assessed in the present article, allowing for improved calculations of hydrodynamic fatigue loads for the design of OWT. For

that purpose a brief summary of wave climate descriptions together with an overview of traditional wave climate lumping methods is presented in section 2. This is followed by the introduction of the new method based on refined fatigue distribution criteria in section 3. All wave lumping methods are subsequently applied and evaluated for various practically relevant fatigue conditions using a representative OWT with a monopile foundation and a realistic wave climate in section 4. The wave climate is taken from the met-ocean database of the actual offshore wind project Gemini [Internet] and has kindly been provided by Typhoon Offshore. Finally, the conclusions are provided in section 5.

2. Existing wave lumping methods for the fatigue design of OWT

This section introduces wave climates and the corresponding met-ocean parameters in the context of wind-wave correlations for the fatigue design of OWT and subsequently summarizes three frequently applied traditional wave lumping methods for SCDs.

2.1. Wave lumping for establishment of wind-wave correlations

Data on the wind and wave climate is in many cases provided by different expert parties in terms of marginal distribution. In consequence only limited information regarding the joint distributions of wind and waves are available.

Establishment of wind and wave load combinations for the fatigue design load cases is commonly grouped according to the following basic parameters:

1. Mean wind speed at hub height.
2. (Mean) wind direction.
3. (Mean) wave direction.
4. Number of seeds for turbulent wind and irregular wave realizations.

The associated waves, defined by combinations of significant wave heights H_s and peak periods T_p, as well as the wind-wave joint probabilities of occurrence are subsequently derived for the aforementioned combination of four basic parameters. In reality a range of H_s-T_p combinations can occur for each set of mean wind speed, wind direction and wave direction. However, for practical applications only one representative H_s-T_p combination is associated for each set of these basic parameters in order to limit the actual number of load simulations but also due to the fact that detailed information on such joint occurrences are often not available. In consequence a lumping of the directional, two-dimensional SCDs is required which is typically established as

directional H_s-T_p relations with one representative peak period associated to each significant wave height or vice versa. The individual steps are indicated in Figure 2.

[Figure 2 below here]

2.1.1. Wave spectra descriptions of sea-states

In this article sea-states as characterized by the significant wave height H_s and the peak period T_p in the SCDs are described by JONSWAP or Pierson-Moskowitz wave energy spectra. The difference in the spectral density distribution of those spectrum types depends on the peak shape factor γ. The Pierson-Moskowitz spectrum formulation according to IEC 61400-3 (2009) is summarized in Eq. 1.

$$S_{PM}(f) = 0.3135 \cdot H_s^2 \cdot {T_p}^{-4} \cdot f^{-5} \cdot e^{\left[-1.25(f \cdot T_p)^{-4}\right]} \quad \text{Eq. 1}$$

Pierson-Moskowitz spectra are special cases of JONSWAP spectra resulting from a peak shape factor γ=1 for description of fully developed sea states. For the formulation of JONSWAP spectra the peak shape factor γ is derived from H_s and T_p according to Eq. 2.

$$\gamma = \begin{cases} 5 \text{ for } \dfrac{T_p}{\sqrt{H_s}} \leq 3.6 \\ \exp\left(5.75 - 1.15\dfrac{T_p}{\sqrt{H_s}}\right) \text{ for } 3.6 \leq \dfrac{T_p}{\sqrt{H_s}} \leq 5 \\ 1 \text{ for } \dfrac{T_p}{\sqrt{H_s}} \geq 5 \end{cases} \quad \text{Eq. 2}$$

The JONSWAP spectrum is summarized in Eq. 3 according to the formulations in IEC 61400-3 (2009) based on the Pierson-Moskowitz spectrum and peak shape factor γ for calculation of the frequency depended peak enhancement factor γ^{α} as well as the normalising factor $C(\gamma)$.

$$S_{JS}(f) = C(\gamma) \cdot S_{PM}(f) \cdot \gamma^{\alpha} \quad \text{Eq. 3}$$

The mean period T_z and the peak period T_p of the spectrum are also related by the peak shape factor γ according to Eq. 4.

$$T_z = T_p \sqrt{\frac{5+\gamma}{11+\gamma}} \quad \text{Eq. 4}$$

2.2. Simplified damage equivalent wave heights

This approach aims at a preservation of the wave period distribution while establishing an associated distribution of wave heights for all wave period classes *j* as indicated in Figure 3. ***[Figure 3 near here]*** The establishment of wave heights (MEWHs) for the individual wave period classes *j* in case of dominant wave inertia loads compared to wave drag loads is based on Eq. 5 taken from Burton et al. (2011) section 11.3.7 in analogy to damage equivalent loads and requires the selection of a representative *S-N* curve slope *m*.

$$H_{s,m,j} = \left(\frac{\sum_i^{N_{Hs}} p_{i,j} \cdot H_{s,i}^m}{p_j} \right)^{1/m} \quad \text{Eq. 5}$$

Eq. 5 is based on the assumption that fatigue loads are linear proportional to wave heights and consequently that fatigue damages are proportional to the probability of occurrence and the m^{th} power of the significant wave height. The representative *S-N* curve slope is typically selected as m=4 or 5 for the design of OWT support structures.

However, the assumed fatigue damage proportionality to the significant wave height in Eq. 5 is only valid under certain similarity conditions of the underlying wave spectra. In detail, this

requires for each wave period class j that all wave spectra $S(f)$ from the individual significant wave heights $H_{s,i}$ in Eq. 5 only differ by the factor $H_{s,i}^2$ for the spectra formulations in Eq. 1 and Eq. 3. For the example of two wave height classes $H_{s,i1}$ and $H_{s,i2}$ this relation for their corresponding spectra $S_{Hs,i1}(f)$ and $S_{Hs,i2}(f)$ is expressed by Eq. 6.

$$S_{H_{s,i2}}(f) = \frac{H_{s,i2}^2}{H_{s,i1}^2} \cdot S_{H_{s,i1}}(f) \qquad \text{Eq. 6}$$

However, given the fact that all significant wave heights $H_{s,i}$ for calculation of a particular lumped wave height $H_{s,m,j}$ are associated to the same peak period $T_{p,j}$ the aforementioned requirement is only met for a constant peak shape factor γ in all corresponding $H_{s,i}$-$T_{p,j}$ combinations. This condition is e.g. fulfilled for the Pierson-Moskowitz spectrum described in Eq. 1. However, Figure 4 shows that the peak shape factor γ depend on the significant wave heights H_s and peak periods T_p according to Eq. 2 for the more general case of JONSWAP spectra. It can be seen that γ is constant over the H_s only for very small and large T_p. For sea state descriptions by JONSWAP wave spectra as applied in this article it can therefore be expected that the MEWH lumping method according to Eq. 5 only yields good results for certain SCD characteristics. In particular, the requirement is that the SCD only has non-zero probabilities for $H_{s,i}$-$T_{p,j}$ combinations with constant γ per wave period class j or at least that the influence of combinations with differing γ are of minor importance e.g. due to low probabilities. The latter case is addressed in more detail in section 4.2.6 while the general influence of γ on the MEWH lumping approach is further elaborated in section 4.2.2.

2.3. Averaging of wave frequencies

This approach aims at a preservation of the significant wave height distribution while establishing an associated wave period distribution for all wave height classes i based on an averaging of the

relative number of waves *n* as the product of probability *p* and wave-frequency $1/T_z$ according to Kühn (2001) in Eq. 7.

$$T_{z,n,i} = \left(\frac{\sum_j^{N_{Tz}} p_{i,j}/T_{z,j}}{p_i} \right)^{-1} \quad \text{Eq. 7}$$

For a given significant wave height $H_{s,i}$ the associated, lumped peak period $T_{p,n,i}$ can easily be converted from $T_{z,n,i}$ with Eq. 4 resulting in an H_s-T_p relation as indicated in Figure 5. ***[Figure 5 near here]*** While the relative number of waves *n* is in average well preserved by this lumping method the actual wave periods have a significant effect on the dynamic responses and therefore on the fatigue damages of the OWT support structure. However, the influence of structural dynamics is disregarded for the individual wave frequencies.

2.4. Averaging of wave periods

Similar to the previous number of waves based averaging method this approach aims at a preservation of the significant wave height distribution as indicated in Figure 5. The wave period distribution is only preserved in average for the individual wave height classes *i* according to Eq. 8 analogously to the wave period lumping approach taken by Mittendorf (2009). Again, the associated peak period $T_{p,ave,i}$ can easily be converted from $T_{z,ave,i}$ by Eq. 4.

$$T_{z,ave,i} = \frac{\sum_j^{N_{Tz}} p_{i,j} \cdot T_{z,j}}{p_i} \quad \text{Eq. 8}$$

Weighting of the individual wave periods is limited to the probability of occurrence while the influence on the structural dynamics is disregarded. It should be noted that this wave period averaging results in a very similar, but not equal H_s-T_p relation compared to the number of waves based averaging introduced in section 2.3. Main differences can especially be found at shorter wave periods which are typically also more relevant for the dynamic responses of the structure.

3. Damage equivalent wave lumping

This section introduces a wave lumping approach that aims at preserving the wave height and fatigue damage distribution while lumping the wave periods or alternatively preserving the wave period and fatigue damage distribution while lumping the wave heights. While similarities exist to the MEWH approach according to section 2.2, the novelty is introduced by equivalence considerations of fatigue damages from each individual H_s-T_p combination. This allows for derivation of damage equivalent wave heights (DEWHs) or alternatively damage equivalent wave periods (DEWPs) based on calculated fatigue damages for the actual structure rather than a generic estimate based only on the slope m of the S-N curve.

3.1. Step-by-step establishment of the damage equivalent lumped waves

The individual steps for the damage equivalent wave lumping are summarized below exemplarily on basis of a time domain approach. It should be noted that steps 1 and 2 could alternatively be based on a frequency domain approach.

1. For each H_s-T_p combination in the SCD[2] a number of time series of irregular waves is established as indicated in Figure 6. The number and length of the irregular wave time series must be sufficiently large to cover stochastic uncertainties adequately. Subsequently, the OWT structure is subjected to these irregular wave realizations in dynamic analyses for representative damping conditions. Section 4 addresses the damping influence in more detail. ***[Figure 6 near here]***
2. Responses from the dynamic analyses are extracted and processed at a representative location. For example at mudline as indicated in Figure 7. For the calculation of damage equivalent moments ΔM_{eq} and fatigue damages d the probability $p_{i,j}$ of each H_s-T_p

[2] This can be limited to H_s-T_p combinations with non-zero probabilities for practical purposes.

combination is set to unity and an adequate *S-N* curve slope *m* is selected. ***[Figure 7 below here]***

Damage equivalent moments (DEMs) are calculated on basis of the well-known Rainflow counting method and subsequently used for derivation of pseudo fatigue damages. DEMs and pseudo fatigue damages are related by the chosen *S-N* curve slope *m* and the scaled section modulus *W* according to Eq. 9. It should be noted that this pseudo damage quantity with the arbitrarily chosen scale value of *10000* does not represent any physical damage. Instead the pseudo damage serves exclusively as a qualitative damage substitute property allowing for a relative quantification of fatigue damages introduced from the investigated methods and conditions. Thus the denominator (10000·*W*) could be set to unity as well since only the proportionality $d \sim \Delta M_{eq}^{\ m}$ needs to be maintained. This is considered acceptable by the authors since only the accuracy of the individual wave lumping methods on the fatigue damages is of interest in the context of the present article.

$$d = \left(\frac{\Delta M_{eq}}{10000 \cdot W}\right)^{m} \qquad \text{Eq. 9}$$

3. The calculated pseudo damages based on unit probabilities from the previous steps, hereinafter called unit damages $d_{i,j}^{\ *}$, for the individual H_s-T_p combinations are derived from calculated DEMs according to Eq. 9. All unit damages $d_{i,j}^{\ *}$ are stored in a unit damage scatter matrix *D** as indicated in Figure 8. ***[Figure 8 near here]***

   Scaling of the unit damages $d_{i,j}^{\ *}$ with the actual probabilities $p_{i,j}$ of a SCD according to Eq. 10 allows for an efficient calculation of the actual, probability based damage scatter matrix *D* for any selected SCD.

$$d_{i,j} = p_{i,j} \cdot d_{i,j}^{*} \qquad \text{Eq. 10}$$

4. Each column sum of the damage scatter matrix D according to Eq. 11 represents the total damage d_j for a particular peak period class j. All damages d_j form the damage distribution over wave period classes T_{pj}.

$$d_j = \sum_i^{N_{Hs}} d_{i,j} = \sum_i^{N_{Hs}} p_{i,j} \cdot d_{i,j}^* \qquad \text{Eq. 11}$$

Analogously, each row sum of D according to Eq. 12 represent the total damage d_i for a particular wave height class i. All damages d_i form the damage distribution over wave heights H_{si}.

$$d_i = \sum_j^{N_{Tp}} d_{i,j} = \sum_j^{N_{Tp}} p_{i,j} \cdot d_{i,j}^* \qquad \text{Eq. 12}$$

5. The last step is to find either the associated DEWPs $T_{p,d,i}$ for a H_{si}-d_i distribution or alternatively the associated DEWHs $H_{s,d,j}$ for a T_{pj}-d_j distribution. Both approaches are equivalent and require analogous steps. They are therefore explained in detail only for the derivation of DEWPs $T_{p,d,i}$. The requirement is that the period $T_{p,d,i}$ in combination with the wave height H_{si} and probability p_i results in the same total damage d_i as introduced by the sum of damages from individual H_{si}-T_{pj}-$p_{i,j}$ combinations over all wave period classes j. A functional description of the damage distribution over wave periods T_p, corresponding to the wave height H_{si} and probability p_i, is established in order to find the DEWP $T_{p,d,i}$. This is achieved by scaling of the unit damages $d_{i,j}^*$ for the individual peak period classes j and the chosen wave height class i with the probability p_i according Eq. 13.

$$d_{i,T_{pj}} = p_i \cdot d_{i,j}^* \qquad \text{Eq. 13}$$

Calculation of scaled wave period class damages is illustrated for the example of wave height class i=3 and the wave period class j=3 in Figure 9. The resulting damage $d_{3,Tp3}$ represents the total damage for wave height class i=3 in case the total probability of

occurrence p_i of this wave height class is assigned exclusively to wave period class j=3.

[Figure 9 below here]

The scaled class damages $d_{i,Tpj}$ provide a number of points for establishment of a functional description of scaled damages over the wave periods T_{pj}. These pairs (T_{pj} - $d_{i,Tpj}$) are subsequently used for the interpolation of a DEWP $T_{p,d,i}$ for each target damage value d_i of the individual wave height classes i.

It should be noted that unit damages for the interpolation are obtained from Eq. 14 instead of Eq. 13 for the alternative case of deriving DEWHs $H_{s,d,j}$ for a given T_{pj}-d_j distribution.

$$d_{j,H_{si}} = p_j \cdot d^*_{i,j} \qquad \text{Eq. 14}$$

3.2. Example for derivation of a damage equivalent wave period

For convenience, the derivation of the associated DEWP $T_{p,d,i}$ is further illustrated for one example H_{si}-d_i pair in Figure 10. ***[Figure 10 below here]***

This example corresponds to the chosen wave height class $H_{s,i}$ =2.625m. The total damage d_i for the chosen wave height class i is extracted as the damage sum over all peak periods T_{pj} according to Eq. 12 and shown as a horizontal line in the figure. The scaled class damages $d_{i,Tpj}$ for the individual wave periods T_{pj} are calculated according to Eq. 13 and included as the red dotted graph in the figure. The intersection of the horizontal total damage graph with the red dotted scaled class damage graph marks the DEWP associated to the chosen wave height class $H_{s,i}$ =2.625m as indicated by the vertical line at $T_{p,i,d}$ = 7.89s. Application of Eq. 9 allows also for a transfer to DEMs in the search of DEWPs. For convenience both, the damage as well as DEM based interpolation are shown in Figure 10 resulting in the same DEWP.

For practical applications the pairs (T_{pj}-$d_{i,Tpj}$) are subjected to an interpolation of $T_{p,i,d}$ for a given damage value d_i rather than to the graphical approach applied in this example. A mix of linear and

cubic spline interpolation has been applied for the derivation of DEWPs $T_{p,d,i}$ as well as for DEWHs $H_{s,d,j}$ for the investigations presented in this article.

4. Assessment of wave lumping methods for monopile structures of OWT

This section investigates all introduced wave lumping methods with respect to hydrodynamic fatigue load calculations for the design of OWT support structures. For that purpose, a hydrodynamically sensitive OWT model with a monopile foundation is established and subjected to dynamic wave loads from a wave climate based on a real site in the Dutch North Sea.

4.1. Example wave climate and OWT

In 2009 the Dutch authorities granted three permits for future offshore wind farms located 55 kilometers north of the island of Schiermonnikoog in the Dutch North Sea. These three projects are named Buitengaats (300MW), Clearcamp (275MW) and ZeeEnergie (300MW), and were fully acquired by Typhoon Offshore in July 2011. Project Gemini is a 600MW offshore wind farm consisting of Buitengaats and ZeeEnergie. The complete wave climate database for the offshore wind farm project Gemini has been provided by Typhoon Offshore for the investigations in the present article. However, this database is still property of Typhoon Offshore and can as such not be fully enclosed in a public article. The corresponding quantities and relations of the met-ocean data are therefore only shown in a qualitative manner, which still allows performing and presenting relevant investigations on basis of real, site specific met-ocean data. The available wave climate consists of directional H_s-T_p SCDs for all of 12 wind directions and 12 wave directions. Figure 11 shows the location of the Gemini project as well as the corresponding omnidirectional SCD. ***[Figure 11 below here]***

A representative, hydrodynamically sensitive OWT configuration is used for the present investigations. The support structure consists of a tubular steel tower with a monopile type foundation using a flanged connection instead of a more traditional transition piece with a grouted connection to the monopile. The rotor-nacelle-assembly is modelled by a simplified, but mass equivalent representation of the NREL 5MW turbine as described by Jonkman et al. (2007).

Figure 12 shows the established OWT model with indicative dimensions. The OWT structure has a first natural frequency of f=0.262Hz and is located at a typical site with medium stiff sand and clay soil at 25m of water depth. All dynamic calculations for the aforementioned OWT structure subjected to various wave climates are performed with the specialised simulation platform ROSAP[3] (2012). ***[Figure 12 below here]***

4.2. Assessment of wave lumping methods

All investigated lumping methods are summarized in Table 1 and shall be denoted by their lumped property in the following. The first three methods aim at a lumping of wave periods while preserving the wave height distribution $H_{s,i}$ while the last two methods aim at a lumping of wave heights while preserving the wave period distribution $T_{p,j}$. Both probability distribution based lumping methods, i.e. $T_{p,ave,i}$ and $T_{p,n,i}$, are independent of the actual structure, dynamic behaviour and fatigue category. The damage equivalent lumping methods $H_{s,m,j}$, $H_{s,d,j}$ and $T_{p,d,i}$ on the other hand have to be based on a variety of conditions covering the *S-N* curve slope *m*, dynamics and a reference location in the structure. ***[Table 1 below here]***

The assessment of the individual wave lumping methods is based on the accuracy of calculated fatigue damages and DEM comprising investigations of influence for the following aspects:

- Location in the structure,
- *S-N* curves,
- Damping,
- SCDs.

---

[3] RAMBOLL Offshore Structure Analysis Package, a finite element based in-house software package of RAMBOLL for offshore structures.

These aspects have been selected due to their relevance for practical fatigue design applications. A starting point is established by a reference scenario used for derivation of the individual lumped waves and the subsequent calculation of corresponding hydrodynamic fatigue damages and DEMs which are compared to reference results from the full SCD.

All dynamic wave load calculations in the following sections are performed as 10-minute simulations for each H_s-T_p combination in the SCD and lumped wave distribution. Uncertainties from the stochastic character of the irregular waves representing the individual H_s-T_p combinations and the limited simulation time are addressed by consideration of a certain number of different wave realizations based on random seeds. In total, 70 wave realizations per H_s-T_p combination in the SCD and 150 wave realizations per H_s-T_p combination of the lumped waves are taken into account for the dynamic simulations. The presented resulting fatigue damages and DEMs are averaged values over all seeds under consideration of the corresponding probability distribution for the underlying SCD. Fatigue damages and DEMs are shown in terms of total values as well as distributions over wave heights $H_{s,i}$ and periods $T_{p,j}$ in the following sections. In case of the SCDs the damage distributions are calculated in accordance to Eq. 11 and Eq. 12.

4.2.1. Lumping of waves for the reference scenario

The reference scenario for the lumping of waves is based on the omnidirectional H_s-T_p SCD of the Gemini project. For the damage equivalent wave lumping methods $H_{s,m,j}$, $H_{s,d,j}$ and $T_{p,d,i}$ a *S-N* curve slope of m=5 is taken into account while the location for extraction of damages and DEMs is defined at mudline level as shown in Figure 12. Furthermore, a damping ratio of 1% critical damping is taken into account for the dynamic wave response calculations, assuming to cover the combined influence from material, soil, radiation and hydrodynamic damping while not including any contributions from aerodynamic damping. The influence of damping is further investigated in section 4.2.4. Table 2 summarizes the reference scenario conditions. ***[Table 2 near here]***

The relative importance of all H_s-T_p combinations in the SCD is illustrated by the *3D* surface plots of unit damages $d_{i,j}^*$ in Figure 13. All damages $d_{i,j}^*$ in the figure are shown in logarithmic scale on the vertical axis and have been derived for the aforementioned conditions in Table 2, however, assuming unit probabilities for all individual H_s-T_p combinations. The following trends are identified:

- For fixed wave heights H_s the unit damage distribution $d_{i,j}^*$ over wave periods T_p follows by tendency a curve similar to a dynamic amplification factor of a single-degree-of-freedom system with the resonance frequency in the vicinity of T_p=4.5s. This corresponds to a mean period of T_z≈3.55s which is located closely to the first natural frequency f=0.262Hz of the structure. Furthermore, it can be seen that a certain range of damage levels can be achieved with two different DEWPs $T_{p,d}$ for fixed wave height values. In such cases only the upper value for $T_{p,d}$ is chosen within this article.
- For fixed wave periods T_p the unit damage distribution $d_{i,j}^*$ follows a trend of increasing damages with increasing wave heights H_s. As indicated in section 2.2 the general trend corresponds approximately to a proportionality factor of H_s^m with m=5 according to Table 2.

[Figure 13 below here]

Figure 14 shows the probability distribution and resulting waves for all lumping methods according to Table 1. Due to the representation of actual met-ocean data from the Gemini offshore wind farm site no values are shown for the ordinates. The upper part shows lumped wave periods over all wave height classes $H_{s,i}$ while the lower part shows the lumped wave height over all wave period classes $T_{p,j}$. ***[Figure 14 below here]***

$T_{p,ave,i}$ and $T_{p,n,i}$ are almost identical for wave heights larger than H_s=1.625m while $T_{p,ave}$ is slightly larger for smaller wave heights. Significant differences can be observed for the damage based wave periods $T_{p,d,i}$ compared to $T_{p,ave}$ and $T_{p,n}$ at small wave heights. Starting with larger values

$T_{p,d,i}$ becomes smaller than the other two lumped wave periods for wave heights larger than 0.875m. For large wave heights all lumped wave periods converge towards one common H_s-T_p-relation.

The lower part of Figure 14 shows that the $H_{s,d}$ is smaller than $H_{s,m}$ in the range of T_p =4.5s to 12.5s. Significant differences in fatigue damage are expected in that wave period range due to the approximate damage proportionality factor of H_s^m.

4.2.2. Assessment of wave lumping methods for the reference scenario

All lumped wave distributions are now subjected to example fatigue calculations and compared against results from the full SCD. The conditions for the reference scenarios are kept in accordance to Table 2, i.e. the same conditions as used for derivation of the lumped wave distributions.

Figure 15 and Figure 16 show the resulting normalized distributions and total values of damages and DEMs for the SCD in comparison to the individual wave lumping methods while Table 3 summarizes the relative errors. ***[Table 3 here]***

It can be seen that the lumping methods $H_{s,d}$ and $T_{p,d}$ show a very good agreement with the reference results from the SCD. The lumped methods $T_{p,ave}$ and $T_{p,n}$ on the other hand underestimate the damages while the lumping method $H_{s,m}$ significantly overestimates the damage.

[Figure 15 below here]

The largest errors for $T_{p,d}$ are observed at H_s=1.875m and 2.125m in Figure 15. Sources for these errors are expected to be a mixture of the applied spline interpolation method for derivation of the individual $T_{p,d,i}$ according to section 3.2 and some minor influences from the large but still limited number of wave realizations. Errors from the lumping methods $T_{p,ave}$ and $T_{p,n}$ are significantly larger and on the non-conservative side which would introduce a risk in real projects.

[Figure 16 here]

The wave lumping method $H_{s,d}$ shows an excellent agreement with the SCD while the largest errors over all lumping methods are introduced by $H_{s,m}$. These errors can especially be observed as overestimations for wave periods between T_p=3.5s to 10.5s. Main source for these differences is the influence of the variable peak shape factor γ as has been explained in section 2.2. This is now addressed in more detail on basis of the example wave period T_p=6.5s. Figure 17 shows the calculated and theoretical unit damages, i.e. for application of unit probabilities for each H_s-T_p combination, in accordance to an assumed damage proportionality factor of H_s^m for m=5. In addition, the figure shows γ together with the actual probabilities for the individual wave heights $H_{s,i}$. It can be seen that the assumed theoretical unit damages starts to differ from the actual damages once γ changes. Constant values of the peak shape factor γ can only be found for wave heights from H_s=0.125m to 1.625m and from H_s=3.375m to 3.875m. In between these regions γ increases with H_s leading to a relative decrease in the resulting damages compared to a scenario with constant γ values based on smallest wave heights. This leads to a deviation from the assumed damage proportionality of H_s^m which forms the basis for calculation of $H_{s,m}$ according to Eq. 5 and would therefore require a higher weighting factor for smaller wave heights relatively to larger waves as a measure of correction. However, since such a weighting factor is neglected in Eq. 5 it is concluded that $H_{s,m}$ might be overestimated when calculated from Eq. 5. This overestimation can e.g. be observed at the wave period T_p=6.5s in Figure 16 leading to an overestimation of fatigue damage and DEM. In this context it should be kept in mind that the probability distribution introduces a further weighting factor for the individual wave heights in Eq. 5, e.g. the influence of H_s-T_p combinations with large variations of γ might be reduced in case of low probabilities.

4.2.3. Variation of the location for fatigue damage extraction

The chosen mudline location in the assessment of the reference scenario represents only one section of the OWT support structure while accurate fatigue loads and damages are required for the entire structure. Therefore, the previously established lumped waves and conditions from section 4.2.1 according to Table 2 are now applied for calculation of fatigue damage and DEMs at another section i.e. interface level according to Figure 12. It is emphasized that $H_{s,d}$ and $T_{p,d}$ are still kept as derived for the mudline location.

Figure 18 and Figure 19 show the resulting normalized distributions and total values of damages and DEMs for the SCD in comparison to the individual wave lumping methods while Table 4 summarizes the relative errors. ***[Table 4 here]***

It can be seen that the fatigue damages and loads at interface level in Table 4 compared to mudline level in Table 3 are

- slightly more underestimated for $T_{p,ave}$ and $T_{p,n}$
- slightly more overestimated for $H_{s,m}$
- slightly less accurate for $H_{s,d,j}$ and $T_{p,d,i}$

Thus, the location variation has a small influence on the accuracy of the individual wave lumping methods for the investigated structure.

[Figure 18 here]

[Figure 19 here]

4.2.4. Variation of damping conditions

OWT are highly dynamic structures subjected to various loading and damping conditions over their lifetime. A damping ratio of 1% critical damping has been used for the reference scenario representing low damping situations without aerodynamic damping such as for idling cases due to technical non-availability or pronounced wind-wave misalignment cases during power

production. However, aerodynamic damping introduces a significant contribution to the overall damping when available which is the case for the majority of lifetime of OWTs. This is due to the typical high likelihood of aligned or only slightly misaligned wind-wave conditions as well as high ratios of OWT being in power production during lifetime. A representative spectrum of dynamic conditions for the assessment of wave lumping methods for the fatigue design of OWT support structures has therefore to cover different damping conditions. For this purpose the previously established lumped waves and conditions from section 4.2.1 are now applied in combination with the conditions in Table 5. The increased structural damping ratio to 4% critical damping is intended to cover the influence of aerodynamic damping on the hydrodynamic response in order to allow for an assessment of sensitivity of the lumped wave against damping variations. It is emphasized that $H_{s,d}$ and $T_{p,d}$ are still kept as derived for the low damping case in Table 2 while all other lumping methods are independent of the dynamic properties and therefore the damping of the structure.

Figure 20 and Figure 21 show the resulting normalized distributions and total values of damages and DEMs for the SCD in comparison to the individual wave lumping methods while Table 6 summarizes the relative errors. ***[Table 6 here]***

It can be seen that the calculated fatigue damages and loads for the higher damping scenario in Table 6 compared to the low damping scenario in Table 3 are

- significantly less underestimated for $T_{p,ave}$ and $T_{p,n}$
- significantly less overestimated for $H_{s,m}$
- slightly less accurate for $T_{p,d,i}$
- significantly less accurate for $H_{s,d,j}$

The damping variation has a significant influence on the accuracy of most wave lumping methods, being beneficial at higher damping situations for $T_{p,ave}$, $T_{p,n}$ and $H_{s,m}$. However, an

unfavourable behaviour towards the non-conservative side is observed for $H_{s,d}$ while the $T_{p,d}$ method is only slightly affected by the changed damping conditions.

[Figure 20 here]

[Figure 21 here]

4.2.5. S-N curve influence

OWTs introduce a large variety of fatigue details covered by different *S-N* curves. In the context of this article the corresponding *S-N* curve slope *m* is of primary interest as particularly the wave lumping methods $H_{s,m}$, $H_{s,d}$ and $T_{p,d}$ are directly influenced by the chosen reference slope *m*. It is therefore important to understand how suitable these wave lumping methods are when applied for fatigue details with other *S-N* curve slopes *m*. For this purpose the previously established lumped waves and conditions from section 4.2.1 are now applied in combination with the conditions in Table 7, i.e. with a representative *S-N* curve slope *m*=3.

Figure 22 and Figure 23 show the resulting normalized distributions and total values of damages and DEMs for the SCD in comparison to the individual wave lumping methods while Table 7 summarizes the relative errors. ***[Table 7 here]***

It can be seen that the calculated fatigue damages and loads for the reduced *S-N* curve slope in Table 7 compared to the reference *S-N* curve slope in Table 3 are:

- significantly less underestimated for $T_{p,ave}$ and $T_{p,n}$
- significantly more overestimated for $H_{s,m}$
- significantly less accurate for $T_{p,d,i}$ and $H_{s,d,j}$

The *S-N* curve slope *m* has a significant influence on the accuracy of all wave lumping methods, being beneficial for the probability based methods $T_{p,ave}$ and $T_{p,n}$ in case of reduced values for *m.* However, large fatigue damage overestimations can be expected for $H_{s,m}$, $T_{p,d}$ and $H_{s,d}$ in case

they have been derived for a larger value of *m*. It is expected that an opposite behaviour can be observed in case $H_{s,m}$, $T_{p,d}$ and $H_{s,d}$ are applied for fatigue details with larger *S-N* curve slopes *m*.

[Figure 22 here]

[Figure 23 here]

4.2.6. Directional wave scatter diagrams

So far all investigations have been limited to the omnidirectional SCD from the Gemini project site applied unidirectionally to the OWT. This approach allowed to assess the individual wave lumping methods for a variety of conditions and introduced as well an adequate representation for fully aligned wind-wave conditions since a large bandwidth of H_s-T_p combinations is considered. However, limitation to the omnidirectional SCD lacks the possibility to provide a more differentiated picture of the wind-wave directionality influence on wave lumping methods for fatigue design purposes, particularly wind-wave misalignment. In this context it should be noted that especially the 90-degree wind-wave misalignment conditions need to be carefully addressed. These misalignment cases potentially govern the fatigue design of hydrodynamically sensitive OWT support structures despite of the rather low probability of occurrence and the trend towards smaller wave heights. This is due to the fact that only limited damping can be utilized for the hydrodynamic response since the large aerodynamic damping is mainly present in wind direction and therefore perpendicular to the wave direction.

Figure 24 shows the SCD for the chosen 90-degree wind-wave misalignment example case. It can be seen that the bandwidth of H_s-T_p combinations is significantly narrower with a very pronounced trend towards smaller wave heights and shorter wave periods compared to the omnidirectional SCD in Figure 11. ***[Figure 24 below here]***

The applied conditions for generation of the lumped waves and the subsequent fatigue calculations are summarized in Table 9. ***[Table 9 here]***

All lumped waves are recalculated for the changed SCD resulting in the distributions shown in Figure 25. ***[Figure 25 below here]***

Figure 26 and Figure 27 show the resulting normalized distributions and total values of damages and DEMs for the SCD in comparison to the individual wave lumping methods while Table 10 summarizes the relative errors. ***[Table 10 here]***

It can be seen that the calculated fatigue damages and loads for the high misalignment SCD in Table 10 compared to the omnidirectional SCD in Table 3 are

- significantly more underestimated for $T_{p,ave}$ and $T_{p,n}$
- significantly less overestimated for $H_{s,m}$
- slightly less accurate for $T_{p,d,i}$ and $H_{s,d,j}$

The changed SCD characteristic has a significant influence on all lumping methods except for $H_{s,d}$ and $T_{p,d}$. Here, a level of high accuracy is achieved since both have been derived for the actually investigated conditions, analogously to the reference case. The significantly improved accuracy for $H_{s,m}$ results from the reduced variation of peak shape factors γ for individual H_s-T_p combinations due to the narrower SCD bandwidth and limitation to smaller wave heights leading to a more valid damage proportionality to H_s^m. Only $T_{p,ave}$ and $T_{p,n}$ show a much poorer accuracy, significantly more underestimating the fatigue damages compared to the reference case. The authors expect this to be a direct consequence from neglecting the influence of dynamics from especially small wave periods in the wave lumping. The influence of dynamics as introduced by these smaller wave periods is significantly more pronounced compared to the omnidirectional SCD. In this context, it can be seen that the errors for the individual wave heights in case of small waves are on similar levels for both SCD cases by comparing Figure 15 and Figure 26. Larger waves on the other hand, for which a good accuracy is achieved in the omnidirectional SCD case,

do not exist for the 90-degree misalignment SCD and can therefore not reduce the influence from the low accuracy of the small waves.

[Figure 26 here]

[Figure 27 here]

4.2.7. Summary and recommendations

Table 11 summarizes the relative errors in total damages compared to the corresponding SCD results as presented in the previous sections. ***[Table 11 below here]***

Non-conservative results are obtained for the wave period based lumping methods $T_{p,ave}$ and $T_{p,n}$ while the wave height based lumping method $H_{s,m}$ significantly overestimates fatigue damages. The best overall results are obtained with the wave period lumping method $T_{p,d}$ while the wave height lumping method $H_{s,d}$ shows larger differences in particular for variations of the *S-N* curve slope *m* and damping conditions. It should be kept in mind that the variation of these conditions introduced a deviation from the reference conditions applied for derivation of lumped wave height $H_{s,d}$. Improvements in the accuracy of calculated fatigue damages from $H_{s,d}$ can therefore be achieved when the lumped wave height $H_{s,d}$ is established e.g. for different damping conditions reflecting different dynamic scenarios during life time of an OWT as indicated in section 4.2.4. However, this requires detailed information on the aerodynamic damping properties for different operational and met-ocean conditions. Analogously, improvements in the accuracy for all damage equivalent lumped waves $H_{s,m}$, $H_{s,d}$ and $T_{p,d}$ can be achieved by an individual derivation for each different *S-N* curve slope *m* of the relevant details for the OWT fatigue design.

5. Conclusions

A selection of existing wave lumping methods together with a new method have been presented and assessed in this article. The investigations of wave lumping methods have been limited to the wave climate alone, although wind conditions are also very important for the fatigue design of OWT. This approach allows for a detailed assessment of the individual condensation methods, while limiting the complexity of combining wind and wave climate. However, it should be noted that wave climate condensation and wind-wave correlations are required simultaneously for most fatigue design load cases of OWT. For practical applications this is typically based on a pre-selection of wind speed bins and associating wave heights and periods rather than maintaining the wave height or period bins from the SCD.

The existing wave lumping methods $T_{p,ave}$ and $T_{p,n}$ are established for the criterion of maintaining the distribution of either wave periods or frequencies in terms of their calculated mean. However, a weighting of the individual periods with respect to dynamics and fatigue damages is disregarded.

The existing wave height lumping method $H_{s,m}$ is established for a simplified damage equivalence assumption which is based on a combination of probabilities and an approximated fatigue damage proportionality factor for the individual wave heights. However, it has been shown that a significant deviation from the assumed damage proportionality factor is introduced by the variability of the peak shape factor γ which consequently introduces errors in the fatigue loads for the $H_{s,m}$ approach. Here, it is recommended to investigate if the influence of γ can be introduced in a refined estimation of $H_{s,m}$.

The new method presented in this article allows for a preservation of the probability and damage distribution over wave heights by a damage equivalent lumping of the wave periods $T_{p,d}$ or

alternatively vice versa for a damage equivalent lumping of wave heights $H_{s,d}$. This damage equivalent lumping approach is based on actual fatigue damage calculations for the underlying wave scatter diagram applied in dynamic analyses to the structure under consideration. Next to the wave scatter diagram it is therefore required to define reference conditions covering the damping, location for extraction of damage and *S-N* curve slope *m*.

All wave lumping methods are based on certain conditions and assumptions. However, in reality OWTs are subjected to a large variety of fatigue relevant conditions during their lifetime. Therefore all wave lumping methods have been assessed for a variety of aspects in this paper including different locations in the structure, *S-N* curve slopes, damping conditions and wave scatter diagrams on basis of a representative OWT. This OWT configuration has been established with a hydrodynamic sensitive support structure using a large diameter monopile foundation. The best overall results for all varying aspects are obtained with the new wave period lumping method $T_{p,d}$. All other wave lumping methods provide good results only for a narrow spectrum of conditions. The new wave height lumping method $H_{s,d}$ showed good performance except in case of *S-N* curve slopes and damping conditions different from those used for derivation of the lumped wave heights. Furthermore, the following general trends have been observed for investigated existing methods:

- Non-conservative results for the wave period based lumping methods $T_{p,ave}$ and $T_{p,n}$ which potentially compromises the safety of the design
- Significant fatigue damage overestimation for the wave height based lumping method $H_{s,m}$ which potentially compromises the economic feasibility of the design

The authors recommend applying the new wave lumping methods $T_{p,d}$ and $H_{s,d}$ for the fatigue design of OWT with hydrodynamic sensitive support structures despite the significantly larger lumping efforts compared to the traditional methods $T_{p,ave}$, $T_{p,n}$ and $H_{s,m}$. However, the observed

superior accuracy of this method compensates for the increased lumping efforts, especially since it can be conveniently addressed by computer tools. The authors encourage further validation and assessment of capabilities and limitations of the new wave lumping methods $T_{p,d}$ and $H_{s,d}$, particularly in OWT design situations that require a simultaneous consideration of wind-wave correlations and wave climate lumping. Furthermore, the authors recommend additional investigations on the validity range of the new wave lumping methods in case of changes in the support structure e.g. during the design process.

Acknowledgement

We thank Bas Kuilman and gratefully acknowledge his support by providing full access to the met-ocean database of the Gemini project on behalf of Typhoon Offshore. This allowed for consideration of realistic wave climate conditions in the presented investigations.

The present article has been established within an industrial PhD project supported by ‘The Danish Council for Technology and Innovation’ and RAMBØLL Wind which is gratefully acknowledged as well.

References

Burton T, Jenkins T, Sharpe D, Bossanyi E. 2011. Wind Energy Handbook, 2nd Edition. John Wiley & Sons. ISBN: 978-0-470-69975-1

Fischer T, de Vries W, Schmidt B. 2010. Upwind Design basis; September 2010; Stuttgart, Germany.

Jonkman J, Butterfield S, Musial W, Scott G. 2007. Definition of a 5MW reference wind turbine for offshore systems development; February 2007; Golden, Colorado: National Renewable Energy Laboratory.

Kühn M. 2001. Dynamics and Design Optimisation of Offshore Wind Energy Conversion Systems, Dissertation, TU Delft, ISBN 90-76468-07-9

Mittendorf K.E. 2009. Joint Description Methods of Wind and Waves for the Design of Offshore Wind Turbines. Marine Technology Society Journal. May 2009; 43(3):23-33. DOI:10.4031/MTSJ.43.3.2

IEC 61400-3. 2009. IEC 61400-3: Wind Turbines – Part 3: Design Requirements for Offshore Wind Turbines, 1st Edition. International Electrotechnical Commission (IEC).

Passon P, Branner K. 2014. Load calculation methods for offshore wind turbine foundations. Ships and Offshore Structures. Vol.9,No.4, June-August 2014. Available from: http://dx.doi.org/10.1080/17445302.2013.820108

ROSAP. 2014. Ramboll Offshore Structural Analysis Program Package, Version 4.80. Copenhagen, Denmark.

GEMINI [Internet]. c2012–2014. Amsterdam, The Netherlands: Typhoon Offshore; [cited 2014 May 5]. Available from: http://www.typhoonoffshore.eu/projects/gemini/.

FIGURES

	Class j	1	2	3	⋯	15	16	17	ALL
	Tp [s]	0.0-1.0	1.0-2.0	2.0-3.0	⋯	14.0-15.0	15.0-16.0	16.0-17.0	p(Hsi)=pi
Class i	Hs [m]								
1	9.00-9.25	p1,1	p1,2	p1,3	⋯	⋯	p1,16	p1,17	∑p1,j
2	8.75-9.00	p2,1	p2,2	⋯	⋯	⋯	p2,16	p2,17	∑p2,j
3	8.50-8.75	p3,1	⋯	p3,3	⋯	⋯		p3,17	∑p3,j
4	8.25-8.50	⋯	⋯	⋯	⋯	⋯	⋯	⋯	∑p4,j
5	8.00-8.25	⋯	⋯	⋯	⋯	⋯	⋯	⋯	∑p5,j
6	7.75-8.00	⋯	⋯			⋯	⋯	⋯	∑p6,j
7	7.50-7.75	⋯	⋯			⋯	⋯	⋯	∑p7,j
⋯	⋯	⋯	⋯			⋯	⋯	⋯	⋯
⋯	⋯	⋯	⋯			⋯	⋯	⋯	⋯
⋯	⋯	⋯	⋯	⋯	⋯	⋯	⋯	⋯	⋯
33	1.00-1.25	⋯	⋯	⋯	⋯	⋯	⋯	⋯	∑p33,j
34	0.75-1.00	p34,1	⋯	⋯	⋯	⋯	⋯	⋯	∑p34,j
35	0.50-0.75	p35,1	p35,2	⋯	⋯	⋯	⋯	p35,17	∑p35,j
36	0.25-0.50	p36,1	p36,2	⋯	⋯	⋯	p36,16	p36,17	∑p36,j
37	0.00-0.25	p37,1	p37,2	⋯	⋯	⋯	p37,16	p37,17	∑p37,j
ALL	p(Tpj)=pj	∑pi,1	∑pi,2	∑pi,3	⋯	∑pi,15	∑pi,16	∑pi,17	∑ = 1.0

$p_{i,j}$

Figure 1: H_s-T_p wave scatter diagram

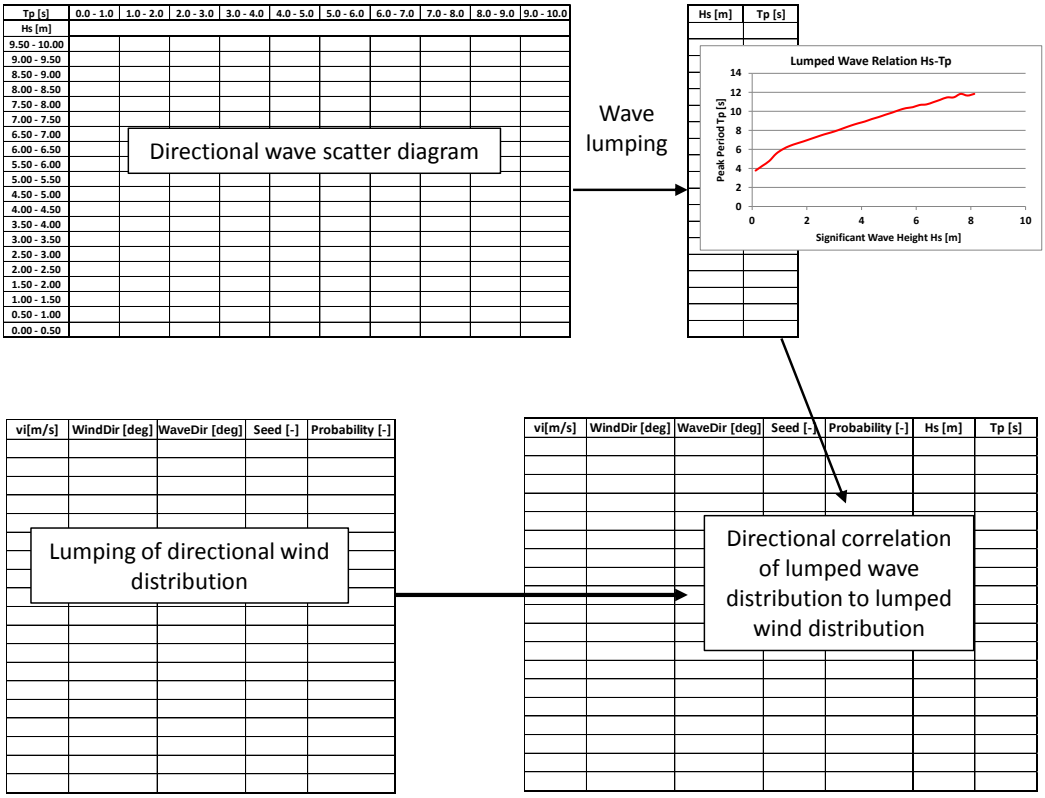

Figure 2: Example wind-wave correlation steps

	Class j	1	2	3	….	15	16	17
	Tp,j [s]	0.0-1.0	1.0-2.0	2.0-3.0	….	14.0-15.0	15.0-16.0	16.0-17.0
Class i	Hs,i [m]							
1	9.00-9.25							
2	8.75-9.00							
3	8.50-8.75							
4	8.25-8.50							
5	8.00-8.25							
6	7.75-8.00							
7	7.50-7.75							
….	….							
….	….							
….	….							
33	1.00-1.25							
34	0.75-1.00							
35	0.50-0.75							
36	0.25-0.50							
37	0.00-0.25							

Wave lumping

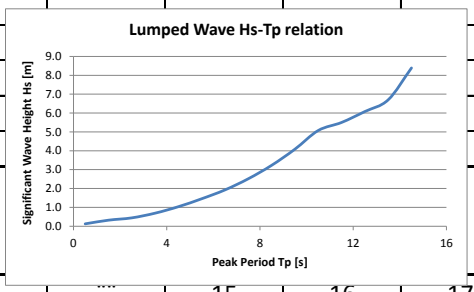

Class j	1	2	3	….	15	16	17
Tp,j [s]	0.0-1.0	1.0-2.0	2.0-3.0	….	14.0-15.0	15.0-16.0	16.0-17.0
Hs,j [m]							

Figure 3: Lumping of wave heights on wave periods

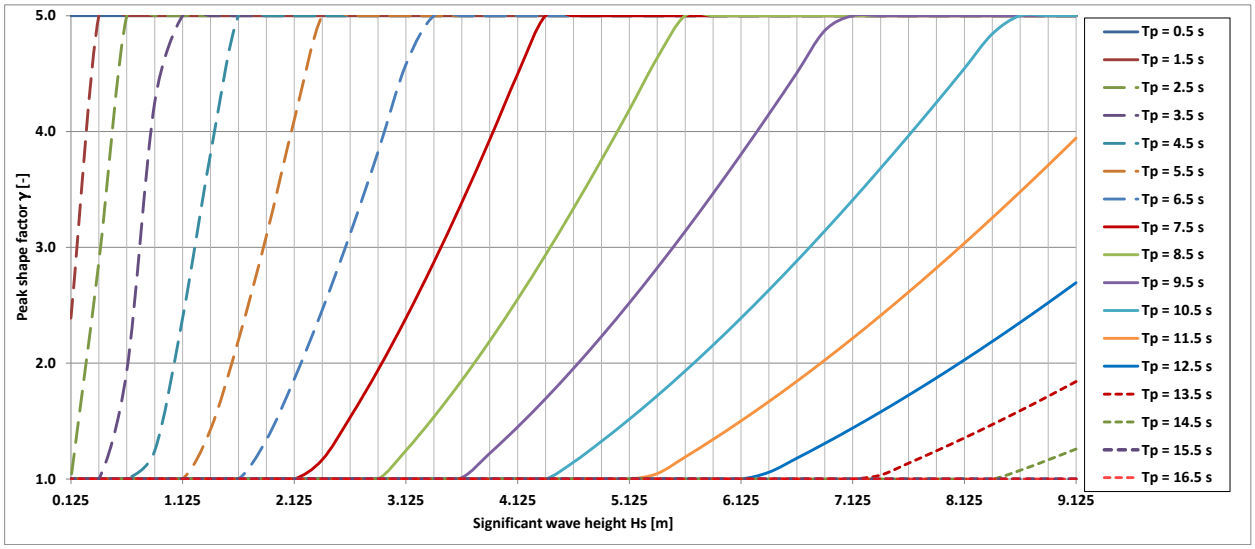

Figure 4: Distribution of peak shape factors γ

	Class j	1	2	3	....	15	16	17
	Tp,j [s]	0.0-1.0	1.0-2.0	2.0-3.0	....	14.0-15.0	15.0-16.0	16.0-17.0
Class i	Hs,i [m]							
1	9.00-9.25							
2	8.75-9.00							
3	8.50-8.75							
4	8.25-8.50							
5	8.00-8.25							
6	7.75-8.00							
7	7.50-7.75							
....	....							
....	....							
....	....							
33	1.00-1.25							
34	0.75-1.00							
35	0.50-0.75							
36	0.25-0.50							
37	0.00-0.25							

Wave lumping

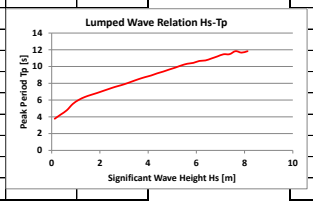

Class i	Hs,i [m]	Tp,i [s]
1	9.00-9.25	
2	8.75-9.00	
3	8.50-8.75	
4	8.25-8.50	
5	8.00-8.25	
6	7.75-8.00	
7	7.50-7.75	
....	....	
....	....	
....	....	
33	1.00-1.25	
34	0.75-1.00	
35	0.50-0.75	
36	0.25-0.50	
37	0.00-0.25	

Figure 5: Lumping of wave periods on wave heights

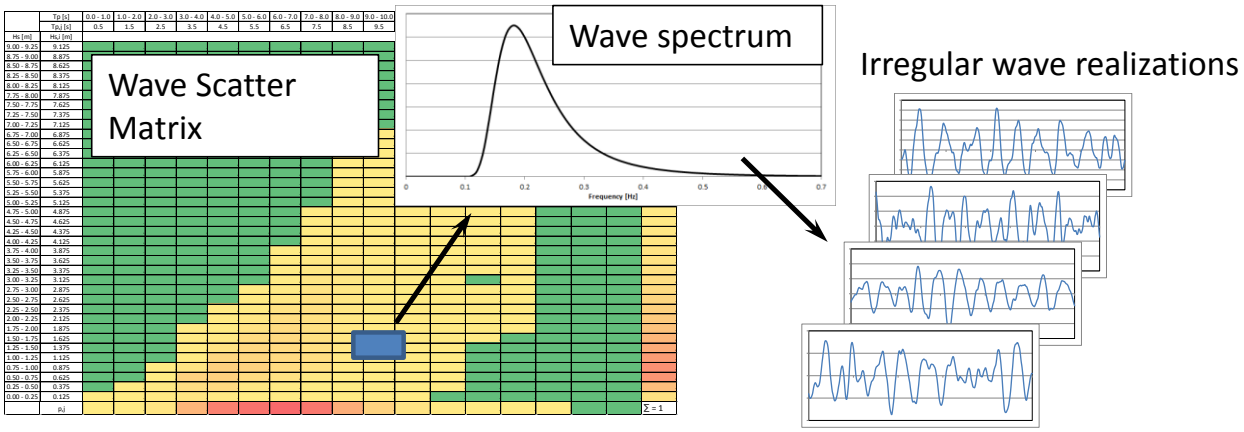

Figure 6: Generation of irregular waves from SCD

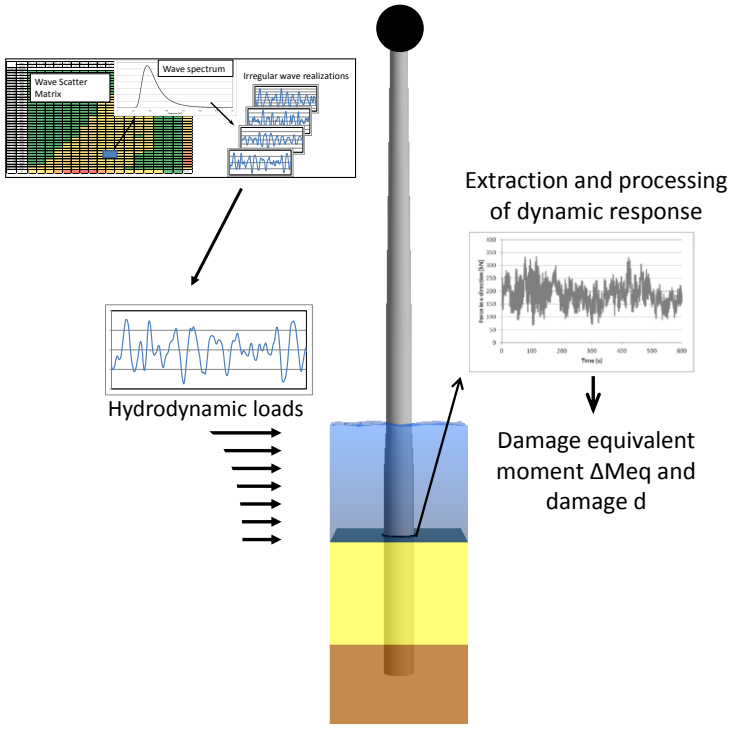

Figure 7: Dynamic analyses for extraction of DEMs and damages

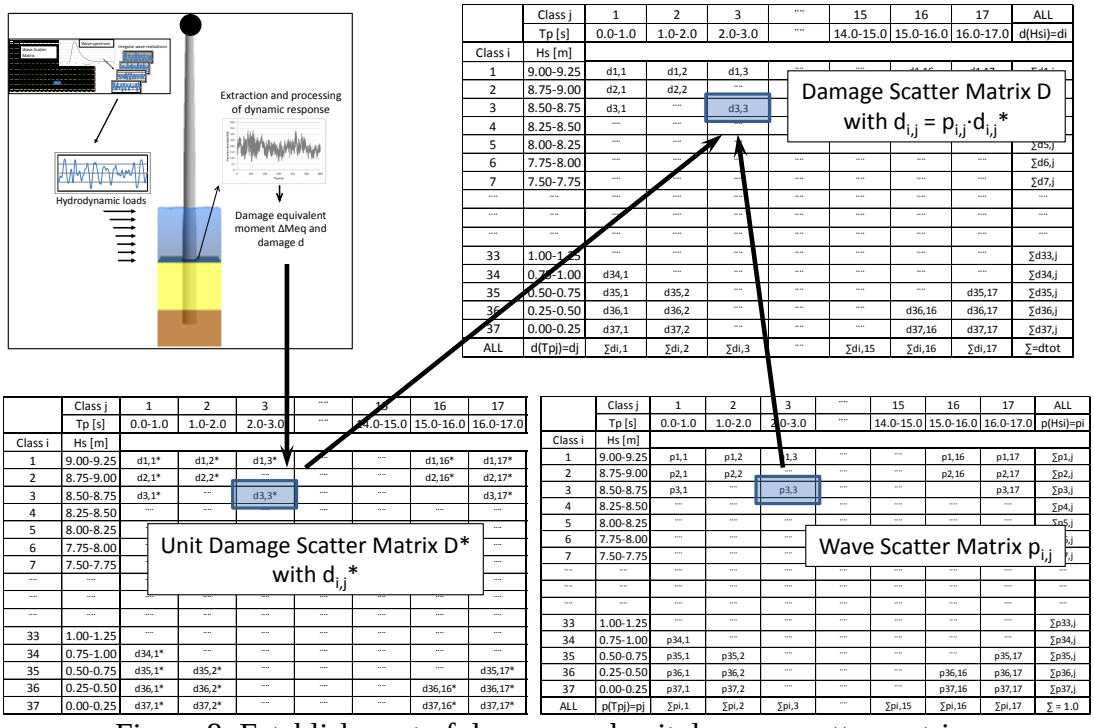

Figure 8: Establishment of damage and unit damage scatter matrix

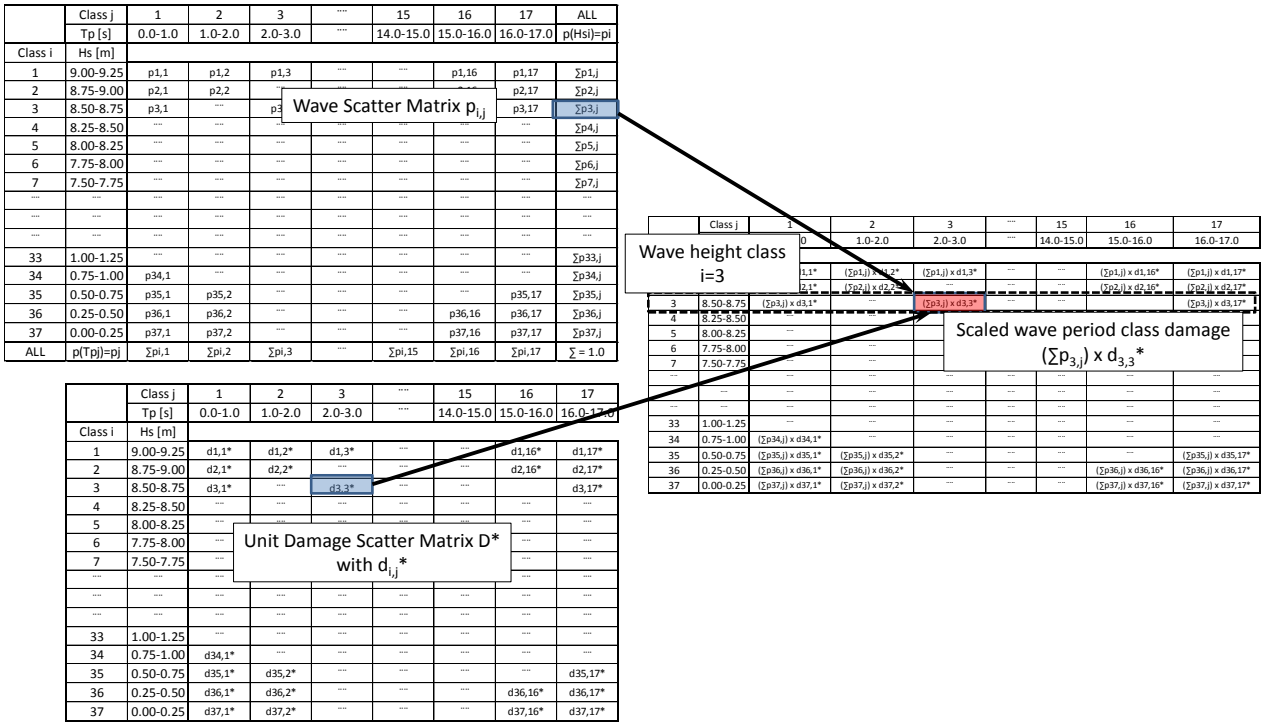

Figure 9: Damage scaling example for wave period class j=3 with total probability p_i for wave height class i=3

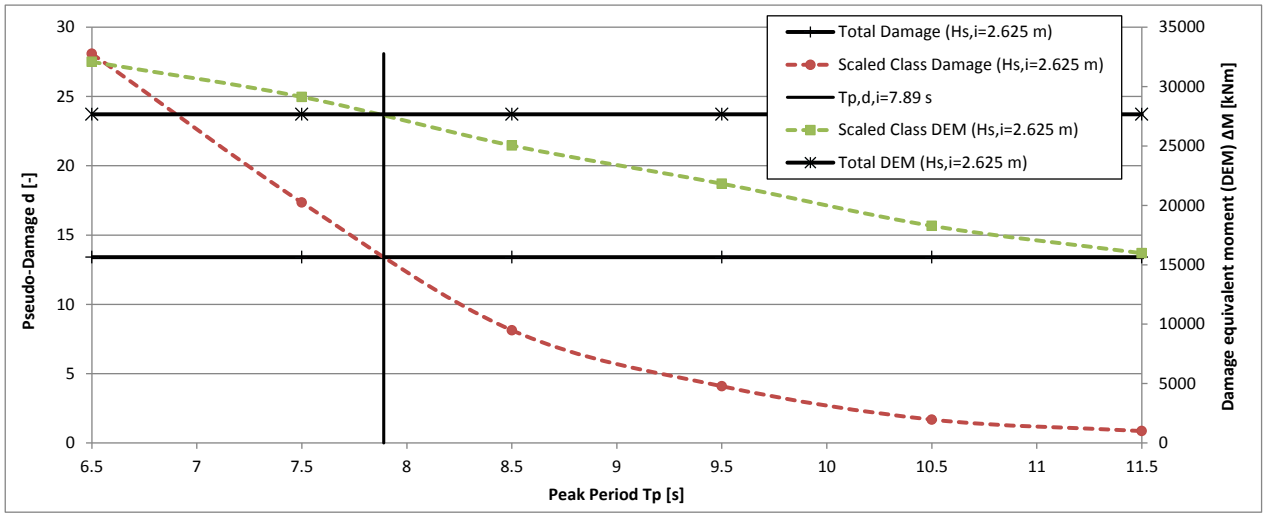

Figure 10: Interpolation of DEWP $T_{p,d,i}$ for significant wave height class $H_{s,i}$ = 2.625m

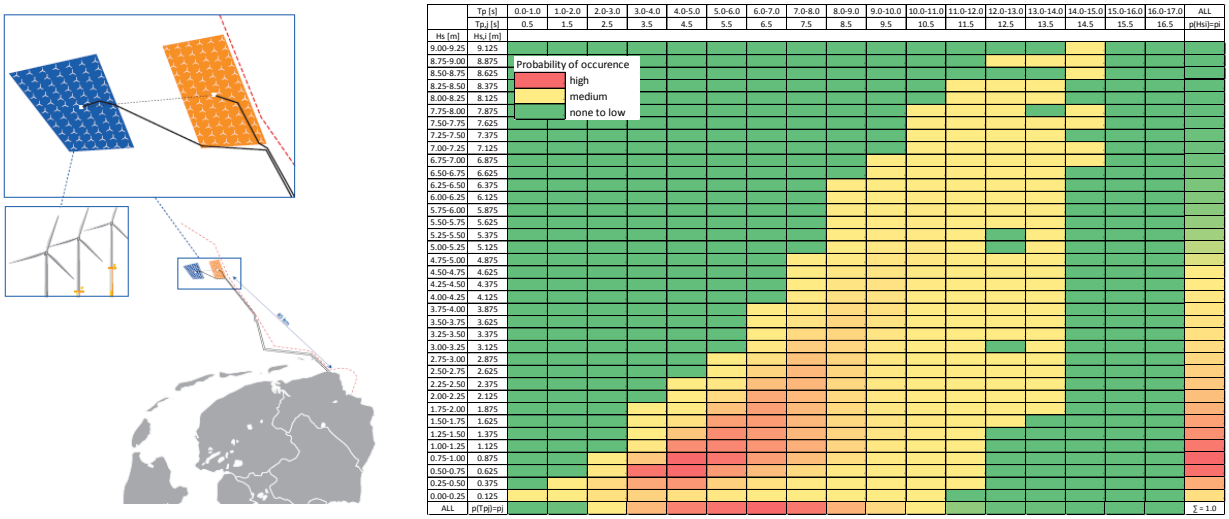

Figure 11: Location of offshore wind farm project Gemini [Internet] from Typhoon Offshore (left) and site-specific omnidirectional SCD (right)

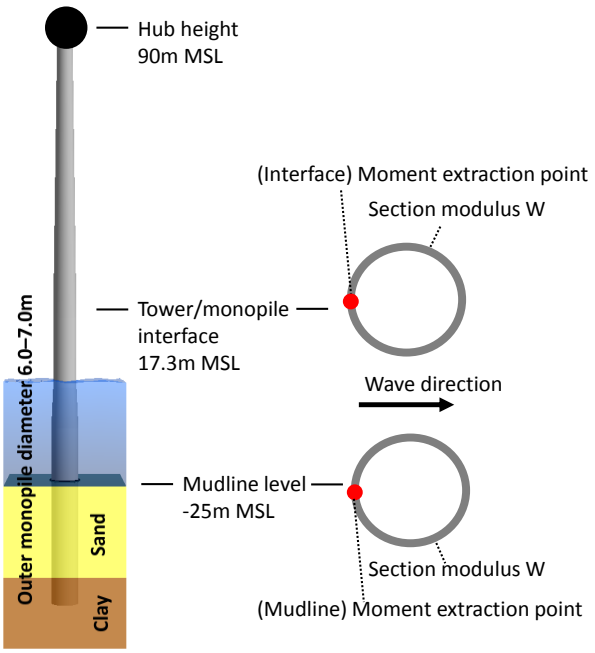

Figure 12: OWT model with interface and mudline locations for extraction of damages and DEMs relative to wave direction

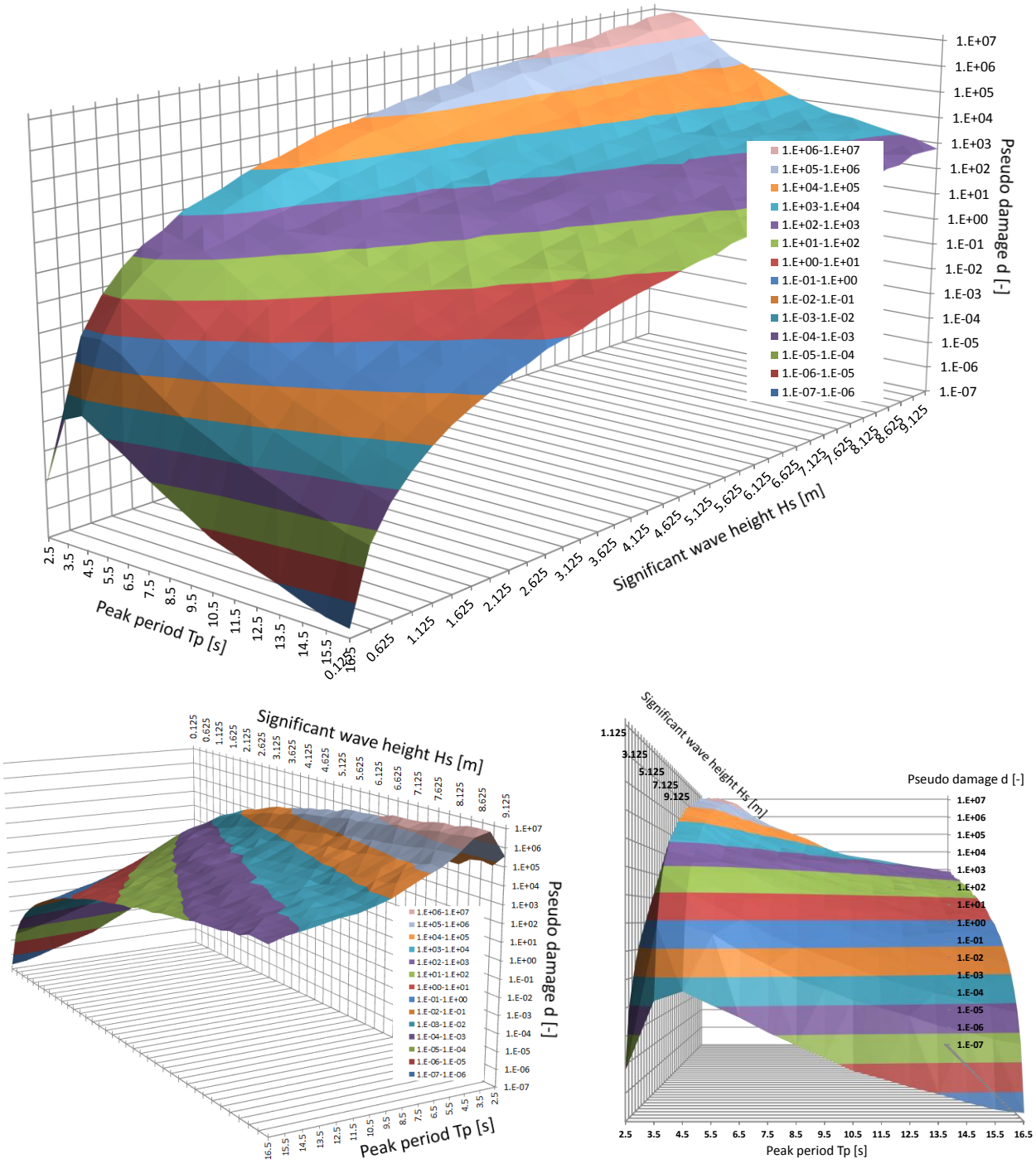

Figure 13: 3D surface plots of unit damage distribution for all Hs-Tp combinations

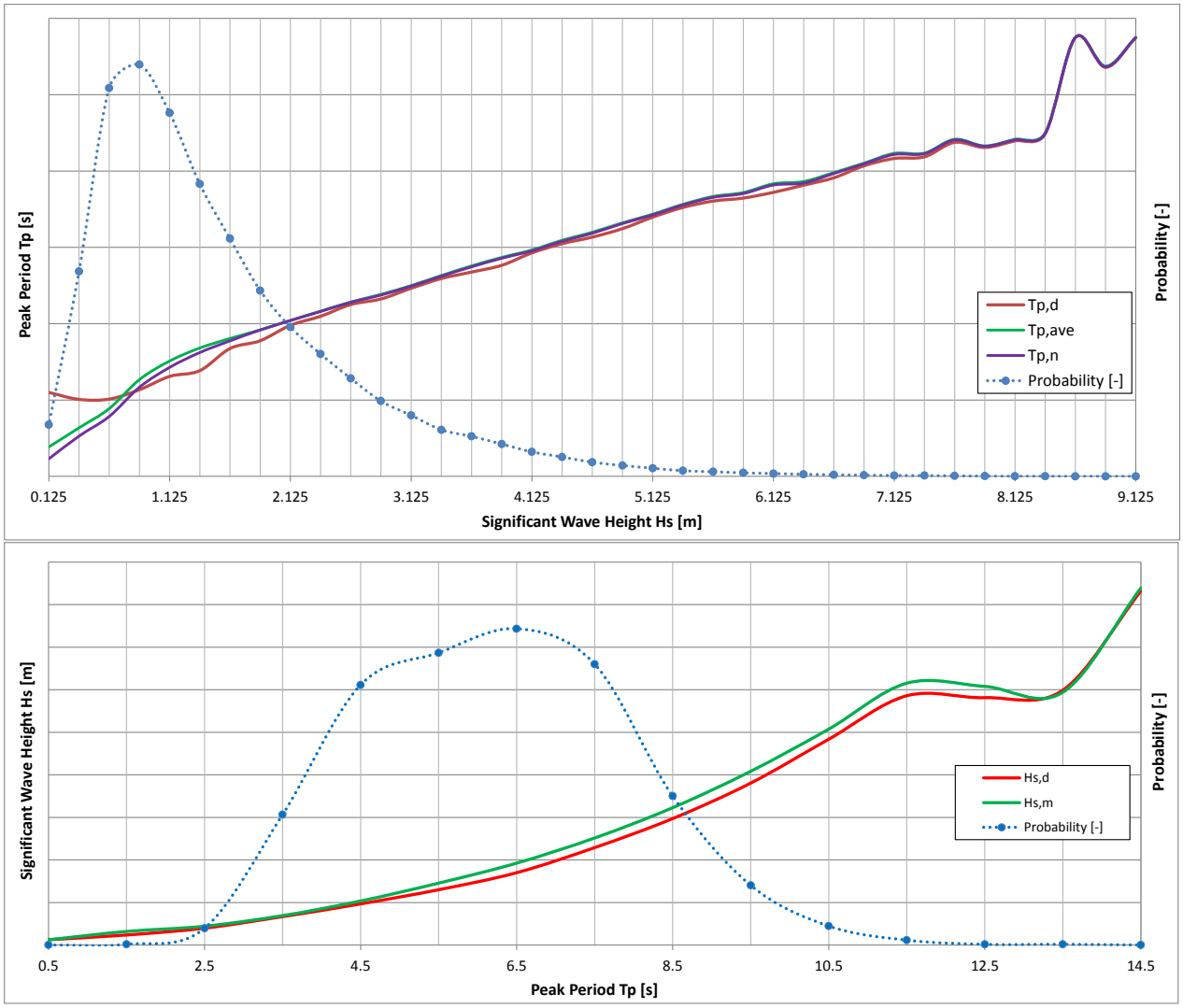

Figure 14: Lumped waves and probability distribution for omnidirectional H_s-T_p SCD of Gemini project (vertical gridlines indicate location of wave height classes *i* and wave period classes *j*)
Upper: Probabilities and wave periods $T_{p,d}$, $T_{p,ave}$ and $T_{p,n}$ for wave height classes $H_{s,i}$
Lower: Probabilities and wave heights $H_{s,d}$ and $H_{s,m}$ for wave period classes $T_{p,j}$

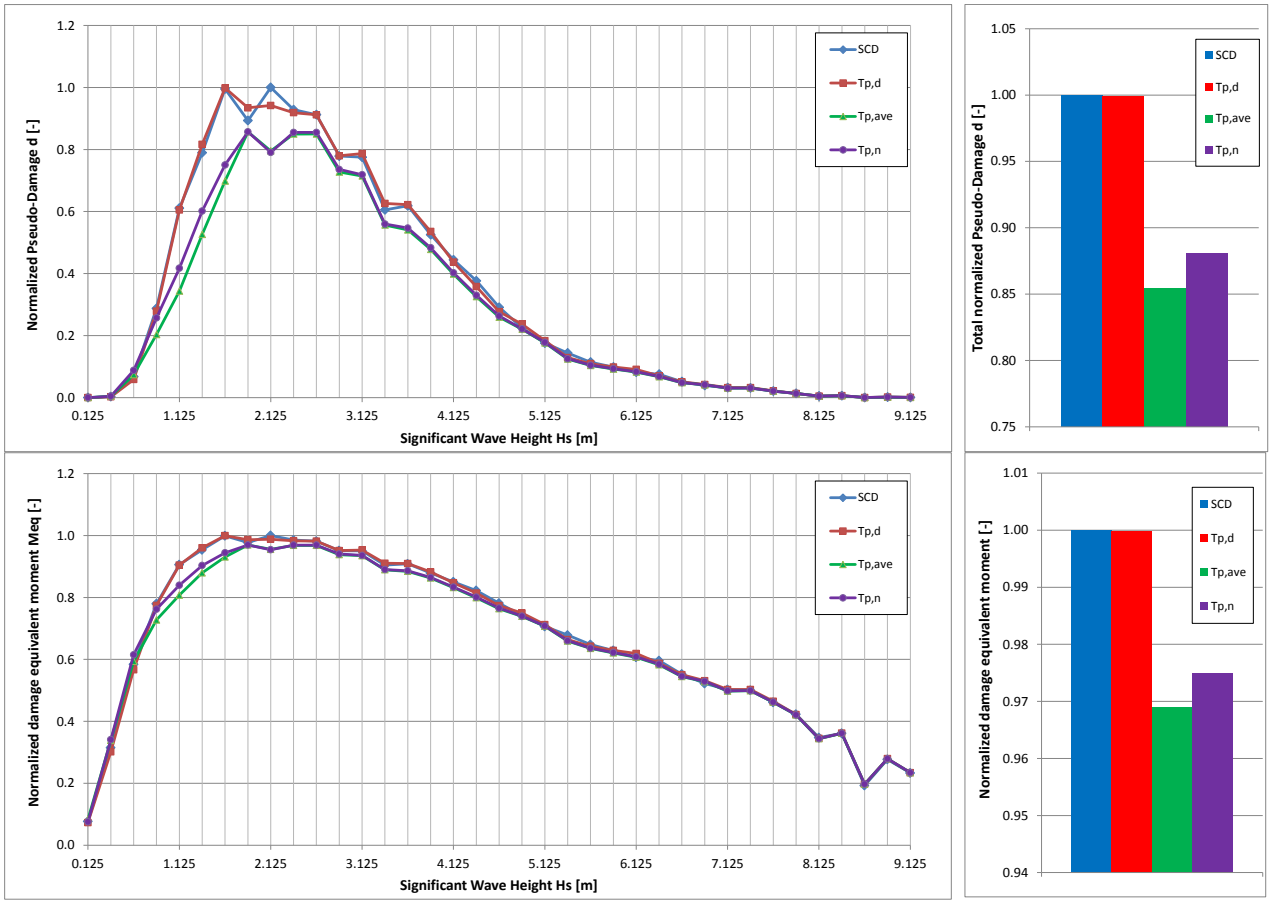

Figure 15: Normalized distributions (*left*) and totals (*right*) of damages (*upper*) and DEMs (*lower*) from SCD compared to lumping approaches $T_{p,d}$, $T_{p,ave}$ and $T_{p,n}$ (vertical gridlines indicate individual locations of wave height classes *i*)

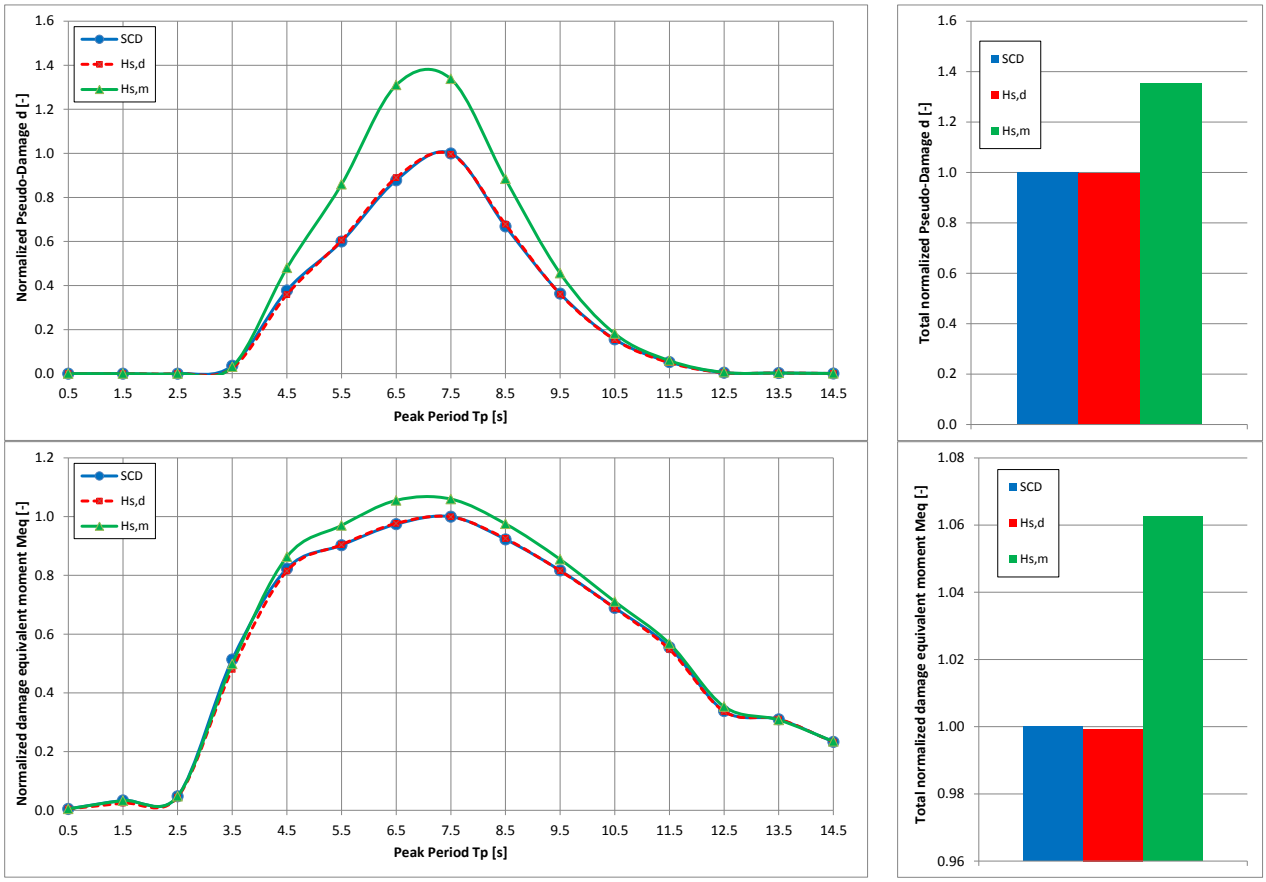

Figure 16: Normalized distributions (*left*) and totals (*right*) of damages (*upper*) and DEMs (*lower*) from SCD compared to lumping approaches $H_{s,d}$ and $H_{s,m}$ (marks on distribution indicate individual locations of wave period classes *j*)

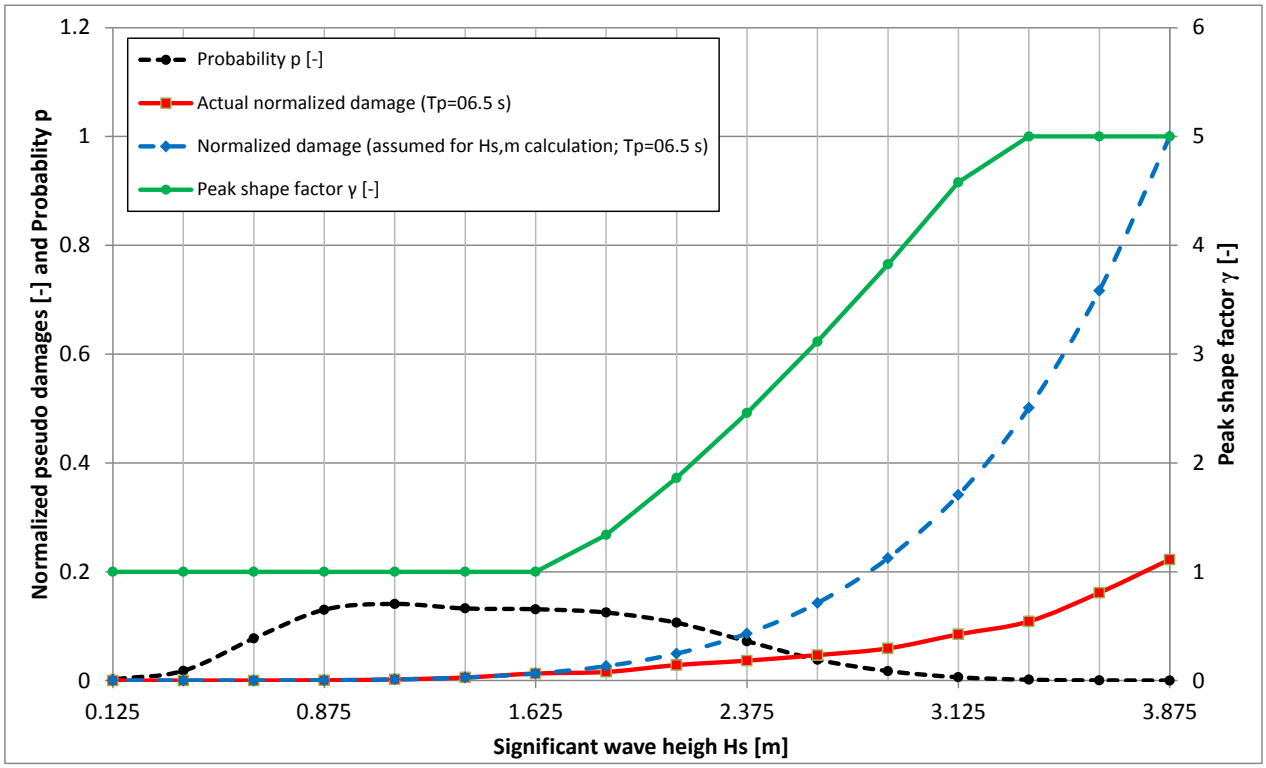

Figure 17: Distribution of calculated and assumed unit damages over wave heights together with peak shape factor and normalized actual probabilities for constant peak period Tp=06.5s

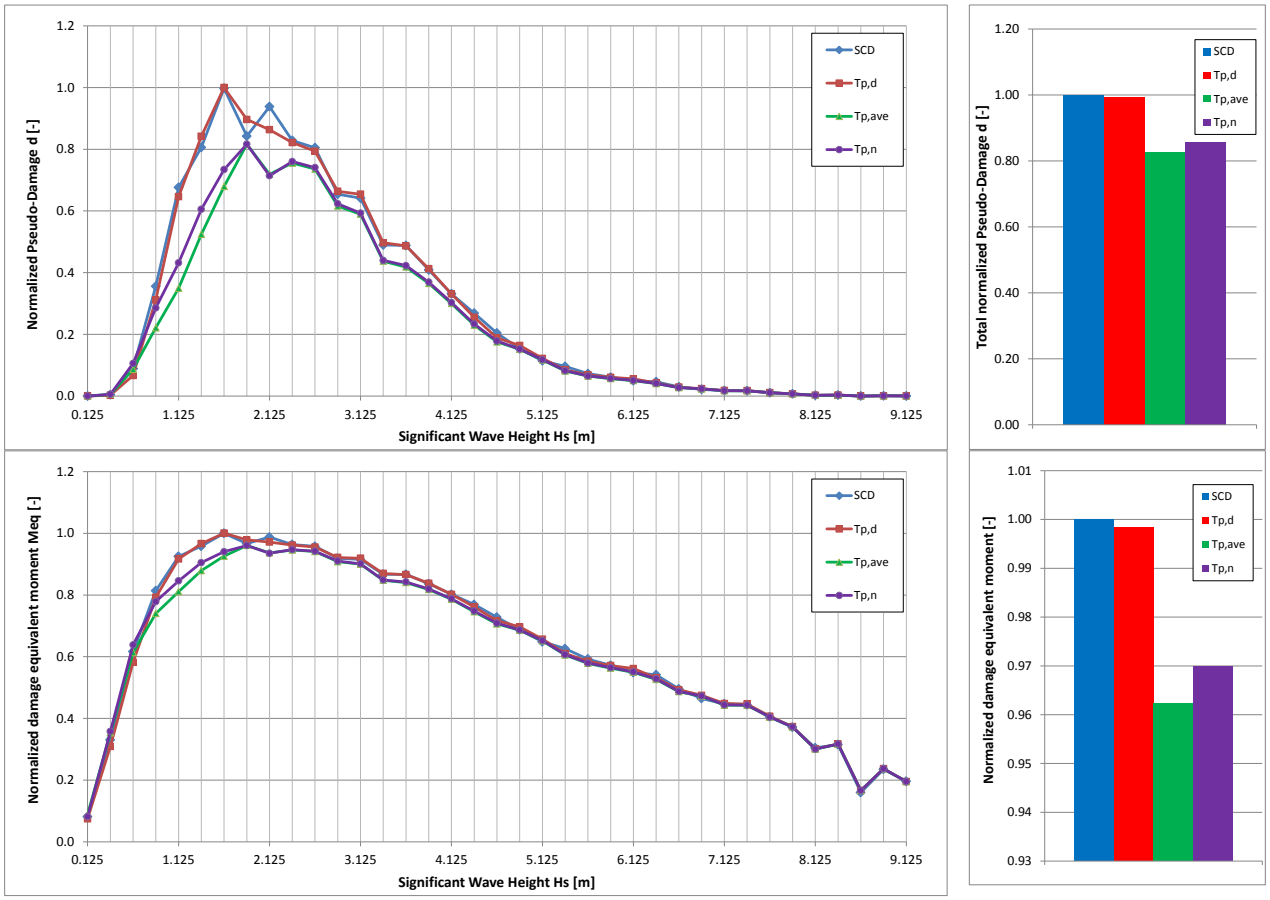

Figure 18: Normalized distributions (*left*) and totals (*right*) of damages (*upper*) and DEMs (*lower*) from SCD compared to lumping approaches $T_{p,d}$, $T_{p,ave}$ and $T_{p,n}$

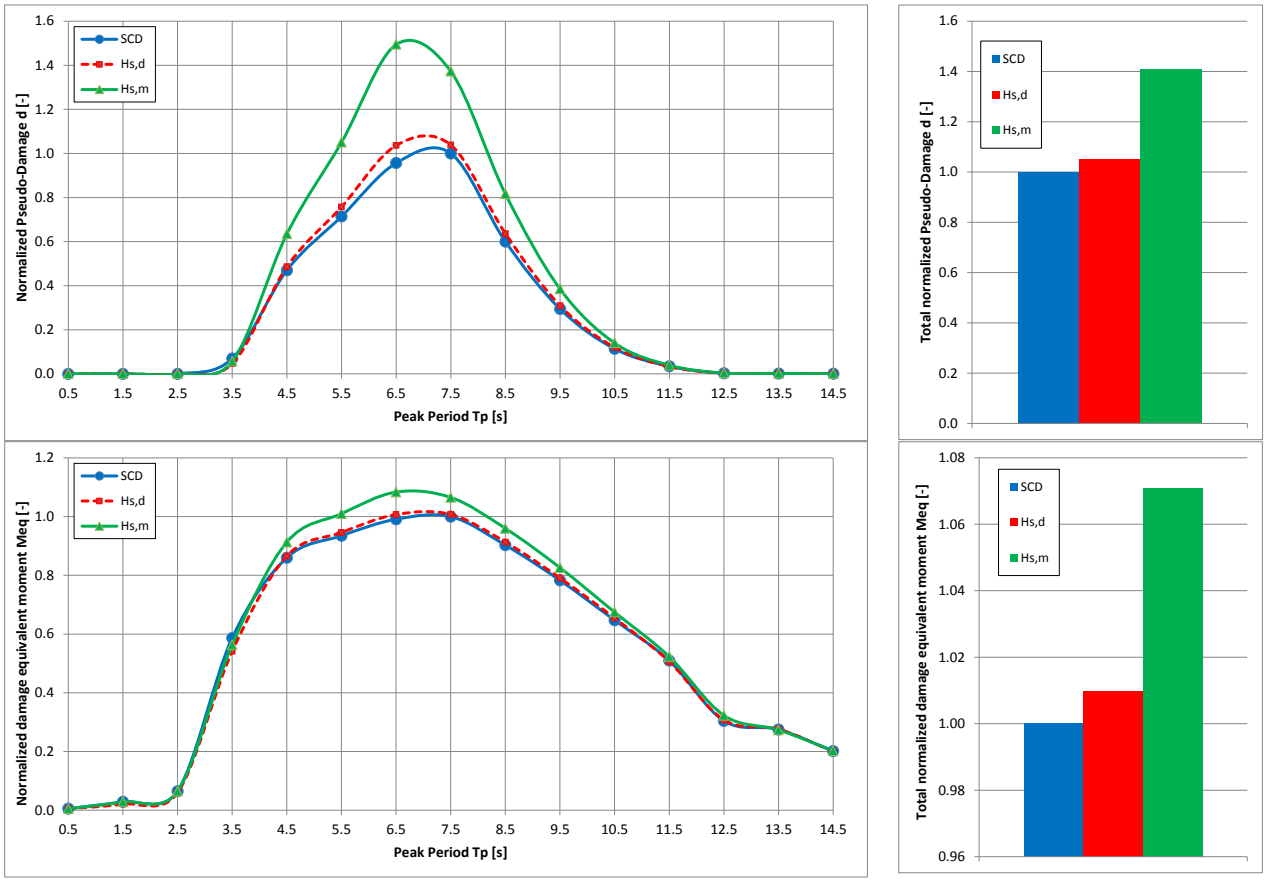

Figure 19: Normalized distributions (*left*) and totals (*right*) of damages (*upper*) and DEMs (*lower*) from SCD compared to lumping approaches $H_{s,d}$ and $H_{s,m}$

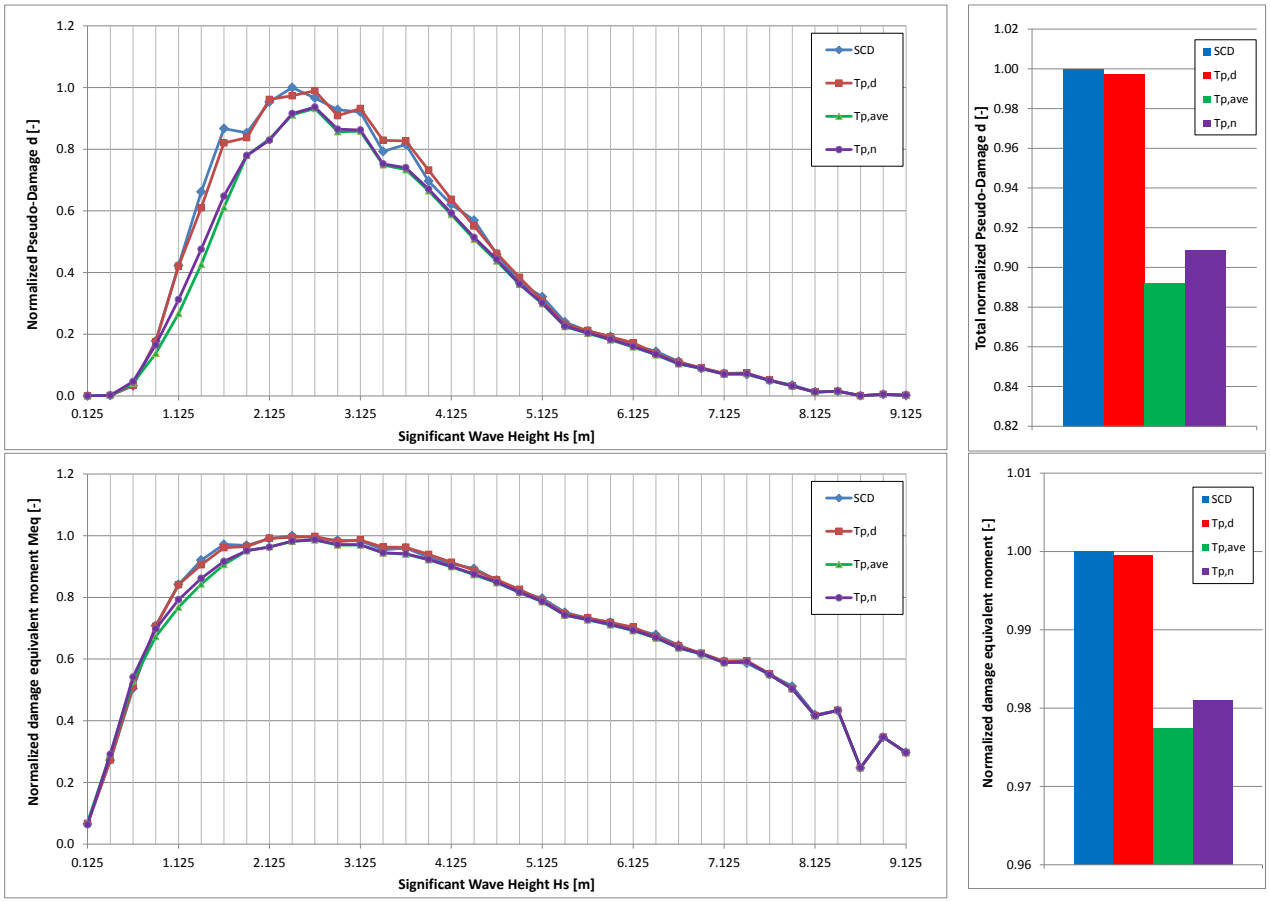

Figure 20: Normalized distributions (*left*) and totals (*right*) of damages (*upper*) and DEMs (*lower*) from SCD compared to lumping approaches $T_{p,d}$, $T_{p,ave}$ and $T_{p,n}$

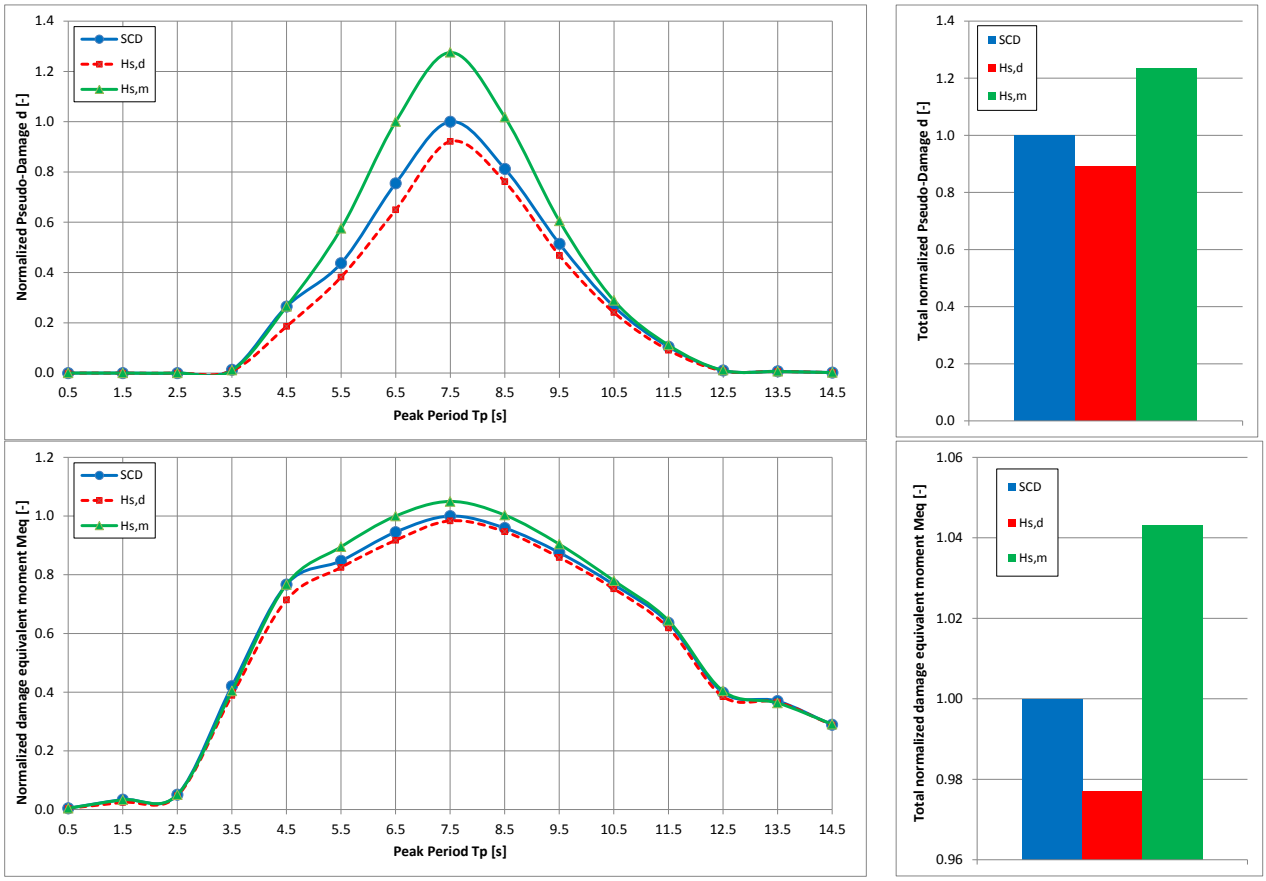

Figure 21: Normalized distributions (*left*) and totals (*right*) of damages (*upper*) and DEMs (*lower*) from SCD compared to lumping approaches $H_{s,d}$ and $H_{s,m}$

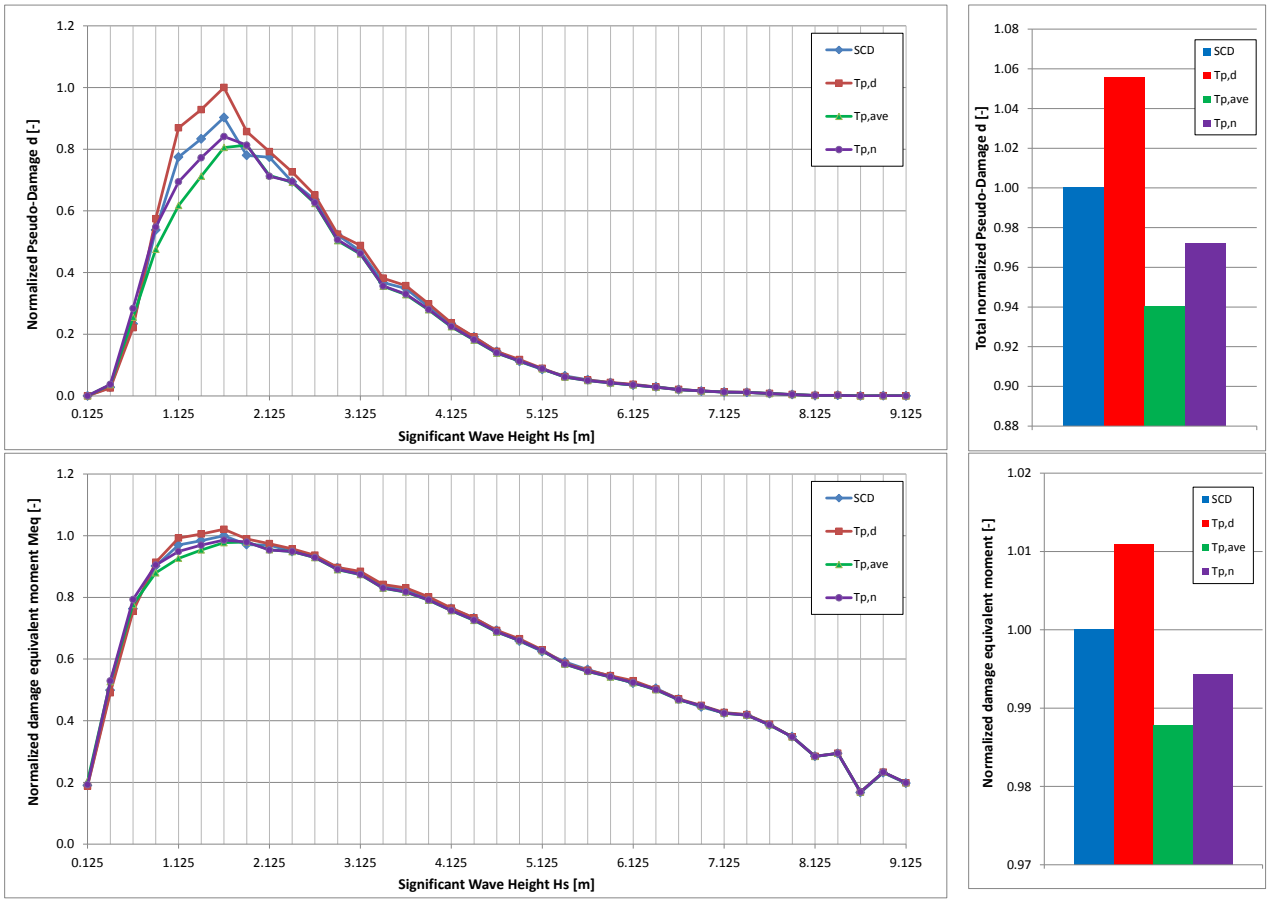

Figure 22: Normalized distributions (*left*) and totals (*right*) of damages (*upper*) and DEMs (*lower*) from SCD compared to lumping approaches $T_{p,d}$, $T_{p,ave}$ and $T_{p,n}$

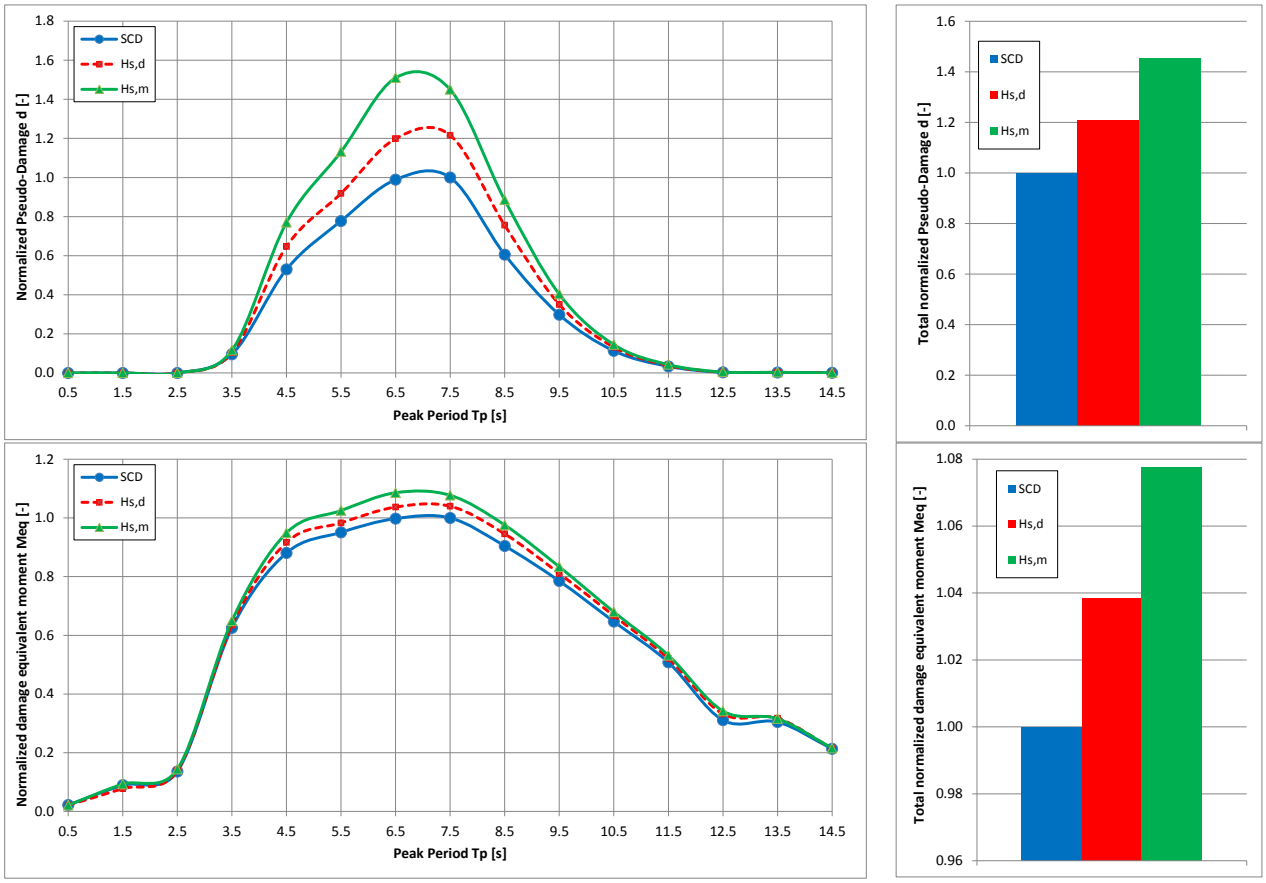

Figure 23: Normalized distributions (*left*) and totals (*right*) of damages (*upper*) and DEMs (*lower*) from SCD compared to lumping approaches $H_{s,d}$ and $H_{s,m}$

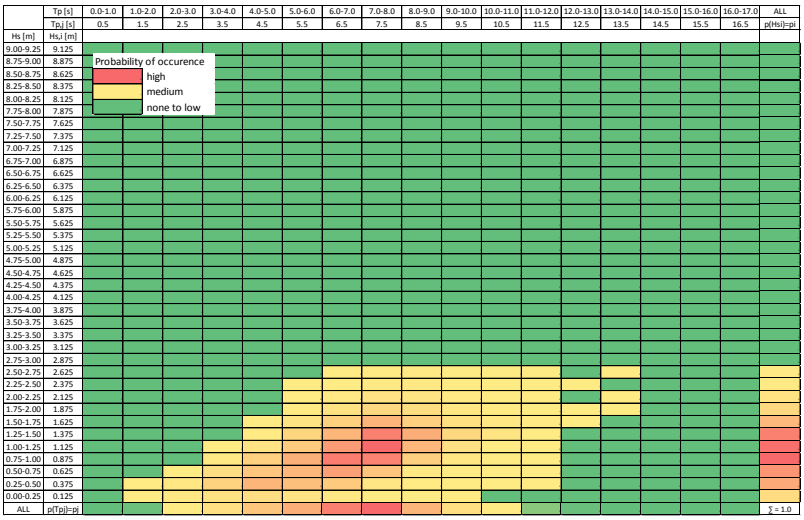

Figure 24: Example SCD for a 90-degree wind-wave misalignment case

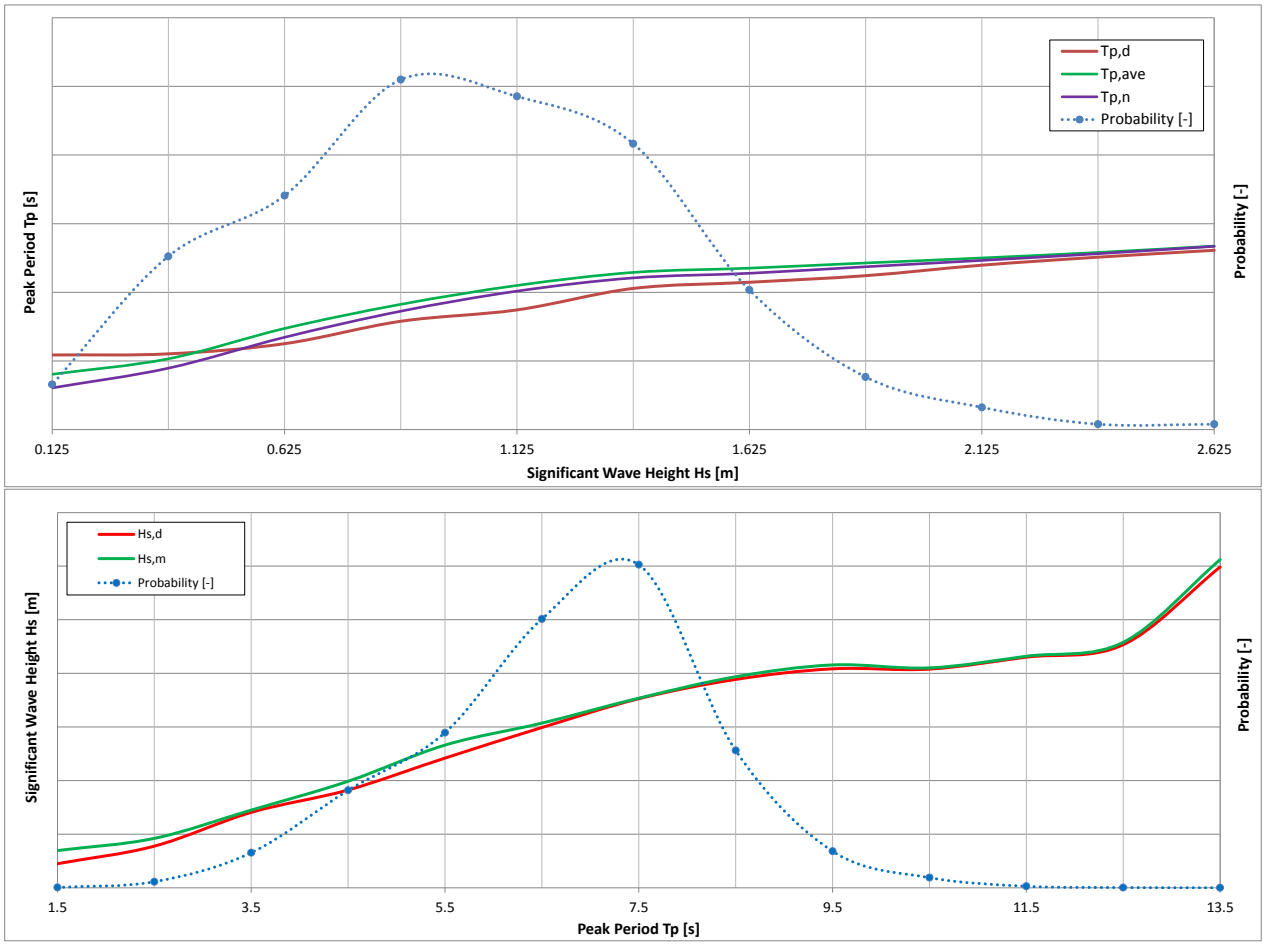

Figure 25: Lumped waves and probability distribution for example 90-degree wind-wave misalignment case H_s-T_p SCD of Gemini project (vertical gridlines indicate location of wave height classes *i* and wave period classes *j*)
Upper: Probabilities and wave periods $T_{p,d}$, $T_{p,ave}$ and $T_{p,n}$ for wave height classes $H_{s,i}$
Lower: Probabilities and wave heights $H_{s,d}$ and $H_{s,m}$ for wave period classes $T_{p,j}$

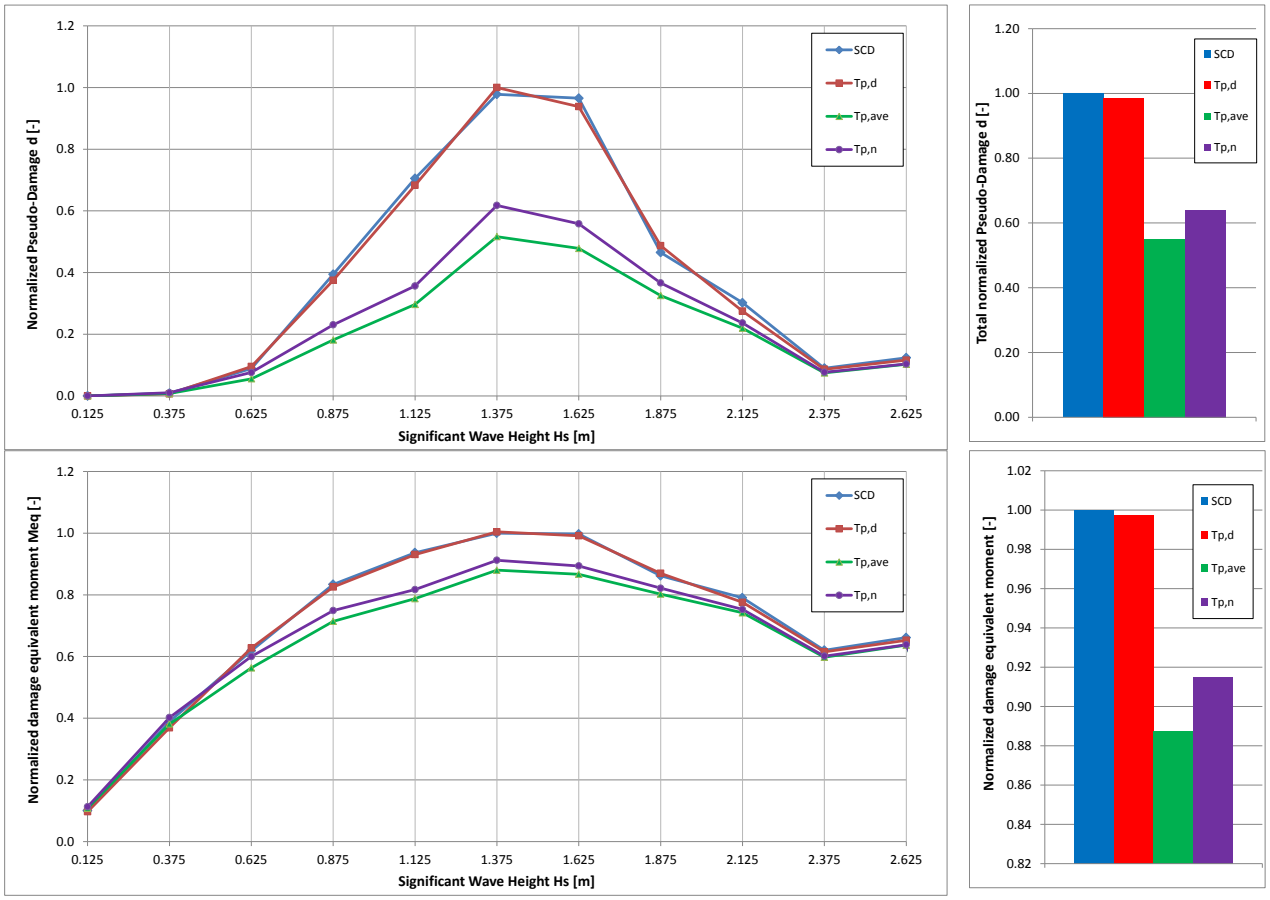

Figure 26: Normalized distributions (*left*) and totals (*right*) of damages (*upper*) and DEMs (*lower*) from SCD compared to lumping approaches $T_{p,d}$, $T_{p,ave}$ and $T_{p,n}$

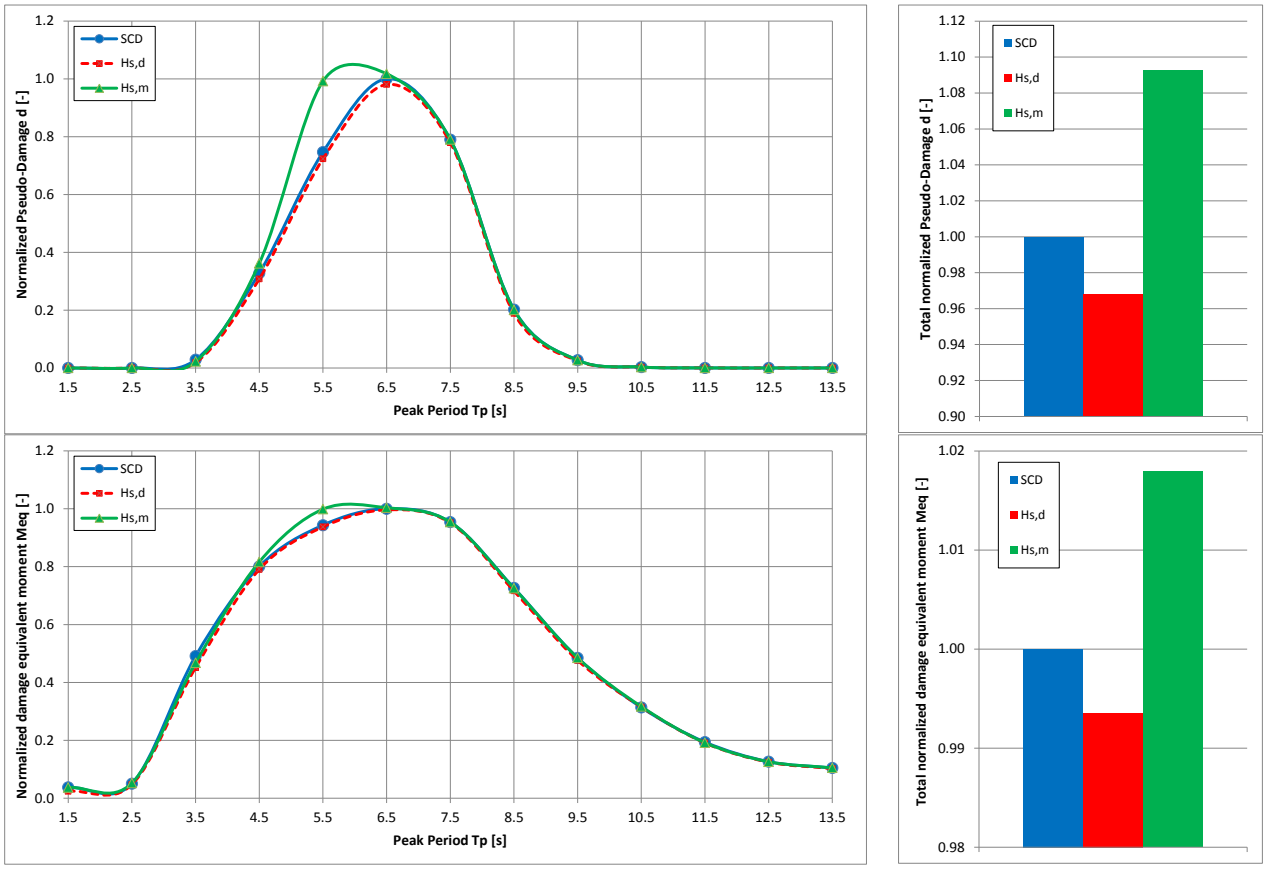

Figure 27: Normalized distributions (*left*) and totals (*right*) of damages (*upper*) and DEMs (*lower*) from SCD compared to lumping approaches $H_{s,d}$ and $H_{s,m}$

Tables

Table 1: Wave lumping methods

Lumped property	Denotation	Reference section
DEWP	$T_{p,d,i}$	3.
Number of wave equivalent period	$T_{p,n,i}$	2.3.
Average wave period	$T_{p,ave,i}$	2.4.
DEWH	$H_{s,d,j}$	3.
MEWH	$H_{s,m,j}$	2.2.

Table 2: Conditions for reference scenario

Reference slope of *S-N* curve *m*	5
Damping ratio (critical) ξ	1%
Reference location in structure	Mudline
SCD	Omnidirectional (H_s-T_p)

Table 3: Damage and DEM error in %

	Wave lumping method				
	$T_{p,d,i}$	$T_{p,ave,i}$	$T_{p,n,i}$	$H_{s,d,j}$	$H_{s,m,j}$
Damage	-0.1	-14.6	-11.9	-0.3	35.4
DEM	0.0	-3.1	-2.5	-0.1	6.2

Table 4: Damage and DEM error in %

	Wave lumping method				
	$T_{p,d,i}$	$T_{p,ave,i}$	$T_{p,n,i}$	$H_{s,d,j}$	$H_{s,m,j}$
Damage	-0.8	-17.5	-14.2	5.0	40.8
DEM	-0.2	-3.8	-3.0	1.0	7.0

Table 5: Conditions for higher damping scenario

Reference slope of *S-N* curve *m*	5
Damping ratio (critical) ξ	4%
Reference location in structure	Mudline
SCD	Omnidirectional (H_s-T_p)

Table 6: Damage and DEM error in %

	Wave lumping method				
	$T_{p,d,i}$	$T_{p,ave,i}$	$T_{p,n,i}$	$H_{s,d,j}$	$H_{s,m,j}$
Damage	-0.2	-10.8	-9.1	-11.0	23.5
DEM	0.0	-2.3	-1.9	-2.3	4.3

Table 7: Conditions for differing S-N curve slope m

Reference slope of *S-N* curve *m*	3
Damping ratio (critical) ξ	1%
Reference location in structure	Mudline
SCD	Omnidirectional (H_s-T_p)

Table 8: Damage and DEM error in %

	Wave lumping method				
	$T_{p,d,i}$	$T_{p,ave,i}$	$T_{p,n,i}$	$H_{s,d,j}$	$H_{s,m,j}$
Damage	5.6	-6.0	-2.8	20.7	45.2
DEM	1.1	-1.2	-0.6	3.8	7.7

Table 9: Conditions for directional SCD case

Reference slope of *S-N* curve *m*	5
Damping ratio (critical) ξ	1%
Reference location in structure	Mudline
SCD	Example 90 degree wind-wave misalignment case (H_s-T_p)

Table 10: Damage and DEM error in %

	Wave lumping method				
	$T_{p,d,i}$	$T_{p,ave,i}$	$T_{p,n,i}$	$H_{s,d,j}$	$H_{s,m,j}$
Damage	-1.4	-45.0	-35.9	-3.2	9.3
DEM	-0.3	-11.3	-8.5	-0.6	1.8

Table 11: Damage error summary in [%]

Case (Section)	Wave lumping method				
	$T_{p,d,i}$	$T_{p,ave,i}$	$T_{p,n,i}$	$H_{s,d,j}$	$H_{s,m,j}$
Reference (4.2.2)	-0.1	-14.6	-11.9	-0.3	35.4
Interface (4.2.3)	-0.8	-17.5	-14.2	5.0	40.8
Damping (4.2.4)	-0.2	-10.8	-9.1	-11.0	23.5
Slope m (4.2.5)	5.6	-6.0	-2.8	20.7	45.2
90-deg SCD (4.2.6)	-1.4	-45.0	-35.9	-3.2	9.3

Paper 3: Damage Equivalent Wind-Wave Correlations on Basis of Damage Contour Lines for the Fatigue Design of Offshore Wind Turbines

Authors:	Patrik Passon
Submitted to:	Journal '*Renewable Energy*'
Status:	Accepted by '*Renewable Energy*'.
Remarks:	Latest submitted revision attached.

Damage Equivalent Wind-Wave Correlations on Basis of Damage Contour Lines for the Fatigue Design of Offshore Wind Turbines

Patrik Passon
RAMBØLL Wind, Esbjerg, Denmark
Telephone: +45 5161 7038, Email: pkp@ramboll.com

An adequate representation of the site-specific wind-wave joint distribution is essential for cost-efficient and reliable designs of offshore wind turbines. Therefore, the wind and wave climates are subjected to a correlation of wind and wave parameters for design purposes. These correlations are often based on a lumping of the directional wave climate and subsequent association of the lumped wave climate to the directional wind climate. Preservation of the hydrodynamic fatigue distribution from the full wave climate is an important aspect in the wind-wave correlation process which requires an adequate consideration of the dynamics from the offshore wind turbine. However, only a few wind-wave correlation methods exist for the fatigue design of offshore wind turbines and none of them take the dynamics of the full structure adequately into account. In this study a new wind-wave correlation method has been developed and introduced. The new method is based on the establishment of damage contour lines which are used to determine the sea-state parameters that ensure simultaneous compliance with damage equivalency criterions at different locations within the offshore wind turbine. This simultaneous damage equivalency throughout the structure together with the straightforward derivation of the corresponding damage equivalent sea-state parameters constitutes the novelty of the presented wind-wave correlation method.

KEY WORDS: Offshore Wind Turbines, Wave Lumping, Wind-Wave Correlation, Damage Contour Lines, Fatigue Design

NOMENCLATURE

$\boldsymbol{D}^*$	Unit damage matrix
$\boldsymbol{D}_s^*$	Scaled unit damage matrix
$\boldsymbol{D}$	Damage matrix
d	Fatigue damage [-]
p	Probability [-]
v	Hub height wind speed [m/s]
H_s	Significant wave height [m]
T_p	Peak period [s]
DCL	Damage contour line
SCD	Wave scatter diagram
OWT	Offshore wind turbine

1 INTRODUCTION

The fatigue design of offshore wind turbines (OWTs) is governed by dynamic responses from simultaneous aerodynamic and hydrodynamic loads. State-of-the-art methods to determine the corresponding design loads in a detailed design process is represented by integrated load calculations with aero-elastic tools under consideration of simultaneous wind and wave conditions as described e.g. by Passon & Branner (2014). The establishment of these simultaneous wind-wave conditions requires a derivation of wind-wave joint parameters from a site- and project-specific met-ocean database. In practice the combined wind-wave parameters are established by a lumping of the wave climate and corresponding association to the wind climate, which hereinafter is denoted as wind-wave correlation. In this wind-wave correlation process it is very important to preserve the fatigue damages introduced from the underlying wind and wave climates in order to ensure a cost-efficient and reliable design. However, accurate wind-wave correlation methods for the fatigue design of OWTs do not exist and guidance is also missing in all relevant design guidelines, e.g. IEC61400-3 (2009), DNV-OS-J101 (2014) and GL-COWT (2012). Hence, designers need to apply simplified correlation methods which do not necessarily capture the dynamics over the entire OWT and consequently introduces an uncertainty in the calculated fatigue design loads, in particular for hydrodynamically sensitive structures.

Passon & Branner (2015) showed that the lumping approach for the wave climate has a significant influence on the accuracy of calculated hydrodynamic fatigue loads. Furthermore, they introduced a damage equivalent lumping method for the wave climate that allows for preservation of the hydrodynamic fatigue damage distribution. However, this method does not consider a coupling of the lumped wave climate with the wind climate as required in the detailed design process of OWTs. Analogously to the wave lumping, the association of the wave climate with the wind climate has a significant influence on accuracy of the fatigue design loads.

Therefore, an improved wind-wave correlation method for the fatigue design of OWT is introduced in the present article. The new method allows for

derivation of damage equivalent sea-state parameters, in terms of wave height and period, for each combination of wind speed, wind direction and wave direction. Here, the lumping of the wave climate and the connection to the wind climate is performed simultaneously in one integral step. The corresponding sea-state parameters are determined from damage contour lines (DCLs) obtained for pre-established target damage levels at different locations within the OWT e.g. at mudline and tower top. Damage equivalency throughout the structure is ensured by selection of coinciding combinations of sea-state parameters from DCLs at different locations within the OWT.

The new wind-wave correlation method presented in this article is an extension of the wave lumping method presented by Passon & Branner (2015). Calculation examples including an assessment of the accuracy with respect to a full wave climate and alternative wave lumping methods complement the introduction of the new method. The met-ocean database of the Veja Mate Offshore Wind Farm project as established by Rambøll Wind is used for that purpose. The database comprises relevant met-ocean information in a high degree of detail and quality. Veja Mate is planned as a 400 MW offshore wind farm located at 40m water depth within the German exclusive economic zone. The project is developed by Veja Mate Offshore Holding GmbH and their representative K2 Management GmbH with SWT-6.0-154 wind turbines from Siemens Wind Power A/S. Furthermore, the monopile type substructures are designed by Rambøll Wind.

2 ORGANIZATION OF WIND-WAVE PARAMETERS FOR FATIGUE DESIGN PURPOSES

Typically, detailed designs of OWTs are based on integrated load calculations under consideration of simultaneous wind and wave conditions. All relevant met-ocean parameters are commonly organized by primary parameters and associated parameters. Primary parameters form the general structure of the fatigue load cases and are defined a priori due to their project-specific but not site-specific character. The primary parameters used in this article are:

- Mean wind speed at hub height v.
- (Mean) wind direction φ_{wind}.
- (Mean) wave direction φ_{wave}.

Associated parameters are site-, project- and structure-specific and derived for the individual combinations of primary parameters. In the context of this article the relevant associated parameters are:

- Significant wave height H_s.
- Peak period T_p.
- Wind-wave joint probability of occurrence p.

Table 1 shows an organization for the relevant selection of primary and associated wind-wave parameters. The pre-defined primary parameters are filled in while the values of the associated parameters are left empty. Each line in the table represents one set of primary and associated parameters used for design load calculations note that e.g. a hub wind speed of 2.5 m/s represents wind speeds in the interval between 2.0 m/s and 3.0 m/s.

Table 1: Example structure of load case table parameters for one directional wind-wave combination used in the fatigue design of OWT

v	φ_{wind}	φ_{wave}	H_s	T_p	p
2.5	30	120			
3.5	30	120			
…	…	…	…	…	…
31.5	30	120			
32.5	30	120			

The calculation of the probabilities of occurrence p from wind distributions and wind-wave misalignment information is rather straightforward. Derivation of adequate wave parameters on the other hand is more complicated since a range of H_s-T_p combinations, described by wave scatter diagrams (SCD), or more properly denoted as wave scatter matrices, can occur for each set of the primary parameters mean wind speed, wind direction and wave direction. However, for practical applications typically only one unique H_s-T_p combination is associated to each individual set of primary parameters, mainly in order to limit the actual number of load simulations. Consequently a lumping of the directional, two-dimensional SCDs conditioned on the individual combinations of wind speed, wind direction and wave direction is required. This lumping and association of the wave climate with the wind climate constitutes the correlation of wind-wave parameters for fatigue design purposes. Unfortunately, detailed information on directional SCDs per set of primary parameters is often not available or disregarded for the sake of simplicity. In such cases the designer needs to complement the missing information on basis of simplifying assumptions which has an uncertain influence on the accuracy of design loads. However, this scenario is not addressed in the present article.

3 CORRELATION OF WIND-WAVE PARAMETERS FOR THE FATIGUE DESIGN

Starting with the full wave climate described by directional SCDs comprising of $i=1..n$ wave height classes $H_{s,i}$ and $j=1..m$ wave period classes $T_{p,j}$ the wave lumping aims at the establishment of directional H_s-T_p relations with one representative peak period associated to each significant wave height or vice versa. Passon & Branner (2015) investigated various lumping approaches for the isolated wave climate and showed that fatigue damages can be significantly over- or underestimated if the lumping approach does not account for the dynamics of the structure and proper damage

equivalency criterions.

Passon & Branner (2015) presented a new method allowing for lumping of wave heights on the given wave periods for all wave period classes $j=1..m$ of a SCD resulting in a damage equivalent $H_{s,d,j}$-$T_{p,j}$ relation for the underlying full wave climate. Alternatively, the method can analogously be applied for lumping of wave periods on the given wave heights for all wave height classes $i=1..n$ resulting in a damage equivalent $H_{s,i}$-$T_{p,d,i}$ relation. In both cases the fatigue damage distribution could be well preserved over $T_{p,j}$ or $H_{s,i}$ respectively. Both relations obtained by Passon & Branner (2015) are plotted for their omnidirectional reference case in Figure 1. However, despite the fact that both relations represent the same SCD and reference conditions it can be seen that they do not coincide. Nevertheless, each relation ensured a very good preservation of the fatigue damage distribution over $H_{s,i}$ and $T_{p,j}$ respectively. The reason for the differences is the fact that each $H_{s,i}$ bin in the $H_{s,i}$-$T_{p,d,i}$ relation comprises a different probability compared to the corresponding $H_{s,d,j}$ value in the $H_{s,d,j}$-$T_{p,j}$ relation. This is of course analogously valid for the $T_{p,j}$ bins. It is therefore not possible to interpolate $H_{s,d,j}$ values for $T_{p,j}$ from the $H_{s,i}$-$T_{p,d,i}$ relation and vice versa. For similar reasons the established relations can also not directly be used for interpolation of associated wave parameters for the sets of primary parameters in the wind-wave correlation process.

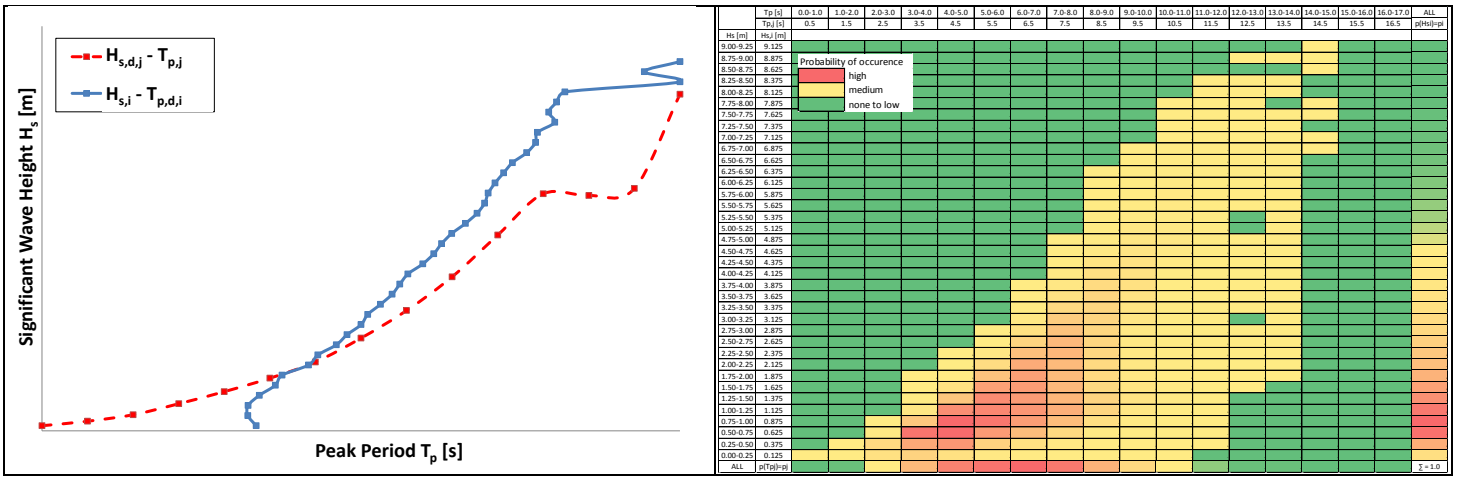

Figure 1: Comparison of the ($H_{s,i}$ - $T_{p,d,i}$) with the ($H_{s,d,j}$ - $T_{p,j}$) relation (left) for the reference case with the omnidirectional SCD (right) from the Gemini offshore wind farm site, taken from Passon & Branner (2015).

Passon & Branner's (2015) method is based on the damage equivalent lumping of a set of wave periods for a given wave height or vice versa without consideration of any correlations to the wind or the simultaneous fulfillment of damage equivalency at different locations of the OWT structure under consideration. Therefore, their wave lumping method is here adjusted and extended for the establishment of wind-wave correlations in terms of a unique, damage equivalent H_s-T_p combination per wind speed bin, wind direction and wave direction. This new wind-wave correlation method does not require a predetermined wave height or period for the lumping of the full wave climate and does furthermore allow for simultaneous preservation of hydrodynamic fatigue damages at different locations in the OWT structure. The new wind-wave correlation method comprises the following three (subsequent) steps:

- Calculation of unit damage matrices.
- Establishment of the hydrodynamic fatigue damage over wind speed.
- Determination of damage equivalent wave height and wave period combinations.

Descriptions and further details on the individual steps are provided in the following sections 3.1 to 3.3. This is complemented by examples using a generic OWT configuration roughly based on the NREL 5MW turbine according to Jonkman et al. (2007), a large diameter (>8m) monopile substructure at 40m water depth and a first (bending) eigenfrequency of f_0 = 0.25 Hz. Met-ocean conditions in terms of wind and wave climates are taken from the detailed Veja Mate project database, where individual SCD are available per combination of wind speed, wind direction and wave direction. This comprises in total 37·144= 5328 SCDs covering 37 wind speeds for the wind speed range from 0 to 37m/s in 1m/s bin sizes and 144 directional combinations per wind speed, i.e. 12 wind directions combined with 12 wave directions. The sum of probabilities of occurrence over all individual H_s-T_p combinations in a SCD corresponds to the total probability of occurrence for that particular wind speed, wind direction and wave direction.

Naturally, many of these primary parameter combinations have a zero probability of occurrence and are consequently excluded from the wind-wave correlation process. For the present article, met-ocean data are exclusively taken from the Veja Mate project in the North Sea as shown in Figure 2. However, the Veja Mate database is property of Veja Mate Offshore Holding GmbH and can as such not be fully enclosed in a public article. The corresponding quantities and relations of the met-ocean data, such as SCDs and wind distributions, are therefore only shown in a qualitative manner in the present article.

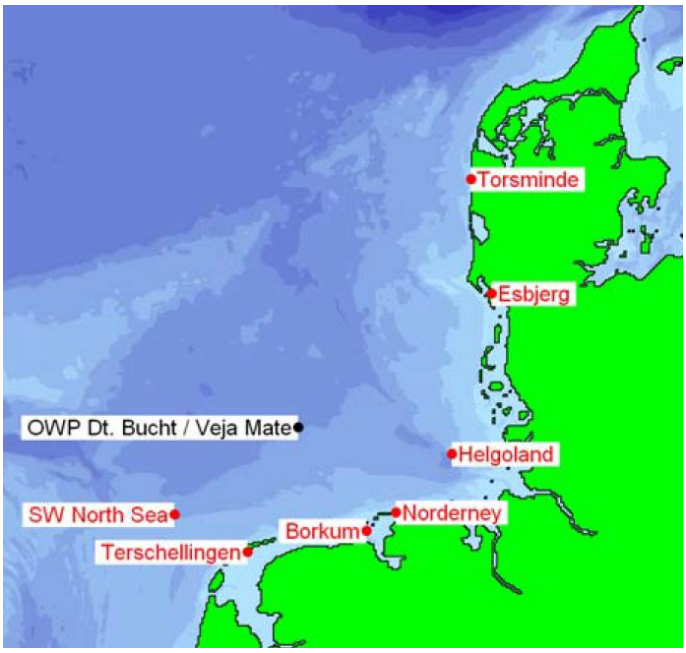

Figure 2: Location of the planned Veja Mate offshore wind farm

3.1 Unit Damage Matrix

Passon & Branner (2015) presented a method for establishment of a unit damage matrix $\boldsymbol{D}^*$ and the corresponding benefits. This unit damage matrix contains fatigue damages d for each individual H_s-T_p combination of a SCD. The individual damages d are obtained from dynamic calculations in time or frequency domain approaches assuming unit probabilities for each H_s-T_p combination. For convenience, a time domain based approach as indicated in Figure 3 is briefly summarized below. Details for a frequency domain based approach can for example be found in Hapel (1990) or Barltrop & Adams (1991).

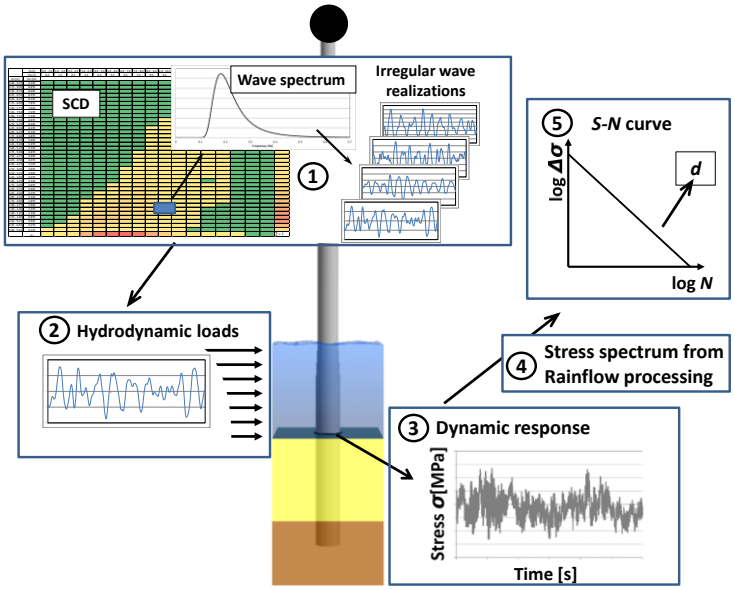

Figure 3: Time domain based calculation of damage per H_s-T_p combination

For each H_s-T_p combination in the SCD a number of irregular wave time series is established. Number and length of these time series must be sufficiently large to cover stochastic uncertainties as analogously shown by Haid et al. (2013) for floating type OWTs. The OWT structure is then subjected to the irregular wave realizations in dynamic analyses. Responses from the dynamic analyses are extracted and processed on basis of the well-known Rainflow counting method in order to obtain stress spectra which are subsequently subjected to a *S-N* curve for determination of the

fatigue damage d.

In analogy to the derivation of damage equivalent loads, the calculation of the individual unit damages $d_{i,j}^{*}$ in $\boldsymbol{D}^{*}$ is based on representative configuration parameters, e.g. with respect to the OWT structure, damping, location of damage extraction and S-N curve slope m. Further details on the influence of configuration parameters are provided by section 4.2 in Passon & Branner (2015).

3.1.1 Damage Calculation

Following the linear damage accumulation hypothesis according to Palmgren (1924) and Miner (1945), actual fatigue damages $d_{i,j}$ for each $H_{s,i}$-$T_{p,j}$ combination in the SCD can be obtained by simple scaling of the unit damages $d_{i,j}^{*}$ in $\boldsymbol{D}^{*}$ with actual probabilities $p_{i,j}$. This is illustrated in Figure 4 for calculation of actual damages $d_{i,j}$ in the damage matrix $\boldsymbol{D}$ for an example $H_{s,i}$-$T_{p,j}$ combination according to Eq. 1.

$$d_{i,l} = p_{i,l} \cdot d_{i,l}^{*} \qquad \text{Eq. 1}$$

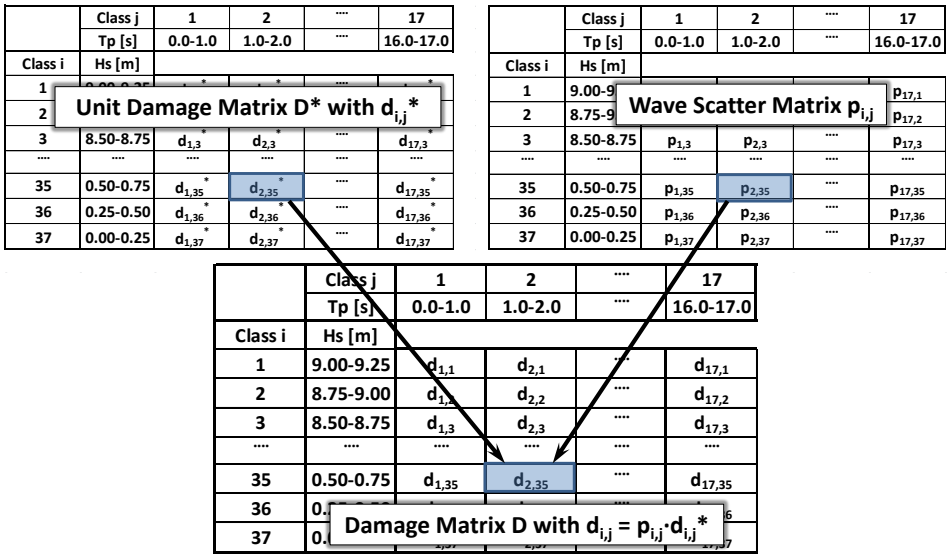

Figure 4: Illustration of damage calculation with the $\boldsymbol{D}^{*}$.

3.1.2 Damage Contour Line

$\boldsymbol{D}^{*}$ can also be used for determination of damage equivalent sea-state parameters for given sets of target damage values d and probability values p. In that case the complete unit damage matrix $\boldsymbol{D}^{*}$ needs first to be scaled by the probability p under consideration in order to obtain the scaled damage matrix $\boldsymbol{D}_s^{*}$ according to Eq. 2.

$$\boldsymbol{D}_s^{*} = p \cdot \boldsymbol{D}^{*} \qquad \text{Eq. 2}$$

This is illustrated in Figure 5 for the OWT configuration described above. The colored surface represent scaled damages $d_{s,i,j}^{*}$ in $\boldsymbol{D}_s^{*}$ for the individual $H_{s,i}$-$T_{p,j}$ combinations obtained from the unit damages $d_{i,j}^{*}$ in $\boldsymbol{D}^{*}$ scaled by the example probability $p = 0.086$ which could e.g. represent the total probability of a SCD. Here, an example target damage level[1] of $d = 0.123$ is assumed and represented by the black plane. The intersection curve forms the DCL for all H_s-T_p combinations resulting in the same target damage d for a probability of occurrence p. It should be highlighted that this is only valid in case the target damage level d has been obtained for the same conditions (S-N curve slope, damping, etc.) as used for establishment of $\boldsymbol{D}^{*}$.

[1] Section 3.2 elaborates in more detail on the determination of target damage levels d.

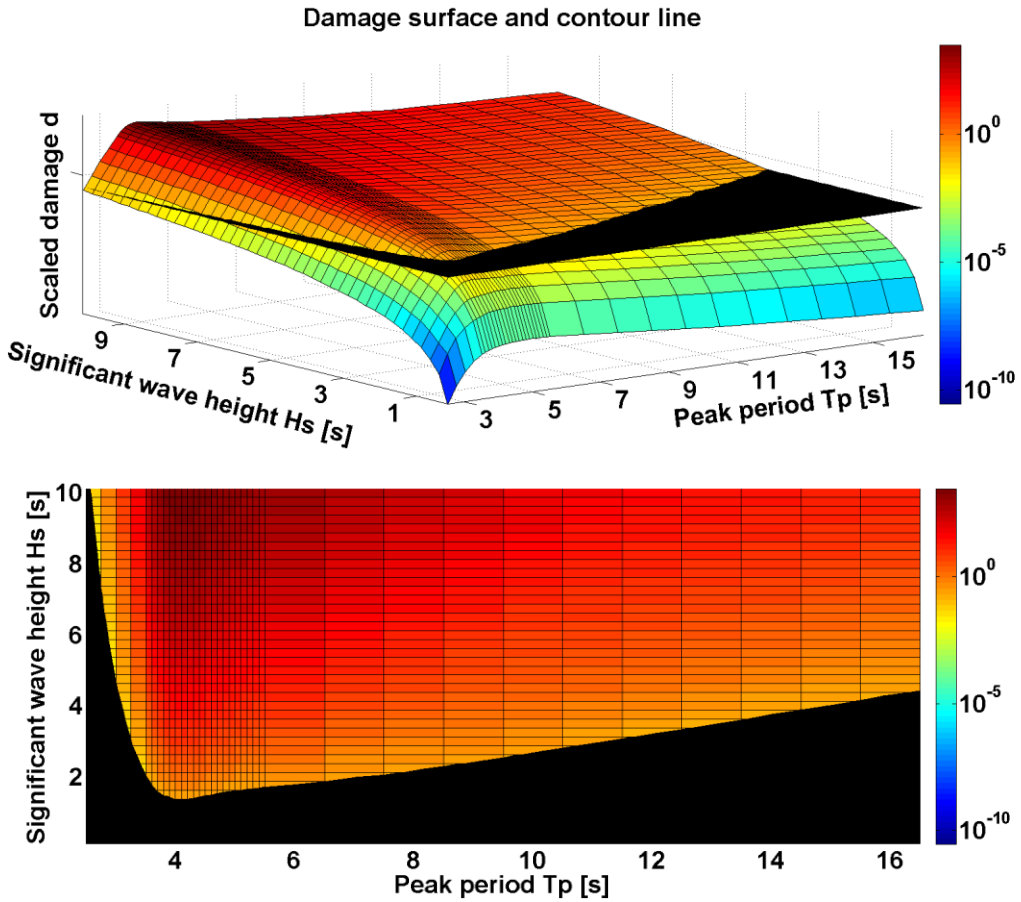

Figure 5: DCL from intersection of probability scaled damage surface with constant target damage level (horizontal black plane).

For example, let the probability p and the target damage level d be known from calculations at mudline for a given OWT configuration. Following the previously introduced approach the corresponding DCL can now be established with the unit damage matrix $\boldsymbol{D}^*$. Each H_s-T_p combination on the DCL is a damage equivalent representation of underlying SCD at mudline. However, almost all H_s-T_p combinations from this DCL are not a damage equivalent SCD representation at other locations within the OWT such as at interface. It is therefore very important to select a H_s-T_p combination from the mudline DCL which introduces an adequate damage equivalent representation of the SCD at all other locations within the OWT as well.

This selection is performed on basis of two DCLs established at sufficiently different locations within the OWT as further addressed in section 3.3. Both DCLs are subsequently projected into the H_s-T_p plane and each of their intersection(s) introduces an adequate, damage equivalent H_s-T_p combination for both locations as well as the entire OWT.

3.1.3 Discussion

Generally, the grid of $H_{s,i}$-$T_{p,j}$ combinations in $\boldsymbol{D}^*$ can be the same as in the SCDs. However, significant changes of the (scaled) unit damage distribution can be observed when T_p is close to the period of the structure's first eigenmode due to pronounced dynamic effects. It is therefore beneficial to establish the unit damage matrix $\boldsymbol{D}^*$ with a finer resolution of T_p in the vicinity of the first eigenperiod as indicated by the narrower gridlines in Figure 5.

Furthermore, a similar trend of significant changes can be observed when moving towards shorter wave periods. Here, the reason for the changes in fatigue damages is introduced from two influences. On one hand the decreased peak period corresponds to a decreased mean wave period T leading to an increased number of load cycles per time $n_{LC} = 1/T$ which linearly increases the fatigue damage. On the other hand the ratio f_e/f_0 of excitation frequency $f_e = 1/T$ to first eigenfrequency f_0 increases as well with decreasing wave periods T which leads to decreasing dynamic responses. This can be well observed for the dynamic amplification function example of a single-degree-of-freedom system in Figure 6. Short wave periods correspond to the right side of the figure with dynamic amplification factors even below 1 while long wave periods correspond to the left side with dynamic responses transforming into quasi-static. This region of very short wave periods is not included in Figure 5, but can for example be observed in Figure 8. However, this wave period region is of low practical interest for the examples presented in this article and is therefore not accounted for by a finer resolution of T_p in the unit damage matrix $\boldsymbol{D}^*$.

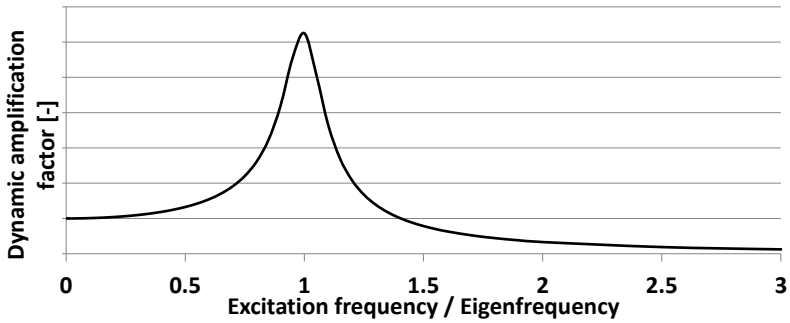

Figure 6: Example dynamic amplification function for an example single-degree-of-freedom system

3.2 Hydrodynamic Fatigue Damage over Wind Speed

An essential task in the establishment of damage equivalent wind-wave correlations is the calculation of hydrodynamic target fatigue damages over wind speeds. These target damages in combination with the corresponding probabilities p are required for establishment of DCLs and the subsequent determination of damage equivalent sea-state parameters. Ideally, this is based on a detailed SCD representation of the wave climate conditioned on wind speed, wind direction and wave direction as has been established for the Veja Mate project and used in the present article.

Damage matrices $\boldsymbol{D}$ for each combination k of wind speed, wind direction and wave direction are calculated by the introduced scaling approach according to Eq. 1. The target damage level d_k is obtained as the sum of all $d_{i,j}$ in $\boldsymbol{D}$ while the total probability p_k is obtained as the sum of all $p_{i,j}$ in the SCD. Based on a given wind and wave direction the individual steps for calculation of the hydrodynamic target fatigue damages are exemplarily illustrated for the wind speed v_k=5.5m/s in Figure 7.

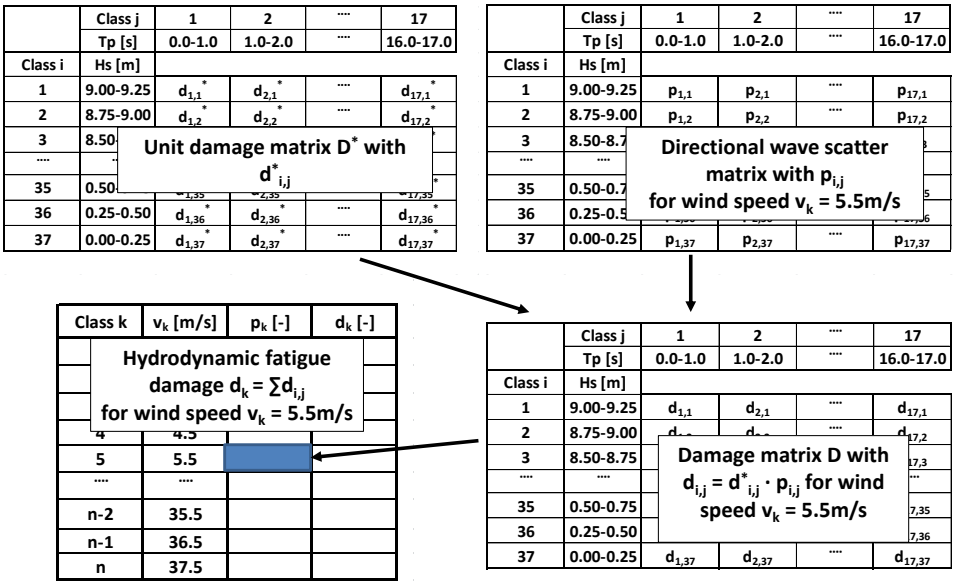

Figure 7: Calculation of hydrodynamic fatigue damage per wind speed

A proper selection of configuration parameters such as damping is very important for the calculation of damages as indicated in section 3.1. It is required to obtain e.g. an adequate guess on the effective aerodynamic damping next to the structural damping for the hydrodynamic response conditioned on a particular combination of wind speed and wind-wave misalignment. This is also valid for the establishment of unit damage matrices $\boldsymbol{D}^*$. However, these configuration parameter considerations do not affect the general methodology for establishment of damage equivalent wind-wave correlations introduced in the present article and are therefore disregarded for the sake of comprehensibility. Instead only fixed configuration parameters are considered in the present article e.g. only structural damping without contributions from aerodynamic damping.

3.3 Damage Equivalent Sea-State Parameters from Damage Contour Lines

The final task in the wind-wave correlation process is to determine the damage equivalent sea-state parameters H_s and T_p. For that purpose the DCLs are established for each wind speed v_k on the basis of the unit damage matrix $\boldsymbol{D}^*$ (step 1), target fatigue damage d_k (step 2) and probability p_k. The probability p_k is used for scaling of the unit damage matrix $\boldsymbol{D}^*$ in order to obtain the scaled damage matrix $\boldsymbol{D}_s^*$ according to Eq. 1. The DCL is subsequently extracted from $\boldsymbol{D}_s^*$ in terms of all H_s-T_p combinations that result in the target fatigue damage level d_k as indicated in Figure 5.

The following characteristics can be observed for the DCL of a given damage level d_k: Exactly one significant wave height exists per peak period due to the monotonous increase of damage over wave height. On the other hand none, one or even more than one peak periods may exist per significant wave height. Both characteristics can for example be observed in the scaled damage surface at interface and mudline in Figure 8. For practical applications it is therefore beneficial to define a series of T_p values covering the full peak period range of the underlying SCD, e.g. up to 16.5s in 0.1s intervals. For each T_p value in that series up to one[2] significant wave height H_s can be interpolated[3] from $\boldsymbol{D}_s^*$ for the given target damage level d_k, i.e. $H_s = f(T_p, \boldsymbol{D}_s^*, d_k)$. The resulting DCL can also be expressed as $H_s = f(T_p)$, corresponding to a projection into the H_s-T_p plane, due to the constant damage level.

However, as stated before, most H_s-T_p combinations from this DCL are not a proper damage equivalent SCD representation at other locations in the OWT. For example, an arbitrary H_s-T_p combination taken from a DCL established at mudline does generally not provide damage equivalency for the underlying SCD at the interface level. The reason is that individual H_s-T_p combinations on the DCL result in different static and dynamic load contributions as well as in a different number of load cycles per time affecting the resulting fatigue damage.

These varying contributions of static loading, dynamic loading and number of load cycles are balanced for all H_s-T_p combinations on the DCL such that the resulting fatigue damage is always the same at that location of the DCL. This is illustrated by the following theoretical example: It is assumed that the H_s-T_p combinations on the mudline DCL are known for the OWT configuration. In this case only the sea states for T_p = 4s and T_p = 10s from the DCL are considered. T_p = 4 seconds corresponds to the eigenperiod of the OWT structure (f_0 = 0.25 Hz) and it can therefore be assumed that the dynamic amplification and therefore the dynamic load contribution to the target damage d is larger than for the case of T_p = 10s. Furthermore, the number of load cycle is larger in case of T_p = 4s as well. A larger static load contribution is therefore required for the T_p = 10s sea state in order to achieve the same target damage d which results in a larger H_s value compared to the first equivalent sea-state with T_p = 4s. This can indicatively be observed in Figure 9 with the trough in H_s roughly corresponding to the eigenperiod of the structure. Contributions from dynamic loading, static loading and the number of load cycles are therefore balanced for all H_s-T_p combinations on the mudline DCL. However, this balance for the H_s-T_p combinations of the mudline DCL is generally not maintained when applied at other locations within the OWT.

Damage equivalency throughout the whole OWT can therefore only be maintained for certain H_s-T_p combinations from the DCL. In order to find such a proper H_s-T_p combination, a second DCL is established at another location of the OWT. The DCLs per wind speed, wind direction and wave direction from the two different locations are subsequently projected into the H_s-T_p plane in order to find their intersection(s) which introduces adequate, damage equivalent H_s-T_p combination(s) for both locations.

These two reference locations for establishment of the DCLs should be in a sufficient distance to each other and also show different ratios of static and dynamic contributions in the overall response. For the investigations in this article the interface and mudline locations are selected. The interface is typically located well above the submerged zone and therefore experiencing hydrodynamic responses dominated by dynamics (inertia loads). The mudline location on the other hand experiences hydrodynamic responses with both contributions, dynamic (inertia loads) and static (direct hydrodynamic forces on the structure). A set of damage equivalent sea-state parameters H_s-T_p which is part of both DCLs, i.e. at interface and mudline, is a damage equivalent representation for both locations. Furthermore, this sea-state parameter set is expected to introduce adequate damage equivalency throughout the entire OWT since it reflects both the dynamic and static contributions of the response adequately.

This is illustrated in Figure 8 for the example OWT configuration at a wind speed of 12.5m/s. The figure shows the scaled damages matrices $\boldsymbol{D}_s^*$ as established at interface and mudline. The individual DCLs are now found as the intersections of $\boldsymbol{D}_s^*$ and the target damage level (black plane) at each location.

[2] If no H_s is found, the range of H_s in $\boldsymbol{D}_s^*$ is too limited. If more than one H_s is found, the stochastic uncertainties of the irregular waves have not been well enough eliminated for establishment of the unit damage matrix $\boldsymbol{D}^*$.

[3] It is beneficial to use logarithmic values in $\boldsymbol{D}_s^*$ and for d_k for interpolation of the DCL. It has been observed that this helped to reduce influences from undesired variations in $\boldsymbol{D}_s^*$, e.g. due to residuals of stochastic uncertainties from time domain calculation approaches.

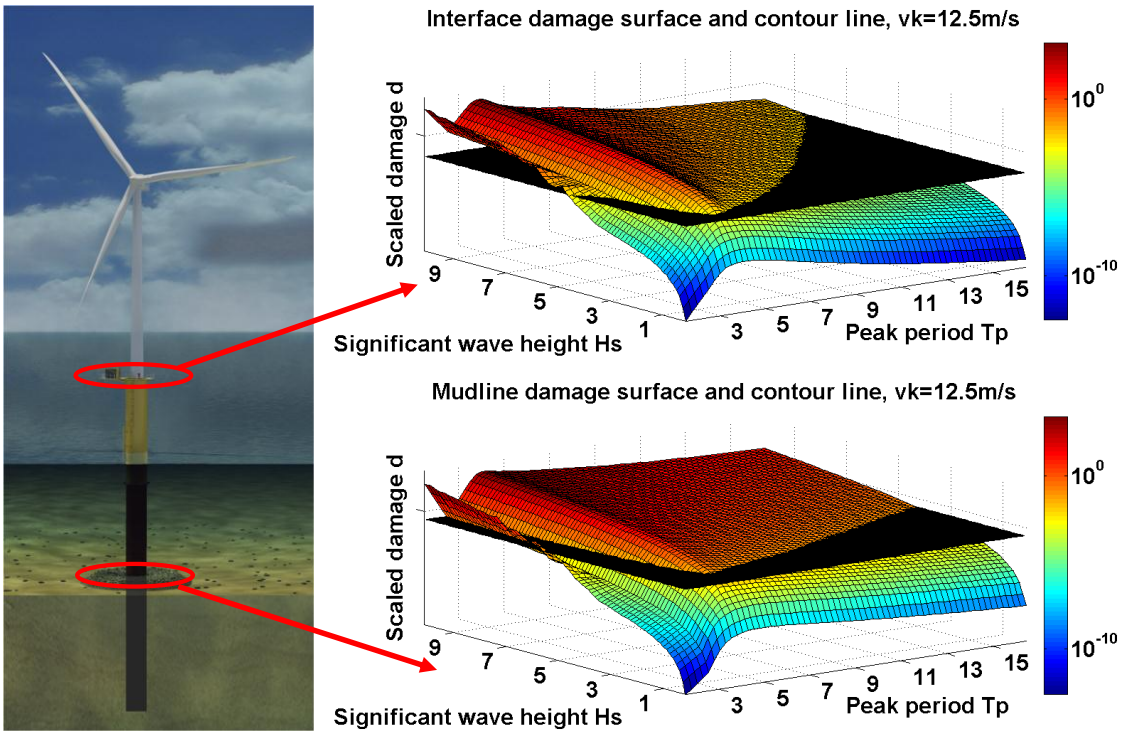

Figure 8: Scaled damage surface and target damage level (black plane) for determination of DCLs at mudline and interface

Both DCLs are plotted together in the H_s-T_p plane in Figure 9 in order to find intersection points. Here, one intersection point is found with the corresponding H_s-T_p combination being the wanted damage equivalent sea-state parameters for the wave climate conditioned on the wind speed v_k=12.5m/s.

285

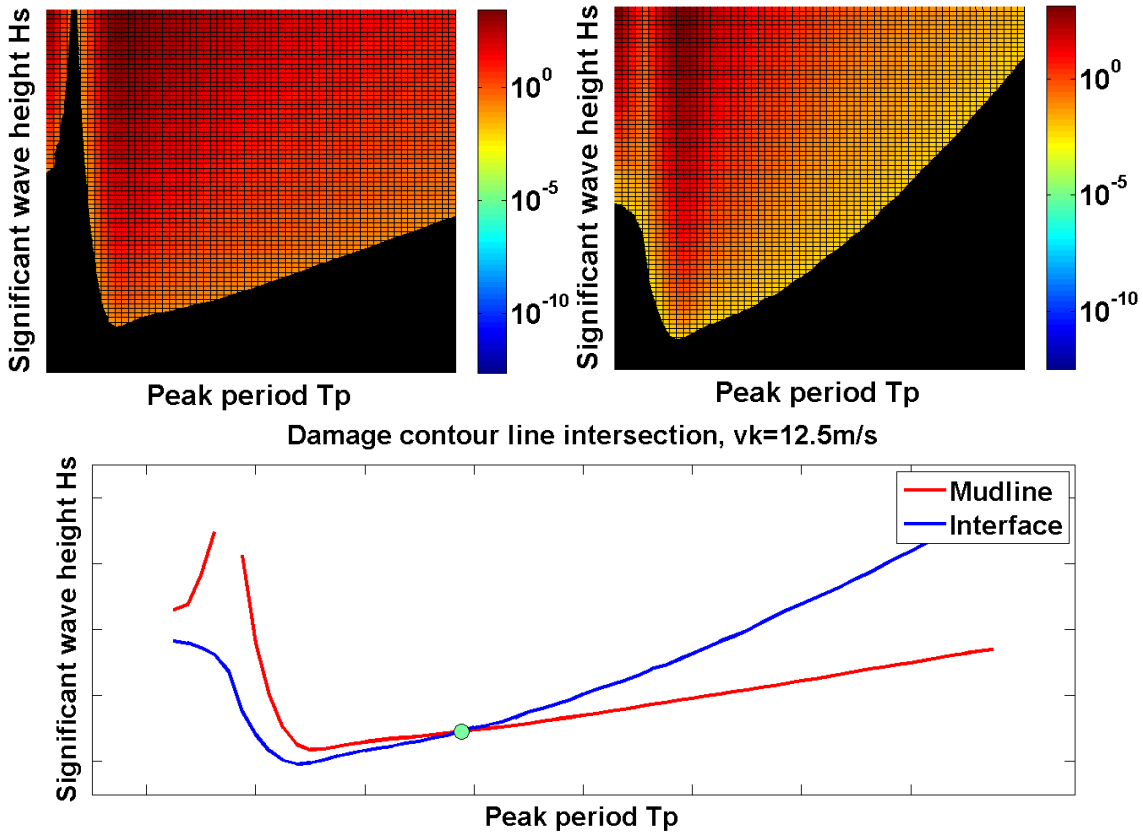

Figure 9: DCL at mudline (upper, left) and interface (upper, right) plotted together for intersection determination (bottom)

Exactly one intersection point has been found in this example, leading to one unique set of damage equivalent sea-state parameters associated to the primary parameter set of wind speed v_k=12.5m/s and aligned wind-wave direction from west. However, various cases with more than one intersection point (typically two or three) have been observed for the investigations in the present work. In such cases an arbitrary intersection point of the two DCLs representing a H_s-T_p combination can be selected. This is due to the fact that all individual intersection points introduce an accurate representation of the underlying SCD in terms of damage equivalent sea-state parameters for the entire OWT. The last possible scenario is that the two DCLs have no intersections even in case of an extension of the H_s and/or T_p range in the scaled damage matrix $\boldsymbol{D}_s^*$. However, this case has not yet been observed by the author and therefore only limited guidance on a theoretical basis is provided for such scenarios in section 3.3.1.

Furthermore, the reader is referred to the DCLs at tower top and interface in Figure 13 as an example for an inadequate selection of DCLs in the determination of damage equivalent sea-state parameters from the intersection approach. Here, both DCLs are very similar with various intersection points due to the fact that they are governed by the dynamic part of the response.

3.3.1 Sea-state Parameters for DCL without Intersections

Now the following scenario is assumed: Mudline (index *mud*) and interface (index *int*) have been used for establishment of DCLs for a particular set of primary parameters, but the DCLs show no intersection. Let d_{mud} and d_{int} be the actual target damages, $D_{s,mud}^*$ and $D_{s,int}^*$ the corresponding probability scaled damage matrices and $H_{s,mud}=f_{mud}(T_p)$ and $H_{s,int}=f_{int}(T_p)$ the DCLs. Fictive fatigue damages $d_{mud,fict}$ are derived at mudline by interpolation from $D_{s,mud}^*$ using the sea-state parameters from the interface DCL $H_{s,int}=f_{int}(T_p)$. Analogously, fictive fatigue damages $d_{int,fict}$ are obtained at interface level, i.e. based on interpolation from $D_{s,int}^*$ using sea-state parameters from the mudline DCL $H_{s,mud}=f_{mud}(T_p)$. Since the DCLs have no intersections all calculated fictive damages $d_{mud,fict}$ are also different from the target damage level d_{mud}, i.e. either $d_{mud,fict}$ is always larger or always smaller. This is also valid for the fictive damages at interface, except for the fact that in case $d_{mud,fict}$ are larger than d_{mud} then $d_{int,fict}$ is smaller than d_{int} and vice versa.

Determination of the desired sea-state parameters can now be based on an error minimization by using either the sea-state parameter set corresponding to smallest error ($d_{mud,fict} - d_{mud}$) or alternatively corresponding to the smallest error ($d_{int,fict} - d_{int}$).
For practical purposes the author would generally recommend to use the sea-state parameters for the case of the smallest positive error. This selection ensures damage equivalency at the location corresponding to the DCL from which the sea-state parameters are taken, while introducing a conservative damage approximation at the other location. However, in such situations it cannot be guaranteed that a conservative damage estimate is achieved at all other locations as well. For example, let the extracted sea-state parameters be a damage equivalent representation at interface but a conservative approximation at mudline. It is then assumed to be a very likely scenario that damages above interface are an approximation on the non-conservative side. However, due to the theoretical character of these considerations it is strongly recommended to investigate the aforementioned recommendations in case situations without intersections of the DCLs do actually occur.

4 EXAMPLE METHOD ASSESSMENT

The established wind-wave correlation method from Chapter 3 is now assessed in a calculation example and furthermore compared against alternative methods. This chapter starts with a brief introduction of the investigated alternative wind-wave correlation methods. Subsequently, all introduced methods are used to calculate lumped wave parameters on basis of the wave climate at the Veja Mate site and a hydrodynamically sensitive OWT configuration. The quality of the lumped wave parameters is assessed on basis of resulting hydrodynamic fatigue damages over wind speed in comparison to reference results obtained from the underlying full wave climate.

4.1 Alternative Wind-Wave Correlation Methods for the Fatigue Design of OWT

Lumping of the full wave climate is a central task in the wind-wave correlation process for the design of OWT. However, established wave lumping methods from the offshore oil & gas industry such as SCD block lumping methods according to DNV-RP-F204 (2010) or from Du et al. (2014) cannot be applied due to the missing correlation with wind speeds. Instead, designers often apply one of the few published wind-wave correlation methods with a lumping of the wave climate for derivation of relevant met-ocean parameters in the FLS design load simulations. In case the structural characteristics are not yet known or for structures that are hydrodynamically not sensitive the probability weighted correlation approach according to Mittendorf (2009) can for example be applied. In case of hydrodynamically sensitive structures a few dynamic approaches exist such as the iterative approach according to Kühn (2001) or a modified version according to Seidel (2014). Application examples of Kühn's (2001) approach can for example be found in Fischer et al. (2010) or Bredmose et al. (2012). However, in comparison to the new damage equivalent wind-wave correlation method from Chapter 3 all aforementioned methods do not necessarily ensure an adequate consideration of the dynamics over the whole OWT and may therefore introduce an uncertain error in the fatigue loads throughout the structure.

Focus in this section is on the wave lumping approaches for the following wind-wave correlation methods for the fatigue design of OWT:

- Probability based averaging of sea-state parameters.
- Iterative, damage equivalent approach according to Kühn (2001).
- Damage equivalent approach according to Seidel (2014).

The wave lumping of a SCD for a given wind speed bin v_k, wind direction and wave direction is in all cases established by the condensation of all $H_{s,i}$ and $T_{p,j}$ combinations to only one representative set of $H_{s,k}$ and $T_{p,k}$. All approaches except of the first are briefly described in the following. The descriptions of Kühn's and Seidel's approach are complemented by graphical illustrations using the DCL. For that purpose, the probability $p_k = \Sigma_i\Sigma_j(p_{i,j})$ for all $i=1..n$ (significant) wave height classes $H_{s,i}$ and all $j=1..m$ (peak) wave period classes $T_{p,j}$ of the SCDs for each $k=1..n_{wind}$ wind speeds

v_k, wind direction and wave direction is used for scaling of the unit damage matrix D^* in Eq. 2 in order to obtain the elements $d_{i,j,s}{}^*$ of the scaled damage matrix $D_s{}^*$ according to Eq. 3. The element $d_{i,j,s}{}^*$ is the theoretical fatigue damage of the sea-state $H_{s,i}$ - $T_{p,j}$ in case the full probability of occurrence p_k of the whole SCD is applied. The corresponding scaled damage surface is a graphical representing the scaled damage matrix $D_s{}^*$ over H_s and T_p as shown in Figure 5.

$$d_{i,j,s}{}^* = p_k \cdot d_{i,j}{}^* \qquad \text{Eq. 3}$$

A DCL for a given target damage level can now be interpolated from the scaled damage matrix $D_s{}^*$ or obtained graphically by the intersection with the scaled damage surface. The target damage level is chosen as $d_k = \Sigma_i\Sigma_j(d_{i,j}) = \Sigma_i\Sigma_j(p_{i,j} \cdot d_{i,j}{}^*)$ which constitutes the total hydrodynamic fatigue damage from the wave climate corresponding to a wind speed v_k of a particular wind direction and wave direction.

4.1.1 Probability based averaging of sea-state parameters

A SCD for a given wind speed bin v_k is lumped to one representative set of $H_{s,k}$ and $T_{p,k}$ by averaging of the significant wave heights $H_{s,i}$ and peak periods $T_{p,j}$ on basis of the probability distribution $p_{i,j}$ according to Eq. 4 and Eq. 5. The probability based averaging is a rather simple and straight forward approach due to the independence from the structure and *S-N* curve slope *m*.

$$H_{s,k} = \frac{\sum_i \sum_j H_{s,i} \cdot p_{i,j}}{\sum_i \sum_j p_{i,j}} \qquad \text{Eq. 4}$$

$$T_{p,k} = \left(\frac{\sum_i \sum_j T_{p,j} \cdot p_{i,j}}{\sum_i \sum_j p_{i,j}} \right) \qquad \text{Eq. 5}$$

4.1.2 Iterative, damage equivalent approach according to Kühn (2001)

The starting point for the iterative wave lumping approach according to section 8.3 in Kühn (2001) is formed by an initial guess on the significant wave height and zero-up crossing or mean wave period according to Eq. 6 and Eq. 7. The initial significant wave height is based on section 11.3.7 in Burton et al. (2011) in analogy to damage equivalent loads and hence requires the selection of a representative *S-N* curve slope *m*.

$$\hat{H}_{s,k} = \sqrt[m]{\frac{\sum_i \sum_j H_{s,i}^m \cdot p_{i,j}}{\sum_i \sum_j p_{i,j}}} \qquad \text{Eq. 6}$$

The initial mean wave period is obtained from an averaging of wave frequencies $f = T_z{}^{-1}$ on basis of the probability distribution $p_{i,j}$.

$$\hat{T}_{z,k} = \left(\frac{\sum_i \sum_j T_{z,j}^{-1} \cdot p_{i,j}}{\sum_i \sum_j p_{i,j}} \right)^{-1} \qquad \text{Eq. 7}$$

A refinement of the initial sea-state parameters in Eq. 6 and Eq. 7 is obtained on basis of a target damage level d_k as introduced from the full wave climate and iterative modification by a factor v_D according to Eq. 8 and Eq. 9 until the target damage level is obtained by $H_{s,k}$ and $T_{z,k}$.

$$H_{s,k} = v_D \cdot \hat{H}_{s,k} \qquad \text{Eq. 8}$$

$$T_{z,k} = v_D^{-1} \cdot \hat{T}_{z,k} \qquad \text{Eq. 9}$$

A graphical illustration of Kühn's iterative approach is provided in Figure 10. Here, the damage for each combination of H_s and T_z is shown as the colored damage surface while the horizontal black plane represents the target damage level d_k. The intersection of the damage surface and the black plane of target damage level is the DCL as introduced in section 3.1.2. Effectively, the initial values from Eq. 6 and Eq. 7 are simultaneously modified by the factor v_D following an iteration path on the scaled damage surface until the DCL is reached.

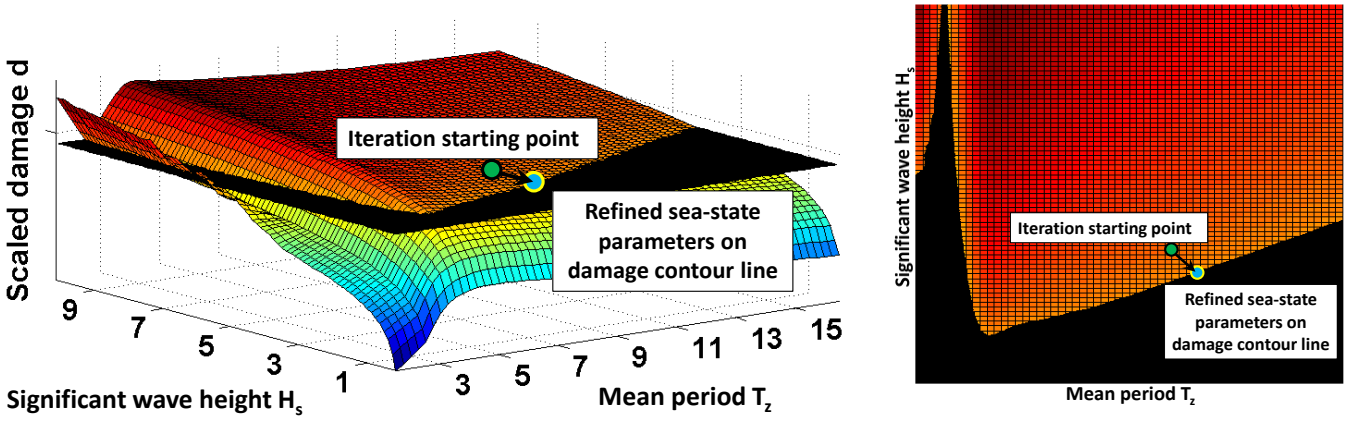

Figure 10: Graphical illustration of Kühn's damage equivalent sea state parameter derivation in a perspective view (left) and top view (right)

4.1.3 Damage equivalent approach according to Seidel (2014)

Seidel's (2014) approach is based on the direct use of the significant wave height in Eq. 7 according to section 11.3.7 in Burton et al. (2011). The corresponding wave period is then interpolated from the damage surface at the predetermined significant wave height for the given target damage level d_k, e.g. according to the approach shown by Passon & Branner (2014). Both Passon & Branner (2014) and Seidel (2014) use the upper wave period value in case more than one wave period is found by the interpolation.

A graphical illustration of Seidel's approach is provided in Figure 11. It can be seen that the largest wave period $T_{p,k}$ on the DCL is chosen for the pre-determined $H_{s,k}$.

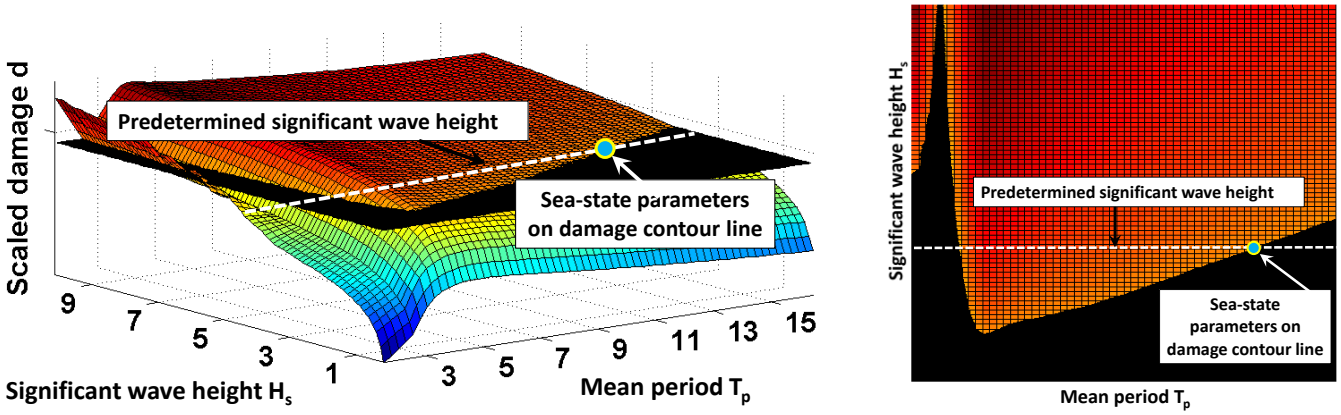

Figure 11: Graphical illustration of Seidel's damage equivalent sea state parameters derivation in a perspective view (left) and top view (right)

4.2 Comparison of hydrodynamic fatigue damage from the different wave lumping approaches

This section assesses the lumped waves from the different wind-wave correlation methods against the full wave climate by comparison of the resulting hydrodynamic fatigue damages over wind speed in an example scenario. The full wave climate in terms of SCDs for individual wind speeds is taken from the met-ocean database of the Veja Mate project conditioned on the directional combination of waves from 270 degrees and wind from 180 degrees. Hydroydnamic fatigue damages over wind speed are calculated for a hydrodynamically sensitive OWT configuration which is roughly based on the NREL 5MW turbine according to Jonkman et al. (2007) with a large diameter (>8m) monopile substructure at 30m water depth and a first (bending) eigenfrequency of f_0 = 0.29 Hz. The hydrodynamic fatigue calculations are comparable to a fault scenario according to design load case 7.2 from IEC 61400-3 (2009) with neglectable aerodynamic load contributions. Hence, the dynamic load calculations are performed with only structural damping, applied as 1% critical damping, while aerodynamic damping is disregarded.

Hydrodynamic fatigue damages are assessed at mudline, tower top, interface and an intermediate location as shown in Figure 12. The figure shows furthermore the SCD of the full wave climate over all wind speeds as well as the derived sea-state parameters for the lumped waves over the whole wind speed range with a non-zero probability of occurrence, i.e. for wind speeds up to v_k=19m/s. Mudline and tower top are used as reference locations for derivation of the damage equivalent sea-state parameters from the intersections of the corresponding DCLs for the new method according to Chapter 3, hereinafter referenced as 'Passon'. Furthermore, the damage levels d_k at mudline are used for derivation of the damage equivalent sea-state parameters for the Kühn's (2001) and Seidel's (2014) method since no further recommendations are provided by any of the two authors.

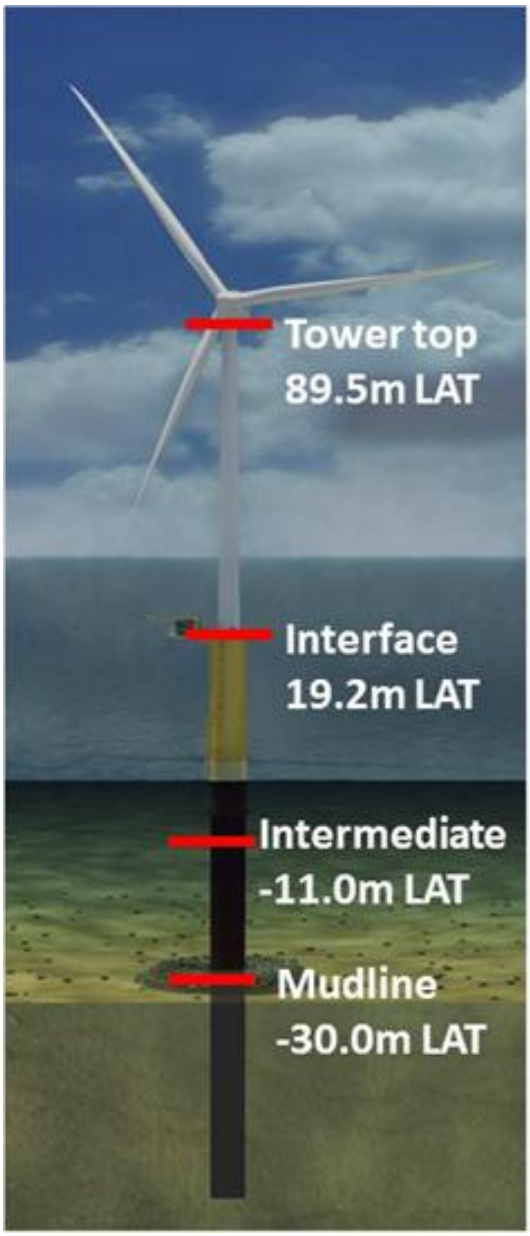

	T_p [s]	0.0 - 1.0	1.0 - 2.0	2.0 - 3.0	3.0 - 4.0	4.0 - 5.0	5.0 - 6.0	6.0 - 7.0	7.0 - 8.0	8.0 - 9.0	9.0 - 10.0	
	$T_{p,i}$ [s]	0.5	1.5	2.5	3.5	4.5	5.5	6.5	7.5	8.5	9.5	
H_s [m]	$H_{s,i}$ [m]											ALL
3.75 - 4.00	3.875											
3.50 - 3.75	3.625											
3.25 - 3.50	3.375											
3.00 - 3.25	3.125											
2.75 - 3.00	2.875											
2.50 - 2.75	2.625											
2.25 - 2.50	2.375											
2.00 - 2.25	2.125											
1.75 - 2.00	1.875											
1.50 - 1.75	1.625											
1.25 - 1.50	1.375											
1.00 - 1.25	1.125											
0.75 - 1.00	0.875											
0.50 - 0.75	0.625											
0.25 - 0.50	0.375											
0.00 - 0.25	0.125											
ALL												

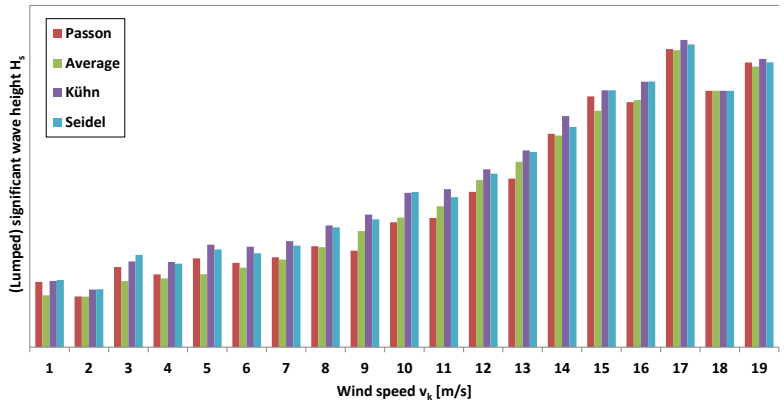

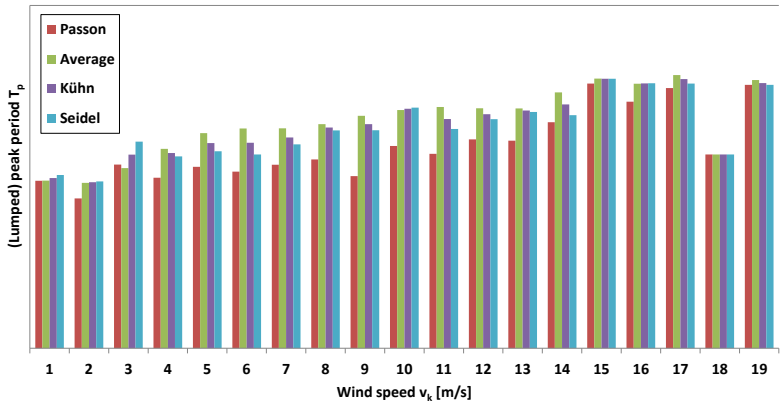

Figure 12: Locations and selected SCDs for assessment of hydrodynamic fatigue damage.

Figure 13 shows exemplarily the SCDs for v_k=9m/and v_k=14m/s which are subsets of the SCD over all wind speeds according to Figure 12. It can be seen that the SCD for v_k=9m/s covers a larger range of wave periods and wave heights while the SCD for v_k=14m/s introduces by tendency larger wave heights and longer wave periods. The figure shows furthermore the calculated DCLs at different locations together with the derived lumped wave parameters. It can be seen that the lumped wave parameters for Passon's new method are located on the intersection point of all DCLs in both cases while the averaging approach results in lumped wave parameters that are not located on any of the DCLs. Sea-state parameters of the lumped wave according to Kühn's and Seidel's method are located on the mudline DCL, but not on the DCLs of any other location. Damage equivalency can therefore be expected at mudline level for both methods while it is uncertain how well the hydrodynamic fatigue damages are preserved at the other locations. However, it can be seen that their lumped wave parameters are located significantly closer to the other DCLs for the v_k =14m/s case which might therefore lead to a better approximation of the hydrodynamic fatigue damages compared to the v_k =9m/s case.

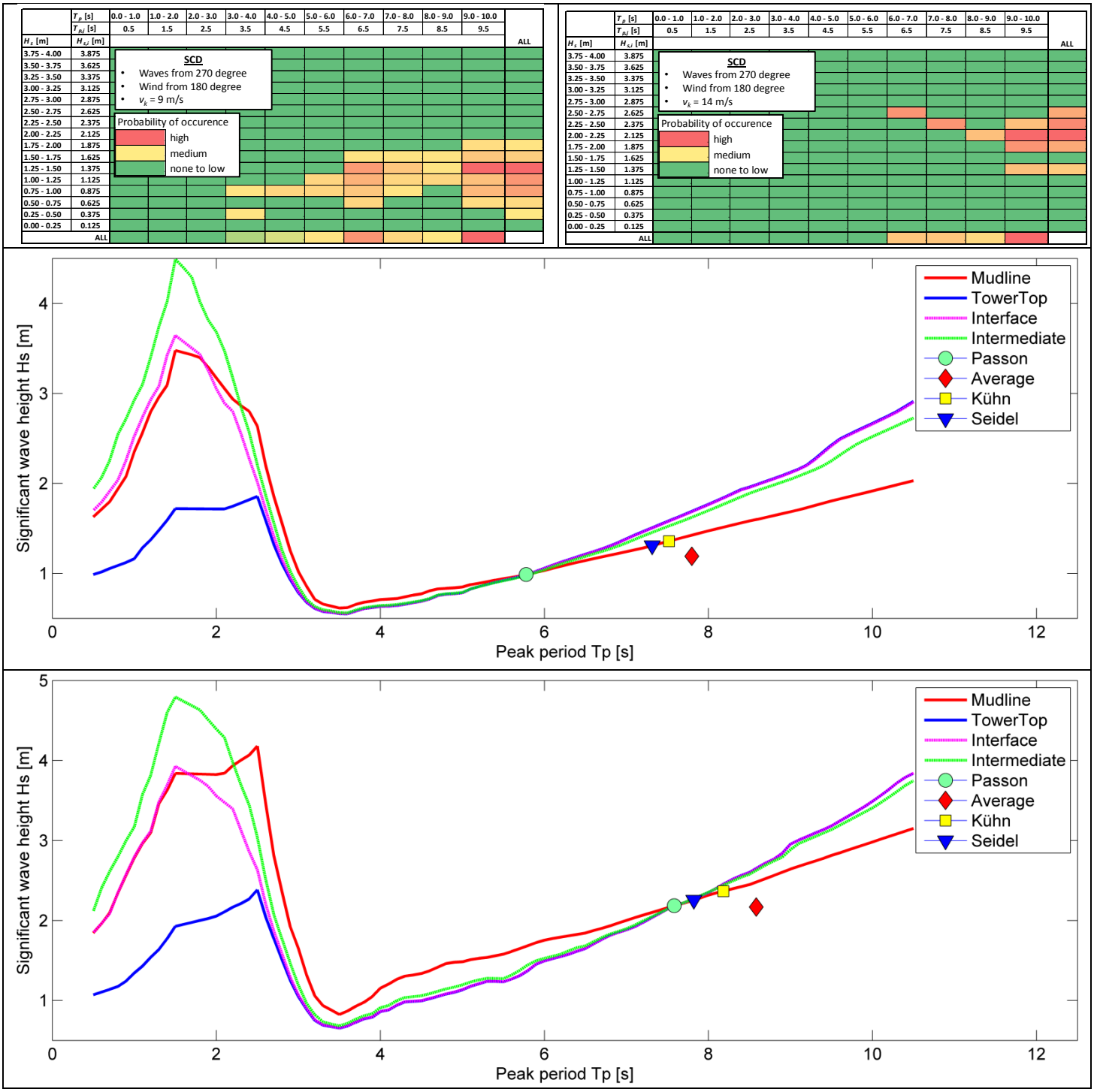

Figure 13: SCDs (top) and corresponding DCLs at mudline, tower top, interface and the intermediate location for v_k=9m/s (center) and v_k=14m/s (bottom) together with the lumped wave parameters for the different wind-wave correlation methods

The calculated individual and cumulative hydrodynamic fatigue damages at the four locations within the OWT are shown in Figure 14 together with the probability of occurrence as normalized values over wind speeds. Reference results from the full wave climate are denoted as 'SCD'.

It can be seen that the averaging method underestimates the hydrodynamic fatigue damages significantly over the whole wind speed range at all locations. The largest difference is found at tower top with an underestimation of the total hydrodynamic fatigue damage by 67%.

Kühn's and Seidel's methods yield very accurate hydrodynamic fatigue damages at mudline in comparison to the reference results of the full wave climate. This is due to the fact that damage equivalent sea-state parameters of the lumped waves have been derived on basis of full wave climate

damage levels at this specific location for both methods. However, significant differences on the non-conservative side are present at all other locations. The largest difference is found at tower top with an underestimation of the total hydrodynamic fatigue damage of 31% by Kühn's method and 27% by Seidel's method. It can furthermore be seen that the differences in hydrodynamic fatigue damage are significantly larger for v_k=9m/s than for v_k=14m/s as expected from the resulting lumped wave parameters in relation to the DCLs in Figure 13.

Only Passon's new method allows for a good preservation of hydrodynamic fatigue damages at all locations. Here, the largest difference in total hydrodynamic damage is found at the intermediate location with an overestimation of 2%. The author considers this as an excellent agreement although differences at individual wind speeds are in some cases larger such as for example at the intermediate location for v_k=9m/s.

It should be mentioned that the author observed a better match for the averaging method as well as for Kühn's and Seidel's method in case of different wind-wave directions and for different damping conditions, e.g. corresponding to design load case 1.2 from IEC 61400-3 (2009) with aligned or only slightly misaligned wind-wave conditions. The investigations and corresponding results are expected to be published soon in Passon (2015).

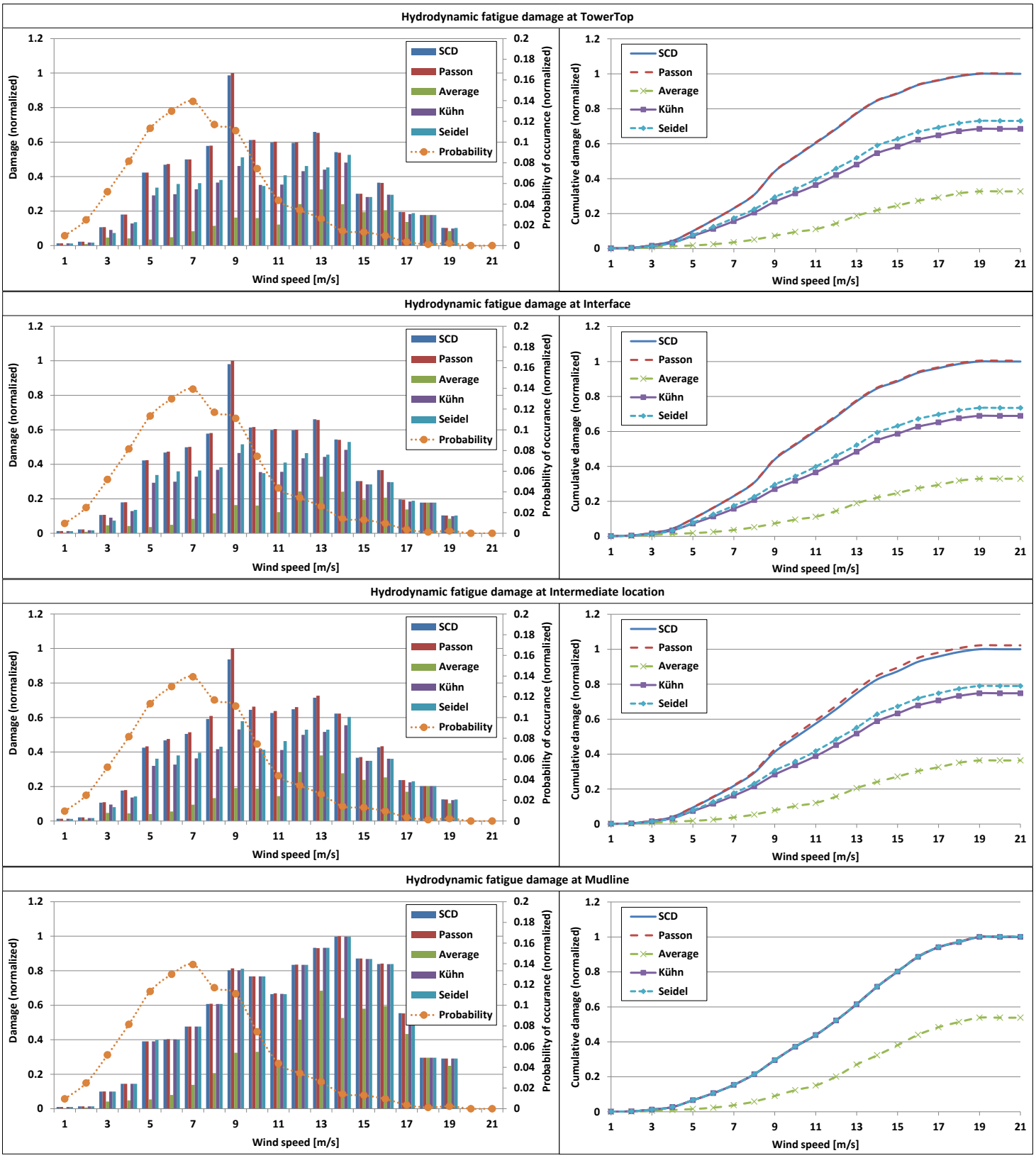

Figure 14: Distribution of hydrodynamic fatigue damage from full wave climate and lumped waves over wind speed at different locations for waves from 270 degree and wind from 180 degree

475

5 CONCLUSIONS AND RECOMMENDATIONS

A new wind-wave correlation method based on the selection of sea-state parameters from calculated DCLs has been introduced. The new method addresses the current lack of wind-wave correlation methods with an appropriate consideration of dynamics for the fatigue design of OWT. Based on example calculations using the very detailed met-ocean database of the Veja Mate project it has been shown that the new method allows for establishment of very accurate damage equivalent wind-wave correlations for the whole OWT structure. This is achieved by a simultaneous lumping of the wave climate and association to the wind climate in one integral step.

The present article focuses on the introduction of the new wind-wave correlation method for the design of OWT. Hence, application examples and calculations are based on a limited set of conditions. However, in reality OWTs are subjected to a large variety of fatigue relevant conditions during their lifetime, such as different damping conditions. The author recommends consideration of these parameters in more detail when establishing wind-wave correlations. Some guidance can be obtained from Passon & Branner (2015), but further investigations under simultaneous wind-wave loading are necessary.

It is important to establish high quality met-ocean databases with detailed wind-wave joint occurrence information early in the design process of offshore wind farms. In this context, the scenario of limited information in the met-ocean database with only marginal wind and wave distributions is of high practical relevance since it occurs quite often in real design situations. The author therefore recommends subjecting this scenario in future studies.

The establishment of wind-wave correlations for the fatigue design of OWT has a direct influence on the accuracy of calculated design loads and therefore on the safety and economics of offshore wind farms. However, the lack of guidance on the establishment of wind-wave correlations in relevant design standards such as IEC61400-3 (2009), DNV-OS-J101 (2014) and GL-COWT (2012) does not reflect the high importance of this topic. The author strongly recommends addressing the subject of the damage equivalent wind-wave correlations for the fatigue design of OWT in future revisions of these standards and guidelines.

Furthermore, the author recommends additional investigations on the validity range of established, damage equivalent wind-wave correlations with respect to changes in the structural configuration. Such changes are e.g. expected during the optimization process within the detailed design of the support structures for OWT. Implications on the structural dynamics from the changes in this particular situation are typically rather limited. Observations by the author indicate a very limited influence on the wind-wave correlations in such situations. However, this has to be assessed in more detail on a case-by-case base.

ACKNOWLEDGEMENTS

The present article has been established within an industrial PhD project supported by ‘The Danish Council for Technology and Innovation’ and RAMBØLL Wind which is gratefully acknowledged. Furthermore, I thank Veja Mate Offshore Holding GmbH and K2 Management GmbH and gratefully acknowledge their support by providing full access to the very detailed met-ocean database of the Veja Mate project. This allowed for consideration of realistic wind and wave climate conditions in the presented investigations.

REFERENCES

Barltrop, N, Adams, A (1991). “Dynamics of fixed Offshore Structures,” *3rd Edition. Butterworth Heinemann 1991.*

Bredmose, H, Larsen, SE, Matha, D, Rettenmeier, A, Marino, E, Eichstaedt, R, Saettran L (2012). “D2.04: Collation of offshore wind wave dynamics,” *in Marine Renewables Infrastructure Network. Available at:* http://orbit.dtu.dk/ws/files/60086212/Collation_of_offshore.pdf (Accessed: 16th January 2015)

Burton, T, Jenkins, T, Sharpe, D, Bossanyi, E (2011). “Wind Energy Handbook, 2nd Edition,” *John Wiley & Sons. ISBN: 978-0-470-69975-1*

DNV-OS-J101 (2014). “Design of Offshore Wind Turbine Structures,” *Offshore Standard. Det Norske Veritas AS.*

DNV-RP-F204 (2010). “Riser Fatigue,” *Offshore Standard. Det Norske Veritas AS.*

Du, J, Chang, A, Wang, S, Li, H (2014). “A Novel Lumping Block Method for Fatigue Damage Assessment of Mooring Chain,” *In The Twenty-fourth International Ocean and Polar Engineering Conference. International Society of Offshore and Polar Engineers.*

Fischer, T, de Vries, W, Schmidt, B (2010). ”Upwind Design basis,” *EU-Upwind project, Stuttgart, Germany.*

GL-COWT (2012). “Guideline for the Certification of Offshore Wind Turbines, Rules and Guidelines, IV – Industrial Services, Part 2,” *Germanischer Lloyd.*

Haid, L, Stewart, G, Jonkman, J, Robertson, A, Lackner, M, Matha, D (2013). “Simulation-length requirements in the loads analysis of offshore floating wind turbines,” *In: Proceedings of the 32nd international conference on ocean, offshore and arctic engineering, Nantes, France; 2013. Available at (preprint):* http://www.nrel.gov/docs/fy13osti/58153.pdf (Accessed 19th January 2015)

Hapel, KH (1990). ”Festigkeitsanalyse dynamisch beanspruchter Offshore-Konstruktionen,” *ISBN-13: 978-3528063689. Vieweg+Teubner Verlag. Germany.*

IEC 61400-3 (2009). “IEC 61400-3: Wind Turbines – Part 3: Design Requirements for Offshore Wind Turbines,” *1st Edition. International Electrotechnical Commission (IEC).*

Jonkman, J, Butterfield, S, Musial, W, Scott, G (2007). "Definition of a 5MW reference wind turbine for offshore systems development," *National Renewable Energy Laboratory, Golden, Colorado.*

Kühn, M (2001). "Dynamics and Design Optimisation of Offshore Wind Energy Conversion Systems," *Dissertation, Technische Universiteit Delft, The Netherlands, ISBN 90-76468-07-9.*

Miner, MA (1945). "Cumulative damage in fatigue," *J Appl Mech*;12: A159–A64.

Mittendorf, KE (2009). "Joint Description Methods of Wind and Waves for the Design of Offshore Wind Turbines," *Marine Technology Society Journal*. 43(3):23-33. DOI:10.4031/MTSJ.43.3.2.

Palmgren, A (1924). "Die Lebensdauer von Kugellagern," *Zeitschrift des Vereins Deutscher Ingenieure*;68:339–41.

Passon, P, Branner, K (2014). "Load calculation methods for offshore wind turbine foundations," *Ships and Offshore Structures*, Vol.9, No.4, pages 433-449.

Passon, P, Branner, K (2015). "Condensation of long-term wave climates for the fatigue design of hydrodynamically sensitive offshore wind turbine support structures," *Ships and Offshore Structures, (in press). DOI: 10.1080/17445302.2014.967994. Available at:* http://www.tandfonline.com/doi/full/10.1080/17445302.2014.967994. (Accessed: 16th January 2015)

Passon, P (2015). "Design of Offshore Wind Turbine Foundations," *Dissertation, Technical University of Denmark (submitted).*

Seidel, M (2014). "Wave induced fatigue loads on monopiles - New approaches for lumping of scatter tables and site specific interpolation of fatigue loads," *Conference Proceedings IWEC, Hannover.*